REVIEWS IN MINERALOGY
AND GEOCHEMISTRY

Volume 76 2013

Thermodynamics of Geothermal Fluids

EDITORS

Andri Stefánsson
University of Iceland
Reykjavík, Iceland

Thomas Driesner
ETH Zurich
Zurich, Switzerland

Pascale Bénézeth
CNRS-Université de Toulouse
Toulouse, France

ON THE FRONT COVER:

Background picture: SEM image of synthesized magnesite ($MgCO_3$). Scale bar = 10 μm. See Figure 21 in Chapter 4 by Bénézeth et al.

Inset images (from top left clockwise): ❧ Cartoon illustrating the aqueous speciation of CO_2-bearing solutions (see Chapter 4 by Bénézeth et al.). ❧ Great Geysir area in Iceland (picture taken by Pascale Bénézeth). ❧ Snapshot from a molecular dynamics simulation of aqueous NaCl at near critical temperature-pressure conditions, showing the formation of an NaCl contact ion pair (yellow and green balls on top left). Courtesy of Thomas Driesner. ❧ Water phase diagram showing the domains of the different aqueous phases (liquid, vapor *sensu stricto*, and supercritical fluid). See Figure 1 in Chapter 6 by Pokrovski et al. ❧ A geothermal well in Iceland (picture taken by Andri Stefánsson).

Series Editor: ***Jodi J. Rosso***

MINERALOGICAL SOCIETY OF AMERICA
GEOCHEMICAL SOCIETY

Reviews in Mineralogy and Geochemistry, Volume 76

Thermodynamics of Geothermal Fluids

ISSN 1529-6466
ISBN 978-0-939950-91-1

COPYRIGHT 2013

THE MINERALOGICAL SOCIETY OF AMERICA
3635 CONCORDE PARKWAY, SUITE 500
CHANTILLY, VIRGINIA, 20151-1125, U.S.A.
WWW.MINSOCAM.ORG

The appearance of the code at the bottom of the first page of each chapter in this volume indicates the copyright owner's consent that copies of the article can be made for personal use or internal use or for the personal use or internal use of specific clients, provided the original publication is cited. The consent is given on the condition, however, that the copier pay the stated per-copy fee through the Copyright Clearance Center, Inc. for copying beyond that permitted by Sections 107 or 108 of the U.S. Copyright Law. This consent does not extend to other types of copying for general distribution, for advertising or promotional purposes, for creating new collective works, or for resale. For permission to reprint entire articles in these cases and the like, consult the Administrator of the Mineralogical Society of America as to the royalty due to the Society.

Thermodynamics of Geothermal Fluids

76 *Reviews in Mineralogy and Geochemistry* **76**

FROM THE SERIES EDITOR

This volume, edited by Andri Stefánsson, Thomas Driesner, and Pascale Bénézeth, presents an extended review of the topics covered in a short course on Geothermal Fluid Thermodynamics held prior to the 23rd Annual V.M. Goldschmidt Conference in Florence, Italy (August 24-25, 2013). The experimentalists and modelers who contributed to this volume have presented material that the expert, as well as those who are new to the field, will find useful. Both the course and this volume summarize the thermodynamics of aqueous fluids over a wide range of temperatures and pressures, spanning from molecular to macroscopic view, and its power in quantifying geochemical and geological processes in the Earth's crust.

All supplemental materials associated with this volume can be found at the MSA website. Errata will be posted there as well.

Jodi J. Rosso, Series Editor
West Richland, Washington
July 2013

1529-6466/13/0076-0000$00.00 http://dx.doi.org/10.2138/rmg.2013.76.0

Thermodynamics of Geothermal Fluids

76 *Reviews in Mineralogy and Geochemistry* **76**

TABLE OF CONTENTS

1 Thermodynamics of Geothermal Fluids

Andri Stefánsson, Thomas Driesner, Pascale Bénézeth

INTRODUCTION TO THE VOLUME 1
REFERENCES 4

2 The Molecular-Scale Fundament of Geothermal Fluid Thermodynamics

Thomas Driesner

INTRODUCTION 5
BASIC RELATIONS BETWEEN THE MOLECULAR SCALE AND THE MACROSCOPIC THERMODYNAMIC PROPERTIES OF GEOFLUIDS 8
  Simplified descriptions of molecular interactions 9
  Basic concepts of statistical thermodynamics 10
  Fluctuations and thermodynamic properties 12
  Understanding fluid thermodynamics from pair correlation functions 13
  Molecular simulation 15
GENERAL MOLECULAR-SCALE FEATURES OF AQUEOUS GEOFLUIDS 16
  Hydration of ions 17
  Ion pairing and clustering 18
  Speciation 19
EFFECTS OF TEMPERATURE, PRESSURE/DENSITY, AND CONCENTRATION ON THE HYDRATION OF IONS IN SOLUTION 20
  Temperature, pressure and concentration effects on the of hydration shell structure 22
FLUID THERMODYNAMICS ON THE MACROSCOPIC AND MOLECULAR SCALES IN THE CRITICAL AND SUPERCRITICAL REGIONS 24
  An explanation of the divergence of derivative thermodynamic properties near the critical point 24
  The molecular-scale picture behind near-critical divergence 25

POSSIBLE FUTURE ROUTES TOWARDS IMPROVED THERMODYNAMIC MODELS FOR GEOTHERMAL FLUIDS FROM AMBIENT TO SUPERCRITICAL CONDITIONS 28
REFERENCES 30

3

Thermodynamics of Aqueous Species at High Temperatures and Pressures: Equations of State and Transport Theory

David Dolejš

INTRODUCTION 35
CONCENTRATION SCALES AND CONVERSION RELATIONSHIPS 36
CONVENTIONS FOR THERMODYNAMIC PROPERTIES 39
BASIC THERMODYNAMIC MODELS FOR AQUEOUS EQUILIBRIA 42
    Approximations to the Gibbs energy function 42
    Predictions using the solvent density 43
    Predictions using the electrostatic theory 45
EQUATIONS OF STATE FOR AQUEOUS SPECIES 46
    Thermodynamics of hydration 46
    Macroscopic thermodynamic models 53
    Electrostatic models 54
    Density models 59
APPLICATIONS OF AQUEOUS THERMODYNAMICS TO FLUID-ROCK INTERACTIONS 64
    Transport theory and estimation of fluid fluxes 65
CONCLUDING REMARKS AND PERSPECTIVES 70
ACKNOWLEDGMENTS 72
REFERENCES 72

4

Mineral Solubility and Aqueous Speciation Hydrothermal Conditions to 300 °C – The Carbonate System as an Example

Pascale Bénézeth, Andri Stefánsson,
Quentin Gautier, Jacques Schott

INTRODUCTION 81
COMMON TECHNIQUES FOR EXPERIMENTS AT HYDROTHERMAL CONDITIONS 85
    Batch reactors 86
    Electrode systems and high temperature pH measurements and titrations 89
    In situ vibrational and electronic spectroscopy 96
SPECIATION AND THERMODYNAMIC STABILITIES IN CARBON-CONTAINING AQUEOUS SOLUTIONS 97

Aqueous speciation of CO_2-bearing solutions 97
Molecular structure of various aqueous carbon species 102
CARBONATE SOLUBILITY AND MINERALIZATION 105
Calcite 106
Magnesium-carbonates 109
Dolomite 120
Siderite 121
CONCLUSION 124
ACKNOWLEDGMENTS 124
REFERENCES 124

5 Thermodynamic Modeling of Fluid-Rock Interaction at Mid-Crustal to Upper-Mantle Conditions

Craig E. Manning

INTRODUCTION 135
CHEMICAL POTENTIALS OF AQUEOUS SPECIES IN HIGH-*PT* FLUIDS 136
Standard state chemical potentials of aqueous species 136
Activity models for aqueous species 139
COMPARISON OF EXPERIMENTAL AND CALCULATED MINERAL SOLUBILITY 142
APPLICATIONS 146
Activity-activity diagrams 146
Homogeneous equilibria 148
The pH dependence of mineral solubility 150
Buffering of pH by rock-forming minerals 152
Salinity and saline brines 154
"Excess" solubility and identification of additional solutes 156
Concluding remarks 159
ACKNOWLEDGMENTS 160
REFERENCES 160

6 Speciation and Transport of Metals and Metalloids in Geological Vapors

Gleb S. Pokrovski, Anastassia Y. Borisova, Andrey Y. Bychkov

INTRODUCTION 165
SPECIATION, THERMODYNAMICS, AND PARTITIONING OF METALS AND METALLOIDS IN GEOLOGICAL VAPORS 167
Volcanic vapors 167
Hydrothermal-magmatic vapors 171
Vapor-brine-supercritical fluid-silicate melt partitioning in experimental and natural systems 186

ROLE OF THE VAPOR-LIKE FLUIDS IN METAL AND METALLOID TRANSPORT IN NATURAL SYSTEMS AND THE FORMATION OF ORE DEPOSITS 192
Low-temperature boiling geothermal systems 192
Magmatic-hydrothermal systems 197
MAJOR CONCLUSIONS 204
REMAINING GAPS AND NEAR-FUTURE CHALLENGES 205
Analytical challenges 205
Experimental challenges 206
Modeling challenges 207
ACKNOWLEDGMENTS 208
REFERENCES 208

7 Solution Calorimetry Under Hydrothermal Conditions

Peter Tremaine, Hugues Arcis

INTRODUCTION 219
THERMODYNAMIC RELATIONS 220
Equations for the temperature and pressure dependence of Gibbs energies and equilibrium constants 220
Solvation effects 221
The temperature dependence of standard partial molar properties 224
"EQUATIONS OF STATE" FOR STANDARD PARTIAL MOLAR PROPERTIES 225
The "density" model 225
The Helgeson-Kirkham-Flowers-Tanger model 226
THERMODYNAMICS OF SOLUTION CALORIMETRY 228
Standard partial molar heat capacities and volumes 228
Standard partial molar enthalpies and heats of mixing 229
Excess properties 230
DENSIMETRY 233
Vibrating-tube densimeters 233
HEAT-CAPACITY CALORIMETRY 235
Pioneering studies 235
The Picker flow microcalorimeter 236
Twin-cell differential scanning nanocalorimeters and Calvet calorimeters 240
Integral heat of solution measurements 243
HEAT OF MIXING CALORIMETRY 245
Pioneering instruments 245
Power-compensated isothermal flow heat of mixing calorimeters 247
Flow heat of mixing cells in Calvet calorimeters 249
Steam-gas mixtures 252
Calibration of isothermal heat-of-mixing calorimeters 253
DISCUSSION 255
Current state-of-the-art for hydrothermal solution calorimetry 255
Data compilations 255
Some current areas for investigation 255

CONCLUDING REMARKS 257
ACKNOWLEDGMENTS 257
REFERENCES 257

8

Structure and Thermodynamics of Subduction Zone Fluids from Spectroscopic Studies

Carmen Sanchez-Valle

INTRODUCTION 265
CHEMISTRY AND STRUCTURE OF SUBDUCTION ZONE FLUIDS 266
    Chemistry of subduction zone fluids 266
    Polymerization of silicate components in high-pressure fluids 267
CONTROLS ON TRACE ELEMENT SPECIATION IN SUBDUCTION ZONE FLUIDS 272
STUDIES ON TRACE ELEMENT SPECIATION IN SUBDUCTION ZONE FLUIDS BY X-RAY ABSORPTION SPECTROSCOPY 273
    X-ray absorption spectroscopy (XAS) 274
    XAS measurements in high-pressure fluids 274
SPECIATION OF TRACE ELEMENTS IN SUBDUCTION ZONE FLUIDS 277
    Speciation of High Field Strength Elements (HFSE) 277
    Speciation of Rare Earth Elements (REE) 281
MOBILIZATION AND FRACTIONATION OF TRACE ELEMENTS IN SUBDUCTION ZONES 284
    High Field Strength Elements (HFSE) 284
    Mobilization of REE and LREE/HREE fractionation 285
PRESSURE-VOLUME-TEMPERATURE-COMPOSITION (*PVTx*) RELATIONS AND THERMODYNAMIC PROPERTIES OF AQUEOUS FLUIDS 285
    Equations of state (EoS) for aqueous fluids 285
    Experimental studies of *PVTx* properties in aqueous systems 286
EQUATIONS OF STATE OF FLUIDS FROM SOUND VELOCITY MEASUREMENTS BY BRILLOUIN SPECTROSCOPY 287
    Principles of Brillouin scattering spectroscopy 288
    Brillouin spectroscopy of fluids under pressure 290
    Determination of density from measured sound velocities 291
PHYSICO-CHEMISTRY OF AQUEOUS FLUIDS AT ELEVATED PRESSURES (> 0.5 GPa) 292
    Volumetric properties of high-pressure aqueous fluids (> 0.5 GPa) 292
    Solute-solvent interactions in salt solutions under pressure 295
    Fugacity and activity of water in high-pressure salt solutions 297
CONCLUDING REMARKS AND OUTLOOK 301
ACKNOWLEDGMENTS 302
REFERENCES 302

9

Thermodynamics of Organic Transformations in Hydrothermal Fluids

Everett L. Shock, Peter Canovas, Ziming Yang, Grayson Boyer, Kristin Johnson, Kirtland Robinson, Kristopher Fecteau, Todd Windman, Alysia Cox

MESSAGES FROM NATURE 311
ORGANIC INVENTORY OF HYDROTHERMAL FLUIDS 311
HYDROTHERMAL ORGANIC TRANSFORMATION PROCESSES 315
THERMODYNAMIC EXPLANATIONS 320
    Hydrocarbon dissolution 320
    Hydration/dehydration 323
    Oxidation/reduction 324
    Relative stabilities 328
EXPERIMENTAL TESTS 332
    Hydration/dehydration reactions 332
    Oxidation/reduction reactions 335
    Relative stabilities and irreversible reactions 337
FUTURE DIRECTIONS FOR HYDROTHERMAL ORGANIC TRANSFORMATIONS 341
REFERENCES 342

Reviews in Mineralogy & Geochemistry
Vol. 76 pp. 1-4, 2013
Copyright © Mineralogical Society of America

Thermodynamics of Geothermal Fluids

Andri Stefánsson

Institute of Earth Sciences
University of Iceland
Sturlugata 7, 101 Reykjavík, Iceland

as@hi.is

Thomas Driesner

Institute of Geochemistry and Petrology
ETH Zurich
Clausiusstrasse 25, 8092 Zurich, Switzerland

thomas.driesner@erdw.ethz.ch

Pascale Bénézeth

Géosciences Environnement Toulouse (GET, ex LMTG)
CNRS-Université de Toulouse
14 Avenue Edouard Belin, 31400 Toulouse, France

pascale.benezeth@get.obs-mip.fr

This volume presents an extended review of the topics conveyed in a short course on Geothermal Fluid Thermodynamics held prior to the 23rd Annual V.M. Goldschmidt Conference in Florence, Italy (August 24-25, 2013).

Geothermal fluids in the broadest sense span large variations in composition and cover wide ranges of temperature and pressure. Their composition may also be dynamic and change in space and time on both short and long time scales. In addition, physiochemical properties of fluids such as density, viscosity, compressibility and heat capacity determine the transfer of heat and mass by geothermal systems, whereas, in turn, the physical properties of the fluids are affected by their chemical properties. Quantitative models of the transient spatial and temporal evolution of geochemical fluid processes are, therefore, very demanding with respect to the accuracy and broad range of applicability of thermodynamic databases and thermodynamic models (or equations of state) that describe the various datasets as a function of temperature, pressure, and composition. The application of thermodynamic calculations is, therefore, a central part of geochemical studies of very diverse processes ranging from the aqueous geochemistry of near surface geothermal features including chemosynthesis and thermal biological activity, through the utilization of crustal reservoirs for CO_2 sequestration and engineered geothermal systems to the formation of magmatic-hydrothermal ore deposits and, even deeper, to the devolatilization of subducted oceanic crust and the transfer of subduction fluids and trace elements into the mantle wedge.

Application of thermodynamics to understand geothermal fluid chemistry and transport requires essentially three parts: first, equations of state to describe the physiochemical system; second, a geochemical model involving minerals and fluid species; and, third, values for various thermodynamic parameters from which the thermodynamic and chemical model can be derived. The two biggest current hurdles for comprehensive geochemical modeling of geothermal systems are that thermodynamic data for species in fluids are often missing, particularly at

1529-6466/13/0076-0001$05.00 http://dx.doi.org/10.2138/rmg.2013.76.1

high temperatures and pressures, and that none of the existing equations of state for aqueous solutes and chemical reaction thermodynamics is valid over the whole range of temperatures, pressures and compositions encountered in Earth's crust and upper mantle. Moreover, it is well recognized that inconsistencies in and between existing thermodynamic databases and theoretical formulations or equations of state that provide thermodynamic data such as equilibrium constants and activity or fugacity coefficients can result in major differences and uncertainties in geochemical modeling.

Another current problem is that the temperature-pressure ranges for which thermodynamic data on fluid species can be considered accurate (typically below 300° to 350° C) often do not overlap with the ranges for which accurate thermodynamic properties of rock-forming minerals such as feldspars, micas, clays, aluminosilicates and iron-magnesium bearing phases such as chlorite or epidote are available. Frequently, modeling of fluid-rock equilibria therefore relies on standard state thermodynamic data for minerals that are extrapolated downwards from high-temperature phase equilibria, solubility and calorimetric studies (e.g., Holland and Powell 2011) and the uncertainty of the extrapolation is often unknown. As the variations of thermodynamic mineral data with temperature and pressure are rather well-behaved, it can be expected that future attempts for deriving internally consistent thermodynamic data sets may reduce this problem by constraining the extrapolations with fluid-rock reaction data at lower temperatures. On the other hand, extrapolating thermodynamic properties of aqueous species to higher temperatures and pressures is often error-prone as extrapolations have to go through regions with rapidly changing bulk fluid properties (such as density, heat capacity, and compressibility near the critical point of water) or may suffer from changes in aqueous speciation along the extrapolation path that cannot be predicted *a priori*. Recent approaches to correlate solute thermodynamic properties with relevant properties of water may be the most promising route to overcome this unsatisfactory situation.

The drawback of methods that determine Gibbs free energies of reactions is that many thermodynamic properties of interest (such as enthalpy, entropy, heat capacity and volume) are derivatives of the measurements with respect to temperature and pressure rather than being directly determined. To derive them requires interpolation between experimental data points, which makes the derived property values sensitive to finding an adequate mathematical formulation for interpolation. Furthermore, the derivation of thermodynamic properties of the individual species from the thermodynamic properties of the reaction often involves the choice of conventions or even extra-thermodynamic assumptions about the physics of the measurement (e.g., a model of ion mobility in conductivity measurements, or a model of the scattering processes in an X-ray absorption experiment).

The most popular model and thermodynamic database used among geochemist over the past two to three decades has been the Helgeson-Kirkham-Flowers (HKF) equation of state and the Supcrt92 database (Helgeson et al. 1981; Tanger and Helgeson 1988; Shock and Helgeson 1988; Johnson et al. 1992; Shock et al. 1992) and the density model (Anderson et al. 1991). However, these models do not work over a large range of temperatures, pressures and compositions that are encountered by different types of geothermal fluids, for example, supercritical fluids that exsolve into high-density saline brines and low-density vapor, high-pressure fluids associated with subduction zones, high-enthalpy and low-pressure fluids like superheated vapor and volcanic gas, to name just a few (Manning 2004; Yardley 2005; Audétat et al. 2008). In recent years, considerable progress has been made with thermodynamic models for aqueous solutions and solutes that can be used over a wide range of temperatures, pressures and compositions and over liquid-vapor phase changes that are based on electrostatic, macroscopic volumetric and microscopic statistical-mechanical approaches (see Palmer et al. 2004). Moreover, linking aqueous solute thermodynamics to the properties of water is also expected to be the key route for accessing the supercritical region that has been known as notoriously difficult in the construction of equations of state. Over the last two or so decades, much insight into the thermodynamics of supercritical fluids has been obtained and a number of rigorous relationships have been derived.

Molecular simulation approaches and statistical mechanics have provided theoretical frameworks that link the molecular scale processes in fluids to macroscopic thermodynamic properties, a subject that is discussed in the second chapter of this volume by Thomas Driesner (Driesner et al. 2013, this volume). These advances go along with the advent of synchrotron radiation sources that allow the direct study of aqueous speciation from ambient to extreme conditions (e.g., chapter 8; Sanches-Valle 2013, this volume). The accumulating insights into the molecular scale of geothermal fluids over very wide ranges of conditions, together with theoretical advances, will likely form the basis for novel equations of state (EoS) that can cover the currently inaccessible conditions mentioned above. Indeed, the need for equations of state over a wide range of compositions, temperatures and pressures describing both bulk fluid properties and thermodynamic properties of solutes for comprehensive geochemical modeling of geothermal systems is shown by the review in the third chapter by David Dolejš, who gives insights into basic thermodynamic models, EoS and transport theory by reviewing the thermodynamics of aqueous solutes at high temperature and pressure (Dolejš 2013, this volume).

Most of our basic thermodynamic parameters come from experimental work on well-defined chemical systems, which allow control of the governing parameters such as temperature, pressure, pH, ionic strength, or redox state with sufficient accuracy. As discussed in more detail in the fourth chapter by Pascale Bénézeth and others, such experiments are often very difficult to carry out at high temperatures and pressures and require laborious efforts (Bénézeth et al. 2013; this volume). A common method is to study mineral solubility as a function of fluid composition, which allows simultaneous determination of the Gibbs free energy of fluid-mineral reactions and inferring the aqueous species that participate in the reactions. Other popular methods for speciation studies are potentiometry and conductivity measurements, as well as various spectroscopic methods. The example of the carbonate systems is used in chapter four to demonstrate the lack of data and the misuse of inconsistent sets of thermodynamic data to model fluid-rock interaction up to hydrothermal conditions. Recent data acquired by using a combination of various experimental tools are compared with previous data and discussed.

In the fifth chapter of this volume, the thermodynamics of fluid-rock interaction continues to be described and discussed by Craig Manning for deeper geological systems at higher pressures and temperatures, from mid-crustal to upper-mantle conditions (Manning 2013, this volume). For instance the predicted and measured solubility of some minerals (corundum, calcite) obtained at high temperature and pressures are compared to demonstrate that some agreement can be obtained via the density-based approach. Vapor-phase transport capacities for metals and metalloids are the motivation of the review given by Gleb Pokrovski and others in the sixth chapter (Pokrovski et al. 2013, this volume). They review recent experimental data and models of the speciation of metals and metalloids and the solubility of their solid phases at conditions spanning from low-density volcanic gases to supercritical fluids and compared them with field observations.

Calorimetric and volumetric (density) measurements, for example, may directly provide fundamental thermodynamic values of the properties that are derivatives of the Gibbs free energy. As most equations of state for the thermodynamic properties of aqueous solutes at elevated temperatures and pressures involve these properties (and derive free energies by integrating them) such experimental data are an invaluable basis for the accurate parameterization of thermodynamic models. Errors that result from integrating derivative properties are normally considered less significant than errors on derivative properties that result from an improper interpolation of free energy data. In chapter seven, Peter Tremaine and Hugues Arcis provide a review of the history and application of solution calorimetry for hydrothermal systems (Tremaine and Arcis 2013, this volume).

More recently, direct determination of the stoichiometry and abundance of aqueous species has become available with X-ray absorption spectroscopy methods using synchrotron radiation. In chapter eight, Carmen Sanchez-Valle reviews recent progress on spectroscopic studies (Raman and XAS) combined with diamond anvil cells at pressure-temperature conditions relevant to subduction zones, discussing in particular the effect of chloride and dissolved silicates on the mobilization and transport of high field-strength elements (HFSE) and rare earth elements (REE) (Sanchez-Valle 2013, this volume).

Finally, Chapter nine by Everett Shock and others gives an overview of the thermodynamics of organic transformations in hydrothermal conditions, combining natural observations, thermodynamic models and experimental data (Shock et al. 2013, this volume).

REFERENCES

Anderson GM, Castet S, Schott J, Mesmer RE (1991) The density model for estimation of thermodynamic parameters of reactions at high temperatures and pressures. Geochim Cosmochim Acta 55:1769-1779

Audétat A, Pettke T, Heinrich CA, Bodnar RJ (2008) The composition of magmatic-hydrothermal fluids in barren and mineralized intrusions. Econ Geol 103:877-908

Bénézeth P, Stefánsson A, Gautier Q, Schott J (2013) Mineral solubility and aqueous speciation under hydrothermal conditions to 300 °C – the carbonate system as an example. Rev Mineral Geochem 76:81-133

Dolejš D (2013) Thermodynamics of aqueous species at high temperatures and pressures: equations of state and transport theory. Rev Mineral Geochem 76:35-79

Driesner T (2013) The molecular-scale fundament of geothermal fluid thermodynamics. Rev Mineral Geochem 76:5-33

Helgeson HC, Kirkham DH, Flowers GC (1981) Theoretical prediction of the thermodynamic behavior of aqueous-electrolytes at high-pressures and temperatures: 4. calculation of activity-coefficients, osmotic coefficients, and apparent molal and standard and relative partial molal properties to 600 °C and 5 kb. Am J Sci 281:1249-1516

Holland TJB, Powell R (2011) An improved and extended internally consistent thermodynamic dataset for phases of petrological interest, involving a new equation of state for solids. J Metamorph Geol 29:333-383

Johnson JW, Oelkers EH, Helgeson HC (1992) SUPCRT92 - A software package for calculating the standard molal thermodynamic properties of minerals, gases, aqueous species, and reactions from 1 bar to 5000 bar and 0 °C to 1000 °C. Comp Geosci 18:899-947

Manning CE (2004) The chemistry of subduction-zone fluids. Earth Planet Sci Lett 223:1-16

Manning CE (2013) Thermodynamic modeling of fluid-rock interaction at mid-crustal to upper-mantle conditions. Rev Mineral Geochem 76:135-164

Palmer DA, Fernandéz-Prini R, Harvey AH (eds) (2004) Aqueous Systems at Elevated Temperatures and Pressures: Physical Chemistry in Water, Steam and Hydrothermal Solutions. Elsevier, Amsterdam, 753 p

Pokrovski GS, Borisova AY, Bychkov AY. (2013) Speciation and transport of metals and metalloids in geological vapors. Rev Mineral Geochem 76:165-218

Sanchez-Valle C (2013) Structure and thermodynamics of subduction zone fluids from spectroscopic studies. Rev Mineral Geochem 76:265-309

Shock EL, Helgeson HC (1988) Calculation of the thermodynamic transport properties of aqueous species at high pressures and temperatures: correlation algorithms for ionic species and equation of state predictions to 5 kb and 1000°C. Geochim Cosmochim Acta 53:2009-2036

Shock EL, Oelkers EH, Johnson JW, Sverjensky DA, Helgeson HC (1992) Calculation of the thermodynamic properties of aqueous species at high pressures and temperatures: Effective electrostatic radii, dissociation constants, and standard partial molal properties to 1000°C and 5 kbar. J Chem Soc Faraday Trans 88:803-826

Shock EL, Canovas P, Yang Z, Boyer G, Johnson K, Robinson K, Fecteau K, Windman T, Cox A (2013) Thermodynamics of organic transformations in hydrothermal fluids. Rev Mineral Geochem 76:311-350

Tanger JC, Helgeson HC (1988) Calculation of the thermodynamic and transport properties of aqueous species at high pressures and temperatures. Am J Sci 288:19-98

Tremaine P, Arcis H (2013) Solution calorimetry under hydrothermal conditions. Rev Mineral Geochem 76:219-263

Yardley BWD (2005) Metal concentrations in crustal fluids and their relationship to ore formation. Econ Geol 100:613-632

Reviews in Mineralogy & Geochemistry
Vol. 76 pp. 5-33, 2013
Copyright © Mineralogical Society of America

The Molecular-Scale Fundament of Geothermal Fluid Thermodynamics

Thomas Driesner
Institute of Geochemistry and Petrology
ETH Zurich
Clausiusstrasse 25, 8092 Zurich, Switzerland
thomas.driesner@erdw.ethz.ch

INTRODUCTION

Chemical interactions between fluids and minerals play a central role in numerous geological processes. In a hydrothermal environment, such reactions are usually referred to as fluid-rock interaction or water-rock interaction and lead to alteration of rocks by changing the mineral assemblages and compositions. During fluid-rock interaction the fluid's chemical composition also changes, some components being depleted upon secondary mineral formation and others being enriched due to primary mineral dissolution. An example is the interaction between rocks at the seafloor and heated seawater during hydrothermal convection at mid-ocean ridges. There, the rocks are altered, extracting Mg and SO_4 from the circulating seawater and releasing metals such as Cu into the fluid. The chemically modified seawater is released back into the ocean at black smoker sites and diffuse discharge sites. This process contributes to buffering the chemical composition of the oceans over geological time periods. In sedimentary systems, the evaporation of aqueous fluids in marine and intracontinental settings leads to the formation of evaporites from complex, multicomponent brines. The diagenesis of sedimentary rocks is closely related to mineral dissolution and precipitation reactions in the presence of pore fluids that often flow over long distances in aquifers. The majority of ore deposits have formed by the interaction of hot hydrothermal fluids with rocks, dissolving the ore constituents as trace elements from a large volume of source material, transporting and focusing them during hydrothermal fluid flow and eventually precipitating them in concentrated form in a smaller rock volume due to chemical precipitation. The precipitation may result from the chemical effects of the reactions between the fluid and the rock. For example, the pH may increase by neutralization of acid fluids, a process that is often key to Pb-Zn sulfide mineralization in limestone and marble. Changes in the physico-chemical conditions (e.g., a temperature decrease) can cause mineral precipitation in response to decreasing solubility. Boiling upon pressure decrease that leads to the re-partitioning of ligands between the liquid and vapor phases that may decrease the solubility of certain metals such as Au.

Hydrothermal fluid processes in the Earth's crust are dynamic, transient in space and time, and operate over broad ranges of temperature, pressure, and fluid composition. A truly quantitative understanding is often only possible by numerical modeling of the physical and chemical effects and how they vary in the system with space and time. Besides the chemical effects, fluid properties such as density, heat capacity, viscosity, and compressibility determine the efficiency of mass and heat transfer in hydrothermal systems. Several studies have provided evidence that the temperature and pressure dependencies of these properties can induce self-organization of the thermo-hydraulic dynamics and spatial structure of hydrothermal systems to optimize the dissipation of heat from a magmatic source (Jupp and Schultz 2000; Coumou et al. 2008). In addition, the interplay between fluid properties and heat transfer determines

1529-6466/13/0076-0002$05.00 http://dx.doi.org/10.2138/rmg.2013.76.2

the physical state of fluids in a hydrothermal systems (Hayba and Ingebritsen 1997; Driesner and Geiger 2007), thereby controlling the thermal structure of the system, the spatial extent of boiling zones, the relative proportions of liquid and steam/vapor, and ultimately preparing the ground for chemical fluid-rock interactions, including the precipitation of minerals in fractures to make—sometimes economically mineralized—veins.

Understanding all these effects is also important for the exploitation of geothermal resources, as the optimization of energy output is the key variable for economic success. Mineral precipitation in wells and installations (referred to as scaling) and damage due to the corrosive nature of fluids often constitutes a major obstacle for a sustainable operation. Analogous to the chemical interactions introduced above, modeling the system's evolution in space and time is crucial for a quantitative understanding of fluid flow and energy and mass transfer. The source region of natural, high-enthalpy systems is believed to lie in the supercritical region of the water phase diagram and is currently being targeted as a future, very high enthalpy geothermal resource (Fridleifsson and Elders 2005; Elders et al. 2011). One of the major obstacles for exploitation of these resources is an almost complete lack in understanding of what chemical processes can be expected in wells under supercritical conditions, resulting from both a lack of experimental data and the nonexistence of a thermodynamic formalism for predictive modeling under these temperature and pressure conditions.

Ideally, one would like to be able to simulate both the chemical and physical processes in geothermal systems simultaneously and in a self-consistent way. For this, equations of state that can describe both bulk fluid properties and the thermodynamic properties of dissolved components (solutes) over wide ranges of temperature, pressure, and composition are required. Equations of state for bulk fluid properties are the fundament for such modeling of hydrothermal processes and accurate formulations for water as the geologically most relevant fluid have been available for several decades. Arguably, the most accurate ones are provided by the International Association for the Properties of Water and Steam (IAPWS, *www.iapws.org*). The current version for scientific use is the IAPWS95 formulation (Wagner and Pruß 2002). Other high accuracy water equations of state are those by Hill (1990), or the earlier release IAPS84 by Haar et al. (1984). Equations of state for mixtures of water with significant amounts of other components such as CO_2 and salts are also available, though basically all of them are either accurate only over limited ranges in temperature, pressure, and composition and/or are limited in accuracy or the number of properties they can reliably provide. Some empirical models that are not true equations of state are accurate over wide ranges of conditions (e.g., Driesner 2007; Driesner and Heinrich 2007) but have only very limited potential to be combined with formulations that describe reaction thermodynamics of solutes dissolved in the respective fluids.

The biggest current obstacle for comprehensive geochemical modeling of geothermal systems is that none of the existing equations of state for aqueous solutes and chemical reaction thermodynamics is valid over the whole range of temperature, pressure and composition encountered in the Earth's crust. The most popular model, the revised Helgeson-Kirkham-Flowers (HKF) equation of state (Helgeson et al. 1981; Tanger and Helgeson 1988) that forms the basis for the popular Supcrt92 database and computer program (Johnson et al. 1992) cannot be used over wide ranges of geothermally relevant conditions at temperatures above ca. 350 °C (Fig. 1) that pertain also to important types of hydrothermal systems such as mid-ocean ridge hydrothermal convection, ore-forming magmatic-hydrothermal systems, and the deep root zone of continental, high-enthalpy systems. Traditionally, this has been attributed to the vicinity of the critical point of water towards which derivative properties of the Gibbs free energy such as the partial molar volume of a solute diverge to plus or minus infinity (Fig. 2). Small errors in the mathematical formulations of the derivative properties lead to large errors

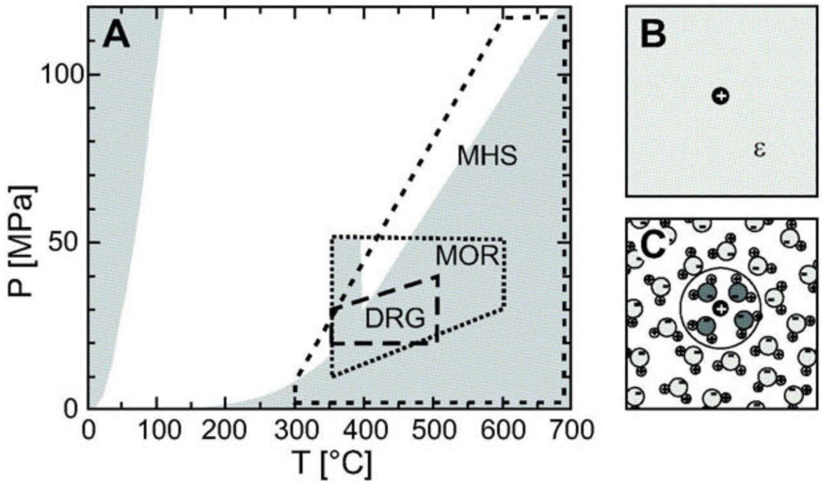

Figure 1. (A) Range of applicability of the popular HKF equation of state (white region) compared to the temperature-pressure conditions (schematic) of important types of natural hydrothermal systems. MHS: magmatic-hydrothermal systems; MOR: mid-ocean ridge hydrothermal systems; DRG: deep roots of continental, high-enthalpy geothermal systems. The applicability of the HKF equation of state is also somewhat restricted at temperatures above 350 °C for pressures below 100 MPa and its accuracy in the "supercritical" region is unknown for many species. (B) Schematic, molecular-scale picture of the Born model for an ion in aqueous solution, on which the HKF model is based: an ion is inserted into a homogeneous dielectric medium with a permittivity ε that represents water. (C) Schematic molecular-sale picture of the actual solution showing the distribution of partial charges on water molecules surrounding the ion, and the formation of a tighter "hydration shell" of water molecules around the ion (inside dashed circle). The local structuring, the distribution of partial charges, and other interactions that are not pictured strongly change as a function of temperature and density, and render the Born model a rather crude approximation that does not capture the physical essence of molecular-scale contributions to geothermal fluid dynamics. In the HKF model these effects are accounted for by empirical terms.

in the Gibbs free energy upon integration and so far, eliminating these problems from the existing equations of state has proven very difficult.

The difficulties of incorporating near-critical thermodynamics and the poor performance of the existing equations of state at high temperatures for upper crustal conditions result partly from their semi-empirical nature and, more importantly, from the fact that they are based on physical models that were developed for liquids at subcritical conditions and in which some contributions to solute thermodynamic properties that become relevant in the vicinity of the critical point are simply ignored. For example, the popular HKF model is based on Born's discovery (Born 1920) that the hydration energy of an ion in liquid water at ambient conditions can semi-quantitatively be understood as the immersion of a charged particle into an incompressible homogeneous dielectric medium (Fig. 1B). However, water is neither incompressible (it is only slightly compressible at ambient conditions but at the critical point, the isothermal compressibility diverges to infinity) nor can its structure near a dissolved ion or molecule be considered homogeneous. While perturbations that a dissolved species exerts on the molecular-scale water structure have a well-behaved effect on the solute's solution thermodynamics at ambient conditions, they have dramatic effects at near-critical conditions.

The construction of improved equations of state for solute thermodynamic properties will, therefore, require improving the physical model, incorporating relevant effects that have so far been ignored. Over the last two decades or so, much has been learned about the molecular-scale

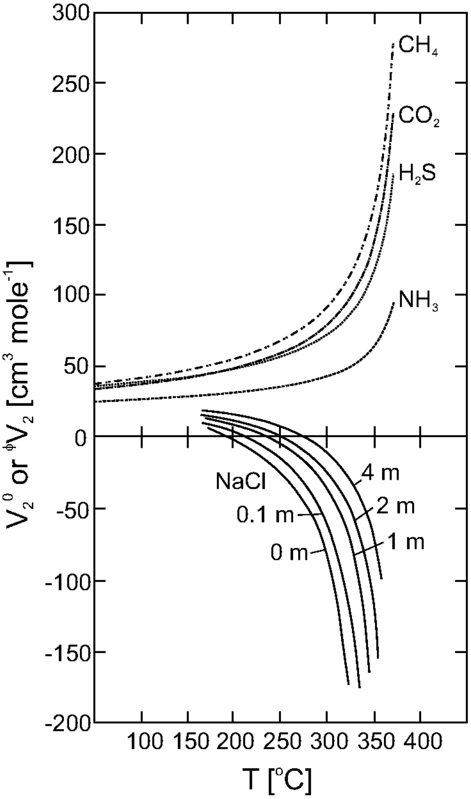

Figure 2. Divergence of the solute partial molar volume towards the critical point of water. The upper set of curves shows the partial molar volume at infinite dilution for four volatile solutes at 28 MPa, taken from Plyasunov et al. (2000b) who used the experimental data of Hnedkovsky et al. (1996). The lower set of curves shows the apparent partial molar volume of aqueous NaCl at 20 MPa for several concentrations, taken from Grant-Taylor (1981). Both sets of curves are not at exactly the critical pressure (22 MPa) of water but the strong divergence to large positive values (+∞ at the critical point) for the volatile solutes and to large negative values (–∞ at the critical point) for the non-volatile NaCl is clearly visible.

behavior of geofluids from spectroscopic and molecular simulation techniques. In addition, some groups have revived theoretical research on the links between molecular-scale phenomena and macroscopic thermodynamic properties under the extreme conditions encountered in natural hydrothermal systems. These theoretical studies have resulted in a much more profound understanding of which molecular-scale phenomena cause the extreme behavior of some thermodynamic properties at near-critical critical conditions. The improved insights on the molecular scale may form the basis for the development of improved conceptual physical models from which equations of state may be engineered.

This chapter reviews the molecular-scale phenomena that are relevant to geothermal fluid thermodynamics and what has been learned about their temperature, pressure, and composition dependency and their links to macroscopic thermodynamics. Some theoretical discoveries that appear to reduce the previous difficulties with "supercritical" fluid thermodynamics will be reviewed. The choice of topics in this chapter is highly selective and does not aim to provide a comprehensive review of the vast literature of aqueous solute species or of the related statistical mechanical concepts. Rather, I have tried to give a rather simplistic and subjective introduction for the non-specialist with a focus on the aspects that appear most relevant for future developments that will allow us to accurately model the thermodynamic properties of geothermal fluids, including the previously inaccessible near-critical and supercritical regimes.

BASIC RELATIONS BETWEEN THE MOLECULAR SCALE AND THE MACROSCOPIC THERMODYNAMIC PROPERTIES OF GEOFLUIDS

The macroscopic thermodynamic properties of fluids reflect the interactions between molecules in the fluid. In a real fluid, these interactions are complicated and their full incorporation into a single theory is still out of reach. Even today, after more than a century of research, there is no unified model of real liquids that is able to quantitatively reproduce the thermodynamic properties of all types of fluids with high accuracy. Quantitative models have been established for some fluid types with well-behaved and rather simple interactions, such as noble gases or certain types of fluids consisting of electrically non-polar molecules. Unfortunately, aqueous solutions and, hence, geothermal fluids, are a particularly difficult case as the interactions between the dipolar water molecules are strong and complex. Solutes in geothermal fluids may interact with water molecules in a very different way than the water molecules interact among themselves, thereby changing the local interaction environment and disturbing the local water structure.

Quantitative links between the molecular interactions and macroscopic thermodynamic properties are provided by the mathematical tools developed in the field of statistical thermodynamics. Due to the heavy mathematics involved, statistical thermodynamics seems often incomprehensible to geochemists and the focus of most standard textbooks is not on topics that are of immediate relevance to geothermal fluids (e.g., McQuarrie 2000; Tuckerman 2010). An excellent, focused, and relevant introduction to molecular theories related to the more modern approaches for equations of state of geothermal fluids (e.g., O'Connell et al. 1996; Plyasunov et al. 2000a,b; Sedlbauer et al. 2000; Akinfiev and Diamond 2003; Dolejš and Manning 2010) is the book of Ben-Naim (2006), which is a good entry point for geochemists who are considering working on new thermodynamic models of geothermal fluids. The overview of statistical thermodynamic concepts given below is a short summary of the introductory chapters of that book. Further information on statistical thermodynamics of geomaterials can be obtained from the chapters in an earlier volume in this series (Cygan and Kubicki 2001).

Simplified descriptions of molecular interactions

While a truly quantitative treatment of the molecular interactions would require a fully quantum-mechanical description, much insight can be gained from simplified, classical approximations in which molecular interactions are treated as pairwise and additive. One way for writing the potential energy of a system of N atoms is to split it into terms that depend on the coordinates $\mathbf{r}$ (written in vector form) of individual atoms, pairs of atoms, triplets, etc. (Allen and Tildesley 1987). A similar expression would apply for molecules, but more coordinates would then be needed to fully describe their position and orientation:

$$V = \sum_{i} v_1\left(\mathbf{r}_i\right) \quad \sum_{i}\sum_{j>i} v_2\left(\mathbf{r}_i,\mathbf{r}_j\right) \quad \sum_{i}\sum_{j>i}\sum_{k>j>i} v_3\left(\mathbf{r}_i,\mathbf{r}_j,\mathbf{r}_k\right) \quad \ldots \tag{1}$$

The first term—the potential energy of the individual atoms i due to the presence of an external field—does not contribute to the particle interactions. For these, the second term with the pair potential v_2 is a function of the distance $r_{ij} = \left|\mathbf{r}_i - \mathbf{r}_j\right|$ between atoms i and j and is the strongest contribution to the molecular interactions. The importance of higher order interactions (e.g., v_3 that represents the contribution to the total potential energy resulting from interaction specific to triplets) becomes significant as density increases towards liquid-like values.

A large number of studies, mostly using numerical simulation techniques (typically molecular dynamics or Monte Carlo simulations) have shown that a good parameterization of the pairwise interactions in a classical rather than quantum form is sufficient to compute numerous thermodynamic, structural, and transport properties of a given fluid with reasonable accuracy. In such cases, the molecular interactions are condensed into a pairwise additive potential. The best-known example is the Lennard-Jones potential

$$v^{LJ}\left(\boldsymbol{\varepsilon}\right) = 4 \left[\left(\frac{\sigma}{r}\right)^{12} \quad \left(\frac{\sigma}{r}\right)^{6}\right] \tag{2}$$

that simply adds up a steep repulsive r^{-12} term that dominates at short distances between the two particles and a long attractive tail represented by the r^{-6} term. The general form as a function of r is given in Figure 3. Many mathematical forms for effective pairwise potentials have been suggested but essentially all have a shape qualitatively similar to the Lennard-Jones potential.

Particles in a system are constantly moving and the distance between any two particles will change. As a result they move along the potential energy curve and the force that is acting between them is the derivative of the potential with distance. The force is attractive at distances larger than the position of the minimum and would accelerate the particles if they were already moving towards each other, converting potential energy to kinetic energy. They would experience a restoring force if moving away from each other at such distances but this force becomes essentially zero at a few molecular diameters, i.e., these interactions are short-ranged. If the molecules are close to each other and pass through the minimum towards shorter distances, the force becomes repulsive and potential energy is gained at the expense of kinetic energy, slowing the movement down until it is reverted and they move away from each other, losing the potential energy and gaining kinetic energy again. The actual direction of movement will be influenced by the pairwise interactions that the two particles have with other particles, making the actual trajectories complicated and leading to a continuous fluctuation of the potential and kinetic energies in the system. The average value of potential energy and kinetic energy are related to the macroscopic properties internal energy and temperature. To derive the exact relations between statistical thermodynamic properties and macroscopic thermodynamic properties, it is essential to specify the independent variables that define the system when the averages and fluctuations are being computed.

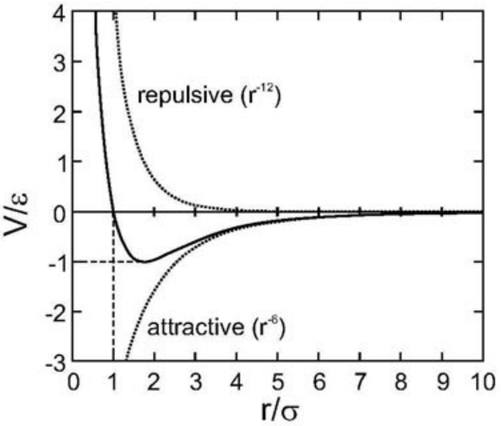

Figure 3. The 12-6 Lennard-Jones potential for the interaction between two particles (atoms) as a function of distance between the particles (*solid line*). The vertical axis is the potential in multiples of the parameter ε in Equation (2), the horizontal axis is distance in multiples of the parameter σ in Equation (2). Dotted curves are the repulsive (*top*) and attractive (*bottom*) components of the potential. The slope of the potential curve gives the force and is attractive between the two particles if positive and repulsive if negative. The potential is zero at a distance of 1σ, which is sometimes used as the definition for the molecular diameter.

The attractive tail of the Lennard-Jones potential decays with r^{-6} leading to the short-ranged nature of non-electrostatic interactions. If the particles bear electrical (partial) charges, long-ranged electrostatically interactions that decay as r^{-2} enter the picture and contribute significantly to the thermodynamics of the solutions, particularly at finite solute concentrations. The water molecule itself can be considered as bearing partial positive and negative charges that interact between various water molecules and between water molecules and ions.

Basic concepts of statistical thermodynamics

Although most computer simulations use classical interaction potentials successfully, the theoretical formulations for statistical thermodynamics are based on quantum formulations that can then be simplified for the classic case. A most fundamental property of a system is the number of possible quantum mechanical states W if the system is isolated, with fixed values of internal energy (E), volume (V), and particle number (N). According to Boltzmann's formula, W is directly connected to the system's entropy S:

$$S(E,V,N) = k \ln W(E,V,N) \tag{3}$$

There will be many states *i* for which a system of *N* particles can fulfill the condition of having the specified *E* and *V*. Statistical thermodynamics postulates that the collection of these states has the fundamental property that each state *i* occurs with the same probability p_i, leading to the simple but important relation

$$p_i = \frac{1}{W(E,V,N)} \tag{4}$$

Such a collection of states is called an ensemble. Many fundamental relations in statistical thermodynamics are derived from or are closely related to this postulate.

There is a 1:1 correspondence between the independent variables used in the definition of macroscopic thermodynamic properties and those used in statistical thermodynamics. For example, a system with constant temperature (*T*), volume (*V*), and particle number (*N*) is connected to the Helmholtz Free Energy *A* (which is defined in terms of *T*, *V* and the number of moles when dealing with macroscopic systems) via

$$A\left(T,V,N\right) = -kT \ln Q(T,V,N) \tag{5}$$

where *k* is the Boltzmann constant. *Q*(*T*,*V*,*N*) is the so-called partition function of the *T*,*V*,*N* ensemble (also called the microcanonical ensemble), and is given by

$$Q(T,V,N) = \sum_E W(E,V,N) e^{-\frac{E}{kT}} \tag{6}$$

Mathematically, the partition function is a normalization constant that ensures that the probabilities for the system having an internal energy *E* add up to 1 if summed over all possible *E*. The probability *p*(*E*) of the system having a specific internal *E* is then

$$p(E) = \frac{W\left(E,V,N\right) e^{-\frac{E}{kT}}}{Q\left(T,V,N\right)} \tag{7}$$

Notice how the number of states *W*(*E*,*V*,*N*) is carried over to this expression in the *T*,*V*,*N* ensemble, underlining its fundamental importance. Notice also that by now having a system that is at constant temperature the condition of it being isolated has been abandoned and heat is allowed to be exchanged between the system and its surroundings. From the statistical thermodynamic Helmholtz free energy other thermodynamic properties can be derived using the same standard relationships as in macroscopic thermodynamics.

The Gibbs free energy, *G*, is analogously defined in an isothermal-isobaric ensemble with constant temperature (*T*), pressure (*P*), and particle number (*N*), i.e., the condition of constant volume is abandoned. The system and its surroundings can now also attain mechanical equilibrium by performing work and, accordingly, a term for pressure-volume work, *PV*, will come into play. The Gibbs free energy is related to a different partition function Δ(*T*,*P*,*N*) via

$$G\left(T,P,N\right) = -kT \ln \Delta\left(T,P,N\right) \tag{8}$$

where the respective partition function now carries the *PV* term and builds on the above derived *Q* and *W* according to

$$\begin{aligned} \Delta\left(T,P,N\right) &= \sum_V Q\left(T,V,N\right) e^{-\frac{PV}{kT}} \\ &= \sum_V \sum_E W\left(E,V,N\right) e^{-\frac{E}{kT}-\frac{PV}{kT}} \end{aligned} \tag{9}$$

Fluctuations and thermodynamic properties

In the ensembles discussed above, properties that are not fixed will fluctuate around an average value. In the E,V,N ensemble, the internal energy is fixed but temperature, pressure, and other properties will fluctuate. The various constituents of the internal energy, e.g., potential, kinetic, and possibly intra-molecular stretching or torsion energies will also fluctuate as the overall constant energy is continuously redistributed between these different forms. Temperature can then be computed from the time-averaged value of the kinetic energy via

$$T = \frac{2}{3Nk}\left\langle \sum_{i=1}^{N} \frac{m_i \mathbf{v}_i^2}{2} \right\rangle \tag{10}$$

where the angular brackets indicate a time average taken of the sum over the kinetic energy of all particles i (m_i being the particles mass and $\mathbf{v}_i$ its velocity). Pressure can be computed as

$$P = \frac{NkT}{V} \quad \frac{1}{3V}\left\langle -\sum_{i=1}^{N} \mathbf{r}_i \mathbf{F}_i \right\rangle \tag{11}$$

where the time average is now taken over the so-called internal virial, i.e., summing over the dot products of coordinate vectors $\mathbf{r}_i$ and force vectors $\mathbf{F}_i$.

Similarly, in the T,V,N ensemble, temperature is fixed but E as well as pressure and other properties can fluctuate. There are a series of other ensembles, all with specific fixed, independent and fluctuating, dependent variables.

The fluctuations themselves are related to thermodynamic properties. For example, in the T,V,N ensemble, it can be shown that the isochoric heat capacity, c_V, which is formally defined as the temperature derivative of E, is directly linked to the fluctuations of E (Ben-Naim 2006) such that

$$c_V = \left(\frac{\partial \langle E \rangle}{\partial T} \right)_{V,N} \quad \frac{\langle E^2 \rangle - \langle E \rangle^2}{kT^2} = \tag{12}$$

where the angular brackets denote averages. In the right-hand side expression, the numerator represents the fluctuations of the internal energy, defined as

$$\sigma^2 = \langle E^2 \rangle \ \langle E \rangle^2 - \tag{13}$$

Similarly, the isobaric heat capacity, c_P, is related to fluctuations in enthalpy, H, in the T,P,N ensemble:

$$c_P = \left(\frac{\partial \langle H \rangle}{\partial T} \right)_{P,N} = \frac{\langle H^2 \rangle - \langle H \rangle^2}{kT^2} \tag{14}$$

A particularly relevant relation can be derived for the fluctuation of the number of particles, N, in systems at constant temperature, volume and chemical potential, the grand or T,V,μ ensemble:

$$\langle N^2 \rangle - \langle N \rangle^2 = kTV\rho^2 \kappa_T \tag{15}$$

The right-hand side of Equation (15) contains the isothermal compressibility κ_T and has been found to be a very useful property to describe the thermodynamics of solutes in the near-critical and supercritical regimes (e.g., O'Connell 1971; O'Connell et al. 1996; Plyasunov et al. 2000a,b). Interestingly, it is also related to approaches for defining and separating short-ranged solute-solvent contributions to thermodynamic properties from long-ranged, solvent compressibility-driven contributions that dominate the divergence of derivative properties in the near- and supercritical regimes, and which will be discussed towards the end of this paper.

Understanding fluid thermodynamics from pair correlation functions

As mentioned above the statistical thermodynamics of fluids can successfully predict macroscopic thermodynamic properties with reasonable accuracy even if the interactions are simplified to be pairwise additive only. Although this is clearly too simple an approach towards a full understanding, molecular dynamics and Monte Carlo simulations using such simplified models in are still a major tool that continues to advance our understanding of fluids. A major advantage is that pairwise additive interaction potentials allow understanding fluid thermodynamics in quite some detail once the pair correlation functions for the various types of interacting particles are available. If explicitly written in terms of the distance r between particles they are usually denoted as $g(r)$ and are often also referred to as radial distribution functions.

The radial distribution function gives the probability of finding a pair of particles in a fluid and separated at a distance r, relative to the same probability expected for a completely random distribution of particles at the same density (particles per volume). In a molecular simulation it is typically computed by looping over all particles of a given type i and for each such particle i counting the number of particles of type j (depending on the pairs of interest, i and j can be different, e.g., for ion-water pairs, or the same, e.g., for water-water interactions) in a thin spherical shell (at distance r and of thickness $2\Delta r$) around it. This procedure is repeated for many simulation configurations (randomly generated in Monte Carlo simulation or taken at different times in a Molecular Dynamics simulation) to obtain good statistics, and the $g(r)$ is computed as

$$g_{ij}(r) = \frac{\left\langle N_{ij}\left(r - \Delta r, r + \Delta r\right)\right\rangle}{\rho V_{r\pm\Delta r}} \tag{16}$$

where the numerator is the time-averaged number of type j particles found in the spherical shell between $r - \Delta r$ and $r + \Delta r$ around the particle of type i. The denominator is the volume of that layer ($V_{r\pm\Delta r}$) times the number density (ρ) and represents the number of particles to be expected in the spherical layer if the particle distribution were completely random. Obviously, if $g(r) = 1$ for all r, the distribution of particles would be completely random, a behavior only to be expected for an ideal gas. Any molecular interactions will induce a non-random distribution with some short-range structuring. For the example of the simple "Lennard-Jones fluid" (i.e., a fluid of spherical particles interacting via the Lennard-Jones potential described above), Figure 4 shows how increasing density leads to increasing interactions and stronger structuring in a fluid. Notice that at high densities the structuring includes a packing density effect as particles cannot move around freely since they cannot easily pass neighboring particles while at low densities any structuring seen in the $g(r)$ does reflect molecular interactions due to some kind of potential energy function.

Besides providing information about the time-averaged solution structure[1], the $g(r)$ has close links to the thermodynamic properties of the fluid. Since $g(r)$ gives the distribution of how many particles can be expected to at a given distance, information about average particle interactions in the fluid can be computed by combining $g(r)$ with the potential function that

---

[1] Although the term "fluid structure" has long been established in the literature and is used abundantly (for the lack of a better expression) it should be emphasized that it does NOT refer to an ordered, long-range structure as in crystalline solids but rather to an averaged picture of transiently changing short-ranged correlations in an otherwise unstructured medium.

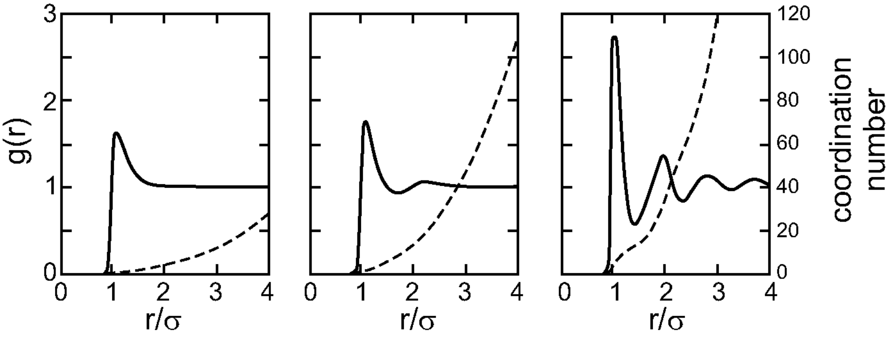

Figure 4. Radial distribution function $g(r)$ (solid lines, and numbers on left vertical axes) for particles with a simple Lennard-Jones interaction (cf. Fig. 3) at low (*left*), intermediate (*middle*), and high (*right*) densities. For the lowest density, only one peak of moderate intensity is seen, indicating occasional interactions with about one molecular diameter where particles get "trapped" in the potential energy minimum seen in Figure 3. Beyond this distance, $g(r)$ rapidly approaches a value of 1 indicating that particles have rather long mean free path lengths and move randomly without interacting. At intermediate densities, some structuring (clustering) is seen as a weak second peak, and at high density, strong structuring extends over several molecular diameters, indicated by the increasing number and height of peaks. The fluid particles get closer to each other and can no longer move around freely. Dashed lines and numbers on the right vertical axes are the radially integrated $g(r)$, which gives the number of particles inside a sphere with the respective radius (coordination or solvation number). This number at the position of the first minimum in the $g(r)$ is often referred to as the first shell coordination number.

describes the interaction between the particles. In fact, $g(r)$ is related to a property called the potential of mean force (PMF), which is the work that is involved when bringing two particles from fixed positions with infinite separation to fixed positions with a finite distance R. For illustration, in the simple case of spherical particles in the T,V,N ensemble, it can be shown (Ben-Naim 2006) that

$$g(R) = e^{-\frac{W(R)-W(\infty)}{kT}} \qquad e^{-\frac{A(R)-A(\infty)}{kT}} = \tag{17}$$

where W is the PMF if the particles are separated by the distance indicated in brackets and A is the Helmholtz Free Energy of the system if the two particles are separated by that distance. If the PMF can be determined as a function of *distance*, $W(R) - W(\infty)$ can therefore be used to evaluate the work involved for bringing the particles from an infinite distance to a separation of R without a need to know the Helmholtz Free Energy of the system. Similar expressions can be derived for other ensembles and more complicated cases.

For the same simple model system, a direct combination of $g(r)$ and the pairwise additive potential energy function $U(r)$ (which could, for example, be the Lennard-Jones potential v^{LJ} given by Equation (2), the average interaction energy in a system would be (Ben-Naim 2006)

$$\frac{1}{2}N\rho\int_0^{\infty} U(r)g(r)4\pi r^2 dr \tag{18}$$

which, if combined with other energy contributions $N\varepsilon$ (translational kinetic energy, which would be $1.5NkT$ in this simple model system, rotational, and vibrational energies) gives the internal energy

$$E = N\varepsilon + \frac{1}{2}N\rho\int_0^{\infty} U(r)g(r)4\pi r^2 dr \tag{19}$$

Again, extension to other ensembles or to mixtures is possible (Ben-Naim 2006) but analytical expressions can only be derived for rather simplistic model systems such as the spherical particles with pairwise additive interactions described above. Depending on the property of interest, $g(r)$ has to be obtained in different ensembles and care has to be taken for the mathematically correct treatment when computing it as some results are sensitive to even small inaccuracies. In any case, for applying these equations $g(r)$ needs to be known, which cannot be done analytically except for the most trivial cases. An accurate $g(r)$ is difficult to determine experimentally (and then typically limited to a short r) and, therefore, numerical simulation methods have been the prime tool to study the radial distribution functions of fluids.

Molecular simulation

Due to the availability of powerful and well-maintained computer codes, molecular simulation techniques have become a popular tool that has made the power of statistical thermodynamics available to the broader scientific community, including geochemists. These methods have the advantage that—besides mostly semi-quantitative thermodynamic data—they provide insight into the molecular structure and dynamics of solutions. Thereby they allow the development and exploration of conceptual models of how the variations in solution thermodynamics with temperature, pressure, and concentration are rooted in changes at the molecular scale. Most current molecular simulation techniques are based on either Monte Carlo (MC), classical molecular dynamics (MD) or *ab initio* molecular dynamics (AIMD) approaches. Introductions to the various methods may be found, for example, in Allen and Tildesley (1987), Cygan and Kubicki (2001), and Frenkel and Smit (2002).

MC methods randomly generate a large number of molecular configurations of interacting particles. For each configuration the potential energy is computed and fed into some acceptance routine that ensures that after a large number of configurations have been generated the potential energy surface of the system has adequately been sampled. MD methods on the other hand start with an initial configuration and then solve the classical equations of motion for the particles in the virtual simulation box with forces between particles being computed from a predefined "force field" (in the simplest case something like a Lennard-Jones potential). As initial configurations are usually generated randomly they are rarely physically meaningful and the simulation requires an initial equilibration phase during which constant values of properties such as E, T, or P (depending on the ensemble chosen) are enforced until they remain constant during subsequent simulation steps.

The currently most advanced simulation techniques are AIMD simulations, mostly using the Carr-Parinello method. In these, the motions of the molecules are computed according to the classical equations of motion, but forces between the particles are derived from quantum mechanical electronic structure calculations at each time step. The quantum chemical computations are typically done by density functional theory approaches (DFT). The method is, in principle, extremely powerful as it avoids prescribing a rigid, simplified force field to describe the intra- and intermolecular interactions and thereby naturally allows for effects such as polarization. However, the current descriptions of the quantum mechanical interactions are somewhat incomplete, and different descriptions result in variations in simulated hydration shell structures that are comparable to the variation of results obtained with classical MD (Bankura et al. 2013). However, with future developments it can be expected that the accuracy of the methods will improve to a degree that the simulated structures will be the most reliable information obtainable. The major drawback of this method—when looking at the potential for providing information about the variations of the molecular-scale interactions with temperature, pressure, and concentration—is the requirement of very large computational resources. This is a particularly strong drawback in the near- and supercritical regions where large systems need to be simulated to avoid artifacts from system sizes that are smaller than the compressibility-dictated correlation length of the fluid. Hence, in spite of the expected detailed and quantitative insights that AIMD can provide, the likelihood that it will become a routine tool to accurately explore wide regions of the parameter space of geochemical relevance is currently low.

GENERAL MOLECULAR-SCALE FEATURES OF AQUEOUS GEOFLUIDS

The thermodynamics of an aqueous geofluid can phenomenologically be understood by the temperature and density variations of the fluid's molecular-scale structure and dynamics. These reflect the competing interactions between the solute and solvent species that the solution is composed of. In the vast majority of hot fluids in the crust, water is the solvent. In a highly simplified classical picture, the water molecule can be considered as an approximately tetrahedral arrangement of partial charges, with two negative partial charges representing the lone pair orbitals of the oxygen site and two positive charges representing the hydrogen sites. This geometry promotes strong local ordering in ordinary water under ambient conditions where a tetrahedral network of hydrogen bonded water molecule is being formed and reaches over several molecular diameters (Figs. 1C and 5A). The geometry also gives the individual water molecules a strong electrical dipole moment, and the ordered network of water molecules is responsible for the high dielectric permittivity of water. The latter is the cause of the high solubility of salts in water and, accordingly, the solutes with highest abundance in natural fluids are typically electrolytes (mostly alkali and alkali earth chlorides), which dissolve in water as ions. More generally, charged species are rather abundant in water compared to other solvents, and it is the charged nature that makes the development of equations of state for aqueous solutes a non-trivial task compared to, for example, fluid mixtures of molecular species. Such molecular, i.e., uncharged species that do not dissociate into ions typically have lower solubilities, and often represent volatile components. Again, this reflects the nature of the molecular interactions with the solvent water molecules. For example, the rather large, linear, and non-polar CO_2 molecule does not easily bond with small, dipolar water molecules. The macroscopic expression of this molecular-scale behavior is the large miscibility gap between H_2O and CO_2, which is only overcome at high temperatures (Diamond 2001) where the ordering of the hydrogen-bonded network of water molecules becomes much less pronounced.

The thermodynamics of solutes in aqueous fluids, in particular those with (partial) charges, is controlled by the phenomena of hydration and speciation. The term "hydration" is a special case of solvation, which denotes the phenomenon that solvent molecules tend to attach to dissolved solute species, and "hydration" is used if the solvent is water. The effect is particularly strong for ions to which the water molecules might bind quite strongly via interactions with a significant electrostatic component, leading to a structured "hydration shell" around the ion. Generally, this binding can be expected to be stronger the smaller and/or the higher charged the ion is. The geometric arrangement of water molecules in the hydration shell typically differs from that of the tetrahedral arrangement in the bulk solvent water. The different bonding environments experienced by water molecules in the hydration shells differ so strongly that they can significantly alter O and H isotope fractionation factors between water and minerals or gases (e.g., Feder and Taube 1952; Taube 1954; Sofer and Gat 1972; Horita et al. 1995; Bopp et al. 1974; Driesner et al. 2000; Driesner and Seward 2000). While a hydration shell that consists of one layer of water molecules is formed around basically all ions, several structured layers may develop around small and/or highly charged ions. A vast number of studies have dealt with these local structuring effects, mostly at ambient conditions, and numerous theoretical concepts have been developed to classify and understand them. For a first overview, the interested reader is referred to the review by Marcus (2009). Most of the concepts, however, appear to be of little quantitative use when dealing with geothermal fluids over wide ranges of temperature and density.

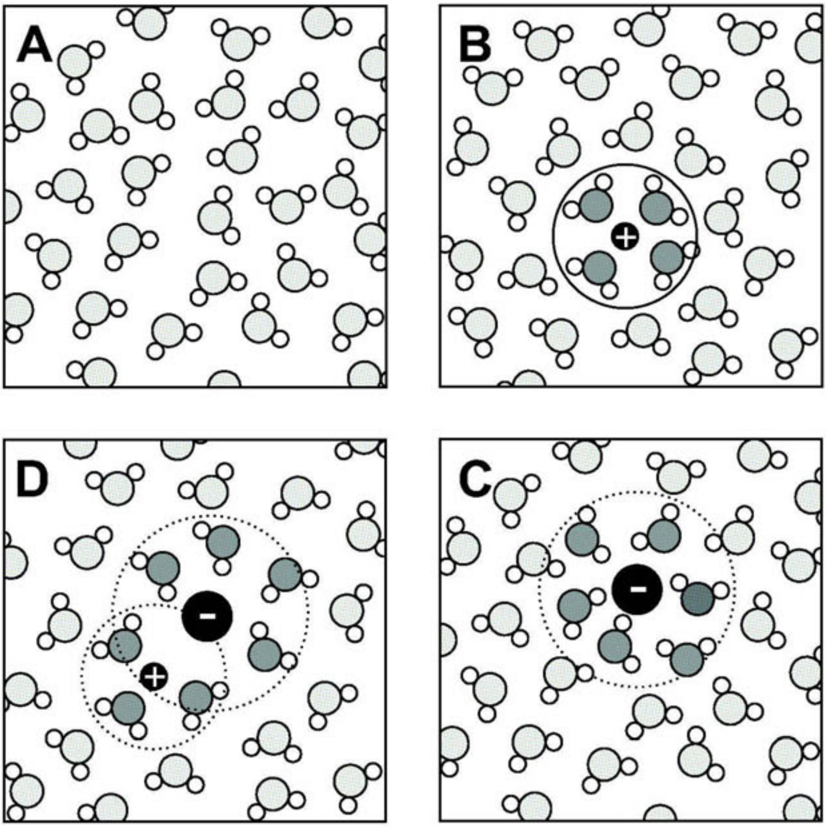

Figure 5. Schematic two-dimensional sketches of the structure of aqueous fluids. Water molecules are depicted by three circles, the bigger gray one representing the oxygen site and the two smaller white ones the hydrogen sites. In clockwise order: (A) Pure water. Notice how neighboring water molecules can have similar orientation, representing the ordering effect of hydrogen bonding. (B) Small cation in aqueous solution. The first hydration shell (water molecules in dark gray) is somewhat tighter packed than the bulk solvent water (light gray) and shows a strong orientation of the water molecules with their oxygen pointing towards the cation. (C) Anion in aqueous solution. Water molecules in the first hydration shell have an orientation with one of the hydrogens pointing towards the ion while the other takes part in the hydrogen bonding network of the bulk water. The structuring in the hydration shell is less pronounced than in the cation case and bulk water molecules frequently penetrate into the shell. (D) Contact ion pair. Both ions largely retain a hydration shell that is similar to that of the single ions in B and C. Only where the hydration shells overlap may some significant re-orientation is expected.

Hydration of ions

The hydration of cations is often characterized by relatively strong bonds between the cation and the oxygen site of water molecules in the hydration shell. Geometrically, this results in the arrangement schematically pictured in Figure 5B. This general geometry has been verified for numerous cations by molecular simulation and spectroscopic techniques that are able to deliver radial distribution functions $g(r)$ (e.g. Enderby and Neilson 1981; Enderby 1995; and references therein). At a low r, the cation-oxygen $g(r)$ is zero, indicating a region that cannot be penetrated by the water molecule due to strong repulsive forces. This effect is strongly related to the concept of an effective radius of the ion in solution, which is typically somewhat larger than the "crystallographic" ion radius. The first peak in $g(r)$ cation oxygen shows the preferred location of water molecules in the first hydration shell. The higher and narrower the peak, the stronger is the structuring in the first hydration shell compared to the bulk solvent. Both spectroscopic and molecular simulation techniques have demonstrated that this peak moves to smaller distances with increasing temperature, which also implies that the effective ionic radius of cations decreases with increasing temperature. It is interesting to note that some authors in the construction of semi-empirical equations of state realized that a temperature-dependence of the effective ionic radius aids in fitting experimental data (Tanger and Helgeson 1988; Shock et al. 1992). Future equations of state may relate to an increasing body of experimental and simulation data (see further below) on this effect, thereby possibly reducing the need for "overfitting" or enforcing empirical correlations.

The hydration of anions is often considered less strong than that of cations. This is reflected in less pronounced peaks in the $g(r)$ and probably indicates a more transient nature of the bonding between the hydrogens in the hydration shell and the anion. The qualitative geometry of these bonds is shown in Figure 5C and can be inferred from the anion-water $g(r)$'s (Enderby and Neilson 1981). The nearest peak is in the anion-hydrogen $g(r)$, followed by anion-oxygen and another anion-hydrogen peak, indicating that the anion and the water molecule are forming a hydrogen bond not unlike the one between neighboring water molecules. The second hydrogen is pointing away from the cation and available for hydrogen bonding with bulk solvent water. Unlike for cations, the first minima in the anion-hydrogen and anion-oxygen $g(r)$ are at finite values, clearly not zero, which shows that the respective components of the water molecule spend significant times at the respective distances, i.e., the water molecules move around more freely than those in cation hydration shells.

Ion pairing and clustering

An often overlooked phenomenon is that species and ion pairs are also hydrated. Figure 5D schematically shows the geometry of a hydrated ion pair. The general orientation of the water molecules on the Na^+ end is similar to that of a single hydrated Na^+ ion and that at the Cl^- end close to that of a single hydrated Cl^- ion. Around the contact zone of the two ions, there is competition between both orientations. To the best of my knowledge, the energetic effects of hydration of ion pairs have not been studied in detail. However, the geometry pictured seems to imply that there is a rather smooth transition from the hydration of single ions to ion pairs.

Traditionally, three types of ion pairs have been distinguished, depending on the presence of water molecules between the ions (e.g., Marcus and Hefter 2006). A contact ion pair is represented by the configuration shown in Figure 5D while a solvent-shared ion pair would have a single layer of water molecules between the two ions. In addition, solvent-separated ion pairs have been defined as configurations where the hydration shells of both ions remain largely intact and touch each other, leading to two layers of water molecules between the ions. Molecular simulations of the potential of mean force (PMF) for the ion pairing process at near-critical conditions (Chialvo et al. 2000, 2002; Chialvo and Simonson 2003) indicate that the contact ion pair is the more stable configuration while the solvent-shared ion pair configuration represents only a weak minimum (Fig. 6) and no particular structure of the PMF curves occurs where a solvent-separated geometry would be expected. This result underlines the difficulty of defining "species" in aqueous solution—a geometrically intuitive definition may energetically be irrelevant. In addition, while such criteria may be useful in establishing a classification in a dilute solution they become semantically difficult in concentrated solutions: if we assume an aqueous solution of NaCl, fully dissociated with an average first-shell coordination number of 6-7 per ion, a 4 molal solution would arithmetically consist of solvent-shared ion pairs although we'd rather see a purely geometric effect distribution of ions. This semantic problem (cf. Marcus and Hefter 2006) has remained unsolved for decades and has influenced the formulation of important thermodynamic models of aqueous electrolytes. For example, the Pitzer model (largely) ignores ion pairing because the lack of a thermodynamically (rather

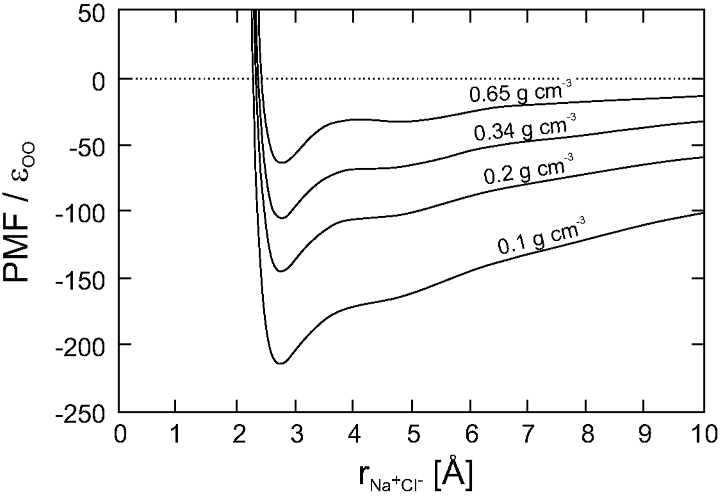

Figure 6. Potential of mean force (PMF) for the Na^+Cl^- ion pair in water along the critical isotherm as computed from classical molecular simulations (modified from Chialvo and Simonson 2003). PMF is given as multiples of the oxygen-oxygen Lennard-Jones ε parameter (Eqn. 2) of the SPCE water model used in the simulations. The minimum near 2.7 Å represents the contact ion pair while a weak depression (at higher densities) or inflection (for lower densities) near 5 Å is indicative of the solvent-shared ion pair configuration. The absence of further minima at larger distances indicates that the solvent-separated ion pair configuration would not represent a species but rather a geometric coincidence.

than geometrically) meaningful and consistent definition renders building a consistent model virtually impossible. It is further complicated by the occurrence of larger associated entities (ion clusters) as concentration increases (Oelkers and Helgeson 1993; Driesner et al. 1998; Sherman and Collings 2002; Hassan 2008). These interactions are the molecular-scale origin of the concentration-dependence of activity coefficients in aqueous electrolyte solutions but their complexity is not well understood and, therefore, a rigorous molecular-based framework for the calculation of these activity coefficients is unlikely to emerge and replace semi-empirical approaches such as the Pitzer model.

Speciation

As discussed above for the example of ion pairs, the definition of what can be called a distinct species in an aqueous solution is not trivial on the molecular scale. From a pragmatic experimentalist's perspective, a species is a molecular entity that can be identified by characteristic spectroscopic responses. However, many species that are used in geochemical databases have not been proven spectroscopically, for example because of very low solubilities or very weak responses to spectroscopic methods. Many species have empirically been introduced to help interpret macroscopic experiments such as solubility studies of sparingly solubility materials in terms of a series of species with increasing ligand numbers.

The most fundamental aspect of speciation in aqueous geofluids is that it involves bonding of some type. This may be electrostatically dominated between cations and anions, or covalent between other solute species and in some cases may be extended to define hydrated ions or atoms as species in solution. The resulting species may be neutral or charged. While the picture of hydration of simple, "hard" ions (i.e., charged species that have a preference for binding with a strong electrostatic component) is quite established, there is comparatively little insight into the interactions between geometrically more complex ions and the solvent water as well as into the interactions between "soft" ions (i.e., those that have a preference for covalent bonds, e.g. Au^+) and bulk solvent water. Evidence from metal solubilities in high temperature vapor indicates that hydration plays a key role in drastically enhancing solubility in such low-density aqueous fluids (e.g., Archibald et al. 2001, 2002; Williams-Jones and Heinrich 2005; Rempel et al. 2008). As covalent bonding and speciation cannot well be represented by classical molecular simulation, AIMD methods will be essential in unraveling the molecular-scale picture of such species in solution. Some first studies have shown the great potential by demonstrating good agreement between AIMD simulation and spectroscopic data (e.g., Brugger et al. 2007; Sherman 2007; Fulton et al. 2012; Mei et al. 2013). Reviewing the topic of speciation for the broad diversity of species found in geothermal solutions is beyond the scope of this paper. However, some additional discussion with examples of measured and calculated speciation are given by Bénézeth et al. (2013, this volume).

EFFECTS OF TEMPERATURE, PRESSURE/DENSITY, AND CONCENTRATION ON THE HYDRATION OF IONS IN SOLUTION

Understanding the solution "structure" as a function of temperature, pressure, and composition will likely be the key to future equation of state models since the proportions of different energetic contributions to the thermodynamic properties of the solution change with these parameters. On a molecular level, solvent-solvent, solute-solvent, and solute-solute interactions have different strengths, act over different length scales, and will react differently to the effects of temperature, pressure and concentration. The competition between them will ultimately determine the variation of thermodynamic properties with these parameters.

Increasing temperature will enhance the kinetic energy of the particles that comprise a solution, allowing them to "escape" from bonded configurations with other particles more easily. Whether a significant fraction of bonds can be broken by the thermal effect depends on the bond strength. The bond strength can simplistically be visualized by the depth of the potential minimum in Figure 2, and kinetic energy would allow a particle to "climb up" the tail (the more kinetic energy, the higher and more distant). As a particle interacts simultaneously with many other particles the overall potential energy surface will be much more complex that the simple one-dimensional function in Figure 2 and the particle may eventually become detached from the particle that it was bonded to. At the same time, higher kinetic energy causes particles to collide more frequently, increasing the chance for exchange reactions or, in simple words, jumps between different potential minima. The higher the kinetic energy the less time a given particle will spend in these minima or be "bonded." This is nicely seen in the residence times of water molecules in the hydration shell of ions (for example, for water in the first hydration shell of the Na^+ ion the residence time at ambient conditions is 26 ps and decreases to less than 3 ps at near-critical temperatures (Driesner et al. 1998)).

Increasing pressure will compress the solution, leading to smaller inter-particle distances. These, in turn, lead to stronger particle-particle interactions, typically with a rapid increase of repulsive components (Fig. 2). Extreme pressure can lead to strong changes in the hydrogen bond geometry between water molecules to optimize the packing density.

Increasing solute concentration will naturally increase the contribution of solute-solvent and solute-solute contributions to bulk thermodynamic properties but at the same time disrupts the water network as smaller and smaller regions of "bulk water" exist, leading to similar semantic problems in defining different species than those discussed above for the definition of ion pairs. For example, assuming a fully dissociated 1:1 electrolyte and considering typical hydration numbers around 6-7 per ion all water would be bound in hydration shells at a concentration of ca. 4 molal. If the second shells are included (typically on the order of 20 water molecules), then all water in a ca. 1 molal solution would be located in hydration shells and no bulk solvent would be present.

For many years, knowledge about the interaction between solutes and hydration shell waters has been obtained from various spectroscopic techniques, namely from Raman and infrared techniques. While these methods allow insights into the nature and strength of bonds and sometimes provide constraints on the number of water molecules in the hydration shell, they generally do not provide information about the actual hydration shell geometry. However, in the last two decades, new experimental and simulation methods have provided fundamental insights into hydration shell geometries and how these change as a function of temperature, pressure, and concentration. The main experimental methods are Neutron Diffraction with Isotopic Substitution (NDIS, e.g. Enderby 1995), and various X-ray absorption spectroscopic methods (XAS), namely Extended X-Ray Absorption Fine Structure Spectroscopy (EXAFS, e.g., Ferlat et al. 2005). These two experimental approaches are complementary in what they can probe but have rarely been combined (e.g. Bowron 2009). NDIS can provide important information about the bulk water structure but has often required high solute concentrations of several molal when the contribution of hydration shells to the diffraction pattern is to be evaluated (Enderby 1995; Enderby and Neilson 1981). More recent experiments were able to explore aqueous solutions at lower concentrations down to 1 molal or below (Botti et al. 2003, 2004; Mancinelli et al. 2007a, b). Furthermore, in the most typical experimental setups, NDIS will average the contribution of hydration shells of anions and cations although experiments with isotopic substitution of the ions may help to obtain more selective information. EXAFS, in contrast, is mostly insensitive to the effect of bulk water but can provide detailed information about the local environment around a solute particle and is selective with respect to the type of solute particle, i.e., anion and cation hydration shells can be studied separately (e.g., Ferlat et al. 2001; Seward et al. 2002; Filipponi et al. 2003; Dang et al. 2006; Fulton et al. 2006, 2010; Migliorati et al. 2009). For both experimental approaches, advancements in experimental setups, combined with novel methods for inverting the raw experimental data into structural information have provided unprecedented information on the molecular level that will benefit the development of new equations of state. However, the range of solutes that have been studied and the ranges of temperature, pressure and concentrations over which each solute has been studied are still rather limited. Detailed insights, complementary to the experimental data, have come from molecular simulation approaches. In particular, classical molecular dynamics simulation techniques (MD) have been invoked since the early 1990s to study changes in water structure and ion hydrations from ambient to supercritical conditions (e.g., Driesner et al. 1998; Chialvo et al. 1999a; Driesner and Cummings 1999; Chialvo et al. 2001; Ferlat et al. 2001; Sherman and Collings 2002; Sherman 2007).

An exciting methodological advance since the mid-1990s (and still far from the end of its development) has been the adaptation of molecular simulation methods for the direct interpretation of spectral data. Early X-ray absorption studies used methods for ordered, solid compounds to derive information about the local configuration around ions in solution. First comparisons between synthetic spectra computed from averaged configurations from molecular dynamics simulations indicated sensitivity to both the dynamics of the system and to what would have to be included in the refinement to find a best fit (Palmer et al. 1996; Ferlat et al. 2001). It became clear that a single local configuration as obtained from conventional data processing may give a somewhat misleading structural interpretation of the signal (Fig. 7) (Ferlat et al. 2001). Rather, performing structural refinements on a number of configurations derived from MD can actually give much better insights (Ferlat et al. 2005). At about the same time, a controversy between the molecular simulation and neutron diffraction communities about hydrogen bonding and water structure under supercritical conditions indicated that the then conventional way of neutron diffraction data processing was insufficient for these highly dynamic systems as well (see Chialvo and Cummings 1999). As a constructive outcome,

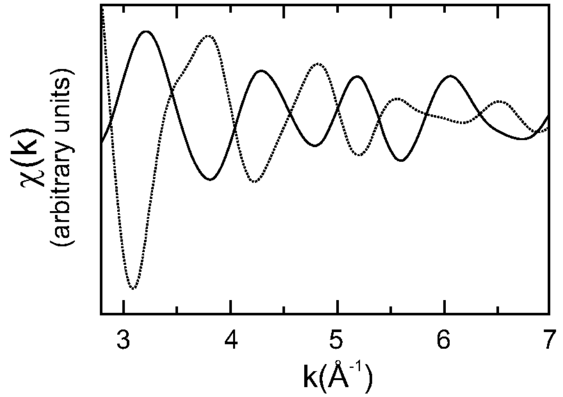

Figure 7. EXAFS spectra for the Br^- ion in supercritical water computed from two different snapshots of a molecular dynamics simulation (modified from Ferlat et al. 2001). The strong difference between the two spectra indicates that the hydration structure is highly transient and that representing it by a single static interpretation of an experimental EXAFS spectrum may be misleading.

methods were developed in which, in an iterative procedure of synthetic spectra computation from simulated configurations and comparison to the measured ones, the molecular simulation model systems are refined until the experimental data can precisely be reproduced. For example, neutron scattering experiments are now often interpreted with the empirical structure refinement method (EPSR, Soper 2012), in which a Monte Carlo simulation approach is used to generate configurations at the same density as the experiment, and using classical models of the water molecule. In the course of the refinement, the classical potential acting between the molecules is allowed to vary and its parameters are refined until no further improvement in representing the experimental spectra is reached. Using the refined potentials, an average solution structure can be obtained by standard Monte Carlo simulations. Recently, it has been shown that the method can be used to refine structural models by simultaneously using complementary spectroscopic data (neutron diffraction and EXAFS) obtained under identical conditions (Bowron 2009).

In spite of the apparent success of the simulation-aided structural interpretation methods, severe challenges still exist. Namely, (1) different spectroscopic methods probe different scales and, hence, an excellent representation of short-range information may not necessarily provide a correct information beyond a first hydration shell, (2) the signals to be fitted by the simulation step may be dominated by some partial contributions that are insufficient to constrain the full structure, and (3) non-uniqueness may arise from the fact that most spectroscopic methods measure a time-averaged signal that may can be interpreted as a mix of different sets of simulated instantaneous configurations, none of which may accurately represent the real solution.

Temperature, pressure and concentration effects on the of hydration shell structure

The hydration shells of cations and anions behave differently with increasing temperature: cation hydration shells tend to contract slightly while anion hydration shells tend to expand (e.g., Seward and Driesner 2004). The hydration shell of cations generally remains a well-developed feature even at high temperature and the number of water molecules in the first hydration shell can remain nearly constant or decrease somewhat (weakly bound cation hydration shells). The first hydration shell of anions appears to become less well-developed with increasing temperature (e.g., Driesner et al. 1998; Driesner and Cummings 2000). In fact, the definition of the hydration shell and the calculation of hydration numbers may become ambiguous (Driesner and Cummings 2000).

The interpretation of these effects is non-trivial as the experimental conditions were typically chosen such that the water density changed considerably (towards lower values) with the increasing temperature. Hence, an unknown portion of the observed trends may simply reflect density effects rather than the actual temperature effects. In the lower density, high temperature solutions the number of bulk water molecules interacting with the hydration shell water molecules would be less and, hence, in a simplistic picture the hydration shell water molecules would experience a weaker force attracting them away from the ion. On the other hand, at high temperatures, the hydrogen bonding network in water is less structured due to the thermal movements of water molecules. The interaction between hydration shell waters and the bulk solvent water is expected to become less, again imposing a weaker "restoring force" that tries to attract the hydration shell water molecules away from the ion (Mayanovic et al. 2003). Yet another contribution may arise from a reduction of dielectric screening: as the dielectric permittivity of water decreases with temperature, its reducing effect on the electrostatic interactions between hydration shell water molecules and the ion would decrease, allowing them to approach each other more closely. None of these explanations is satisfactory as one would expect similar behavior then for anion hydration shells, which is not the case (see below). As the effects can also be seen in molecular simulation (Driesner et al. 1998; Driesner and Cummings 1999) it is unlikely that they are a mere artifact of the EXAFS data analysis. The temperature dependence therefore still lacks a quantitative physical explanation.

Studies that systematically explore the change of solution structure with pressure are rather scarce and have mostly addressed conditions at lower temperatures. By means of x-ray absorption spectroscopy, Filipponi et al. (2003) investigated the pressure dependence of ion hydration in an aqueous 0.92 *m* RbBr solution at three different pressure-temperature points near the melting curves of ice-I, -VI and -VII. They saw no significant change in hydration shell structures to 0.2 GPa. Interestingly, although a further increase in pressure leads to a compression of the hydration shell as indicated by the peak position of the respective $g(r)$, the hydration numbers appear to remain nearly constant up to the highest pressure of 2.8 GPa. Filipponi et al. (2003) interpret this as being accommodated by an increase in orientational disorder in the hydration shells that becomes significant at about 0.5-1 GPa, in line with more recent observations that the pure water structure experiences changes from "low density" to "high density" configurations at comparable pressures.

Systematic studies of hydration changes with concentration are equally rare and, again, mostly restricted to low temperatures. Mancinelli et al. (2007a,b) performed a neutron diffraction study on NaCl and KCl solutions at ambient conditions and for concentrations from 0.67 to 5.5 molal. The spectra were interpreted by the EPSR method described above. The hydration shells of both cations appear to be rather insensitive to increasing concentration whereas significant effects are seen for the chloride hydration shell. Some insight has been gained from simulation studies (e.g., Driesner et al. 1998; Sherman and Collings 2002) but a comprehensive picture is still lacking.

In spite of these experimental and simulation advances and the new results and insights obtained from them our knowledge about the systematic dependence of hydration on temperature, pressure and concentration is still highly incomplete. This is due to the fact that the number of different solutes that were studied is quite limited and has a strong bias toward alkali and alkali earth halides (namely, RbBr has been studied intensely as it provides good X-ray spectroscopic response) and that for any given solute the range of conditions studied has remained rather small (as experiments are quite time-consuming to perform). Any developments of new thermodynamic models and equations of state will therefore have to work with a rather limited and patchy set of experimental data. Nevertheless, theoretical insights obtained over the last two decades and reviewed in the next section may allow parameterizing new models with much fewer parameters as they appear to be able to assign much of the non-linearity near the critical point to water properties, the temperature and pressure dependencies of which are known with high accuracy.

FLUID THERMODYNAMICS ON THE MACROSCOPIC AND MOLECULAR SCALES IN THE CRITICAL AND SUPERCRITICAL REGIONS

An explanation of the divergence of derivative thermodynamic properties near the critical point

The divergence of derivative thermodynamic properties such as heat capacities, partial molar volumes etc. has been the major challenge in the development of equations of state for aqueous solutes that are valid over the whole range of temperatures and pressures encountered in the earth's crust. As outlined in the introduction, equations of state that integrate such derivative properties to arrive at an expression for free energies or chemical potentials heavily rely on the accuracy with which the temperature and pressure dependence of the derivative properties is represented mathematically. Small errors in the mathematical representation can lead to large errors upon integration, and the best approach for finding a good mathematical representation remained enigmatic until more recent theoretical studies demonstrated that there is nothing magical about the near-critical divergence of solute thermodynamic properties. Rather, the divergence reflects the extrema in solvent compressibility near the critical point. This is best illustrated (e.g., Levelt-Sengers et al. 1992) for the partial molar volume of a solute, $\bar{V}_{solute}$, which is defined as

$$\bar{V}_{solute} = V_{solution} \quad \left(\frac{\partial V_{solu+tion}}{\partial X_{solute}}\right)_{PT} \tag{20}$$

Where $V_{solution}$ is the molar volume of the solution and X_{solute} is the mole fraction of the solute in the solution. Subscripts at the partial derivative expression indicate the state variables that are constant when taking the derivative. A simple chain rule expansion of the last term results in

$$\bar{V}_{solute} = V_{solution} \quad \left(\frac{\partial V_{solution}}{\partial P}\right)_{TX}\left(\frac{\partial P}{\partial X}\right)_{VT} \tag{21}$$

which can be re-written in terms of the solution's isothermal compressibility, $\kappa_{solution}$:

$$\bar{V}_{solute} = V_{solution} \quad V_{solution} + \quad {}_{solution}\left(\kappa\frac{\partial P}{\partial X}\right)_{VT} = V_{solution}\left(1 \quad {}_{solution} + \left(\kappa\frac{\partial P}{\partial X}\right)_{VT}\right) \tag{22}$$

This relation is completely general, irrespective of the nature of the solute (neutral species or ions, volatile or non-volatile) and applies to all concentrations. In the limit of a single solute at infinite dilution and for water as the solvent, this leads to

$$\bar{V}_{solute,\infty} = V_{water}\left(1 \quad {}_{water}\left(+\kappa\frac{\partial P}{\partial X}\right)_{VT}\right) \tag{23}$$

The term $(\partial P/\partial X)_{VT}$ is called the Krichevskii parameter and is believed to be a finite, well-behaved property at all temperature-pressure conditions including the critical point, and to reflect short-ranged, molecular-scale solute-solvent interactions. The actual divergence can therefore only come from the solvent compressibility, i.e., κ_T. Similar expressions can be derived for other diverging derivative properties, and in all of them the critical divergence can be shown to result from κ_{water}. Since the properties of water are known very accurately, this opens a chance for revised equations of state that can treat even the near-critical region. Therefore, the crucial task in the development of new solute equations of state is to find ways of parameterizing the Krichevskii parameter or related expressions.

The molecular-scale picture behind near-critical divergence

The high solvent compressibility in a near-critical fluid finds its expression also in the radial distribution function. While the short-ranged structuring remains qualitatively similar to non-critical conditions, a long tail with *g*(*r*) values > 1 develops that asymptotically approaches 1 (Fig. 8). This tail is the longer the closer the conditions are to the critical point and reflects a phenomenon often referred to as "critical clustering." This was sometimes interpreted as an increasingly longer-ranged attractive force that a solute exerts on solvent molecules when approaching the critical point. However, it is rather the molecular-scale expression of the relations between the well-behaved solute-solvent contribution and the diverging solvent compressibility contribution implied by Equations (22) and (23). A similar tail evolves in the *g*(*r*) of the pure solvent, reflecting molecular-scale density fluctuations in a near-critical fluid and demonstrating that "critical clustering" rather is a property of the solvent than an increase in solute-solvent interaction. Near the critical point the particle density is strongly varying in space and time, forming liquid-like and gas-like regions next to each other. As more particles are located in the denser regions, these provide an above-average contribution to the *g*(*r*), creating the long tail. Ions will also preferable reside in denser regions.

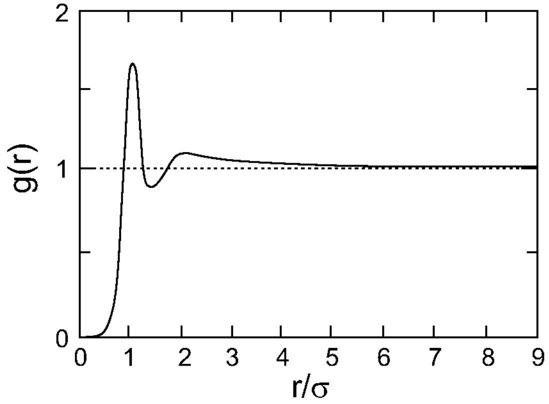

Figure 8. Radial distribution function *g*(*r*) for a near-critical Lennard-Jones fluid (schematic, modified from Levelt Sengers 1994). For small *r* the short-ranged interactions cause structuring seen as maxima and minima in the *g*(*r*) while at larger *r* the *g*(*r*) displays a slowly decaying long-ranged "tail".

In a series of papers, Chialvo and co-workers (Chialvo and Cummings 1994, 1995; Chialvo et al. 1999a,b, 1996, 2001) worked out how the macroscopic findings about the Krichevskii parameter and the effect of the solvent's compressibility are related to the molecular-scale interactions between solute and solvent, namely the effect of solvation/hydration. Their solvation formalism invokes a concept in which the solute-solvent interactions cause local perturbations to the solvent structure and where the solvent's compressibility then allows the perturbation to propagate across the system. In a phenomenological way it can be stated that the solvent's compressibility amplifies the local solute-solvent interactions.

Chialvo et al. developed their formalism from a conceptual process in which solvent particles are converted to solute particles and worked out how the resulting short-ranged and long-ranged contributions may be defined and separated. An important piece in the formulation is the definition of an "excess number" of solvent molecules, N_{ex}, that is different from the conventional coordination number that was discussed earlier. Rather than counting the number of water molecules that reside within a certain distance from the solute particle, the formalism defines N_{ex} as "the number of solvent molecules around a species in solution, in excess (augmentation or depletion) to that number around any solvent molecule" in the pure solvent at the same pressure and temperature, "i.e., the case of a solute in an ideal solution" (Chialvo et al. 1999b, p.1080). Formally, this is given by

$$N_{ex} = 4\pi\rho\int_{0}^{\infty}\left[g^{\infty}_{solute-solvent} - g^{0}_{solvent-solvent}\right]r^{2}dr \tag{24}$$

where $g^{\infty}_{solute-solvent}$ refers to the solute-solvent radial distribution at infinite dilution and $g^{0}_{solvent-solvent}$ to the solvent-solvent radial distribution function for the pure solvent at the same conditions.

From the definition of N_{ex} there is a straightforward relation with the macroscopic partial molar volume:

$$N_{ex} = 1 \quad \rho - \bar{V}_{solute} \tag{25}$$

By comparison with Equation (23) this implies that

$$N_{ex} = -\kappa\left(\frac{\partial P}{\partial X}\right)_{VT} \tag{26}$$

If accurate partial molar volumes are available from experiments, the Krichevskii parameter can be derived from them. The sign of the Krichevskii determines whether the divergence at the critical point will be to $+\infty$ or $-\infty$, and this is clearly related to a negative or positive N_{ex}, respectively. Divergence of the partial molar volume at infinite dilution to $-\infty$ is typical for non-volatile solutes and implies that the solute tends to cause a positive N_{ex}, i.e., the local density perturbation creates a locally denser structure compared to the pure solvent while the opposite applies for volatile solutes. Equation (26) applies for a general solute and, after some straightforward manipulations that take into account the electroneutrality conditions, the formalism can also be applied to the individual contributions of ions to the thermodynamic properties of aqueous electrolytes (Chialvo et al. 1999b).

Figure 9 shows an example of this formalism, applied to a molecular dynamics simulation of a dilute NaCl solution at a near-critical temperature of 643 K and a density of 0.7 g cm^{-3} (Driesner 2010). The *NVT* molecular dynamics simulations were done for 1 Na^{+} plus 1 Cl^{-} ion in 16382 SPCE water molecules (i.e., a 0.0033 molal NaCl solution). Figure 9A shows the different $g(r)$ that indicate that the hydration shell around the Na^{+} ion is located at the shortest distance, followed by the hydration shell of a water molecule in pure water at somewhat larger distances, and that the hydration shell of the Cl^{-} ion indicates an expansion of the structure at least at short distances . The local solvent density effects caused by the ions can be measured by integrating these $g(r)$ and computing N_{ex} according to Equation (24), which results in the curves seen in Figure 9B. It can be seen that Na^{+} induces a denser solution structure with N_{ex} being positive (in line with the position of the first peak in the $g(r)$ being located at a shorter distance than that for pure water) at all r while there is an initial depletion (negative N_{ex}) around the Cl^{-} ion (due to the ion having a somewhat larger effective radius than a water molecule and thus shifting the first peak in the Cl^{-}-water $g(r)$ to larger distances). However, N_{ex} then rapidly changes to positive values at all distances beyond ca. 0.35 nm, i.e., also the Cl^{-} ion induces an overall denser solution structure compared to pure water at the same conditions. The short-range oscillations in the N_{ex} curves reflect the differences in the local structuring seen in Figure 9A and rapidly die out after ca. 3 layers of water molecules. Figures 9D-F provide a schematic visualization of the structural effects.

Using Equation (25) the N_{ex} curves can be converted to the partial molar volumes as a function of r (Fig. 9C). Adding up the resulting contributions from the two ions as they converge at larger r results in a value of -46.8 cm^{3} mol^{-1}. This is difficult to compare directly to values for real NaCl solutions in the infinite dilution limit. The SOCW model of Sedlbauer et al. (2000) is probably the most accurate predictive equation of state in this temperature-pressure region and predicts -115 cm^{3} mol^{-1} at the simulated temperature and pressure. However, when temperature and density are taken in reduced coordinates (i.e., T/T_{crit} and ρ/r_{crit}), the

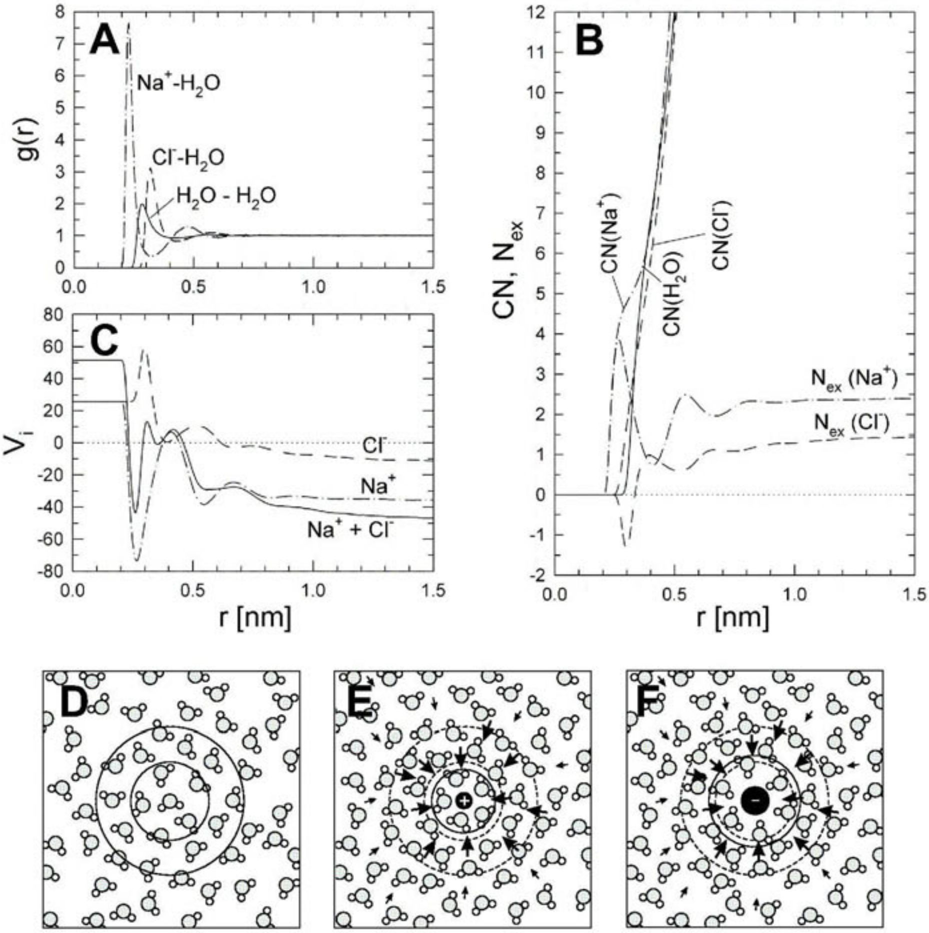

Figure 9. The molecular-scale interpretation of partial molar volumes for the example of a molecular dynamics simulation of a dilute NaCl solution (1 NaCl per 16382 SPCE water molecules at 643 K and 0.7 g cm^{-3}). (A) Radial distribution functions $g(r)$. The key point here is that the first hydration shell of the Na$^+$ ion is at shorter distances than that of a water molecule, which in turn is at shorter distances than that of a Cl$^-$ ion. (B) Running coordination numbers CN (= radially integrated $g(r)$) and excess hydration number N_{ex}, obtained by forming the differences $N_{ex}(\text{Na}^+) = CN(\text{Na}^+) - CN(\text{H}_2\text{O})$ and $N_{ex}(\text{Cl}^-) = CN(\text{Cl}^-) - CN(\text{H}_2\text{O})$. Notice how the oscillations in the N_{ex} curves at small r relate to the differences in the CN curves, which in turn reflect the local density variations at different r seen in the $g(r)$ curves in A. N_{ex} seems to converge at relatively short r for this relatively dense solution (and would converge at large r for near-critical solutions). (C) Partial molar volume contributions of the two ions and total partial molar volume, computed from the N_{ex} curves using Equation (25). Notice that the value of the partial molar volume is established at rather short r while it would converge only at increasingly larger r when approaching the critical point, reflecting the increasing contributions of the solvent compressibility-driven divergence (e.g., Eqn. 27). These relations are thought to be a key for the development of improved equations of state for geothermal fluids when engineering them in terms of conceptual physical models that root in molecular-scale features of the fluids. (D) Schematic picture of molecular-scale structure of water at near-critical conditions. Local density varies strongly and the extent of the first and second hydration shells in a denser region is indicated by circles. (E) If a Na$^+$ ion is present it will attract its nearest neighbor water molecules (big arrows) making the local water density higher than in the pure water case shown in D. The limit of the first hydration shell (solid circle) is at shorter distances compared to pure water (dashed circles indicate the positions in D). The local density perturbation propagates into the compressible solvent (small arrows). (F) Around a Cl$^-$ ion the first hydration shell is somewhat expanded but due to the attractive forces of the ion there is again a local density increase that propagates into the compressible solvent.

agreement is much better. Large series of simulations of the PVT properties of SPCE water were fitted with equations of state that indicate a critical temperature of ca. 640.25 K and a critical density of ca. 0.276 g cm^{-3} (Plugatyr and Svishchev 2009) to 640 K and 0.29 g cm^{-3} (Guissani and Guillot 1993). Hence, using the corresponding states principle, the simulated state should be equivalent to ca. 650 K and 0.78 to 0.82 g cm^{-3} for real water. For this parameter range the SOCW model predicts partial molar volumes between –49.9 cm^3 mol^{-1} and –32.2 cm^3 mol^{-1}. The molecular dynamics simulations show positive N_{ex} for both ions, i.e., both ion contributions to the partial molar volume are of negative sign (–35.6 cm^3 mol^{-1} for Na$^+$ and –11.2 cm^3 mol^{-1} for Cl$^-$). This seems physically more realistic than the contributions computed with the SOCW model (+29.2 for Na$^+$ and –61.4 for Cl$^-$ for the last value of –32.2 cm^3 mol^{-1} given above); however, this mostly reflects the dilemma that the parameterization of equations of state depends on experimental data on bulk electrolytes and therefore the choice of some artificial convention to assign single ion properties. Equations of state will typically be much more accurate than simulations, which provide a much better physical insight but lack accuracy due to the simplifications in representing the details of molecular interactions.

Although the concept of using N_{ex} is intuitive and has a straightforward meaning, it still refers to a bulk number and does not separate the finite solvation contribution and the diverging compressibility-driven contribution. Chialvo and co-workers employed the statistical-mechanical concepts of direct and total correlation function integrals (DCFI and TCFI) to define a finite, solvation and a diverging, compressibility-driven part (e.g., Chialvo and Cummings 1995; Chialvo et al. 1999b). The choice for this convention is based on the fact that DCFI are finite even at the solvent's critical point and is therefore—mathematically—a natural choice for defining the two contributions. Unfortunately, the physical meaning of DCFI is enigmatic (Ben-Naim 2006, p. 309) and it cannot directly be related to experimentally accessible information of the local solvent structure around a solute (e.g., via EXAFS or related spectroscopic methods). Nevertheless, the convention provides mathematical relations that may be useful in exploring possible correlation schemes or equation of state formulations for solutes. For example, the solvation and compressibility-driven contributions to N_{ex} would simply be obtained by multiplying the (bulk) Krichevskii parameter with the ideal gas and residual contributions to the solvent's compressibility:

$$- \; N_{ex} = \kappa\left(\frac{\partial P}{\partial X}\right)_{VT} \qquad \kappa^{IG}\left(\frac{\partial P}{\partial X}\right)_{VT} \qquad \kappa^{r}\left(\frac{\partial P}{\partial X}\right)_{VT} \tag{27}$$

To this end, this approach has not been tested for its ability to represent a wide variety of solutes over broad ranges of temperature and pressure although some studies that built on related concepts have demonstrated the potential for improved geochemical thermodynamic models (e.g., O'Connell et al. 1996; Plyasunov et al. 2000a,b; Sedlbauer et al. 2000; Sedlbauer and Wood 2004; Dolejš and Manning 2010). Possible correlation strategies were discussed by Chialvo et al. (2001) but remain to be explored.

POSSIBLE FUTURE ROUTES TOWARDS IMPROVED THERMODYNAMIC MODELS FOR GEOTHERMAL FLUIDS FROM AMBIENT TO SUPERCRITICAL CONDITIONS

While there seems to be some convergence of the approaches that attempt resolving the difficulties associated with the compressibility-driven contributions to near-critical thermodynamics, these theoretical advances alone do not solve the every-day problems of geochemists dealing with geothermal fluids under these conditions. There are several big tasks ahead: (1) the consolidation of the different theoretical approaches into a single thermodynamic framework that can deal with both charged and neutral solute species; (2) obtaining the experimental data in the near-critical and supercritical regions needed to parameterize such a model; (3) ideally, formulating this model such that its parameterization can build on both molecular-scale, spectroscopic information about the local solution structure and on experiments that determine macroscopic thermodynamic properties; (4) finally, identifying mathematical expressions for the temperature, pressure, and composition dependence of solute thermodynamic properties that allow robust extrapolation to experimentally unstudied conditions. The latter is particularly relevant for conditions that are experimentally difficult to handle, namely at moderate pressures between ca. 10 and 30 MPa for temperatures in excess of 350 °C.

A possible route to explore is whether some pragmatic convention can be formulated for the definition of short-ranged, finite vs. compressibility-driven contributions. As stated earlier, DCFI/TCFI-based conventions have mathematical characteristics that allow such a distinction but lack a direct interpretation in terms of measurable structural properties of a fluid. Although originally derived within such a convention, the property N_{ex} (e.g., Chialvo and Cummings 1994, 1995; Chialvo et al. 1999b) may be the most promising candidate as its physical interpretation does not rely on that convention and has a clear meaning in terms of changes in local solution density. This is pictured in Figure 9, where the local restructuring of solvent-molecules around a solute particle is visible in the $g(r)$, the resulting N_{ex}, and a cartoon representing the physical interpretation. The local, short-range perturbation is visible as an oscillatory pattern in the diagram, representing the region where the maxima and minima the solvent-solvent and ion-solvent $g(r)$ are located at different r. However, after a few molecular diameters, the $N_{ex}(r)$ curve smooths out and the remainder of the curve can probably be described by a continuum expression for the long-range propagation of the local density perturbation across the solvent. This implies that with sufficiently accurate spectroscopic information about the local $g(r)$'s over just a few molecular diameters it may be possible to derive fundamental thermodynamic information. Thinking further, this picture seems simple enough to allow future correlation schemes as a function of microscopic properties such as the effective solute particle diameter in solution. A good source for such information might be experimentally-constrained molecular simulation.

Given that classical molecular simulation tools are now sufficiently fast to provide microscopic pictures of the solution structure it is tempting to see this as the fastest route to correlation schemes by simply running numerous simulations for a broad variety of solutes under variable conditions and monitoring the trends in N_{ex}. Unfortunately, this is not straightforward because N_{ex} converges only for simulations in the $TV\mu$ ensemble while standard simulations in the NVE and NPT ensemble produce artifacts at large r (Driesner 2010) due to the isolated or closed nature of the system; i.e., the local increase or decrease in density around a solute cannot be compensated for by solvent particles entering or leaving the system. $TV\mu$ molecular simulation, however, is not a routine method for systems with ions and further methodological developments appear necessary to make this approach feasible. However, the local structural changes are probably captured sufficiently in NVE and NPT simulations; if a good theoretical framework for the long-range propagation became available the local information may therefore be sufficient. If true, one might expect that, ultimately, AIMD methods will be able to deliver the necessary information in the future at a high level of accuracy.

Although it may be premature to conclude that a theoretical framework to overcome the current limitations in modeling the near- and supercritical thermodynamics of geothermal fluids is in reach, the progress that has been made over the last two decades or so in understanding the problems from both a molecular and macroscopic perspective is highly encouraging. As this has gone along with major advances in experimental, spectroscopic and numerical simulation techniques, further progress grounded in data of actual systems can be expected. It seems likely that the integration of the various approaches will be the key for success.

REFERENCES

Akinfiev NN, Diamond LW (2003) Thermodynamic description of aqueous nonelectrolytes at infinite dilution over a wide range of state parameters. Geochim Cosmochim Acta 67:613-629

Allen MP, Tildesley DJ (1987) Computer Simulation of Liquids. Oxford University Press, Oxford

Archibald SM, Migdisov AA, Williams-Jones AE (2001) The stability of Au-chloride complexes in water vapor at elevated temperatures and pressures. Geochim Cosmochim Acta 65:4413-4423

Archibald SM, Migdisov AA, Williams-Jones AE (2002) An experimental study of the stability of copper chloride complexes in water vapor at elevated temperatures and pressures. Geochim Cosmochim Acta 66:1611-1619

Bankura A, Carnevale V, Klein ML (2013) Hydration structure of salt solutions from ab initio molecular dynamics. J Chem Phys 138:014501

Bénézeth P, Stefánsson A, Gautier Q, Schott J (2013) Mineral solubility and aqueous speciation under hydrothermal conditions to 300 °C – the carbonate system as an example. Rev Mineral Geochem 76:81-133

Ben-Naim A (2006) Molecular Theroy of Solutions. Oxford University Press, Oxford, New York

Bopp P, Heinzinger K, Vogel PC (1974) Calculations of the oxygen isotope fractionation between hydration water of cations and free water. Z Naturforsch A 29:1608-1613

Born M (1920) Volumen und Hydratationswärme der Ionen. Z Phys 1:45-48

Botti A, Bruni F, Imberti S, Ricci MA, Soper AK (2004) Ions in water: The microscopic structure of a concentrated HCl solution. J Chem Phys 121:7840-7848

Botti A, Bruni F, Isopo A, Modesti G, Oliva C, Ricci MA, Senesi R, Soper AK (2003) Water structure in supercritical mixtures of water and rare gases. J Chem Phys 118:235-241

Bowron DT (2009) Comprehensive structural modelling of aqueous solutions using neutron diffraction and X-ray absorption spectroscopy. J Phys Conf Series 190:012022

Brugger J, Etschmann B, Liu W, Testemale D, Hazemann, JL, Emerich H, van Beek W, Proux O (2007) An XAS study of the structure and thermodynamics of Cu(I) chloride complexes in brines up to high temperature (400 °C, 600 bar). Geochim Cosmochim Acta 71:4920-4941

Chialvo AA, Cummings PT (1994) Solute-induced effects on the structure and thermodynamics of infinitely dilute mixtures. AIChE J 40:1558-1573

Chialvo AA, Cummings PT (1995) Near-critical phase-behavior of dilute mixtures - Comment. Mol Phys 84:41-48

Chialvo AA, Cummings PT (1999) Molecular-based modeling of water and aqueous solutions at supercritical conditions. Adv Chem Phys 109:115-205

Chialvo AA, Cummings PT, Simonson JM (2000) H_3O^+/Cl^- ion-pair formation in high-temperature aqueous solutions. J Chem Phys 113:8093-8100

Chialvo AA, Cummings PT, Simonson JM, Mesmer RE (1999a) Solvation in high-temperature electrolyte solutions. I. Hydration shell behavior from molecular simulation. J Chem Phys 110:1064-1074

Chialvo AA, Cummings PT, Simonson JM, Mesmer RE (1999b) Solvation in high-temperature electrolyte solutions. II. Some formal results. J Chem Phys 110:1075-1086

Chialvo AA, Ho PC, Palmer DA, Gruszkiewicz MS, Cummings PT, Simonson JM (2002) H_3O^+/Cl^- association in high-temperature aqueous solutions over a wide range of state conditions. A direct comparison between simulation and electrical conductance experiment. J Phys Chem B 106:2041-2046

Chialvo AA, Kalyuzhnyi YV, Cummings PT (1996) Solvation thermodynamics of gas solubility at sub- and near-critical conditions. AIChE J 42:571-584

Chialvo AA, Kusalik PG, Cummings PT, Simonson JM (2001) Solvation in high-temperature electrolyte solutions. III. Integral equation calculations and interpretation of experimental data. J Chem Phys 114:3575-3585

Chialvo AA, Simonson JM (2003) Aqueous Na^+Cl^- pair association from liquidlike to steamlike densities along near-critical isotherms. J Chem Phys 118:7921-7929

Coumou D, Driesner T, Heinrich CA (2008) The structure and dynamics of mid-ocean ridge hydrothermal systems. Science 321:1825-1828

Cygan RT, Kubicki JD (eds) (2001) Molecular Modeling Theory: Applications in the Geosciences. Reviews in Mineralogy and Geochemistry. Mineralogical Society of America.

Dang LX, Schenter GK, Glezakou VA, Fulton JL (2006) Molecular simulation analysis and X-ray absorption measurement of Ca^{2+}, K^+ and Cl^- ions in solution. J Phys Chem B 110:23644-23654

Diamond LW (2001) Review of the systematics of CO_2-H_2O fluid inclusions. Lithos 55:69-99

Dolejš D, Manning CE (2010) Thermodynamic model for mineral solubility in aqueous fluids: theory, calibration and application to model fluid-flow systems. Geofluids 10:20-40

Driesner T (2007) The system H_2O-NaCl. Part II: Correlations for molar volume, enthalpy, and isobaric heat capacity from 0 to 1000 °C, 1 to 5000 bar, and 0 to 1 X_{NaCl}. Geochim Cosmochim Acta 71:4902-4919

Driesner T (2010) Molecular-scale thermodynamics of aqueous NaCl to hydrothermal conditions. Geochim Cosmochim Acta 74:A247

Driesner T, Cummings PT (1999) Molecular simulation of the temperature- and density-dependence of ionic hydration in aqueous $SrCl_2$ solutions using rigid and flexible water models. J Chem Phys 111:5141-5149

Driesner T, Cummings PT (2000) Molecular simulation of the temperature-, density- and concentration-dependence of ion hydration shell geometry and composition: Some general trends and implictions for the interpretation of experimental results. *In*: Steam, Water, and Hydrothermal Systems: Physics and Chemistry Meeting the Needs of Industry. Tremaine PR, Hill PG, Irish DE, Balakrishnan PV (eds), NRC Press, Ottawa, p 554-561

Driesner T, Geiger S (2007) Numerical simulation of multiphase fluid flow in hydrothermal systems. Rev Mineral Geochem 65:187-212

Driesner T, Ha TK, Seward TM (2000) Oxygen and hydrogen isotope fractionation by hydration complexes of Li^+, Na^+, K^+, $Mg2^+$, F^-, Cl^-, and Br^-: A theoretical study. Geochim Cosmochim Acta 64:3007-3033

Driesner T, Heinrich CA (2007) The system H_2O-NaCl. Part I: Correlation formulae for phase relations in temperature-pressure-composition space from 0 to 1000 °C, 0 to 5000 bar, and 0 to 1 X_{NaCl}. Geochim Cosmochim Acta 71:4880-4901

Driesner T, Seward TM (2000) Experimental and simulation study of salt effects and pressure/density effects on oxygen and hydrogen stable isotope liquid-vapor fractionation for 4-5 molal aqueous NaCl and KCl solutions to 400 °C. Geochim Cosmochim Acta 64:1773-1784

Driesner T, Seward TM, Tironi IG (1998) Molecular dynamics simulation study of ionic hydration and ion association in dilute and 1 molal aqueous sodium chloride solutions from ambient to supercritical conditions. Geochim Cosmochim Acta 62:3095-3107

Elders WA, Frioleifsson GO, Zierenberg RA, Pope EC, Mortensen AK, Guomundsson A, Lowenstern JB, Marks NE, Owens L, Bird DK, Reed M, Olsen NJ, Schiffman P (2011) Origin of a rhyolite that intruded a geothermal well while drilling at the Krafla volcano, Iceland. Geology 39:231-234

Enderby JE (1995) Ion solvation via neutron-scattering. Chem Soc Rev 24:159-168

Enderby JE, Neilson GW (1981) The structure of electrolyte-solutions. Prog Phys 44:593-653

Feder HM, Taube H (1952) Ionic hydration – an isotope fractionation technique. J Chem Phys 20:1335-1336

Ferlat G, San Miguel A, Jal JF, Soetens JC, Bopp PA, Daniel I, Guillot S, Hazeman JL, Argoud R (2001) Hydration of the bromine ion in a supercritical 1:1 aqueous electrolyte. Phys Rev B 63:134202

Ferlat G, Soetens JC, San Miguel A, Bopp PA (2005) Combining extended x-ray absorption fine structure with numerical simulations for disordered systems. J Phys Condens Matter 17:S145-S157

Filipponi A, De Panfilis S, Oliva C, Ricci MA, D'Angelo P, Bowron DT (2003) Ion hydration under pressure. Phys Rev Lett 91

Frenkel D, Smit B (2002) Understanding Molecular Simulation. From Algorithms to Applications. Academic Press, San Diego

Fridleifsson GO, Elders WA (2005) The Iceland Deep Drilling Project: a search for deep unconventional geothermal resources. Geothermics 34:269-285

Fulton JL, Bylaska EJ, Bogatko S, Balasubramanian M, Cauet E, Schenter GK, Weare JH (2012) Near-quantitative agreement of model-free DFT-MD predictions with XAFS observations of the hydration structure of highly charged transition-metal ions. J Phys Chem Lett 3:2588-2593

Fulton JL, Chen YS, Heald SM, Balasubramanian M (2006) Hydration and contact ion pairing of Ca^{2+} with Cl^- in supercritical aqueous solution. J Chem Phys 125:094507

Fulton JL, Schenter GK, Baer MD, Mundy CJ, Dang LX, Balasubramanian M (2010) Probing the hydration structure of polarizable halides: a multiedge XAFS and molecular dynamics study of the iodide anion. J Phys Chem B 114:12926-12937

Grant-Taylor DF (1981) Partial molar volumes of sodium-chloride solutions at 200 bar, and at temperatures from 175° to 350 °C. J Solution Chem 10:621-630

Guissani Y, Guillot B (1993) A computer-simulation study of the liquid-vapor coexistence curve of water. J Chem Phys 98:8221-8235

Haar L, Gallagher JS, Kell GS (1984) NBS/NRC Steam Tables: Thermodynamic and Transport Properties and Computer Programs for Vapor and Liquid States of Water in SI Units. Taylor & Francis, London.

Hassan SA (2008) Computer simulation of ion cluster speciation in concentrated aqueous solutions at ambient conditions. J Phys Chem B 112:10573-10584

Hayba DO, Ingebritsen SE (1997) Multiphase groundwater flow near cooling plutons. J Geophys Res Solid Earth 102:12235-12252

Helgeson HC, Kirkham DH, Flowers GC (1981) Theoretical prediction of the thermodynamic behavior of aqueous-electrolytes at high-pressures and temperatures. 4. calculation of activity-coefficients, osmotic coefficients, and apparent molal and standard and relative partial molal properties to 600 °C and 5 kb. Am J Sci 281:1249-1516

Hill PG (1990) A unified fundamental equation for the thermodynamic properties of H_2O. J Phys Chem Ref Data 19:1233-1274

Hnedkovsky L, Wood RH, Majer V (1996) Volumes of aqueous solutions of CH_4, CO_2, H_2S, and NH_3 at temperatures from 298.15 K to 705 K and pressures to 35 MPa. J Chem Thermo 28:125-142

Horita J, Cole DR, Wesolowski DJ (1995) the activity composition relationship of oxygen and hydrogen isotopes in aqueous salt-solutions. 3. Vapor-liquid water equilibration of NaCl solutions to 350 °C. Geochim Cosmochim Acta 59:1139-1151

Johnson JW, Oelkers EH, Helgeson HC (1992) SUPCRT92 - A software package for calculating the standard molal thermodynamic properties of minerals, gases, aqueous species, and reactions from 1 bar to 5000 bar and 0 °C TO 1000 °C. Comp Geosci 18:899-947

Jupp T, Schultz A (2000) A thermodynamic explanation for black smoker temperatures. Nature 403:880-883

Levelt Sengers JMH, Harvey AH, Crovetto R, Gallagher JS (1992) Standard states, reference states and finite-concentration effects in near-critical mixtures with applications to aqueous-solutions. Fluid Phase Equilib 81:85-107

Levelt Sengers JMH (1994) Critical behavior of fluids: concepts and applications. *In*: Supercritical Fluids: Fundamentals for Application. Kiran E , Levelt Sengers JMH (eds) Kluwer Academic Publishers, p 3-38

Mancinelli R, Botti A, Bruni F, Ricci MA, Soper AK (2007a) Hydration of sodium, potassium, and chloride ions in solution and the concept of structure maker/breaker. J Phys Chem B111:13570-13577

Mancinelli R, Botti A, Bruni F, Ricci MA, Soper AK (2007b) Perturbation of water structure due to monovalent ions in solution. Phys Chem Chem Phys 9:2959-2967

Marcus Y. (2009) Effect of ions on the structure of water: structure making and breaking. Chem Rev 109:1346-1370

Marcus Y, Hefter G (2006) Ion pairing. Chem Rev 106:4585-4621

Mayanovic RA, Jayanetti S, Anderson AJ, Bassett WA, Chou IM (2003) Relaxation of the structure of simple metal ion complexes in aqueous solutions at up to supercritical conditions. J Chem Phys 118:719-727

McQuarrie (2000) Statistical Mechanics. University Science Books Sausalito.

Mei Y, Sherman DM, Liu WH, Brugger J (2013) *Ab initio* molecular dynamics simulation and free energy exploration of copper(I) complexation by chloride and bisulfide in hydrothermal fluids. Geochim Cosmochim Acta 102:45-64

Migliorati V, Chillemi G, Mancini G, Zitolo A, Tatoli S, Filipponi A, D'Angelo P (2009) Ion hydration in high-density water. J Phys Conf Series 190:012057

O'Connell JP (1971) Thermodynamic properties of solutions based on correlation functions. Mol Phys 20:27-33

O'Connell JP, Sharygin AV, Wood RH (1996) Infinite dilution partial molar volumes of aqueous solutes over wide ranges of conditions. Ind Eng Chem Res 35:2808-2812

Oelkers EH, Helgeson HC (1993) Multiple ion association in supercritical aqueous-solutions of single electrolytes. Science 261:888-891

Palmer BJ, Pfund DM, Fulton JL (1996) Direct modeling of EXAFS spectra from molecular dynamics simulations. J Phys Chem 100:13393-13398

Plugatyr A, Svishchev IM (2009) Accurate thermodynamic and dielectric equations of state for high-temperature simulated water. Fluid Phase Equilib 277:145-151

Plyasunov AV, O'Connell JP, Wood RH (2000a) Infinite dilution partial molar properties of aqueous solutions of nonelectrolytes. I. Equations for partial molar volumes at infinite dilution and standard thermodynamic functions of hydration of volatile nonelectrolytes over wide ranges of conditions. Geochim Cosmochim Acta 64:495-512

Plyasunov AV, O'Connell JP, Wood RH, Shock EL (2000b) Infinite dilution partial molar properties of aqueous solutions of nonelectrolytes. II. Equations for the standard thermodynamic functions of hydration of volatile nonelectrolytes over wide ranges of conditions including subcritical temperatures. Geochim Cosmochim Acta 64:2779-2795

Rempel KU, Williams-Jones AE, Migdisov AA (2008) The solubility of molybdenum dioxide and trioxide in HCl-bearing water vapour at 350 °C and pressures up to 160 bars. Geochim Cosmochim Acta 72:3074-3083

Sedlbauer J, O'Connell JP, Wood RH (2000) A new equation of state for correlation and prediction of standard molal thermodynamic properties of aqueous species at high temperatures and pressures. Chem Geol 163:43-63

Sedlbauer J, Wood RH (2004) Thermodynamic properties of dilute NaCl(aq) solutions near the critical point of water. J Phys Chem B 108:11838-11849

Seward TM, Driesner T (2004) Hydrothermal solution structure: experiments and computer simulations. *In*: Aqueous Systems at Elevated Temperatures and Pressures: Physical Chemistry in Water, Steam and Hydrothermal Solutions. Palmer DA, Fernandez-Prini R, Harvey AH (eds) Elsevier, p 149-182

Seward TM, Henderson CMB, Charnock JM (2002) An EXAFS study of Pd^{2+} solvation in aqueous media and chloride complexing to 340 °C at saturated vapour pressure. Geochim Cosmochim Acta 66:A699

Sherman DM (2007) Complexation of Cu^+ in hydrothermal NaCl brines: *Ab initio* molecular dynamics and energetics. Geochim Cosmochim Acta 71:714-722

Sherman DM, Collings MD (2002) Ion association in concentrated NaCl brines from ambient to supercritical conditions: results from classical molecular dynamics simulations. Geochem Trans 3:102-107

Shock EL, Oelkers EH, Johnson JW, Sverjensky DA, Helgeson HC (1992) Calculation of the thermodynamic properties of aqueous species at high-pressures and temperatures - effective electrostatic radii, dissociation-constants and standard partial molal properties to 1000 °C and 5 kbar. J Chem Soc-Faraday Trans 88:803-826

Sofer Z, Gat JR (1972) Activities and concentrations of O-18 in concentrated aqueous salt solutions - analytical and geophysical implications. Earth Planet Sci Lett 15:232-238

Soper AK (2012) Computer simulation as a tool for the interpretation of total scattering data from glasses and liquids. Mol Simulat 38:1171-1185

Tanger JC, Helgeson HC (1988) Calculation of the thermodynamic and transport-properties of aqueous species at high-pressures and temperatures - revised equations of state for the standard partial molal properties of ions and electrolytes. Am J Sci 288:19-98

Taube H (1954) Use of oxygen isotope effects in the study of hydration of ions. J Phys Chem 58:523-528

Tuckerman ME (2010) Statistical Mechanics: Theory and Molecular Simulation. Oxford University Press, Oxford.

Wagner W, Pruß A (2002) The IAPWS formulation 1995 for the thermodynamic properties of ordinary water substance for general and scientific use. J Phys Chem Ref Data 31:387-535

Williams-Jones AE, Heinrich CA (2005) 100th Anniversary special paper: Vapor transport of metals and the formation of magmatic-hydrothermal ore deposits. Econ Geol 100:1287-1312

Reviews in Mineralogy & Geochemistry
Vol. 76 pp. 35-79, 2013
Copyright © Mineralogical Society of America

Thermodynamics of Aqueous Species at High Temperatures and Pressures: Equations of State and Transport Theory

David Dolejš

Institute of Petrology and Structural Geology
Charles University
128 43 Praha 2, Czech Republic

david.dolejs@natur.cuni.cz

INTRODUCTION

Aqueous fluids are important and essential mass-transfer agents in the Earth's crust and mantle. They are produced by sediment compaction, metamorphic devolatilization and magmatic activity in a variety of settings, including continental and accretionary orogens, subduction zones with magmatic arcs as well as by hydrothermal systems at mid-oceanic ridges and sea floor (Wilson et al. 2000; Kerrick and Connolly 2001; Manning 2004; Breeding et al. 2004; Palandri and Reed 2004; Bucher and Stober 2010). The fluid-mediated mass transfer produces specific major- and trace-element and isotopic patterns in source regions of mantle melting and it imparts characteristic geochemical signatures to magmas in various geodynamic settings, which are used to interpret geodynamic processes (Baier et al. 2008; Beinlich et al. 2010; Mysen 2010). At the final stages of magmatic activity, aqueous fluids are released as a single supercritical phase, a high-density saline brine, or a low-density vapor, each of which can play different roles in hydrothermal and geothermal processes, ore formation or by providing local input to the atmosphere (Yardley 2005; Audétat et al. 2008). Similarly, mass transport by aqueous fluids has now been detected in a number of high-grade metamorphic rocks, providing evidence for flow patterns and chemical changes during devolatilization reactions that accompany metamorphism during plate convergence (Gorman et al. 2006; Zack and John 2007; John et al. 2008). The efficiency of these fluid-mediated interactions, their time scales and implications for fluid flow patterns, have only started to be explored by applications of transport theories (e.g., Konrad-Schmolke et al. 2011).

The mobility and transport of inorganic and organic solutes in aqueous fluids is manifested by alteration or veining, distinct element depletion-enrichment patterns or isotopic disturbances (e.g., Coltorti and Grégoire 2009; Yardley 2013). In addition, high buoyancy and low viscosity of aqueous fluid in a rock environment make their flow universally viable and efficient. The impact of many fluid-mediated processes is promoted by high time-integrated fluid fluxes, 10^1-10^6 $m_f^3 m_r^{-2}$, inferred for diffuse and focused fluid flow through the lithosphere (Ague 2003). In contrast to silicate magmas, fluids are only rarely preserved in their pathways and much of the evidence, including chemical composition, is often reconstructed indirectly from mineral mode and chemical or isotopic variations. This link is provided by thermodynamic equations of state and datasets, which play a central role in interpreting or predicting the fluid-melt-mineral interactions during the reactive fluid flow.

In geological applications, the thermodynamic properties of aqueous solutes are almost exclusively based on the Helgeson-Kirkham-Flowers electrostatic equation of state (Helgeson et al. 1981; Tanger and Helgeson 1988; Shock et al. 1992). Although this model is only partially

1529-6466/13/0076-0003$05.00 http://dx.doi.org/10.2138/rmg.2013.76.3

applicable near the critical point of water, it cannot be used with low-density fluids, and its extrapolation to very high temperatures and pressures is limited owing to lack of data on the dielectric constant of aqueous solvent, it has become a widespread tool for its extensive dataset, which covers numerous inorganic and organic solutes as well as nonelectrolytes (Johnson et al. 1992; Oelkers et al. 1995). By contrast, aqueous physical chemistry now offers a variety of approaches to the thermodynamic properties of aqueous solutes that are applicable in subcritical, near-critical and supercritical conditions, including liquid-vapor partitioning, and are based on electrostatic, macroscopic volumetric and/or microscopic statistical-mechanical arguments (Palmer et al. 2004; Sedlbauer 2008).

In this contribution, we review the state of the art of the thermodynamics of aqueous solutes. The presentation starts with conversion relationships that apply to concentrations, standard thermodynamic properties and activity coefficients related to various standard states. Scales for the thermodynamic state functions are subject to several conventions and we address ambiguities or inconsistencies that may arise in certain portions of thermochemical cycles. The presentation of standard thermodynamic properties is intentionally divided into two sections. In the first one, the fundamental extrapolation schemes are presented and built up into correlation relationships using density or electrostatic terms. These are not self-standing equations of state for they describe differences or changes in thermodynamic properties, often in homogeneous equilibria only, and they may lack the intrinsic or state-conversion terms. In the next section, approaches and derivations leading to equations of state for aqueous solutes are organized from classical macroscopic through hydration, electrostatic, and density-based models. Since various contributions may appear in a single equation of state, a brief illustration of thermochemical cycles should provide a guide towards internal consistency. The contribution concludes with a presentation of basic transport theory, aimed at linking the thermodynamic properties to the reaction progress during reactive fluid flow, extending the theory to include disequilibrium effects, and providing relationships between integrated fluid fluxes and fluid-rock ratios that continue to play a role in mass balancing in the numerical models.

CONCENTRATION SCALES AND CONVERSION RELATIONSHIPS

Concentrations of solutes in aqueous fluids are conventionally expressed using molarity (c), molality (m) and mole fraction (x) scales (e.g., Anderko et al. 2002; Thomsen 2004; Majer et al. 2004). The concentration of solute i is defined as follows:

$$c_i = \frac{n_i}{V} \tag{1}$$

$$m_i = \frac{n_i}{m_\mathrm{w}} \tag{2}$$

$$x_i = \frac{n_i}{\sum_j n_j + n_\mathrm{w}} \tag{3}$$

where V represents volume of solution (dm^3), m_w is mass of H_2O (kg), and n is the number of moles of each solute j, and n_w is the number of moles of H_2O. The molarity scale incorporates the volume of aqueous solution, which makes it inconvenient for geological applications at variable temperature or pressure. The molality scale, normalized to mass of pure solvent, does not suffer from changes in the solvent's volume and has an additional advantage that the concentration of an arbitrary solute is not affected by addition or removal of other solutes; this eliminates the need for renormalization of all concentrations during dissolution or precipitation processes. Standard thermodynamic data for aqueous species are frequently expressed using the one molal standard state referred to infinite dilution (Wagman 1982; Johnson et al. 1992; Oelkers et al. 1995; Hummel et al. 2002). In contrast, applications to mixed-solvent or supercritical fluids require a description using the mole fraction scales (e.g., Kosinki and Anderko 2001; Newton and Manning 2008). Using the definition of molality, we obtain:

$$x_i = \frac{n_i}{\sum_j n_j + n_\mathrm{w}} = \frac{m_i}{\sum_j m_j + 1/M_\mathrm{w}} \tag{4}$$

where M_w represents the molar weight of H_2O (0.018015 kg mol^{-1}). In dilute solutions, the sum of solute molalities becomes negligible, and the conversion formula may be simplified to (e.g., Luckas and Krismann 2001):

$$x_i \approx m_i \cdot M_\mathrm{w} \tag{5}$$

This relationship becomes accurate at the limit of infinite dilution. The choice of concentration scales requires conversion relationships for thermodynamic properties referred to corresponding standard states. The partial molar Gibbs energy (chemical potential, μ) of a solute is expressed as

$$\mu_i = G_i^\mathrm{x} + RT \ln x_i \tag{6}$$

and

$$\mu_i = G_i^\mathrm{m} + RT \ln \frac{m_i}{m_\mathrm{o}} \tag{7}$$

where G_i is the standard Gibbs energy of solute i in the mole-fraction (x) and molality (m)-based standard state, respectively, and m_o = 1 mol kg^{-1} ensures non-dimensionality of the logarithm argument. Since the chemical potential of the solute must be independent of the choice of the standard state and associated concentration scale, subtracting Equations (6) and (7) and substituting Equation (5) yields the relationship between the two standard Gibbs energies:

$$G_i^\mathrm{x} = G_i^\mathrm{m} - RT \ln\left(M_\mathrm{w} \cdot m_\mathrm{o}\right) \tag{8}$$

Thus, G_i^m and G_i^x differ by an additive constant that is linearly related to temperature. This difference by a temperature-multiplied constant propagates into the first temperature derivative of the Gibbs energy; hence the standard molar entropy of a solute is always concentration-scale dependent.

Equations (6) and (7) implicitly define ideal solutions, associated with each concentration scale. The chemical potential of solute and the ideal Gibbs energy of solution are different as illustrated in Figure 1. This effect becomes significant at mole fractions, $x > 0.08$ or molalities, $m > 5$. In order to accurately convert the partial molar properties from one scale to another, we introduce activity coefficients that are concentration-scale and reference-state specific. For the mole fraction based solutions:

$$\mu_i = G_i^\mathrm{x} + RT \ln\left(x_i \gamma_i^\mathrm{x,R}\right) \tag{9}$$

where $\gamma_i^\mathrm{x,R}$ is the Raoultian (symmetrical) activity coefficient that is unity at the (hypothetical) standard state of a pure solute. For solutes, activity coefficients are traditionally normalized to unity at infinite dilution; hence we define the Henrian (unsymmetrical) activity coefficient, $\gamma_i^\mathrm{x,H}$:

$$\gamma_i^\mathrm{x,H} = \frac{\gamma_i^\mathrm{x,R}}{\gamma_{i,\infty}^\mathrm{x,R}} \tag{10}$$

Since the value of the Raoultian activity coefficient at infinite dilution ($\gamma_{i,\infty}^\mathrm{x,R}$) is a constant, we

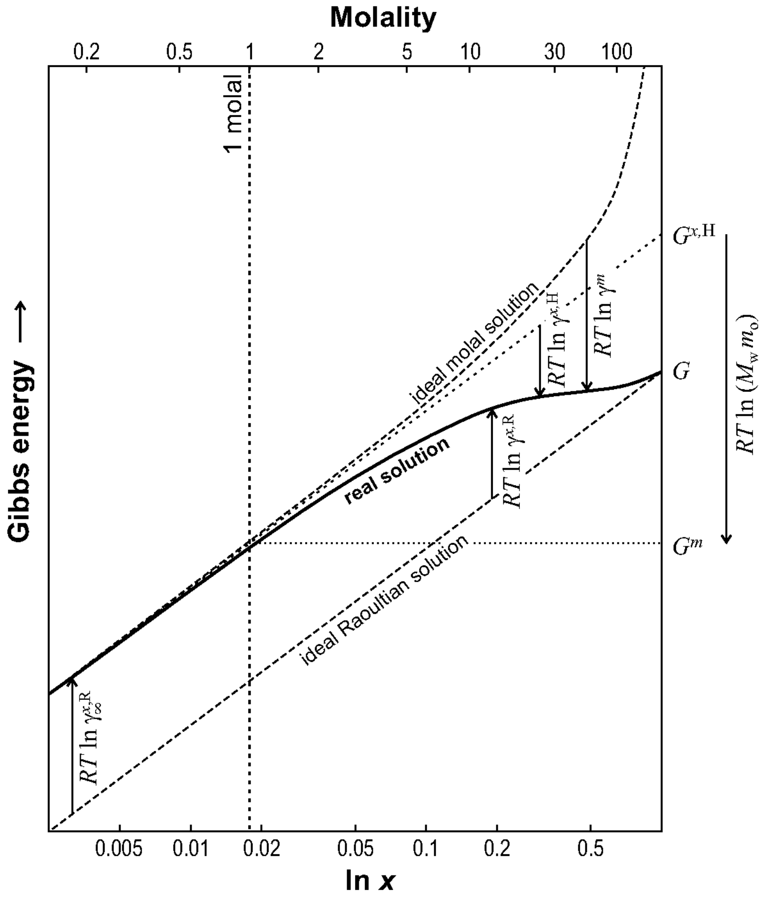

Figure 1. Relationship between mole-fraction concentration and Gibbs energy illustrating the difference between various standard states. The thick line represents mixing behavior of a hypothetical solution, from infinite dilution to the pure liquid (fluid) standard state. The dashed lines are ideal solutions on molality and mole fraction-based scales referred to the Henrian or Raoultian limit.

can separate its contribution and include it into a mole fraction-based standard Gibbs energy referred to infinite dilution:

$$\mu_i = G_i + RT\ln\left(x_i\gamma_i^{\mathrm{x,H}}\gamma_{i,\infty}^{\mathrm{x,R}}\right) = G_i^{\mathrm{H}} + RT\ln\left(x_i\gamma_i^{\mathrm{x,H}}\right) \qquad (11)$$

where G_i^{H} is the Gibbs energy of the rational Henrian standard state. Equation (11) leads to:

$$G_i^{\mathrm{H}} = G_i + RT\ln\gamma_{i,\infty}^{\mathrm{x,R}} \qquad (12)$$

Expanding the mole fraction of a solute in Equation (11) in terms of molality leads to the definition of the Henrian molal (practical) activity coefficient referred to infinite dilution and the corresponding standard Gibbs energy:

$$\mu_i = G_i^{\mathrm{H}} + RT\ln\left(m_i x_\mathrm{w} M_\mathrm{w}\gamma_i^{x,\mathrm{H}}\right) = G_i^{\mathrm{H}} + RT\ln\left(M_\mathrm{w}m_\mathrm{o}\right) + RT\ln\left(\frac{m_i}{m_\mathrm{o}}x_\mathrm{w}\gamma_i^{x,\mathrm{H}}\right) \qquad (13)$$

where x_w is the mole fraction of H_2O in the solution. The first two terms in Equation (13) define the standard Gibbs energy of one molal solute referred to infinite dilution:

$$G_i^{\mathrm{m}} = G_i^{\mathrm{x,H}} + RT\ln\left(M_{\mathrm{w}}m_{\mathrm{o}}\right) \tag{14}$$

and the molal activity coefficient,

$$\gamma_i^{\mathrm{m}} = x_w \gamma_i^{\mathrm{x,H}} \tag{15}$$

As expected, the molal activity coefficient and the Henrian mole activity coefficients become identical as the mole fraction approaches unity because they are both normalized to unity at infinite dilution (*cf.* Fig. 1). The standard molal Gibbs energy is frequently used in tabulations of thermodynamic properties of aqueous species (Wagman 1982; Johnson et al. 1992; Oelkers et al. 1995; Hummel et al. 2002; Anderson 2005).

In applications of standard thermodynamic properties to concentrated or supercritical fluids, relationships between Raoultian and Henrian standard states become essential. Consider the binary system H_2O-SiO_2 ranging from dilute fluid to hydrous silica melt. When the mixing properties of critical mixtures (transitional concentrated fluids) are described by excess mixing parameters (e.g., Newton and Manning 2008; Hunt and Manning 2012), their values must correspond to the difference between Henrian molal and Raoultian mole fraction standard states for SiO_2. When this constraint, arising from Equations (12) and (14), is employed, the functional form and numerical values for the excess properties are directly constrained by the difference in Gibbs energies of the two standard states (Šulák and Dolejš 2011).

CONVENTIONS FOR THERMODYNAMIC PROPERTIES

Absolute values of internal energy of substances cannot be measured directly, but since we are only concerned with energy differences in processes, energetic state functions are defined by conventions. If correct and independent conventions are adopted, then (i) values for reaction enthalpies, entropies and energies are mutually consistent, and (ii) standard properties for transfer processes such as charging or solvation are not violated. This criterion is particularly important for internal consistency of hydration equilibria involving charged species in various standard states (e.g., ideal gas, aqueous species).

Benson (1968), Helgeson et al. (1978, 1981), Robie et al. (1978), and Robie and Hemingway (1995) define the enthalpy and Gibbs energy of all elements in their pure stable standard state at 25 °C and 1 bar to be zero. This convention has been practical for deriving enthalpies and Gibbs energies of substances, particularly in cases when the standard reaction Gibbs energy or equilibrium constant only are known, but it is not consistent with entropy defined by the third law of thermodynamics. Hence:

$$\Delta_{\mathrm{f}}G \neq \Delta_{\mathrm{f}}H - TS \tag{16}$$

where $\Delta_f G$ and $\Delta_f H$ express the Gibbs energy and enthalpy of formation from elements, respectively, and S is the third-law entropy. Calculation of the Gibbs energy from the enthalpy of formation and the third-law entropy is possible *via* the following relationship:

$$\Delta_{\mathrm{f}}G = \Delta_{\mathrm{f}}H - T\Delta_{\mathrm{f}}S \tag{17}$$

where $\Delta_f S$ is the entropy of formation defined as follows:

$$\Delta_{\mathrm{f}}S = S - \sum_i \left(\nu_i S_i\right) \tag{18}$$

where S_i are the third-law entropies of constituting elements (i) in their stable standard states and ν_i is the number of atoms i in the formula unit.

The internal inconsistency in the Benson-Helgeson convention (Eqn. 16) imposes a restriction on the calculation of Gibbs energy at elevated temperatures and pressures:

$$\Delta_f G_{P,T} \neq \Delta_f H_{1,298} + \int_{298}^{T} C_P dT - T\left(S_{1,298} + \int_{298}^{T} \frac{C_P}{T} dT\right) + \int_{1}^{P} V dP \tag{19}$$

where P refers to the pressure, T is the absolute temperature, C_P is heat capacity, and V represents volume. The following relationship maintains the consistency with the convention:

$$\Delta_f G_{P,T} = \Delta_f G_{1,298} + \int_{298}^{T} C_P dT - \left[S_{1,298}\left(T - 298\right) + T\int_{298}^{T} \frac{C_P}{T} dT\right] + \int_{1}^{P} V dP \tag{20}$$

In addition, the Benson-Helgeson convention may lead to inconsistencies in calculations involving internal or Helmholtz energy. For instance, the following equivalences,

$$\Delta A = \Delta_f G - PV \tag{21}$$

and

$$\Delta A = \Delta_f H - TS - PV \tag{22}$$

and analogous expressions for internal energy yield results that differ by a constant, $298\,\Sigma_i(v_i S_i)$ (*cf.* Eqn. 18). This leads to non-unique definitions of internal energy and Helmholtz energy and renders the thermochemical computation cycles to ambiguity. In order to eliminate these drawbacks, Berman (1988) suggested abandoning the extraneous convention for the Gibbs energy and used:

$$\Delta_a G = \Delta_f H - TS \tag{23}$$

where $\Delta_a G$ stands for the apparent Gibbs energy. The term apparent is used here to distinguish this energy scale from that of the formation from elements at 25 °C and 1 bar (Fig. 2), and this usage is more restrictive and different from previous authors (Helgeson et al. 1981; Anderson and Crerar 1993; Anderson 2005) who use this adjective in a broader sense, including formation from elements at temperatures and pressures different from those of interest. The Gibbs energy of formation from elements and its apparent counterpart differ by a constant, which includes entropies of the constituting elements in their stable standard states at 25 °C and 1 bar (*cf.* Eqn. 18; Fig. 2):

$$\Delta_f G = \Delta_a G + 298.15\sum_i \left(\nu_i S_i\right) \tag{24}$$

The concept of apparent energy can be easily and consistently extended to Helmholtz and internal energy, as follows:

$$\Delta_a A = \Delta_f H - TS - PV = \Delta_a G - PV \tag{25}$$

and

$$\Delta_a U = \Delta_f H - PV = \Delta_a G + TS - PV = \Delta_a A + TS \tag{26}$$

The thermodynamic properties of charged species are subject to additional convention, which circumvents the impossibility of isolating a reference species (e.g., free electron in vacuum) and measuring its properties independently. Due to historical and practical reasons, several conventions are in concurrent use and may introduce errors into properties of transfer (Klotz 1950; Rossini 1950; Noyes 1963, 1964): (i) the energy of an electron in an ideal gas state equals its kinetic energy, (ii) enthalpy, Gibbs energy and entropy of electron in a half-reaction are zero, (iii) enthalpy, Gibbs energy and entropy of standard hydrogen electrode are zero, and

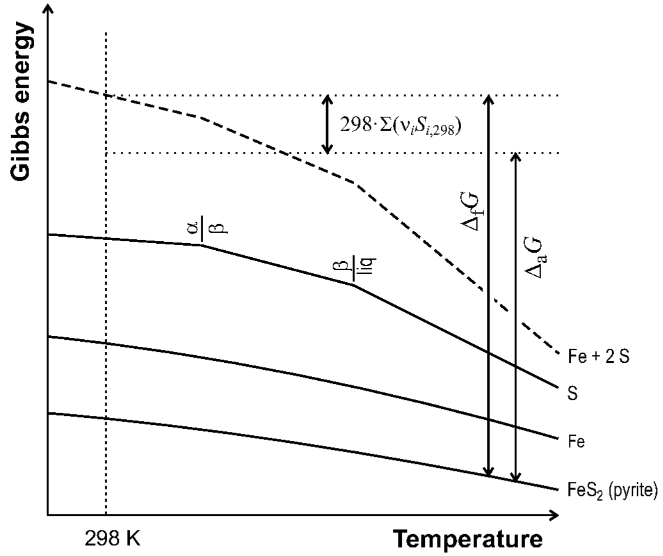

Figure 2. Relationship between temperature and Gibbs energy showing the meaning of the Gibbs energy of formation from elements and the apparent Gibbs energy (Eqns. 23-24). Pyrite (FeS_2) is used an example of a multielement compound.

(iv) enthalpy, Gibbs energy and entropy of aqueous hydrogen ion (H^+) are zero. Note that these conventions may be extended to include zero volume of the species when used at non-ambient pressure.

Thermodynamic data sets for aqueous species assume that enthalpy and the Gibbs energy of formation and standard entropy, heat capacity and volume of aqueous hydrogen ion are zero at all temperatures and pressures (Johnson et al. 1992; Oelkers et al. 1995; Hummel et al. 2002). Thermodynamic properties of charged species are calculated using standard reaction properties and those of elements using

$$z\mathrm{H}^+(\mathrm{aq}) + \mathrm{M} = \frac{z}{2}\mathrm{H}_2(\mathrm{g}) + \mathrm{M}^{z+}(\mathrm{aq}) \tag{27}$$

with $\Delta_a G = -38.96$ kJ mol^{-1}, $S = 130.68$ J K^{-1} mol^{-1} and $C_P = 28.836$ J K^{-1} mol^{-1} for hydrogen gas at 25 °C and 1 bar (Chase 1998). Consider the following reaction:

$$\frac{1}{2}\mathrm{H}_2(\mathrm{g}) = \mathrm{H}^+(\mathrm{aq}) + \mathrm{e}^- \tag{28}$$

where the standard state for an electron is intentionally not assigned (e.g., hydrated electron, e^- (Pt), ideal electron gas etc.). Since some thermodynamic properties of H_2 (g) and H^+ (aq) are defined by conventions, $S_{\mathrm{e}^-} = 65.34$ J K^{-1} mol^{-1} and $C_{P,\mathrm{e}^-} = 14.418$ J K^{-1} mol^{-1} at 25 °C in an unspecified standard state are implicitly set. This will not provide consistency with thermodynamic properties of ions in other standard states (e.g., ideal gas state); hence energies of hydration cannot be directly evaluated. Noyes (1963) suggested the following corrections to be applied at any temperature:

$$C_{P,\mathrm{H}^+(\mathrm{aq})} = \frac{C_{P,\mathrm{H}_2(\mathrm{g})}}{2} \tag{29}$$

$$S_{\mathrm{H^+(aq)}} = \frac{S_{\mathrm{H_2(g)}}}{2} \tag{30}$$

Maintaining that $\Delta_{\mathrm{f}} H_{\mathrm{H^+(aq)}} = 0$ at all temperatures allows for two possible conventions for the Gibbs energy of aqueous hydrogen ion:

$$\Delta_{\mathrm{f}} G_{\mathrm{H^+(aq)}} = 0 \tag{31}$$

or

$$\Delta_{\mathrm{a}} G_{\mathrm{H^+(aq)}} = \Delta_{\mathrm{f}} H_{\mathrm{H^+(aq)}} - T S_{\mathrm{H^+(aq)}} \tag{32}$$

The rationale behind the apparent Gibbs energy for aqueous species is identical to that for uncharged substances (Eqn. 23) and it would lead to internal consistency between enthalpy and Gibbs energy and allow for unambiguous extensions to Helmholtz or internal energy.

BASIC THERMODYNAMIC MODELS FOR AQUEOUS EQUILIBRIA

Interpretation of density measurements, equilibrium constants for homogeneous speciation equilibria, and solubilities of gaseous or solid substances has prompted derivation of simple interpretation and extrapolation thermodynamic models. Such thermodynamic interpolation and extrapolation schemes are simple relationships, mainly caloric expansions of standard reaction Gibbs energy or equilibrium constant, that are applied to predictions of homogeneous and heterogeneous equilibria over several hundred degrees Celsius (e.g., from ambient conditions to critical temperature). They do not represent self-standing equations of state, partly due to the absence of higher-order derivative properties (e.g., heat capacity), which are expected to cancel out in a balanced equilibrium. These approaches are based on (i) assumption that derivative reaction properties such as heat capacity or entropy are negligible, thus may be set to zero, (ii) the correspondence principle for ionic entropies, (iii) the relationship between the thermodynamic properties of aqueous species and those of the solvent, and (iv) incorporation of the Born theory (for reviews see Puigdomenech et al. 1997; Majer et al. 2004; Sedlbauer 2008; Dolejš and Manning 2010).

Approximations to the Gibbs energy function

Consider the temperature dependence of the standard reaction Gibbs energy ($\Delta_{\mathrm{r}} G$):

$$\Delta_{\mathrm{r}} G_T = \Delta_{\mathrm{r}} G_{T_{\mathrm{ref}}} - (T - T_{\mathrm{ref}}) \Delta_{\mathrm{r}} S_{T_{\mathrm{ref}}} + \int_{T_{\mathrm{ref}}}^{T} \Delta_{\mathrm{r}} C_P dT - T \int_{T_{\mathrm{ref}}}^{T} \frac{\Delta_{\mathrm{r}} C_P}{T} dT \tag{33}$$

and for the equilibrium constant (K):

$$\log K_T = \log K_{T_{\mathrm{ref}}} - \frac{\Delta_{\mathrm{r}} H_{T_{\mathrm{ref}}}}{R \ln 10} \left(\frac{1}{T} - \frac{1}{T_{\mathrm{ref}}} \right) - \frac{1}{RT \ln 10} \int_{T_{\mathrm{ref}}}^{T} \Delta_{\mathrm{r}} C_P dT + \frac{1}{R \ln 10} \int_{T_{\mathrm{ref}}}^{T} \frac{\Delta_{\mathrm{r}} C_P}{T} dT \tag{34}$$

where R is the universal gas constant (8.31446 J $\mathrm{K^{-1}}$ $\mathrm{mol^{-1}}$) and the subscript "ref" indicates the reference temperature (e.g., 298.15 K). Depending on the availability of the standard enthalpy and heat capacity of the reaction, Equations (33) and (34) are reduced to approximations. Assuming constant heat capacity, we obtain the three-term approximation (Cobble et al. 1982):

$$\Delta_{\mathrm{r}} G_T = \Delta_{\mathrm{r}} G_{T_{\mathrm{ref}}} - (T - T_{\mathrm{ref}}) \Delta_{\mathrm{r}} S_{T_{\mathrm{ref}}} + \Delta_{\mathrm{r}} C_P \left(T - T_{\mathrm{ref}} - T \ln \frac{T}{T_{\mathrm{ref}}} \right) \tag{35}$$

and

$$\log K_T = \log K_{T_{\mathrm{ref}}} - \frac{\Delta_{\mathrm{r}} H_{T_{\mathrm{ref}}}}{R \ln 10} \left(\frac{1}{T} - \frac{1}{T_{\mathrm{ref}}} \right) + \frac{\Delta_{\mathrm{r}} C_P}{R \ln 10} \left(\frac{T_{\mathrm{ref}}}{T} - 1 + \ln \frac{T}{T_{\mathrm{ref}}} \right) \tag{36}$$

For high-quality experimental data, the three-term approximation is used over a temperature range exceeding approximately 20 °C (Puigdomenech et al. 1997). Temperature effects in the last term tend to cancel each other out. These relationships are further simplified when the standard heat capacity of the reaction is assumed to be zero, that is, the standard reaction enthalpy becomes constant (two-term approximation or third-law method):

$$\Delta_r G_T = \Delta_r G_{T_{\text{ref}}} - \left(T - T_{\text{ref}}\right)\Delta_r S_{T_{\text{ref}}} \tag{37}$$

and

$$\log K_T = \log K_{T_{\text{ref}}} - \frac{\Delta_r H_{T_{\text{ref}}}}{R\ln 10}\left(\frac{1}{T} - \frac{1}{T_{\text{ref}}}\right) \tag{38}$$

Note that Equation (38) corresponds to the integrated van't Hoff equation. These relationships are particularly useful and more accurate for reactions that have isoelectric or isocoulombic form (Mesmer and Baes 1974; Wood and Samson 1998). Considering that both the reaction entropy and the heat capacity are related to ion-solvent interactions, an isocoulombic equilibrium should minimize both quantities simultaneously. Thus, the standard Gibbs energy of the reaction tends to be constant and independent of temperature:

$$\Delta_r G_T = \Delta_r G_{T_{\text{ref}}} \tag{39}$$

and

$$\log K_T = -\frac{\Delta_r G_{T_{\text{ref}}}}{RT\ln 10} \tag{40}$$

This one-term equation, rejected by Anderson (2005), provides reasonable predictions of isocoulombic homogeneous equilibria for a variety of acid-base neutralization, hydrolysis, redox and exchange reactions that are solely based on the knowledge of the standard Gibbs energy or equilibrium constant at a single reference temperature (Gu et al. 1994).

None of the above approximations (Eqns. 33-40) contains provision for a pressure effect on thermodynamic properties. These models were frequently applied at liquid-vapor saturation, and the effect of pressure is usually neglected. Application to high pressures or at isothermal conditions would require inclusion of an additional volume term. In the models discussed below the effect of pressure will be implicitly accounted for by variations of solvent density or dielectric constant.

Predictions using the solvent density

The temperature and pressure dependence of the standard reaction properties for homogeneous and heterogeneous equilibria has been successfully described by the density model, which is based on a linear relationship between the logarithm of the equilibrium constant and the logarithm of the H_2O density, and a polynomial caloric expansion (Franck 1956; Marshall and Franck 1981). This versatile tool is applicable to association-dissociation equilibria and solid phase solubilities over a wide range of solvent densities, that is, from aqueous vapor to high-pressure fluids (Fig. 3). The original empirical form of the model has frequently been reduced to a three-parameter version (Mesmer et al. 1988; Anderson et al. 1991) that appears sufficient for reactions involving aqueous species and minerals (as corrected in Anderson 1995):

$$\begin{aligned}\Delta_r G_{P,T} &= \Delta_r G_{P_{\text{ref}},T_{\text{ref}}} - \Delta_r S_{P_{\text{ref}},T_{\text{ref}}}\left(T - T_{\text{ref}}\right) \\ &+ \frac{\Delta_r C_{P,P_{\text{ref}},T_{\text{ref}}}}{T_{\text{ref}}\left(\dfrac{\partial \alpha_w}{\partial T}\right)_{P_{\text{ref}},T_{\text{ref}}}}\left[\alpha_{w,P_{\text{ref}},T_{\text{ref}}}\left(T - T_{\text{ref}}\right) + \ln\frac{\rho_w}{\rho_{w,P_{\text{ref}},T_{\text{ref}}}}\right]\end{aligned} \tag{41}$$

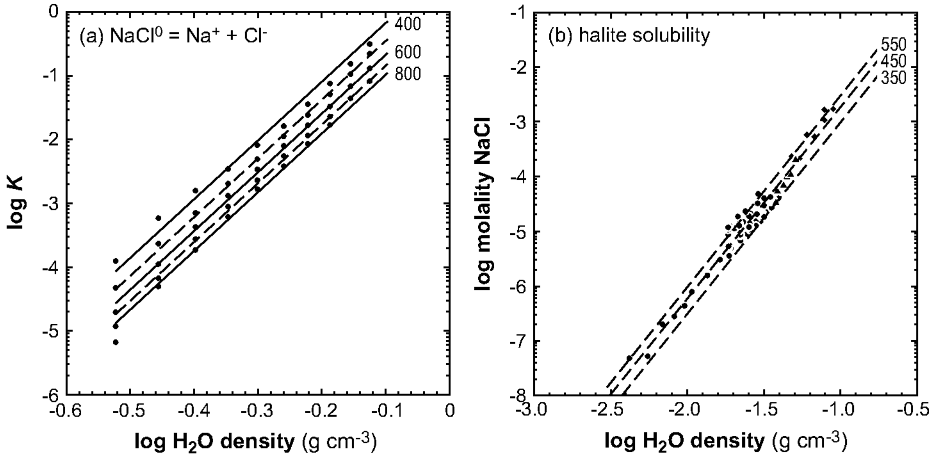

Figure 3. Linear relationships between the logarithmic density of aqueous solvent and logarithmic equilibrium constants for homogeneous dissociation equilibria and mineral solubility: (a) dissociation of NaCl. Experimental data by Quist and Marshall (1968) are shown by point symbols at 400, 500, 600, 700 and 800 °C, with isotherms fitted to the data set; (b) halite solubility in aqueous vapor. Experimental measurements are indicated by the following symbols: circles – Galobardes et al. (1981), diamonds – Armelini and Tester (1993), triangles – Higashi et al. (2005). Dashed lines are isotherms at 350, 450 and 550 °C fitted to the data set.

and

$$\log K = \log K_{P_{ref},T_{ref}} - \frac{\Delta_r H_{P_{ref},T_{ref}}}{R\ln 10}\left(\frac{1}{T}-\frac{1}{T_{ref}}\right) + \frac{\Delta_r C_{P,P_{ref},T_{ref}}}{RT_{ref}\ln 10\left(\dfrac{\partial \alpha_w}{\partial T}\right)_{P_{ref},T_{ref}}}\left[\frac{1}{T}\ln\frac{\rho_w}{\rho_{w,P_{ref},T_{ref}}} - \frac{\alpha_{w,P_{ref},T_{ref}}}{T}\left(T-T_{ref}\right)\right] \qquad (42)$$

where ρ_w is the H_2O density ($\rho_{w,P_{ref},T_{ref}}$ = 0.9998 g cm^{-3}), $\alpha_{w,P_{ref},T_{ref}}$ is the thermal expansion of H_2O at reference conditions of 25 °C and 1 bar (2.593×10^{-4} K^{-1}), and $(\partial\alpha_w / \partial T)_{P_{ref},T_{ref}}$ is the isobaric temperature derivative of the thermal expansion of H_2O (9.5714×10^{-6} K^{-2}). This model is a three-term relationship based on the standard reaction Gibbs energy (equilibrium constant), enthalpy (entropy), and heat capacity, and it has proven to be successful for extrapolations from ambient conditions to 600 °C and 2 kbar (Anderson 1995).

The density model for the self-dissociation of H_2O (Marshall and Franck 1981) forms the basis for the three-parameter modified Ryzhenko-Bryzgalin model for the standard Gibbs energy of association (Borisov and Shvarov 1992; Shvarov and Bastrakov 1999; Wagner and Kulik 2007):

$$\Delta_r G_{P,T} = \Delta_r G_{P_{ref},T_{ref}} - \frac{R\ln 10}{1.0107}\left(T\log K_{w,P,T} - 298.15\log K_{w,P_{ref},T_{ref}}\right)\left(A+\frac{B}{T}\right) \qquad (43)$$

where A and B are associate-dependent parameters and K_w represents the dissociation constant of pure H_2O, defined by Marshall and Franck (1981) as follows:

$$\log K_w = a + \frac{b}{T} + \frac{c}{T^2} + \frac{d}{T^3} + \left(e + \frac{f}{T} + \frac{g}{T^2}\right)\log\rho_w \qquad (44)$$

where $a = -4.098$, $b = -3245.2$ K, $c = 2.2362\times10^5$ K^2, $d = -3.984\times10^7$ K^3, $e = 13.957$, $f = -1262.3$ K, $g = 8.5641\times10^5$ K^2. The modified Bryzgalin-Ryzhenko model represents the main tool for computing the thermodynamic properties of aqueous complexes in the hCh software package (Shvarov and Bastrakov 1999). Although it appears to be less accurate, the parameters of the model are correlated with fundamental chemical properties such as charge or ionic radius and therefore, the formation equilibrium constants for a large number of complexes were derived (Ryzhenko and Bryzgalin 1987; Ryzhenko et al. 1991).

Predictions using the electrostatic theory

Models for the standard Gibbs energy of ionic association are frequently described as the sum of electrostatic and non-electrostatic contributions (Gurney 1953):

$$\Delta_r G = \Delta_r G_{\text{el}} + \Delta_r G_{\text{nonel}} \tag{45}$$

The non-electrostatic standard Gibbs energy ($\Delta_r G_{\text{nonel}}$) can be conventionally expanded into enthalpic and entropic contributions, but at the same time realizing that $T\Delta S >> \Delta H$ for ion-solvent interactions (e.g., Walther 1992) suggests a constant non-electrostatic contribution to the overall equilibrium constant of the association reaction. The electrostatic Gibbs energy is formulated as a Coulomb-type equation (Ryzhenko et al. 1985; Bryzgalin 1989):

$$\Delta_r G_{\text{el}} = -\frac{\left|z^+_{\text{eff}} z^-_{\text{eff}}\right| e^2 N_A}{4\pi\varepsilon_o \varepsilon r_{\text{eff}}} \tag{46}$$

where z^+_{eff} and z^-_{eff} are the effective ionic charges of the cation and anion, respectively, related to their formal charges, r_{eff} is an effective bond distance approximated by the sum of the radii of the central ion and ligand, e is the elementary charge, N_A is Avogadro's number, ε_o is the absolute permittivity of the vacuum (8.8542×10^{-12} F m^{-1}), and ε is the relative permittivity (dielectric constant) of the solvent. Equations (45) and (46), with substitution of the equilibrium constant at reference temperature and pressure, yield:

$$\log K_{P,T} = \frac{T_{\text{ref}}}{T}\log K_{P_{\text{ref}},T_{\text{ref}}} + \frac{\left|z^+_{\text{eff}} z^-_{\text{eff}}\right| e^2 N_A}{4\pi\varepsilon_o r_{\text{eff}} RT \ln 10}\left(\frac{1}{\varepsilon_{P,T}} - \frac{1}{\varepsilon_{P_{\text{ref}},T_{\text{ref}}}}\right) - \sum_i \nu_i \log \rho_{P,T} \tag{47}$$

where ρ is the solvent density; this term ensures conversion between molar and molal concentration scales. The model contains only two parameters, the equilibrium constant at reference conditions and the effective bond distance. If the value for $\Delta_r H$ or $\Delta_r S$ at reference conditions is known, the r_{eff} may be directly calculated. In an opposite case, the distance parameter r_{eff} is approximated by the sum of the crystallographic radii of the central ion and the ligand. This allows calculation of $K_{P,T}$ solely from its value at reference conditions when all other data are not available.

In an alternative formulation, we will consider the association of ions due to electrostatic attraction to be a continuous function of the dielectric constant of the aqueous solvent (Denison and Ramsay 1955; Fuoss 1958). Including non-electrostatic ion-solvent interactions into the Fuoss-Bjerrum treatment of association equilibrium constant leads to (Gilkerson 1970; Brady and Walther 1990):

$$K = K' \frac{4\pi 10^{-24} N_A d^3 e^b}{3000} \tag{48}$$

where K' is the equilibrium-constant contribution arising from non-electrostatic interactions, d represents the center-to-center distance (Å) between ions in the aqueous complex, and

$$b = \frac{z^+ z^- e_o^2}{\varepsilon d k T} \tag{49}$$

where k is Boltzmann's constant, and ε is the dielectric constant of H_2O. By substituting the constants and rearranging, we obtain

$$\log K = -2.60 + 3\log d + \frac{72800 z^{+} z^{-}}{d\varepsilon T} + \log K' \tag{50}$$

Since d and K' appear to be independent of temperature and pressure (Walther and Schott 1988; Brady and Walther 1990), the plot of log K vs. $1/(\varepsilon T)$ becomes linear at constant pressure. In practice, in particular at low values of the dielectric constant of H_2O, the following equation can be used to represent association equilibria up to 750 °C and 5 kbar (Walther 1992):

$$\log K = a_1 + a_2 P + \frac{a_3 + a_4 P}{\varepsilon T \times 10^5} \tag{51}$$

where a_1 to a_4 are the complex-specific parameters of the model. Representative parameters were calibrated for hydrogen, alkali and alkali-earth chloride complexes (Walther 1992).

EQUATIONS OF STATE FOR AQUEOUS SPECIES

A successful description of the equilibrium and transport properties of aqueous fluids and associated speciation, redox and precipitation reactions requires equations of state for solvent and dissolved species, which cover a wide range of temperatures (up to 1100 °C) and pressures (up to 30 kbar). The construction of equations of state has been approached from empirical, macroscopic, microscopic (statistical) and electrostatic perspective, or their combinations (Fig. 4). This scheme emphasizes that the individual approaches are neither strictly complementary nor exclusive. Frequently, they provide additive thermodynamic contributions, whose forms or approximations may depend on the range of temperature and/or pressure that is addressed.

Presently, the Helgeson-Kirkham-Flowers equation of state (Helgeson et al. 1981; Tanger and Helgeson 1988; Shock et al. 1992; Oelkers et al. 1995) remains the most widely accepted tool in geochemical applications, promoted by its extensive aqueous database (Johnson et al. 1992). Other, mainly non-electrostatic approches (e.g., Mesmer et al. 1988; Tanger and Pitzer 1989a; Akinfiev and Diamond 2003; Sedlbauer 2008; Djamali and Cobble 2009) have never reached comparable acceptance because their coverage and generality appears to be smaller, although their performance for specific solutes (e.g., non-electrolytes), or at near-critical or extreme temperature and pressure conditions is much more accurate.

Thermodynamics of hydration

The hydration of aqueous species involves changes in standard thermodynamic properties arising from species transfer from its pure state (ideal gas state, real fluid or solid) to infinite dilution in an aqueous solvent, and from solute-solvent interactions. Careful examination of various equations of state reveals that some of their forms are incomplete or confuse thermodynamic contributions that represent: (i) property changes due to intensive variables (e.g., with temperature or pressure such as $\Delta_{PT}G$ or $\Delta_{PT}G_B$), (ii) changes due to processes and transfers at constant conditions (e.g., change due to the Born energy, $\Delta_B G$), and (iii) standard state conversion terms. Inconsistencies arise when the transfer terms are not strictly isothermal and isobaric but may inadvertently represent change between two standard states referring to two distinct reference states. Furthermore, it has been shown that various thermochemical paths may lead to more appropriate or advantageous treatments (e.g., Djamali and Cobble 2009). A simple scheme that portrays individual standard states in the pressure-temperature space is provided in order to facilitate construction and verification of thermochemical cycles, in particular for hydration or dissolution properties (Fig. 5).

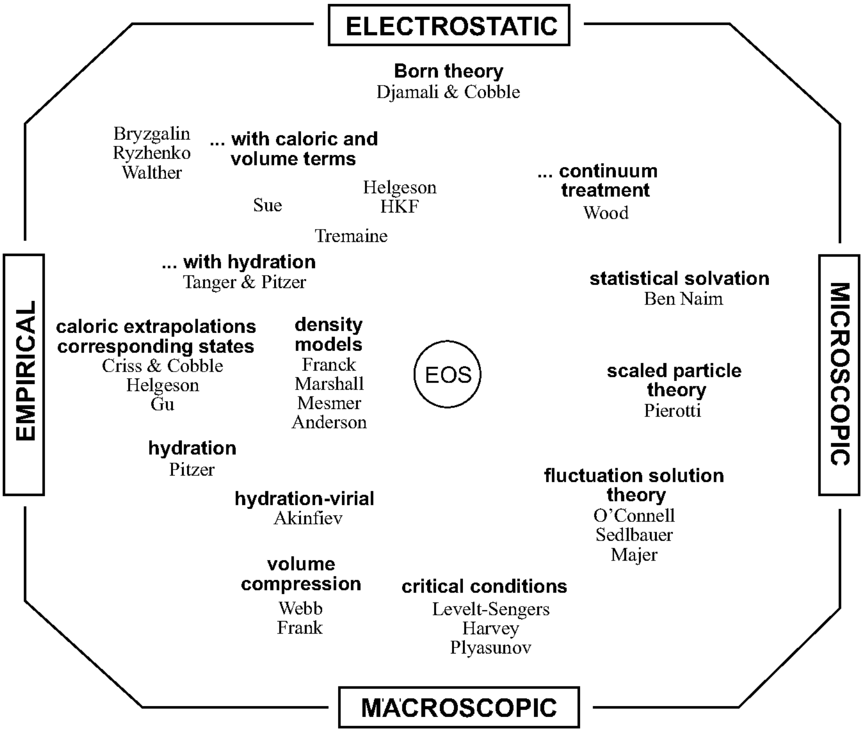
ELECTROSTATIC
Born theory
Djamali & Cobble
Bryzgalin
Ryzhenko
Walther
... with caloric and volume terms
Helgeson
HKF
Sue
... continuum treatment
Wood
Tremaine
... with hydration
Tanger & Pitzer
statistical solvation
Ben Naim
EMPIRICAL
MICROSCOPIC
caloric extrapolations
corresponding states
Criss & Cobble
Helgeson
Gu
density models
Franck
Marshall
Mesmer
Anderson
EOS
scaled particle theory
Pierotti
hydration
Pitzer
fluctuation solution theory
O'Connell
Sedlbauer
Majer
hydration-virial
Akinfiev
volume compression
Webb
Frank
critical conditions
Levelt-Sengers
Harvey
Plyasunov
MACROSCOPIC

Figure 4. Overview of thermodynamic models and equations of states for aqueous solutes. Simple or empirical approaches are portrayed near the sides, whereas more complex and accurate models are placed in the center.

Solute transfer. Changes in standard thermodynamic properties arising from transfer of solute species from the ideal gas state to an aqueous solvent are evaluated from the condition of equilibrium, i.e.,

$$\mu^{ig} = \mu^{aq,x} = \mu^{aq,m} \tag{52}$$

From statistical thermodynamics, the chemical potential of a species in the ideal gas state is as follows (e.g., Ben-Naim 1985, 1987):

$$\mu^{ig} = kT\ln\frac{\Lambda^3}{q} + kT\ln\frac{N}{V} \tag{53}$$

where Λ represents the translational partition function, q is the internal (i.e., rotational, vibrational, electronic, etc.) partition function, and the ratio N/V describes the equilibrium number density, which is equivalent to the molar concentration (c). When considering the transfer of a species from one phase (a) to another (b), the standard Gibbs energy of the transfer ($\Delta_{tr}G$) is calculated from the equilibrium number densities (or, analogously, densities or molar concentrations), as follows (e.g., Bryantsev et al. 2008):

$$\Delta_{tr}G = kT\ln\frac{V_a}{V_b} = kT\ln\frac{\rho_b}{\rho_a} \tag{54}$$

where V and ρ are the molar volume and density at each standard state, respectively. Converting

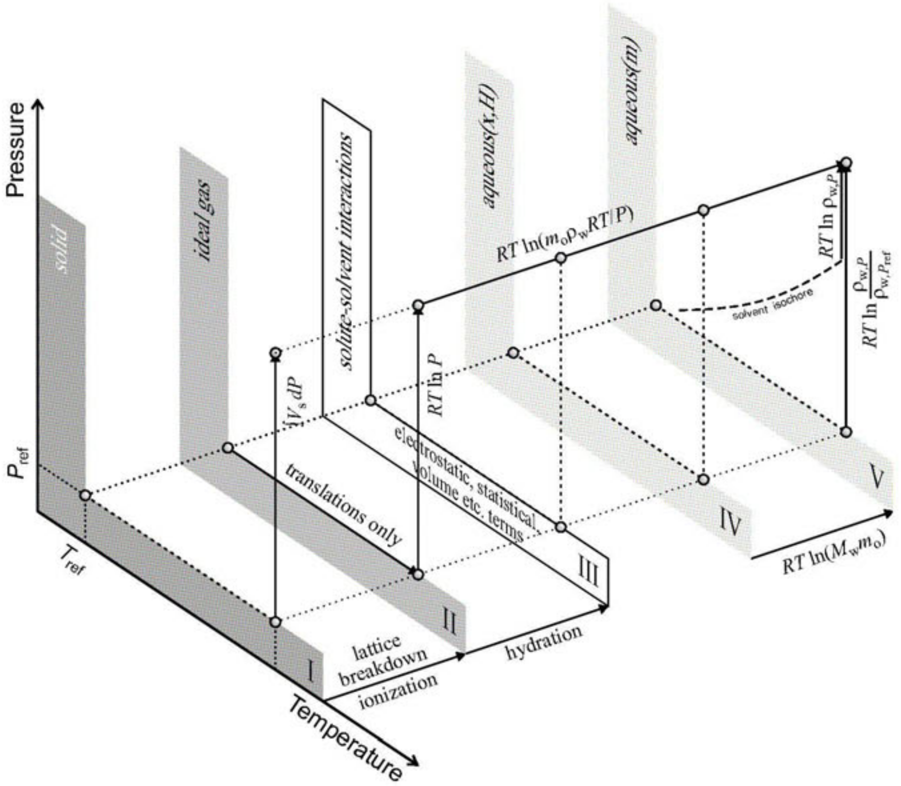
Pressure
Temperature
P_ref
T_ref
solid
ideal gas
solute-solvent interactions
aqueous(x,H)
aqueous(m)
RT ln(m_o ρ_w RT/P)
RT ln ρ_w,P
RT ln ρ_w,P/ρ_w,Pref
solvent isochore
∫V_s dP
RT ln P
electrostatic, statistical, volume etc. terms
translations only
I
II
III
IV
V
lattice breakdown
ionization
hydration
RT ln(M_w m_o)

Figure 5. Pressure-temperature space with projection of various standard states illustrating individual steps in thermochemical cycles and standard state conversion during hydration.

to one mole of solute and expanding densities using the ideal gas law and the definition of appropriate concentration scale in the solvent, we obtain the standard Gibbs energy of transfer from the pure ideal gas state to the hypothetical mole fraction-based solution (Ben-Naim and Marcus 1984; Ben-Naim 2006):

$$\Delta_{\mathrm{II}\rightarrow\mathrm{IV}}G = RT\ln\frac{RT\rho_{\mathrm{w}}}{PM_{\mathrm{w}}} \tag{55}$$

where the subscript II→IV refers to standard states, as indicated in Figure 5. The standard Gibbs energy of transfer from the pure ideal gas state to one molal solution at infinite dilution becomes:

$$\Delta_{\mathrm{II}\rightarrow\mathrm{V}}G = RT\ln\frac{RTm_{\mathrm{o}}\rho_{\mathrm{w}}}{P} \tag{56}$$

where units must be chosen to fulfill the non-dimensionality of the logarithm argument. Equation (56) is often simplified as

$$\Delta_{\mathrm{II}\rightarrow\mathrm{V}}G = RT\ln\frac{RT\rho_{\mathrm{w}}}{1000} \tag{57}$$

where RT is the volume of an ideal gas at 1 bar, with the universal gas constant given in bar cm^3 K^{-1} mol^{-1}, and $1000/\rho_{\mathrm{w}}$ is the volume of 1 kg H_2O, with density in g cm^{-3} (e.g., Tremaine and Goldman 1978; Tanger and Pitzer 1989a; Majer et al. 2004).

The standard Gibbs energies in Equations (56) and (57) correspond to the work needed to transfer one mole of stationary species from one to another standard state, but they neither contain any contribution from the translational entropy, nor from attractive solute-solvent or solvent-solvent interactions (Vitha and Carr 2000). Consequently, hydration is treated as a stepwise process, which adds additional interaction contributions: (i) transfer of the species into the solution, associated with the creation of a free space within the solvent structure (i.e., cavitation), (ii) solute-solvent interactions due to insertion to the aqueous environment, including translational contributions to entropy, and (iii) electrostatic and non-electrostatic (e.g., compression) perturbations arising due to solute-solvent interactions.

Born theory. The electrostatic contribution arising from ion charging in a dielectric medium is described by the Born theory (Born 1920; Atkins and MacDermott 1982). The difference between the Gibbs energy of species uncharged in a vacuum, transferred and charged in an aqueous solvent ($\Delta_B G$) at a temperature and pressure of interest is given by:

$$\Delta_B G_{P,T} = \frac{(ze)^2 N_A}{2r}\left(\frac{1}{\varepsilon}-1\right) = \omega\left(\frac{1}{\varepsilon}-1\right) \tag{58}$$

where r is the ionic radius, and ω represents the absolute Born parameter of aqueous species. The agreement between the calculated and experimental Born parameter decreases with increasing charge (Fletcher 1993), subject to additional uncertainty arising from the definition of ionic radius. In practical applications, the Born parameter has been fitted to reproduce the entropy and the Gibbs energy of hydration (Shock and Helgeson 1988; Djamali and Cobble 2009). Equation (58) can be manipulated to describe the change in energy of hydration with temperature and pressure, as follows:

$$\Delta_{PT} G_B = G_{B,P,T} - G_{B,P_{ref},T_{ref}} = \omega\left(\frac{1}{\varepsilon_{P,T}} - \frac{1}{\varepsilon_{P_{ref},T_{ref}}}\right) \tag{59}$$

As Equation (58) indicates, the Born parameter has physical significance but its value is subject to several restrictions or approximations: (i) the conventional Born parameter is defined as the difference between the absolute value and that of the hydrogen ion, in accordance with the hydrogen ion convention for the Gibbs energy (Helgeson et al. 1981); (ii) the Born parameter is zero for neutral species by definition, although a non-physical small positive value is often used in order to reproduce experimental data (e.g., Johnson et al. 1992; Oelkers et al. 1995); (iii) the divergence of derivative thermodynamic properties near the critical point of H_2O may lead to non-physical negative values and this indicates the predominance of mechanical (volumetric) over electrostatic effects in the near-critical region (e.g., Tremaine et al. 1997; Plyasunov and Shock 2001); (iv) the Born parameter may become pressure- and temperature-dependent in harmony with changes in ionic radius or to more accurately reproduce hydration properties (e.g., Tanger and Helgeson 1988; Shock et al. 1992).

Electrostatic properties of aqueous solvent. The electrostatic permittivity (dielectric constant) of H_2O is essential for the Born electrostatic term over a wide range of pressures and temperatures. Future development of electrostatic models must rely on accurate data, while approaches to calculation of the dielectric constant include: (i) dielectric polarization model for polar liquids (Kirkwood 1939; Pitzer 1983a; Wassermann et al. 1995; Fernandéz et al. 1997); (ii) approximation by a hard-sphere fluid with dipole moments (Patey et al. 1979; Franck et al. 1990); (iii) semiempirical models based on the Tait equation (Bradley and Pitzer 1983; Floriano and Nascimento 2004); (iv) empirical temperature-density models (Uematsu and Franck 1980; Marshall 2008a).

Using an extension of the Onsager polarization theory and its application to liquid water with tetrahedral coordination and directed bonds between molecules, Kirkwood (1939) derived the following relationship for the dielectric constant of H_2O:

$$\frac{(2\varepsilon+1)(\varepsilon-1)}{9\varepsilon}=\frac{4\pi N_A\rho}{3M_w}\left(\alpha+\frac{\mu^2 g}{3kT}\right) \tag{60}$$

where M_w is the molar weight of H_2O (18.015 g mol^{-1}), α is the polarizability (1.444×10^{-24} cm^3), μ is the permanent dipole moment of the H_2O molecule (1.84×10^{-18} esu cm), k is the Boltzmann constant, and g is the Kirkwood correlation factor. This factor has been fitted by empirical function in temperature and density (Pitzer 1983a):

$$g=1+2.68\rho+6.69\rho^5\left[\left(\frac{565}{T}\right)^{0.3}-1\right] \tag{61}$$

or, following Wasserman et al. (1995),

$$g=1+2.5117\rho+16.0801\rho^5\left[\left(\frac{657.16}{T}\right)^{0.15302}-1\right] \tag{62}$$

The Kirkwood equation or its alternatives (*cf.* Harris and Alder 1953) provide the basis for the main formulations for the dielectric constant of H_2O (e.g., Pitzer 1983a; Wasserman et al. 1995; Fernandéz et al. 1997). By contrast, the density models for the dielectric constant of H_2O have been inspired by simple correlation relationships between these two variables (Franck 1956; Quist and Marshall 1965), and lead to an empirical formulation of the dielectric constant as a function of powers in temperature and solvent density (Uematsu and Franck 1980). The discovery of linear relationship between log (ε-1) and log ρ, motivated by the approach of ε to unity as the H_2O density decreases towards zero (Yeatts et al. 1971) forms the basis for the empirical model for the dielectric constant of H_2O up to 1000 °C and 1.1 g cm^{-3}, as follows (Marshall 2008a):

$$\log(\varepsilon-1)=y\left[c+(s-1)\log\rho\right]+d+\log\rho \tag{63}$$

where

$$y=\frac{1}{1+0.0012/\rho^2} \tag{64}$$

$$c=0.4117+\frac{366.6}{T}-\frac{1.491\times10^5}{T^2}+\frac{9.190\times10^6}{T^3} \tag{65}$$

$$d=0.290+\frac{275.4}{T}+\frac{0.3245\times10^5}{T^2} \tag{66}$$

$$s=\left.\frac{\partial\log(\varepsilon-1)}{\partial\log\rho}\right|_T=1.667-\frac{11.41}{T}-\frac{3.526\times10^4}{T^2} \tag{67}$$

At H_2O densities from 0.25 to above 1.1 g cm^{-3}, the y term approaches unity within uncertainty and Equation (63) reduces to a simple form applicable up to greater than 900 °C:

$$\log(\varepsilon-1)=a+s\log\rho \tag{68}$$

where

$$a=0.7017+\frac{642.0}{T}-\frac{1.167\times10^5}{T^2}+\frac{9.190\times10^6}{T^3} \tag{69}$$

while noting that the term a represents log (ε–1) at ρ = 1 g cm^{-3}. This model reproduces experimental measurements within uncertainty (Δε = 0.05-0.3) with eleven coefficients, which compares with the twelve coefficients and twenty-two exponents of Fernandéz et al. (1997).

The representative models for the dielectric constant of H_2O have been evaluated along the water liquid-vapor coexistence and critical isochore, and along the geotherm of 25 °C kbar^{-1}, corresponding to ~7 °C km^{-1}, characteristic of subduction zones (Fig. 6). At subcritical temperatures and vapor saturation, all models converge with the exception of that by Uematsu and Franck (1980) and Franck et al. (1990), which overestimate ε by up to 15. Above the critical temperature, individual calibrations differ by as much as 5% in 1/ε (chosen to be proportional to the electrostatic Born energy). At $T > 700$ °C, the model of Shock et al. (1992) significantly deviates from other formulations reaching an underestimation of 18% in 1/ε at 1000 °C. Along the 25 °C kbar^{-1} geotherm, the models substantially diverge above 400 °C, forming a gently rising trend of 1/ε (Fernandéz et al. 1997; Marshall 2008a), and a steeply rising group (Pitzer 1983a; Shock et al. 1992; Wasserman et al. 1995). As before, the trend of the IAPWS formulation (Fernandéz et al. 1997) is best reproduced by the empirical density model of Marshall (2008a) (Fig. 6).

Solvent compression. In addition to the electrostatic energy of charging, additional contribution results from the compression of the solvent in the vicinity of the solute species. By fundamental thermodynamic identities, the compression work per unit volume (W_r) is as follows (Webb 1926):

$$W_r = \int_{V_1}^{V_2} P\frac{dV}{V} = \int_{P_{\text{ref}}}^{P} \frac{P}{V}\frac{dV}{dP}dP = \int_{P_{\text{ref}}}^{P} \kappa P dP \tag{70}$$

where κ is the compressibility of the solvent. The total compression work (W) is obtained by integrating over the entire volume of solvent:

$$W = \int_{r_0}^{\infty} W_r 4\pi r^2 dr \tag{71}$$

By applying the scaled particle theory (Pierotti 1963, 1976), we can evaluate the reversible work required to produce a cavity of radius, r:

$$W = kT\ln\left(1 - \frac{4}{3}\pi r^3 \rho_w\right) \tag{72}$$

The scaled particle theory as well as previous statistical mechanical studies by Reiss et al. (1959), Frisch (1963), and Harris and Tully-Smith (1971) produced a number of approximate expressions for calculating the reversible work of cavitation that, however, remain empirical. In an alternative approach, the hydration energy is considered to be the sum of translation and internal contributions (int), solvent reorganization (ss) upon solute insertion, and solute-solvent (sw) interaction (Lazaridis 1998; Ben-Amotz et al. 2005):

$$G = G_{\text{int}} + G_{\text{ss}} + G_{\text{sw}} \tag{73}$$

The partial molar volume of the solute is obtained by differentiating the standard molar Gibbs energy by pressure at constant temperature:

$$V = \sum \kappa RT + V_{\text{ss}} + V_{\text{sw}} \tag{74}$$

where the first term represents the sum of all compressibility terms arising from the internal (thermal) motion of the solute and the standard state conversion, and

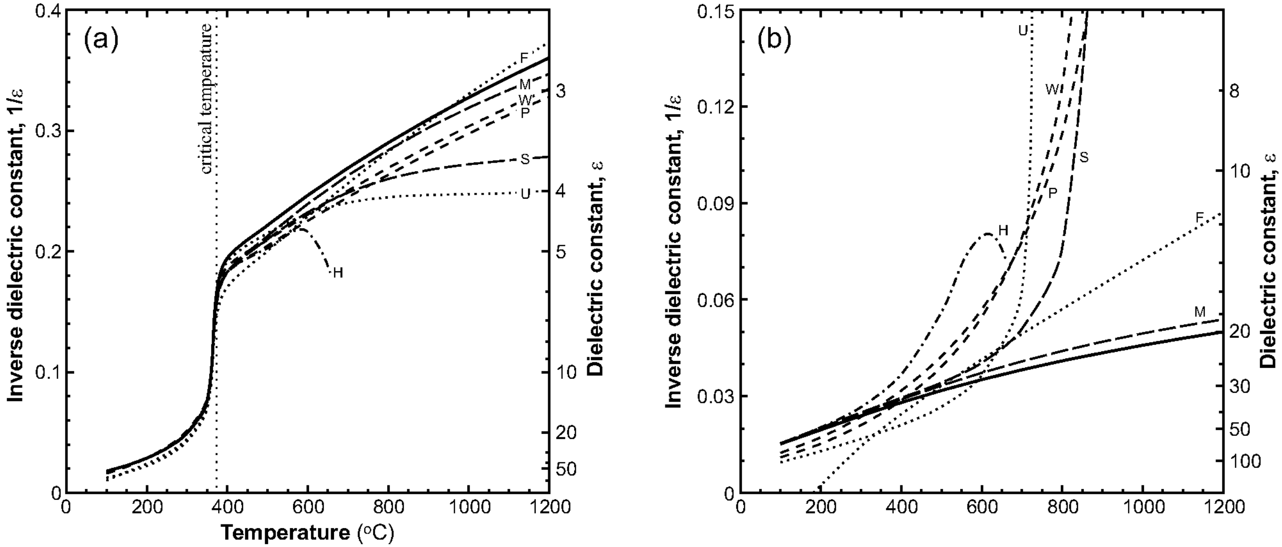

Figure 6. Prediction of the inverse dielectric constant of H_2O (proportional to Born electrostatic energy) at (a) liquid-vapor saturation and critical isochore ($\rho = 0.322$ g cm^{-3}), and (b) geothermal gradient, dT/dP = 25 °C $kbar^{-1}$, corresponding to the subduction thermal regime. Abbreviations: F – Franck et al. (1990), H – Helgeson and Kirkham (1974), M – Marshall (2008a), P – Pitzer (1983a), S – Shock et al. (1992), U – Uematsu and Franck (1980), W – Wassermann et al. (1995). The thick curve represents the IAPWS formulation (Fernandéz et al. 1997).

$$V_{\mathrm{sw}} = \kappa RT = N_{\mathrm{A}} \int \left(1 - g_{\mathrm{sw}}\right) dr \tag{75}$$

where g_{sw} is the grand-canonical solute-solvent pair correlation function (Kirkwood and Buff 1951). Note that this integral scales with the κRT term arising from the other contributions. By applying the chain rule to the pressure derivative of the remaining portion of the Gibbs energy due to solvent reorganization (Ben-Amotz et al. 2005), we obtain:

$$V_{\mathrm{ss}} = \left(\frac{\partial G_{\mathrm{ss}}}{\partial P}\right)_T = \left(\frac{\partial G_{\mathrm{ss}}}{\partial \rho_{\mathrm{w}}}\right)_T \left(\frac{\partial \rho_{\mathrm{w}}}{\partial P}\right)_T = \kappa \rho_{\mathrm{w}} \left(\frac{\partial G_{\mathrm{ss}}}{\partial \rho_{\mathrm{w}}}\right)_T \tag{76}$$

The last expression has a close relationship to the Krichevskii parameter, A_{Kr} (Ben-Amotz 2005):

$$A_{\mathrm{Kr}} = \rho_{\mathrm{w}}^2 \left(\frac{\partial U}{\partial \rho_{\mathrm{w}}}\right)_T \tag{77}$$

The generalized Krichevskii parameter (Levelt Sengers 1991; Plyasunov et al. 2000) represents the change in pressure upon replacement of an infinitesimal amount of solvent by solute, evaluated at the solvent critical point (Plyasunov 2012):

$$A_{\mathrm{Kr}} = -\lim_{x_i \to 0} \left(\frac{\partial^2 A}{\partial V \partial x_i}\right)_T = \lim_{x_i \to 0} \left(\frac{\partial P}{\partial x_i}\right)_{T,V} = \frac{V_i}{\kappa RT} = 1 - C_{12} \tag{78}$$

where A is the Helmholtz energy of the solvent-solute system, x_i is the mole fraction of the solute, and C_{12} is the dimensionless spatial integral of the infinite dilution solute-solvent direct correlation function arising in the fluctuation solution theory (Kirkwood and Buff 1951; O'Connell 1971, 1990; O'Connell et al. 1996). The Krichevskii parameter has the advantage of behaving as a finite smooth function in the vicinity of the critical point and it is nearly independent of temperature when applied to both electrolyte and non-electrolyte systems (Cooney and O'Connell 1987; Crovetto et al. 1990). It provides a linear proportionality constant between the partial molar volume of solute and the solvent compressibility (Eqn. 78) that has been experimentally confirmed at elevated temperatures for inorganic solutes in aqueous and organic solvents (Hamann and Lim 1954; Ellis 1966; Criss and Wood 1996).

Macroscopic thermodynamic models

Macroscopic thermodynamic models are equations of state that are constructed from equality of the solute chemical potential in coexisting phases (e.g., solution vs. saturating gas or solid phase):

$$\mu^{\mathrm{aq}} = \mu^{\mathrm{g}} \tag{79}$$

Expanding Equation (79) as an ideal aqueous solution and real gas (fluid) leads to:

$$G^{\mathrm{aq}} + RT \ln m = G^{\mathrm{g}} + RT \ln f \tag{80}$$

where f stands for the fugacity of the gas, and G^{g}, the standard Gibbs energy of the pure gas, refers to the temperature of interest and the pressure of 1 bar. The purpose of this expansion is to express the standard molal Gibbs energy of an aqueous solute as a function of the standard Gibbs energy of the pure gas and of the non-ideal contribution, that is, a fugacity coefficient referred to infinite dilution. Following Akinfiev (2000) and Akinfiev and Diamond (2003, 2004), the fugacity coefficient of H_2O is evaluated using the virial equation of state referred to infinite dilution:

$$G^{aq} = G^{g} + (1-\xi)RT\ln f + RT\ln\frac{1000}{M_w} + \xi RT\ln\frac{RT\rho_w}{M_w} + RT\rho_w\left(a + b\sqrt{\frac{1000}{T}}\right) \quad (81)$$

where ξ is a dimensionless empirical scaling factor (Plyasunov et al. 2000), and a and b are parameters that describe the change in the second virial coefficient by comparing the solvent-solvent and solute-solvent interactions.

This equation of state provides an accurate description of the partial molal properties of aqueous electrolytes that continuously and correctly approach the ideal gas law as the fluid density decreases (Fig. 7); it has also been successfully applied to the description of the volume and heat capacity of the NaCl electrolyte up to 4 kbar (Akinfiev and Diamond 2004), and, with addition of the Born electrostatic term, to the solubility of SiO_2 up to 600 °C and 1 kbar (Akinfiev 1999). The model has been derived from the truncated virial equation of state for nonelectrolytes (low-density fluids) and its parameters remain largely empirical.

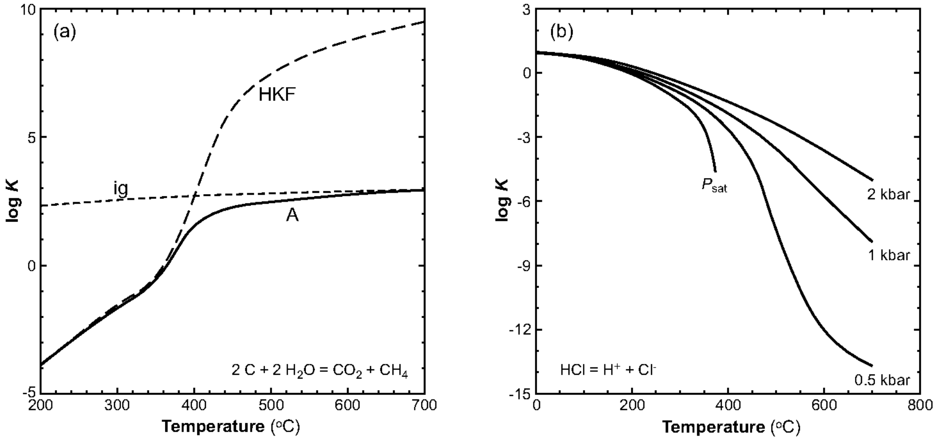

Figure 7. Prediction of equilibrium constants for (a) graphite dissociation to carbon dioxide and methane in aqueous environment, and (b) dissociation of hydrochloric acid using the equation of state by Akinfiev and Diamond (2003). Abbreviations: A – Akinfiev and Diamond (2003), HKF – Shock et al. (1992), ig – ideal gas.

Electrostatic models

Electrostatic models include equations of state, which use the Born theory to describe the thermodynamic properties of species hydration and their dependence on temperature and pressure. The Born contribution is generally augmented by caloric intrinsic, caloric single or stepwise hydration, volumetric and/or standard-state conversion terms, which may have physical justification or be chosen empirically. Hydration *sensu stricto* is a transfer process at constant temperature and pressure only and therefore, individual models differ in the extent in which the pressure-temperature changes in the thermodynamic properties are apportioned between the electrostatic and other contributions.

Djamali-Cobble model. This is a simple electrostatic model which illustrates the essential features of combining the caloric, Born and standard state conversion terms rather well (Djamali and Cobble 2009, 2010). It is applicable to all partial molal properties of electrolytes or ionization equilibria from ambient conditions to 1000 °C and 1 GPa, although its performance at high pressures has not yet been rigorously tested. The standard energy of hydration ($\Delta_h G$)

incorporates both the effect of pressure and temperature and the species transfer from an ideal gas state to that of a one molal solution, and is defined as follows:

$$\Delta_{\mathrm{h}}G = \Delta G_{\mathrm{nel}} + \Delta_{\mathrm{B}}G + \Delta_{\mathrm{ss}}G \tag{82}$$

with the non-electrostatic (nel), Born (B) and standard-state conversion (ss) terms:

$$\Delta G_{\mathrm{nel}} = \Delta H - T\Delta S \tag{83}$$

where ΔH and ΔS represent the enthalpy and entropy loss of the solvent molecules in the primary hydration shell, respectively, and are independent of pressure and temperature,

$$\Delta_{\mathrm{B}}G = \frac{N_{\mathrm{A}}e^2}{2r_{\mathrm{B}}}\left(\frac{1}{\varepsilon_{P,T}} - 1\right) \tag{84}$$

with r_{B} representing the Born radius parameter, which incorporates ionic radii, ionic charges and stoichiometry in the species by applying the following weighting scheme:

$$\frac{1}{r_{\mathrm{B}}} = \sum_i \frac{\nu_i z_i^2}{r_i} \tag{85}$$

where r_i is the effective electrostatic radius of the spherical cavity in the dielectric continuum, defined as the distance beyond which the bulk dielectric constant of the solvent is applicable (Djamali and Cobble 2009). The single value of r_{B} can be adjusted in order to improve reproducibility of experimental data, and

$$\Delta_{\mathrm{ss}}G = \nu RT \ln \frac{m_{\mathrm{o}}\rho RT}{1000P_{\mathrm{o}}} \tag{86}$$

where ν is the number of ions in the species or electrolyte, ρ is the density of the pure solvent (g cm^{-3}) at the pressure and temperature of interest, $m_{\mathrm{o}} = 1$ mol kg^{-1}, and $P_{\mathrm{o}} = 1$ bar. For calculation of the standard thermodynamic properties of arbitrary species, the energy of hydration is added to the standard Gibbs energies of constituting ions in an ideal gas state (e.g., Chase 1998). In order to calculate the standard Gibbs energy at elevated temperatures and pressures, it appears to be more accurate to apply the following thermodynamic cycle: (i) transfer from one molal aqueous standard state to that of an ideal gas at the reference temperature and pressure; (ii) apply temperature and pressure effects in the ideal gas state to the temperature and pressure of interest; (iii) transfer from the ideal gas state to one molal aqueous solution at the temperature and pressure of interest. More detailed discussion of alternative thermochemical cycles is provided by Tremaine and Goldman (1978).

The Djamali-Cobble model reproduces the standard Gibbs energies, entropies, volumes and heat capacities of ionization equilibria rather accurately. However, it has only been tested at subcritical temperatures and pressures less than 1 kbar. In this region, the thermodynamic properties are dictated by the divergence at the solvent critical point and, by contrast, the decrease in partial molal heat capacities and volumes observed experimentally at $T < 100$ °C cannot be reproduced. Application of the model to high pressures of geological relevance remains unexplored but the necessity of including non-electrostatic volumetric terms is to be expected.

Tanger-Pitzer model. The design of the Tanger-Pitzer semicontinuum model (Tanger and Pitzer 1989a) is similar to that of Djamali and Cobble (2009, 2010) but the non-electrostatic contribution is described more accurately as successive hydration dictated by increasing H_2O fugacities as pressure in the system increases. The standard Gibbs energy of ion hydration at pressure and temperature of interest is defined by

$$\Delta_{\mathrm{h}}G = \Delta_{\mathrm{h,is}}G + \Delta_{\mathrm{h,os}}G + \Delta_{\mathrm{ss}}G \tag{87}$$

where subscripts is and os refer to the inner- and outer-shell contribution to hydration, respectively. The standard-state conversion term is identical to Equation (56) ($\nu = 1$) and the outer-shell hydration term is equated with the Born electrostatic term (Eqn. 59). The inner-shell contribution accounts for the Gibbs energies of the solute hydrated by up to six H_2O molecules according to the reaction:

$$\mathrm{A\ (g)} + n\ \mathrm{H_2O} = \mathrm{A(H_2O)}_n \tag{88}$$

where $n = 1$ to 6. The stepwise equilibrium constant for individual hydration reaction:

$$\mathrm{A(H_2O)}_{n-1} + \mathrm{H_2O} = \mathrm{A(H_2O)}_n \tag{89}$$

becomes

$$K_n = \frac{f_n}{f_{n-1} \cdot f_{\mathrm{H_2O}}} \tag{90}$$

where f represent fugacities of individual hydrated states and of H_2O (g). Standard reaction enthalpies and entropies for these equilibria are available experimentally or computationally (e.g., Kebarle 1977; Pitzer 1983b; Likholyot et al. 2007; Lemke and Seward 2008). The standard Gibbs energy of the inner-shell hydration is then:

$$\Delta_{\mathrm{h,is}}G = -RT \ln\left[1 + \sum_{i=1}^{6}\left(f^{n}_{\mathrm{H_2O}} \frac{\gamma_g}{\gamma_n} \prod_{j=1}^{n} K_j\right)\right] \tag{91}$$

The ratio of the fugacity coefficients between n-hydrated (γ_n) and unhydrated (γ_g) species can be set to unity at low pressures (vapor-like fluid densities; Pitzer 1982) but otherwise is evaluated through the contribution of the effective volume increment per hydration step ($V^{*}_{\mathrm{H_2O}}$), assumed to be independent of pressure:

$$\ln \frac{\gamma_{\mathrm{n}}}{\gamma_{\mathrm{g}}} = \frac{\int_{P_{\mathrm{ref}}}^{P} nV^{*}_{\mathrm{H_2O}}dP}{RT} \tag{92}$$

therefore

$$\ln \frac{\gamma_{\mathrm{n}}}{\gamma_{\mathrm{g}}} = -\frac{nPV^{*}_{\mathrm{H_2O}}}{RT} \tag{93}$$

where the volume increment is empirically fitted to a five-term polynomial in temperature and crystallographic radius of the ion (Tanger and Pitzer 1989b). This model has been successfully applied to standard properties of aqueous sodium chloride covering the high-temperature and low-pressure region, and its setup also permits evaluation of the mean hydration numbers and separation of the inner- and outer-shell hydration contributions as a function of temperature and pressure.

Application of Equations (87) and (91) allows calculation of the equilibrium constants for self-dissociation of an aqueous solvent (Bandura and Lvov 2006) and predicts a progressive increase in ion hydration as the fugacity of water increases (Pitzer 1982; Tanger and Pitzer 1989b). The complete formation of the inner hydration shell, i.e., when the maximum hydration number has been reached, necessarily results in a linear relationship between the logarithm of solvent fugacity and the partial fugacity or concentration of the aqueous species (Fig. 8). At low densities, where the solvent properties are close to those of an ideal gas,

$$\rho_{\mathrm{w}} = \frac{M_{\mathrm{w}}P}{RT} \tag{94}$$

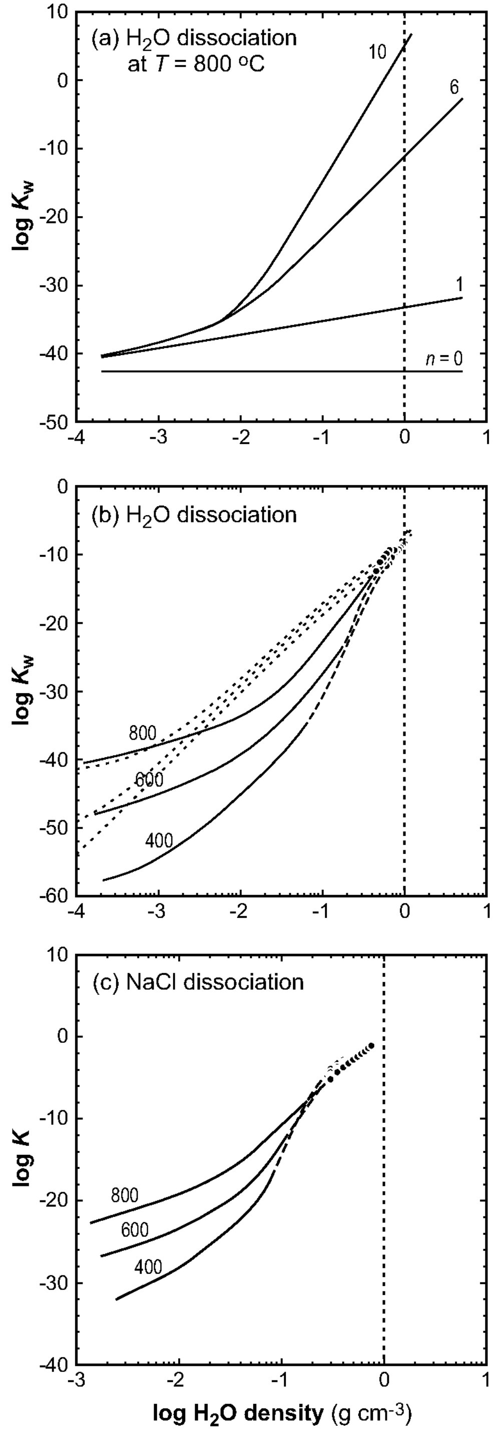

Figure 8. Relationships between logarithmic density of aqueous solvent and logarithmic equilibrium constants for homogeneous solvent and salt dissociation predicted by stepwise hydration models: (a) ideal-gas hydration model for self-dissociation of H_2O (Pitzer 1982). The symbol n represents the maximum hydration number of aqueous species and it is related to the $\log K_w/\log \rho$ slope in the ideal-gas approximation; (b) ideal-gas hydration model for self-dissociation of H_2O (Pitzer 1982), which merges with experimental data at liquid-like densities (Quist 1970) when a maximum of 6-7 H_2O molecules in the inner hydration shell is reached (solid curves represents formulation of Pitzer 1982; dotted curves were computed using the model of Bandura and Lvov 2006, at 400, 600 and 800 °C); (c) ideal-gas hydration model for dissociation of NaCl (aq) (Pitzer 1983b). Symbols represent experimental data of Quist and Marshall (1968), at 400, 600 and 800 °C.

Therefore, the plot of the logarithm of equilibrium constant vs. the logarithm of solvent density has a constant linear slope corresponding to the maximum hydration number (Fig. 8a). This behavior has been confirmed for H^+, OH^- and other electrolytes (Pitzer 1982; Tanger and Pitzer 1989b) and is illustrated in Figures 8b and 8c. With increasing solvent densities, $\rho_w > 0.4$ g cm^{-3}, deviations from the non-ideal gas behavior of water and of hydrated species become significant.

Helgeson-Kirkham-Flowers model. The Helgeson-Kirkham-Flowers model represents the main equation of state for calculating the standard partial molal thermodynamic properties of aqueous species at elevated temperatures and pressures (Helgeson et al. 1981; Tanger and Helgeson 1988; Shock et al. 1992; Oelkers et al. 1995). The model treats the thermodynamics of charged species, neutral aqueous complexes and dissolved fluids (gases) as a combination of three contributions: (i) reference state properties at 25 °C and 1 bar; (ii) energetic contribution from charging in the aqueous solvent furnished by the Born theory, with a pressure- and temperature-dependent Born parameter; (iii) an empirical (non-solvation) contribution, which improves the prediction of the partial molar volume and heat capacity of aqueous species resulting from solvent collapse and electrostriction effects. The standard partial molar Gibbs energy of formation of aqueous species at the pressure and temperature of interest referred to infinite dilution is defined as follows:

$$\Delta_f G_{P,T} = \Delta_f G_{P_{\mathrm{ref}},T_{\mathrm{ref}}} + \int_{T_{\mathrm{ref}}}^{T} C_P dT - S_{T_{\mathrm{ref}}}\left(T - T_{\mathrm{ref}}\right) - T\int_{T_{\mathrm{ref}}}^{T} \frac{C_P}{T} dT + \int_{P_{\mathrm{ref}}}^{P} V dP + \Delta_B G_{P,T} - \Delta_B G_{P_{\mathrm{ref}},T_{\mathrm{ref}}} \quad (95)$$

The heat capacity (C_P) and volume (V) terms incorporate empirical non-solvation contributions, as follows (Helgeson et al. 1981; Tanger and Helgeson 1988; Shock et al. 1992):

$$V^\circ = a_1 + a_2 \frac{1}{\Psi + P} + a_3 \frac{1}{T - \Theta} + a_4 \frac{1}{(T - \Theta)^2} \quad (96)$$

and

$$C_P = c_1 + c_2 \frac{1}{(T - \Theta)^2} \quad (97)$$

where $\Theta = 228$ K and $\Psi = 2600$ bar, and a_1-a_4 and c_1-c_2 are the species-specific parameters. The non-solvation terms empirically describe the divergence of heat capacity and volume as the supercooled liquid-liquid critical point is approached at very low temperatures (Angell 1983; Fuentevilla and Anisimov 2006; Bertrand and Anisimov 2011; Holten et al. 2012). By contrast, at high temperatures and pressures the non-solvation terms become smaller and tend to linearize; thus prediction of the Gibbs energy is largely determined by the standard enthalpy, entropy, and the Born electrostatic term only. Furthermore, significant correlations exist between individual model parameters (Shock and Helgeson 1988; Shock et al. 1989, 1997; Sverjensky et al. 1997), and therefore the model is effectively a low-parametric one where much of the variations are linked, and probably reflect more universal species-solvent interactions.

The Helgeson-Kirkham-Flowers model is conventionally restricted to 1000 °C and 5 kbar at liquid-like fluid densities ($\rho_w > 0.35$ g cm^{-3}). In addition, it becomes increasingly inaccurate in the vicinity of the critical point of solvent, thus it is not applicable at a temperature range of 350-400 °C and pressure lower than 500 bar. Application of the Helgeson-Kirkham-Flowers model requires accurate data for volumetric and electrostatic properties of the aqueous solvent, and their pressure and temperature derivatives. Their paucity prevented use and development of this model to address fluid-mediated mass transfer in the lower crust and upper mantle, release of volatiles from magmas at low fluid densities, or element partitioning during fluid ascent and boiling. Extrapolations to very high temperatures and pressures, while preserving the framework of the model, can be tested and verified by replacing the original formulations for the density and the dielectric constant of H_2O with newer data applicable at a wider range of conditions, as proposed by Mungall (2002) and Manning et al. (2013). Figure 9 illustrates the consequences of this approach for the dissociation of H_2O and the solubility of quartz. Prediction of the equilibrium constant for the H_2O dissociation progressively deviates from the current scientific standard (Bandura and Lvov 2006); the difference reaches 0.2 log units at 700 °C and 9 kbar, and 0.5 log units at 900 °C and 12 kbar but it remains within the range bracketed by the density models (Marshall and Franck 1981; Holland and Powell 1998). Above 900 °C at $\rho_w = 0.9$ g cm^{-3}, inaccurate description of the solvent properties by Haar et al. (1984) and Shock et al. (1992) prevents acceptable prediction, which, however, is significantly improved by using the IAPWS formulations (Wagner and Pruß 2002; Fernandéz et al. 1997); the remaining deviation from the standard trend (Bandura and Lvov 2006) can be accounted for by adjusting the standard partial molal enthalpy and volume of the OH^- anion. By contrast, predictions of quartz solubility using different density and dielectric constant formulations for H_2O are nearly identical up to 800 °C and 16 kbar. However, the solubility trend significantly deviates from linearity and density model predictions above 5 kbar, i.e., $\rho_w = 0.7$ g cm^{-3} (Fig. 9b). At these conditions, the changes in the Born energy become negligible, and therefore, the progressive deviation is related to inadequate representation of the solute non-solvation volumetric properties implicit in the Helgeson-Kirkham-Flowers model.

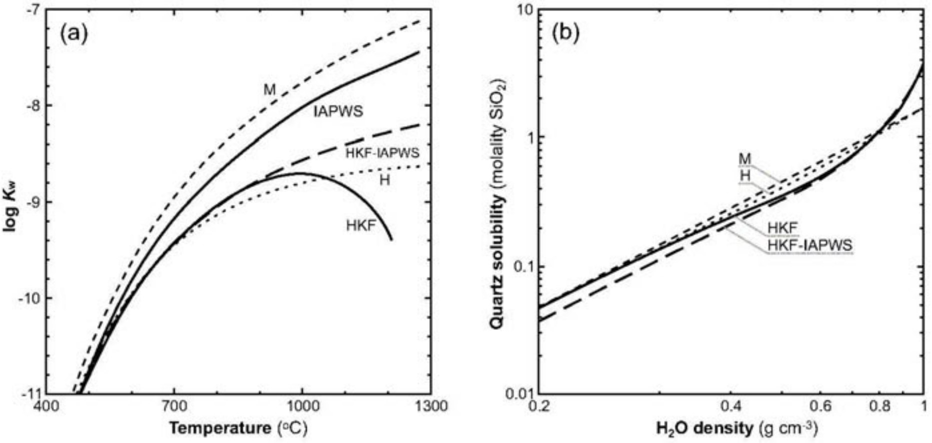

Figure 9. Comparison of prediction of (a) self-dissociation of H_2O along the H_2O isochore $\rho_w = 0.9$ g cm^{-3} and (b) quartz solubility at $T = 800$ °C, with the Helgeson-Kirkham-Flowers, density and IAPWS models. Abbreviations: H – Holland and Powell (1998), HKF – Shock et al. (1992), HKF-IAPWS – Shock et al. (1992) using the international calibration for the solvent density and dielectric constant (Wagner and Pruß 2002, Fernandéz et al. 1997), IAPWS – Bandura and Lvov (2006), M – Manning (1994).

Density models

The density models provide equations of state for association and dissociation equilibria, solid solubilities and for standard molal properties of aqueous species that are based on caloric and volumetric properties as functions of temperature and solvent density, and they do not include explicit provision for electrostatic interactions (e.g., Mesmer et al. 1988; Anderson et al. 1991; Sedlbauer et al. 2000; Dolejš and Manning 2010). Their development has been motivated by empirical observations of log-log linear relationships between equilibrium constant and solvent density ($\ln K \propto \ln\rho_w$, $\Delta_r G \propto RT\ln\rho_w$), which is consistent with the proportionality between the standard molal volume of the reaction or solute and the solvent compressibility ($V^{aq} \propto \kappa RT$). The latter relationship arises from the statistical mechanics (Eqns. 74-75), standard state conversion (Eqns. 55-56) as well as from the analysis of critical behavior in binary fluid mixtures (Eqn. 78), and thus has recently become a cornerstone of new equations of state for aqueous electrolytes and nonelectrolytes (e.g., Sedlbauer et al. 2000; Sedlbauer and Wood 2004).

The density models discussed below do not contain explicit provision for the electrostatic contribution to the standard properties of the solute despite their applications to weak and strong electrolytes (Ho et al. 1994; Ho and Palmer 1997; Sedlbauer and Wood 2004; Ballerat-Busserolles et al. 2007). The individual effects of the electrostatic contribution and the solvent compression due to electrostriction have not been independently addressed but the universal utility of the models with electrostatic or density terms only suggests that these two may be significantly correlated. The Gibbs energy contributions scale with the inverse dielectric constant (Eqn. 58) and with the $T \ln \rho_w$ (Eqn. 74, upon integration). Mutual correlation of these two variables is shown in Figure 10, and demonstrates that the density models can replace the lack of constraints on the dielectric constant at very high temperatures or pressures.

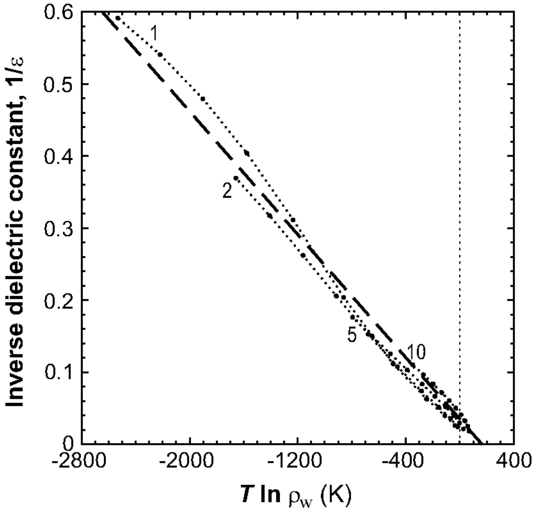

Figure 10. Correlation between the solvent density and dielectric constant terms. The inverse dielectric constant of H_2O proportionally scales with the reduced Born energy, $\Delta_B G/\omega$. Data of Fernandéz et al. (1997) are illustrated for isobars of 1, 2, 5 and 10 kbar (dotted curves labels) at a temperature range of 200-1100 °C (point symbols in 100 °C steps). Dashed line is a linear fit to the data set: $1/\varepsilon = -1.135 \times 10^{-3}\ T \ln\rho_w + 3.497 \times 10^{-2}$.

Sedlbauer-O'Connell-Wood model. This equation of state provides formalism for the standard molal properties of aqueous nonelectrolytes and electrolytes based on the standard thermodynamic properties of hydration derived from the fluctuation solution theory and the standard properties of species in the ideal gas state (Sedlbauer et al. 2000; Sedlbauer and Wood 2004; Ballerat-Busserolles et al. 2007; Majer et al. 2008; Sedlbauer 2008).

The partial molal volume of aqueous species is related to the compressibility of the aqueous solvent as follows (*cf.* Eqn. 78):

$$V^{aq} = A_{Kr} \kappa RT \qquad (98)$$

The Krichevskii parameter (A_{Kr}) may be expressed using the virial expansion (Majer et al. 1999):

$$A_{Kr} = 1 + \frac{2}{M_w} \rho_w B_w + \ldots \qquad (99)$$

where B_w is the second cross (solute-water) virial coefficient. This truncated expansion leads to a two-parameter expression for the partial molal volume of aqueous solute (O'Connell 1995):

$$V^{aq} = RT\kappa\left\{1+\rho_w\left[a+b\left(e^{v\rho_w}-1\right)\right]\right\} \tag{100}$$

where a and b are the solute-specific parameters, and v is a constant (5 cm^3 g^{-1}) (O'Connell et al. 1996). By comparing the virial expansions of the solute and those of the aqueous solvent, and introducing the scaling factor (d), the molar volume becomes:

$$V^{aq} = RT\kappa + d(V_w - RT\kappa) + RT\kappa\rho_w\left[a+b\left(e^{v\rho_w}-1\right)+ce^{\Theta/T}+\delta\left(e^{\lambda\rho_w}-1\right)\right] \tag{101}$$

where v = 0.005 m^3 kg^{-1}, λ = –0.01 m^3 kg^{-1}, δ = 0.35a (for nonelectrolytes), 0 m^3 kg^{-1} (for cations) or –0.645 m^3 kg^{-1} (for anions), respectively, and Θ = 1500 K. The a-d coefficients are solute-specific adjustable parameters (Sedlbauer et al. 2000; Sedlbauer 2008). Individual terms correspond to a series of hydration steps and represent insertion of an ideal gas species into the solvent (κRT), the cavity formation effect scaled to the solvent volume (dV_w – dκRT), and the solute-solvent interaction contribution (change in the potential field from the solvent-solvent to the solute-solvent interaction); the last term is mostly empirical and optimized by analysis of experimental data for electrolyte and nonelectrolyte solutions. The standard Gibbs energy of hydration ($\Delta_h G$) is obtained by integrating Equation (101) and introducing the conversion term between the ideal gas and aqueous molal standard states, respectively:

$$\Delta_h G = RT\ln\frac{P}{P_{ref}} + \int_{P_{ref}}^{P}\left(V^{aq}-\frac{RT}{P}\right)dP - dRT\ln\frac{RT\rho_w}{P_{ref}M_w} + \Delta_{cor}G \tag{102}$$

where $\Delta_{cor}G$ is a correction representing the Gibbs energy difference that occurs during the integration path when crossing the liquid-vapor boundary at subcritical temperatures (Sedlbauer and Wood 2004). The standard molal Gibbs energy of the aqueous solute is defined by adding the hydration contribution to the species properties in the ideal gas state, as follows:

$$G^{aq} = G^{ig} + \Delta_h G \tag{103}$$

This equation of state is valid for both electrolytes and nonelectrolytes including organic solutes, and its major advantage is a close reproduction of derivative properties (such as volume or heat capacity) near the solvent critical region and at low fluid densities. Its complexity arises from the desire to accurately describe the variations of the Krichevskii parameter in a solvent's near-critical region by a multiple-term empirical function. As shown below, the Krichevskii parameter for representative solutes of geochemical relevance remains constant over wide range of temperature and pressure, and hence reduction of the hydration properties to one volumetric and a constant Krichevskii term may provide a versatile tool for geological applications.

Empirical density models. Development of empirical density models was motivated by a universal linear relationship between the logarithm of the equilibrium constant for homogeneous and heterogeneous aqueous equilibria and the logarithm of the solvent density at constant temperature (Mosebach 1955; Franck 1956; Martynova 1964; Marshall and Quist 1967; Quist and Marshall 1968; Sweeton et al. 1974; Fournier and Potter 1982; Marshall and Mesmer 1984; Eugster and Baumgartner 1987; Mesmer et al. 1988; Anderson et al. 1991; Ho et al. 1994; Manning 1994; Ho and Palmer 1997; Marshall 2008b; Fig. 11). These correlation relationships for homogeneous and heterogeneous equilibria have only recently been developed into equations of state for aqueous species. The original polynomial expansion in temperature and solvent density (Mesmer et al. 1988):

$$\ln K = -\frac{\Delta_r G}{RT} = \sum_{i=0}^{3} a_i T^{-i} + \ln\rho_w \sum_{j=0}^{2} b_j T^{-j} \tag{104}$$

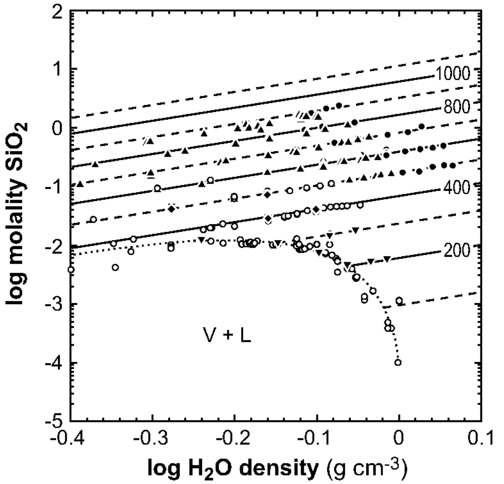

Figure 11. Quartz solubility at isotherms of 25, 100 through 900 °C illustrated as a function of logarithmic solvent density. Sources of experimental data: (a) solid upright triangles – Anderson and Burnham (1965); solid inverted triangles – Hemley et al. (1980); solid diamonds – Walther and Orville (1983); solid circles – Manning (1994), open circles – Kennedy (1950), Morey and Hesselgesser (1951), Wyart and Sabatier (1955), Kitahara (1960), Morey et al. (1962), Weill and Fyfe (1964), and Crerar and Anderson (1971).

where K is the equilibrium constant, and a_i and b_j are empirical parameters, has been reduced to a three parameter form (Mesmer et al. 1988; Anderson et al. 1991; Anderson 2005):

$$\ln K = a_0 + \frac{a_1}{T} + \frac{b_1}{T}\ln\rho_w \tag{105}$$

where the parameters a_0, a_1 and b_1 are directly derived from the standard properties of equilibrium at reference conditions (e.g., Gibbs energy, enthalpy, and heat capacity). The choice of individual terms is purely empirical, based on the fits to experimental association and dissociation equilibria, but the last term is inconsistent with the proportionality between ln$K$ and lnρ from statistical mechanics and critical conditions (Eqns. 78 and 98).

Anderson (1995) adopted this form directly for the standard Gibbs energy of formation for individual aqueous species:

$$\begin{aligned}\Delta_f G_{P,T} &= \Delta_f G_{P_{ref},T_{ref}} - S_{P_{ref},T_{ref}}\left(T - T_{ref}\right) \\ &+ \frac{C_{P,P_{ref},T_{ref}}}{T_{ref}\left(\dfrac{\partial\alpha_w}{\partial T}\right)_{P,P_{ref},T_{ref}}}\left[\alpha_{w,P_{ref},T_{ref}}\left(T - T_{ref}\right) + \ln\frac{\rho_w}{\rho_{w,ref}}\right]\end{aligned} \tag{106}$$

where the standard Gibbs energy, entropy and heat capacity of aqueous species at reference conditions (i.e., 25 °C and 1 bar) are substituted instead of the original parameters, and the solvent volumetric parameters at reference conditions have the following values (Anderson et al. 1991): $\rho_{P_{ref},T_{ref}} = 0.9998$ g cm^{-3}, $\alpha_{P_{ref},T_{ref}} = 2.593\times10^{-4}$ K^{-1}, and $(\partial\alpha / \partial T)_{P_{ref},T_{ref}} = 9.5714\times10^{-6}$ K^{-2}. It should be noted that this equation of state does not contain any volume term, which should ensure consistency between homogeneous vs. mineral-aqueous species equilibria. This density model was extended by Holland and Powell (1998), who (i) included the volume term, (ii) included a heat capacity term linear in absolute temperature, and (iii) proposed a temperature correction to the density term applicable at $T > 500$ K, which brings the model to consistency with the definition of the Krichevskii parameter at high temperatures:

$$\Delta_{\mathrm{a}}G_{P,T} = \Delta_{\mathrm{f}}H_{P_{\mathrm{ref}},T_{\mathrm{ref}}} - TS_{P_{\mathrm{ref}},T_{\mathrm{ref}}} + PV_{P_{ref},T_{ref}} + b\left(T_{ref}T - \frac{T_{ref}^2}{2} - \frac{T^2}{2}\right)$$
$$+ \frac{C_{P,P_{\mathrm{ref}},T_{\mathrm{ref}}}}{T_{\mathrm{ref}}\left(\dfrac{\partial\alpha_{\mathrm{w}}}{\partial \mathrm{T}}\right)_{P,P_{ref},T_{ref}}}\left[\alpha_{\mathrm{w},P_{\mathrm{ref}},T_{\mathrm{ref}}}\left(T - T_{\mathrm{ref}}\right) - \kappa_{P_{ref},T_{ref}}P + \frac{T}{T'}\ln\frac{\rho_{\mathrm{w}}}{\rho_{\mathrm{w,ref}}}\right] \tag{107}$$

where b is the heat capacity term linear in temperature, and $T' = T$ below 500 K and $T' = 500$ above 500 K. This equation of state has been calibrated for 21 aqueous species (Holland and Powell 1998, 2011) but its accuracy and applications have not yet been tested.

Recently, Dolejš and Manning (2010) evaluated mineral solubilities in aqueous fluids up to very high temperatures and pressures by a modified density model, which is internally consistent with hydration energetics and should provide a foundation for a new equation state for aqueous species. Their approach is based on two heuristic observations: (i) the intrinsic volumetric properties of unhydrated species are closely approximated by those of the corresponding solid phase, and (ii) the caloric hydration properties become a simple expansion of enthalpy, entropy and heat capacity when evaluated at constant solvent density. This allows the intrinsic and hydration properties to be described by two distinct pressure-temperature paths, which leads to a particularly simple, low-parameter equation of state. The standard Gibbs energy of dissolution ($\Delta_{\mathrm{ds}}G$) is conventionally defined as:

$$\Delta_{\mathrm{ds}}G = G^{\mathrm{aq}} - G^{\mathrm{sol}} \tag{108}$$

Expanding the standard Gibbs energies for both standard states in temperature and pressure yields:

$$\Delta_{\mathrm{ds}}G_{P,T} = G^{\mathrm{aq}}_{P_{\mathrm{ref}},T_{\mathrm{ref}}} + \Delta_{PT}G^{\mathrm{aq}} - \left(G^{\mathrm{sol}}_{P_{\mathrm{ref}},T_{\mathrm{ref}}} + \Delta_{PT}G^{\mathrm{sol}}\right) \tag{109}$$

where $\Delta_{PT}G$ indicates the change in the standard Gibbs energy from a reference temperature and pressure to those of interest. For the solid phase, we use the conventional integration path at variable temperatures and a constant reference pressure, followed by that at variable pressures and a constant temperature of interest, as follows:

$$\Delta_{PT}G^{\mathrm{sol}} = G^{\mathrm{sol}}_{P,T} - G^{\mathrm{sol}}_{P_{\mathrm{ref}},T_{\mathrm{ref}}} = \int_{T_{\mathrm{ref}}}^{T}\left(\frac{\partial G^{\mathrm{sol}}}{\partial T}\right)_{P_{\mathrm{ref}}} dT + \int_{P_{\mathrm{ref}}}^{P}\left(\frac{\partial G^{\mathrm{sol}}}{\partial P}\right)_{T} dP \tag{110}$$

The standard Gibbs energy of aqueous solute is separated into an intrinsic term, which represents the properties of bare unhydrated species, and a hydration term, which accounts for solute-solvent interactions and solvent reorganization. This separation allows us to treat the dependence of both terms on temperature and pressure independently, and choose a distinct integration path for $\Delta_{PT}G$ of each term. The intrinsic term (aq,int) is expanded conventionally along isobaric and isothermal paths:

$$\Delta_{PT}G^{\mathrm{aq,int}} = G^{\mathrm{aq,int}}_{P,T} - G^{\mathrm{aq,int}}_{P_{\mathrm{ref}},T_{\mathrm{ref}}} = \int_{T_{\mathrm{ref}}}^{T}\left(\frac{\partial G^{\mathrm{aq,int}}}{\partial T}\right)_{P_{\mathrm{ref}}} dT + \int_{P_{\mathrm{ref}}}^{P}\left(\frac{\partial G^{\mathrm{aq,int}}}{\partial P}\right)_{T} dP \tag{111}$$

whereas the hydration term (aq,hyd) is evaluated along an isochoric (constant solvent density), followed by an isothermic path:

$$\Delta_{PT}G^{\mathrm{aq,hyd}} = G^{\mathrm{aq,hyd}}_{P,T} - G^{\mathrm{aq,hyd}}_{P_{\mathrm{ref}},T_{\mathrm{ref}}} = \int_{T_{\mathrm{ref}}}^{T}\left(\frac{\partial G^{\mathrm{aq,hyd}}}{\partial T}\right)_{\rho_{\mathrm{w,ref}}} dT + \int_{P_{\rho_{\mathrm{w,ref}}}}^{P}\left(\frac{\partial G^{\mathrm{aq,hyd}}}{\partial P}\right)_{T} dP \tag{112}$$

where $\rho_{w,ref}$ is the solvent density at reference conditions (e.g., 25 °C and 1 bar, that is, $\rho_{w,ref} \sim 1$ g cm^{-3}). This choice of integration path is motivated by the empirical simplicity of the density model (Mesmer et al. 1988, Anderson et al. 1991), where the caloric properties of hydration become a simple function of temperature, tractable by expansion into enthalpy, entropy and constant or linear (isochoric) heat capacity.

Integrals in Equations (110)-(112) incorporate conventional caloric and volumetric equations of state, but differences in properties become particularly simple when the higher-order derivative properties are assumed to be equal and cancel out. The mineral solubility data at 25-1100 °C and 0.001-20 kbar permit the following approximations (Dolejš and Manning 2010, Šulák and Dolejš 2012):

$$V_{P,T}^{\text{sol}} = V_{P,T}^{\text{aq,int}} \tag{113}$$

and

$$\int_{T_{\text{ref}}}^{T} \left[\left(\frac{\partial G^{\text{aq,int}}}{\partial T} \right)_{P_{\text{ref}}} + \left(\frac{\partial G^{\text{aq,hyd}}}{\partial T} \right)_{\rho_{\text{w,ref}}} - \left(\frac{\partial G^{\text{aq,hyd}}}{\partial T} \right)_{P_{\text{ref}}} \right] dT = a + bT + cT\ln T + dT^2 \tag{114}$$

where the coefficients *a*-*d* have dimension of enthalpy, entropy, and constant and linear heat capacity, respectively, and do not need to explicitly distinguish the isobaric and isochoric properties. Note that the term *a* also incorporates any energy changes due to hydration and standard-state conversion that are constants at 25 °C and 1 bar. Substituting Equations (110)-(112) and (114) into Equations (108)-(109), and expressing the pressure dependence of the standard Gibbs energy of hydration as discussed above (Eqns. 74 and 98) gives:

$$\int_{P_{\rho_{\text{w,ref}}}}^{P} \left(\frac{\partial G^{\text{sol}}}{\partial P} \right)_T dP = eT \ln \frac{\rho_{\text{w,P,T}}}{\rho_{\text{w,ref}}} \tag{115}$$

where $\rho_{w,ref} = 1$ g cm^{-3}, leads to the following equation for the standard Gibbs energy of mineral solubility in pure H_2O (Dolejš and Manning 2010):

$$\Delta_{\text{ds}}G = a + bT + cT\ln T + dT^2 + eT\ln\rho_{\text{w}} \tag{116}$$

This five-parameter model or its reduced, three-parameter version ($c = d = 0$) has been remarkably successful in reproducing and predicting solubilities of main rock-forming minerals in aqueous fluids up to 1100 °C and 20 kbar (Dolejš and Manning 2010). In particular, it reproduces temperature and pressure dependence including the retrograde solubility behavior of phases forming either neutral solutes or charged species with significant electrostriction effects (Fig. 12). Evaluation of the quartz solubility measurements in the vicinity of the critical point of H_2O indicates that the density approach is more accurate (Manning 1994; Dolejš and Manning 2010; Fig. 11) than conventional electrostatic models (Tanger and Helgeson 1988; Shock et al. 1992). The solubility model provides a basis for a new equation of state for aqueous species to very high temperatures and pressures (Šulák and Dolejš 2012).

APPLICATIONS OF AQUEOUS THERMODYNAMICS TO FLUID-ROCK INTERACTIONS

Recent advances in our knowledge of mineral solubility and speciation at elevated temperatures and pressures, ranging from upper-crustal geothermal systems to slab devolatilization in the Earth's mantle, permit applications of equilibrium thermodynamics to modeling of reactive fluid flow (e.g., Garven 1995; Reed 1997; Steefel et al. 2005; Comou et al. 2008; Putnis and Austrheim 2010). The nature of the fluid flow determines and predicts the extent and efficiency of element enrichment and depletion in the Earth's lithosphere (e.g., Oliver and

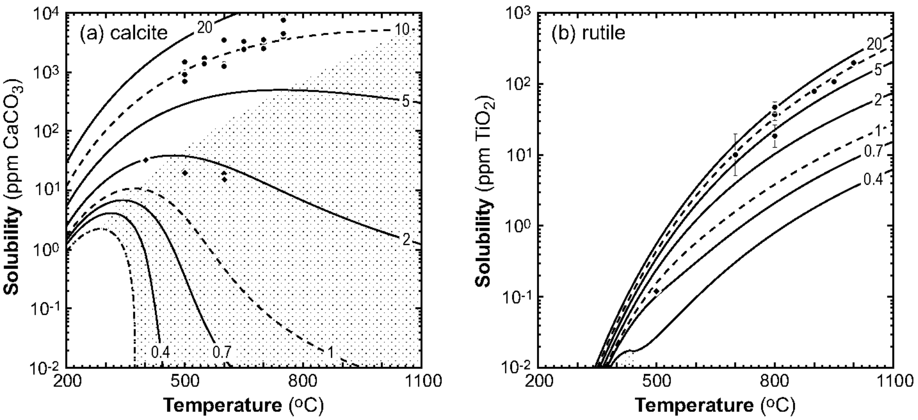

Figure 12. Predictions of the (a) calcite and (b) rutile solubility in pure H_2O using the density model of Dolejš and Manning (2010). Experimental solubility measurements are plotted along selected isobars: (a) diamonds – Fein and Walther (1989) at 2 kbar; circles – Caciagli and Manning (2003) at 10 kbar; (b) diamond – Ryzhenko et al. (2006) at 1 kbar; circles – Antignano and Manning (2008) at 10 and 20 kbar. Dotted shading indicates regions where the isobaric mineral solubility decreases with increasing temperature.

Bons 2001; Zack and John 2007), and the hydrodynamic models were successfully applied to numerous upper crustal environments, e.g., sedimentary basins, mid-ocean ridges, ore deposits and geothermal systems, but requisite equilibrium and transport properties of aqueous fluids applicable in lower crustal and upper mantle conditions are often not available. We will examine the transport theory, derive the relationships between reaction progress and thermodynamic properties at local equilibrium, and introduce possible extensions of this limiting case to treat disequilibrium flow as well.

Transport theory and estimation of fluid fluxes

Aqueous fluids generally migrate along paths of increasing temperature and decreasing pressure owing to buoyancy forces (Manning 2004; Zhu et al. 2009). The flow occurs either in a porous, pervasive manner accompanied by intimate interaction with the rock matrix, or in a channelized way whereby the fluid-to-rock ratios are higher but equilibration times become inevitably lower. Porous and channelized flow velocities are expected to be significantly different, and they vary from 10^0 to 10^3 m yr^{-1} (Thompson 1997; Ague 2003). The relationships between the time-integrated fluid flux, fluid-rock ratio and petrographic observables such as mineral mode can be derived using the mass balance considerations or from the transport theory. General mass conservation expression in one spatial dimension with the assumption of constant porosity (ϕ) and constant combined diffusion-dispersion coefficient in aqueous fluids (D) is as follows (e.g., Lasaga 1998; Philpotts and Ague 2009):

$$\varphi\frac{\partial c_{i,\mathrm{f}}}{\partial t}=-\varphi\frac{\partial\left(vc_{i,\mathrm{f}}\right)}{\partial z}+\varphi D\frac{\partial^2 c_{i,\mathrm{f}}}{\partial z^2}+\varphi R_{i,\mathrm{f}} \qquad (117)$$

where $c_{i,\mathrm{f}}$ represents the concentration of the constituent i in the fluid, v is the flow velocity in the z-direction, R is the reaction term representing the rate of consumption or production of i, and z denotes the distance. The meaning of individual terms in Equation (117) is illustrated in Figure 13.

We utilize the local equilibrium constraint and relate $R_{i,\mathrm{f}}$ to the rate of the reaction of the solid, which is a petrographic observable:

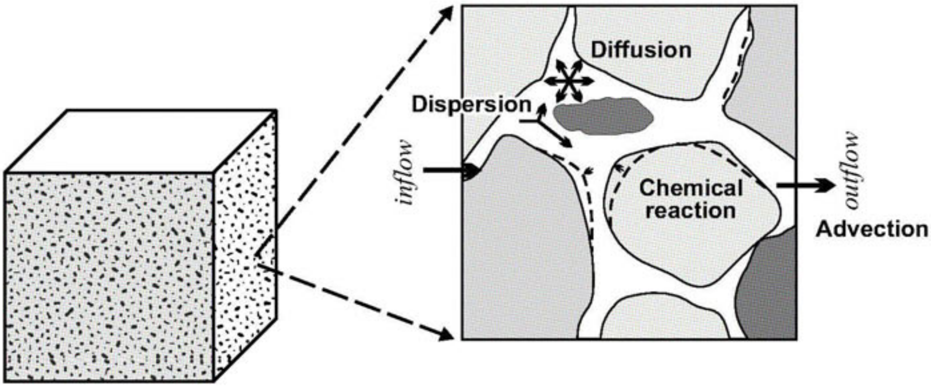

Figure 13. Schematic illustration of a rock control volume with interactions during one-dimensional fluid flow. Sources and sinks of chemical constituents are chemical reaction such as dissolution or precipitation within the control volume, diffusion and dispersion of solution within the fluid, and advection by the fluid flow.

$$-\phi R_{i,\mathrm{f}} = (1-\phi) R_{i,\mathrm{s}} \tag{118}$$

where $R_{i,\mathrm{s}}$ is the solid reaction rate (e.g., mol i $\mathrm{m_s}^{-3}$ time^{-1}) and the complementary porosity term on the right-hand side has the dimension of $\mathrm{m_s}^{-3}\ \mathrm{m_r}^{-3}$. Note that

$$R_{i,\mathrm{s}} = \frac{\partial c_{i,\mathrm{s}}}{\partial t} \tag{119}$$

For the quantification of the time-integrated fluid fluxes based on the reaction progress in the rock, it is convenient to recast Equation (117) as

$$\phi \frac{\partial c_{i,\mathrm{f}}}{\partial t} + (1-\phi) \frac{\partial c_{i,\mathrm{s}}}{\partial t} = -v\phi \frac{\partial c_{i,\mathrm{f}}}{\partial z} + \phi D \frac{\partial^2 c_{i,\mathrm{f}}}{\partial z^2} \tag{120}$$

Realizing that the second term on the left-hand side of Equation (120) has units of moles of i per unit rock volume per unit time, it may be represented as follows:

$$(1-\phi) \frac{\partial c_{i,\mathrm{s}}}{\partial t} = \frac{\partial c_{i,\mathrm{r}}}{\partial t} \tag{121}$$

where $c_{i,\mathrm{r}}$ is now the concentration of species i per unit rock volume (moles of i $\mathrm{m_r}^{-3}$). Assuming a steady state for fluid composition with time, the transport expression (Eqn. 120) reduces to:

$$\frac{\partial c_{i,\mathrm{r}}}{\partial t} = -v\phi \frac{\partial c_{i,\mathrm{f}}}{\partial z} \tag{122}$$

This expression is integrated over the total time interval of flow (t) and concentration change in the rock ($c_{i,\mathrm{r}}$) (Philpotts and Ague 2009):

$$v\phi \int_0^t dt = -\frac{1}{\left(\dfrac{\partial c_{i,\mathrm{f}}}{\partial z}\right)} \int_{c_{i,\mathrm{r}}^0}^{c_{i,\mathrm{r}}^t} dc_{i,\mathrm{r}} \tag{123}$$

where $c_{i,\mathrm{r}}^0$ and $c_{i,\mathrm{r}}^t$ are the concentration of i in the rock at the beginning and end of a reaction or a reaction front. The integrated expression

$$v\phi t = q = -\frac{c_{i,\mathrm{r}}^{t} - c_{i,\mathrm{r}}^{0}}{\left(\dfrac{\partial c_{i,\mathrm{f}}}{\partial z}\right)} = -\frac{n_{i,\mathrm{r}}}{\left(\dfrac{\partial c_{i,\mathrm{f}}}{\partial z}\right)} \qquad (124)$$

relates the time-integrated fluid flux, q ($\mathrm{m_f}^3\mathrm{m_r}^{-2}$) to the change in moles of i in the rock due to a reaction, $n_{i,\mathrm{r}}$ (mol i $\mathrm{m_r}^{-3}$). Note that Equation (124) represents a simple mass balance expression:

$$\frac{q}{\Delta z} = -\frac{n_{i,\mathrm{r}}}{\Delta c_{i,\mathrm{f}}} = f_{\mathrm{V}} \qquad (125)$$

where the left-hand side has the dimension of $\mathrm{m_f}^3\mathrm{m_r}^{-3}$, and is analogous to the fluid-rock ratio per volume, f_{V}. In other words, the overall loss or gain of i from the fluid (mol i $\mathrm{m_f}^{-3}$) must be scaled to the gain or loss of i in the rock (mol i $\mathrm{m_r}^{-3}$) through the volume ratio of these two phases. As noted by Ague (2003) and Bucholz and Ague (2010), the integrated fluid flux and the fluid-rock ratio can be interrelated if the length scale of alteration or mass transport is considered. This is because the dimensions of the fluid-rock ratio ($\mathrm{m_f}^3\mathrm{m_r}^{-3}$) or the time-integrated fluid flux ($\mathrm{m_f}^3\mathrm{m_r}^{-2}$) differ by $\mathrm{m_r}$, the characteristic distance of alteration or front propagation, parallel to the flow direction (z). The fluid-rock ratio does not necessarily express the total amount of fluid that has passed through the rock but only that amount which has caused the change in the rock composition due to the reaction (Philpotts and Ague 2009). The same expression (Eqn. 125) is used to calculate the displacement of a reaction front, that is, the length scale of the metasomatic alteration (Ferry and Gerdes 1998):

$$\Delta z = -\frac{q\Delta c_{i,\mathrm{f}}}{n_{i,\mathrm{r}}} \qquad (126)$$

For the calculation of the time-integrated fluid flux from the petrological record, we need to evaluate the concentration gradient in Equation (125). This gradient is due to precipitation and dissolution caused by fluid flow along the temperature and pressure gradient, and attainment of local equilibrium within the reference volume of length z when the infiltrating fluid is out of equilibrium with the rock (Fig. 14). The denominator in Equation (125) is expanded using the chain rule and extended to account for attainment of local equilibrium at the end of the reaction zone:

$$\frac{\partial c_{i,\mathrm{f}}}{\partial z} = \frac{\partial c_{i,\mathrm{f}}}{\partial T}\frac{\partial T}{\partial z} + \frac{\partial c_{i,\mathrm{f}}}{\partial P}\frac{\partial P}{\partial z} + \frac{\partial c_{i,\mathrm{f(rxn)}}}{\partial z} \qquad (127)$$

The first two terms on the right-hand side of Equation (127) represent the change in the concentration of i in the fluid due to the change in temperature and pressure assuming local equilibrium throughout the reference volume (Baumgartner and Ferry 1991; Ferry and Dipple 1991). This applies to the situation when a fluid is constantly in local equilibrium and any reaction is induced by changing temperature and/or pressure. The last term, newly introduced here, is a change in concentration of i from a disequilibrium value at the fluid inlet to attainment of equilibrium at the end of the reaction front, or by additional solute precipitation or interaction with the surrounding rock. In strongly reacting systems, or where gradients of temperature and pressure are negligible across the reaction front, the third term determines the overall concentration gradient (Fig. 14).

The gradients in Equation (127) include terms dictated by the local geological situation and thermodynamic properties of the system. Because the thermodynamic properties of aqueous species are referred to the molality scale (Johnson et al. 1992; Shock et al. 1992; Oelkers et al. 1995; Holland and Powell 1998), Equation (127) may be recast as

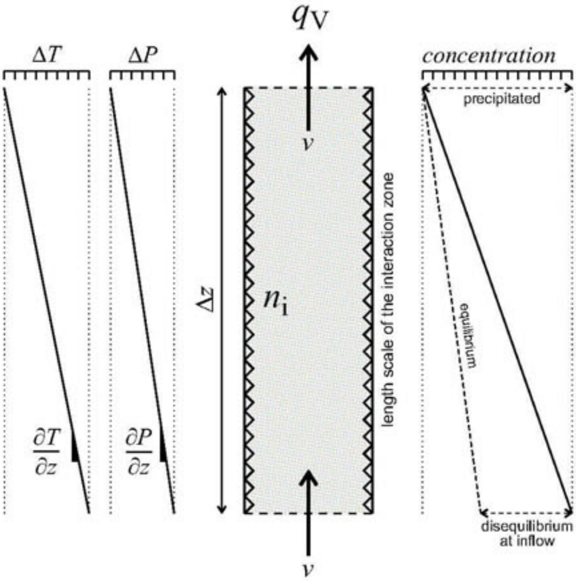

Figure 14. Relationships between the length scale of the alteration zone, reaction progress (amount precipitated) due to local equilibrium along the temperature and pressure gradient and with contribution from disequilibrium at the inflow.

$$\frac{\partial c_{i,\mathrm{f}}}{\partial z} = \rho_\mathrm{f}\left(\frac{\partial m_{i,\mathrm{f}}}{\partial T}\frac{\partial T}{\partial z} + \frac{\partial m_{i,\mathrm{f}}}{\partial P}\frac{\partial P}{\partial z} + \frac{\partial m_{i,\mathrm{f(rxn)}}}{\partial z}\right) \tag{128}$$

where ρ_f is the solvent (fluid) density (kg m^{-3}) and m represents the molality of i in the fluid (mol kg^{-1}). The gradients of molality with temperature and pressure are related to the standard thermodynamic properties of the bulk metasomatic reaction, and for a dissolution reaction producing the bulk solute i they can be calculated as follows (Dolejš and Manning 2010):

$$\frac{\partial m_i}{\partial T} = K\frac{\partial \ln K}{\partial T} = K\frac{\Delta_\mathrm{r} H}{RT^2} \tag{129}$$

$$\frac{\partial m_i}{\partial P} = K\frac{\partial \ln K}{\partial P} = -K\frac{\Delta_\mathrm{r} V}{RT} \tag{130}$$

where K is the equilibrium constant, and $\Delta_\mathrm{r}H$ and $\Delta_\mathrm{r}V$ are the standard enthalpy and volume, respectively, of the dissolution reaction. In more complex solid-fluid reactions, the values of concentration gradients are obtained by numerical differentiation using appropriate temperature and pressure steps. The gradients $\partial T/\partial z$ and $\partial P/\partial z$ in Equation (128) are geothermal (hydrothermal) and lithostatic (hydrostatic) gradients, respectively, at the site of fluid-rock interaction.

This development provides a phenomenological framework for relating the mineralogical or petrological record of fluid-rock interaction through standard thermodynamic properties of fluid-mineral reactions to environmental variables of the flow such as integrated fluid flux. As shown in Equation (125), the fluid-rock ratios, which are required in path-independent mass-balance or phase-equilibrium calculations, can still be unambiguously defined when the above variables are scaled to the flow direction. To illustrate these concepts consider various geometries of a permeable interaction zone, where the precipitation of solutes A and B due to local equilibrium under an external temperature or pressure gradient and initial disequilibrium, respectively, occurs (Fig. 15). All scenarios assume identical time-integrated fluid flux of 100 $m_\mathrm{f}^3 m_\mathrm{r}^{-2}$, but the cross section as well as the distance of alteration change. Consequently,

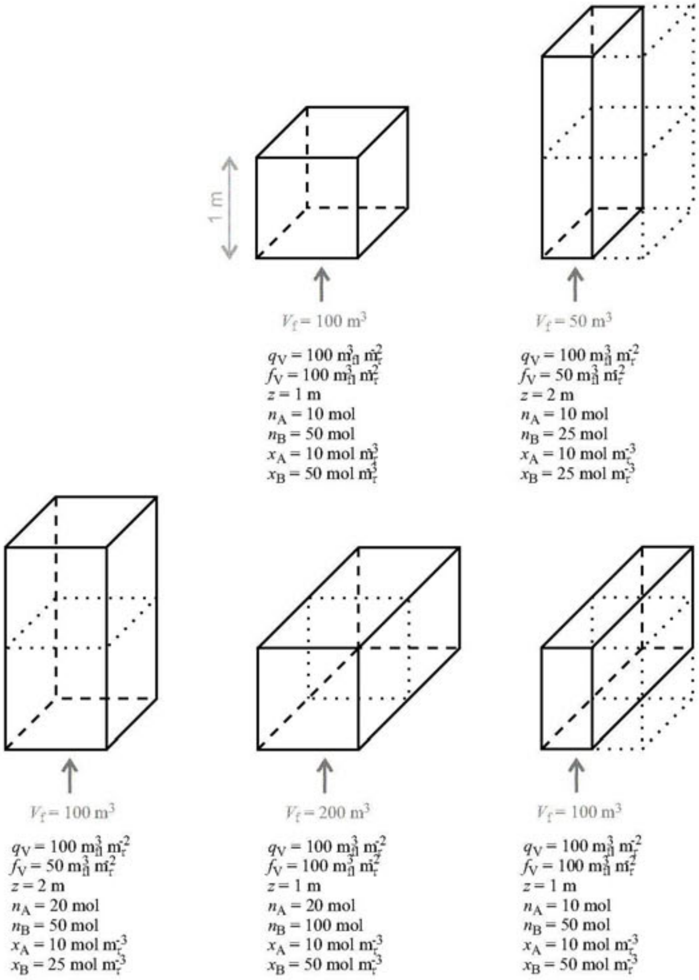
1 m
$V_f = 100\ m^3$
$q_V = 100\ m_{fl}^3\ m_r^{-2}$
$f_V = 100\ m_{fl}^3\ m_r^{-2}$
$z = 1\ m$
$n_A = 10\ mol$
$n_B = 50\ mol$
$x_A = 10\ mol\ m_r^{-3}$
$x_B = 50\ mol\ m_r^{-3}$
$V_f = 50\ m^3$
$q_V = 100\ m_{fl}^3\ m_r^{-2}$
$f_V = 50\ m_{fl}^3\ m_r^{-2}$
$z = 2\ m$
$n_A = 10\ mol$
$n_B = 25\ mol$
$x_A = 10\ mol\ m_r^{-3}$
$x_B = 25\ mol\ m_r^{-3}$
$V_f = 100\ m^3$
$q_V = 100\ m_{fl}^3\ m_r^{-2}$
$f_V = 50\ m_{fl}^3\ m_r^{-2}$
$z = 2\ m$
$n_A = 20\ mol$
$n_B = 50\ mol$
$x_A = 10\ mol\ m_r^{-3}$
$x_B = 25\ mol\ m_r^{-3}$
$V_f = 200\ m^3$
$q_V = 100\ m_{fl}^3\ m_r^{-2}$
$f_V = 100\ m_{fl}^3\ m_r^{-2}$
$z = 1\ m$
$n_A = 20\ mol$
$n_B = 100\ mol$
$x_A = 10\ mol\ m_r^{-3}$
$x_B = 50\ mol\ m_r^{-3}$
$V_f = 100\ m^3$
$q_V = 100\ m_{fl}^3\ m_r^{-2}$
$f_V = 100\ m_{fl}^3\ m_r^{-2}$
$z = 1\ m$
$n_A = 10\ mol$
$n_B = 50\ mol$
$x_A = 10\ mol\ m_r^{-3}$
$x_B = 50\ mol\ m_r^{-3}$

Figure 15. Various geometries of the fluid-rock interaction zone showing differences between the length scale of alteration, the integrated fluid flux and the fluid-rock ratio during one-dimensional fluid flow. Calculations assume local equilibrium precipitation of A = 0.1 mol $m_f^{-3}\ m_r^{-1}$, and disequilibrium supersaturation in B = 0.5 mol m_f^{-3}.

the fluid-rock ratios change proportionally, according to Equation (125), and so do the total amounts of A and B precipitated and their concentrations (per unit rock volume). This cautionary example illustrates that the geometry of the alteration zone and the orientation of the fluid flow must be known a priori, before the time-integrated fluid fluxes can be meaningfully calculated. In turn, numerical simulations of hydrodynamic modeling of geothermal, hydrothermal, magmatic or metamorphic systems can now be extended to predict the resulting record of fluid flow in rocks (e.g., Connolly 2010). Similarly, the mineral-assemblage record can be inverted using reaction thermodynamic properties to hydrodynamic variables and, in addition, to fluid flow rates if the duration of the flow event is known or can be independently estimated. The flow rates provide constraints on the hydrological properties of rocks, e.g., *in situ* permeabilities, data for which are not available otherwise (Ingebritsen and Manning 2002, 2010).

CONCLUDING REMARKS AND PERSPECTIVES

The thermodynamic properties of aqueous solutes represent essential data and tools for our interpretation and modeling of hydrothermal systems in the Earth's interior. Considerable progress has been achieved in hydrothermal geochemistry and aqueous physical chemistry in formulating diverse correlation relationships and self-standing equations of state that are potentially applicable at near-critical and supercritical conditions or at very high temperatures and pressures. In geological applications, the Helgeson-Kirkham-Flowers model (Helgeson et al. 1981; Tanger and Helgeson 1988; Shock et al. 1992) has been the most extensively used equation of state for aqueous species, both for its temperature and pressure range of applicability and for extensive coverage of inorganic and organic species (Johnson et al. 1992; Oelkers et al. 1995). Other approaches, mainly simple extrapolation schemes for equilibrium constants and other properties for speciation and fluid-mineral equilibria, have been embodied in hydrochemical software packages such as PHREEQC or Geochemist's Workbench (Parkhurst 1995; Bethke 2008). By contrast, developments of the equations of state for aqueous solutes in physical chemistry and chemical engineering have addressed liquid-vapor, critical and supercritical regions and equally span volumetric (pressure-volume-temperature) and electrostatic approaches (e.g., Wood et al. 1994; Palmer et al. 2004). The remaining issues are: (i) applicability to electrolytes (charged and neutral species) and nonelectrolytes (dissolved gases) alike, (ii) accuracy in the critical region of aqueous solvent, (iii) prediction of solute properties at low densities and application to liquid-vapor partitioning, (iv) temperature and pressure limits of applicability in relation to our knowledge of the volumetric and electrostatic properties of the aqueous solvent, and (v) extension to concentrated fluids or multicomponent supercritical mixtures.

Equations of state for geological applications are expected to provide reasonable extrapolation stability in respect to temperature and pressure or solvent density, possibly at the expense of accurate performance close to the critical point of water. Statistical mechanics and thermodynamics has offered several important theories for solute-solvent interactions – the scaled particle theory (Pierotti 1976; L'vov 1982), the fluctuation solution theory (Kirkwood and Buff 1951; O'Connell 1971, 1991; Matteoli 1997; Shulgin and Ruckenstein 2006), or detailed insights into the statistical thermodynamics of cavitation and hydration (Matubayasi and Levy 1996; Lazaridis 1998; Ben-Amotz et al. 2005). Spatial integrals over electric or pressure field gradients of correlation functions dictate inspiration for the form of macroscopic terms, which constitute the equations of state, although direct analytical transformation is often impossible. So far, some equations of state suffer from inaccurate or incomplete application of thermochemical cycles and appropriate state conversion terms. In particular, more rigorous application of individual steps of compression, hydration and interaction, and the functional form of their property variation in the pressure-temperature space in dependence on the choice of the standard state are expected to contribute to identifying significant terms, correlations with other species-specific properties, or separate the common solvent effects. The validity of the functional forms can be tested by comparison with experimental data of primary properties and, preferably, their higher-order derivatives such as partial volume or heat capacity. In addition, model verification using the reaction properties (i.e., equilibrium constants, standard reaction enthalpies) is not conclusive because these properties represent differences only. Typically, homogeneous speciation equilibria (e.g., from electrical conductivity measurements) do not address the absolute magnitudes of the Gibbs energy of individual species, and therefore it is desirable to employ heterogeneous equilibria which involve other phases whose thermodynamic properties are established with confidence (e.g., mineral or gas solubilities).

Analysis of performance of several electrostatic (Helgeson-Kirkham-Flowers), hydration (Tanger-Pitzer) and density models (Mesmer-Anderson, Holland-Powell, Dolejš-Manning, Sedlbauer-O'Connell-Wood) using H_2O self-dissociation and NaCl dissociation equilibria, and salt and mineral solubilities indicates several general observations:

1. Hydration models that link the stability of hydrated species to H_2O fugacity appear to be applicable at low pressures and low fluid densities. Increasing hydration number leads to progressively increasing ln$K$/lnρ slopes. Attainment of the constant slope corresponds to complete formation of the hydration shell while provision for the stepwise hydration becomes redundant.
2. In the vicinity of the critical point of the aqueous solvent, the accuracy of density models is superior to the electrostatic approach. Positive or negative divergence of thermodynamic properties as the solvent critical point is approached can be treated by volumetric terms whereas use of the electrostatic theory would require non-physical meaning of the Born parameter.
3. The Born electrostatic theory does not predict the linear relationship between ln$K$ and lnρ at high solvent densities, that is, at very high pressures.
4. The proportionality of ln$K$ vs. (lnρ)/T in previous empirical density models is incorrect and should be replaced by ln$K$ vs. lnρ, in agreement with the definition of the Krichevskii parameter and the form of the standard state conversion terms. This modification significantly improves the reproducibility of mineral solubilities over wide range of temperature and pressure.
5. Inclusion of the ρ and/or ρlnρ terms in the Gibbs energy definition, proposed empirically from critical conditions or liquid-vapor partitioning, is not supported by temperature and pressure dependence of speciation or solubility equilibria.
6. Progressive decrease in partial molal volumes and heat capacities at temperatures below 100 °C at 1 bar, related to the approach to the second liquid-liquid critical point of subcooled H_2O, is not captured by variations of the solvent dielectric constant and is therefore not reproduced by the electrostatic term. It is marginally predicted by the Krichevskii-type volumetric term.

These preliminary observations should guide future development of equations of state for aqueous solutes. The thermodynamic models reviewed here refer to standard partial properties at infinite dilution. In order to extend this approach to concentrated or mixed-solvent fluids, which are typical for the lower crust and upper mantle (Glasley 2001; Manning 2004; Newton and Manning 2008; Hunt and Manning 2012), the infinite dilution properties have to be self-consistently associated with non-ideal mixing contribution and linked to the pure liquid standard state. Current equilibrium, transport and reactive flow models at high temperatures and pressures often use the Debye-Hückel theory or the mean spherical approximation to extrapolate the infinite-dilution properties to concentrations typical of natural fluids (Oelkers and Helgeson 1991; Sharygin et al. 2002; *cf.* Lin et al. 2010). This allows for calculating the fluid speciation but cannot often reproduce the mineral solubilities and gas saturation limits adequately. This is a fundamental restriction because the fluid composition in nature is mainly controlled by mineral equilibria in the surrounding rocks (Newton 1995). In addition, constituents which are present at the highest concentrations mostly contribute to the whole-rock mass changes, formation and destruction of porosity (Dolejš and Wagner 2008). These limitations also apply to modeling of gas saturation and subcritical phase separation, in particular in the system H_2O-NaCl-CO_2, which is representative of crustal fluids. The activity-composition relationships predicted by the Anderko-Pitzer-Kosinski model (Kosinski and Anderko 2001) are in a remarkable contrast to those obtained by dehydration equilibria which were used to postulate the complete dissociation of NaCl at pressures exceeding 5 kbar (Aranovich and Newton 1996). These open questions must await additional experimental or simulation studies but the formulation of the new equations of state for infinite dilution properties should pave the way by appropriate choice and careful use of standard states that may facilitate future extension to the pure liquid (fluid) properties.

ACKNOWLEDGMENTS

Preparation of this contribution was financially supported by the Czech Science Foundation Project Nr. P210/12/0986 and the Charles University Science Support Program P44. I would like to acknowledge the infrastructure and hospitality over several years of the Bayerisches Geoinstitut, University of Bayreuth, where much of this work was initiated and developed. Critical comments by Jón Örn Bjarnason and Terry G. Lacy as well as editorial handling by Andri Stefánsson helped to improve the manuscript and are appreciated.

REFERENCES

Ague JJ (2003) Fluid flow in the deep crust. *In*: The Crust. Rudnick RL (ed) Treatise Geochem 3:195-228

Akinfiev NN (1999) Equation of state of SiO_{2aq} for description of silica dissolution at temperatures of 0-600 °C and pressures of 1-1000 bar. Geochem Int 39:1242-1244

Akinfiev NN (2000) A low-parameter description of aqueous nonelectrolytes in a wide range of parameters of state. Geochem Int 38:S221-S226

Akinfiev NN, Diamond LW (2003) Thermodynamic description of aqueous nonelectrolytes at infinite dilution over a wide range of state parameters. Geochim Cosmochim Acta 67:613-627

Akinfiev NN, Diamond LW (2004) A three-parameter EoS to describe aqueous non-electrolytes at infinite dilution over a wide range of state parameters, with preliminary application to 1:1 electrolytes. Fluid Phase Equilib 222-223:31-37

Anderko A, Wang P, Rafal M (2002) Electrolyte solutions: from thermodynamic and transport property models to the simulation of industrial processes. Fluid Phase Equilib 194-197:123-142

Anderson GM (1995) Is there alkali-aluminum complexing at high temperatures and pressures? Geochim Cosmochim Acta 59:2155-2161

Anderson GM (2005) Thermodynamics of Natural Systems (2nd ed). Cambridge University Press, Cambridge

Anderson GM, Burnham CW (1965) The solubility if quartz in supercritical water. Am J Sci 263:494-511

Anderson GM, Castet S, Schott J, Mesmer RE (1991) The density model for estimation of thermodynamic parameters of reactions at high temperatures and pressures. Geochim Cosmochim Acta 55:1769-1779

Anderson GM, Crerar DA (1993) Thermodynamics in Geochemistry: The Equilibrium Model. Oxford University Press, New York

Angell CA (1983) Supercooled water. Ann Rev Phys Chem 34:593-630

Antignano A, Manning CE (2008) Rutile solubility in H_2O, H_2O-SiO_2, and H_2O-$NaAlSi_3O_8$ fluids at 0.7-2.0 GPa and 700-1000 °C: Implications for mobility of nominally insoluble elements. Chem Geol 255:283-293

Aranovich LY, Newton RC (1996) H_2O activity in concentrated NaCl solutions at high pressures and temperatures measured by the brucite-periclase equilibrium. Contrib Mineral Petrol 125:200-212

Armelini FJ, Tester JW (1993) Solubility of sodium chloride and sulfate in sub- and supercritical water vapor from 450-500°C and 100-250 bar. Fluid Phase Equilib 84:123-142

Atkins PW, MacDermott AJ (1982) The Born equation and ionic solvation. J Chem Educ 59:359-360

Audétat A, Pettke T, Heinrich CA, Bodnar RJ (2008) The composition of magmatic-hydrothermal fluids in barren and mineralized intrusions. Econ Geol 103:877-908

Baier J, Audétat A, Keppler H (2008) The origin of the negative niobium tantalum anomaly in subduction zone magmas. Earth Planet Sci Lett 267:290-300

Ballerat-Busserolles K, Sedlbauer J, Majer V (2007) Standard thermodynamic properties of H_3PO_4(aq) over a wide range of temperatures and pressures. J Phys Chem 111:181-190

Bandura AV, Lvov SN (2006) The ionization constant of water over a wide range of temperatures and densities. J Phys Chem Ref Data 35:15-30

Baumgartner LP, Ferry JM (1991) A model for coupled fluid-flow and mixed-volatile mineral reactions with applications to regional metamorphism. Contrib Mineral Petrol 106:273-285

Beinlich A, Klemd R, John T, Gao J (2010) Trace-element mobilization during Ca-metasomatism along a major fluid conduit: Eclogitization of blueschist as a consequence of fluid-rock interaction. Geochim Cosmochim Acta 74:1892-1922

Ben-Amotz D (2005) Global thermodynamics of hydrophobic cavitation, dewetting, and hydration. J Chem Phys 123:184504

Ben-Amotz D, Raineri FO, Stell G (2005) Solvation thermodynamics: theory and applications. J Phys Chem B 109:6866-6878

Ben-Naim A (1985) Solvation thermodynamics of inert-gas molecules in inert-gas liquids. J Phys Chem 89:5738-5743

Ben-Naim A (1987) Solvation Thermodynamics. Plenum Press, New York

Ben-Naim A (2006) Molecular Theory of Solutions. Oxford University Press, Oford

Ben-Naim A, Marcus Y (1984) Solvation thermodynamics of nonionic solutes. J Chem Phys 81:2016-2027

Benson SW (1968) Thermochemical kinetics. Methods for the estimation of thermochemical data and rate parameters. John Wiley & Sons, New York

Berman RG (1988) Internally-consistent thermodynamic data for minerals in the system Na_2O-K_2O-CaO-MgO-FeO-Fe_2O_3-Al_2O_3-SiO_2-TiO_2-H_2O-CO_2. J Petrol 29:445-522

Bertrand CE, Anisimov MA (2011) Peculiar thermodynamics of the second critical point in supercooled water. J Phys Chem B 115:14099-14111

Bethke CM (2008) Geochemical and biogeochemical reaciton modeling (2nd ed). Cambridge University Press, Cambridge

Borisov MV, Shvarov YV (1992) Thermodynamics of Geochemical Processes. Moscow University, Moscow (in Russian)

Born M (1920) Volumen und Hydratationswärme der Ionen. Zeitschr Physik 1:45-48 (in German)

Bradley DJ, Pitzer KS (1983) Thermodynamics of electrolytes. 12. Dielectric properties of water and Debye-Hückel parameters to 350 °C and 1 kbar. J Phys Chem 83:1599-1603

Brady PV, Walther JV (1990) Algorithms for predicting ion association in supercritical H_2O fluids. Geochim Cosmochim Acta 54:1563-1574

Breeding CM, Ague JJ, Broecker M (2004) Fluid-metasedimentary rock interactions in subduction-zone mélange: Implications for the chemical composition of arc magmas. Geology 32:1041-1044

Bryantsev VS, Diallo MS, Goddard III WA (2008) Calculation of solvation free energies of charged solutes using mixed cluster/continuum models. J Phys Chem B 112:9709-9719

Bryzgalin OV (1989) Electrostatic-model estimates of electrolyte dissociation constants up to 800 °C and 5 kbar. Geochem Int 26/10:63-70

Bucher K, Stober I (2010) Fluids in the upper continental crust. Geofluids 10:241-253

Bucholz CE, Ague JJ (2010) Fluid flow and Al transport during quartz-kyanite vein formation, Unst, Shetland Islands, Scotland. J Metamorph Geol 28:19-39

Caciagli NC, Manning CE (2003) The solubility of calcite in water at 5-16 kar and 500-800 °C. Contrib Mineral Petrol 146:275-285

Chase MW Jr. (1998) NIST-JANAF Thermochemical Tables (4th ed). J Phys Chem Ref Data Monogr 9

Cobble JW, Chen K, Turner PJ, Murray RC (1982) High-temperature thermodynamic data for species in aqueous solution. Final report. Electr Power Res Inst NP-2400

Coltorti M, Grégoire M (eds) (2009) Metasomatism in oceanic and continental lithospheric mantle. Geol Soc Spec Pub 293

Connolly JAD (2010) The mechanics of metamorphic fluid expulsion. Elements 6:165-172

Cooney WR, O'Connell JP (1987) Correlation of partial molar volumes at infinite dilution of salts in water. Chem Eng Comm 56:341-349

Coumou D, Driesner T, Heinrich CA (2008) The structure and dynamics of mid-ocean ridge hydrothermal systems. Science 321:1825-1828

Crerar DA, Anderson GM (1971) Solubility and solvation reactions of quartz in dilute hydrothermal solutions. Chem Geol 8:107-122

Criss CM, Wood RH (1996) Apparent molar volumes of aqueous solutions of some organic solutes at the pressure 28 MPa and temperatures to 598 K. J Chem Thermodyn 28:723-741

Crovetto R, Wood RH, Majer V (1990) Densities of carbon dioxide + water $\{x\mathrm{CO_2} + (1-x)\mathrm{H_2O}\}$ with $x < 0.014$ at supercritical conditions. Molar volumes, partial molar volumes of carbon dioxide at infinite dilution, and excess molar volumes. J Chem Thermodyn 22:231-243

Denison JT, Ramsey JB (1955) The free energy, enthalpy and entropy of dissociation of some perchlorates in ethylene chloride and ethylidene chloride. J Am Chem Soc 77:2615-2621

Djamali E, Cobble JW (2009) A unified theory of the thermodynamic properties of aqueous electrolytes to extreme temperatures and pressures. J Phys Chem B 113:2398-2403

Djamali E, Cobble JW (2010) Thermodynamic properties of aqueous polyatomic ions at extreme temperatures and pressures. J Phys Chem B 114:3887-3893

Dolejš D, Manning CE (2010) Thermodynamic model for mineral solubility in aqueous fluids: theory, calibration, and application to model fluid-flow systems. Geofluids 10:20-40

Dolejš D, Wagner T (2008) Thermodynamic modeling of non-ideal mineral-fluid equilibria in the system Si-Al-Fe-Mg-Ca-Na-K-H-O-Cl at elevated temperatures and pressures: Implications for hydrothermal mass transfer in granitic rocks. Geochim Cosmochim Acta 72:526-553

Ellis AJ (1966) Partial molal volumes of alkali chlorides in aqueous solution to 200°. J Chem Soc A 1966:2579-2584

Eugster HP, Baumgartner L (1987) Mineral solubilities and speciation in supercritical metamorphic fluids. Rev Mineral 17:367-403

Fein J, Walther JV (1989) Calcite solubility and speciation in supercritical NaCl-HCl aqueous fluids. Contrib Mineral Petrol 103:317-324

Fernández DP, Goodwin ARH, Lemmon EW, Levelt Sengers JMH, Williams RC (1997) A formulation for the static permittivity of water and steam at temperatures from 238 K to 873 K at pressures up to 1200 MPa including derivatives and Debye-Hückel coefficients. J Phys Chem Ref Data 26: 1125-1166

Ferry JM, Dipple GM (1991) Fluid flow, mineral reactions, and metasomatism. Geology 19:211-214

Ferry JM, Gerdes ML (1998) Chemically reactive fluid flow during metamorphism. Ann Rev Earth Planet Sci 26:255-287

Fletcher P (1993) Chemical Thermodynamics for Earth Scientists. Longman Scientific & Technical, Essex

Floriano WB, Nascimento MAC (2004) Dielectric constant and density of water as a function of pressure at constant temperature. Brazil J Phys 34:38-41

Fournier RO, Potter II RW (1982) An equation correlating the solubility of quartz in water from 25° to 900 °C at pressures up to 10,000 bars. Geochim Cosmochim Acta 46:1969-1973

Franck EU (1956) Zur Löslichkeit fester Stoffe in verdichteten Gasen. Zeitschr Physikal Chemie Neue Folge 6:345-355 (in German)

Franck EU, Rosenzweig S, Christoforakos M (1990) Calculation of the dielectric constant of water to 1000 °C and very high pressures. Ber Bundesges Phys Chem 94:199-203

Frisch HL (1963) The equation of state of the classical hard sphere fluid. Adv Chem Phys 6:229-289

Fuentevilla DA, Anisimov MA (2006) Scaled equation of state for supercooled water near the liquid-liquid critical point. Phys Rev Lett 97:195702

Fuoss RM (1958) Ionic association. III. The equilibrium between ion pairs and free ions. J Am Chem Soc 80:5059-5061

Galobardes JV, Van Hare DR, Rogers LB (1981) Solubility of sodium chloride in dry steam. J Chem Eng Data 26:363-365

Garven G (1995) Continental-scale groundwater flow and geologic processes. Ann Rev Earth Planet Sci 23:89-117

Gilkerson WR (1970) The importance of the effect of the solvent dielectric constant on ion-pair formation in water at high temperatures and pressures. J Phys Chem 74:746-750

Glasley WE (2001) Elemental composition of concentrated brines in subduction zones and the deep continental crust. Prec Res 105:371-383

Gorman PJ, Kerrick DM, Connolly JAD (2006) Modeling open system metamorphic decarbonation of subducting slabs. Geochem Geophys Geosyst 7:4

Gu Y, Gammons CH, Bloom MS (1994) A one-term extrapolation method for estimating equilibrium constants of aqueous reactions at elevated temperatures. Geochim Cosmochim Acta 58:3545-3560

Gurney RW (1953) Ionic Processes in Solution. McGraw-Hill, New York

Haar L, Gallagher JS, Kell GS (1984) NBS/NRC Steam Tables. Thermodynamic and transport properties and computer programs for vapor and liquid states of water in SI units. Hemisphere Publishing, Washington

Hamann SD, Lim SC (1954) The volume changes on ionization of weak electrolytes. Aust J Chem 7:329-334

Harris FE, Alder BJ (1953) Dielectric polarization in polar substances. J Chem Phys 21:1031-1038

Harris SJ, Tully-Smith DM (1971) Radial distribution functions and superficial quantities for rigid sphere fluids; method of "point" chemical potential using scaled particle theory. J Chem Phys 55:1104-1112

Helgeson HC, Delaney JM, Nesbitt HW, Bird DK (1978) Summary and critique of the thermodynamic properties of rock-forming minerals. Am J Sci 278A:1-229

Helgeson HC, Kirkham DH (1974) Theoretical prediction of the thermodynamic behavior of aqueous electrolytes at high pressures and temperatures. I. Summary of the thermodynamic/electrostatic properties of the solvent. Am J Sci 274:1089-1198

Helgeson HC, Kirkham DH, Flowers GC (1981) Theoretical prediction of the thermodynamic behavior of aqueous electrolytes at high pressures and temperatures. Am J Sci 281:1249-1516

Hemley JJ, Montoya JW, Marinenko JW, Luce RW (1980) Equilibria in the system Al_2O_3-SiO_2-H_2O and some general implications for alteration/mineralization processes. Econ Geol 75:210-228

Higashi H, Iwai Y, Matsumoto K, Kitani Y, Okazaki F, Shimoyama Y, Arai Y (2005) Measurement and correlation for solubilities of alkali metal chlorides in water vapor at high temperature and pressure. Fluid Phase Equilib 228-229:547-551

Ho PC, Palmer DA (1997) Ion association of dilute aqueous potassium chloride and potassium hydroxide solutions to 600 °C and 300 MPa determined by electrical conductance measurements. Geochim Cosmochim Acta 61:3027-3040

Ho PC, Palmer DA, Mesmer RE (1994) Electrical conductivity measurements of aqueous sodium chloride solutions to 600 °C and 300 MPa. J Solution Chem 23:997-1018

Holland TJB, Powell R (1998) An internally consistent thermodynamic data set for phases of petrological interest. J Metamorph Geol 16:309-343

Holland TJB, Powell R (2011) An improved and extended internally consistent thermodynamic dataset for phases of petrological interest, involving a new equation of state for solids. J Metamorph Geol 29:333-383

Holten V, Bertrand CE, Anisimov MA, Sengers JV. (2012) Thermodynamics of supercooled water. J Chem Phys 136:094507

Hummel W, Berner U, Curti E, Pearson FJ, Thoenen T (2002) Nagra/PSI chemical thermodynamic data base 01/01. Universal Publishers

Hunt JD, Manning CE (2012) A thermodynamic model for the system SiO_2-H_2O near the upper critical end point based on quartz solubility experiments at 500-1100 °C and 5-20 kbar. Geochim Cosmochim Acta 86:196-213

Ingebritsen SE, Manning CE (2002) Diffuse fluid flux through orogenic belts: implications for the world ocean. Proc Natl Acad Sci 99:9113-9116

Ingebritsen SE, Manning CE (2010) Permeability of the continental crust: dynamic variations inferred from seismicity and metamorphism. Geofluids 10:193-205

John T, Klemd R, Gao J, Garbe-Schönberg D (2008) Trace-element mobilization in slabs due to non-steady state fluid-rock interaction: Constraints from an eclogite-facies transport vein in blueschist (Tianshan, China). Lithos 103:1-24

Johnson JW, Oelkers EH, Helgeson HC (1992): SUPCRT92: a software package for calculating the standard molal thermodynamic properties of minerals, gases, aqueous species, and reactions from 1 to 5000 bar and 0 to 1000 °C. Comp Geosci 18:899-947

Kebarle P (1977) Ion thermochemistry and solvation from gas phase ion equilibria. Ann Rev Phys Chem 28:445-476

Kennedy GC (1950) A portion of the system silica-water. Econ Geol 45:629-653

Kerrick DM, Connolly JAD (2001) Metamorphic devolatilization of subducted oceanic metabasalts: Implications for seismicity, arc magmatism and volatile recycling. Earth Planet Sci Lett 189:19-29

Kirkwood JG (1939) The dielectric polarization of polar liquids. J Chem Phys 7:911-919

Kirkwood JG, Buff FP (1951) The statistical mechanical theory of solutions. I. J Chem Phys 19:774-777

Kitahara S (1960) The solubility equilibrium and the rate of solution of quartz in water at high temperatures and high pressures. Rev Phys Chem Japan 30:122-130

Klotz IM (1950) Chemical Thermodynamics. Basic Theory and Methods. Prentice-Hall, New York

Konrad-Schmolke M, O'Brien PJ, Zack T (2011) Fluid migration above a subducted slab-constraints on amount, pathways and major element mobility from partially overprinted eclogite-facies rocks (Sesia Zone, Western Alps). J Petrol 52:457-486

Kosinski JJ, Anderko A (2001) Equation of state for high-temperature aqueous electrolyte and nonelectrolyte systems. Fluid Phase Equilib 183-184:75-86

L'vov SN (1982) Calculation of the standard thermodynamic characteristics for the dissolution of non-polar gases in water at high temperatures and pressure. Russ J Phys Chem 56:1326-1328

Lasaga AC (1998) Kinetic Theory in the Earth Sciences. Princeton University Press, Princeton

Lazaridis T (1998) Inhomogeneous fluid approach to solvation thermodynamics. 1. Theory. J Phys Chem 102:3531-3541

Lemke KH, Seward TM (2008) Solvation processes in steam: ab initio calculations of ion-solvent structures and clustering equilibria. Geochim Cosmochim Acta 72:3293-3310

Levelt Sengers JMH (1991) Solubility near the solvent's critical point. J Supercrit Fluids 4:215-222

Liebscher A (2010) Aqueous fluids at elevated pressure and temperature. Geofluids 10:3-19

Likholyot A, Lemke KH, Hovey JK, Seward TM (2007) Mass spectrometric and quantum chemical determination of proton water clustering equilibria. Geochim Cosmochim Acta 71:2436-2447

Lin Y, ten Kate A, Mooijer M, Delgado J, Fosbøl PL, Thomsen K (2010) Comparison of activity coefficient models for electrolyte systems. AIChE J 56:1334-1351

Luckas M, Krissmann J (2001) Thermodynamik der Elektrolytlösungen. Eine einheitliche Darstellung der Berechnung komplexer Gleichgewichte. Springer, Berlin (in German)

Majer V, Degrange S, Sedlbauer J (1999) Temperature correlation of partial molar volumes of aqueous hydrocarbons at infinite dilution: test of equations. Fluid Phase Equilib 158-160:419-428

Majer V, Sedlbauer J, Bergin G (2008) Henry's law constant and related coefficients for aqueous hydrocarbons, CO_2 and H_2S over a wide range of temperature and pressure. Fluid Phase Equilib 272:65-74

Majer V, Sedlbauer J, Wood RH (2004) Calculation of standard thermodynamic properties of aqueous electrolytes and non-electrolytes. *In*: Aqueous Systems at Elevated Temperatures and Pressures. Physical Chemistry in Water, Steam and Hydrothermal Solutions. Palmer DA, Fernández-Prini R, Harvey AH (eds) Elsevier, Amsterdam, p 99-147

Manning CE (1994) The solubility of quartz in H_2O in the lower crust and upper mantle. Geochim Cosmochim Acta 58:4831-4839

Manning CE (2004) The chemistry of subduction-zone fluids. Earth Planet Sci Lett 223:1-16

Manning CE, Shock EL, Sverjensky DA (2013) The chemistry of carbon in aqueous fluids at crustal and upper-mantle conditions: experimental and theoretical constraints. Rev Mineral Geochem 75:109-148

Marshall WL (2008a) Dielectric constant of water discovered to be simple function of density over extreme ranges from –35 to +600°C and to 1200 MPa (12000 atm), believed universal. Nature Prec doi: 10.1038/npre.2008.2472.1

Marshall WL (2008b) Aqueous electrolyte ionization over extreme ranges as simple fundamental relation with density and believed universal; sodium chloride ionization from 0° to 1000 °C and to 1000 MPa (10000 Atm.). Nature Prec doi: 10.1038/npre.2008.2476.1

Marshall WL, Franck EU (1981) Ion product of water substance, 0-1000 °C, 1-10,000 bars. New international formulation and its background. J Phys Chem Ref Data 10:295-304

Marshall WL, Mesmer RE (1984) Pressure-density relationships and ionization equilibria in aqueous solutions. J Solution Chem 13:383-391

Marshall WL, Quist AS (1967) A representation of isothermal ion-ion-pair-solvent equilibria independent of changes in dielectric constant. Proc Natl Acad Sci 58:901-906

Martynova OI (1964) Some problems of the solubility of involatile inorganic compounds in water vapour at high temperatures and pressures. Russ J Phys Chem 38:587-592

Matteoli E (1997) A study on Kirkwood-Buff integrals and preferential solvation in mixtures with small deviations from ideality and/or size mismatch of components. Importance of proper reference system. J Phys Chem B 101:9800-9810

Matubayasi N, Levy RM (1996) Thermodynamics of the hydration shell. 2. Excess volume and compressibility of a hydrophobic solute. J Phys Chem 100:2681-2688

Mesmer RE, Baes CF Jr. (1974) Phosphoric acid dissociation equilibria in aqueous solutions to 300 °C. J Solution Chem 3:307-321

Mesmer RE, Marshall WL, Palmer DA, Simonson JM, Holmes HF (1988) Thermodynamics of aqueous association at high temperatures and pressures. J Solution Chem 17:699-718

Morey GW, Fournier RO, Rowe JJ (1962) The solubility of quartz in water in the temperature interval from 25° to 300 °C. Geochim Cosmochim Acta 26:1029-1043

Morey GW, Hesselgesser JM (1951) The solubility of some minerals in superheated steam at high pressures. Econ Geol 46:821-835

Mosebach R (1955) Die hydrothermale Löslichkeit des Quarzes als heterogenes Gasgleichgewicht. N Jahrb Mineral Abh 87:351-388 (in German)

Mungall JE (2002) Roasting the mantle: Slab melting and the geneis of major Au and Au-rich Cu deposits. Geology 30:915-918

Mysen BO (2010) Speciation and mixing behavior of silica-saturated aqueous fluid at high temperature and pressure. Am Mineral 95:1807-1816

Newton RC (1995) Simple-system mineral reactions and high-grade metamorphic fluids. Eur J Mineral 7:861-881

Newton RC, Manning CE (2008) Thermodynamics of SiO_2-H_2O fluid near the upper critical end point from quartz solubility measurements at 10 kbar. Earth Planet Sci Lett 274:241-249

Noyes RM (1963) Conventions defining thermodynamic properties of aqueous ions and other chemical species. J Chem Educ 40:2-10 (addendum 40:116)

Noyes RM (1964) Assignment of individual ionic contributions to properties of aqueous ions. J Am Chem Soc 86:971-979

O'Connell JP (1971) Thermodynamic properties of solutions based on correlation functions. Mol Phys 20:27-33

O'Connell JP (1990) Thermodynamic properties of mixtures from fluctuation solution theory. *In*: Fluctuation Theory of Mixtures. Matteoli E, Mansoori GA (eds) Taylor and Francis, New York, p 45-67

O'Connell JP (1991) Thermodynamics and fluctuation solution theory with some applications to systems at near- or supercritical conditions. *In*: Supercritical Fluids. Kiran E, Levelt Sengers JMG (eds) Kluwer Academic Publishers, Dordrecht, p 191-229

O'Connell JP (1995) Application of fluctuation solution theory to thermodynamic properties of solutions. Fluid Phase Equilib 104:21-39

O'Connell JP, Sharygin AV, Wood RH (1996) Infinite dilution partial molar volumes of aqueous solutes over wide ranges of conditions. Ind Eng Chem Res 35:2808-2812

Oelkers EH, Helgeson HC, Shock EL, Sverjensky DA, Johnson JW, Pokrovskii VA (1995) Summary of the apparent standard partial molal Gibbs free energies of formation of aqueous species, mineral, and gases at pressures 1 to 5000 bars and temperatures 25 to 1000°C. J Phys Chem Ref Data 24:1401-1560

Oliver NHS, Bons PD (2001) Mechanisms of fluid flow and fluid-rock interaction in fossil metamorphic hydrothermal systems from vein-wallrock patterns, geometry and microstructure. Geofluids 1:137-162

Palandri JL, Reed MH (2004) Geochemical models of metasomatism in ultramafic systems: serpentinization, rodingitization, and sea floor carbonate chimney precipitation. Geochim Cosmochim Acta 68:1115-1133

Palmer DA, Fernandéz-Prini R, Harvey AH (eds) (2004) Aqueous Systems at Elevated Temperatures and Pressures. Physical Chemistry in Water, Steam and Hydrothermal Solutions. Elsevier, Amsterdam

Parkhurst DL (1995) User's guide to PHREEQC, a computer model for speciation, reaction-path, advective transport and inverse geochemical calculations. US Geol Survey Water Res Invest Rep 95-4227, 143 p

Patey GN, Levesque D, Weis JJ (1979) Integral equation approximations for dipolar fluids. Mol Phys 38:219-239

Philpotts AR, Ague JJ (2009) Principles of Igneous and Metamorphic Petrology (2nd ed). Cambridge University Press, Cambridge

Pierotti RA (1963) The solubility of gases in liquids. J Phys Chem 67:1840-1845

Pierotti RA (1976) A scaled particle theory of aqueous and nonaqueous solutions. Chem Rev 76:717-726

Pitzer KS (1982) Self-ionization of water to high temperature and the thermodynamic properties of the ions. J Phys Chem 86:4704-4708

Pitzer KS (1983a) Dielectric constant of water at very high temperature and pressure. Proc Natl Acad Sci 80:4575-4576

Pitzer KS (1983b) Thermodynamics of sodium chloride solutions in steam. J Phys Chem 87:1120-1125

Plyasunov AV. (2012) Thermodynamics of $Si(OH)_4$ in the vapor phase of water: Henry's and vapor-liquid distribution constants, fugacity and cross virial coefficients. Geochim Cosmochim Acta 77:215-231

Plyasunov AV, O'Connell JP, Wood RH (2000) Infinite dilution partial molar properties of aqueous soluions of nonlectrolytes. I. Equations for partial molar volumes at infinite dilution and standard thermodynamic functions of hydration of volatile nonelectrolytes over wide ranges of conditions. Geochim Cosmochim Acta 64:495-512

Plyasunov AV, Shock EL (2001) Estimation of the Krichevskii parameter for aqueous nonelectrolytes. J Supercrit Fluids 20:91-103

Puigdomenech I, Plyasunov AV, Rard JA, Grenthe I (1997) Temperature corrections to thermodynamic data and enthalpy calculations. *In*: Modelling in Aquatic Chemistry. Grenthe I, Puigdomenech I (eds) Nuclear Energy Agency, Paris, p 427-493

Putnis A, Austrheim H (2010) Fluid-induced processes: metasomatism and metamorphism. Geofluids 10:254-269

Quist AS (1970) The ionization constant of water to 800 °C and 4000 bars. J Phys Chem 74:3393-3402

Quist AS, Marshall WL (1965) Estimation of the dielectric constant of water to 800°. J Phys Chem 69:3165-3167

Quist AS, Marshall WL (1968) Electrical conductances of aqueous sodium chloride solutions from 0 to 800° and at pressures to 4000 bars. J Phys Chem 72:684-703

Reed MH (1997) Hydrothermal alteration and its relationship to ore fluid composition. *In*: Geochemistry of hydrothermal ore deposits (3ed edition) Barnes HL (ed) John Wiley & Sons, Hoboken, p 303-365

Reiss H, Frisch HL, Lebowitz JL (1959) Statistical mechanics of rigid spheres. J Chem Phys 31:369-380

Robie RA, Hemingway BS (1995) Thermodynamic properties of minerals and related substances at 298.15 K and 1 bar (10^5 Pascals) pressure and at higher temperatures. US Geol Surv Bull 2131, 461 pp

Robie RA, Hemingway BS, Fisher JR (1978) Thermodynamic properties of minerals and related substances at 298.15 K and 1 bar (10^5 Pascals) pressure and at higher temperatures. US Geol Surv Bull 1452, 456 pp

Rossini FD (1950) Chemical thermodynamics. John Wiley & Sons, New York

Ryzhenko BN, Bryzgalin OV. (1987) Dissociation of acids under hydrothermal conditions. Geochem Int 24/8:122-127

Ryzhenko BN, Bryzgalin OV, Artamkina IY, Spassenykh MY, Shapkin AI (1985) An electrostatic model for the electrolytic dissociation of inorganic substances dissolved in water. Geochem Int 22/9:138-144

Ryzhenko BN, Bryzgalin OV, Shapkin AI (1991) Dissociation of salts and bases in aqueous solution at 25 °C and 1 bar. Geochem Int 28/5:77-83

Ryzhenko BN, Kovalenko NI & Prisyagina NI (2006) Titanium complexation in hydrothermal systems. Geochem Int 44:879-895

Sedlbauer J (2008) Modeling approaches to hydration properties of aqueous nonelectrolytes at elevated temperatures and pressures. Collect Czech Chem Commun 73:322-343

Sedlbauer J, O'Connell JP, Wood RH (2000) A new equation of state for correlation and prediction of standard molal thermodynamic properties of aqueous species at high temperatures and pressures. Chem Geol 163:43-63

Sedlbauer J, Wood RH (2004) Thermodynamic properties of dilute NaCl(aq) near the critical point of water. J Phys Chem B 108:11838-11849

Sharygin AV, Wood RH, Zimmerman GH, Balashov VN (2002) Multiple ion association versus redissociation in aqueous NaCl and KCl at high temperatures. J Phys Chem 106:7121-7134

Shock EL, Helgeson HC (1988) Calculation of the thermodynamic and transport properties of aqueous species at high pressures and temperatures: Correlation algorithms for ionic species and equation of state predicitions to 5 kb and 1000 °C. Geochim Cosmochim Acta 52:2009-2036

Shock EL, Helgeson HC, Sverjensky DA (1989) Calculation of the thermodynamic and transport properties of aqueous species: Standard partial molal properties of inorganic neutral species. Geochim Cosmochim Acta 53:2157-2183

Shock EL, Oelkers EH, Johnson JW, Sverjensky DA, Helgeson HC (1992) Calculation of the thermodynamic properties of aqueous species at high pressures and temperatures: Effective electrostatic radii, dissociation constants and standard partial molal properties to 1000 °C and 5 kbar. J Chem Soc Farad Trans 88:803-826

Shock EL, Sassani DC, Willis M, Sverjensky DA (1997) Inorganic species in geologic fluids: Correlations among standard molal thermodynamic properties of aqueous ions and hydroxide complexes. Geochim Cosmochim Acta 61:907-950

Shulgin IL, Ruckenstein E (2006) The Kirkwood-Buff theory of solutions and the local composition of liquid mixtures. J Phys Chem B 110:12707-12713

Shvarov Y, Bastrakov E (1999) HCh: A Software Package for Geochemical Equilibrium Modeling – User's Guide. Australian Geological Survey Organization Record 1999/25, 61 pp

Steefel CI, DePaolo DJ, Lichtner PC (2005) Reactive transport modeling: An essential tool and a new research approach for the Earth sciences. Earth Planet Sci Lett 240:539-558

Šulák M, Dolejš D (2011) The system SiO_2-H_2O revisited: equation of state to very high temperatures and pressures including critical behavior. Mineral Mag 75:1961

Šulák M, Dolejš D (2012) Thermodynamic of aqueous solutes at high temperatures and pressures: application of the hydration theory and implications for fluid-mediated mass transfer. Geophys Res Abstr 14:13566

Sverjensky DA, Shock EL, Helgeson HC (1997) Prediction of the thermodynamic properties of aqueous metal complexes to 1000 °C and 5 kb. Geochim Cosmochim Acta 61:1359-1412

Sweeton FH, Mesmer RE, Baes CF (1974) Acidity measurements at elevated temperatures. VII. Dissociation of water. J Solution Chem 3:191-214

Tanger IV JC, Helgeson HC (1988) Calculation of the thermodynamic and transport properties of aqueous species at high pressures and temperatures. Revised equations of state for the standard partial molal properties of ions and electrolytes. Am J Sci 288:19-98

Tanger IV JC, Pitzer KS (1989a) Calculation of the thermodynamic properties of aqueous electrolytes to 1000 °C and 5000 bar from a semicontinuum model for ion hydration. J Phys Chem 93:4941-4951

Tanger IV JC, Pitzer KS (1989b) Calculation of the ionization constant of H_2O to 2,273 K and 500 MPa. AICHE J 35:1631-1638

Thompson AB (1997) Flow and focusing of metamorphic fluids. *In*: Fluid Flow and Transport in Rocks. Mechanisms and Effects. Yardley BWD, Jamtweit B (eds) Chapman and Hall, London, p 297-314

Thomsen K (2004) Thermodynamics of electrolyte systems for industry. *In*: Chemical Thermodynamics for Industry. Letcher TM (ed) Royal Soc Chem, Cambridge, p 219-229

Tremaine PR, Goldman S (1978) Calculation of Gibbs free energies of aqueous electrolytes to 350 °C from an electrostatic model of ionic hydration. J Phys Chem 82:2317-2321

Tremaine PR, Shvedov D, Xiao C (1997) Thermodynamic properties of aqueous morpholine and morpholinium chloride at temperatures from 10 to 300 °C: apparent molar volumes, heat capacities, and temperature dependence of ionization. J Phys Chem B 101:409-419

Uematsu M, Franck EU (1980) Static dielectric constant of water and steam. J Phys Chem Ref Data 9:1291-1306

Vitha MF, Carr PW (2000) The chemical meaning of the standard free energy of transfer: use of von der Waals' equation of state to unravel the interplay between free volume, volume entropy, and the role of standard states. J Phys Chem B 104:534-5349

Wagman DD (ed, 1982) The NBS tables of chemical thermodynamic properties: Selected values for inorganic and C1 and C2 organic substances in SI units. Am Chem Soc Am Inst Phys, New York

Wagner T, Kulik DA (2007) TP-corrections applying to electrostatic and density models. *In*: GEM-Selektor v. 3 on-line documentation. Paul Scherrer Institut, Villigen

Wagner W, Pruß A (2002) The IAPWS formulation 1995 for the thermodynamic properties of ordinary water substance for general and scientific use. J Phys Chem Ref Data 31:387-535

Walther JV (1992) Ionic association in H_2O-CO_2 fluids at mid-crustal conditions. J Metamorph Geol 10:789-797 (erratum 11:460)

Walther JV, Orville P (1983) The extraction-quench technique for determination of the thermodynamic properties of solute complexes: application to quartz solubility in fluid mixtures. Am Mineral 68:731-741

Walther JV, Schott J (1988) The dielectric constant approach to speciation and ion pairing at high temperature and pressure. Nature 332:635-638

Wasserman E, Wood B, Davies A (1995) Equation of state for aqueous silica species at pressures from 1 bar to 20 kbar and temperatures from 25° to 900 °C based on simulated values of the dielectric constant. Chem Geol 121:3-9

Webb TJ (1926) The free energy of hydration of ions and the electrostriction of the solvent. J Am Chem Soc 48:2589-2603

Weill DF, Fyfe WS (1964) The solubility of quartz in H_2O in the range 1000-4000 bars and 400-550 °C. Geochim Cosmochim Acta 28:1243-1255

Wilson AM, Boles JR, Garven G (2000) Calcium mass transport and sandstone diagenesis during compaction-driven flow: Stevens Sandstone, San Joaquin Basin, California. Geol Soc Am Bull 112:845-856

Wood RH, Carter RW, Quint JR, Majer V, Thompson PT, Boccio JR (1994) Aqueous electrolytes at high temperatures: comparison of experiment with simulation and continuum models. J Chem Thermodyn 26:225-249

Wood SA, Samson IM (1998) Solubility of ore minerals and complexation of ore metals in hydrothermal solutions. Rev Econ Geol 10:33-80

Wyart J, Sabatier G (1955) Nouvelles mesures de la solubilité du quartz, de la tridymite et de la cristobalite dans l'eau sous pression au-dessus de la température critique. Compt Rendu Acad Sci 240:1905-1907 (in French)

Yardley BWD (2005) Metal concentrations in crustal fluids and their relationship to ore formation. Econ Geol 100:613-632

Yardley BWD (2013) The chemical composition of metasomatic fluids. *In*: Metasomatism and the chemical transformation of rock. Harlov DE, Austrheim H (eds) Springer Verlag, Berlin, p 17-51

Yeatts LB, Dunn LA, Marshall WL (1971) Electrical conductances and ionization behavior of sodium chloride in dioxane-water solutions at 100° and pressures to 4000 bars. J Phys Chem 75:1099-1106

Zack T, John T (2007) An evaluation of reactive fluid flow and trace element mobility in subducting slabs. Chem Geol 239:199-216

Zhu G, Gerya TV, Yuen DA, Honda S, Yoshida T, Connolly JAD (2009) Three-dimensional dynamics of hydrous thermal-chemical plumes in oceanic subduction zones. Geochem Geophys Geosyst 10:11

Reviews in Mineralogy & Geochemistry
Vol. 76 pp. 81-133, 2013
Copyright © Mineralogical Society of America

4

Mineral Solubility and Aqueous Speciation Under Hydrothermal Conditions to 300 °C – The Carbonate System as an Example

Pascale Bénézeth[a], Andri Stefánsson[b],
Quentin Gautier[a,c], Jacques Schott[a]

[a]*Géosciences Environnement Toulouse (GET, ex LMTG)*
CNRS-Université de Toulouse
14 Avenue Edouard Belin, 31400 Toulouse, France

[b]*Institute of Earth Sciences*
University of Iceland
Sturlugata 7, 101 Reykjavík, Iceland

[c]*Université Paris-Est, Laboratoire Navier*
6/8 avenue Blaise Pascal, Champs-sur-Marne
77455 Marne-La-Vallée, France

pascale.benezeth@get.obs-mip.fr

INTRODUCTION

Carbon is a major element in the Earth's system and plays an important role in many geochemical processes including metamorphism, volcanism, oceanic systems and atmospheric evolution. Knowledge and understanding of chemical speciation, mineral solubility and reactivity involving carbon are very important in order to qualitatively and quantitatively understand these processes. Indeed, dissolved inorganic carbon is among the major components of natural geothermal fluids. It originates from various sources including magmatic degassing, rock dissolution and organic matter degradation (e.g., Giggenbach 1992; Giggenbach et al. 1993; Simmons and Cristenson 1994; Sanoa and Marty 1995). Dissolved CO_2 is the most common form of dissolved inorganic carbon in these systems, though other forms exist like CH_4 and CO but usually in much lower concentrations than CO_2 (e.g., Chiodini and Marini 1998; Stefánsson and Arnórsson 2002). The concentrations of dissolved inorganic carbon (DIC) in geothermal fluids from active geothermal systems throughout the world are shown in Figure 1a together with the pH of the fluids. In general, the DIC concentration increases in geothermal fluids with increasing temperature from a few mmol per kg up to half a mole per kg of fluid. This increase is accompanied by a decrease in the fluid pH (Fig. 1b). Higher concentrations (not shown) are observed in fumarole fluids discharging volcanic gases (e.g., Chiodini et al. 1996). At Earth's surface, CO_2 also degasses through the soils in active geothermal systems (e.g., Chiodini et al. 1998).

The chemistry and transport of DIC in natural geothermal systems is influenced by many processes including magma degassing, water-rock interaction and partitioning of CO_2 between liquid and vapor phases upon boiling and phase separation. It has been concluded that the concentration of DIC and all other major elements besides incompatible elements such as Cl are controlled by fluid-secondary mineral equilibria (e.g., Giggenbach 1980, 1981; Arnórsson et al. 1983). The most common carbonate mineral observed in geothermal systems is calcite

1529-6466/13/0076-0004$10.00 http://dx.doi.org/10.2138/rmg.2013.76.4

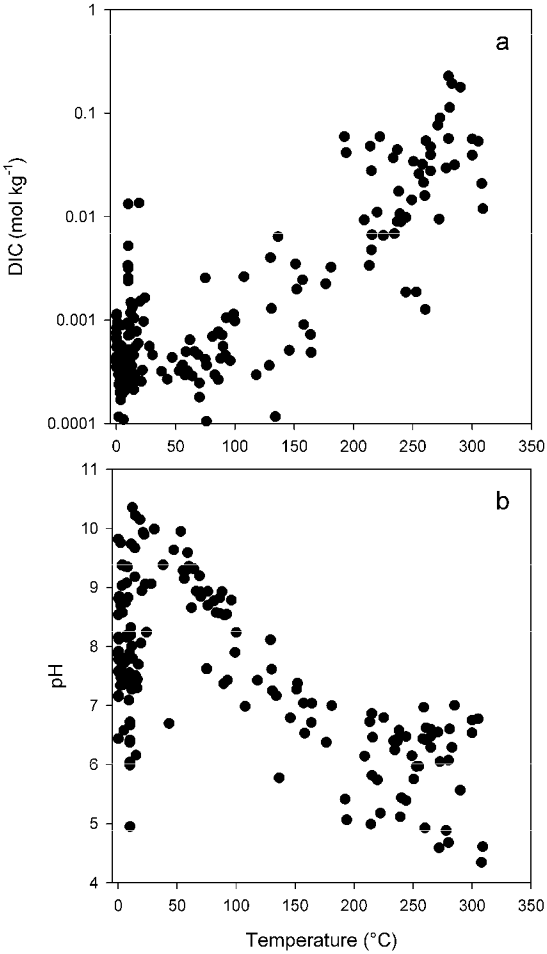

Figure 1. The concentration of dissolved inorganic carbon (ΣCO_2) and pH as a function of temperature in geothermal fluids from several geothermal systems in the world. Data include fluids in Iceland, New Zealand, Philippines, Japan, Nicaragua, Guatemala, El Salvador and Yellowstone. Data are from Stefánsson and Arnórsson (2000). The pH was calculated at reservoir temperatures with the aid of the WATCH program (Bjarnason 1994).

($CaCO_3$) (Browne 1978). It follows that geothermal fluids, at all temperatures and neutral to alkaline pH, are often saturated with respect to calcite (Fig. 2). Other carbonate minerals including siderite ($FeCO_3$), magnesite ($MgCO_3$), dolomite ($CaMg(CO_3)_2$) and ankerite ($Ca(Mg,Fe)(CO_3)_2$) are less common. However, geothermal fluids are observed to be saturated with respect to siderite and ankerite at $T < 100$-150 °C and to be close to saturation with dolomite at $T > 200$ °C. The abundance of these carbonate minerals may be limited due to the availability of Fe and Mg in the geothermal fluids.

The interpretation of the chemical behavior of dissolved inorganic carbon and most other major elements in geothermal systems relies on consistent data on the fluids chemical compositions and the thermodynamic properties of species in the gas and liquid phases as well as of the minerals. The calculation of fluid saturation indices with respect to calcite,

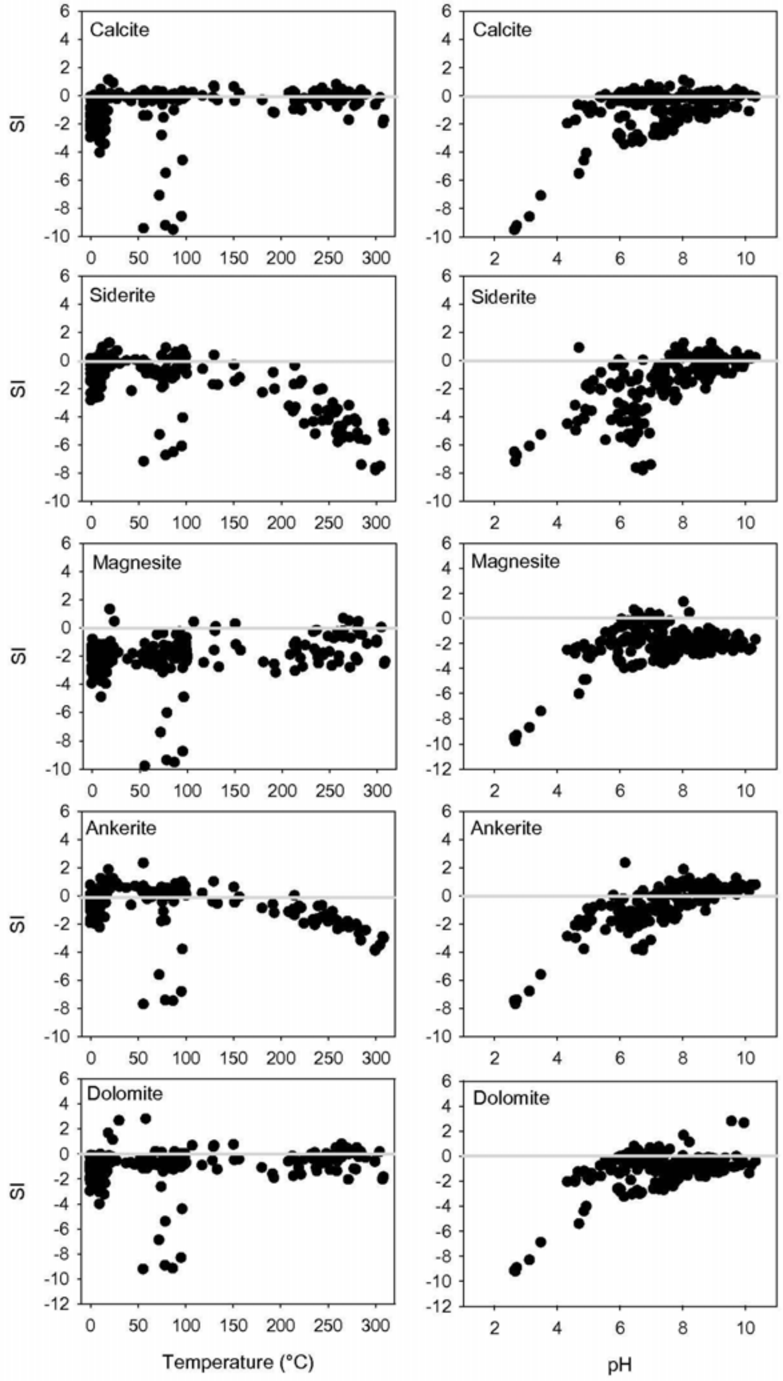

Figure 2. Saturation indices of geothermal fluids from several geothermal systems in the world (see Fig. 1) with respect to common carbonate minerals The saturation indices were calculated with the aid of the WATCH program (Bjarnason 1994).

as presented in Figure 2, is based on such data. As shown in this figure, many minerals plot close to saturation and therefore small errors in the thermodynamic properties of the aqueous and gas species and minerals involved may result in drastic changes in the interpretation of the data. The need for high quality thermodynamic data within geothermal fluid chemistry is therefore of key interest and importance for quantitative understanding of geothermal fluid chemistry and transport.

To overcome the increase in anthropogenic atmospheric CO_2 concentration and to help mitigate climate change, research efforts have been focusing for more than a decade on assessing the feasibility of sequestering CO_2 in subsurface aquifers, either as trapped CO_2 gas and aqueous species or, ideally, as stable secondary carbonate phases—dubbed "mineral trapping" (e.g., Benson and Cole 2008). Geochemical and reactive transport codes (e.g., PHREEQC, EQ3/6, CHESS, Geochemist's Workbench, MINTEQA2, THOUGHREACT, CrunchFlow, to name a few, see Gaus et al. 2008, Oelkers et al. 2009 and references cited) can simulate the fate of CO_2 injected into deep sedimentary formations and ultramafic rocks, shown in Figure 3, indicating the formation of various carbonate minerals, including calcite, dolomite, magnesite and siderite, but also dawsonite, $NaAlCO_3(OH)_2$ (e.g., Xu et al. 2004) depending upon the type of reservoir. Some of these carbonate minerals are also present, as primary minerals, in carbonate or carbonate-bearing sandstones as host reservoirs considered for CO_2 injection, mainly for enhanced oil recovery (CO_2-EOR), as well as in various caprock formations (e.g., Gherardi et al. 2007; Andreani et al. 2008; Griffith et al. 2011). In these types of reservoirs it is therefore important to quantify the impact, during and after CO_2 injection, of the carbonate mineral dissolution and/or precipitation reactions on the physical (porosity, permeability, flow) and chemical properties of the geologic formation and subsequently on the efficiency and integrity of the sequestration. In addition, several recent studies have investigated the carbonation of silicate-rich mafic and ultramafic rocks and minerals because of the large perspectives it offers for CO_2 mineral sequestration. Such studies, in particular, focused on Mg-silicates due to their known potential for *in situ* or *ex situ* CO_2 mineral sequestration (e.g., O'Connor et al. 2001; Giammar et al. 2005; Béarat et al. 2006; Gerdemann et al. 2007; Garcia et al. 2010; Daval et al. 2011). The reaction of CO_2 with common mineral silicates to form carbonates like magnesite, calcite or siderite, following the general Reaction (1) below,

$$(\mathrm{Mg, Ca, Fe})_x\mathrm{Si}_y\mathrm{O}_{x+2y} + x\mathrm{CO}_2 \rightarrow x(\mathrm{Mg, Ca, Fe})\mathrm{CO}_3 + y\mathrm{SiO}_2 \qquad (1)$$

is exothermic and thermodynamically favored, mimicking the natural weathering of silicate minerals which contributes to the regulation of atmospheric CO_2. However, many challenges in mineral carbonation remain to be resolved.

Mineral scale formation causes major problems to geothermal energy production and oil field operations such as reduction in fluid production and injection rates. The formation of carbonate scale is mainly associated with changes in fluid pressure, boiling and pH. For example, a decrease in pressure reduces the solubility of carbonate minerals, leading in some cases to mineral deposition on the inner walls of pipes such as calcite and magnesite (see Villafáfila-García et al. 2006). Additionally, the boiling of geothermal fluids often leads to an increase in pH and the formation of calcite (e.g., Simmons and Christenson 1994).The use of supercritical CO_2 instead of water or brine as the heat-exchange fluid in Enhanced Geothermal Systems (EGS) has recently raised interest due to its hydraulic and thermal properties (e.g., Brown 2000; Fouillac et al. 2004; Pruess 2006; Xu et al. 2008), but also because it avoids scaling problems and formation plugging (e.g., Brown 2000; García et al. 2006). But here again, the development of CO_2 sequestration, modeling carbonate mineral scaling and CO_2-aided EGS, requires a thorough understanding of CO_2-water rock interactions.

As carbonate minerals are also used in many industrial processes (e.g., construction, oil, food processing and the pharmaceutical industry), we could reasonably expect that knowledge

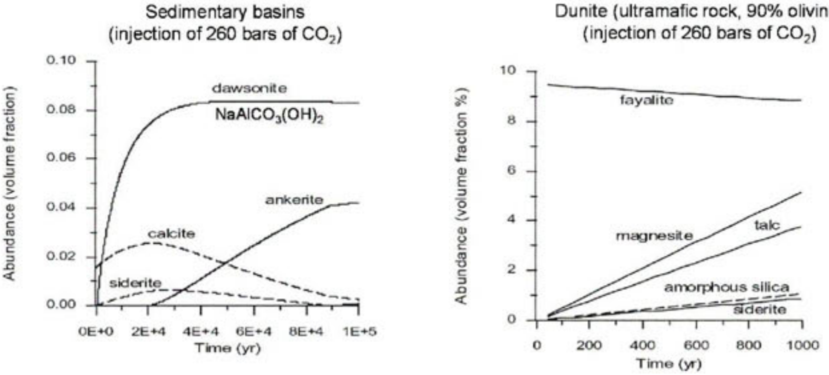

Figure 3. Distribution of precipitated mineral phases due to CO_2 injection (260 bars) as a function of time for two geological settings: sedimentary basins and olivine rock. After Xu et al. (2004).

of their formation, stability and transformations in these natural and industrial processes, including geochemical cycles and petroleum reservoir characteristics, is well known, not only at room temperature but also up to hydrothermal conditions. Indeed, reservoir simulations rely on the molecular understanding of the fluids of interest as well as on a good knowledge of the thermodynamics and kinetics of involved chemical reactions under conditions of varying solution composition, temperature and pressure. Nevertheless, a review of experimental and compiled data that we started almost a decade ago shows that we are far from reaching this goal. This is mainly due to the inconsistency of experimental data at room temperature and their scarcity at higher temperatures. One of the main reasons for this lack of data above room temperature is the difficulties in carrying out experiments at higher temperatures and pressures and/or predicting them from empirical calculations.

Considering these evidences and towards the goal of providing accurate thermodynamic data to bridge some of the existing gaps, a number of state-of-the-art techniques have been developed in our groups and will be presented here, together with examples of data obtained on the aqueous speciation of CO_2, including cation-ion pair formation and the solubility of some carbonate minerals up to high temperatures (<300 °C).

COMMON TECHNIQUES FOR EXPERIMENTS AT HYDROTHERMAL CONDITIONS

Various experimental techniques have been used to investigate mineral solubilities and speciation under hydrothermal conditions. Following Ulmer and Barnes (1987), many of these techniques as well as data analyses have been summarized during recent decades (e.g., Palmer et al. 2004; Oelkers and Schott 2009). This section is not intended to provide an exhaustive review of all available techniques but rather to focus on a few techniques that have been used and combined in recent years to encompass the lack of fundamental thermodynamic (and kinetic) parameters to adequately assess CO_2-fluid-mineral interactions from ambient temperatures to hydrothermal systems. These include an array of state-of-the-art tools such as high temperature batch reactors, pH sensors for *in situ* measurements, *in situ* vibrational spectroscopy (IR and Raman) and ultraviolet and visible spectrophotometry. These techniques have been used for studying water-carbonate mineral interaction as well as speciation of CO_2-containing solutions in hydrothermal conditions. The techniques and tools are briefly described below.

Batch reactors

Batch reactors offer a very versatile technique commonly operated for hydrothermal experiments at water vapor saturation pressure (P_{sat}) including mineral solubility, mineral transformations and mineral dissolution and crystal growth kinetics. Commonly, the solid is introduced in a known amount (volume or mass) of solution at a fixed pH, by using various buffers, and fixed ionic strength, using a background electrolyte (e.g., NaCl). The solution and solid phases are generally agitated by *in situ* stirring or rocking and samples can be collected as a function of time or reaction progress.

A "home-made" batch reactor that has been used since the mid-nineties in our laboratory in Toulouse to measure the reactivity and solubility of several minerals including aluminum hydroxide (Castet et al. 1993; Bénézeth et al. 1994), gallium and germanium hydroxides (Bénézeth et al. 1997a; Diakonov et al. 1997; Pokrovski and Schott 1998), and more recently for the study of iron isotope fractionation between minerals and aqueous solutions (Saunier et al. 2011) is shown in Figure 4. The system allows injection of the solids/solutions at the experimental temperature avoiding possible supersaturation with respect to some of the

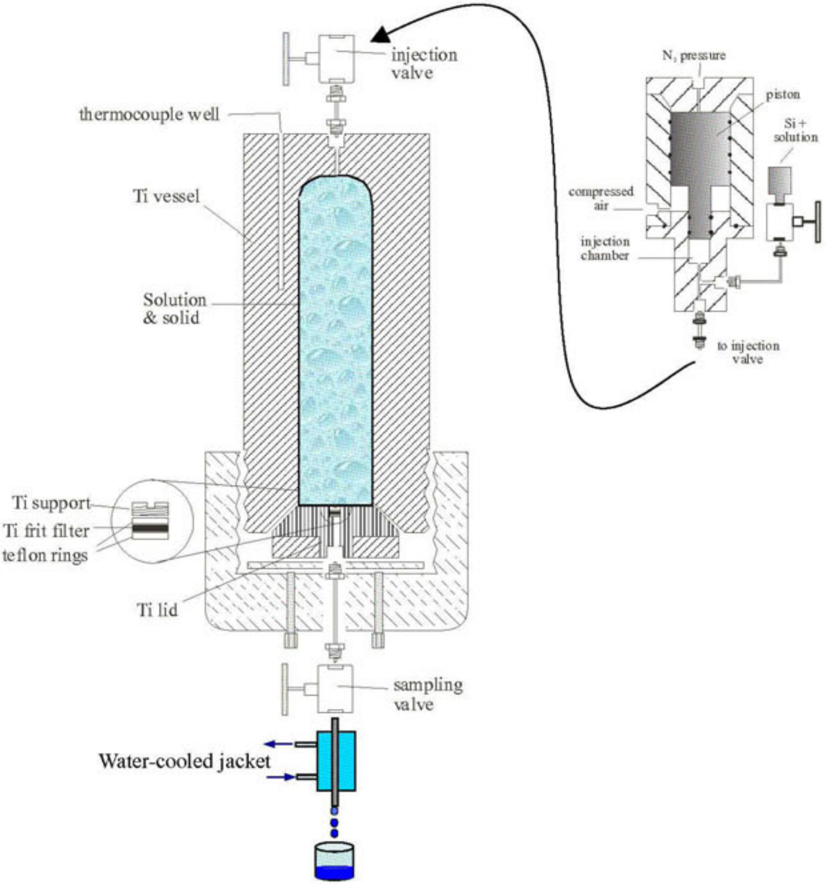
injection valve
thermocouple well
Ti vessel
Solution & solid
Ti support
Ti frit filter
teflon rings
Ti lid
sampling valve
Water-cooled jacket
N_2 pressure
piston
Si + solution
compressed air
injection chamber
to injection valve

Figure 4. Schematic illustration of a titanium pressure vessel used mainly for solubility measurements (at Geosciences Environment Toulouse laboratory) showing the *in situ* 2 µm Ti frit, valve and cooling systems for sampling the fluid, as well as the injection system (see text for details).

minerals mentioned above which tend to become less soluble with increasing temperature in acidic conditions. The injection system (see Fig. 4) consists of a detachable cylinder in which a piston is moved in response to N_2 overpressure. The piston pushes into the vessel a suspension made of the solid phase and sample of the solution previously drawn from the reactor. Solution samples are collected by inverting the system and passing the solution first through an *in situ* 2 μm Ti filter positioned in the head of the reactor, and then through another 0.01 μm filter after rapid cooling by means of a water-cooled sampling tube (Fig. 4).

Similar hydrothermal batch reactors are available commercially, such as stirred Parr reactors made of titanium metal (Figs. 5 and 6). The Parr reactors are continuously stirred with a magnetically driven stirrer and the temperature controlled to ± 1 °C by a heating mantel and temperature controller. A gas bottle can be connected to the reactor via a titanium tube and a manometer in order to pressurize the system, while the reactor's internal pressure is followed with a solid-state pressure transducer connected to a computer. Samples are collected regularly through a Ti-valve furnished with a 2 μm titanium frit.

Flexible-cell rocking reactors (Seyfried et al. 1987), commercialized by Coretest, should also be mentioned. They allow the investigation of hydrothermal reactions to 500 °C and pressure up to 2 kb, and sampling or addition of solution during the course of the experiments. This experimental setup, described in Figure 7, consists of a flexible Ti (or Au) reaction cell (volume ~ 150 ml), where the solids and the experimental solution are loaded. The reaction cell is placed into a large volume (~1.2 L) stainless steel pressure vessel with water as a pressure medium which, in turn, is placed into a rocking furnace. Only Ti/Au is allowed to come into contact with the experimental solution during sampling. A gas-driven pump is used for delivery of water into the pressure vessel to maintain pressure during sampling, and a back pressure regulator serves to release water from the pressure vessel during heating or addition of solution into the reaction cell. Samples are taken, and solution is added into the reaction cell via a Ti/Au sampling tube connected to the external Ti sampling valve. Addition of solution into the reaction cell is performed with the help of a Ti hand pump connected to the external Ti sampling valve. This type of reactor has been operated by our group to determine, at hydrothermal conditions to 500 °C and 1kb, gold solubility and gold-hydrosulfide complexing (Tagirov et al. 2005), arsenopyrite stability and the vapor-liquid fractionation of metals (Pokrovski et al. 2002, 2008). In these experiments mineral buffers could be added to the reaction cell to simultaneously constrain pH, $f(S_2)$ and $f(H_2)$.

Hydrothermal experiments using batch reactors are generally straightforward. However, the measurements are usually lengthy and time consuming and arduous as each one can only be carried out at one temperature and solution composition (including ionic strength and pH).

If pH is among the main variables controlling aqueous species distribution, reaction kinetics, mineral solubility and the transport of elements in natural systems, its measurement (activity or concentration of the H^+ ion) is mostly limited to temperatures <80 °C by the use of commercial glass electrodes, and is rarely achieved above this temperature. In most cases, the pH of the solutions in experiments conducted in batch reactors (or hydrothermal water samples from natural systems as well) at high temperatures is calculated from the pH measured on a quenched solution at room temperature combined with mass and charge balances and in some cases also by including the charge balance equation and the equilibrium constants for all reactions involved (e.g., acids/bases dissociations, complexation and redox). However, a number of chemical reactions and processes may occur during sample collection and cooling off, for example precipitation, gas exsolution and oxidation, which can cause significant modifications to the solution pH and aqueous speciation. This is one of the reasons why many solubility measurements have been carried out in buffered solutions, not only to fix the pH but also to be able to calculate it at elevated temperatures.

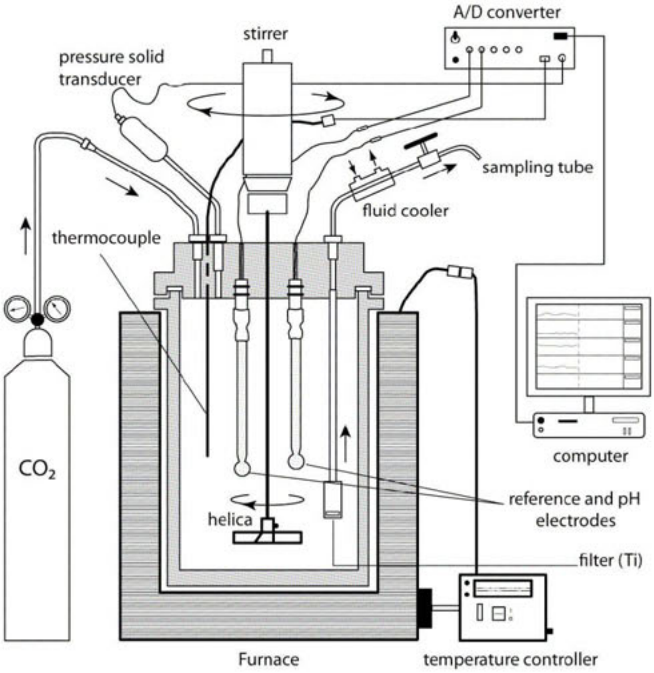
A/D converter
stirrer
pressure solid transducer
sampling tube
fluid cooler
thermocouple
CO_2
computer
reference and pH electrodes
helica
filter (Ti)
Furnace
temperature controller

Figure 5. Classical Parr batch reactor modified to include *in situ* pH electrodes (solid-contact glass-electrodes) (modified from Saldi 2009).

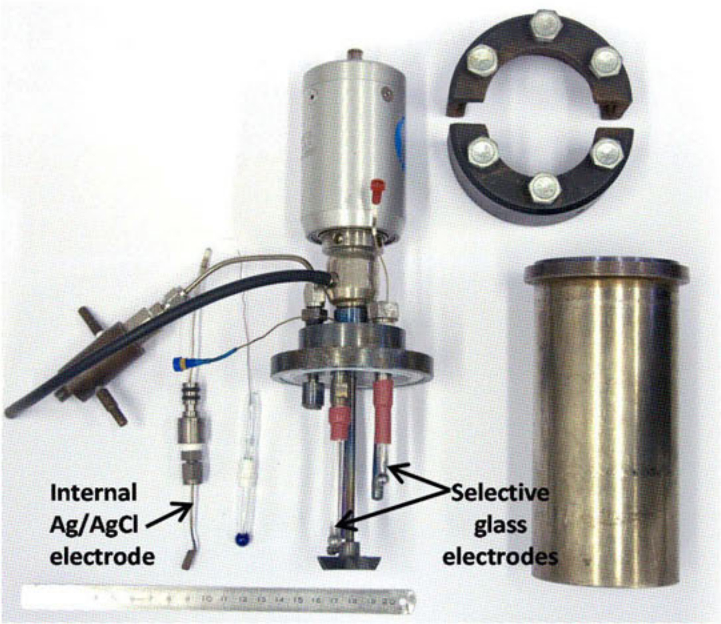
Internal Ag/AgCl electrode
Selective glass electrodes

Figure 6. Titanium Parr reactor adapted to insert various types of *in situ* pH electrodes (see text).

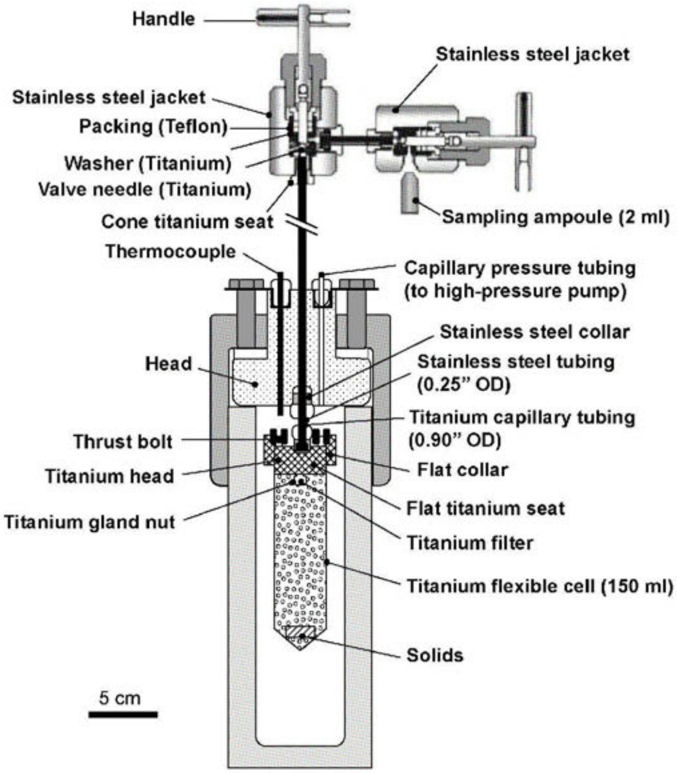
Handle
Stainless steel jacket
Stainless steel jacket
Packing (Teflon)
Washer (Titanium)
Valve needle (Titanium)
Cone titanium seat
Sampling ampoule (2 ml)
Thermocouple
Capillary pressure tubing
(to high-pressure pump)
Stainless steel collar
Head
Stainless steel tubing
(0.25" OD)
Titanium capillary tubing
(0.90" OD)
Thrust bolt
Titanium head
Flat collar
Flat titanium seat
Titanium gland nut
Titanium filter
Titanium flexible cell (150 ml)
Solids
5 cm

Figure 7. Schematic illustration of the Coretest flexible-cell rocking reactor.

Electrode systems and high temperature pH measurements and titrations

Despite numerous efforts devoted to the development of pH sensors, there are only a few electrode systems that have been successful for *in situ* pH measurements at temperatures above 100 °C. Most of them, for example the Yttria-stabilized zirconia (YSZ) membrane electrodes (150-500 °C) and the metal-metal oxide (e.g., Pt-PtO_2, Ir-IrO_2) electrodes (100-300 °C), were described in detail by Lvov and Palmer (2004). Here, we would like to focus on the development, application and limitations of two pH sensors that have been used successfully in our laboratory at 100-300 °C, selective glass electrodes and the hydrogen electrodes, as well as pH indicators.

High temperature Na^+- and H^+-selective glass electrodes. Na^+- and H^+-selective glass electrodes were developed in the early 90's by the Russian company "Potential" (Beliustin et al. 1992). They were combined in early studies with an *external* AgCl/Ag, 3.2 M KCl reference electrode. An example is shown in Figure 8 (Pokrovski et al. 1995; Pokrovski and Schott 1998). The electrochemical cell configuration is:

Sn-Cu, Li-Sn alloy | Na-selective glass | test sol. containing Na^+ || 3.2M KCl, Ag/AgCl

or

Sn-Cu, Li-Sn alloy | H^+-selective glass | test sol. || 3.2M KCl, Ag/AgCl

which uses a liquid junction (||) salt bridge. The Na^+- and H^+-selective glass electrodes have been used for the determination of the stability constants of various sodium-anion ion pairs,

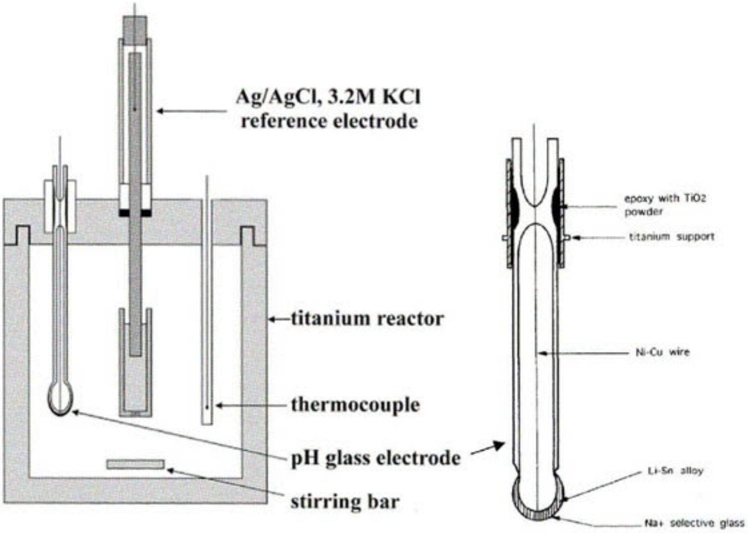

Figure 8. Schematic illustration of the potentiometric cell and the sodium-selective electrode (see Pokrovski et al. 1995).

for example sulfate, borate, aluminate ion pairs (Pokrovski et al. 1995; Diakonov et al. 1996), Al-silicate and Al-borate complexes (Pokrovski et al. 1996; Tagirov et al. 2004) as well as metal-hydroxide complexes (Pokrovski and Schott 1998). The main characteristic of this type of electrode is that there is no internal solution as it has an electrochemically reversible solid contact (provided by a thin Li-Sn alloy) with the glass-ion conducting membrane. Moreover, as the resistance of the electrode decreases with increasing temperature, the optimal temperature range is 50 to 200 °C. The upper temperature limitation of this pH electrode is essentially due to the melting point of the electrode alloy, which is around 215±10 °C. The advantage of using a room temperature reference electrode is that it provides more stable and reproducible potential and prevents dissolution of the reference element that may be the case when using an *internal* Ag/AgCl electrode immersed in a NaCl-containing solution. Alternatively, the cell may be set up without transfer, as shown in the configuration below and in Figure 6:

Sn-Cu, Li-Sn alloy | H^+-selective glass | test sol. containing Cl^- | AgCl/Ag

This electrochemical cell configuration has been used for carbonate dissolution kinetics studies at 100-150 °C and pCO_2 up to 55 bars (Pokrovsky et al. 2009a,b; Golubev et al. 2009). More recently, the internal Ag/AgCl reference electrode has been replaced by the Na^+ selective glass electrode (used earlier) coupled to the solid contact Li-Sn alloy commercial electrode to obtain the electrochemical cell described by:

Sn-Cu, Li-Sn alloy | H^+-selective glass | Na-bearing buffer solution | Na^+-selective glass | Sn-Cu, Li-Sn alloy

These coupled electrodes, allow continuous pH measurements in circumneutral and alkaline solutions with fixed activity of the Na^+ ion. They have been used, for instance, to measure the dissolution/precipitation kinetics and solubility of magnesite (Saldi et al. 2010, 2012; Bénézeth et al. 2011) and to assess the stability of $CaCO_3^{\circ}$, $CaHCO_3^+$ and $NaCO_3^-$ complexes at 100, 120, 140 and 160 °C and 1 to 50 atm pCO_2 (Bychkov et al. 2007). The experimental setup of such an electrode system is also shown in Figure 6.

As specified above, the stability of these different combined electrodes can be uncertain above 150 °C, mainly due to the dissolution of the glass and/or the reference electrode components in the test solution (Ag/AgCl here), which precludes their use for long term experiments. Furthermore, the derived data (dissociation constants, solubility, rates) are affected by uncertainties linked to i) the nernstian behavior and precision of the electrodes (of by ±5-10% of the Nernst values), ii) liquid junction potentials estimation (±15%), and finally iii) the need for external and frequent calibrations at the temperature of the experiments which has to be performed in several types of solutions/buffers (e.g., NaCl, NaCl/Na_2CO_3, NaCl/$B(OH)_3$/NaOH and NaCl/CH_3COOH/HCl) to cover a wide range of pH values. Indeed, the pH of the buffer solutions is calculated with PHREEQC and HCh (Shvarov and Bastrakov 1999; Shvarov 2008), which in turn rely on thermodynamic constants available in the databases coupled to these software programs, activity coefficients calculations, and so on.

The hydrogen-electrode-concentration cell (HECC). The use of hydrogen electrodes in the following simplified concentration cell configuration:

H_2, Pt, | reference solution (e.g., HCl, NaCl) || test solution (e.g., HCl, NaCl) | Pt, H_2

was pioneered at Oak Ridge National Laboratory almost 45 years ago (Mesmer et al. 1970) and has been improved and used since then in a large number of studies (over 150) to not only study homogeneous aqueous reactions including acid-base ionization, metal ion hydrolysis and complexation, but also solubility measurements, adsorption studies and, more recently, dissolution/precipitation rates very near equilibrium (e.g., Tremaine et al. 2004; Wesolowski et al. 2004; Machesky et al. 2006; Bénézeth et al. 2008; Davis et al. 2011; Schott et al. 2012). It has been used over the last few years to measure precisely the solubility of a number of carbonate minerals relevant for carbon sequestration, including dawsonite, siderite and magnesite (Bénézeth et al. 2007, 2009, 2011, respectively). The hydrogen electrode concentration cell (HECC) (see Palmer et al. 2001 and Bénézeth et al. 2009 for details) allows very precise measurement of pH (±0.005 pH units), *in situ* fluid sampling and injection (fluids and/or gas) at temperatures up to 290 °C and 0-5 mol/kg salt-like NaCl. The cell, shown in Figure 9, consists of a 300 mL Stainless Steel pressure vessel containing two concentric Teflon cups holding the reference and test solutions, separated by a porous Teflon liquid junction, sharing a common hydrogen fugacity at their headspace. The solutions in each cup are stirred magnetically. Teflon-insulated platinum wires coated with platinum black protrude in each cup and serve as electrodes, which have been proven in numerous studies to obey the Nernst's potential equation:

$$\Delta E = \frac{RT}{F}\ln\left(\frac{[H^+]_t}{[H^+]_r}\right) + E_{lj} \tag{2}$$

and from which the hydrogen ion concentration in the test solution ($[H^+]_t$) is calculated relative to its known concentration in the reference solution ($[H^+]_r$). ΔE refers to the measure potential difference between the two platinum electrodes, E_{lj} the estimated liquid junction potential, and F, R and T represent the Faraday constant, the gas constant, and the temperature in Kelvin, respectively. Activity coefficients of H^+ are assumed to be identical in both solutions due to the presence of a supporting electrolyte (e.g., NaCl or NaF_3CSO_3), which keeps the ionic strength constant and also minimizes the liquid junction potential. So the working definition of pH in this case is pH = $-\log[H^+]$ in molal concentration units, and not the conventional activity scale.

Because of the use of a supporting electrolyte, most of the experiments are performed at various ionic strengths ($I \geq 0.03$ molal) so that the obtained parameters are equilibrium quotients (Q) which are then regressed by semi-empirical equations to obtain equilibrium constants at infinite dilution (K). An example of an equation that is frequently used is:

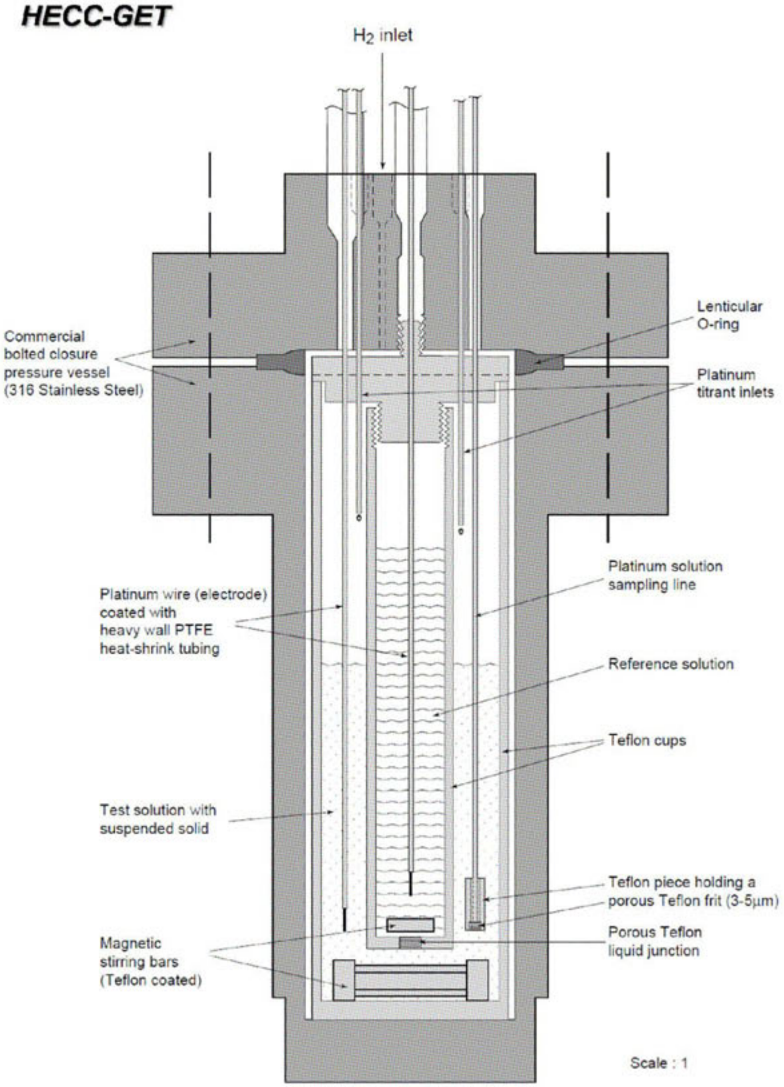
HECC-GET
H2 inlet
Commercial bolted closure pressure vessel (316 Stainless Steel)
Lenticular O-ring
Platinum titrant inlets
Platinum solution sampling line
Platinum wire (electrode) coated with heavy wall PTFE heat-shrink tubing
Reference solution
Teflon cups
Test solution with suspended solid
Teflon piece holding a porous Teflon frit (3-5µm)
Porous Teflon liquid junction
Magnetic stirring bars (Teflon coated)
Scale : 1

Figure 9. The hydrogen electrode concentration cell (HECC) at GET laboratory.

$$\log_{10} Q = \log_{10} K \quad \left(\frac{\Delta z^2 A_\varphi}{2.303}\right)\left\{\frac{\sqrt{I}}{1+1.2\sqrt{I}} + \quad 1.667\ln\left(1 \quad 1.2\sqrt{I}\right)\right\} \tag{3}$$

$$+a_1 I + a_2 I^2 + a_3 F(\mathrm{I}) + 0.0157\phi I$$

where I is the ionic strength (IS), $\Delta z^2 = \Sigma z^2$(products) – Σz^2(reactants), A_φ corresponds to the Debye-Hückel limiting slope for the osmotic coefficient, ϕ, proposed by Pitzer (1991), a_1, a_2 and a_3 are independent adjustable parameters determined from fitted data at various ionic strengths, and the function $F(I)$ corresponds to:

$$F(I) = \frac{1-\left(1+2\sqrt{I}-2I\right)\exp\left(-2\sqrt{I}\right)}{4I} \tag{4}$$

However, in the case of measurements at only one or two ionic strengths, the calculation of activity coefficients, for $I \leq 0.1$ molal, can be performed using Debye-Hückel, b_γ-dot (Helgeson 1969) or Davies equations (Davies 1962) that are implemented in various geochemical software. Another approach suggested by Lindsay (1989) can be useful in NaCl-dominated medium where the mean stoichiometric activity coefficients are derived from the Meissner equation (Meissner and Tester 1972) with the implicit assumption that for an ion charge, z:

$$\gamma_{|z|} = \gamma_{\pm(\text{NaCl})}^{z^2} \tag{5}$$

where $\gamma_{\pm(\text{NaCl})}$ is the mean molal stoichiometric activity coefficient of NaCl calculated from Archer (1992). It has been shown that this approximation can provide a reasonable estimation for activity coefficients at ionic strengths up to 1.0 molal (e.g., Bénézeth et al. 2007). More complex and more accurate activity models, such as the Specific ion Interaction Theory (SIT) (e.g., Guggenheim 1966) or the Pitzer (Pitzer and Mayorga 1973) models exist, but such models require the knowledge of ion interaction coefficients that are not always known. Finally, the effect of ionic strength can be minimized by writing the chemical reaction in an "isocoulombic form" (Lindsay 1980, 1989) so that the charges of the reactants and products are the same. It has been demonstrated in numerous experimental studies (Lindsay 1980, 1989; Bénézeth et al. 1997b) that the equilibrium quotients (Q) are then independent from the IS, allowing an easier extrapolation of these constants to infinite dilution.

The HECC is probably the most reliable technique known today to measure the pH at hydrothermal conditions (< 300 °C). It can operate at variable temperatures (0-290 °C), pH (2-11) and ionic strength (0.03 to 6 M), and it is highly accurate, within ±0.005 pH log unit. No calibration and/or use of a buffer are needed, and it is very stable for a long period of time, over two months, suitable then for solubility measurements (Bénézeth et al. 2011). Finally, reaction progress can be directly monitored during solubility experiments. Once the system attains this steady state it can be perturbed chemically (e.g., pH jump by addition of acid/base titrants via 2 hastelloy pumps or by injecting $CO_{2(g)}$) or thermally (temperature jump) in order to undersaturate or supersaturate the system. This allows precise determination of mineral solubilities by approaching equilibrium from undersaturation and/or reaction rates very close to equilibrium, as pioneered by Bénézeth et al. (2008) in the case of aluminum hydroxide (50 and 100 °C), by Davis et al. (2011) for quartz (125-200 °C) and more recently for magnesite (Schott et al. 2012), as presented in this chapter. The HECC has a few drawbacks, however; first the cell is limited to temperatures below 300 °C, due to the use of Teflon for its inner components, and second, it is not very suitable for studying elements with various oxidation states due to the use of hydrogen gas.

Colorimetric measurement of H^+ concentration. Among the oldest techniques for measuring pH is the use of color pH-indicators. This technique is based on the pH dependent ionization of colored compounds, commonly organic compounds. Some of these pH indicators are thermally stable and have been used for determination of solution pH to temperatures as high as ~400 °C, but they may be used with confidence to temperatures of 200-300 °C (e.g., Xiang and Johnston 1994; Boily and Seward 2005; Bulemela et al. 2005; Clarke et al. 2005; Suleimenov and Boily 2006; Ehlerova et al. 2008; Minubayeva et al. 2008; Bulemela and Tremaine 2009). Examples of pH indicators that have been used under hydrothermal conditions include acridinium, methyl orange, 4-nitrophenol and 2-napthol.

This technique determines the concentration of H^+ in solution. The colorimetric pH measurement involves two steps, first the determination of the absorbtivity (ε) of the protonated

(ROH) and deprotonated (RO^-) forms of a given pH-indicator and second the pH measurements in solutions containing both forms of the pH indicator. The former is carried out by spectral scans under acidic and alkaline conditions to obtain the molar absorbtivities of the two forms (ε_{ROH} and ε_{RO^-}), respectively (Eqn. 6). The latter is done by spectral scan of the test solution in which the pH is to be measured. The measured molar absorbance (A) is related to the Beer-Lambert law according to:

$$A = \rho l \ (m_{RO^-}\varepsilon_{RO^-} + m_{ROH}\varepsilon_{ROH}) \tag{6}$$

where l is the cell path length, ρ is the solution density, and m_{ROH} and m_{RO^-} are the molar (mol/L) concentration of the protonated and deprotonated forms of the pH indicator. The concentrations of the two forms are then fitted using the least-squares procedure to the measured absorbance (Fig. 10).

The relationship between the protonated and deprotonated forms of the pH indicator is given by the ionization reaction:

$$ROH_{(aq)} = H^+ + RO^-_{(aq)} \tag{7}$$

The respective equilibrium ionization constant is defined by:

$$K = \frac{m_{H^+}\gamma_{H^+} m_{RO^-_{(aq)}}\gamma_{RO^-_{(aq)}}}{m_{ROH_{(aq)}}} \tag{8}$$

where m_i and γ_i stand for the i^{th} aqueous species molal concentration (mol/kg) and activity coefficient, respectively. Rearranging Equation (8) results in the solution pH:

$$pH = -\log K + \log\left(\frac{m_{RO^-}}{m_{ROH}}\right) + \log \ _{RO^-} \tag{9}$$

An example of the procedure is shown in Figure 10.

Spectrophotometric determination using pH indicators is relatively straightforward when the experimental setup is in place and can be done using the commercial spectrophotometers that are in most laboratories for carrying out solution chemistry analysis. The measurements can be made in a timely manner and continuously to monitor pH changes. pH values are easily calculated from the measurements. They can be used over a wide range of ionic strengths and solution composition, do not need background electrolyte solution, and can be carried out on dilute solutions where activity coefficients are relatively easy to calculate. However, there are several problems with this technique. pH can only be determined in a solution where both forms of the pH indicator coexist. This results in a relatively short operational pH range for each indicator, no more than 2 pH units. Therefore, in order to span a wide range of pH, several indicators have to be used. The precision of the calculated pH value is largely dependent on the equilibrium ionization constant. These may not always be accurately known under hydrothermal conditions. Moreover, the errors associated with the equilibrium ionization constants cumulate in the uncertainties of the pH value (Eqn. 9). Finally, the measurement involves determining the concentration of a particular aqueous species in solution. These species, the protonated and deprotonated forms of the pH indicator may react and complex with other solutes in solution. In addition, they may undergo structural changes following changes in solution composition, temperature and pressure as well as decomposition. It is therefore clear that spectrophotometric determinations using pH indicators involve several shortcomings and associated problems that are not always easy to deal with or to quantify.

pH determination by UV-Vis spectrophotometry

$$\mathrm{ROH(aq)} = \mathrm{RO^-(aq)} + \mathrm{H^+(aq)}$$

$$A = l\rho(m_{\mathrm{RO^-(aq)}}\varepsilon_{\mathrm{RO^-(aq)}} + m_{\mathrm{ROH(aq)}}\varepsilon_{\mathrm{ROH(aq)}})$$

$$\mathrm{pH} = -\log K + \log(m_{\mathrm{RO^-(aq)}}/m_{\mathrm{ROH(aq)}}) + \log\gamma_{\mathrm{RO^-(aq)}}$$

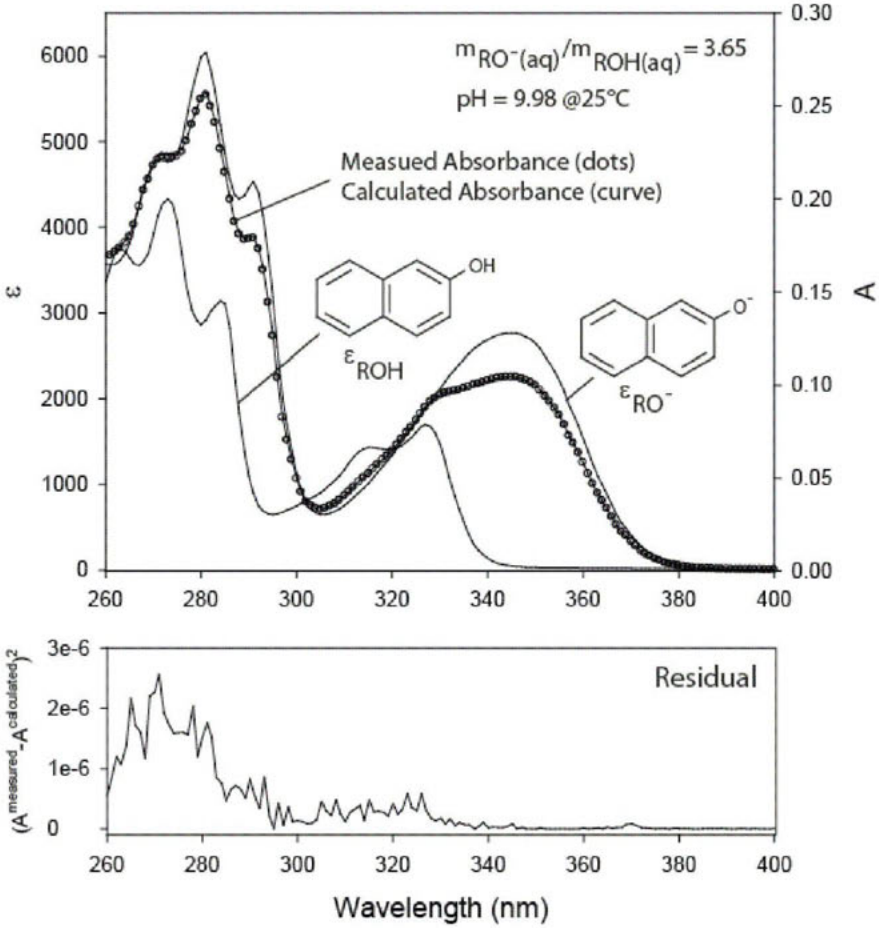

Figure 10. UV-Vis Spectrophotometric measurements of pH using 2-napthol as a pH indicator at 25 °C and 1 bar. Shown are the molar absorptivities for the protonated and deprotonated forms of 2-napthol, the measured absorbance for a given test solution together with the data regression using the Beer-Lambert law and the respective residual of the fit.

In situ vibrational and electronic spectroscopy

In recent years, several *in situ* spectroscopic techniques have been employed in the studies of aqueous speciation under hydrothermal conditions. These include X-ray and neutron techniques to obtain detailed information on ion hydration and complexation (e.g., Seward et al. 1999; Fulton et al. 2003; Evans et al. 2009; Bazarkina et al. 2010) and solubility (e.g., Pokrovski et al. 2005, 2009; Testemale et al. 2009), UV-Vis-IR and Raman spectroscopy for both structural information and to measure reaction kinetics and thermodynamics at ambient to hydrothermal conditions (e.g., Kruse and Franck 1982; Seward 1984; Belsky and Brill 1998; Rudolph et al. 1999; Murphy et al. 2000; Suleimenov and Seward 2000; Boily and Seward 2005; Stefánsson and Seward 2008) and NMR (e.g., Gerardin et al. 1999). Each technique has its advantages and drawbacks, which often depend on the system under study. Here again, this section is not intended to give an exhaustive description of each of these techniques but rather to emphasize a few that are related to our carbonate studies in hydrothermal conditions.

Vibrational and electronic spectroscopies have proven to be very useful for studying C-containing systems, including Raman and IR spectroscopy and UV-Vis spectrophotometry. These spectroscopic techniques can be applied to obtain molecular structures and symmetry, vibrational and electronic energy changes and levels, and can be quantified in terms of molecular species concentrations. Using such methods, it is possible to derive aqueous speciation and thermodynamic equilibrium constants for reactions in solution. Moreover, the position and shape of IR and Raman bands can give insight into solvation and the bonding environment. The various experimental setup used for vibrational and electronic spectroscopy under hydrothermal conditions have been reviewed by Buback et al. (1987).

UV-Vis and vibrational spectroscopic measurements of hydrothermal solutions usually consist of commercial spectrometers, an optical cell or sample tube and sometimes pumps to load the solutions to the cell. The UV-Vis cells may either be placed within the light path of the spectrophotometer or externally connected with fiber optics. The preferred setup in practice today for hydrothermal experiments at 25-300 °C is probably the flow-through system for which the experimental solution is pumped through the cell and the pressure maintained by a pressure valve or a back pressure regulator (BPR, Fig. 11). Such systems are relatively easy to operate including loading the experimental solutions, maintaining constant pressure, and keeping the system as a single liquid phase.

Various types of optical cells are available. Commercial UV-Vis cells that can be operated to ~ 80 °C are usually made of quartz glass. For higher temperatures the cells are usually made of inert metals like titanium and titanium alloys and/or lined with an inert metal like gold or platinum (Trevani et al. 2001; Suleimenov 2004; Cox and Seward 2007) to prevent interaction between the solution and the cell body. Common window materials are sapphire or quartz. Commercial cells and tubes are available for Raman and IR measurements at low temperatures. For higher temperatures and pressures most optical cells have been designed based on the pioneering work of Franck's group at Karlsruhe University (Buback 1987). These are either single window or transmission type cells with various path lengths from a few μm to several hundred μm with windows made of sapphire, ZnSe, AgCl or optical grade diamond, for instance. An example of cells used by our group is shown in Figure 11.

Vibrational and electronic spectroscopy can be quantified for measuring aqueous species concentrations either using known standard solutions or by applying the Beer-Lambert law. In particular, transmission type measurements are useful for such work given that the path length of the optical cell is known or can be determined. Common path lengths for UV-Vis spectrophotometry are in the range of 0.1-5 cm, whereas for IR measurements much shorter path lengths are often used (10-100 μm) due to the background absorbance of the solvent. Recently, two types of short-path length flow-through cells using diamond windows have been

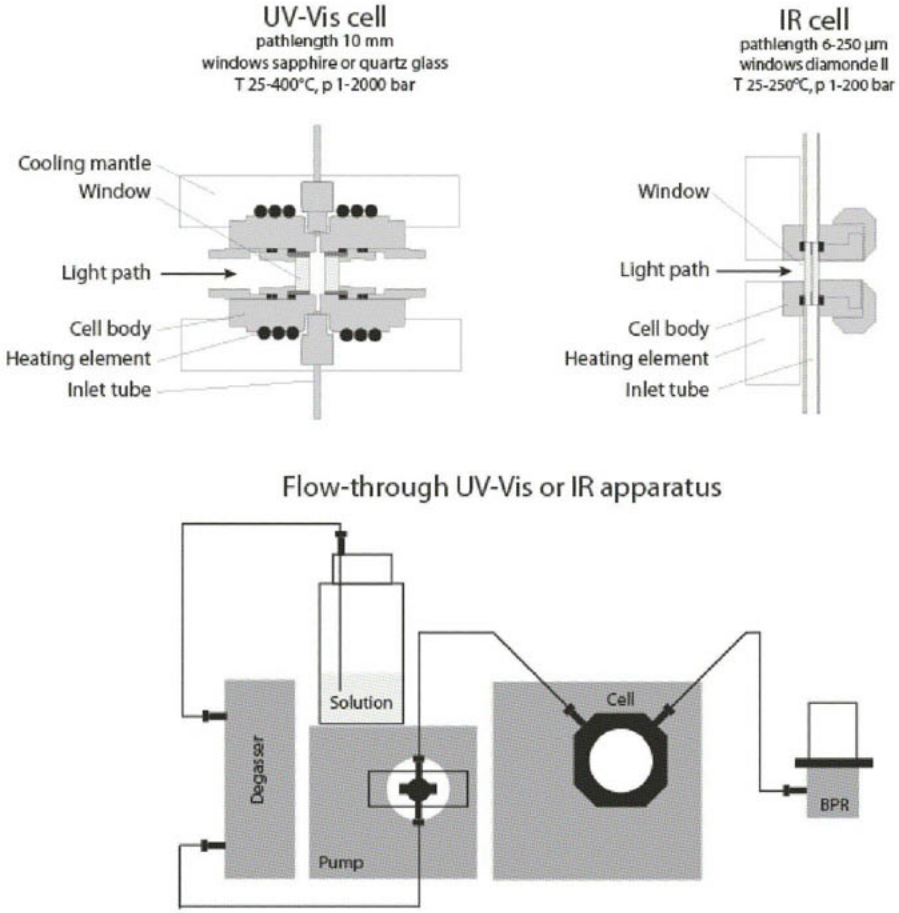
UV-Vis cell
pathlength 10 mm
windows sapphire or quartz glass
T 25-400°C, p 1-2000 bar
Cooling mantle
Window
Light path
Cell body
Heating element
Inlet tube
IR cell
pathlength 6-250 µm
windows diamonde II
T 25-250°C, p 1-200 bar
Window
Light path
Cell body
Heating element
Inlet tube
Flow-through UV-Vis or IR apparatus
Solution
Degasser
Pump
Cell
BPR

Figure 11. A schematic of high-temperature and high-pressure UV-Vis cell, IR cell and flow-through spectroscopic setup.

used successfully, either by welding special washers to the inlet and outlet capillary tubes, or by drilling the diamond windows (Schoppelrei et al. 1996; Hoffmann et al. 2000).

SPECIATION AND THERMODYNAMIC STABILITIES IN CARBON-CONTAINING AQUEOUS SOLUTIONS

Aqueous speciation of CO_2-bearing solutions

Calculating accurately aqueous dissolved inorganic carbon speciation is a prerequisite for modeling the chemistry and reactive transport of CO_2-bearing fluids. Indeed, the speciation is a function of many variables, including solution composition, pH, ionic strength, temperature and pressure, which means that most of the equilibria are interdependent and must be solved simultaneously. Carbon dioxide gas ($CO_{2(g)}$) dissolves in water to form carbonic acid ($CO_{2(aq)}$) that is known to hydrolyze to form bicarbonate (HCO_3^-) and carbonate (CO_3^{2-}) aqueous species with increasing pH. The hydrolysis of $CO_{2(aq)}$ is described by the reactions:

$$CO_{2(aq)} + H_2O = H^+ + HCO_3^- \qquad (10)$$

$$HCO_3^- = H^+ + CO_3^{2-} \qquad (11)$$

and the respective equilibrium constants are given by

$$K_1 = \frac{m_{H^+} m_{HCO_3^-}}{m_{CO_{2(aq)}} a_{H_2O}} \frac{\gamma_{H^+} \gamma_{HCO_3^-}}{\gamma_{CO_{2(aq)}}} \cdot \qquad (12)$$

$$K_2 = \frac{m_{H^+} m_{CO_3^{2-}}}{m_{HCO_3^-}} \frac{\gamma_{H^+} \gamma_{CO_3^{2-}}}{\gamma_{HCO_3^-}} \qquad (13)$$

where m_i and γ_i are the aqueous species concentrations and activity coefficients, respectively.

Experimental measurements under hydrothermal conditions are few and reported values are often dispersed. The ionization of carbonic acid is probably among the most important reactions in natural geothermal fluids at temperatures <300 °C, as well as high temperatures and pressures. Data on the ionization of carbonic acid are available over a wide range of temperatures, from ambient temperature to 250 °C and high ionic strengths (e.g., Shedlovsky and MacInnes 1935; Harned and Bonner 1945; Ellis 1959; Nakayama 1970; Dyrssen and Hansson 1973; Read 1975; Patterson et al. 1982, 1984; Thurmond and Millero 1982; He and Morse 1993; Park et al. 1998, 1999; Crea et al. 2006; Millero et al. 2007; Li and Duan 2007; Stefánsson et al. 2013a). However, as can be seen in Figure 12, some differences still exist between the various experimental studies at hydrothermal conditions, in particular for the second ionization constant (K_2) above 125 °C, the differences being up to 0.4 log units at 200 °C. However, such disagreements in studied thermodynamic values for reactions of geothermal importance are not uncommon, making aqueous speciation calculations often uncertain at high temperatures. The reasons for the differences in values among various studies may be numerous and include experimental difficulties and errors and also the way the experimental data are treated, i.e. which aqueous species are included and how the activity coefficients are calculated. Our recent data (Stefánsson et al. 2013a) for K_1 compare well with previous results and for K_2 they agree reasonably well with Patterson et al. (1984). However, significant errors were associated with the equilibrium constants derived from the spectrophotometric pH measurements, particularly above 100 °C. This was primarily related to the errors assigned to the ionization constants of the pH indicators as well as the fraction of the protonated and deprotonated forms of a given pH indicator.

The interaction of cations in solution with HCO_3^- and CO_3^{2-} ions to form ion pairs according to the general reactions:

$$Me^{x+} + HCO_3^- = MeHCO_3^{x-1} \qquad (14)$$

$$Me^{x+} + CO_3^{2-} = MeHCO_3^{x-2} \qquad (15)$$

is even less characterized and sometimes ignored in the aqueous speciation schemes. As will be discussed in the solubility section, uncertainties on aqueous speciation can affect solubility product calculations, as well as predictions of solid phase reaction rates.

In the case of natural geothermal fluids, the cations (Me^{x+}), Na^+, Ca^{2+}, Mg^{2+} and Fe^{2+} may be among the more important ones for ion pairing with HCO_3^- and CO_3^{2-} ions. Until very recently, the values of equilibrium ion pair formation constants for Na^+, Ca^{2+} and Mg^{2+} have been obtained primarily from carbonate mineral solubility measurements and acid-base titration at low temperatures, either in pure water or in H_2O-CO_2 solutions (e.g., Greenwald 1941; Garrels et al. 1961; Hostetler 1963; Lafon 1970; Nakayama 1971; Reardon and Langmuir 1974; Riesen et al. 1977; Siebert and Hostetler 1977a,b; Plummer and Busenberg 1982; Gamsjäger 1989). Equilibrium formation constants are available in the literature for the

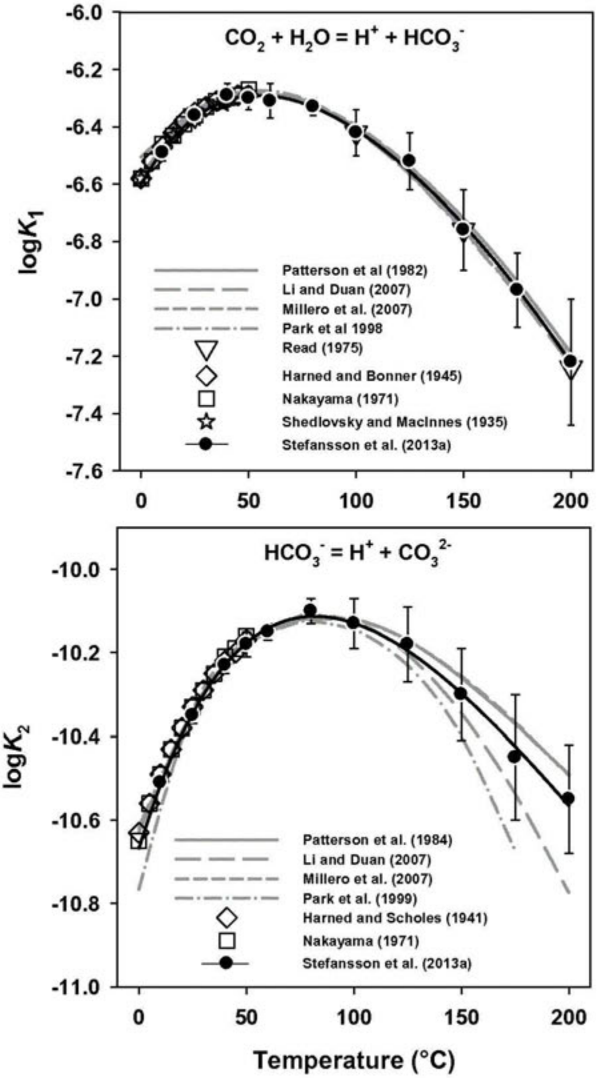

Figure 12. The first (K_1) and second (K_2) ionization constant of carbonic acid to hydrothermal conditions.

Na^+, Ca^{2+} and Mg^{2+} ion pairs at low temperatures, but no data were available until recently for temperatures above 100 °C (Stefánsson 2013a,b). It is not our intent here to give a thorough review of these data, but rather to point out the problems of discrepancy among the data and estimations, as well as the lack of data at hydrothermal conditions.

As can be seen from Figure 13, even at 25 °C the experimental values for the log*K* of $MeHCO_3^+$ and $MeCO_3^\circ$ are in poor agreement for all ion pairs. The difference among the low and high values in some cases at 25 °C is >1 log unit, which can be due to either ignorance of species, experimental problems or difficulties in computing ionic strength and activity coefficients. Values calculated by SUPCRT92 (Johnson et al. 1992), based on the revised HKF thermodynamic model, are also shown in Figure 13. The calculated parameters

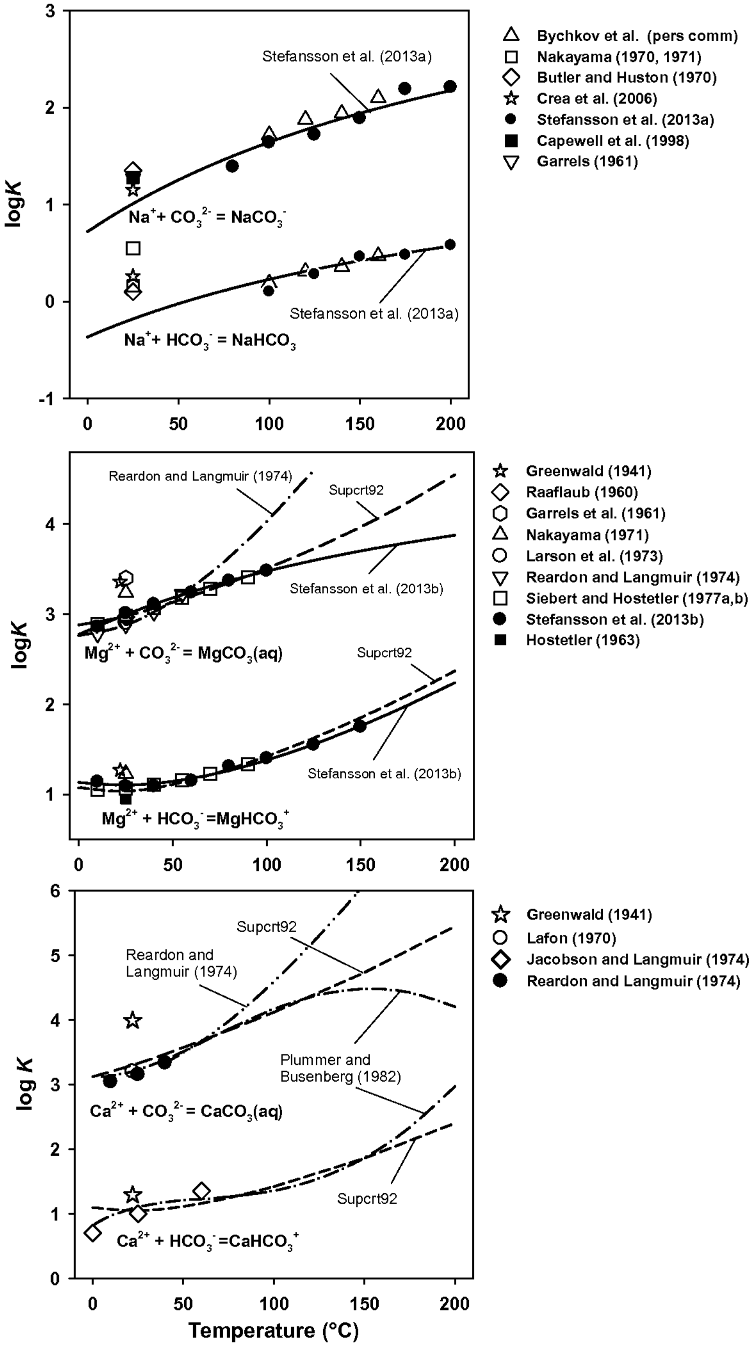

Figure 13. Equilibrium formation constants for Na^+, Mg^{2+} and Ca^{2+} and HCO_3^- and CO_3^{2-} ion pairs to hydrothermal conditions. As noted, few studies have reported values >100 °C, however, extrapolations to elevated temperatures from data obtained at low temperatures often result in very different predicted values above 100-150 °C.

for the bicarbonate-complexes come from Shock and Koretsky (1995), who used the data from Plummer and Busenberg (1982) for $CaHCO_3^+$, and Siebert and Hostetler (1977a) for $MgHCO_3^+$, as a basis for their calculations. On the other hand, the calculated parameters for the carbonate-complexes come from Sverjensky et al. (1997), who used the data from Plummer and Busenberg (1982) for $CaCO_{3(aq)}$, and Siebert and Hostetler (1977b) and Reardon and Langmuir (1974) for $MgCO_{3(aq)}$. Moreover, the standard molal entropies of cations and ligands from Shock and Helgeson (1988) were used. It is interesting to note that although Sverjensky et al. (1997) and Shock and Koretsky (1995) used the data from Plummer and Busenberg (1982) for the Ca-complexes as a basis for their thermodynamic calculations, the values generated with SUPCRT92 deviate quite substantially from the Plummer and Busenberg data in the range 0-70 °C, especially the $CaHCO_3^+$ data. Note that in Figure 13, the dotted lines for Reardon and Langmuir (1974) and Plummer and Busenberg (1982) were computed from fitting equations given by the authors, however, outside the temperatures of their experimental data, so they should be taken very cautiously. Note also that in the case of Ca and Mg, the datasets from Plummer and Busenberg (1982) and Siebert and Hostetler (1977a,b), respectively are used in the PHREEQC databases. The recent data of Stefánsson et al. (2013b) for $MgHCO_3^+$ and $MgCO_{3(aq)}$ ion pairs compare well with the work of Siebert and Hostetler (1977a,b) and result in similar extrapolation to higher temperatures, whereas the values of Reardon and Langmuir (1974) show different slopes resulting in extrapolations that predict very high stabilities, particularly for $MgCO_{3aq)}$, which is not supported by later measurements.

Among the most common methods for determining equilibrium constants in solution involving protons is the measurement of pH change (concentration or activity of the H^+ ion) to the addition of acid or base to a solution. As discussed previously, pH measurements under hydrothermal conditions are not trivial in practice and systemic errors may result in inaccurate values of equilibrium ionization constants. Nonetheless, the experimental measurements are commonly fitted to a given scheme of aqueous species and activity model in two ways. The first one, the ion-association approach, assumes the formation of many weak ion pairs between the solution constituting ions and approximate the activity coefficients using the Debye-Hückel, b_γ-dot (Helgeson 1969), Davies (Davies 1962) or Meissner (Meissner and Tester 1972) equations, for instance. The second approach, the Pitzer ion interaction formalism, involves a limited number of aqueous species and a more comprehensive activity coefficient model (Pitzer 1973; Harvie and Weare 1980; Harvie et al. 1984; Christov et al. 2007). These two different approaches may result in very similar values for the equilibrium ionization constants at infinite dilution ($I = 0$) but differ at higher ionic strengths in terms of aqueous species distribution and activities. Moreover, a salt like NaCl is commonly used as a background electrolyte to fix the solution ionic strength. This may result in difficulties in obtaining ion pair formation constants between the supporting electrolyte and the other ions. These differences are explored below, as well as the molecular nature and solvation of aqueous species present in CO_2-bearing solutions.

The aqueous speciation of CO_2-bearing solutions is a good example of the variable results generated by the two approaches described above for calculation of aqueous speciation. An example is given in Figure 14 for the aqueous species distribution at 100 °C in a solution containing 0.01 m CO_2, 0.5 m NaCl and 0.1 m $MgCl_2$. The calculations were carried out with the aid of the PHREEQC program (Parkhurst and Appelo 1999). For the ion-association approach, several carbon containing aqueous species were included in addition to $CO_{2(aq)}$, HCO_3^- and CO_3^{2-}: $NaHCO_{3(aq)}$, $NaCO_3^-$, $MgHCO_3^+$ and $MgCO_{3(aq)}$ whose equilibrium constants were taken from the llnl.dat database of the PHREEQC program with updates from Stefánsson et al. (2013a,b) while the aqueous species activity coefficients were calculated using the extended Debye-Hückel b_γ-dot method (Helgeson 1969) (Fig. 14a). In the ion interaction formalism, many fewer species are included c.a., $CO_{2(aq)}$, HCO_3^-, CO_3^{2-}, whereas $MgCO_{3(aq)}$ and the weak

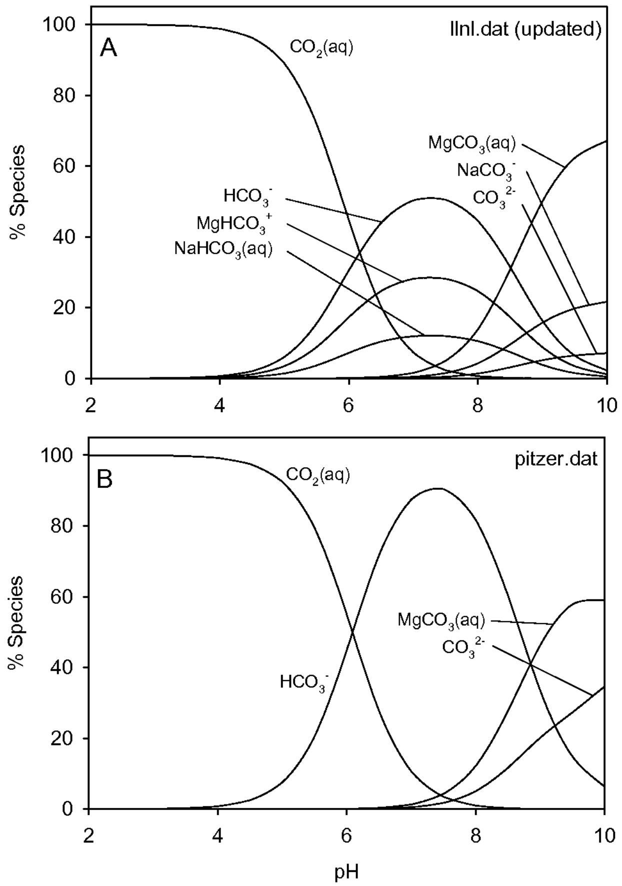

Figure 14. Aqueous species distribution as a function of pH at 100 °C for aqueous solutions containing 0.5 *m* NaCl, 0.1 *m* $MgCl_2$ and 0.01 *m* Na_2CO_3. The calculations were carried out with the aid of the PHREEQC program (Parkhurst and Appelo 1999), (A) using the ion-association approach (updated llnl.dat database) and (B) the Pitzer ion interaction formalism (pitzer.dat) (see text).

ion pairs, $NaHCO_{3(aq)}$, $NaCO_3^-$, and $MgHCO_3^+$ were not included in the speciation scheme. The equilibrium constants were taken from the pitzer.dat database of the PHREEQC program, and ion-ion and ion-solvent interactions were calculated applying the Pitzer approach using data given in the pitzer.dat database (Parkhurst and Appelo 1999) (Fig. 14b). As can be seen in Figure 14, if the predicted aqueous speciation under acid conditions is similar for both models, the results are very different above pH 5. According to the Pitzer specific interaction model, the HCO_3^- ion predominates at pH ~6-9, whereas, according to the ion-association approach, HCO_3^- predominates at low to moderate salt content and the $NaHCO_{3(aq)}$ and particularly $MgHCO_3^+$ ion pairs become important with increasing NaCl and $MgCl_2$ concentrations. Moreover, at alkaline pH, the two models predict very different CO_3^{2-} activities and thus different saturation indexes of the solution with respect to carbonate minerals.

Molecular structure of various aqueous carbon species

The molecular structure of aqueous dissolved inorganic carbon (CO_2) species in solution as well as their solvation environment have been investigated by theoretical calculations and vibrational spectroscopy (e.g., Capewell et al. 1999; Sipos et al. 2000; Rudolph et al. 2006, 2008; Garand et al. 2010; Di Tommaso and Leeuw 2009, 2010a,b; Dopieralski et al. 2011).

The isolated unhydrated HCO_3^- anion has a C_s symmetry (Rudolph et al. 2006). Stepwise solvation of the HCO_3^- moiety modifies slightly the HCO_3^- structure, the most important change being the strong preference of H_2O molecules to bind to the negatively charged -CO_2 part of the HCO_3^- anion. Moreover, the maximum number of H_2O molecules in the first solvation shell has been suggested to be 4-6, whereas six H_2O molecules are predicted to form the second hydration shell (Fig. 15) (Rudolph et al. 2006; Garand et al. 2010; Dopieralski et al. 2011).

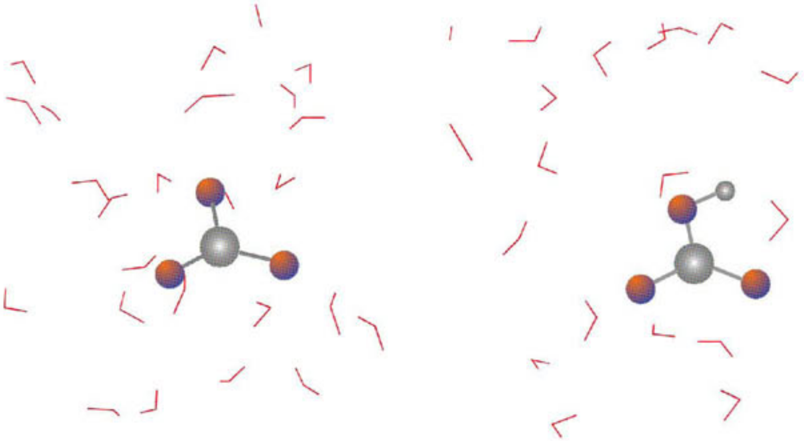

Figure 15. The simulated structure of water solvated CO_3^{2-} (*left*) and HCO_3^- (*right*). As shown, the CO_3^{2-} is solvated by 8-9 water molecules whereas HCO_3^- is solvated by 5-6 water molecules. Reproduced from Dopieralski et al. (2011).

The isolated and unhydrated CO_3^{2-} anion has a trigonal planar structure with D_{2h} symmetry (Rudolph et al. 2006). Upon hydration, the structure of the CO_3^{2-} does not change much, with the number of solvated H_2O molecules being 8-9 (Leung et al. 2007; Dopieralski et al. 2011). The nature of the solvated CO_3^{2-} anion is rigid with a maximum of three water molecules connected via hydrogen bonds to the O-atoms of the CO_3^{2-} anion.

The hydration and interaction of metal cations and HCO_3^- and CO_3^{2-} provides interesting features on ion solvation and ion pair formation. The aqueous Mg^{2+} ion has a six-fold coordination (Lightstone et al. 2001; Ikeda et al. 2007; Di Tommaso and de Leeuw 2010a,b). However, upon substitution of CO_3^{2-} and HCO_3^- in the hydration shell, Mg^{2+} coordination number is reduced to five, which is not observed in the case of Ca^{2+} upon CO_3^{2-} and HCO_3^- substitution. The hydration and ion pair formation of Na^+ concentration. Such shifts are indicative of the formation of contact ion pairs (Fig. 16). Recent IR measurements performed by the authors of this chapter indicate similar trends for the aqueous speciation of $NaHCO_3^+$ $MgCl_2$+NaOH+H_2O solutions (Fig. 17). In <0.1 M $NaHCO_3$ and $MgCl_2$-free solutions at pH = 8.66-12.17, the only absorbing species in solution were HCO_3^- and CO_3^{2-}. However, in an aqueous solution containing 0.052 M $NaHCO_3$ and 0.11 M $MgCl_2$ at pH = 9.21 the measured IR spectra cannot be calculated by only taking into account HCO_3^- and CO_3^{2-}, $NaHCO_{3(aq)}$, $MgHCO_3^+$, $NaCO_3^-$ and $MgCO_{3(aq)}$; ion pairs also need to be added to the speciation scheme. The results suggest that the $MgHCO_3^+$, and $MgCO_{3(aq)}$ ion pairs truly exist in solution, and that macroscopic changes in solution pH can not only be explained by the non-ideal behavior of ion-ion and ion-solvent interactions.

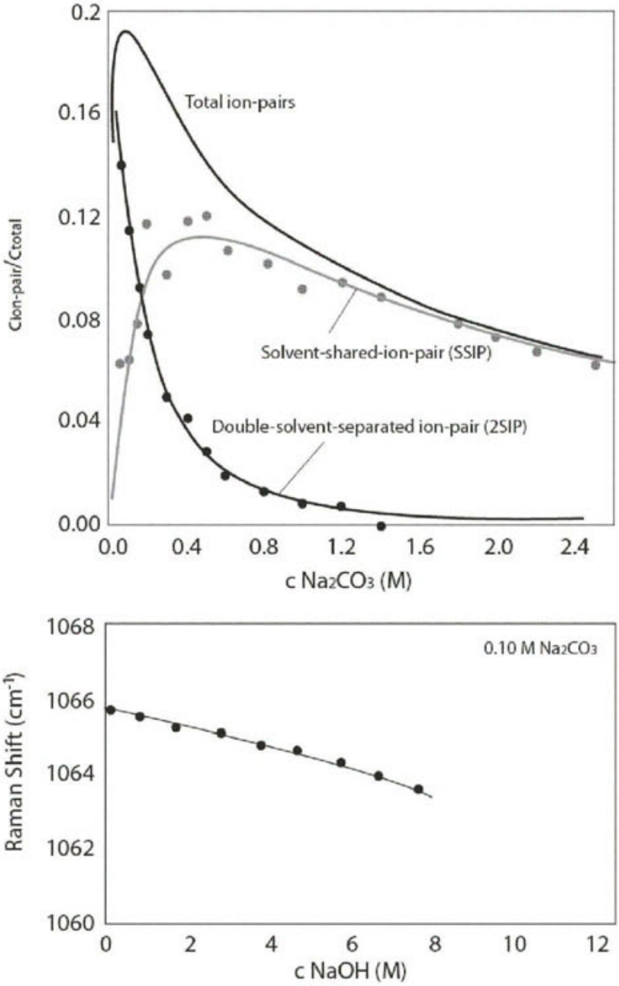

Figure 16. *Above*: Relative concentrations of ion pairs in aqueous Na_2CO_3 solutions at 25 °C calculated from solute relaxation. The two ion pairs that were found to contribute were double solvent separated (2SIP) and solvent-shared (SSIP) $NaCO_3^-$. *Below*: Raman shift of 0.1 M Na_2CO_3 solution at 25 °C as a function of NaOH concentration. Based on shift and symmetry of vibrational stretching of CO_3^{2-} observed by Raman spectroscopy, contact ion pair has further been suggested in very concentrated NaOH and NaCl solutions. Reproduced from Capewell et al. (1999) and Sipos et al. (2000).

Aqueous speciation schemes and respective equilibrium constants between species must incorporate the true molecular nature of the solution. However, ions forming complexes and ion pairs in solution may not be in direct contact with each other but are instead separated by one or more solvated layers of water. Whether such solvent separate ions should be considered as true aqueous species and taken into account in aqueous speciation or as part of the non-ideal contribution of ion-ion and ion-solvent interaction is not straightforward. However, from the point of view of thermodynamics, both approaches may be valid.

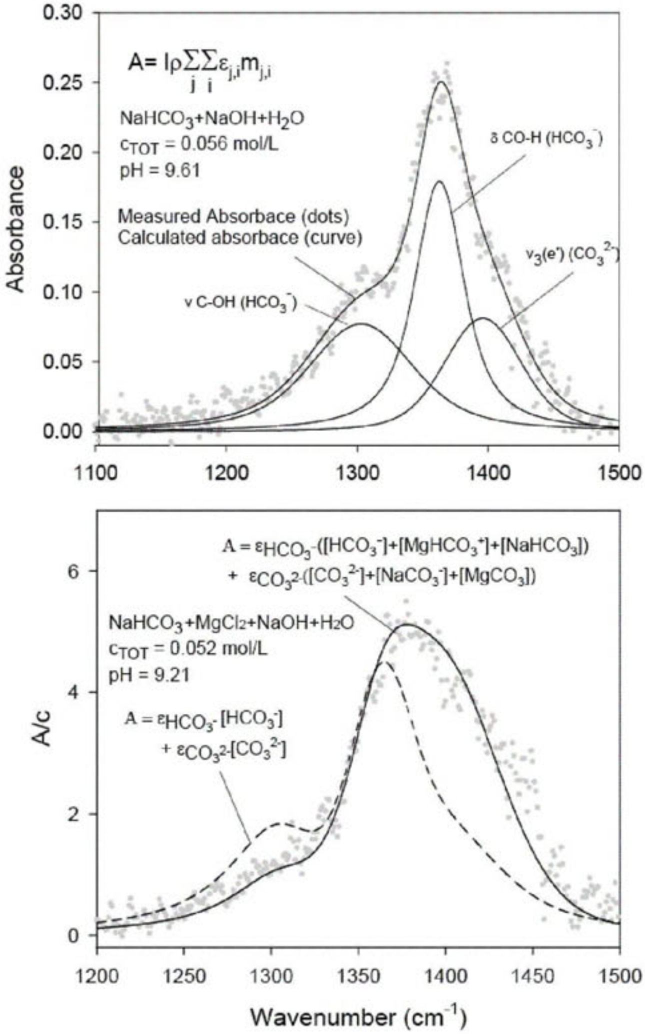

Figure 17. *Above*: An example of IR measurements (grey dots) and fitted (lines) spectra at 25 °C in $NaHCO_3$+$NaOH$+H_2O solution. The peaks observed are due to HCO_3^- and CO_3^{2-} vibrations and stretching. *Below*: An example of an IR measurement (grey dots) and fitted (lines) spectra at 25 °C in the $NaHCO_3$+$MgCl_2$+$NaOH$+H_2O solution. Two types of fit are shown, one assuming only HCO_3^- and CO_3^{2-} to be present in solution (broken line) and the other (solid line) assuming HCO_3^-, $NaHCO_{3(aq)}$ and $MgHCO_3^+$ contributing to total measured HCO_3^- concentration and CO_3^{2-}, $NaCO_3^-$ and $MgCO_{3(aq)}$ contributing to the total CO_3^{2-} concentration. As indicated, the model taken the respective ion pairs into account satisfactorily explains the measured values whereas, ignoring the ion pairs fails to fit the measured data. Reproduced from Stefánsson et al. (2013b).

CARBONATE SOLUBILITY AND MINERALIZATION

The purpose of this section is to provide an outline of the solubility products of major carbonate mineral phases which may form at high temperatures in hydrothermal and industrial systems, assess the important discrepancies that exist between published datasets, and recall how experimental techniques described above have been used to bring new information on these systems, particularly at high temperatures, including near-equilibrium mineral reactivity. A particular focus will be made on the Mg-carbonate system, which has been recently thoroughly investigated.

The solubility product of a pure carbonate mineral is the thermodynamic constant of the general reaction:

$$MCO_{3(cr)} = M^{2+} + CO_3^{2-} \tag{16}$$

where M represents the divalent cation M^{2+} (e.g., Ca, Mg, Fe). Assuming that the solid phases are pure and stoichiometric $a_{MCO_{3(cr)}} = 1$

$$K_{sp-carbonate} = a_{M^{2+}} a_{CO_3^{2-}} \tag{17}$$

where a_i represents the activity of the i^{th} ion.

For the experiments carried out with the HECC (see the common techniques section) the apparent solubility products of Reaction (16), defined as $Q_{sp\text{-}carbonate} = m_{M^{2+}} m_{CO_3^{2-}}$, where m_i stands for the molality of the i^{th} aqueous species, are measured at fixed ionic strength and the solubility product (at infinite dilution) can then be expressed as:

$$K_{sp-carbonate} = Q_{sp-carbonate} \quad {}_{Mg^{2+}} \quad {}_{CO_3^{2-}}\gamma \quad \gamma \tag{18}$$

where γ_i defines the activity coefficient of the i^{th} aqueous species calculated according to Equation (5).

An empirical equation for the temperature dependence of the carbonate solubility constants such as Equation (19) can be fitted onto the obtained data, including their uncertainties, usually in a wide range of temperatures (between 50 to 250 °C).

$$\log K_{s\text{-}carbonate} += a \quad bT(+K) \quad \frac{c}{T(K)} + \quad d\log_{10} T(K) \tag{19}$$

Based on this equation and its first and second derivatives with respect to T the equations for the standard free energy, enthalpy, entropy, and heat capacity for Reaction (16) are given respectively by:

$$\Delta_r G^\circ = \quad R\ln(10)T\log K = \quad R\ln(10)\left(aT \quad bT^2 + \quad c \quad dT\ \log T\right) \tag{20}$$

$$\Delta_r H^\circ = R\ln(10)T^2\left(\frac{d\ \ln K}{dT}\right) = R\ln(10)\left(bT^2 \quad c \quad \frac{dT}{\ln(10)}\right) + \tag{21}$$

$$\Delta_r S^\circ = \frac{\left(\Delta_r G^\circ - \Delta_r H^\circ\right)}{T} \tag{22}$$

$$\Delta C_P{}^\circ = \frac{\partial \Delta_r H^\circ}{\partial T} \quad R\ln(10)\left(2bT \quad \frac{d}{\ln(10)}\right) \tag{23}$$

where R stands for the gas constant and T is in kelvins. Combining these values with the thermodynamic parameters for the divalent cations and CO_3^{2-} taken from the literature (e.g., Shock and Helgeson 1988; Shock et al. 1997), the thermodynamic properties of the solid carbonates at 25 °C and 1 bar can be calculated.

Calcite

The solubility of calcite ($CaCO_3$) below 100 °C has been studied quite extensively in open and/or closed systems in pure water or in CO_2-H_2O solutions (e.g., Jacobson and Langmuir 1974; Berner 1976; Sass et al. 1983). The most widely recognized and used data are those of

Plummer and Busenberg (1982) obtained between 0 and 90 °C ($\log K_{sp} = -8.48$ at 25 °C, see Table 1), which were used as a basis for the SUPCRT92 (Johnson et al. 1992) database as well as in PHREEQC databases (Parkhurst and Appelo 1999). Jacobson and Langmuir (1974) determined the $\log K_{sp}$ for calcite at 5, 15, 35 and 50 °C, also reviewed earlier works, and selected a value of −8.42 at 25 °C. Berner (1976) determined $\log K_{sp} = -8.45 \pm 0.01$. However, both of these studies omitted the formation of the ion pairs formed between calcium and bicarbonate and carbonates species ($CaHCO_3^+$ and $CaCO_3^\circ$, respectively, see Eqns. 14, 15), which is not the case for the study of Plummer and Busenberg (1982) as their model includes both complexes as well as revised data on CO_2 solubility and dissociation of carbonic acid. In 1983, Sass et al. performed experiments in both closed and open systems at 25 °C and deduced a value for $\log K_{sp}$ of −8.49 and −8.48, respectively, using the ion pairing model to calculate the activity coefficients. By adjusting an equation given by Millero (1979), Sass et al. (1983) provided an equation valid from 0 to 50 °C (see Table 1), which gave values in agreement with Plummer and Busenberg (1982), as can be seen in Figure 18. In this figure, some selected low temperature values are reported as well as the value recently obtained by Gledhill and Morse (2006) from solubility measurements performed in Na-Ca-Mg-Cl brines ($\log K_{sp} = -8.41 \pm 0.12$). It appears from this figure that if the solubility of calcite seems fairly well established from 25 °C to 90 °C, experimental data are scarce above 90 °C with only two published datasets: Ellis (1959, 1963) who performed experiments between 98 and 201 °C, and Segnit et al. (1962) between 75 and 200 °C. Both studies, which were performed at pCO_2 up to 65 bars, are in close agreement. The values of Ellis (1959) have been recalculated by the same authors (Ellis 1963) using updated data for CO_2 solubility in water (Fig. 18). Even though SUPCRT92 deviates substantially from Ellis' experimental data, as shown in Figure 18, these two sets of experimental high temperature data have been used recently by Duan and Li (2008) for the parameterization of their model. This was later developed for the calculation of coupled phase and aqueous species equilibrium in the H_2O-CO_2-NaCl-$CaCO_3$ system from 0 to 250 °C, 1 to 1000 bar with NaCl concentrations up to halite saturation.

In order to provide additional experimental data above 90 °C, the solubility of calcite and the formation constants of $CaCO_3^\circ$, $CaHCO_3^+$ and $NaCO_3^-$ complexes were measured at

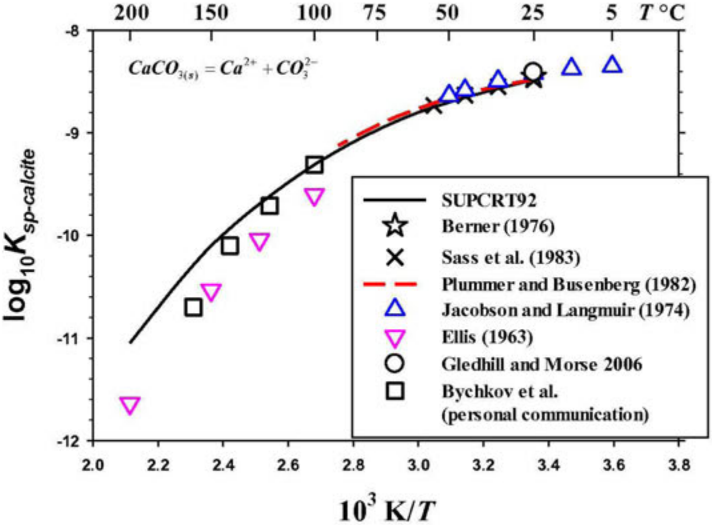

Figure 18. Calcite solubility product as a function of the reciprocal of temperature.

Table 1. Fitting parameters for the solubility products of calcite, magnesite, dolomite, siderite and solubility constant for dawsonite according to an equation similar to Equation (19) as well as the values at 25 °C.

Carbonates	**Reactions**	***a***	***b***	***c***	***d***	***e***	**logK_{sp} (25 °C)**
calcite[a]	$CaCO_3 = Ca^{2+} + CO_3^{2-}$	−171.9065	−0.077993	2839.319	71.595	–	−8.48
calcite[b]	$CaCO_3 = Ca^{2+} + CO_3^{2-}$	13.87	−0.04035	−3059		–	−8.42
calcite[c]	$CaCO_3 = Ca^{2+} + CO_3^{2-}$	131.601		−5797	−48.7537	–	−8.48
calcite[d]	$CaCO_3 = Ca^{2+} + CO_3^{2-}$	1213.62115	0.569484	−29347.93096	−513.23148	-2.64412×10^{-4}	−8.48
magnesite[e]	$MgCO_3 = Mg^{2+} + CO_3^{2-}$	7.267	−0.033918	−1476.604			−7.80
dolomite[d]	$0.5CaMg(CO_3)_2 = 0.5Ca^{2+} + 0.5Mg^{2+} + CO_3^{2-}$	1222.32845	0.577404	−29226.0615	−517.97734	-2.68077×10^{-4}	−9.07
siderite[f]	$FeCO_3 = Fe^{2+} + CO_3^{2-}$	175.568	0.0139	−6738.483	−67.898		−10.90
dawsonite[g]	$NaAlCO_3(OH)_2 + 2H_2O = Al(OH)_4^- + HCO_3^- + Na^+ + H^+$	8.797	−0.01625	−6510.1			−17.88

[a] Plummer and Busenberg (1982) ($0 < T < 90$ °C)
[b] Jacobson and Langmuir (1974) ($0 < T < 50$ °C)
[c] Sass et al. (1983) ($0 < T < 50$ °C)
[d] SUPCRT92 (note that the parameters were extracted from a fit of the values generated by SUPCRT92 using Equation (19) which needed an additional fitting parameter: $e\times T^2$ to reproduce the data within 0.1 log unit)
[e] Bénézeth et al. (2011) (25-200 °C)
[f] Bénézeth et al. (2009) (25-250 °C)
[g] Bénézeth et al. (2007) (25-250 °C).

100, 120, 140 and 160 °C and 1 to 50 atm pCO_2 by Bychkov et al. (2007) using solid contact electrodes (see the common techniques section). These data have been refined very recently so these as yet unpublished results will not be presented in detail here, but the calcite solubility products are reported in Figure 18 as a personal communication. Bychkov et al. (2007) found that the existing SUPCRT92 parameters of the HKF model for the Ca^{2+} ion and its aqueous complexes do not allow an accurate description of calcite solubility in the wide range of solution conditions and temperatures explored in their study, as seen in Figure 18 (for example, the measured Ca concentration at 100 °C and $pCO_2 = 55$ bars was 40% lower than that calculated with SUPCRT92). From the recent data acquired by Bychkov et al. (personal comm.), the solubility of calcite at pH = 5 to 6 will be quantitatively predicted using available computer codes (SUPCRT92 -- Jonhson et al. 1992; GIBBS and HCh --Shvarov and Bastrakov 1999) with some modifications of the heat capacitance c_1, c_2 (HKF) parameters for Ca^{2+} ion and its carbonate and bicarbonate complexes. The new model will precisely describe calcite solubility up to 60 bar pCO_2 and 300 °C and will be compared to the Duan and Li (2008) model.

Magnesium-carbonates

In the MgO-CO_2-H_2O system, magnesite is thermodynamically the stable Mg-carbonate mineral in a wide range of temperatures (Könisberger et al. 1999; Bénézeth et al. 2011), but its precipitation is very sluggish below *c.a.* 50 °C, which is widely ascribed to the highly hydrated character of the Mg^{2+} cation (Lippmann 1973; Sayles and Fyfe 1973; Hänchen et al. 2008). The recent studies on magnesite growth kinetics have confirmed the slow precipitation rate of magnesite (Saldi et al. 2009, 2012). As a result of its reluctance to dehydrate, magnesium has a strong tendency to form a variety of hydrated magnesium carbonates at ambient temperatures (barringtonite, nesquehonite and lansfordite) and hydrated magnesium carbonate hydroxides (pokrovskite, artinite, hydromagnesite, giorgiosite and dypingite) (see Bénézeth et al. 2011 and Hopkinson et al. 2012 for the details). However, little is known about the solubility and precipitation kinetics of these mineral phases, as well as their reaction path in the MgO-CO_2-H_2O system. Nonetheless, recent studies (e.g., Kwak et al. 2011; Loring et al. 2011; Felmy et al. 2012; Schaef et al. 2013) have shown that the precipitation of magnesite occurs during the carbonation of magnesium silicates (mainly forsterite) in experiments performed in wet supercritical CO_2 (90 bars) and at temperature as low as 35 °C (Felmy et al. 2012).

In an attempt to bridge some of the existing gaps regarding the formation of magnesium-carbonates, either in natural (e.g., Mg-silicates weathering) or industrial systems (e.g., CO_2 mineral trapping in mafic and ultramafic rocks), we have been studying very thoroughly magnesite solubility (Bénézeth et al. 2011) and reactivity (Saldi et al. 2009, 2012), including near-equilibrium reactivity (Schott et al. 2012). The effect of organic ligands on its solubility and precipitation rate has also been assessed (Gautier et al. 2009, 2010; Gautier 2012). A brief summary of recent results on magnesite solubility, including the presence of organic ligands and near-equilibrium reactivity, is presented below.

Magnesite solubility from 50 to 200 °C. Previously published data on the solubility products of magnesite show large discrepancies even at 25 °C (more than 3 orders of magnitude in $\log K_{sp}$), with few values acquired at temperatures above 30 °C, as can be seen on Figure 19. These lacks or discrepancies among the data can lead to uncertainties in the calculation of chemical equilibrium and on the relative stability of the various mineral phases of the system MgO-CO_2-H_2O as a function of pCO_2 and temperature, which can then be in disagreement with field observations (Trommsdorff and Connolly 1990). Moreover, the lack of reliable thermodynamic data on magnesium-aqueous carbonate and bicarbonate complexes ($MgHCO_3^-$ and $MgCO_3^\circ$, respectively), especially above 100 °C, as discussed in the previous section, can also lead to uncertainties on aqueous speciation and carbonate mineral surface speciation, affect solubility products calculations as well as predictions of carbonate solid phases reaction

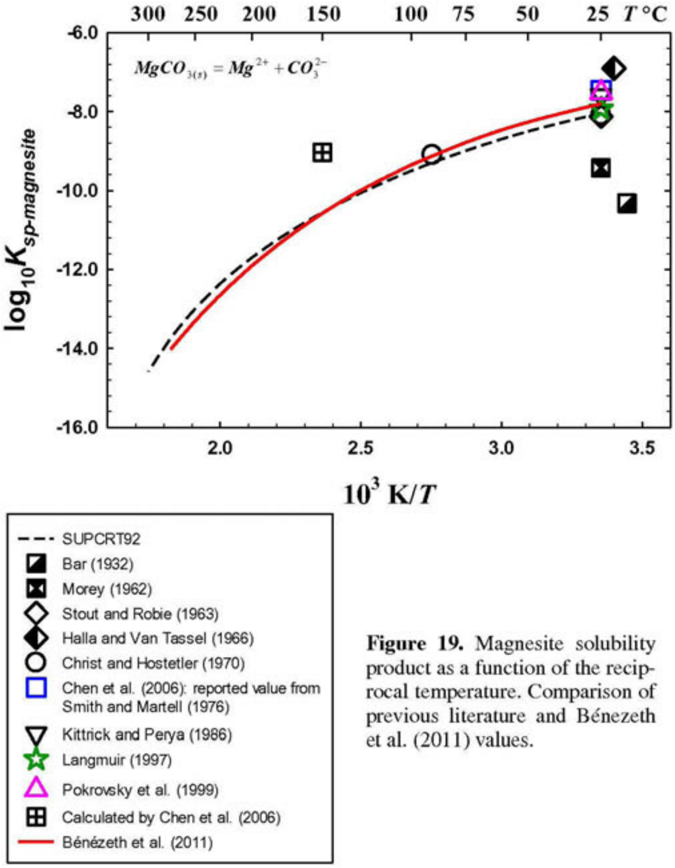

Figure 19. Magnesite solubility product as a function of the reciprocal temperature. Comparison of previous literature and Bénezeth et al. (2011) values.

rates (e.g., Pokrovsky and Schott 2002; Pokrovsky et al. 2009b; Saldi et al. 2010, 2012). For example, Figure 20 represents the predicted solubility of magnesite calculated at 200 °C and pH 7 using two distinct databases available within the geochemical code PHREEQC: llnl.dat and USGS wateq4f.dat. It can be seen that the solubilities are quite different, which prompted Saldi et al. (2010) to change the logarithm of magnesite solubility product from −10.51 to −10.04 at 150 °C ($\delta\Delta_r G = -3.80$ kJ/mol) and −11.70 to −11.23 at 200 °C ($\delta\Delta_r G = -4.25$ kJ/mol) in the 1ln1 thermodynamic PHREEQC database to insure that all the reactive solutions in which magnesite dissolution occurs at $4.6 < \mathrm{pH} < 8.4$, were actually undersaturated with respect to magnesite. In both cases, these important errors were mainly attributed to incorrect values reported in the thermodynamic databases for the stability of $MgHCO_3^-$ and $MgCO_3^\circ$ complexes.

Due to the large uncertainties shown in Figure 19, the solubility of synthetic magnesite (Fig. 21) was investigated (Bénézeth et al. 2011) using a batch Ti-reactor (Figs. 5 and 6) (120-200 °C) and *in situ* pH measurements (HECC, Fig. 9) (50-200 °C) from both undersaturated and supersaturated solutions. The parameters of Equation (19) obtained from the regression of the data are reported in Table 1. Table 2 lists the standard state properties of magnesite deduced from Equations (20) to (23). It can be seen from Figure 19 that the temperature dependence of the magnesite solubility constants derived by Bénézeth et al. (2011) (red solid line), is in very good agreement with the value of Christ and Hostetler (1970) at 90 °C, and reproduced

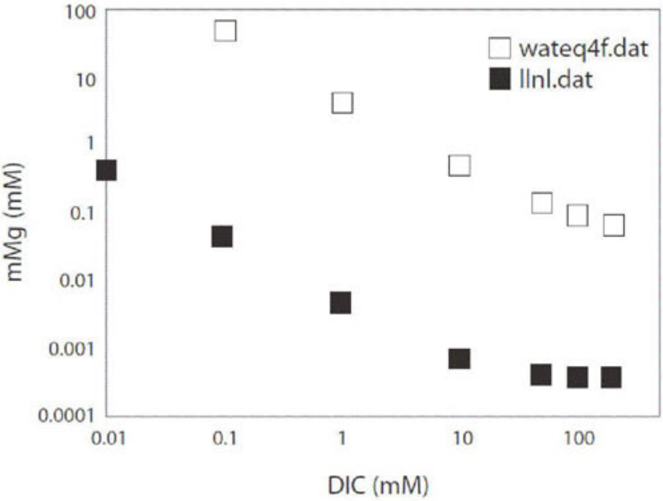

Figure 20. Calculated magnesite solubility at 200 °C and 0.1 M NaCl using two different thermodynamic databases with the PHREEQC geochemical code (see text).

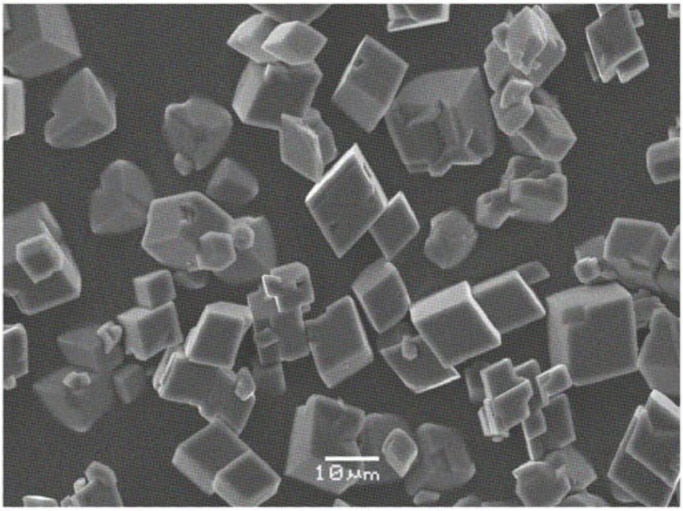

Figure 21. Hydrothermally synthesized magnesite single crystals (see Saldi et al. 2010; Bénézeth et al. 2011).

fairly well the SUPCRT92 results. The extrapolated 25 °C value (log$K_{\text{sp-magnesite}} = -7.80 \pm 0.3$) is also in relatively good agreement (within the uncertainty) with either the value recalculated by Langmuir (1997) (log$K_{\text{sp-magnesite}} = -7.93$) or the one measured by Kittrick and Peryea (1986) (log$K_{\text{sp-magnesite}} = -7.59 \pm 0.30$) and Pokrovsky et al. (1999) (log$K_{\text{sp-magnesite}} = -7.52 \pm 0.25$). Moreover, this recent study confirmed that below 75-50 °C, the very slow kinetics of magnesite dissolution-precipitation is responsible for the more scattered solubility values. This can very well explain, in part, the large inconsistencies among the K_{sp} values reported in the literature at 25 °C, for which equilibrium with respect to magnesite was probably not attained. As a consequence, the reported thermodynamic properties of magnesite also show large

Table 2. Standard state properties of carbonates at 25 °C and 1 bar.

Carbonates	$\Delta G_f°$ kJ mol^{-1}	$S_f°$ J mol^{-1} K^{-1}	$\Delta H_f°$ kJ mol^{-1}	$C_P°$ J mol^{-1} K^{-1}	Ref.
calcite	−1129.18	92.68	−1207.30	82.01	[1]
magnesite	−1026.48±2	60.00±2	−1111.75±2	75.91±2	[2]
0.5 Dolomite	−1083.15	77.59	−1164.47	78.66	[1]
siderite	−680.71±2	109.54±2	−749.59±2	83.26±2	[3]
dawsonite	−1782±2	131±2	−1960±7	–	[4]

References: [1] SUPCRT92; [2] Benezeth et al. (2011); [3] Bénézeth et al. (2009); [4] Bénézeth et al. (2007)

discrepancies (see the review given by Bénézeth et al. 2011), in particular a $\delta\Delta G_f°$ of −18 kJ/mol, and a $\delta\Delta H_f°$ of −22 kJ/mol. The values obtained by Bénézeth et al. (2011) are in close agreement with previous calorimetric measurements as well as high pressure and temperature phase equilibrium studies, thus proving that reliable thermodynamic data can be also obtained from solubility measurements.

Recently, magnesite column-scale rate data obtained by Salehikhoo et al. (2013) in acidic conditions at room temperature and under low flow velocities, were best described by changing only one reaction constant in the database of EQ3/6 computer code (Wolery 1983) they used, which is the solubility product of magnesite. Under their experimental conditions, the system reaches local equilibrium and so is very sensitive to the solubility constant used in their calculation. Without this adjustment, the code underestimates the magnesium effluent concentrations. The corrected value appears to be in excellent agreement with the value determined by Bénézeth et al. (2011). Note that in most measurements performed by Bénézeth et al. (2011), the solubility has been approached by both undersaturation and supersaturation, insuring that steady state has been reached, and allowing simultaneously measurements of dissolution/precipitation kinetics very close to equilibrium, as presented in the next sub-sections.

Magnesite near-equilibrium reactivity. The operation of the hydrogen-electrode concentration cell has recently made possible the investigation of the magnesite approach to equilibrium ($|\Delta G|$ less than a few hundreds J/mol) during both its dissolution and growth (Schott et al. 2012). Experiments were performed at 100 °C and pH = 5.6 using synthetic magnesite crystals (Fig. 21). Near-equilibrium rates were determined by changing temperature (increase and decrease for crystal growth and dissolution, respectively) and following the evolution of the system to a new equilibrium. In experiments where magnesite growth was provoked by the perturbation of the system after a long period of equilibrium (452 h), magnesite growth follows a parabolic rate law (r_p/mol cm^{-2} s^{-1} = $10^{-14.7}(\Omega-1)^{1.8}$) consistent with spiral growth step generation controlling magnesite precipitation (Fig. 22a). Magnesite near-equilibrium dissolution, also triggered by the disruption of a long magnesite-solution equilibrium, follows a linear rate law (r_d/mol cm^{-2} s^{-1} = $10^{-13.52}(1-\Omega)$ for $\Delta G \leq -2$ kJ mol^{-1}; see curve A of Fig. 22a). However the value of the dissolution rate constant ($k_d = 10^{-13.52}$ mol cm^{-2} s^{-1} at 100 °C and pH = 5.6) is almost 2 orders of magnitude lower than that determined by Pokrovsky et al. (2009b) on ground powders of natural magnesite at the same temperature and solution pH but far from equilibrium ($k_d = 10^{-11.63}$ mol cm^{-2} s^{-1}, $\Delta G < -15$ kJ mol^{-1}). The strong discontinuity observed between magnesite near-to-equilibrium and far-from-equilibrium dissolution rates observed in Figure 22b is consistent with a change in controlling dissolution mechanisms as equilibrium is approached. It is generally acknowledged (see Schott et al. 1989, 2012; Arvidson and Lüttge 2010; Fischer et al. 2012) that the bulk crystal dissolution or growth proceeds via parallel reactions occurring at active surface sites located at edges, corners,

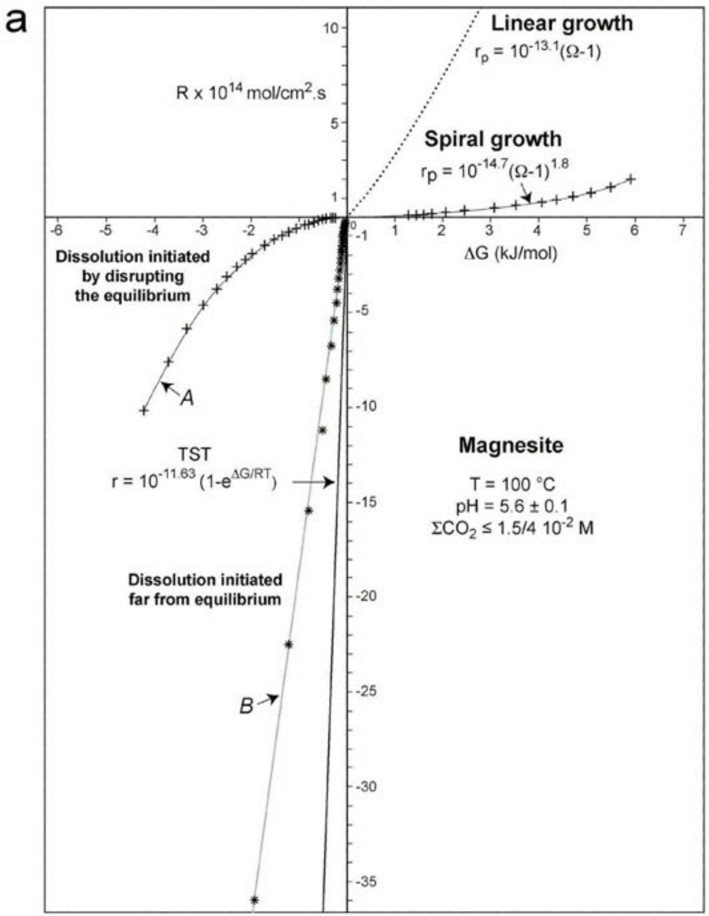

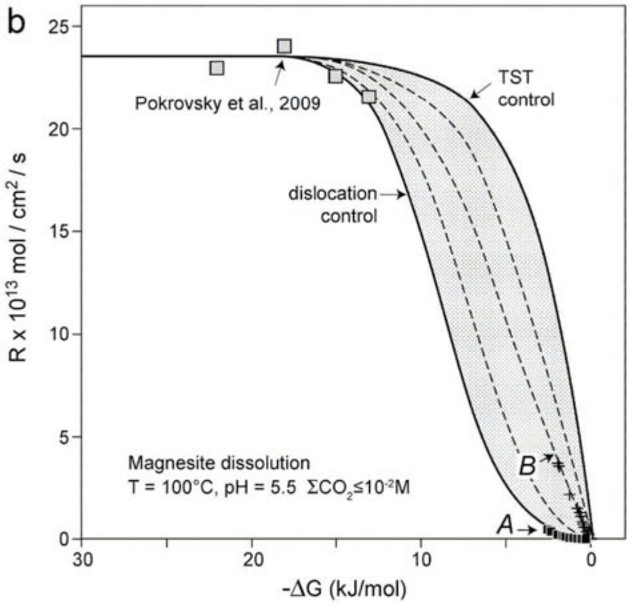

Figure 22. Magnesite dissolution and growth rates measured at near to equilibrium conditions at 100 °C and pH = 5.5 in a hydrogen electrode concentration cell (HECC). (a) Dissolution and growth rates of synthetic single crystals as a function of ΔG, *A*: dissolution initiated by perturbing magnesite-solution equilibrium, *B*: dissolution initiated far from equilibrium; (b) Magnesite near equilibrium (data from Fig. 22a) and far from equilibrium (data from Pokrovsky et al. 2009b) dissolution rates as a function of ΔG. The "dislocation control" solid line has been generated using Equation (24) with $r_{+,1}$ and $r_{+,2}$ equal to $10^{-11.63}$ and $10^{-13.52}$ mol cm^{-2} s^{-1}, respectively, and n and m equal to $10^{-1.623}$ and 3.2, respectively. The 'TST' solid line has been generated with $r_+ = 10^{-11.63}$ mol cm^{-2} s^{-1}. The dashed lines represent possible intermediate rate functions including a fit of run *B*, the shaded area corresponds to the zone delimited by the TST- and dislocation-derived rate laws (modified after Schott et al. 2012).

surface pits, point defects, twins or grain boundaries, microfractures, etc. The overall bulk dissolution rate is determined by the relative concentration of the different active sites, the rate constant for each corresponding elementary reaction and the dependence on the rates of these reactions on the departure from equilibrium. The lack of data on the nature, energetics and distribution of the active sites present at the surface of magnesite crystals used in the above experiments prevented a rigorous modeling of its dissolution as a function of the chemical affinity of the overall reaction. However, a simplified approach, which consists of considering two limiting cases for the density and nature of active sites, can provide useful information on near-equilibrium rates. One limiting case is observed with single crystals of large sizes and low surface roughness whose faces, therefore, exhibit a low density of active sites. Following Burch et al. (1993), Lasaga and Luttge (2001), Hellmann and Tisserand (2006), Schott et al. (2012), it can be assumed that the dissolution of such crystals is defect-driven and controlled by two parallel reactions. Far from equilibrium, dissolution is driven by the nucleation at dislocation outcrops of etch pits that are the source of steps traveling across the crystal surface. Closer to equilibrium, below a critical ΔG value, etch pits stop nucleating and dissolution occurs only at pre-existing edges and corners at a much lower rate. The overall dissolution rate can thus be described by the following rate law representing the sum of the two parallel reactions mentioned above (Burch et al. 1993; Hellmann and Tisserand 2006):

$$r = r_{+,1} f_1(\Delta G) + r_{+,2} f_2(\Delta G) = r_{+,1}\left\{1 - \exp\left(-\left(\frac{n|\Delta G|}{RT}\right)^m\right)\right\} + r_{+,2}\left\{1 - \exp\frac{\Delta G}{RT}\right\} \tag{24}$$

where $r_{+,1}$ and $r_{+,2}$, stand for the forward rates of the two parallel reactions and n, and m are adjustable fit parameters.

The second limiting case corresponds to fine-grained microcrystalline powders of high surface area and surface roughness which have many active sites (kinks, steps, corners, twins or grain boundaries, microfractures) where dissolution and growth reactions can occur. The dissolution (growth) of these crystals is driven by the direct and reversible attachment of reactants at the numerous active sites available at their surface (Schott et al. 2012) and can be described within the framework of Transition State Theory (TST; Eyring 1935) according to:

$$r = r_+\left(1 - \exp\left(\frac{\Delta G}{\sigma RT}\right)\right) \tag{25}$$

where r_+ stands for the forward rate and σ designates the Temkin's stoichiometric number equal to the ratio of the rate of destruction of the activated complex to the overall reaction rate (see Schott et al. 2009 for more details).

Using the magnesite forward dissolution rates determined by Pokrovsky et al. (2009b) at 100 °C and pH = 5.5, the magnesite near-to-equilibrium dissolution rates predicted respectively by Equations (24) and (25) are compared in Figure 22b. It can be seen that the near equilibrium dissolution of magnesite synthetic single crystals having well-developed smooth faces with little active sites (curve A, Fig. 22b) can be accurately described by the dislocation-assisted rate law (Eqn. 24) whereas the TST-derived rate law (Eqn. 25) leads to near-equilibrium estimates that are almost 2 orders of magnitude faster than measured rates. The near-equilibrium rate data plotted in Figure 22 (curve A) contrast with those measured by Saldi et al. (2010) at 150 °C and 4.5 < pH < 8.4 for grounded powders of natural magnesite exhibiting much a higher surface roughness (defined as the ratio of the BET specific area to the geometric specific surface area: 5.2 vs. 2.2). These latter rates do not exhibit any discontinuity as a function of ΔG and obey the TST rate law near equilibrium (not shown).

It seems likely that an infinity of different $f(\Delta G)$ functions, between the limiting TST and dislocation-assisted rate laws, can describe near-equilibrium dissolution rates depending on the density and nature of active sites present on the crystal faces. This assumption is supported by a duplicate of a magnesite dissolution experiment performed using the same hydrogen-electrode concentration cell (HECC), temperature, pH, and synthetic magnesite crystals but initiated far from equilibrium instead of by disrupting a long-term equilibrium. This run reported in Figure 22a (curve B) resulted in much faster near-equilibrium dissolution rates (r_d/mol cm^{-2} s^{-1} = $10^{-12.19}(1-\Omega)$ for $\Delta G \leq -2$ kJ mol^{-1}) but still significantly lower than the TST-derived rate based on the magnesite dissolution rate constant determined by Pokrovsky et al. (2009b) (see Fig. 22). It is believed that the preliminary etching at far-from-equilibrium conditions of magnesite single crystals generates active sites (i.e., at steps, edges, corners and pits) where dissolution can proceed via the direct attachment of reactants even near to equilibrium. Therefore, these observations suggest that the form of the $f(\Delta G)$ function describing the dissolution of minerals, like magnesite having well-developed high surface energy smooth faces, depends on the availability of reactive sites at the crystal surfaces and thus on the history of the mineral-fluid interaction and the hydrodynamic conditions under which the crystals are reacted.

The distribution of active sites on the surface controls as well the form of the $f(\Delta G)$ function describing magnesite near-equilibrium growth (Saldi 2009; Saldi et al. 2009, 2012; Schott et al. 2012). This is shown in Figure 23 which compares the growth rates measured at 150 °C in a mixed flow reactor (Fig. 23a) and in a batch reactor (Fig. 23b) of the same synthetic magnesite crystals as those used in the near-equilibrium dissolution experiments described above. Magnesite growth measured in a mixed flow reactor, where a supersaturated solution flows on magnesite single crystals having few growth sites (e.g., pits, kinks, edges, and steps), occurs primarily by defect-assisted nucleation and is proportional to $(\Omega-1)^2$ in accordance with a spiral growth control. In the batch reactor experiment, magnesite growth was provoked by a temperature increase following ~250 hours of magnesite dissolution; this initial dissolution step generated active sites to which reactants could directly fasten in agreement with TST and a linear rate law (rates are proportional to $\Omega-1$ with a rate constant about 40 times larger than that measured in the mixed flow reactor). Thus, when precipitation occurs just after a long dissolution episode it obeys a linear TST law, but when it occurs via the disruption of a long period of equilibrium it obeys a parabolic rate law. Note that because active sites are destroyed with time during linear growth, this process is inevitably transient and eventually a spiral growth mechanism will dominate in the long term.

These results demonstrate that the near-equilibrium dissolution and growth of magnesite heavily depend on the density of the active sites present on the crystal faces. Depending on the preliminary treatment undergone by the crystals and the selected experimental protocol, the same magnesite single crystals can dissolve/precipitate near equilibrium and under the same T and pH conditions at very different rates (to up 2 orders of magnitude) obeying distinct $f(\Delta G)$ functions. These functions, which reflect the nature and the distribution of the rate-controlling active sites, can have different forms, from the simple linear TST law describing the direct attachment of reactants to active sites to more complex laws such as Equation (24) reflecting defect-assisted controls at different types of defects. It follows that the accurate description of magnesite (as well as that of many other minerals) near-equilibrium dissolution and growth rates require quantitative information on the nature and density of the main active sites present at the crystals faces. The crystal surface roughness has the potential to be a proxy of the density of the active sites but extensive experimental calibration would be necessary before this parameter could help in the selection of the most accurate rate law for describing the near-equilibrium reactivity of magnesite given crystals. Moreover, as the nature and density of active sites change over time with the physical and chemical conditions at the crystal-solution interface, the simulation of slow mineral-water interactions in natural environments over large time and length scales represents a challenging task.

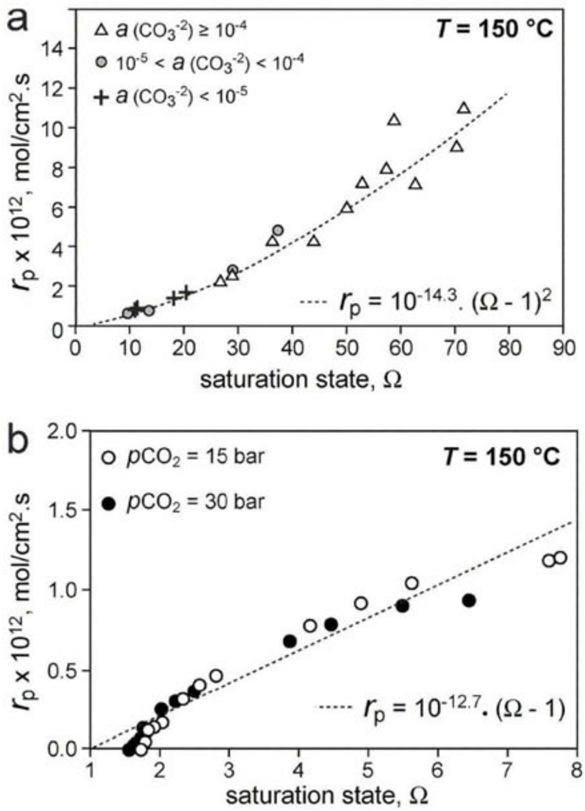

Figure 23. Comparison of magnesite growth rates measured at 150 °C on identical magnesite synthetic single crystals in an open (mixed flow) and in a closed reactor. (a) magnesite growth rate versus solution saturation state measured in a mixed flow reactor where a supersaturated solution directly flows on the magnesite crystals: a parabolic rate law is observed, consistent with a spiral growth mechanism; (b) magnesite growth rate versus solution saturation state measured in a closed reactor where magnesite growth is provoked by a temperature increase following a long (~ 250 h) stage of magnesite dissolution: a linear rate law is observed in accord with TST (modified after Schott et al. 2012).

Effect of citrate on the solubility of magnesite at 120 °C: retrieving the Mg-Citrate complexation constant at high temperature. The need to reduce anthropogenic CO_2 emissions has generated much interest in the possibilities of storing CO_2 under a mineral form through "*ex situ*" Mg-silicates carbonation (see Reaction 1). The process is slow, however, and several authors have proposed using organic ligands such as oxalate, citrate or EDTA to accelerate the slow dissolution of the silicate phase (e.g., Park et al. 2003; Krevor and Lackner 2011; Prigiobbe and Mazzoti 2011 and references cited). However, the influence of such ligands on the subsequent Mg-carbonate precipitation is unknown. It is expected that, by complexing free cations such as Mg^{2+} in aqueous solution, organic ligands reduce their chemical activity and therefore reduce the saturation state of the solution with respect to minerals containing these cations. This would in turn decrease the rate of carbonate mineral precipitation, as recently shown by Gautier (2012). Correctly estimating the effect of organic ligands on Mg-carbonate solubility however requires knowing precisely the extent of complexation between organic ligands and Mg^{2+} at the temperature of interest.

Although the most usual carboxylic ligands, their dissociation constants, the type of complexes they form with metal cations and their stability constants have been studied at ambient temperature (see for instance reviews by Smith et al. 1987, 1998; Hummel et al. 2005), this is much less the case at higher temperatures. Here, citrate and its interactions with Mg^{2+} will be taken as an example to illustrate the scarcity of data, and how high temperature solubility studies may be used to better constrain metal-ligands complexation constants, provided that the solubility of the mineral of interest is well known.

The following complexation reactions between Mg^{2+} and citrate species have been mentioned in the literature:

$$\mathrm{Citrate}^{3-} + \mathrm{Mg}^{2+} = \mathrm{MgCitrate}^{-} \tag{26}$$

$$\mathrm{HCitrate}^{2-} + \mathrm{Mg}^{2+} = \mathrm{MgHCitrate} \tag{27}$$

$$\mathrm{H_2Citrate}^{-} + \mathrm{Mg}^{2+} = \mathrm{MgH_2Citrate}^{+} \tag{28}$$

$$2\mathrm{Citrate}^{3-} + \mathrm{Mg}^{2+} = \mathrm{Mg(Citrate)_2}^{4-} \tag{29}$$

The strongest complex by far is $MgCitrate^{-}$ (Reaction 26). The CRITICAL database (Smith et al. 1998) reports values for $\log Q_{\mathrm{MgCitrate-}}$ (the complexation quotient) ranging from 3.43 to 3.64 at 25 °C and an ionic strength of 0.1 M. Complexation constants for Reactions (27) and (28) can be found in CRITICAL, while that of Reaction (29) can be extrapolated to zero ionic strength from the data reported at 37 °C and 0.15 M ionic strength by Covington and Danish (2009). However, given their reported stability constant at low temperatures, these species are not expected to play an important role on citrate and Mg speciation. All equilibrium constants (including those extrapolated from non-zero ionic strength) are reported in Table 3.

Here, we wish to estimate the extent of Mg-citrate complexation at hydrothermal temperatures. Temperature extrapolation may be performed using different methods (see for

Table 3. Summary of thermodynamic data for the Mg-Na-citrate system, used for the calculation of solution chemical speciation during magnesite solubility experiment with citrate. For $MgCitrate^{-}$, two possibilities of temperature extrapolation existed, and both are reported here. The bold values designate which option was eventually retained.

Chemical reaction	**log*K* (25°C)**	**$\Delta_r H°$ (kJ mol^{-1})**	**$\Delta_r C_P°$ (J K^{-1} mol^{-1})**	**log*K* (100 °C)**	**log*K* (120 °C)**
$H_3Citrate = H_2Citrate^{-} + H^{+}$	–3.127 [a]	4.1 ± 0.2 [a]	–162 ± 7 [a]	–3.137	–3.176
$H_2Citrate^{-} = HCitrate^{-} + H^{+}$	–4.759 [a]	2.2 ± 0.1 [a]	–192 ± 15 [a]	–4.874	–4.945
$HCitrate^{2-} = Citrate^{3-} + H^{+}$	–6.397 [a]	–3.6 ± 0.3 [a]	–231 ± 7 [a]	–6.761	–6.896
$Mg^{2+} + Citrate^{3-} = MgCitrate^{-}$	4.74 [b]	8.7	–	5.49	5.76
	5.00 [b]	**7.7**	**–**	**5.77**	**6.05**
$HCitrate^{2-} + Mg^{2+} = MgHCitrate$	2.59 [b]	–	–	–	–
$H_2Citrate^{-} + Mg^{2+} = MgH_2Citrate^{+}$	1.0 [b]	–	–	–	–
$2\ Citrate^{3-} + Mg^{2+} = Mg(Citrate)_2^{4-}$	5.49 [c]	–	–	–	–
$Na^{+} + Citrate^{3-} = NaCitrate^{2-}$	1.00 [d]	–0.47 ± 0.36 [d]	120 ± 30 [d]	1.08	1.12
$Citrate^{3-} + 2\ Na^{+} = Na_2Citrate^{-}$	1.81 [b]	–5.1 [e]	–	–	–
$Na^{+} + Citrate^{3-} + H^{+} = NaHCitrate^{-}$	6.45 [e]	–3.6 [e]	–	–	–

[a]Bénézeth et al. (1997b); [b]CRITICAL (Smith et al. (1998); [c]Covington and Danish (2009); [d]Zelenina and Zelenin (2005); [e]minteq.dat.

instance Tremaine et al. 2004; Oelkers et al. 2009 for a review), but these depend upon the knowledge of thermodynamic constants (in particular reaction enthalpy, calorific capacity) at ambient temperature for the chemical reaction of interest. There is to our knowledge no calorimetric study of the reaction enthalpy and heat capacity of Reaction (26). CRITICAL mentions for its reaction enthalpy $\Delta_r H_{\mathrm{MgCitrate-}} = 8$ kJ/mol at a 0.1 M ionic strength, but we were not able to determine the original research source of these data, which should therefore be considered with caution. The temperature dependence of Reactions (27) to (29) is unknown. Given the uncertainties of both complexation constants at ambient temperature and reaction thermodynamic constants, any attempt to estimate the extent of Mg-citrate complexation at hydrothermal temperatures may be affected by large errors. Thus, in the present case, we will confront the result of a temperature extrapolation of Reaction (26) complexation constant with the result of a solubility experiment performed at 120 °C.

In order to minimize extrapolation errors, Reaction (26) was written in an isoelectric fashion (Lindsay 1980, see the common techniques section), after which the van't Hoff equation was used to extrapolate the equilibrium quotient at 0.1 M to 120 °C. The obtained value for $Q_{\mathrm{MgCitrate-}}$ was then extrapolated to zero ionic strength (for more details see Gautier 2012). The extrapolation procedure was applied to the two extreme values for $Q_{\mathrm{MgCitrate-}}$ reported at 25 °C. Temperature extrapolation for the two extremes is shown in Figure 24. An accurate chemical speciation calculation in the presence of citrate at 120 °C should allow us to retrieve, in the presence of citrate, the exact magnesite solubility product measured experimentally by Bénézeth et al. (2011) and described above.

The corresponding solubility experiment at 120 °C was carried out in a 400 mL titanium batch reactor (Figs. 5 and 6) on synthetic magnesite seeds (see Fig. 21), with 1 mM of citrate under the form of Na_3Citrate. The ionic strength was fixed at ~0.1 M with NaCl. In the absence of *in situ* electrodes, pH was controlled through CO_2 pressurization (15.2 bars) controlled by mean of a solid-state pressure transducer, while 0.03 M $NaHCO_3$ was added to buffer the solution. In order to calculate the chemical speciation of the solution, it was assumed that the solution was in equilibrium with the applied CO_2 partial pressure, thus fixing the pH and the total dissolved inorganic carbon (TDIC) concentration. Equilibrium was reached within 150

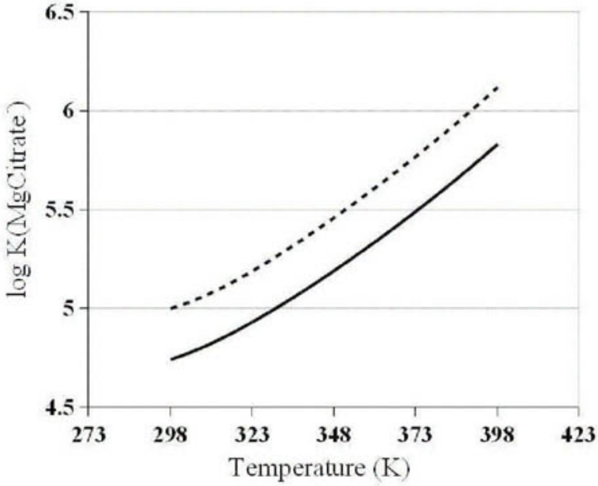

Figure 24. Extrapolation with temperature of MgCitrate$^-$ complexation constant (Reaction 26). The two curves delimit a range of plausible values for the complexation constant (see text).

hours, as shown in Figure 25, and the chemical composition of the solution at equilibrium with magnesite is summarized in Table 4. PHREEQC was used to calculate the corresponding solution speciation with its llnl.dat thermodynamic database, which was modified to include the same thermodynamic dataset as used by Bénézeth et al. (2011), data for citric acid dissociation constants (Bénézeth et al. 1997b), Na-citrate complexation, and one or the other Mg-Citrate⁻ complexation constant hypotheses (summarized in Table 2). The corresponding magnesite solubility product was then calculated using Equation (18) and the results of the calculations with our two hypotheses for $K_{\text{MgCitrate}^-}$ are reported in Table 5. Given that the actual value of $\log K_{\text{sp-magnesite}}$ determined at 120 °C by Bénézeth et al. (2011) is –9.82, it can then be concluded that the higher hypothesis for Mg-Citrate⁻ stability constant ($\log K_{\text{MgCitrate}^-}$ (120 °C) = 6.05 and $\log K_{\text{MgCitrate}^-}$(25 °C) = 5.00, in bold in Table 2) gives the best agreement with Bénézeth et al. (2011). This is confirmed by Figure 25, which compares the actual Mg concentration measured from aliquots, and the predicted concentration at equilibrium with magnesite in the presence of 1 mM of citrate. The higher complexation hypothesis is clearly in better agreement with the measured Mg concentrations. This hypothesis may therefore be used to estimate the influence of citrate on magnesite saturation state in aqueous solutions.

This solubility experiment was used as a way to confirm a doubtful thermodynamic dataset and calculate the chemical speciation of solutions containing Mg^{2+} and citrate at hydrothermal

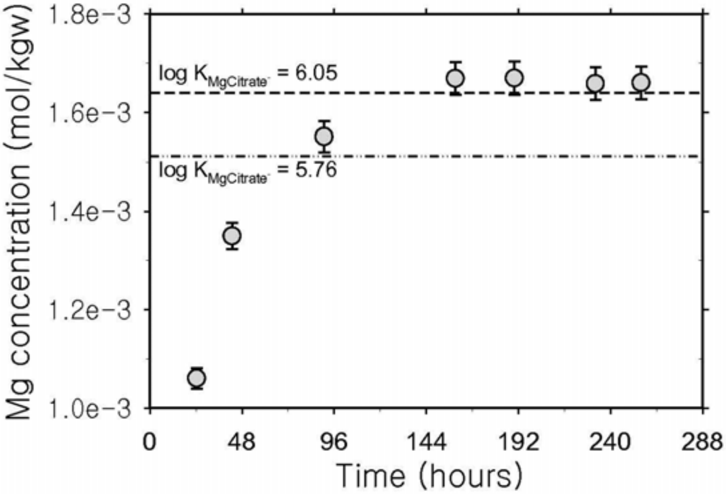

Figure 25. Evolution of Mg concentration with time during the course of the magnesite solubility experiment at 120 °C in the presence of citrate. Stability of Mg concentration (as symbolized by the dashed line) indicates equilibrium is reached. The two dashed lines materialize the total Mg concentration at equilibrium with magnesite in the presence of 1 mM citrate, as calculated using the two selected hypotheses for Mg-citrate complexation. The higher complexation hypothesis convincingly fits the obtained results

Table 4. Result of the magnesite solubility experiment in presence of citric acid performed at 120 °C in a Ti-batch reactor.

T **(°C)**	**Citrate (mol kg⁻¹)**	**Mg_{tot} (mol kg⁻¹)**	**pCO_2 (bars)**
120	10^{-3}	$1.660\times10^{-3} \pm 2.5\times10^{-5}$	15.2 ± 0.1

Table 5. Results of chemical speciation calculation at 120 °C from solution chemistry reported in Table 4, and calculation of $K_{\text{sp-magnesite}}$ with the two hypotheses for MgCitrate^- stability constant. Uncertainties for $\log K_{\text{sp-magnesite}}$ were calculated based on estimated uncertainties for the concentration of Mg^{2+} and pCO_2.

	Hypothesis 1	Hypothesis 2
$\log K_{\text{MgCitrate}^-}$ (120°C)	6.05	5.76
pH	5.7	5.7
I (mol kg^{-1})	0.1035	0.1039
TDIC (mol kg^{-1})	1.829×10^{-1}	1.829×10^{-1}
Mg^{2+} (mol kg^{-1})	6.293×10^{-4}	7.054×10^{-4}
CO_3^{2-} (mol kg^{-1})	2.934×10^{-6}	2.947×10^{-6}
$\log Q_{\text{sp-magnesite}}$	−8.734	−8.682
$\gamma_{\pm\text{NaCl}}$	0.7313	0.7310
$\log K_{\text{sp-magnesite}}$ (120 °C)	−9.82 ± 0.04	−9.77 ± 0.04

temperatures with a relative confidence. This was only possible, however, because the mineral solubility had been studied in detail by Bénézeth et al. (2011).

Dolomite

Dolomite, $CaMg(CO_3)_2$ is a double carbonate in which Mg^{2+} and Ca^{2+} are segregated into separate planes of the crystal structure. It is a common mineral in sedimentary rocks, ubiquitous in the past, yet rarely found in modern environments (Arvidson and MacKenzie 1999). Stoichiometric dolomite, also called "ordered," "ideal" or "primary" dolomite (as opposed to disordered or protodolomite) is also hard to synthesize under laboratory conditions (Usdowski 1994). Its behavior and the uncertainties about its origin, the "dolomite problem," have attracted the attention of scientists for more than a century. In addition, because of its slow dissolution rate (Pokrovsky and Schott 2001; Pokrovsky et al. 2005) and incongruent dissolution behavior, the solubility products, $K_{sp\text{-}carbonate} = a_{Ca^{2+}} a_{Mg^{2+}} (a_{CO_3^{2-}})^2$, yielded inconsistent and unreliable results. Experimental values obtained at room temperature in pure water and 1 bar pCO_2 range from −16.5 to −19.35 (Yanat'yeva 1952; Garrels et al. 1960; Halla and Van Tassel 1965). Yanat'eva (1952) reported a $\log K_{sp}$ of −18.37 at 25 °C, measured in pure water for 100 days. Garrels et al. (1960) performed dissolution experiments with dolomite in pure water at 25 °C and 1 atm pCO_2 for 18 h. The pH at equilibrium between solution and dolomite (grain size <0.1 mm) was measured as 5.68±0.02. These results yield a $\log K_{sp}$ value of −19.34. However, Garrels et al. reported that adding well-ground dolomite powder into their experimental solutions when they were close to the point of equilibrium (at pH ~5.6), resulted in a rapid increase of the pH, up to 6.2. These results yield a $\log K_{sp}$ value of −16.44 which may indicate failure to reach equilibrium. Halla and Van Tassel (1965) reported a $\log K_{sp}$ of −17.76 at 21 °C. More recently, Sherman and Barak (2000) performed solubility experiments at 25 °C and in Ca-Mg-HCO_3/CO_3 solutions for almost 2 years and gave a mean value of −17.2±0.2, which is in agreement with the value that can be calculated from the thermodynamic properties of dolomite given by Robie et al. (1978) ($\log K_{sp} = -17.12$), as can be seen in Figure 26, where some K_{sp} values are reported as a function of the reciprocal temperature including the values generated from SUPCRT92.

The Robie et al. (1978) value is the most widely used value. The results of Halla and Van Tassel and Yanat'yeva yield considerably lower values than Robie et al. (1978) and Sherman

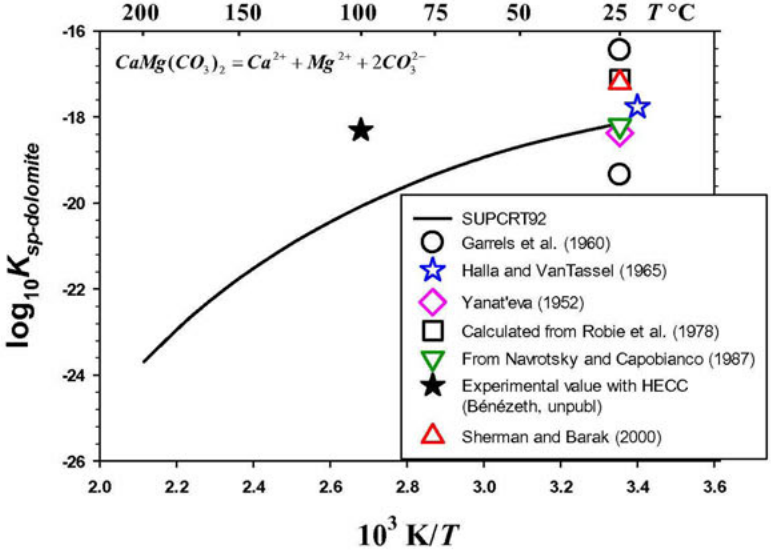

Figure 26. Dolomite solubility product as a function of the reciprocal temperature.

and Barak (2000) but closer to the value generated by SUPCRT92 ($\log K_{sp} = -18.15$) and the one calculated by Navrotsky and Capobianco (1987) from their HCl solution calorimetry experiments performed at 85 °C ($\log K_{sp} = -18.2$). The SUPCRT92 database uses thermodynamic data of dolomite from Helgeson et al. (1978) to calculate the solubility products. These data are based on phase equilibrium for the reaction: 4 talc + 5 dolomite = 5 diopside + 6 forsterite + $10CO_2$ + $4H_2O$, at $P = 2$ kbar and temperatures in the range 400-600 °C, and yield quite different solubility products from the ones calculated with the data from Robie et al. (1978).

Incongruent dissolution has been reported in many kinetic studies (Pokrovsky and Schott 2001; Pokrovsky et al. 2005; Zhang et al. 2007; Debure et al. 2013) with a Ca/Mg concentration ratio ranging between 2 and 6. The lower hydration energy of Ca^{2+} compared to Mg^{2+} and the lower stability of Ca^{2+} at the dolomite/water interface could explain the preferential release of Ca (Pokrovsky and Schott 2001; Zhang et al. 2007). However, Urosevic et al. (2012) did not find any evidence to support those mechanisms with their Atomic Force Microscopy (AFM) observations. They suggest that dolomite dissolves via a dissolution-precipitation reaction at all pH and slow solution flow, with the formation of an Mg-rich surface precipitate, nesquehonite. According to these authors, this newly formed precipitate should redissolve as dissolution progresses, as could also be the case for the incongruent observation during dissolution kinetic experiments performed far from equilibrium.

Recent scoping solubility experiments performed on a natural dolomite with the HECC at 100 °C (Bénézeth, unpublished data) show that the Ca/Mg concentration ratio in the solution is close to 1 (1.06), leading to a $\log K_{sp}$ value of -18.3, as reported in Figure 26 where it can be seen that it disagrees with the prediction of SUPCRT92 by 1.8 log unit. However, it should be noted that more measurements are needed in order to verify these preliminary data as well as the behavior of dolomite solubility as a function of temperature.

Siderite

Siderite, $FeCO_3$, is a common mineral occurring for example in bedded sedimentary iron ores, in gangue minerals of Au-Ag or Pb-Zn hydrothermal vein deposits and as a concretion in shales and sandstones. Its stability is controlled by O_2 and CO_2 fugacity so that its formation is complex and involves abiotic and biotic mediations. Under specific conditions, siderite formation has also been observed experimentally from mineral carbonation (e.g., Palandri et al. 2005; Lammers et al. 2011; Qafoku et al. 2012) or in some industrial fields as, for example, in geothermal pipes and the oil industry (Heuer and Stubbins 1999). Due to its low solubility, once deposited it can act as a good barrier against steel corrosion forming passivation layers.

A review of siderite solubility products made by Bénézeth et al. (2009) shows that the previous values reported at 25 °C were dispersed, ranging from $-11.03 < \log K_{sp} < -10.24$ and only three sets of data were available above room temperature (Reiterer et al. 1981; Braun 1991; Greenberg and Tomson 1992), showing large scatter as well. In Figure 27, these previous data are reported together with the ones measured by Bénézeth et al. (2009) from 25 to 250 °C and 0.1 mol/kg ionic strength using the HECC and natural siderite. As can be seen in Table 1, the temperature-dependent equation used to fit the siderite data included a fourth term involving $\log T$. A function with only 3 terms as used for magnesite could reproduce the experimental data up to 150 °C, but not to 250 °C, given a poorest fit and unreliable thermodynamic data, particularly the enthalpy of formation and heat capacity of siderite, which are very well known from Robie et al. (1984) and Chai and Navrotsky (1994) direct measurements, respectively. If the data of Bénézeth et al. (2009) seem in very good agreement with the data of Reiterer et al. (1981) at 50 °C, they deviate considerably from the values reported by Braun (1991) and to a lesser extent by Greenberg and Tomson (1992). It should be emphasized here that in most of the previous studies, siderite was synthesized by precipitation at low temperatures which produced poor crystallinity and very fine grains, prone to rapid oxidation. Moreover, Greenberg and Tomson used a de-ionized water solution and assumed that the ionic strength was zero, whereas Braun (1991) used buffer solutions at pH 4-7 (potassium hydrogen phthalate-NaOH-potassium dihydrogen phosphate-disodium hydrogen phosphate), but only used the pH 7 data to determine the K_{sp} of siderite as, according to this author, faster equilibrium was obtained

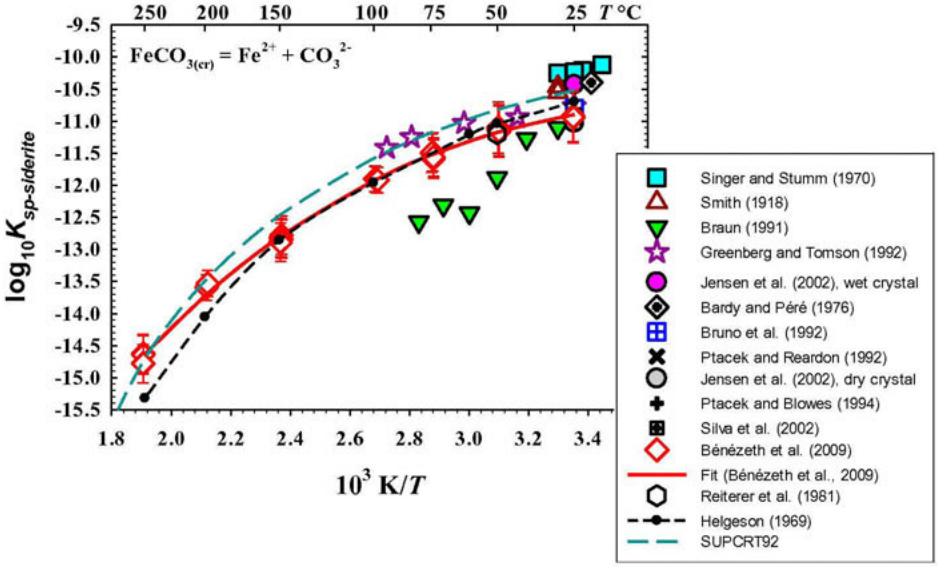

Figure 27. Siderite solubility product as a function of the reciprocal temperature: previous data, including the most recent values of Bénézeth et al. (2009) obtained between 25-250 °C (see text).

without too much change in the pH, which could in fact be the main problem associated also with a possible complexation between the phosphate buffer and iron.

The solubility products of the carbonate minerals discussed and described above are reported in Figure 28 for comparison. Note that the $\log K_{sp}$ values for dolomite were halved to convert to a per mole CO_3 basis and in order to be compared with the other carbonates. Magnesite and calcite have similar solubility products although calcite precipitation rates exceed by far those of magnesite (Saldi et al. 2009, 2012), which is attributed to the strong hydration of the Mg^{2+} ion and its slow dehydration rate compared to the Ca^{2+} ion (4 orders of magnitude lower, Bleuzen et al. 1997; Larentzos and Criscenti 2008). Siderite is by far the least soluble and thus more stable, followed by dolomite which is more stable than the minerals made of single cations, magnesite and calcite. Based on Equation (19) and its first and second derivatives with respect to T, the thermodynamic properties of these three carbonates have then been generated and reported in Table 2, together with the data for dawsonite (not discussed here) from Bénézeth et al. (2007), calcite and dolomite from SUPCRT92. It should be emphasized here that deriving the thermodynamic properties of a solid phase from Equation (19) implies that the thermodynamic properties of other species (aqueous species) involved in the reactions are well known and that it is possible to extract the activities of both the free metal ions and carbonate/bicarbonate species, as discussed in the previous section. So far, the close agreement we obtained for siderite, magnesite and dawsonite (Bénézeth et al. 2011, 2009, 2007, respectively) between our estimations and previous thermodynamic data obtained from calorimetric measurements and high pressure/temperature phase equilibrium studies demonstrate that direct solubility measurements are a reliable tool for the determination of the thermodynamic properties of minerals. Note also that the fitting parameters reported in Table 1 for calcite and dolomite were extracted from a fit of the values generated by SUPCRT92 (25 to 300 °C), using Equation (19), which needed an additional fitting parameter (eT^2) to reproduce the data within 0.1 log unit. Finally, for a thorough list of previously available standard state properties of carbonate minerals, the authors strongly encourage the reader to look at the PNNL-19766 report, by Krupta et al. (2010).

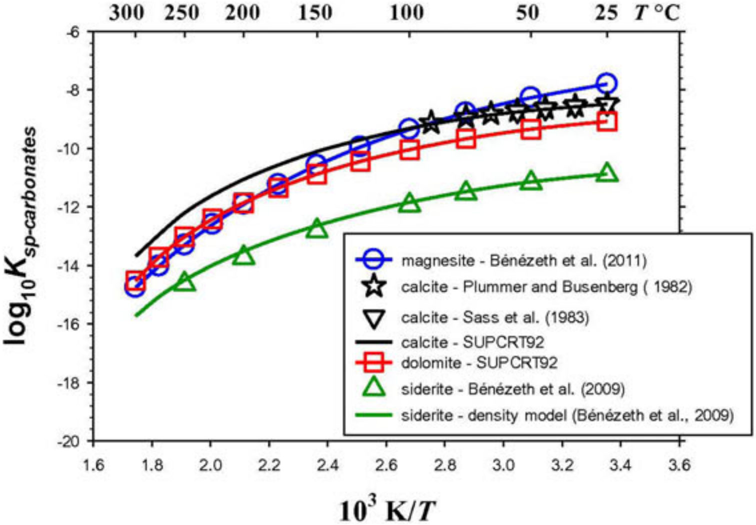

Figure 28. Comparison of calcite, magnesite, siderite and dolomite solubility products. Note that the $\log K_{sp}$ values for dolomite were halved to convert to a per mole CO_3 basis and compared with the other carbonates.

CONCLUSION

The present chapter has aimed at illustrating a few examples where a good knowledge of the thermodynamic properties of the carbonate system is crucial for the understanding of natural or industrial processes. We demonstrated here that in geothermal systems, CO_2 species largely control the fluid chemistry and the transport of elements, and therefore calculating accurately aqueous CO_2 chemical speciation is a prerequisite to model reactive transport induced by CO_2-bearing fluids. Moreover, precisely modelling CO_2-water-rock interactions is crucial for the prediction of the long-term fate of CO_2 in subsurface storage sites, and the optimization of its mineral sequestration. EGS and mineral scaling also pose various challenges to the energy industry, which all point towards a strong need for good knowledge of the properties of carbonate species and minerals.

Drawing an exhaustive synthesis of all known data regarding the carbonate system, however, was far beyond the purpose of this chapter. Rather, we wished to illustrate how various experimental techniques, including *in situ* pH measurements and *in situ* spectroscopic and spectrophotometric techniques may be used to slowly fill the gap that still prevents the scientific community from a good knowledge of the system.

Despite the amount of data obtained so far, numerous gaps and inconsistencies remain. For instance, the exact knowledge of Fe-CO_3 and Fe-HCO_3 formation constants at 25 °C and higher temperatures are urgently needed as well as the complexation constants of Mg^{2+} with most organic ligands that may be encountered in sedimentary settings or be part of industrial processes. Concerning mineral phases, very little is known on hydrated carbonate phases and their mineralogical transitions, which may develop at low temperatures and be precursors for their anhydrous counterparts. This is particularly the case of hydrated Mg-carbonates, which form in natural environments as well during carbonation of Mg-silicates. Solubility data are scarce and prompted us, for example, to directly measure hydromagnesite solubility from 25 to 75 °C, a prerequisite to study its growth kinetics as well (Gautier et al. 2012, and in preparation) and to compare with data on magnesite. As pointed out earlier, we also started the measurement of dolomite solubility, which is not an easy one to study due to its incongruent dissolution (dedolomitization). Finally, solid-solution carbonates like ankerite $Ca(Mg,Fe)(CO_3)_2$, for which thermodynamic data and kinetic rate parameters are scarce in the literature, have not received much attention either.

ACKNOWLEDGMENTS

Research sponsored by the French national programs: INSU (Institut National des Sciences de l'Univers du CNRS) and ANR (National Agency for Research, within the framework of the GEOCARBONE-CARBONATATION and CO_2-FIX projects under the contracts ANR-05-CO2-009-02 and ANR-08-PCO2-003, respectively), and the Icelandic Research Centre (RANNÍS, through grant #1102233021). The visiting professorship granted to Andri Stefánsson by the CNRS and the Université Paul Sabatier is gratefully acknowledged.

REFERENCES

Andreani M, Gouze P, Luquot L, Jouanna P (2008) Changes in seal capacity of fracture claystone caprocks induced by dissolved and gaseous CO_2 seepage. Geophys Res Lett 35:L14404

Archer DG (1992) Thermodynamic properties of the NaCl+H_2O system. II. Thermodynamic properties of $NaCl_{(aq)}$, $NaCl{\cdot}2H_2O_{(cr)}$, and phase equilibria. Journal of Physical and Chemical Reference Data 21:793-829

Arnórsson S, Gunnlaugsson E, Svavarsson H (1983) The chemistry of geothermal waters in Iceland: 2. Mineral equilibrium and independent variables controlling water compositions. Geochim Cosmochim Acta 47:547-566

Arvidson RS, Lüttge A (2010) Mineral dissolution kinetics as a function of distance from equilibrium – New experimental results. Chem Geol 269:79-88

Arvidson RS, Mackenzie FT (1999) The dolomite problem: control of precipitation kinetics by temperature and saturation state. Am J Sci 299:257-288

Bär O (1932) Beitrag zum Thema dolomitentstehung. Zentralblatt für Mineralogie und Paläontologie pp. 46-62

Bardy J, Péré C (1976) Détermination expérimentale du coefficient de solubilité du carbonate ferreux en milieux aqueux. Tribune du CEBEDEAU (Centre Belge d'Etude et de Documentation des Eaux) 29:75-81

Bazarkina EF, Pokrovski GS, Zotov AV, Hazemann J-L (2010) Structure and stability of cadmium chloride complexes in hydrothermal fluids. Chem Geol 276:1-17

Béarat H, McKelvy MJ, Chizmeshya AVG, Gormley D, Nunez R, Carpenter RW, Squires K, Wolf GH (2006) Carbon sequestration via aqueous olivine mineral carbonation: role of passivating layer formation. Environ Sci Technol 40:4802-4808

Beliustin A, Pisarevsky A, Lepnev G, Sergeyev A, Shultz M (1992) Glass electrodes: a new generation. Sensors Actuat B10:61-66

Belsky AJ, Brill TB (1998) Spectroscopy of hydrothermal reactions. 9. IR and Raman spectroscopy of hydrolysis and self-reaction of cyanamide and dicyandiamide at 130-270 °C and 275 bars. J Phys Chem A 102:4509-4516

Bénézeth P, Castet S, Dandurand J-L, Gout R, Schott J (1994) Experimental study of aluminum-acetate complexing between 60 and 200 °C, Geochim Cosmochim Acta 58:4561-4571

Bénézeth P, Diakonov I, Pokrovski G, Dandurand J-L, Schott J, Khodakovsky I (1997a) Gallium speciation in aqueous solution - Experimental study and modeling: Part II. Solubility of α-GaOOH in acidic solutions from 150 to 250 °C and hydrolysis constants of gallium (III) to 300 °C. Geochim Cosmochim Acta 61:1343-1357

Bénézeth P, Palmer DA, Wesolowski DJ (1997b) Dissociation constants for citric acid in aqueous sodium chloride media to 150°C. J Solution Chem 26:63-84

Bénézeth P, Palmer DA, Anovitz LM, Horita J (2007) Dawsonite synthesis and reevaluation of its thermodynamic properties from solubility measurements: Implications for mineral trapping of CO_2. Geochim Cosmochim Acta 71:4438-4455

Bénézeth P, Palmer DA, Wesolowski DJ (2008) Dissolution/Precipitation kinetics of boehmite and gibbsite: Application of a pH-Relaxation technique to study near-equilibrium rates. Geochim Cosmochim Acta 72:2429-2453

Bénézeth P, Dandurand J-L, Harrichoury J-C (2009) The solubility product of siderite ($FeCO_3$) as a function of temperature. *In:* Special Issue on CO_2 Geological Sequestration. Bénézeth P, Ménez B, Noiriel C (eds) Chem Geol 265:3-12

Bénézeth P, Saldi G, Dandurand J-L, Schott J (2011) Experimental determination of the solubility product of magnesite at 50 to 200 °C. Chem Geol 286:21-31

Benson SM, Cole DR (2008) CO_2 sequestration in deep sedimentary formations. Elements 4:325-331

Berner RA (1976) The solubility of calcite and aragonite in seawater at one atmosphere and 34.5 parts per thousand. Am J Sci 276:713-730

Bjarnason JO (1994) The Speciation Program WATCH, version 2.1. Icelandic Nat. Energy Auth. Report

Bleuzen A, Pittet PA, Helm L, Merbach AE (1997) Water exchange on Magnesium(II) in aqueous solution: A variable temperature and pressure ^{17}O NMR study. Magn Reson Chem 35:765-773

Boily JF, Seward TM (2005) Palladium(II) chloride complexation: Spectrophotometric investigation in aqueous solutions from 5 to 125 °C and theoretical insight into Pd-Cl and Pd-OH_2 interactions. Geochim Cosmochim Acta 69:3773-3789

Braun RD (1991) Solubility of iron (II) carbonate at temperatures between 30 and 80 °C. Talanta 38:205-211

Brown D (2000) A hot dry rock geothermal energy concept utilizing supercritical CO_2 instead of water. *In*: Proceedings of the twenty-fifth workshop on geothermal reservoir engineering. Stanford University, p 233-238

Browne PRL (1978) Hydrothermal alteration in active geothermal fields. Ann Rev Earth Planet Sci 6:229-250

Bruno J, Wersin P, Stumm W (1992) On the influence of carbonate in mineral dissolution: II. The solubility of $FeCO_3(s)$ at 25 °C and 1 atm total pressure. Geochim Cosmochim Acta 56: 1149-1155

Buback M, Crerar DA, Vogel-Koplitz LM (1987) Vibrational and Electronic Spectroscopy of Hydrothermal Systems, Chap 14. *In*: Hydrothermal Experimental Techniques. Ulmer GC, Barnes HL (eds) Wiley, New York, p 333-359

Bulemela E, Tremaine PR (2009) D_2O isotope effects on the ionization of β-naphthol and boric acid at temperatures from 225 to 300 °C using UV-visible spectroscopy. J Solution Chem 38:805-826

Bulemela E, Trevani LN, Tremaine PR (2005) Ionization constants of aqueous glycolic acid at temperatures up to 250 °C using hydrothermal pH indicators and UV-visible spectroscopy. J Solution Chem 34:769-788

Burch TE, Nagy KL, Lasaga AC (1993) Free energy dependence of albite dissolution kinetics at 80 °C and pH 8.8. Chem Geol 105:137-162

Butler JN, Huston R (1970) Activity coefficients and ion pairs in the systems sodium chloride – sodium bicarbonate – water and sodium chloride – sodium carbonate – water. J Phys Chem 74:2976-2983

Bychkov AYu, Bénézeth P, Pokrovsky OS, Shvarov Yu V, Schott J (2007) Experimental determination of calcite solubility and stability at 120-160 °C and 2-50 bar pCO_2 using in situ pH measurements. First French-German Symposium on Geological Storage of CO_2. Potsdam, Germany. Geotechnologien Science Report 9, ISSN 1619-7399, p 47-48

Capewell SG, Hefter G, May PM (1998) Potentiometric investigation of the weak association of sodium and carbonate ions at 25 °C. J Sol Chem 27:865-877

Capewell SG, Buchner R, Hefter G, May PM (1999) Dielectric relaxation of aqueous Na_2CO_3 solutions. Phys Chem Chem Phys 1:1933-1937

Castet S, Dandurand J-L, Schott J, Gout R (1993) Boehmite solubility and aqueous aluminum speciation in hydrothermal solutions (90-350 °C) Experimental study and modeling. Geochim Cosmochim Acta 57:4869-4884

Chai L, Navrotsky A (1994) Enthalpy of formation of siderite and its application in phase equilibrium calculation. Am Mineral 79:921-929

Chen Z Y, O'Connor WK, Gerdemann SJ (2006) Chemistry of aqueous mineral carbonation for carbon sequestration and explanation of experimental results. Environ Prog 25:161-166

Chiodini G, Marini L (1998) Hydrothermal gas equilibria: the H_2O-H_2-CO_2-CO-CH_4 system. Geochim Cosmochim Acta 62:2673-2687

Chiodini G, Frondini F, Raco B (1996) Diffuse emission of CO_2 from the Fossa crater, Vulcano Island (Italy). Bull Volcanol 58: 41-50

Chiodini G, Cioni R, Guidi M, Raco B, Marini L (1998) Soil CO_2 flux measurements in volcanic and geothermal areas. Appl Geochem 13:543-552

Christ CL, Hostetler PB (1970) Studies in the system MgO-SiO_2-CO_2-H_2O (II): the activity product constant of magnesite. Am J Sci 268:439-453

Christov C, Dickson AG, Møller N (2007) Thermodynamic modeling of aqueous aluminum chemistry and solid-liquid equilibria to high solution concentration and temperature: I. The acidic H-Al-Na-K-Cl-H_2O system from 0 to 100 °C. J Solution Chem 36: 1495-1523

Clarke RGF, Collins CM, Roberts JC, Trevani LN, Bartholomew RJ, Tremaine PR (2005) Ionization constants of aqueous amino acids at temperatures up to 250 °C using hydrothermal pH indicators and UV-visible spectroscopy: glycine, α-alanine and proline. Geochim Cosmochim Acta 69:3029-3043

Covington AK, Danish EY (2009) Measurement of magnesium stability constants of biologically relevant ligands by simultaneous use of pH and ion-selective electrodes. J Solution Chem 38:1449-1462

Cox JS, Seward TM (2007) The reaction kinetics of alanine and glycine under hydrothermal conditions. Geochim Cosmochim Acta 71:2264-2284

Crea F, De Stefano C, Gianguzza A, Piazzese D, Sammartano S (2006) Protonation of carbonate in aqueous tetraalkylammonium salts at 25 °C. Talanta 68:1102-1112

Daval D, Sissmann O, Menguy N, Saldi G.D, Guyot F, Martinez I, Corvisier J, Garcia B, Machouk I, Knauss KG, Hellmann R (2011) Influence of amorphous silica layer formation on the dissolution rate of olivine at 90 °C and elevated pCO_2. Chem Geol 284:193-209

Davies CW (1962) Ion Association. Butterworths London.

Davis MC, Wesolowski DJ, Rosenqvist J, Brantley SL, Mueller KT (2011) Dissolution/precipitation kinetics of boehmite and gibbsite: Application of pH-relaxation technique to study near-equilibrium rates. Geochim Cosmochim Acta 75:401-415

Debure M, Frugier P, De Windt L, Gin S (2013) Dolomite effect on borosilicate glass alteration. Appl Geochem 33:237-251

Di Tommaso D, de Leeuw NH (2009) Theoretical study of the dimerization of calcium carbonate in aqueous solution under natural water conditions. Geochim Cosmochim Acta 73:5394-5405

Di Tommaso D, de Leeuw NH (2010a) Structure and dynamics of the hydrated magnesium ion and of the solvated magnesium carbonates: Insights from first principles simulations. Phys Chem Chem Phys 12:894-901

Di Tommaso D, de Leeuw NH (2010b) First principles simulations of the structure and dynamical properties of hydrated metal ions Me^{2+} and solvated metal carbonates (Me = Ca, Mg and Sr). Crystal Growth Des 10:4292-4302

Diakonov I, Pokrovski GS, Schott J, Castet S, Gout R (1996) An experimental and computational study of sodium-aluminum complexing in crustal fluids. Geochim Cosmochim Acta 60:197-211

Diakonov I, Pokrovski G, Bénézeth P, Schott J, Dandurand J-L, Escalier J (1997) Gallium speciation in aqueous solution - Experimental study and modeling: Part I. Thermodynamic properties of $Ga(OH)_4^-$ to 300 °C. Geochim Cosmochim Acta 61:1333-1343

Dopieralski PS, Burakowski A, Latajka Z, Olavsson I (2011) Hydration of $NaHCO_3^-$, KCO_3, $(HCO_3^-)_2$, HCO_3^- and CO_3^{2-} from molecular dynamics simulation and speed of sound measurements. Chem Phys Lett 507:89-95

Dyrssen D, Hansson I (1973) Ionic medium effect in seawater – A comparison of acidity constants of carbonic acid and boric acid in sodium chloride and synthetic seawater. Mar Chem 1: 137-150

Duan Z, Li D (2008) Coupled phase and aqueous species equilibrium of the H_2O-CO_2-NaCl-$CaCO_3$ system from 0 to 250 °C, 1 to 1000 bar with NaCl concentrations up to saturation of halite. Geochim Cosmochim Acta 72:5128-5145

Ehlerova J, Trevani LN, Sedlbauer J, Tremaine PR (2008) Spectrophotometric determination of the ionization constants of aqueous nitrophenols at temperatures up to 225 °C. J Solution Chem 37:854-857

Ellis AJ (1959) The solubility of calcite in carbon dioxide solutions. Am J Sci 257:354-365

Ellis AJ (1963) The solubility of calcite in sodium chloride solutions at high temperatures. Am J Sci 261:259-267

Evans KA, Gordon RA, Mavrogenes JA, Taiby N (2009) The effects of CO_2 on the speciation of RbBr in solution at temperatures to 579 °C and pressures to 0.26 GPa. Geochim Cosmochim Acta 73:2631-2644

Eyring H (1935) The activated complex in chemical reactions. J Chem Phys 3:107-115

Felmy AR, Qafoku O, Arey BW, Hu JZ, Hu M, Schaef HT, Ilton ES, Hess NJ, Pearce CI, Feng J, Rosso KM (2012) Reaction of water-saturated supercritical CO_2 with forsterite: Evidence for magnesite formation at low temperatures. Geochim Cosmochim Acta 91:271-282

Fischer C, Arvidson RS, Lüttge A (2012) How predictable are dissolution rates of crystalline material? Geochim Cosmochim Acta 98:177-185

Fouillac C, Sanjuan B, Gentier S, Czernichowski-Lauriol I (2004) Could sequestration of CO_2 be combined with the development of Enhanced Geothermal Systems? Poster presented at the third annual conference on carbon capture and sequestration, Alexandria, VA, May 3-6, 2004. ***http://www.netl.doe.gov/publications/*** *proceedings/04/carbon-seq/212.pdf*

Fulton JL, Heald SM, Badyal YS, Simonson JM (2003) Understanding the effects of concentration on the solvation structure of Ca^{2+} in aqueous solutions. I: the perspective on local structure from EXAFS and XANES. J Phys Chem A 107:4688-4696

Gamsjäger H (1989) Thermodynamic aspects of dissolution reactions in the system Mg^{+2}-Ca^{+2}-CO_2-H_2O. Mon Ser Nin Dep 28:269-285

Garand E, Wende T, Goebbert DJ, Bergmann R, Meijer G, Neumark DM, Asmis KR (2010) Infrared spectroscopy of hydrated bicarbonate anion clusters: HCO_3–$(H_2O)1$–10. J Am Chem Soc 132:849-856

García AV, Thomsen K, Stenby EH (2006) prediction of mineral scale formation in geothermal and oilfield operations using the Extended UNIQUAC model: Part II. Carbonate-scaling minerals. Geothermics 35:239-284

Garcia B, Beaumont V, Perfetti E, Rouchon V Blanchet D, Oger P, Dromart G, Huc A-Y, Haeseler F (2010) Experiments and geochemical modeling of CO_2 sequestration by olivine: potential, quantification. Appl Geochem 25:1383-1396

Garrels R Thompson ME, Siever R (1960) Stability of some carbonates at 25 °C and one atmosphere total pressure. Am J Sci 258:402-418

Garrels RM, Thompson ME, Siever R (1961) Control of carbonate solubility by carbonate complexes. Am J Sci 258:402-418

Gaus I, Audigane P, Andre L, Lions J, Jacquemet N, Dutst P, Czernichowski-Lauriol I, Azaroual M (2008) Geochemical and solute transport modelling for CO_2 storage, what to expect from it? Int J Greenhouse Gas Cont 2:605-625

Gautier Q (2012) Cinétiques de précipitation de minéraux carbonatés magnésiens, influence de ligands organiques, et conséquences pour la séquestration minérale du CO_2. PhD Dissertation, Université Paris-Est, France, 269 pp. (in French)

Gautier Q, Saldi GD, Bénézeth P, Oelkers E, Schott J (2009) Effects of organic ligands on magnesite precipitation rates. 19th annual V.M. Goldschmidt Conference, Davos, Suisse, June 21-26, 2009. Geochim Cosmochim Acta 73: Issue: 13, p A419

Gautier Q, Jordan G, Bénézeth P, Schott J (2010) Influence of organic ligands on the crystal growth of magnesite ($MgCO_3$): Mechanistic aspects and implications for the mineral sequestration of CO_2. American Geophysical Union, Fall meeting 2010, abstract GC31B-0880

Gerardin C, In M, Allouche L (1999) In situ pH probing of hydrothermal solutions by NMR. Chem Mater 11:1285-1292

Gerdemann SJ, O'Connor WK, Dahlin DC Penner LR, Rush H (2007) Ex situ aqueous mineral carbonation. Environ Sci Technol 41:2587-2593

Gherardi F, Xu T, Pruess K (2007) Numerical modeling of self-limiting and self-enhancing caprock alteration induced by CO_2 storage in a depleted gas reservoir. Chem Geol 244:103-129

Giammar DE, Bruant RG, Peters CA (2005) Forsterite dissolution and magnesite precipitation at conditions relevant for deep saline aquifer storage and sequestration of carbon doxide. Chem Geol 217:257-276

Giggenbach WF (1980) Geothermal gas equilibria. Geochim Cosmochim Acta 44:2021-2032

Giggenbach WF (1981) Geothermal mineral equilibria. Geochim Cosmochim Acta 45:393-410

Giggenbach WF (1992) Isotopic shifts in waters from geothermal and volcanic systems along convergent plate boundaries and their origin. Earth Planet Sci Lett 113:495-510

Giggenbach WF, Sano Y, Wakita H (1993) Isotopic composition of helium and CO_2 and CH_4 contents in gases produced along the New Zealand part of a convergent plate boundary. Geochim Cosmochim Acta 57:3427-3455

Gledhill DK, Morse JW (2006) Calcite solubility in Na-Ca-Mg-Cl brines. Chem Geol 233:249-256

Golubev S, Bénézeth P, Schott J, Dandurand J-L, Castillo A (2009) Siderite dissolution kinetics in acidic aqueous solutions from 20 to 100 °C and 0 to 50 atm pCO_2. *In:* Special Issue on CO_2 geological sequestration. Bénézeth P, Ménez B, Noiriel C (eds) Chem Geol 265:13-19

Greenberg J, Tomson M (1992) Precipitation and dissolution kinetics and equilibria of aqueous ferrous carbonate vs. temperature. Appl Geochem 7:185-190

Greenwald I (1941) The dissolution of calcium and magnesium carbonates. J Biol Chem 141:789-796

Griffith CA, Dzombak DA, Lowry GV. (2011) Physical and chemical characteristics of potential seal strata in regions considered for demonstrating geological saline CO_2 sequestration. Environ Earth Sci 64:925-948

Guggenheim EA (1966) Applications of Statistical Mechanics. Clarendon Press

Halla VF, Van Tassel R (1965) Auflosungserscheinungen bei erdalkalikarbonaten I. (Dissolution phenomena of alkaline earth aquacarbonates) Radex-Rundschau 4:595-599 (in German)

Hänchen M, Prigiobbe V, Baciocchi R, Mazzotti M (2008) Precipitation in the Mg-carbonate system – effects of temperature and CO_2 pressure. Chem Eng Sci 63:1012-1028

Harned HS, Bonner FT (1945) The first ionization of carbonic acid in aqueous solution of sodium chloride. J Am Chem Soc 67:1026-1031

Harned HS, Scholes SR (1941) The ionization constant of HCO_3^- from 0 to 50 °C. J Am Chem Soc 63:1706-1709

Harvie CE, Weare JH (1980) The prediction of mineral solubilities in natural waters: The system Na-K-Mg-Ca-Cl-SO_4-H_2O from zero to high concentration at 25 °C. Geochim Cosmochim Acta 44:981-997

Harvie CE, Møller N, Weare JH (1984) The prediction of mineral solubilities in natural waters - The Na-K-Mg-Ca-H-Cl-SO_4-OH-HCO_3-CO_3-CO_2-H_2O system to high ionic strengths at 25 °C. Geochim Cosmochim Acta 48:723-751

He S, Morse JW (1993) The carbonic acid system and calcite solubility in aqueous Na-K-Ca-Mg-Cl-SO_4 solutions from 0 to 90 °C. Geochim Cosmochim Acta 57:3533-3554

Helgeson HC (1969) Thermodynamics of hydrothermal systems at elevated temperatures and pressures. Am J Sci 267:729-804

Helgeson HC, Delany JM, Nesbitt HW, Bird DK (1978) Summary and critique of the thermodynamic properties of rock-forming minerals. Am J Sci 278A:229p

Hellmann R, Tisserand D (2006) Dissolution kinetics as a function of the Gibbs free energy of reaction: An experimental study based on albite feldspar. Geochim Cosmochim Acta 70:364-383

Heuer JK, Stubbins JF (1999) An XPS characterization of $FeCO_3$ films from CO_2 corrosion. Corros Sci 41:1231-1243

Hoffmann MM, Addleman RS, Fulton JL (2000) Short-pathlength, high-pressure flow cell for static and time-resolved infrared spectroscopy suitable for supercritical fluid solutions including hydrothermal systems. Rev Sci Instrum 71:1552-1556

Hopkinson L, Kristova P, Rutt K, Cressey G (2012) Phase transitions in the system MgO-CO_2-H_2O during CO_2 degassing of Mg-bearing solutions. Geochim Cosmochim Acta 76:1-13

Hostetler PB (1963) Complexing of magnesium with bicarbonate. J Phys Chem 67:720

Hummel W, Anderegg G, Puigdomènech I, Rao L, Tochiyama O (eds) (2005) Chemical Thermodynamics of Compounds and Complexes of U, Np, Pu, Am, Tc, Se, Ni, and Zr, with Selected Organic Ligands. OECD Nuclear Energy Agency Chemical Thermodynamics, Vol. 9. Elsevier Science

Ikeda T, Boero M, Terakura K (2007) Hydration properties of magnesium and calcium ions from constrained first principles molecular dynamics. J Chem Phys 127:074503-074511

Jacobson RL, Langmuir D (1974) Dissociation constants of calcite and $CaHCO_3^+$ from 0 to 50 °C. Geochim Cosmochim Acta 38:301-318

Jensen DL, Boddum JK, Tjell JC, Christensen TH (2002) The solubility of rhodochrosite ($MnCO_3$) and siderite ($FeCO_3$) in anaerobic aquatic environments. Appl Geochem 17:503-511

Johnson JW, Oelkers EH, Helgeson HC (1992) SUPCRT92 – A software package for calculating the standard molal thermodynamic properties of minerals, gases, aqueous species, and reactions from 1 bar to 5000 bar and 0 degrees C to 100 degrees C. Comput Geosci 18:899-947

Kittrick JA, Peryea FJ (1986) Determination of the Gibbs free energy of formation of magnesite by solubility methods. Soil Sci Soc Am J 50:243-247

Königsberger E, Königsberger L-C, Gamsjäger H (1999) Low-temperature thermodynamic model for the system Na_2CO_3-$MgCO_3$-$CaCO_3$-H_2O. Geochim Cosmochim Acta 63:3105-3119

Krevor SCM, Lackner KS (2011) Enhancing serpentine dissolution kinetics for mineral carbon dioxide sequestration. Int J Greenhouse Gas Control 5:1073-1080

Krupta KM, Cantrell KJ, McGrail BP (2010) Thermodynamic Data for Geochemical Modelling of Carbonate Reactions Associated with CO_2 Sequestration – Literature Review. PNNL-19766, 135p

Kruse R, Franck EU (1982) Raman-spectra of hydrothermal solutions of CO_2 and $KHCO_3$ at high temperatures and pressures. Ber Buns Ges Phys Chem Chem Phys 86:1036-1038

Kwak JH, Hu JZ, Turcu RVF, Rosso KM, Ilton ES, Wang C, Sears JA, Engelhard MH, Felmy AR, Hoyt DW (2011) The role of H_2O in the carbonation of forsterite in supercritical CO_2. Int J Greenhouse Gas Control 5:1081-1092

Lafon GM (1970) Calcium complexing with carbonate ion in aqueous solutions at 25 °C and 1 atmosphere. Geochim Cosmochim Acta 34:935-940

Lammers K, Murphy R, Riendeau A, Smirnov AL, Schoonen MAA, Strongin DR (2011) CO_2 sequestration through mineral carbonation of iron oxyhydroxides, Environ Sci Technol 45:10422-10428

Langmuir D (1997) Aqueous Environmental Geochemistry. Prentice Hall, 600 pp.

Larentzos JP, Criscenti LJ (2008) A molecular dynamics study of alkaline earth metal-chloride complexation in aqueous solution. J Phys Chem B 112:14243-14250

Larson TE, Sollo FW, McGurk FF (1973) Complexes affecting the solubility of calcium carbonate in water. Urbana, III, Univ. Illinois Water Resources Center, Research Rept 68, 49 p.

Lasaga AC, Luttge A (2001) Variation of crystal dissolution rate based on dissolution stepwave model. Science 291:2000-2004

Li D, Duan Z (2007) The speciation equilibrium coupling with phase equilibrium in the H_2O-CO_2-NaCl system from 0 to 250 °C, from 0 to 1000 bar, and from 0 to 5 molality of NaCl. Chem Geol 244:730-751

Lightstone FC, Schwegler E, Hood RQ, Gygi F, Galli G (2001) A first principles molecular dynamics simulation of the hydrated magnesium ion. Chem Phys Lett 343:549-555

Lindsay WT (1980) Estimation of concentration quotients for ionic equilibria in high temperature water: The model substance approach. Proceedings of the 41st International Water Conference, p 284-294

Lindsay WT Jr (1989) Chemistry of steam cycle solutions: principles. *In:* The ASME Handbook on Water Technology for Thermal Power Systems. Paul Cohen (ed) ASME, New York, NY p 341-544

Lippmann F (1973) Sedimentary Carbonate Minerals. Springer-Verlag Berlin.

Loring JS, Thompson CJ, Wang Z, Joly AG, Sklarew DS, Schaef HT, Ilton ES, Rosso KM, Felmy AR (2011) In situ infrared spectroscopic study of forsterite carbonation in wet supercritical CO_2. Environ Sci Technol 45:6204-6210

Lvov SN, Palmer DA (2004) Electrochemical processes in high-temperature aqueous solutions. *In:* Aqueous Systems at Elevated Temperatures and Pressure. Physical Chemistry in Water Steam and Hydrothermal Solutions. Palmer DA, Fernández-Prini R, Harvey AH (eds) Elsevier/Academic Press, p 377-408

Machesky ML, Wesolowski DJ, Palmer DA, Ridley MK, Bénézeth P, Lvov SN, Fedkin MV (2006) Ion adsorption into the hydrothermal regime: Experimental and modeling approaches. *In:* Surface Complexation Modeling. Volume 11 Interface Science and Technology. Lützenkirchen J (ed) Academic Press, p 324-358

Meissner HP, Tester JW (1972) Activity coefficients of strong electrolytes in aqueous solutions. Ind Eng Chem Proc Design Development 11:128-133

Mesmer RE, Baes CF Jr, Sweeton FH (1970) Acidity measurement at elevated temperatures. IV. Apparent dissociation constants of water in 1 m potassium chloride up to 292 °C. J Phys Chem 74:1937-1942

Millero FJ (1979) The thermodynamics of the carbonate system in seawater. Geochim Cosmochim Acta 43:1651-1661

Millero FJ, Huang F, Graham T, Pierrot D (2007) The dissociation of carbonic acid in NaCl solutions as a function of concentration and temperature. Geochim Cosmochim Acta 71:46-55

Minubayeva Z, Suleimenov OM, Seward TM (2008) Acridinium ion ionization at elevated temperatures and pressures to 200 °C and 2000 bar. J Solution Chem 37:291-305

Morey GW (1962). The action of water on calcite, magnesite, and dolomite. Am Mineral 47:1456-1460

Murphy PJ, Stevens G, LaGrange MS (2000) The effects of temperature and pressure on gold-chloride speciation in hydrothermal fluids: A Raman spectroscopic study. Geochim Cosmochim Acta 64:479-494

Nakayama FS (1970) Sodium bicarbonate and carbonate ion pairs and their relation to the estimation of the first and second dissociation constants of carbonic acid. J Phys Chem 74:2726-2728

Nakayama FS (1971) Magnesium complex and ion pair in $MgCO_3$-CO_2 solution system. J Chem Eng Data 16:178-181

Navrotsky A, Capobianco C (1987) Enthalpies of formation of dolomite and magnesian calcites. Am Mineral 75:782-787

O'Connor WK, Dahlin DC, Rush GE, Dahlin CL, Collins WK (2001) Carbon dioxide sequestration by direct mineral carbonation: process mineralogy of feed and products. Mineral Metallurg Proc 19:95-101

Oelkers EH, Schott J (eds) (2009) Thermodynamics and Kinetics of Water-rock Interaction. Reviews in Mineralogy Geochemistry, Volume 70. Mineralogical Society of America

Oelkers EH, Bénézeth P, Pokrovski GS (2009) Thermodynamic databases for water-rock interaction. Rev Mineral Geochem 70:1-46

Palandri JL, Rosenbauer RJ, Kharaka YK (2005) Ferric iron in sediments as a novel CO_2 mineral trap: CO_2-SO_2 reaction with hematite. Appl Geochem 20:2038-2048

Palmer DA, Bénézeth P, Wesolowski DJ (2001) Aqueous high temperature solubility studies. I. The solubility of boehmite at 150°C as a function of ionic strength and pH as determined by "in situ" measurements. Geochim Cosmochim Acta 65:2081-2095

Palmer DA, Fernández-Prini R, Harvey AH (2004) Aqueous Systems at Elevated Temperatures and Pressures. Physical Chemistry in Water, Steam and Hydrothermal Solutions. Elsevier. 766 pp.

Park SN, Kim CS, Kim MH, Lee IJ, Kim K (1998) Spectrophotometric measurement of the first dissociation constants of carbonic acid at elevated temperatures. J Chem Soc Farad Trans 94:1421-1425

Park SN, Kim H, Kim K, Lee J, Lho DS (1999) Spectroscopic measurement of the acid dissciation constant of 2-naphthol and the second dissociation of carbonic acid at elevated temperatures. Phys Chem Chem Phys 1:1893-1898

Park AHA, Jadhav R, Fan LS (2003) CO_2 mineral sequestration: chemically enhanced aqueous carbonation of serpentine. Can J Chem Engin 81:885-890

Parkhurst DL, Appelo CAJ (1999) User's guide to PHREEQC (version 2): A computer program for speciation, batch-reaction, one-dimensional transport, and inverse geochemical calculations. US Geological Survey Water-Resources Investigations Report, 99(4259), 312 pp

Patterson CS, Slocum GH, Busey RH, Mesmer RE (1982) Carbonate equilibrium in hydrothermal systems – First ionization of carbonic acid in NaCl media to 300 °C. Geochim Cosmochim Acta 46:1653-1663

Patterson CS, Busey RH, Mesmer RE (1984) Second ionization of carbonic acid in NaCl media to 250 °C. J Solution Chem 9:647-661

Pitzer KS (1991) Activity Coefficients in Electrolyte Solutions. 2nd Edition. CRC Press, Boca Raton, FL

Pitzer KS, Mayorga G (1973) Thermodynamics of electrolytes. II. Activity and osmotic coefficients for strong electrolytes with one or both ions univalent. J Phys Chem 77:2300-2308

Plummer LN, Busenberg E (1982) The solubilities of calcite, aragonite and vaterite in CO_2-H_2O solutions between 0 and 90 °C and the evaluation of the aqueous model for the system $CaCO_3$-CO_2-H_2O. Geochim Cosmochim Acta 46:1011-1040

Pokrovski GS, Schott J, Sergeyev AS (1995) Experimental determination of the stability constants of $NaSO_4^-$ and $NaB(OH)_4^0$ in hydrothermal solutions using a new high-temperature sodium-selective glass electrode — Implications for boron isotopic fractionation. Chem Geol 124:253-265

Pokrovski GS, Schott J, Harrichoury J-C, Sergeyev AS (1996) The stability of aluminum silicate complexes in acidic solutions from 25 to 150 °C. Geochim Cosmochim Acta 60:2495-2501

Pokrovski GS, Schott J (1998) Thermodynamic properties of aqueous Ge(IV) hydroxide complexes from 25 to 350 °C: Implications for the behavior of germanium and the Ge/Si ratio in hydrothermal fluids. Geochim Cosmochim Acta 62:1631-1642

Pokrovski GS, Kara S Roux J (2002) Stability and solubility of arsenopyrite, FeAsS, in crustal fluids. Geochim Cosmochim Acta 66:2361-2378

Pokrovski GS, Roux J, Hazemann JL, Testemale D (2005) An X-ray absorption spectroscopy study of argutite solubility and germanium aqueous speciation in hydrothermal fluids to 500 °C and 400 bar. Chem Geol 217:127-145

Pokrovski GS, Borisova AYu, Harrichoury J-C (2008) The effect of sulfur on vapor-liquid fractionation of metals in hydrothermal systems. Earth Planet Sci Lett 266:345-362

Pokrovski GS, Tagirov BR, Schott J, Hazemann J-L, Proux O (2009) A new view on gold speciation in sulfur-bearing hydrothermal fluids from in situ X-ray absorption spectroscopy and quantum-chemical modelling. Geochim Cosmochim Acta 73:5406-5427

Pokrovsky OS, Schott J (2001) Kinetics and mechanism of dolomite dissolution in neutral to alkaline solution revisited. Am J Sci 301:597-626

Pokrovsky OS, Schott J (2002) Surface chemistry and dissolution kinetics of divalent metal carbonates. Environ Sci Technol 36:426-432

Pokrovsky OS, Schott J, Thomas F (1999) Processes at the magnesium-bearing carbonates/solution interface. I. A surface speciation model for magnesite. Geochim Cosmochim Acta 63:863-880

Pokrovsky OS, Golubev SV, Schott J (2005) Dissolution kinetics of calcite, dolomite and magnesite at 25 °C and 0 to 50 atm pCO_2. Chem Geol 217:239-255

Pokrovsky OS, Golubev SV, Jordan G (2009a) Effect of organic and inorganic ligands on calcite and magnesite dissolution rates at 60 °C and 30 atm pCO_2. Chem Geol 265:33-43

Pokrovsky OS, Golubev SV, Schott J, Castillo A (2009b) Calcite, dolomite and magnesite dissolution kinetics in aqueous solutions at acid to circumneutral pH, 25 to 150 °C and. Special Issue on CO_2 Geological Sequestration. Bénézeth P, Ménez B, Noiriel C (eds) Chem Geol 265:20-32

Prigiobbe V, Mazzotti M (2011) Dissolution of olivine in the presence of oxalate, citrate, and CO_2 at 90 °C and 120 °C. Chem Eng Sci 66:6544-6554

Pruess K (2006) Enhanced Geothermal Systems (EGS) using CO_2 as working fluid – A novel approach for generating renewable energy with simultaneous sequestration of carbon. Geothermics 35:351-367

Ptacek CJ, Blowes DW (1994) Influence of siderite on the pore-water chemistry of inactive mine-tailings impoundments. *In:* Alpers CN, Blowes DW (eds), Environmental Geochemistry of Sulfide Oxidation. American Chemical Society, Washington, DC, p 172-189

Ptacek CJ, Reardon EJ (1992) Solubility of siderite ($FeCO_3$) in concentrated NaCl and Na_2SO_4 solutions at 25 °C. Water-Rock Interaction. Proc. Int. Symp., 7th, p 181-183

Qafoku O, Kovarik L, Kukkadapu RK, Ilton ES, Arey BW, Tucek J, Felmy AR (2012) Fayalite dissolution and siderite formation in water-saturated supercritical CO_2. Chem Geol 332-333:124-135

Rafflaub J (1960) Untersuchungen uber die magnesium komplex verbindungen von oxalat und carbonat. Helv Chim Acta 274:629-634 (in German)

Read AJ (1975) The first ionization constant of carbonic acid from 25 to 250 °C and to 2000 bar. J Solution Chem 4:53-70

Reardon EJ, Langmuir D (1974) Thermodynamic properties of the ion pairs $MgCO_3°$ and $CaCO_3°$ from 10 to 50 °C. Am J Sci 274:599-612

Reiterer F, Johannes W, Gamsjäger H (1981) Semimicro determination of solubility constants: copper (II) carbonate and iron (II) carbonate. Mikrochim Acta 1:63-72

Riesen W, Gamsjäger H, Schindler PW (1977) Complex formation in the ternary system Mg(II)-CO_2-H_2O. Geochim Cosmochim Acta 41:1019-1200

Robie RA, Hemingway BS, Fisher JR (1978) Thermodynamic properties of minerals and related substances at 298.15 K and 1 bar (10^5 Pascals) pressure and at higher temperatures. U.S. Geological Survey Bulletin 1452. Reprinted with corrections, 1979

Robie RA, Haselton HT Jr., Hemingway BS (1984) Heat capacities and entropies of rhodochrosite ($MnCO_3$) and siderite ($FeCO_3$) between 5 and 600 K. Am Mineral 69:349-357

Rudolph WW, Brooker MH, Tremaine PR (1999) Raman spectroscopy of aqueous $ZnSO_4$ solutions under hydrothermal conditions: Solubility, hydrolysis, and sulfate ion pairing. J Solution Chem 28:621-630

Rudolph WW, Fischer D, Irmer G (2006) Vibrational spectroscopy studies and density functional theory calculations of speciation in the CO_2-water system. Appl Spectro 60 130-144

Rudolph WW, Irmer G, Königsberger E (2008) Speciation studies in aqueous HCO_3^--CO_3^{2-} solutions: A combined Raman spectroscopy and thermodynamic study. Dalton Trans 900-908

Saldi GD (2009) Les cinétiques de dissolution et précipitation de la magnésite aux conditions hydrothermales. PhD Dissertation Toulouse University, 184 pp. (In French)

Saldi GD, Jordan G, Schott J, Oelkers EH (2009) Magnesite growth rates as a function of temperature and saturation state. Geochim Cosmochim Acta 73:5646-5657

Saldi GD, Schott J, Pokrovsky OS, Oelkers EH (2010) An experimental study of magnesite dissolution rates at neutral to alkaline conditions and 150 and 200 °C as a function of pH, total dissolved carbonate concentration, and chemical affinity. Geochim Cosmochim Acta 74:6344-6356

Saldi GD, Schott J, Pokrovsky OS, Gautier Q, Oelkers EH (2012) An experimental study of magnesite precipitation rates at neutral to alkaline conditions and 100 to 200 °C as a function of pH, aqueous solution composition and chemical affinity. Geochim Cosmochim Acta 83:93-109

Salehikhoo F, Li L, Brantley SL (2013) Magnesite dissolution rates at different spatial scales: the role of mineral spatial distribution and flow velocity. Geochim Cosmochim Acta 108:91-106

Sanoa Y, Marty B (1995) Origin of carbon in fumarolic gas from island arcs. Chem Geol 119 265-274

Sass E, Morse JW, Millero FJ (1983) Dependence of the values of calcite and aragonite thermodynamic solubility products on ionic models. Am J Sci 283:218-229

Saunier G, Pokrovski GS, Poitrasson F (2011) First experimental determination of iron isotope fractionation between hematite and aqueous solution at hydrothermal conditions. Geochim Cosmochim Acta 75:6629-6654

Sayles FL, Fyfe WS (1973) The crystallization of magnesite from aqueous solution. Geochim Cosmochim Acta 37:87-99

Schaef HT, McGrail BP, Loring JS, Bowden ME, Arey BW, Rosso KM (2013) Forsterite [Mg_2SiO_4] carbonation in wet supercritical CO_2: An in situ high pressure X-ray diffraction study. Environ Sci Technol 45:6204-6210

Schoppelrei JW, Kieke ML, Brill TB (1996) Spectroscopy of hydrothermal reactions. 2. Reactions and kinetic parameters of [NH_3OH]NO_3 and equilibria of (NH_4)(2)CO_3 determined with a flow cell and FT Raman spectroscopy. J Phys Chem 100:7463-7470

Schott J, Brantley S, Crerar D, Guy C, Borcsik M, Willaime C (1989) Dissolution kinetics of strained calcite. Geochim Cosmochim Acta 53:373-382

Schott J, Pokrovsky OS, Oelkers EH (2009) The link between mineral dissolution/precipitation kinetics and solution chemistry. Rev Mineral Geochem 70:207-258

Schott J, Oelkers EH, Bénézeth P, Goddéris Y, François L (2012) Can accurate kinetic laws be created to describe chemical weathering? CR Geosci 344:568-585

Segnit ER, Holland HD, Biscardi CJ (1962) The solubility of calcite in aqueous solutions; I, The solubility of calcite in water between 75 degrees and 200 degrees at CO_2 pressures up to 60 atm. Geochim Cosmochim Acta 26:1301-1331

Seward TM (1984) The formation of lead(II) chloride complexes to 300 °C – a spectrophotometric study. Geochim Cosmochim Acta 48:121-134

Seward TM, Henderson CMB, Charnock JM, Dobson BR (1999) An EXAFS study of solvation and ion pairing in aqueous strontium solutions to 300 °C. Geochim Cosmochim Acta 63:2409-2418

Seyfried WE Jr, Janecky DR, Berndt ME (1987) Rocking autoclaves for hydrothermal experiments II: The flexible reaction-cell system. *In:* Hydrothermal Experimental Techniques. Ulmer GC, Barnes HL (eds) New York, Wiley Interscience, p 216-240

Shedlovsky T, MacInnes DA (1935) The first ionization constant of carbonic acid, 0 to 38 °C, from conductance measurements. J Am Chem Soc 57:1705-1710

Sherman LA, Barak P (2000) Solubility and dissolution kinetics of dolomite in Ca-Mg-HCO_3/CO_3 solutions at 25 °C and 0.1 MPa carbon dioxide. Soil Sci Soc Am J 64:1959-1968

Shock EL, Helgeson HC (1988) Calculation of the thermodynamic and transport properties of aqueous species at high temperatures and pressures: Correlation algorithms for ionic species and equation of state predictions to 5 kbar and 1000 °C. Geochim Cosmochim Acta 52:2009-2036

Shock EL, Koretsky CM (1995) Metal-organic complexes in geochemical processes: Estimation of standard partial molal thermodynamic properties of aqueous complexes between metal cations and monovalent organic acid ligands at high pressures and temperatures. Geochim Cosmochim Acta 59:1497-1352

Shock EL, Sassani DC, Willis M, Sverjensky DA (1997) Inorganic species in geological fluids: Correlations among standard molal thermodynamic properties of aqueous ions and hydroxide complexes. Geochim Cosmochim Acta 61:907-950

Shvarov Y (2008) HCh: new potentialities for the thermodynamic simulation of geochemical systems offered by Windows. Geochem Int 46:834-839

Shvarov Y, Bastrakov E (1999) UNITHERM: A Software Package for Geochemical Equilibrium Modeling. User's Guide. Australian Geological Survey Organisation, Department of Industry, Science and Resources.

Siebert RM, Hostetler PB (1977a) The stability of the magnesium bicarbonate ion pair from 10 to 90 °C. Am J Sci 277:697-715

Siebert RM, Hostetler PB (1977b) The stability of the magnesium carbonate ion pair from 10 to 90 °C. Am J Sci 277:716-734

Silva CAR, Liu X, Millero FJ (2002) Solubility of siderite ($FeCO_3$) in NaCl solutions. J Solution Chem 31:97-108

Simmons SF, Christenson BW (1994) Origin of calcite in a boiling geothermal system. Am J Sci 294:361-400

Singer PC, Stumm W (1970) The solubility of ferrous iron in carbonate-bearing waters. J Am Water Works Assoc 62:198-202

Sipos P, Bolden L, Hefter G, May PM (2000) Raman spectroscopic study of ion pairing of alkali metal ions with carbonate and sulfate in aqueous solutions. Aust J Chem 53:887-890

Smith HJ (1918) On equilibrium in the system ferrous carbonate, carbon dioxide, and water. J Am Chem Soc 40:879-883

Smith RM, Martell AE (1976) Critical Stability Constants. Vol 4 Inorganic ligands, Plenum New York

Smith RM, Martell AE (1987) Critical stability constants, enthalpies and entropies for the formation of metal complexes of aminopolycarboxylic acids and carboxylic acids. Sci Total Environ 64:125-147

Smith RM, Martell AE, Motekaitis RJ (1998) NIST Critically selected stability constants of metal complexes database. National Institute of Standards and Technology (NIST)

Stefánsson A, Arnórsson S (2000) Feldspar saturation state in natural waters. Geochim Cosmochim Acta 64:2567-2584

Stefánsson A, Arnorsson S (2002) Gas pressures and redox reactions in geothermal fluids in Iceland. Chem Geol 190:251-271

Stefánsson A, Seward TM (2008) A spectrophotometric study of iron(III) hydrolysis in aqueous solutions to 200°C. Chem Geol 249:227-235

Stefánsson A, Bénézeth P, Schott J (2013a) Carbonic acid ionization and the stability of sodium bicarbonate and carbonate ion pairs to 200 °C – A potentiometric and spectrophotometric study. Geochim Cosmochim Acta, http://dx.doi.org/10.1016/j.gca.2013.04.023

Stefánsson A, Bénézeth P, Schott J (2013b) Potentiometric and spectrophotometric study of the stability of magnesium carbonate and bicarbonate ion pairs to 150 °C and aqueous inorganic carbon speciation and magnesite solubility in $MgCl_2$-NaCl solutions (in prep.)

Stout JW, Robie RA (1963) Heat capacity from 11 to 300 K, entropy, and heat of formation of dolomite. J Phys Chem 67:2248-2252

Suleimenov OM (2004) Simple, compact, flow-through, high temperature high pressure cell for UV-Vis spectrophotometry. Rev Sci Instrum 75:3363-3364

Suleimenov OM, Boily JF (2006) Pressure dependence of the acid/base equilibria of methyl orange in aqueous solutions to 1000 bar at 20 °C. J Solution Chem 35:541-549

Suleimenov OM, Seward TM (2000) Spectrophotometric measurements of metal complex formation at high temperatures: the stability of Mn(II) chloride species. Chem Geol 167:177-192

Sverjensky DA, Shock EL, Helgeson HC (1997) Prediction of the thermodynamic properties of aqueous metal complexes to 1000 °C and 5 kbar. Geochim Cosmochim Acta 61:1359-1412

Tagirov B, Schott J, Harrichoury J-C, Escalier J (2004) Experimental study of the stability of aluminate-borate complexes in hydrothermal solutions. Geochim Cosmochim Acta 68:1333-1345

Tagirov BR, Salvi S, Schott J, Baranova NN (2005) Experimental study of gold-hydrosulphide complexing in aqueous solution at 350-500 °C, 500 and 1000 bars using mineral buffers. Geochim Cosmochim Acta 69:2119-2132

Testemale D, Dufaud F, Martinez I, Bénézeth P, Hazemann J-L, Schott J, Guyot F (2009) An X-ray absorption study of the dissolution of siderite at 300 bar between 50 °C and 100 °C. *In:* Experimental Techniques for the Study of Hydrothermal Fluids and Silicate Melts. Chemical Geology Special Issue. Berry A, Rickers K (eds) Chem Geol 259:8-16

Thurmond V, Millero FJ (1982) Ionization of carbonic acid in sodium chloride solutions at 25 °C. J Solution Chem 11:447-456

Tremaine P, Zhang K, Bénézeth P, Xiao C (2004) Dissociation equilibria of weak acids and bases. *In:* Aqueous Systems at Elevated Temperatures and Pressure. Physical Chemistry in Water Steam and Hydrothermal Solutions. Palmer DA, Fernández-Prini R, Harvey AH (eds) Elsevier/Academic Press, p 441-492

Trevani LN, Roberts JC, Tremaine PR (2001) Copper(II)-ammonia complexation equilibria in aqueous solutions at temperatures from 30 to 250 °C by visible spectroscopy. J Solution Chem 30:585-622

Trommsdorff V, Connolly JAD (1990) Constraints on phase diagram topology for the system CaO-MgO-SiO_2-CO_2-H_2O. Contrib Mineral Petrol 104:1-7

Ulmer GC, Barnes HL (1987) Hydrothermal Experimental Techniques. Wiley-Intersciences

Urosevic M, Rodriguez-Navarro C, Putnis CV, Cardell C, Putnis A, Ruiz-Agudo E (2012) In situ nanoscale observations of the dissolution of dolomite cleavage surfaces. Geochim Cosmochim Acta 80:1-13

Usdovski E (1994) Synthesis of dolomite and geochemical implications. *In* Dolomites: A Volume in Honour of Dolomieu. Purser B, Tucker M, Zenger D (ed) Blackwell Sci. Publ, Oxford, UK, p 345-360

Villafáfila-García A, Thomsen K, Stenby EH (2006) Prediction of mineral scale formation in geothermal and oilfield operations using extended UNIQUAC model Part II. Carbonate-scaling minerals. Geothermics 35:239-284

Wesolowski DJ, Ziemniak SE, Anovitz LM, Machesky ML, Bénézeth P, Palmer DA (2004) Solubility and surface adsorption characteristics of metal oxides. *In:* Aqueous Systems at Elevated Temperatures and Pressure. Physical Chemistry in Water Steam and Hydrothermal Solutions. Palmer DA, Fernández-Prini R, Harvey AH (eds) Elsevier/Academic Press, p 493-595

Wolery TJ (1983) *EQ3NR,* A Computer Program for Geochemical Aqueous Speciation-Solubility Calculations: User's Guide and Documentation: UCRL-53414, Lawrence Livermore National Laboratory, Livermore, California.

Xiang T, Johnston KP (1994) Acid-base behavior of organic compounds in supercritical water. J Phys Chem 98:7915

Xu T, Apps J, Pruess K (2004) Numerical simulation of CO_2 disposal by mineral trapping in deep aquifers. Appl Geochem 19:917-936

Xu T, Pruess K, Apps J (2008) Numerical studies of fluid-rock interactions in enhanced geothermal systems (EGS) with CO_2 as a working fluid. Proceedings of the thirty-third workshop on Geothermal Reservoir Engineering, Stanford University, 8 pp., SGP-TR-185

Yanat'eva OK (1952) Solubility of dolomite in water salt solutions. Izvestiya Sektora FkhA Akademii Nauk SSSR 20:252-268 (In Russian)

Zelenina TE, Zelenin OY (2005) Complexation of citric and tartaric acids with Na and K ions in aqueous solution. Russian J Coordination Chem 31:235-242

Zhang R, Hu S, Zhang X, Yu W (2007) Dissolution kinetics of dolomite in water at elevated temperatures. Aq Geochem 13:309-338

Reviews in Mineralogy & Geochemistry
Vol. 76 pp. 135-164, 2013
Copyright © Mineralogical Society of America

Thermodynamic Modeling of Fluid-Rock Interaction at Mid-Crustal to Upper-Mantle Conditions

Craig E. Manning

Department of Earth and Space Sciences
University of California, Los Angeles
Los Angeles, California 90095, U.S.A.

manning@ess.ucla.edu

INTRODUCTION

Fluid-rock interaction is important in a wide range of settings in the middle crust to the upper mantle. Fluids are liberated in the crust during prograde metamorphism in convergent-margin settings. At greater depth, devolatilization of subducting lithosphere plays a major role in global element cycling, metasomatic alteration of the mantle, and the genesis of arc magmas. Mafic magmas produced in these settings may stall in the lower crust and liberate volatiles that metasomatize surrounding rocks and trigger production of silicic magmas of crustal derivation. Mounting evidence points to an important role for metasomatic alteration by saline brines in the genesis of some lower-crustal granulite-facies metamorphic terranes.

Unlike shallow geothermal systems or low-grade metamorphic environments, there has been only limited progress in modeling the fluid-rock interaction that characterizes the deeper geologic systems enumerated above. Such phase-equilibrium models require as input the chemical potential, μ_i

$$\mu_i \equiv \left(\frac{\partial G_i}{\partial n_i} \right)_{P,T} \tag{1}$$

of the participating phases or species i, where G_i is the Gibbs free energy of i, n_i is the number of moles of i, P is pressure, and T is temperature. At the P and T of interest,

$$\mu_i = \mu_i^\circ + RT \ln a_i \tag{2}$$

Where μ° is standard state chemical potential, a is activity, R is the gas constant, and T is absolute temperature.

It is challenging to quantify the right-hand terms in Equation (2) at P and T ranging from the middle crust to the upper mantle. This is chiefly because of (1) limitations in our quantitative knowledge of key properties of relevant solutes and H_2O, and (2) uncertainty in how properly to model solute activities at the requisite conditions. As a consequence, aqueous geochemists have been discouraged from plying their trade in the numerous deep geologic systems in which fluid-rock interaction may play a major role in the Earth's chemical and physical evolution.

Here, I discuss strategies for determining the standard-state chemical potential and the activity of a dissolved solute at conditions corresponding to the lower crust and upper mantle. I show that simple approaches can be used to derive reasonable approximations of standard-state properties. The parameters necessary for constraining activity coefficients of aqueous

1529-6466/13/0076-0005$05.00 http://dx.doi.org/10.2138/rmg.2013.76.5

solutes can be calculated or estimated, leading to the conclusion that activity models for dilute aqueous species yield accurate representations of solute behavior at the concentrations observed or predicted in a wide range of H_2O-rich aqueous solutions at high P and T. This provides the foundation for study of fluid-mineral interaction in a variety of high-PT scenarios.

CHEMICAL POTENTIALS OF AQUEOUS SPECIES IN HIGH-*PT* FLUIDS

Standard state chemical potentials of aqueous species

The conventional standard-state for aqueous species in relatively dilute solutions is unit activity of the hypothetical 1.0 molal solution, referenced to infinite dilution. Standard-state thermodynamic properties of an aqueous solute therefore account for the consequences of its transfer to, and influence on, the solvent H_2O. When dissolved in H_2O, an ion such as Na^+ attracts H_2O dipoles so that they form a coordinating cluster, or shell, in which the H_2O molecules are more densely packed and more ordered than they would otherwise be in the ion's absence. For octahedral coordination of H_2O around the sodium ion, we can describe the hydration process as

$$\mathrm{Na^+ + 6H_2O = Na(H_2O)_6^+} \tag{3}$$

Structures such as $Na(H_2O)_6{}^+$ constitute entities in which the number of H_2O molecules may vary on short time scales but attain some long-term average that varies with P and T. Accordingly, for the purposes geochemical applications that must address a wide range conditions, it is conventional to neglect the hydration waters when writing reactions (i.e., Na^+, not $Na(H_2O)_6{}^+$). Any variations in hydration are implicit, and accounted for in the standard state thermodynamic properties of the solutes. This is the same as assuming that the change in any state property associated with Equation (3) is zero.

The Helgeson-Kirkham-Flowers equation of state. The hydration process involves energetic changes that must be taken into account in characterizing the thermodynamic properties of a solute. There are numerous thermodynamic models for the standard state properties of aqueous species (for a review see Dolejš 2013). In geochemistry, the most widely used thermodynamic model is the Helgeson-Kirkham-Flowers equation of state, or HKF EOS (Helgeson and Kirkham 1976; Helgeson et al. 1981; Tanger and Helgeson 1988). The HKF EOS accounts for the energetics of transferring a solute to H_2O as the sum of the intrinsic properties of the solute, the structural change of solvent H_2O around the solute ("collapse", because solution volume decreases), and the electrostatic interactions between the solvent H_2O dipoles and the solute ("solvation"). Hence, the standard Gibbs free energy change of bringing a solute into solution may be written

$$\Delta G_i^\circ = \Delta G_{i,\mathrm{intrinsic}}^\circ + \Delta G_{i,\mathrm{collapse}}^\circ + \Delta G_{i,\mathrm{solvation}}^\circ \tag{4}$$

(All properties considered here are implicitly "conventional"; i.e., relative to those of H^+.) The terms on the right in Equation (4) are not strictly separable (Helgeson and Kirkham 1976). Because solvation effects may be taken into account through electrostatic theory, it is convenient to distinguish them explicitly from nonsolvation effects defined as

$$\Delta G_{\mathrm{non\text{-}solvation}}^\circ = \Delta G_{i,\mathrm{intrinsic}}^\circ + \Delta G_{i,\mathrm{collapse}}^\circ \tag{5}$$

This leads to

$$\Delta G_i^\circ = \Delta G_{i,\mathrm{non\text{-}solvation}}^\circ + \Delta G_{i,\mathrm{solvation}}^\circ \tag{6}$$

In the HKF EOS, nonsolvation contributions are quantified through species-specific, P-T independent EOS coefficients. The solvation contributions are treated via Born theory, which describes the Gibbs energy change of solvation as a function of the static dielectric constant, $_{H\ O}$, of H_2O:

$$\Delta G^{\circ}_{i,\mathrm{solvation}} = \omega_i\left(\frac{1}{\varepsilon_{H_2O}}\quad 1\right) \tag{7}$$

where ω is a species-specific, *P*-*T* independent EOS coefficient. The requisite parameters have been derived for a wide variety of aqueous species (Shock and Helgeson 1988; Shock et al. 1989; Shock and Helgeson 1990; Shock et al. 1992; Pokrovskii and Helgeson 1995, 1997; Shock et al. 1997; Sverjensky et al. 1997; Plyasunov and Shock 2001). Thus, the Gibbs energies and other thermodynamic properties of solutes can be computed in the HKF EOS framework, provided that the dielectric constant of pure H_2O (Eqn. 7) is well known.

Unfortunately, deploying HKF theory at deep crustal and upper mantle conditions is problematic because ε_{H_2O} has only been measured to 5 kbar and 550 °C (Heger et al. 1980) (Fig. 1). Estimates using the Kirkwood equation (Pitzer 1983; Fernández et al. 1997) or other approaches (Franck et al. 1990) have been employed to extend values of ε_{H_2O} to 10 kbar and 1000 °C, and there has been recent progress in using *ab initio* molecular dynamics to compute ε_{H_2O} to very high pressures (Pan et al. 2013). Nevertheless, the most widely used implementation of the HKF thermodynamic database and computational framework (SUPCRT92, Johnson et al. 1992) is based on the ε_{H_2O} extension of Pitzer (1983), and is limited to a maximum pressure to 5 kbar. The absence of high-*P* ε_{H_2O} data thus prevents use of the HKF EOS to study mineral-fluid equilibria in the high-*PT* environments of interest here.

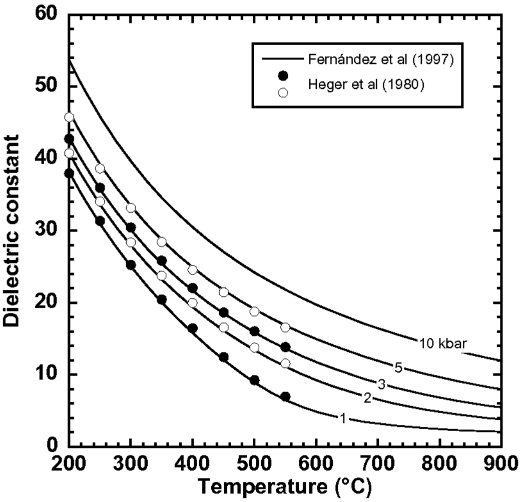

Figure 1. Dielectric constant of H_2O as a function of temperature at constant pressure. Data are from Heger et al. (1980). Solid lines show fitted and extrapolated values from Fernández et al. (1997).

Density models. There are several alternate approaches that can be used to derive high-*P* standard state Gibbs energies of aqueous species (Dolejš 2013). For work at high *P* and *T*, density correlations offer the best prospects because they can be tied to well-calibrated EOS for H_2O (Marshall and Franck 1981; Marshall and Mesmer 1984; Eugster and Baumgartner 1987; Anderson et al. 1991; Dolejš and Manning 2010). Density models are based on the observation that isothermal changes in the logarithms of the equilibrium constants (*K*) for many dissociation reactions display linear correlations with $\log\rho_{H_2O}$. An example is the variation in the equilibrium constant for the self-dissociation of H_2O

$$H_2O = H^+\quad OH^- \tag{8}$$

(Sweeton et al. 1974; Marshall and Franck 1981) (Fig. 2). The relations shown in Figure 2 suggest that at constant temperature

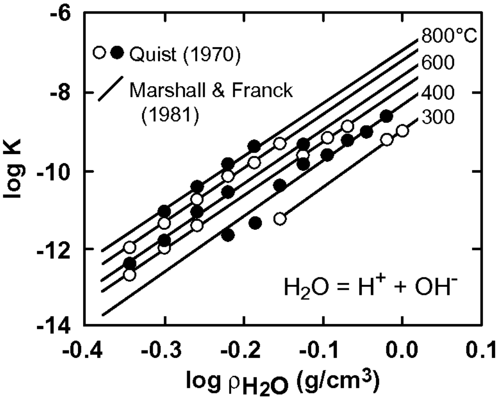

Figure 2. Variation in the equilibrium constant for H_2O self-dissociation with the logarithm of the density of H_2O (g/cm^3). Circles are from Quist (1970). Lines show values calculated using the equation of Marshall and Franck (1981).

$$\log K = m + n \log \rho_{H_2O} \tag{9}$$

where m and n are fit parameters, which may be treated as polynomials in T, e.g.

$$m = m_0 + m_1 T^{-1} + m_2 T^{-2} + m_3 T^{-3} \tag{10}$$

$$n = n_0 + n_1 T^{-1} + n_2 T^{-2} \tag{11}$$

(Marshall and Quist 1967; Mesmer et al. 1988; Anderson et al. 1991). Numerous other dissociation reactions display similar behavior, including alkali-halide dissociation (Franck 1956; Quist and Marshall 1968b; Frantz and Marshall 1982; Ho and Palmer 1997), acid and base dissociation (Frantz and Marshall 1984; Mesmer et al. 1988; Mesmer 1991; Ho and Palmer 1997), and the dissolution of oxide and halide minerals (Fournier and Potter 1982; Manning 1994; Caciagli and Manning 2003; Antignano and Manning 2008a,b; Dolejš and Manning 2010).

Manning (1998) showed that log$K$ values for homogeneous and heterogeneous equilibria derived from the HKF EOS also display linear correlations with $\log \rho_{H_2O}$ at high P. Similar behavior was demonstrated for $\Delta G°$ for individual aqueous species. Figure 3 gives example correlations, which were derived using SUPCRT92 and thermodynamic data from Pokrovskii and Helgeson (1995). Log$K$ values were computed at 3.0, 3.5, 4.0, 4.5, and 5.0 kbar and 400-600 °C. In Figure 3A, it can be seen that calculated log$K$ for the homogeneous equilibrium $HAlO_2 = H^+ + AlO_2^-$ varies linearly with with $\log \rho_{H_2O}$. Also shown for selected isotherms are the ±0.5 kcal/mol average uncertainties in the predictions estimated by Shock and Helgeson (1988). The distribution of predicted log$K$ values along isotherms is demonstrably linear within the stated uncertainties. Similar results are obtained for the equilibrium constant for corundum hydrolysis and $\Delta G°$ of Al^{+3} (Fig. 3), as well as for many other species and equilibria (Manning 1998, 2007; Manning et al. 2010, 2013).

The linear correlations displayed in Figure 3 imply that

$$\left(\frac{\partial \ln K}{\partial \ln \rho_{H_2O}}\right)_T = -\frac{\Delta V°}{RT\beta_{H_2O}} = \textit{constant} \tag{12}$$

where $\Delta V°$ refers to the volume change of the reaction or species of interest and β_{H_2O} is the isothermal compressibility of H_2O. Taking Ca^{+2} as an example, Figure 4 illustrates that the HKF EOS predicts that the ratio in Equation (12) approaches a constant value at pressures ≥ 3 kbar. This is probably because at high P, the nonsolvation contributions to $\Delta G°$ approach

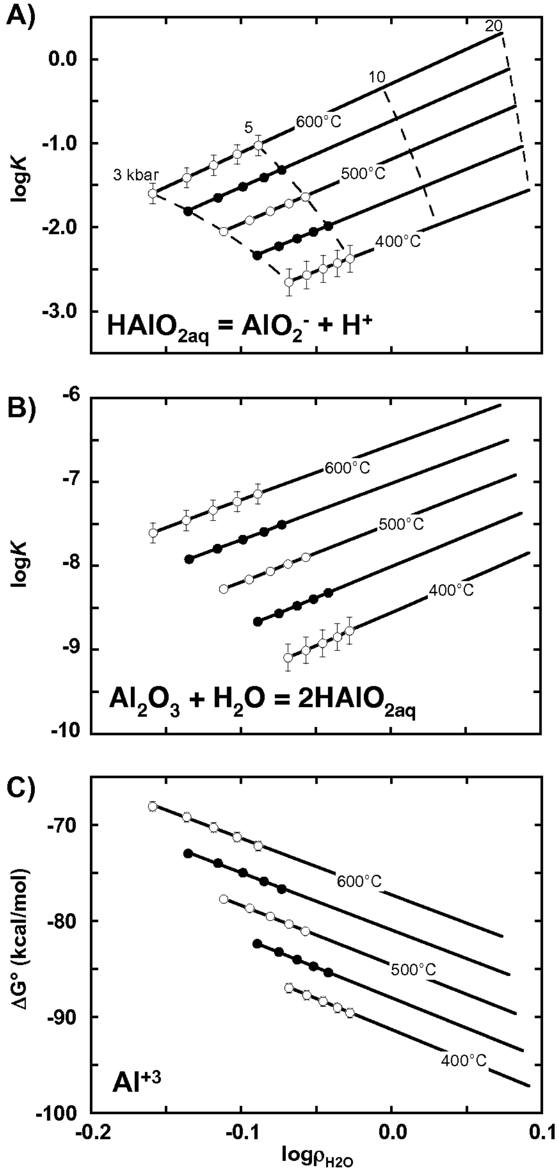

Figure 3. Values of log*K* and $\Delta G°$ vs. $\log \rho_{H_2O}$ (in g/cm^3) illustrating density-based extrapolations for a representative homogeneous equilibrium (A), heterogeneous equilibrium (B), and single species (C). Data from Pokrovskii and Helgeson (1995) were employed with SUPCRT92 to compute properties at 3-5 kbar (500 bar increments) at 400-600 °C (50 °C increments). Solid lines represent linear fits to calculated properties along each isotherm, extrapolated to 20 kbar. Dashed lines in (A) show isobars. Representative error bars correspond to ±0.5 kcal/mol (Shock and Helgeson 1988).

constant values while the solvation contributions depend on ε_{H_2O} which is strongly correlated with ρ_{H_2O} (Dolejš and Manning 2010).

The nearly linear isothermal variation of log*K* and $\Delta G°$ with $\log \rho_{H_2O}$ to 5 kbar supports extrapolation to higher *P* (Fig. 3). It is not expected that behavior is exactly linear, but several arguments support the conclusion that such extrapolations are reasonable approximations of high-*PT* thermodynamic properties. First, the range of ρ_{H_2O} over which the extrapolation is performed is relatively small, owing to the progressively decreasing compressibility of H_2O. At any *T*, the difference in $\log \rho_{H_2O}$ between 3 and 5 kbar is about the same as that between 5 and 10 kbar and about half that between 5 and 20 kbar (Fig. 3A). Second, variations in the density of water are significantly less nonlinear at the high pressures of interest than in the vicinity of the critical point. Neither discontinuities nor strong variations in derivative properties occur in dense H_2O. Finally, the uncertainties in log*K* and $\Delta G°$ are large relative to potential nonlinearity. Higher order fits are not justified at the accuracy level of the predictions.

Activity models for aqueous species

Activity models have also been a major limitation to high-*PT* studies of aqueous chemistry, fluid-rock interaction, and reactive fluid flow. The activity of a solute accounts for the energetic consequence of departure from standard-state behavior due to interactions with other solutes present at finite concentration. Activity is related to concentration through

$$a_i = \gamma_i m_i \qquad (13)$$

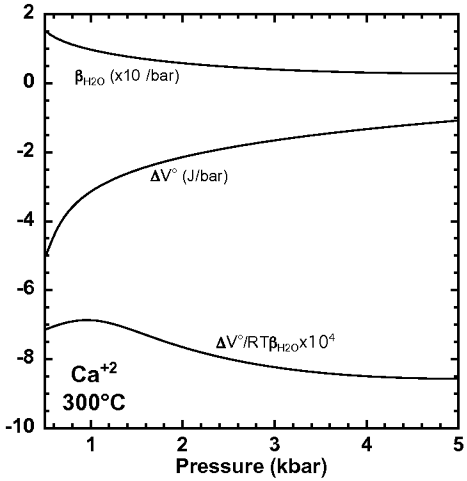

Figure 4. Isothermal variation at 300 °C of the compressibility of H_2O, the standard molal volume of Ca^{+2}, and their ratio multiplied by $1/RT$. The ratio approaches a constant value at $P > 3$ kbar, consistent with the linear slopes in Figure 3 (see text). Data from Helgeson and Kirkham (1974) and SUPCRT92.

where γ_i is the activity coefficient and m_i is molal concentration. (Alternate concentration scales are necessary at very high solute concentrations.)

In addition to the interactions with H_2O discussed above, solutes will also interact with each other, and the magnitudes of these interactions may vary significantly depending on solute identities. The largest energetic contributions arise from coulombic forces operating on solute ions. The hydrated ions of a simple electrolyte like NaCl exert forces of attraction and repulsion on each other over relatively large distance, leading to nonrandom ion distributions in the solution. The resulting average cluster distribution has lower energy than would a random distribution in an ideal solution. The chemical potential of each ionic solute at finite but low concentration is thus lower than in it would be if $\gamma_i = 1$, requiring that the activity coefficient is less than unity. The number of hydrated clusters increases with rising electrolyte concentration. Because the magnitudes of coulombic forces vary with the inverse of separation distance, progressively tighter packing of the charged clusters leads to progressively greater negative departures from ideality, and hence decreasing activity coefficients.

With continued increase in the concentration of a dissociated NaCl electrolyte in H_2O, the ion abundance eventually becomes so great that two effects cause activity to cease decreasing, and then to rise. First, the added ions eventually involve so much H_2O in the formation of hydration shells that availability for further hydration is affected. In addition, in tightly packed ionic solutions the domination of repulsive over attractive forces reduces “ordering”, which diminishes the departure from ideality. Note that in this hypothetical process, the effects of association of ions are ignored; i.e., we are taking no account of the possibility of $Na^+ + Cl^- = NaCl_{(aq)}$, the forward progress of which will limit the rise in ion concentration.

Estimation of activity coefficients for geochemical applications has chiefly followed two separate lines of investigation. One approach has been the development of “specific-ion interaction” approaches based on virial equations (e.g., Pitzer 1977, 1979). This method is largely empirical and does not account for the different species of a particular solute ion that may be present in solution; i.e., the concentration of Na^+ or Cl^- is equivalent to the total concentration of Na or Cl. Virial equations are especially useful at very high concentrations, for example in evaporite brines, but they preclude evaluation of the contributions of distinct solute forms of the same element to the interactions among solutions and minerals. Moreover, the empirical nature of virial approaches means that a substantial body of experimental data is required to implement the approach. Such a body of data simply does not exist at high P and T.

Ion activity models are generally based on a version of the Debye-Hückel equation, which was developed for a solution of completely dissociated ions. These models take the form

$$\log\gamma_i = -\frac{A z_i^2 \sqrt{I}}{1 + \mathring{a}_i B \sqrt{I}} + b_i I \tag{14}$$

where A and B are solvent parameters, z_i is the ion charge, $\mathring{a}_i$ is the ion size parameter (in cm), b_i is a constant characteristic of the electrolyte and dependent on P and T, and I is ionic strength.

Ionic strength is computed from

$$I = \frac{1}{2}\sum_i m_i z_i^2 \tag{15}$$

and has units of concentration, here molality. Debye-Hückel-type equations were developed for solutions without ion pairing. However, significant ion pairing is expected at high P and T (see below). This can be accounted for by including only unpaired ions in the summation (e.g., Helgeson 1969; Helgeson et al. 1981). In this case, I is termed the "true" ionic strength.

In Equation (14), the å parameter is nominally a function of electrostatic radius and hence could vary with P and T. However, Helgeson et al. (1981) showed that this need not be considered. The A and B solvent parameters are defined by

$$A \equiv \frac{\left(2\pi N \rho_{H_2O}\right)^{\frac{1}{2}} e^3}{2.303 \times 1000^{\frac{1}{2}} \left(\varepsilon_{H_2O} kT\right)^{\frac{3}{2}}} = \frac{1.825 \times 10^6 \left(\rho_{H_2O}\right)^{\frac{1}{2}}}{\left(\varepsilon_{H_2O} T\right)^{\frac{3}{2}}} \tag{16}$$

and

$$B \equiv \left(\frac{8\pi N \rho_{H_2O} e^2}{1000 \varepsilon_{H_2O} kT}\right)^{\frac{1}{2}} = \frac{5.029 \times 10^9 \left(\rho_{H_2O}\right)^{\frac{1}{2}}}{\left(\varepsilon_{H_2O} T\right)^{\frac{1}{2}}} \tag{17}$$

(e.g., Helgeson and Kirkham 1974), where N is Avagadro's number, e is electron charge, k is Boltzmann's constant, and T is absolute temperature. Dimensions of A and B are $\mathrm{kg}^{1/2}\ \mathrm{mol}^{-1/2}$ and $\mathrm{kg}^{1/2}\ \mathrm{mol}^{-1/2}\ \mathrm{cm}^{-1}$, respectively.

Equations (16) and (17) demonstrate that A and B depend on H_2O density and dielectric constant. As discussed above, while ρ_{H_2O} is reasonably well known from H_2O equations of state (e.g., Haar et al. 1984; Saul and Wagner 1989; Wagner and Pruß 2002), ε_{H_2O} is not. However, estimates of A and B may be made from extrapolations of ε_{H_2O} to high P and T (Fig. 1). Figure 5 shows values of A and B from Manning et al. (2013).

Attempts to use Equation (14) have a long and storied history in solution chemistry in general, and aqueous geochemistry in particular. The various, widely used forms of Equation (14) can be derived from simplifying assumptions. For example, the Debye-Hückel equation is obtained if $b_i = 0$. Assuming $\mathring{a}_i B = 1$ and $b_i = 0$ yields the Güntelberg equation. Because positive values of b_i are required for γ_i to increase in concentrated solutions, the Debye-Hückel and Güntelberg equations nominally pertain to electrolyte behavior only in dilute solutions. This problem is partly circumvented by the Davies (1938, 1962) equation, in which $\mathring{a}_i B = 1$ and $b_i = CAz^2$ where C is 0.2 or 0.3. But the appropriateness of using these (or any other) fixed values of C might logically be questioned at high P and T.

Recognizing the importance of investigating fluid-rock interaction in geological settings of widely varying P and T, Helgeson and coworkers (Helgeson 1969; Helgeson et al. 1981) de-

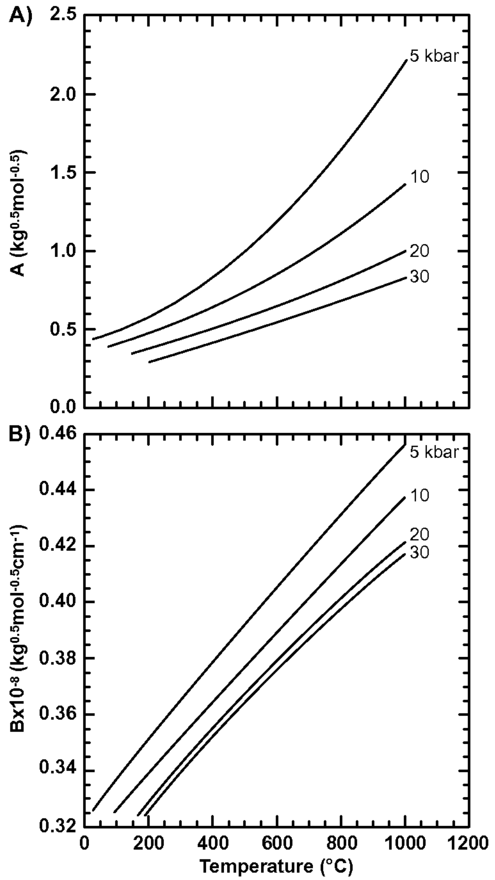

Figure 5. Variation in the A and B solute parameters with temperature at a range of pressures (from Manning et al. 2013).

veloped a framework in which values of the b_i parameter (variably referred to as the "extended term parameter," or "B-dot" after an alternate symbol definition) were derived for a wide range of electrolytes as a function of P and T. In practice, it is impractical to account separately for å and b for each ion, so it is typically assumed that these parameters may be approximated as those of the dominant electrolyte in solution, which for geochemical applications is in many cases NaCl. As with the A and B parameters, b_{NaCl} has been limited to ≤5 kbar (Helgeson et al. 1981). However, Manning et al. (2013) recently used correlations with $\rho_{\mathrm{H_2O}}$ to extrapolate b_{NaCl} to high P and T (Fig. 6).

Activity coefficients calculated from the various modifications of Equation (14) differ dramatically. Figure 7 shows calculated activity coefficient for a monovalent ion (e.g., $\mathrm{Na^+}$ or $\mathrm{Cl^-}$) at 700 °C, 10 kbar, conditions relevant to the high-PT environments under consideration here. At these conditions, A = 1.0 kg$^{1/2}$/mol$^{1/2}$, B = 0.4×10^{-8} kg$^{1/2}$/mol$^{1/2}$cm, å = 3.72×10^{-8} cm, and b_{NaCl} = 0.28 kg/mol (Figs. 5 and 6; Manning et al. 2013). The Güntelberg equation is similar to the Debye-Hückel equation and yields steadily decreasing value of γ_i with rising ionic strength. In contrast, the Davies and B-dot equations yield similar forms, with minima at I = 0.5-0.8 molal and rapid rise in activity coefficient at higher I.

COMPARISON OF EXPERIMENTAL AND CALCULATED MINERAL SOLUBILITY

Taken together, the need for extrapolations of log$K$ and $\Delta G°$, the disparate forms of solute activity models, and the uncertainties in solute parameters might discourage any attempt to carry out quantitative modeling of speciation, mineral solubility, and/or reactive transport in high-P environments. Such reservations would be strengthened by absence of experimental data with which to test the accuracy of any models. However, with the developments of hydrothermal-piston cylinder methods (Ayers et al. 1992; Manning 1994; Manning and Boettcher 1994) and hydrothermal diamond-anvil cell techniques (Bassett et al. 1996), there is now a growing data set on high-PT mineral solubility that can be used to assess the computational approaches

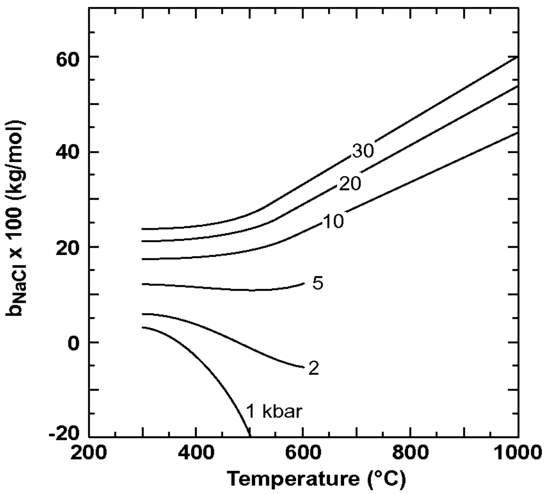

Figure 6. Variation in the extended term parameter for NaCl with temperature at a range of pressures (from Manning et al. 2013).

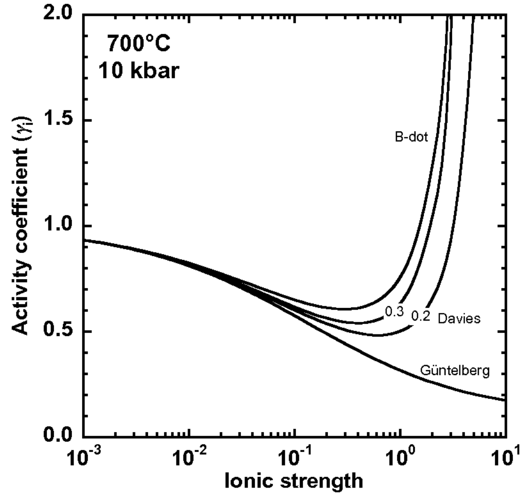

Figure 7. Comparison of activity models for monovalent ions at 700 °C, 10 kbar. Parameter values: A = 1.0 kg$^{1/2}$/mol$^{1/2}$, B = 0.4×10^{-8} kg$^{1/2}$/mol$^{1/2}$cm, å = 3.72×10^{-8} cm, and b_{NaCl} = 0.28 kg/mol (Figs. 5 and 6; Manning et al. 2013).

outlined above at mid-crustal to upper-mantle conditions. A simple example serves to show that in nearly every respect, concerns about extending these methods to the lower crust and upper mantle are largely misplaced.

The solubility of corundum in H_2O and in KOH solutions has been measured at 700 °C, 10 kbar, to a total K concentration ($[K]_{\mathrm{total}}$) of ~4 molal (Becker et al. 1983; Tropper and Manning 2007a; Wohlers and Manning 2009). The data allow evaluation of the density extrapolation method and of the consequences of adopting different activity-coefficient models. For these solutions we can assume the presence of seven main aqueous species in solution: H^+, OH^-, K^+, $KOH_{(aq)}$, $HAlO_{2(aq)}$, AlO_2^-, and $KAlO_{2(aq)}$. The density model can be used to derive equilibrium constants from SUPCRT92 and Ho and Palmer (1997) at 700 °C, 10 kbar, for the following equilibria:

$$\underset{corundum}{Al_2O_3} + 2H_2O = 2HAlO_2 \qquad \log K = -5.883 \tag{18}$$

$$HAlO_{2(aq)} = H^+ + AlO_2^- \qquad \log K = -4.877 \qquad (19)$$

$$KOH_{(aq)} = K^+ + OH^- \qquad \log K = -1.206 \qquad (20)$$

$$KAlO_{2(aq)} = K^+ + AlO_2^- \qquad \log K = -0.299 \qquad (21)$$

(Wohlers and Manning 2009). Using these equilibrium constants, the log*K* for Equation (8) (Marshall and Franck 1981), the constraint of electrical neutrality, one of the ion-activity models, and known $[K]_{total}$, the solubility of corundum in H_2O and aqueous KOH solutions can be computed independent of the experiments by iterative solution of the resulting system of equations.

Becker et al. (1983) and Tropper and Manning (2007a) reported corundum solubility in pure H_2O at 700 °C, 10 kbar, to be 1.08±0.08 and 1.19±0.14 millimolal, respectively. Using the Güntelberg equation for ion activity coefficients, $A = 1.0$, and unit activity coefficients for neutral species, the predicted solubility derived from the density extrapolation is 1.14 millimolal, in close agreement with the measured values. Other activity formulations give an essentially identical result because the solution is so dilute (Fig. 7).

While the result above is encouraging, the low total solubility of corundum in pure H_2O means that the comparison does not meaningfully distinguish potential differences between activity models. For this it is necessary to compare predicted and calculated solubility as a function of increasing concentration of an electrolyte such as KOH. Figure 8 shows corundum solubilities measured in KOH solutions at 700 °C, 10 kbar (Wohlers and Manning 2009) and those independently calculated using the Güntelberg, Davies ($C = 0.2$ and 0.3) and B-dot formulations for activity coefficient. Parameter values were the same as those used in Figure 7, and it was again assumed that $\gamma = 1$ for neutral species. The various equations for ion activity coefficient yield calculated solubilities that differ negligibly from one another at $[K]_{total} \leq 0.1$ molal (Fig. 8). But even at the highest $[K]_{total}$ of 4 molal, predicted $[Al]_{total}$ ranges from a minimum of 2.0 molal (Davies with $C = 0.3$) to 2.4 molal (Güntelberg) as compared to the experimental value of 2.7 molal, a surprisingly small difference given the high concentration. In general, it is clear that differences in predicted solubility arising from adopting any of the activity models are minor over a wide range of concentration and ionic strength. Note that Wohlers and Manning (2009) used the Güntelberg formulation to refine the log*K* for Equation (21), which explains why corundum solubility calculated using Güntelberg activity coefficients best matches the experimental data (Fig. 8); however, the relative differences between the formulations would remain similar if one of the other activity models had been used.

Both the Güntelberg and Davies formulations depend on knowledge of only one solvent parameter, *A*. Manning and coworkers have argued that calculations of mineral solubility at high *P* and *T* are relatively insensitive to variations in *A*, and that it can be assumed equal to unity (Manning 1998, 2007; Wohlers and Manning 2009; Manning et al. 2010; Wohlers et al. 2011). This is supported by the relatively narrow range in values exhibited by *A* away from the critical region of H_2O (Fig. 5A) (Helgeson and Kirkham 1974), and by tests indicating that results varied little with changes in this parameter. But assuming $A = 1.0$ may have been fortuitous, as Figure 5A shows that the new high-*P* estimations yield $A = 1.0$ at 700 °C, 10 kbar. As a check, values of *A* were arbitrarily varied by ±20%, and corundum solubility was then recalculated and compared to the experiments of Wohlers and Manning (2009). Figure 9 illustrates that the calculations are insensitive to relatively extreme and arbitrary variations in *A*. Although accurate knowledge of this parameter is useful for high precision, uncertainties in *A* should not prevent thermodynamic modeling of aqueous solutions at high *P* and *T*.

The insensitivity of calculated solubility to activity-model form or solvent parameters is due at least in part to the effects of ion pairing. As will be shown below, ion pair formation in H_2O is significantly more extensive at high *P* and *T* than in surficial or shallow crustal settings. This will tend to limit the rise in true ionic strength, at least in compositionally simple systems.

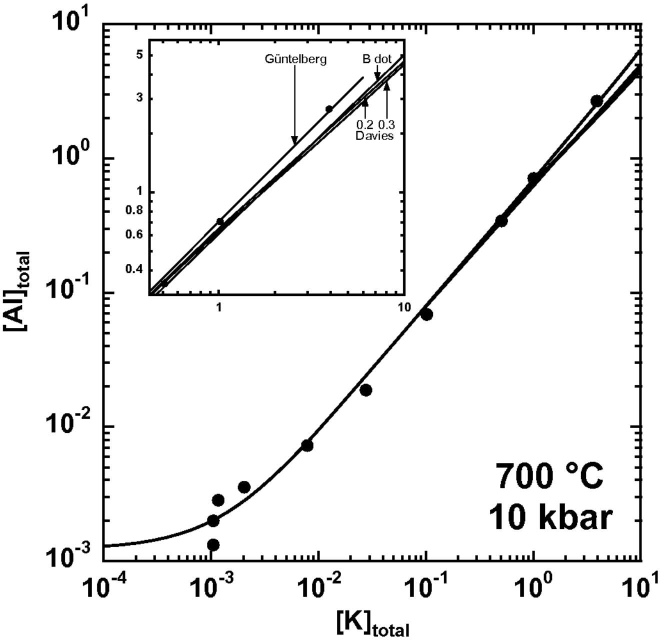

Figure 8. Comparison of experimentally determined corundum solubility in KOH solutions with independently calculated solubility using different ion activity models, at 700 °C, 10 kbar. Filled circles are data of Wohlers and Manning (2009); solid lines are calculated solubility according to the Güntelberg, Davies, and B-dot equations (see text). Inset shows expanded view of high-concentration range. Parameter values: $A = 1.0$ kg$^{1/2}$/mol$^{1/2}$, $B = 0.4\times10^{-8}$ kg$^{1/2}$/mol$^{1/2}$cm, $å = 3.72\times10^{-8}$ cm, and $b = 0.28$ kg/mol (Figs. 5 and 6; Manning et al. 2013).

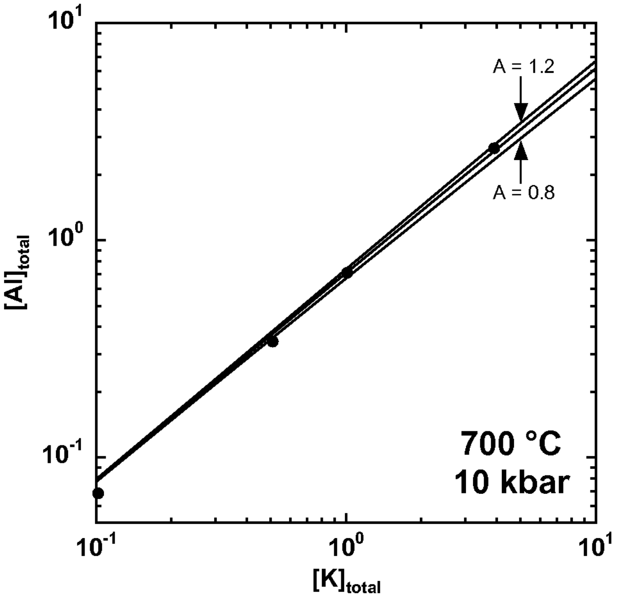

Figure 9. Effect of varying A parameter on calculated corundum solubility at 700 °C, 10 kbar. Activities calculated using the Güntelberg equation. Experimental data from Wohlers and Manning (2009).

The example of corundum solubility in H_2O and KOH solutions suggests that use of density-based models to extrapolate standard state thermodynamic data, when coupled with the observation that speciation calculations are relatively insensitive to choice of activity model and solute parameters, is a promising approach for calculation of mineral solubility at high P and T. Similar results have been obtained for calcite in H_2O at a range of high P and T (Manning et al. 2013) and albite + paragonite + quartz in H_2O at 10 kbar and $T < 500$ °C (Manning et al. 2010) (see below).

Several important caveats should be noted. The calculations outlined above incorporate data from a variety of sources; no attempt at internal consistency was made. Use of the density-based fitting procedure for extrapolation to high P can lead to subtle but potentially aggravating inconsistencies with calculations at 3-5 kbar using unsmoothed thermodynamic data (e.g., from SUPCRT92). More fundamentally, the derivation of the properties of aqueous species or equilibria from solubility or conductance data may lead to nonunique solutions that depend on a priori assumptions about the identities of participating species. An example is NaCl, for which the same data sets have been used to obtain fundamentally different conclusions about its extent of dissociation at low to moderate P (c.f. Frantz and Marshall 1984; Oelkers and Helgeson 1991). Results of calculations of species abundances are frequently provisional, subject to significant refinement upon the arrival of more and better experimental data. Nevertheless, it is clear from the tests above that reasonably accurate estimates of equilibrium constants and activity coefficients can be made and applied to investigate metasomatic environments ranging from the middle crust to the upper mantle.

APPLICATIONS

The agreements between experimentally determined mineral solubility at high P and T on one hand, with those predicted using the density model and a combination of the HKF EOS and low-P experimental data on the other, lends confidence to the quantitative investigation of fluid-rock interaction at $P > 5$ kbar. Below I discuss examples that highlight the utility of extending many of the tools familiar to those working at lower P to the high-P environments of interest here.

Activity-activity diagrams

Standard state properties of ions, H_2O, and minerals can be used to compute equilibrium activity-activity diagrams, which are useful for illustrating metasomatic phase relations at a P and T of interest (e.g., Bowers et al. 1984). Such diagrams are projections of mineral saturation surfaces onto a coordinate system involving fluid compositional variables. For example, consider the equilbrium

$$\underset{\textit{K-feldspar}}{3KAlSi_3O_8} + 2H^+ = \underset{\textit{muscovite}}{KAl_3Si_3O_{10}(OH)_2} + 2K^+ + 6SiO_{2(aq)} \qquad (22)$$

Here, the equilibrium is written so that Al is conserved in the minerals, and $SiO_{2(aq)}$ corresponds to total SiO_2 in solution, neglecting polymeric silica speciation (see below). The logarithm of the equilibrium constant for Equation (22) is

$$\log K = 2\log\frac{a_{K^+}}{a_{H^+}} + 6\log a_{SiO_{2(aq)}} + \log a_{muscovite} - \log a_{K\text{-feldspar}} \qquad (23)$$

Assuming pure, stoichiometric minerals in their standard state of unit activity at any P and T, the two right-hand terms equal zero, and Equation (23) can be rearranged to obtain

$$\log\frac{a_{K^+}}{a_{H^+}} = \frac{1}{2}\log K - 3\log a_{SiO_{2(aq)}} \qquad (24)$$

which is the equation for a straight line if we adopt plotting coordinates of $\log(a_{K+}/a_{H+})$ and $\log a_{SiO_{2(aq)}}$. Writing similar Al-conserving reactions between minerals in the system of interest (e.g., K_2O-Al_2O_3-SiO_2-H_2O, or KASH) and then computing equilibrium constants from standard state thermodynamic properties allows identification of equilibrium mineral stability fields and phase boundaries as functions of fluid compositional variables.

Figure 10A illustrates equilibrium fluid-mineral phase relations in the KASH system at 700 °C, 10 kbar. At constant *P* and *T*, the saturation surface for each stable aluminum-bearing mineral defines a divariant field; mineral-mineral phase boundaries yield univariant phase boundaries; assemblages of three minerals are invariant. Quartz is Al-free (neglecting trace substitution), so it defines a saturation surface which projects onto Figure 10A as a vertical line. Because the diagram portrays equilibrium phase relations, quartz saturation defines the upper limit of $SiO_{2(aq)}$ activity, and any fluid with higher a_{SiO_2} is metastably supersaturated with respect to quartz. The diagram is useful for exploring how isothermal-isobaric changes in mineral assemblages record variation in activities of aqueous species at local equilibrium, which aids interpretation of metasomatic mineral zoning observed in outcrop. For example, at constant *P* and *T*, mineral zonation from quartz + kyanite → kyanite + muscovite →

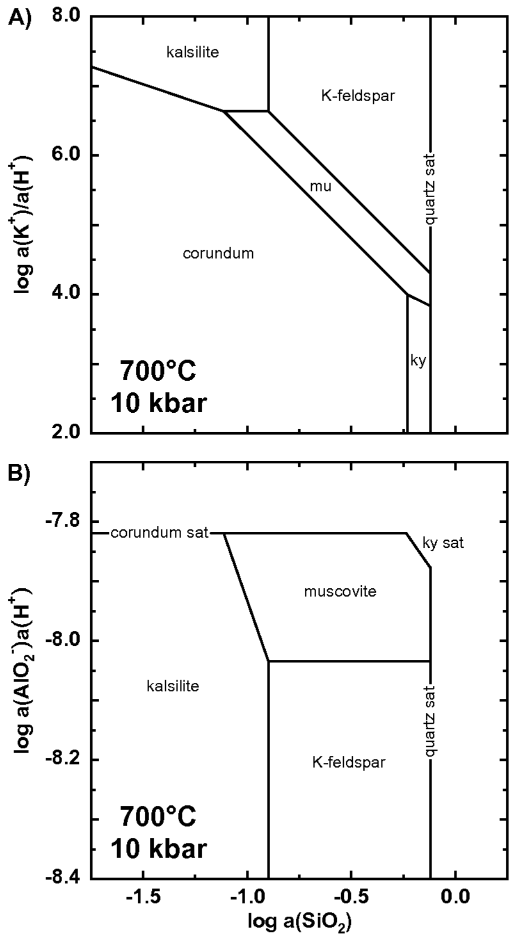

Figure 10. Equilibrium activity-activity diagrams depicting phase relations among minerals and H_2O in the system K_2O-Al_2O_3-SiO_2-H_2O at 700 °C, 10 kbar. Sources of thermodynamic data: minerals, Holland and Powell (1998; 2002 update, as implemented in the PERPLEX software package (*http://www.perplex.ethz.ch*)); H_2O, Haar et al. (1984); Al and K species, density-based extrapolations of data from Pokrovskii and Helgeson (1997); SiO_2, Manning (1994). Abbreviations: mu, muscovite; ky, kyanite; sat, saturation.

muscovite + corundum indicates decreasing $a_{\mathrm{SiO_2}}$ and rising $a_{\mathrm{K+}}/a_{\mathrm{H+}}$ in the coexisting pore fluid. At quartz saturation, rising acidity along a flow path at constant $a_{\mathrm{K+}}$ would produce mineral zoning of K-feldspar → muscovite → kyanite.

The choice of species is arbitrary and strictly a matter of convenience. Common practice is use of the simple cations of the oxides of interest, except for silica. However, these need not—and in many cases at high *P* and *T*, do not—correspond to the most abundant species in solution. Species choice is immaterial because the topology of the fluid-mineral phase relations must be the same, though the numeric values of the activity ratios and products change. Figure 10B illustrates phase relations in the KASH system, again at 700 °C and 10 kbar, but with the aqueous Al species AlO_2^-. As described above, this species is likely to predominate in high-*PT* fluids in this system at pH only slightly above neutrality. Nevertheless, the topology is the same as if Al^{+3} were used instead. Examples of other quantitative high-*PT* activity-activity diagrams can be found in Manning (1998, 2007).

Homogeneous equilibria

Experimental data constraining the equilibrium constant for the self-dissociation of water (Eqn. 8) (Quist 1970; Sweeton et al. 1974) have been fit using a density model (Marshall and Franck 1981). Figure 11 shows variation in the equilibrium constant (log*K*) for Reaction (8) with pressure along isotherms (200, 400, 600, 800 °C), and along geothermal gradients (10, 20, 40 °C/km) that model *dP/dT* associated with burial/exhumation and heating/cooling in a range of crustal and upper-mantle settings. It can be seen that log*K* becomes less negative with increasing *P* along the plotted isotherms, with increasing *T* along isobars, and with greater burial along geotherms. This means that Reaction (8) is driven to the right to ever-greater degrees with progress along these paths; that is, the self-dissociation of water becomes more extensive. The opposite obtains for cooling and decompression paths.

The greater extent of H_2O self-dissociation in high *P-T* environments has important consequences. Figure 11 shows that neutral pH is dramatically lower than in shallower environments. In addition, in contrast to shallow-crustal environments, the H_2O self-dissociation products H^+ and OH^- contribute significantly to ionic strength in deep crustal environments. For example, at 600 °C and 25 kbar, conditions that may be expected to attain along the tops of subducting slabs (e.g., Syracuse et al. 2010), the ionic strength of pure H_2O is ~1 millimolal.

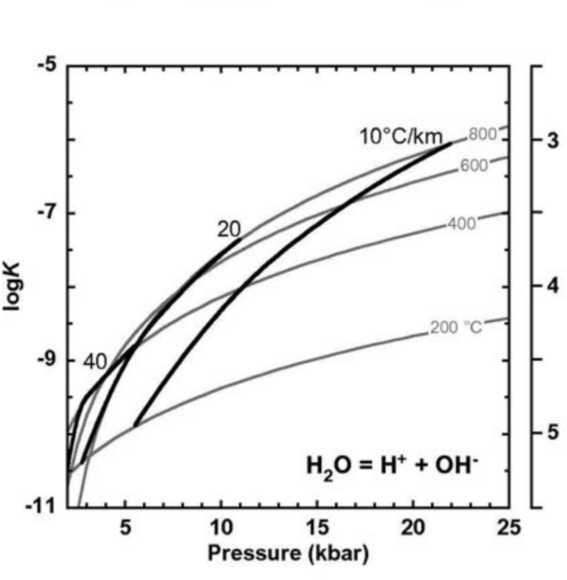

Figure 11. Variation in the equilibrium constant for H_2O self-dissociation with pressure along isotherms (light gray lines) and model linear geotherms (bold lines). Values of log*K* calculated from Marshall and Franck (1981). Neutral pH is displayed on the right, assuming unit activity coefficients of H^+ and OH^-.

NaCl is likely to be an important electrolyte in high *P-T* environments. Figure 12A illustrates that the equilibrium constant for

$$\mathrm{NaCl_{(aq)}} = \mathrm{Na^+} + \mathrm{Cl^-} \tag{25}$$

rises with increasing depth along any isotherm (Quist and Marshall 1968a). In contrast, the coupled rise in *P* and *T* with burial along a geotherm leads to a decrease in log*K*.

The extent of dissociation of electrolyte *AB* is usefully characterized as

$$\alpha_{AB} \equiv 1 - \frac{\left[AB_{(\mathrm{aq})}\right]}{\left[AB\right]_{\mathrm{total}}} \tag{26}$$

Where $[AB_{(\mathrm{aq})}]$ and $[AB]_{\mathrm{total}}$ denote the concentration of associated electrolyte in the solution, and the electrolyte total concentration, respectively. According to Equation (26), α_{AB} varies from 0 to 1 as electrolyte *AB* changes from fully associated to fully dissociated, and it therefore represents a simple parameter for tracking the extent of electrolyte dissociation or association.

Figure 12B illustrates the variation in α_{NaCl} with *P* along the same isotherms and geotherms as in Figure 12A, assuming dilute solutions in which activity coefficients can be approximated

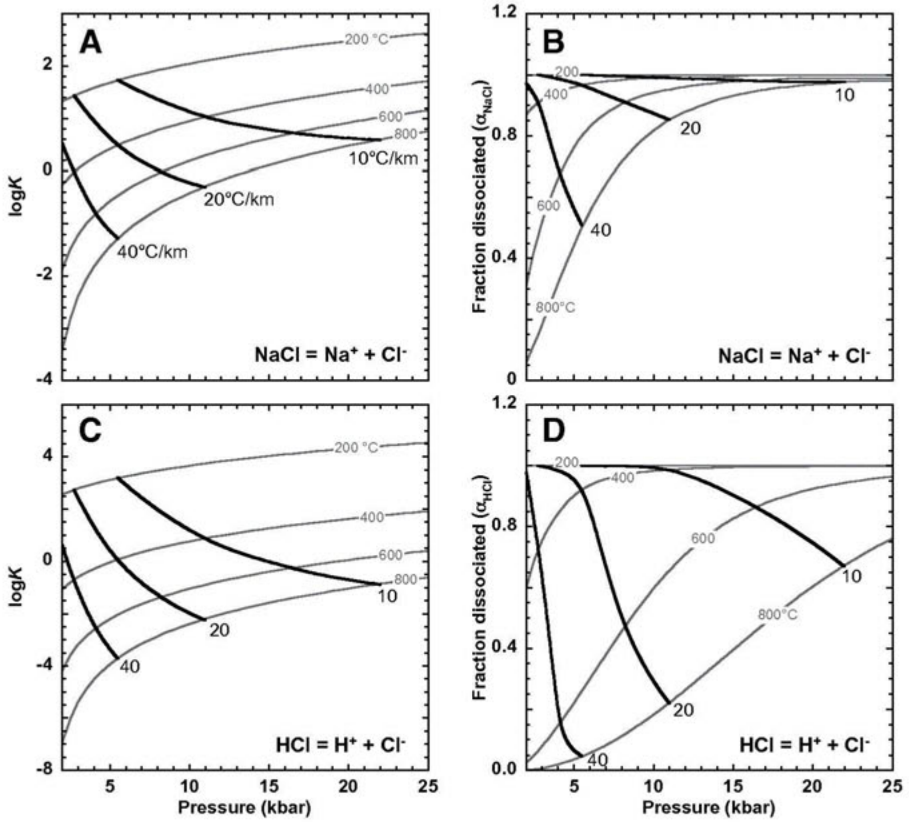

Figure 12. Variation in equilibrium constant and dissociation parameter (a) for NaCl (A and B) and HCl (C and D) along isotherms (light gray lines) and model geotherms (bold black lines) (Quist and Marshall 1968a; Frantz and Marshall 1984). Activity coefficients assumed to be 1.

as unity. The extent of dissociation rises with P along isotherms. With isobaric heating at <5 kbar, NaCl changes from fully dissociated at low T to strongly associated at high T. This contrasts with behavior along the same path at high P, where less association is induced by heating. These relations mean that solute NaCl compressed along model geothermal gradients is more dissociated than it would be if isobarically heated to the same extent. In general, the extent of NaCl association is greater at all elevated P and T than at 25 °C and 1 bar, but when high-T igneous and metamorphic environments are compared, the extent of electrolyte dissociation is greater in deep settings (e.g., subduction zones) than in their shallow equivalents (e.g., contact metamorphic aureoles).

At fixed P and T, rising NaCl concentration in dilute solutions will initially inhibit dissociation, owing to the decrease in activity coefficient (Fig. 7). However, continued increase in concentration will eventually cause activity coefficients to exceed unity and yield more extensive dissociation. In the saline brines that may accompany metamorphism and melting in deep-crustal amphibolites and granulites (Touret 1985; Newton et al. 1998; Aranovich et al. 2013), NaCl is effectively completely dissociated (Aranovich and Newton 1996) (see below). Similar observations can be made for KCl (Aranovich and Newton 1997; Ho and Palmer 1997), as well as for AB_2 electrolytes such as $CaCl_2$ and $MgCl_2$ (Fig. 13) (Frantz and Marshall 1982).

At ambient conditions HCl is a strong acid by virtue of its large log$K$ of 9.3, which indicates nearly complete dissociation. However, Frantz and Marshall (1984) showed that HCl becomes much weaker at high P and T. Figure 12C illustrates that variation in log$K$ along isotherms and geotherms is similar to that of NaCl, although values exhibit a wider range. The equilibrium constants translate to α_{HCl} indicating that burial along all geotherms yields significant HCl association (Fig. 12D). The extent of association is greatest along elevated geotherms, but is still prounounced even along subduction-type geotherms that are here modeled as 10 °C/km. Similar effects can be seen in strong bases such as KOH (Ho and Palmer 1997). In general, strong acids and bases become significantly weaker in high P-T fluids.

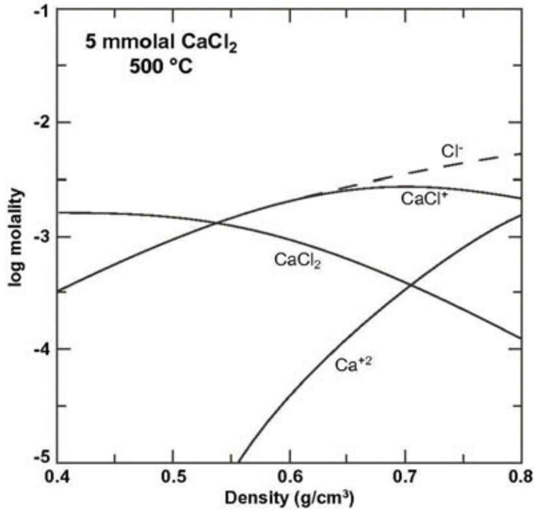

Figure 13. Species abundances in a 0.005 molal $CaCl_2$ solution at 500 °C, as a function of H_2O density (Frantz and Marshall 1982).

The pH dependence of mineral solubility

Mineral dissolution in H_2O is a strong function of pH. However, the substantial changes with P and T in H_2O self-dissociation and in mineral and solute stabilities translate to differences in the pH dependence of mineral dissolution. This can be seen using two examples, calcite and corundum.

Calcite dissolution is the primary contributor to groundwater alkalinity, but the magnitude of this effect depends on the prevailing pH and the relative stabilities of $CO_{2(aq)}$, HCO_3^- and

CO_3^{-2}. This effect arises from the modest solubility of calcite in H_2O, which can be seen by writing the equilibria

$$\underset{calcite}{CaCO_3} = Ca^{+2} + CO_3^{-2} \tag{27}$$

$$HCO_3^- = H^+ + CO_3^{-2} \tag{28}$$

$$CO_{2(aq)} + H_2O = H^+ + HCO_3^- \tag{29}$$

Equilibrium constants for Equations (27-29) can be combined with Equation (8) and charge and mass balance to derive the well-known pH dependence of calcite solubility (Fig. 14A). Calcite solubility corresponds to the sum of all carbonate species in solution, which together must equal the total dissolved calcium (only Ca^{+2} is considered for simplicity). The minimum calcite solubility of 0.06 millimolal exists in alkaline solutions of pH >12. However, decreasing pH progressively increases solubility as Equations (28) and (29) are driven to the left due to H^+ addition. Figure 14A illustrates that reaction with acidic solutions can yield very high

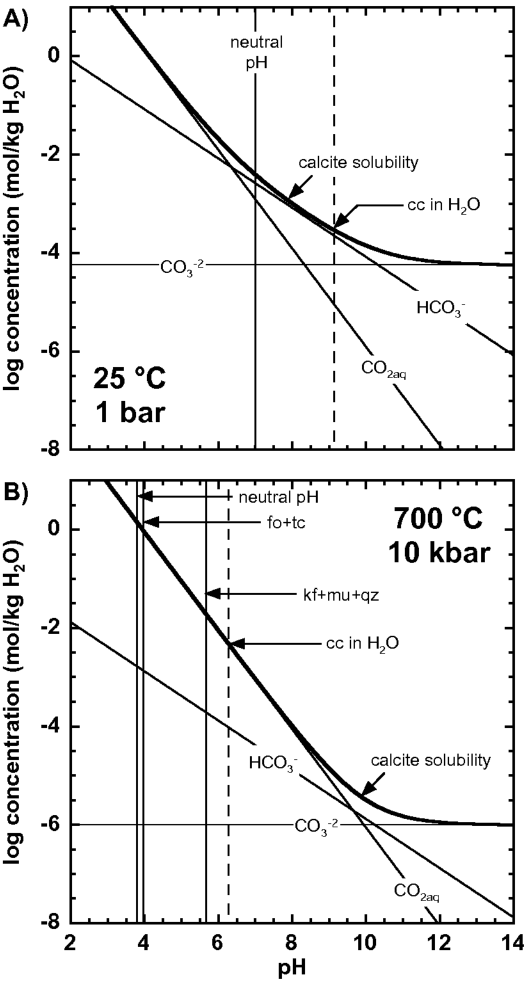

Figure 14. Solubility of calcite as a function of pH at 25 °C, 1 bar (A), and 700 °C, 10 kbar (B). Calcite solubility (bold line) is the sum of the concentrations of the carbonate species (thin lines). Vertical dashed lines show pH in pure H_2O equilibrated with calcite; intersections with bold curves define the solubility of calcite in H_2O. Vertical solid lines are neutral pH and pH values imposed by relevant silicate mineral buffers (see text). Figures calculated assuming unit activity coefficients and the only calcium species is Ca^{+2}. Calculations in (B) used density extrapolation methods with data from Marshall and Frank (1981) and SUPCRT92 using the slop98 data set. Abbreviations: cc, calcite; fo, forsterite; kf, K-feldspar; mu, muscovite; qz, quartz; tc, talc.

calcite solubility. In the absence of external controls on pH, initially neutral H_2O brought into equilibrium with calcite acquires a pH of 9.1 at ambient conditions, solubility is 0.30 millimolal, and the predominant form of dissolved carbon will be HCO_3^-.

Calcite solubility relations exhibit similar form at deep-crustal conditions of 700 °C and 10 kbar (Fig. 14B). Solubility is at a minimum in alkaline solutions, and it increases with decreasing pH. In addition, calcite solubility is essentially identical in the most acidic solutions at the two *P-T* conditions shown. However, there are three important differences from relations at ambient conditions. First, the minimum solubility in alkaline solutions is predicted to be *lower* than at 25 °C, 1 bar. Second, the relative stabilities of the carbonate species vary with *P* and *T*, and it can be seen that the HCO_3^- predominates over a narrower pH range at 700 °C than at ambient conditions. Finally, the pH of initially pure H_2O equilibrated with calcite shifts to 6.2 relative to neutral pH of 3.8 at these conditions. The magnitude of the shift is similar to that at 25 °C, 1 bar, but the solubility of 11 millimolal at the acquired pH is higher and the predominant dissolved carbon species is carbonic acid ($CO_{2(aq)}$).

In contrast to carbonate minerals, aluminum-oxide compounds are amphoteric owing to the ability of dissolved Al and its hydrates to form stable cations and anions. The effects of changing *P* and *T* from ambient conditions to those of the deep crust and upper mantle can be examined using corundum (Al_2O_3). In the presence of H_2O, corundum is metastable with respect to gibbsite ($Al(OH_3)$) at 25 °C, 1 bar; however, differences in pH dependence between corundum and gibbsite are negligible at these conditions. At 25 °C, 1 bar, metastable corundum solubility in H_2O displays a deep minimum of 1×10^{-7} molal at pH = 6.2 (Fig. 15A). Shifts in pH to more acidic or more alkaline values yield dramatic enhancement in dissolved Al concentration. The depth of the solubility minimum is partly a consequence of the fact that neutral $HAlO_{2(aq)}$ is only marginally stable at these conditions, and it accounts for the limited solubility of Al in near-neutral H_2O. Initially neutral H_2O acquires a very weakly acidic pH of 6.8 by equilibrating with corundum, and the dominant species is AlO_2^- (Fig. 15A).

As with calcite, the pH dependence of corundum solubility at 700 °C, 10 kbar, is similar in form to that at low *P* and *T* (Fig. 15B), but in detail there are important differences. The minimum in the solubility curve is substantially broader and shallower due to the significantly greater relative stability of neutral $HAlO_{2(aq)}$. The solubility of corundum is therefore predicted to be much higher at elevated *P* and *T*, consistent with experimental studies (Becker et al. 1983; Tropper and Manning 2007a). Neutral $HAlO_{2(aq)}$ is predicted to become predominant over AlO_2^- in initially pure H_2O equilibrated with corundum. Though the solution still shifts to slightly acid pH, the magnitude of this shift is smaller.

These conclusions have important implications for Al mobility as a consequence of H^+ metasomatism. At near-surface conditions, H^+ metasomatism leads to substantial Al solubility and mobility and is widely recognized where acidity is produced for example by oxidation and/or cooling of dissolved volcanic gases in hydrothermal systems. However, Figure 15B illustrates that acids do not have the same effect at high *P* and *T*, and the significant weakening of otherwise strong acids such as HCl (Fig. 12) at high-grade conditions makes it even more difficult to mobilize Al by this mechanism. Though H^+ metasomatism has been proposed in medium- to high-grade metamorphic contexts (Vernon 1979; Zaraisky 1994; Nabelek 1997; McLelland et al. 2002), the constraints imposed by Figure 15B make this scenario unlikely except in very unusual cases.

Buffering of pH by rock-forming minerals

The elevated log*K* for H_2O dissociation and the relative weakness of acids and bases at high *P* and *T* also mean that the nature of pH buffering by rock-forming mineral assemblages changes significantly with depth of metasomatic environment. For example, at ambient conditions, the consumption of H^+ during transformation of olivine to hydrous serpentine

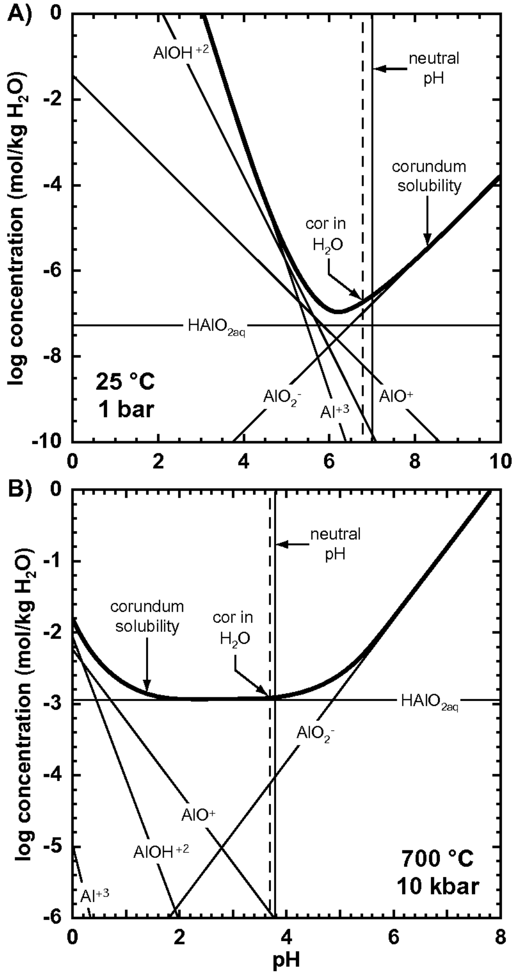

Figure 15. Solubility of corundum as a function of pH at 25 °C, 1 bar (A), and 700 °C, 10 kbar (B). Corundum solubility (bold line) is the sum of the concentrations of the Al species (thin lines). Vertical dashed lines show pH in pure H_2O equilibrated with corundum; vertical solid lines are neutral pH; intersection with the bold curve defines the solubility of calcite in H_2O; intersections with bold curves define the solubility of corundum in H_2O. Vertical solid line shows neutral pH. Figures calculated assuming unit activity coefficients. Mineral pH buffers calculated with density model with data from Marshall and Franck (1981), and SUPCRT92 using the slop98 data set. Abbreviation: cor, corundum.

minerals generates strongly alkaline waters. Springs issuing from actively serpentinizing ultramafic rocks may have pH in excess of 10 (e.g., Barnes and O'Neil 1969; Barnes et al. 1978). Does this also occur at high P and T? The relevant equilibria change with P and T due to variations in mineral stability; however, we can use the pH-buffering equilibrium between forsterite and talc

$$\underset{\textit{forsterite}}{4Mg_2SiO_4} + 10H^+ = \underset{\textit{talc}}{Mg_3Si_4O_{10}(OH)_2} + 5Mg^{+2} + 4H_2O \qquad (30)$$

as a model. Though this equilibrium is metastable with respect to others involving serpentine minerals at low P and T, it usefully illustrates how the consequences of H^+ consumption change with burial depth. At ambient conditions, pH buffered (metastably) by Equation (30) is 10.79, which differs from neutral pH (ΔpH) by 3.79 pH units. In geothermal systems of modest temperature (100 °C, P_{sat}), pH = 8.63 and ΔpH = 2.51. The disparity between the buffer equilibrium and neutrality is smaller, but buffered pH is still quite alkaline, consistent with observations of alkaline, ultramafic-hosted submarine warm springs (e.g., Kelley et al. 2001).

This trend continues as *P* and *T* increase: at 300 °C and 2 kbar, pH = 5.89 and ΔpH = 0.87; at 700 °C and 10 kbar, pH = 3.97 and ΔpH = 0.18. These calculations show that pH buffered by Equation (30) declines significantly with rising *P* and *T*. The buffered pH remains alkaline, as required by H^+ consumption (Eqn. 30); however, the most striking result is that the difference between buffered pH and neutrality declines to the point of insignificance at 700 °C and 10 kbar.

Similar results are obtained with other silicate pH buffers. At ambient conditions, the (metastable) assemblage K-feldspar + muscovite + quartz buffers pH at 9.40, whereas at 700 °C, pH is 4.09. As with forsterite + talc, ΔpH declines but remains alkaline—from 2.40 to 1.88. Note that, at 700 °C and 10 kbar, the pH buffered by the K-feldspar + muscovite + quartz is significantly more alkaline than that imposed by forsterite + talc. The results of these calculations indicate that as *P* and *T* increase to lower crustal and upper mantle conditions, less extreme pH shifts away from acid-base neutrality should be expected in fluids internally buffered by silicate rock mineral assemblages.

The effects of pH buffering by silicate mineral assemblages are important for deep fluids. Consider calcite, which is sparingly soluble in pure H_2O at 700 °C, 10 kbar. Figure 14B illustrates that aqueous pore fluids in which pH is controlled by equilibrium with a rock matrix dominated by silicate minerals such as K-feldspar + muscovite + quartz or forsterite + talc, will in effect act as moderate to strong acids and raise calcite solubility. For example, at forsterite-talc-buffered pH of 4.09, calcite solubility is 0.88 molal, or ~80 times higher than in H_2O equilibrated with calcite alone (Fig. 14B). Clearly, consideration of pH effects is essential in evaluating carbon transport in deep metasomatic environments.

Salinity and saline brines

Chlorine is likely an important ligand in high *P-T* fluids, and variation in its concentration will strongly influence dissolved element solubility and speciation. As discussed above, it is unlikely that externally derived solutions in these environments are strongly acidic. It is therefore more appropriate to examine the consequences of changing chlorinity by modeling Cl addition as a dissolved alkali-chloride, such as NaCl. Manning (1998) examined the role of varying dissolved NaCl concentration on solubilities of the model mineral assemblage glaucophane + garnet + omphacite + quartz near the blueschist-eclogite transition at 550 °C, 17.5 kbar (Fig. 16). Dissolved NaCl was varied from 0.001 to 1.0 molal, or 0.006 to 6 wt%. Figure 16 shows that Cl^- is the dominant form of chlorine in solution. Solute concentrations are generally low, even at the highest $[NaCl]_{total}$. Changes in speciation reflect the combination of the relative stabilities of association/dissociation equilibria and the large equilibrium constant for H_2O dissociation ($\log K = -6.91$).

As summarized by Newton and Manning (2010), highly concentrated brines may play an important role in high-grade metamorphism, especially at granulite-facies conditions in the lower crust. These brines may attain salt mole fractions of 0.3 or greater, and it is highly likely that the supporting cations include not just Na^+, but in addition K^+, Ca^{+2}, Mg^{+2}, and other major rock-forming metals. While a comprehensive treatment of these solutions is beyond the scope of this review, it is important to note that the standard state adopted here is inappropriate at such high concentrations. Newton and Manning (2010) showed that the brines can successfully be modeled as ideal solutions of fully dissociated salts diluted by H_2O. With the exception of quartz, solubilities of rock-forming minerals in such solutions are dramatically higher than in dilute aqueous solutions like those modeled in Figure 16 (Newton and Manning 2000, 2002, 2005, 2006, 2007, 2008a; Tropper and Manning 2007a,b; Antignano and Manning 2008a; Wykes et al. 2008; Tropper et al. 2011). Such solutions can be expected to be powerful metasomatic agents wherever they occur.

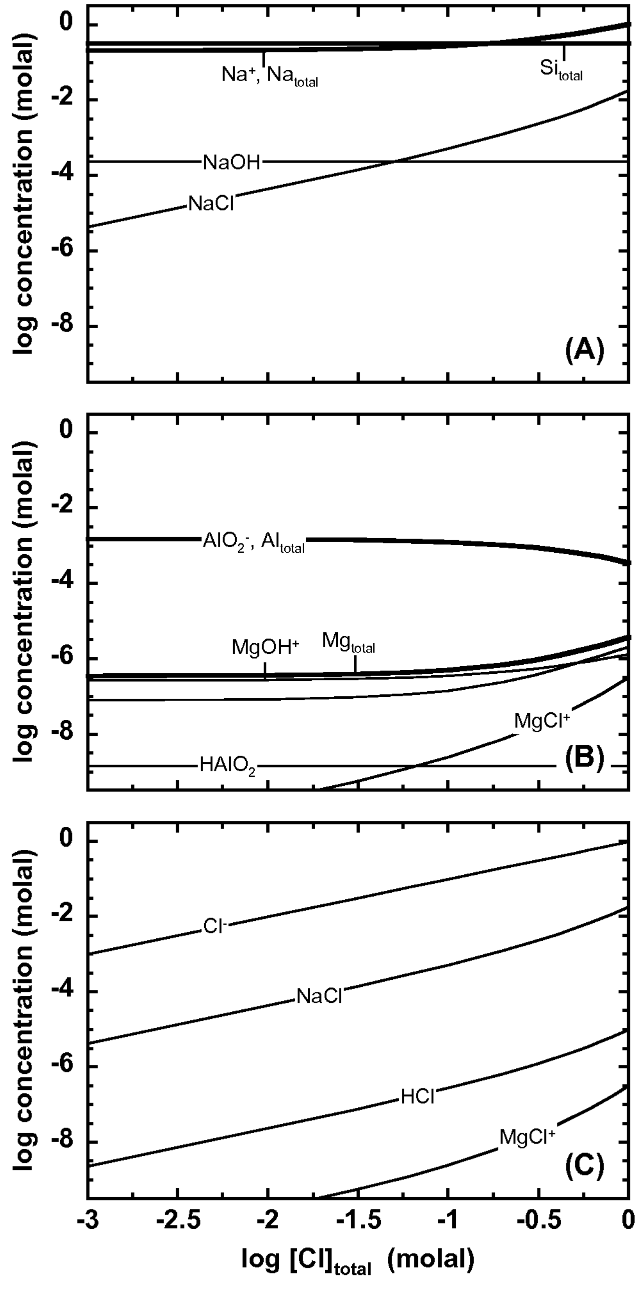

Figure 16. Variation in species concentrations with total Cl in aqueous fluid equilibrated with model glaucophane ecolgite at 550 °C, 17.5 kbar (after Manning 1998). Bold lines denote total element concentrations; thin lines, concentrations of individual species. The pH decreases from 6 to 5.3 as $\log Cl_{total}$ increases from –3 to 0; neutral pH is 3.5.

"Excess" solubility and identification of additional solutes

The methods described above also provide a framework for identifying new solute species and quantifying their concentrations. This is exemplified by experimental studies of the solubility of aqueous silica in equilibrium with various mineral assemblages. It was long assumed that in crustal metamorphic settings, all dissolved silica exists as monomeric silicic acid (H_4SiO_4, for which we will adopt here the anhydrous notation $SiO_{2(m)}$) (e.g., Walther and Helgeson 1977). This can be tested by comparing measured silica solubility associated with different assemblages which fix, or "buffer," the activity of SiO_2 at constant P and T. Examples are:

$$\underset{corundum}{Al_2O_3} + SiO_{2(m)} = \underset{kyanite}{Al_2SiO_5} \tag{31}$$

$$\underset{forsterite}{Mg_2SiO_4} + SiO_{2(m)} = \underset{enstatite}{2MgSiO_3} \tag{32}$$

If only monomeric SiO_2 is present, then assuming unit activity coefficient for neutral $SiO_{2(m)}$ (i.e., ${}_{SiO_{2(m)}} = a_{SiO_{2(m)}}$; see above) and stoichiometric minerals permits determination of the solubility of either assemblage constrains $\Delta G^{\circ}_{SiO_{2(m)}}$ at that P and T from:

$$\Delta G^{\circ}_{SiO_{2(m)}} = RT \ln m^{buffer}_{SiO_{2(m)}} + \Delta G^{\circ}_{kyanite} - \Delta G^{\circ}_{corundum} \tag{33}$$

Experimental measurements of SiO_2 concentrations associated with these assemblages (Zhang and Frantz 2000; Newton and Manning 2002, 2003) allow prediction of the solubility of other silica buffers, such as quartz:

$$\underset{quartz}{SiO_2} = SiO_{2(m)} \tag{34}$$

$$\ln m^{quartz}_{SiO_{2(m)}} = \frac{\Delta G^{\circ}_{SiO_{2(m)}} - \Delta G^{\circ}_{quartz}}{RT} \tag{35}$$

which have been measured independently (e.g., Anderson and Burnham 1965; Manning 1994). Newton and Manning (2002, 2003) showed that using Equations (33) and (35) underpredicts quartz solubility at ≥5 kbar and ≥600 °C, and that the extent of underprediction grows with rising P and T. These observations require the presence of additional dissolved silica species whose concentrations increase with P and T. This is consistent with spectroscopic observation of polymerization of aqueous silica to form dimers ($Si_2O_{4(d)}$, Zotov and Keppler 2000 2002) at high P, T, and Si concentration. That is, the reaction

$$2SiO_{2(m)} = Si_2O_{4(d)} \tag{36}$$

is driven to the right at high P and T, and

$$[Si]_{total} = [SiO_{2(aq)}] = [SiO_{2(m)}] + 2[Si_2O_{4(d)}] \tag{37}$$

Figure 17 illustrates the consequences of recognizing the presence of SiO_2 dimers in addition to monomers. If all dissolved silica were assumed to be monomers and quartz solubility measurements alone had been used to derive $\Delta G^{\circ}_{SiO_{2(m)}}$, then the phase relations would predict more restricted stability fields than when polymerization is taken into account. Newton and Manning (2008b) and Hunt and Manning (2012) extended this approach to higher T and showed that further polymerization to trimers and other structures must occur as the hydrous melting curve is approached and crossed. As pointed out by Manning (2004), polymerization in the aqueous phase is the chemical behavior that makes possible fully miscible mixing of hydrous silicate melt and solute-rich aqueous fluid. Simple mixing models of the system SiO_2-H_2O that account for homogeneous polymerization reactions successfully reproduce melting relations and solubilities (Hunt and Manning 2012).

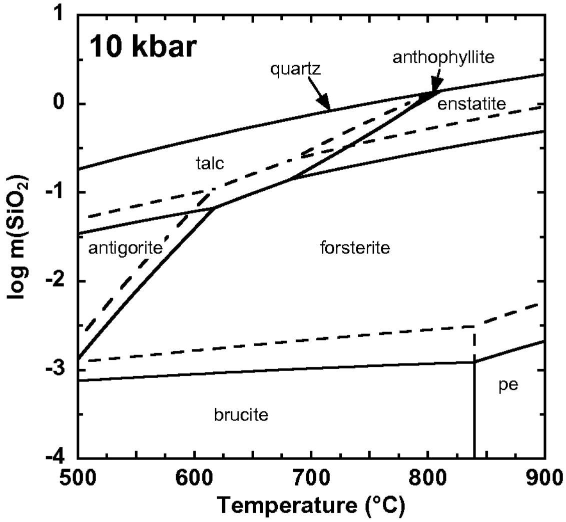

Figure 17. Equilibrium temperature-activity diagram depicting equilibrium phase relations in the system MgO-SiO_2-H_2O at 10 kbar (after Newton and Manning 2002). Dashed lines show phase relations assuming the presence of SiO_2 monomers only, derived from the solubility of quartz in H_2O (Manning 1994). Solid lines show phase relations accounting for the presence of silica monomers and dimers (Newton and Manning 2002). Abbreviation: pe, periclase.

Identification of excess solubility relative to that predicted via the density-model has been extended to other compositional systems and leads to the conclusion that aqueous polymerization of dissolved rock-forming oxide components is an unanticipated but pervasive feature of high-*PT* fluids. Manning (2007) identified Si and Al solubilities in corundum + kyanite equilibrated H_2O that were greater than predicted assuming only monomeric species of Si and Al (Fig. 18A). The excess solubility was used to predict the Gibbs free energy of an assumed Al-Si dimer, $HAlSiO_{4(aq)}$, and evaluate changes in species abundances as a function of addition of dissolved silica (Fig. 18B). Increasing $[Si]_{total}$ produces rising $[Al]_{total}$ due to increasing concentration of $HAlSiO_{4(aq)}$. This leads to the surprising prediction that the maximum dissolved Al concentration should be observed at quartz saturation rather than at corundum saturation, a result entirely a consequence of aluminosilicate cluster formation.

Manning et al. (2010) determined the solubility of the assemblage albite + paragonite + quartz at 350-620 °C, 10 kbar. Using simple dissolved solutes in this system, they showed that measured solubilities agreed with those predicted using the density-modeling approach at 350 to ~500 °C, indicating that calculations based on simple ions, monomers, and ion pairs of species in this system are adequate to explain the observations. However, measured solubilities are greater than predicted from 500 to 620 °C (Fig. 19). Moreover, the discrepancy grows with increasing *T*, and yields a predicted maximum at the melting point of 635 °C. The agreement at lower *T*, coupled with independent observations that density-based extrapolations are robust in simple solute systems even at higher *T* (see above), indicate that the discrepancy is caused by increasing concentrations of species not taken into account in the calculations; i.e., polymeric clusters. The results of Manning et al. (2010) make it clear that such species are in fact the most abundant solutes in the solutions. At the melting point, 81% of the dissolved solutes are in polymerized clusters. Polymerized silica is the most abundant dissolved constituent (6 wt%). Of this polymerized silica, 1.5 wt% is Si_2O_4 dimers and the rest is Si-Al, Si-Na, and Si-Al-Na clusters. Aluminum and sodium are present in roughly equal concentrations on a molar basis (Na/Al = 1.1). Similar conclusions have been reached for this system at higher *P* (Wohlers et al. 2011) and in the system K_2O-Al_2O_3-SiO_2-H_2O (Wohlers and Manning 2013).

Utilization of the density model for simple aqueous solutes for comparison with experimental results has thus led to critical insights into the important differences between

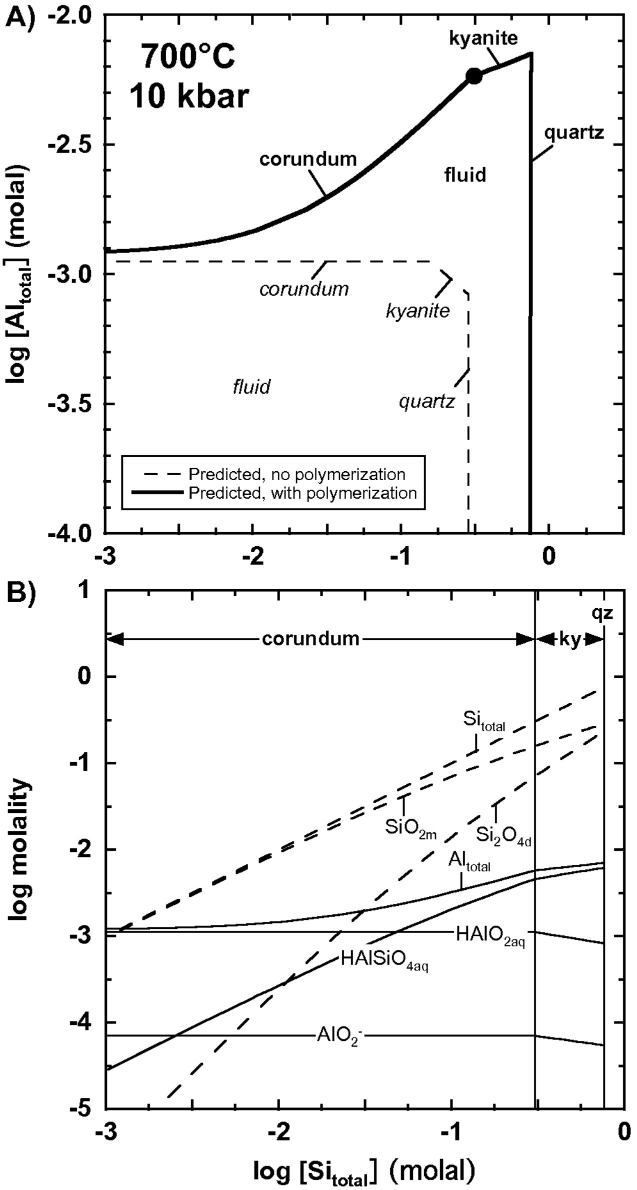

Figure 18. (A) Comparison of variations in predicted concentration of $[\mathrm{Al}]_{\mathrm{total}}$ and $[\mathrm{Si}]_{\mathrm{total}}$ with (solid lines) and without (dashed lines) polymerization at corundum, kyanite and quartz saturation, 700 °C, and 10 kbar (after Manning 2007). The filled circle denotes measure fluid composition from Manning (2007). The difference between the dashed and solid lines illustrates that Al_2O_3-SiO_2 and SiO_2 polymerization leads to significantly higher Al concentration, and the previously unexpected conclusion that maximum dissolved Al occurs at kyanite + quartz equilibrium rather than in equilibrium with corundum. (B) Equilibrium abundances of aqueous species coexisting with corundum, kyanite, and quartz, as a function of total Si molality at 700 °C, 10 kbar. Dashed lines, major Si species; solid lines, major Al species (after Manning 2007). Abbreviation: ky, kyanite.

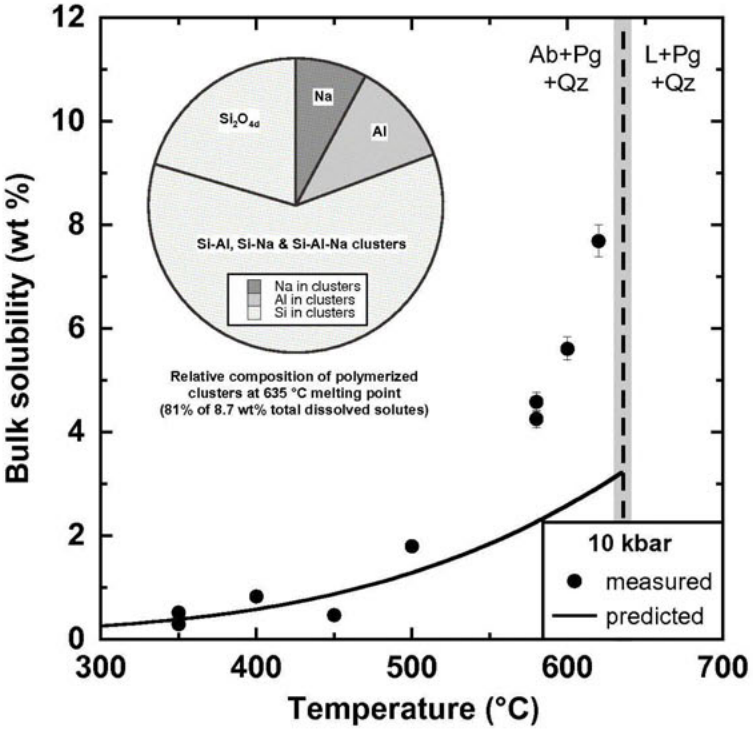

Figure 19. Comparison of experimentally determined and predicted solubilities of ablite + paragonite + quartz at 10 kbar (after Manning et al. 2010). Filled circles show experimental measurements; black line, predicted solubility using density-based modeling. Species used in the calculations were H^+, OH^-, Na^+, $NaOH_{(aq)}$, $HAlO_{2(aq)}$, AlO_2^-, $NaAlO_{2(aq)}$, $SiO_{2(m)}$, $Si_2O_{4(d)}$, and $NaHSiO_{3(aq)}$ ($HSiO_3^-$ was considered, but is omitted here). The divergence between predicted and measured bulk solubility indicates increasing concentrations of polymerized species. Inset shows the predicted relative composition of the 8.7 wt% of polymerized species at the solidus (635 °C), estimated from the difference between calculated solubility and extrapolation of the experimental results to the melting point.

shallow-crustal hydrothermal fluids and those in deep-crustal and upper mantle settings. The experimental observation that mineral solubilities are generally quite high at elevated P and T can be seen to arise in part from the tendency of rock forming oxides to form SiO_2-dominated polymeric clusters. Silica tends to be the most abundant dissolved solute in high a_{H_2O} fluids equilibrated with silicate rocks, so polymerized complexes with SiO_2 can be anticipated to be the predominant dissolved form of many elements. This is especially true for aluminum, for which low solubility in H_2O has long conflicted with ample geologic evidence for Al mobility as evidenced by aluminosilicates in high-PT veins and segregations (Manning 2007). The elevated Al solubility arising from the formation of polymerized Al-Si-hydroxide clusters offers a simple mechanism for dissolving and transporting significant Al. Similar conclusions have been drawn for elements such as Ti and Zr, whose oxides display low solubility in pure H_2O despite geologic evidence for fluid mobility in certain high P and T settings (Antignano and Manning 2008b; Manning et al. 2008; Ayers et al. 2012; Wilke et al. 2012; Louvel et al. 2013).

Concluding remarks

Thermodynamic modeling of interactions between aqueous fluids and rocks at high P and T require as input standard-state properties of solute species and a model for quantifying departures from ideality. Work at middle crustal to upper mantle conditions has been hindered by uncertainties in solute properties and activity models at > 5 kbar. I have shown here that extrapolations based on the density of H_2O afford reasonable estimates of equilibrium constants and Gibbs free energies of equilibria and solutes. Moreover, calculations of the effects of non-ideality appear to be relatively insensitive to activity models and input parameters, at least to moderate total dissolved solids. Agreement between extrapolated data and experiment provides confidence for carrying out thermodynamic modeling of fluid-rock interaction at high P and T, which leads to the conclusion that fluids and their interaction with minerals differ in fundamental ways in deep terrestrial environments as compared to shallow settings.

The approach outlined must be viewed as an initial attempt to make deep fluid-rock interaction accessible to the widely used tools of aqueous geochemistry. The density-based approach has the advantages that it extends the commonly utilized HKF EOS, that any simple linear extrapolation is reasonable within HKF EOS uncertainties, that there is a thermodynamic basis for the approach to linearity, and that the range of extrapolation is relatively small. In addition, the approach allows simple combination of HKF data set with important homogeneous equilibria that are not included. On the other hand, the methods used are empirical, and the extrapolations will compound any errors in accuracy inherent to equations of state or experimental data. Mixing data sources can introduce serious accuracy and internal consistency problems. Nevertheless, the advantages strongly outweigh the shortcomings, as the approach makes possible quantitative aqueous geochemical modeling in a wide range of high-pressure geologic systems.

ACKNOWLEDGMENTS

This work was prepared while the author was in residence at the Lamont Doherty Earth Observatory of Columbia University. I thank P. Kelemen and T. Plank for their hospitality and probing discussions. The research was supported by grants from the National Science Foundation (EAR-1049901) and the Deep Carbon Observatory.

REFERENCES

Anderson GM, Burnham CW (1965) The solubility of quartz in supercritical water. Am J Sci 263:494-511

Anderson GM, Castet S, Schott J, Mesmer RE (1991) The density model for estimation of thermodynamic parameters of reactions at high temperatures and pressures. Geochim Cosmochim Acta 55:1769-1779

Antignano A, Manning CE (2008a) Fluorapatite solubility in H_2O and H_2O-NaCl at 700 to 900 °C and 0.7 to 2.0 GPa. Chem Geol 251:112-119

Antignano A, Manning CE (2008b) Rutile solubility in H_2O, H_2O-SiO_2, and H_2O-$NaAlSi_3O_8$ fluids at 0.7-2.0 GPa and 700-1000 °C: Implications for mobility of nominally insoluble elements. Chem Geol 255:283-293

Aranovich LY, Newton RC (1996) H_2O activity in concentrated NaCl solutions at high pressures and temperatures measured by the brucite-periclase equilibrium. Contrib Mineral Petrol 125:200-212

Aranovich LY, Newton RC (1997) H_2O activity in concentrated KCl and KCl-NaCl solutions at high temperatures and pressures measured by the brucite-periclase equilibrium. Contrib Mineral Petrol 127:261-271

Aranovich LY, Newton RC, Manning CE (2013) Brine-assisted anatexis: experimental melting in the system haplogranite-H_2O-NaCl-KCl at deep-crustal conditions. Earth Planet Sci Lett, doi: 10.1016/j.epsl.2013.05.027

Ayers J, Zhang L, Luo Y, Peters T (2012) Zircon solubility in alkaline aqueous fluids at upper crustal conditions. Geochim Cosmochim Acta 96:18-28

Ayers JC, Brenan JB, Watson EB, Wark DA, Minarik WG (1992) A new capsule technique for hydrothermal experiments using the piston-cylinder apparatus. Am Mineral 77:1080-1086

Barnes I, O'Neil JR (1969) The relationship between fluids in some fresh Alpine-type ultramafics and possible modern serpentinization, western United States. Geol Soc Am Bull 80:1947-1960

Barnes I, O'Neil JR, Trescases JJ (1978) Present day serpentinization in New Caledonia, Oman and Yugoslavia. Geochim Cosmochim Acta 42:144-145

Bassett WA, Wu T-C, Chou I-M, Haselton HT Jr., Frantz J, Mysen BO, Huang W-L, Sharma SK, Schiferl D (1996) The hydrothermal diamond anvil cell (HDAC) and its applications. *In:* Mineral Spectroscopy: A Tribute to Roger G. Burns. Dyar MD, McCammon C, Schaefer MW (eds) The Geochemical Society, Special Publication No. 5, p 261-272

Becker KH, Cemic L, Langer KEOE (1983) Solubility of corundum in supercritical water. Geochim Cosmochim Acta 47:1573-1578

Bowers TS, Jackson KJ, Helgeson HC (1984) Equilibrium activity diagrams: for coexisting minerals and aqueous solutions at pressures and temperatures to 5 kb and 600 °C. Springer, Berlin

Caciagli NC, Manning CE (2003) The solubility of calcite in water at 6-16 kbar and 500-800 °C. Contrib Mineral Petrol 146:275-285

Davies CW (1938) The extent of dissociation of salts in water. Part VIII. An equation for the mean ionic activity coefficient of an electrolyte in water, and a revision of the dissociation constants of some sulphates. J Chem Soc 1938:2093-2098

Davies CW (1962) Ion Association. Butterworths, Washington, D.C.

Dolejš D (2013) Thermodynamics of aqueous species at high temperatures and pressures: equations of state and transport theory. Rev Mineral Geochem 76:35-79

Dolejš D, Manning CE (2010) Thermodynamic model for mineral solubility in aqueous fluids: theory, calibration and application to model fluid-flow systems. Geofluids 10:20-40

Eugster HP, Baumgartner L (1987) Mineral solubilities and speciation in supercritical metamorphic fluids. Rev Mineral 17:367-403

Fernández DP, Goodwin ARH, Lemmon EW, Levelt Sengers JMH, Williams RCA (1997) A formulation for the static permittivity of water and steam at temperatures from 238 K to 873 K at pressures up to 1200 MPa, including derivatives and Debye-Huckel coefficients. J Phys Chem Ref Data 26:1125-1166

Fournier RO, Potter RW II (1982) An equation correlating the solubility of quartz in water from 25° to 900 °C at pressures up to 10,000 bars. Geochim Cosmochim Acta 46:1969-1973

Franck EU (1956) Hochverdichteter Wasserdampf III. Ionen-dissoziation von HCl, KOH und Wasser. Z Phys Chem 6:192-206

Franck EU, Rosenzweig S, Christoforakos M (1990) Calculation of the dielectric constant of water to 1000 °C and very high pressures. Bunsen-Ges Phys Chem 94:199-203

Frantz JD, Marshall WL (1982) Electrical conductances and ionization constants of calcium chloride and magnesium chloride in aqueous solutions at temperatures to 600 °C and pressures to 4000 bars. Am J Sci 282:1666-1693

Frantz JD, Marshall WL (1984) Electrical conductances and ionization constants of salts, acids, and bases in supercritical aqueous fluids: 1. Hydrochloric-acid from 100° to 700 °C and at pressures to 4000 bars. Am J Sci 284:651-667

Haar L, Gallagher JS, Kell GS (1984) NBS/NRC Steam Tables. Hemisphere, New York

Heger K, Uematsu M, Franck EU (1980) The static dielectric constant of water at high pressures and temperatures to 500 MPa and 550°C. Ber Bunsen Ges Phys Chem 84:758-762

Helgeson HC (1969) Thermodynamics of hydrothermal systems at elevated temperatures and pressures. Am J Sci 267:729-804

Helgeson HC, Kirkham DH (1974) Theoretical prediction of the thermodynamic behavior of aqueous electrolytes at high pressures and temperatures: II. Debye-Hückel parameters for activity coefficients and relative partial molal properties. Am J Sci 274:1199-1261

Helgeson HC, Kirkham DH (1976) Theoretical prediction of the thermodynamic behavior of aqueous electrolytes at high pressures and temperatures: III. Equation of state for aqueous species at infinite dilution. Am J Sci 276:97-240

Helgeson HC, Kirkham DH, Flowers GC (1981) Theoretical prediction of the thermodynamic behavior of aqueous electrolytes at high pressures and temperatures: IV. Calculation of activity coefficients, osmotic coefficients, and apparent molal and standard and relative partial molal properties to 600 °C and 5 kb. Am J Sci 281:1249-1516

Ho PC, Palmer DA (1997) Ion association of dilute aqueous potassium chloride and potassium hydroxide solutions to 600 °C and 300 MPa determined by electrical conductance measurements. Geochim Cosmochim Acta 61:3027-3040

Holland TJB, Powell R (1998) An internally consistent thermodynamic data set for phases of petrological interest. J Metamorph Geology 16:309-343, doi: 10.1111/j.1525-1314.1998.00140.x

Hunt JD, Manning CE (2012) A thermodynamic model for the system SiO_2-H_2O near the upper critical end point based on quartz solubility experiments at 500-1100 °C and 5-20 kbar. Geochim Cosmochim Acta 86:196-213

Johnson JW, Oelkers EH, Helgeson HC (1992) SUPCRT92: A software package for calculating the standard molal thermodynamic properties of minerals, gases, aqueous species, and reactions from 1 to 5000 bar and 0 to 1000 °C. Computers & Geosciences 18:899-947

Kelley DS, Karson JA, Blackman DK, Fruh-Green GL, Butterfield DA, Lilley MD, Olson EJ, Schrenk MO, Roe KK, Lebon GT, Rivizzigno P, Party ATS (2001) An off-axis hydrothermal vent field near the Mid-Atlantic Ridge at 30°N. Nature 412:145-149

Louvel M, Sanchez-Valle C, Malfait WJ, Testemale D, Hazemann JL (2013) Zr complexation in high pressure fluids and silicate melts and implications for the mobilization of HFSE in subduction zones. Geochim Cosmochim Acta 104:281-299

Manning CE (1994) The solubility of quartz in H_2O in the lower crust and upper mantle. Geochim Cosmochim Acta 58:4831-4839

Manning CE (1998) Fluid composition at the blueschist-eclogite transition in the model system Na_2O-MgO-Al_2O_3-SiO_2-H_2O-HCl. Schweiz Mineral Petrogr Mitt 78:225-242

Manning CE (2004) The chemistry of subduction-zone fluids. Earth Planet Sci Lett 223:1-16

Manning CE (2007) Solubility of corundum plus kyanite in H_2O at 700 °C and 10 kbar: evidence for Al-Si complexing at high pressure and temperature. Geofluids 7:258-269

Manning CE, Antignano A, Lin HA (2010) Premelting polymerization of crustal and mantle fluids, as indicated by the solubility of albite + paragonite + quartz in H_2O at 1 GPa and 350-620 °C. Earth Planet Sci Lett 292:325-336

Manning CE, Boettcher SL (1994) Rapid-quench hydrothermal experiments at mantle pressures and temperatures. Am Mineral 79:1153-1158

Manning CE, Shock EL, Sverjensky DA (2013) The chemistry of carbon in aqueous fluids at crustal and upper-mantle conditions: experimental and theoretical constraints. Rev Mineral Geochem 75:109-148

Manning CE, Wilke M, Schmidt C, Cauzid J (2008) Rutile solubility in albite-H_2O and $Na_2Si_3O_7$-H_2O at high temperatures and pressures by in-situ synchrotron radiation micro-XRF. Earth Planet Sci Lett 272:730-737

Marshall WL, Franck EU (1981) Ion product of water substance, 0-1000 °C, 1-10,000 bars: new international formulation and its background. J Phys Chem Ref Data 10:295-304

Marshall WL, Mesmer RE (1984) Pressure-density relationships and ionization equilibria in aqueous solutions. J Solution Chem 13:383-391

Marshall WL, Quist AS (1967) A representation of isothermal ion–ion-pair–solvent equilibria independent of changes in dielectric constant. Proc Natl Acad Sci USA 58:901-906

McLelland J, Morrison J, Selleck B, Cunningham B, C. O, Schmidt K (2002) Hydrothermal alteration of late- to post-tectonic Lyon Mountain Granite Gneiss, Adirondack Mountains, New York: origin of quartz-sillimanite segregations, quartz-albite lithologies and associated Kiruna-type low-Ti Fe-oxide deposits. J Metamorph Geol 20:175-190

Mesmer RE (1991) A new approach to measuring pH in brines and other concentrated electrolytes - comment. Geochim Cosmochim Acta 55:1175-1176

Mesmer RE, Marshall WL, Palmer DA, Simonson JM, Holmes HF (1988) Thermodynamics of aqueous association and ionization reactions at high temperatures and pressures. J Solution Chem 17:699-718

Nabelek PI (1997) Quartz-sillimanite leucosomes in high-grade schists, Black Hills, South Dakota: A perspective on the mobility of Al in high-grade metamorphic rocks. Geology 25:995-998

Newton RC, Aranovich LY, Hansen EC, Vandenheuvel BA (1998) Hypersaline fluids in Precambrian deep-crustal metamorphism. Precambrian Res 91:41-63

Newton RC, Manning CE (2000) Quartz solubility in H_2O-NaCl and H_2O-CO_2 solutions at deep crust-upper mantle pressures and temperatures: 2-15 kbar and 500-900°C. Geochim Cosmochim Acta 64:1993-3005

Newton RC, Manning CE (2002) Solubility of silica in equilibrium with enstatite, forsterite, and H_2O at deep crust/upper mantle pressures and temperatures and an activity-concentration model for polymerization of aqueous silica. Geochim Cosmochim Acta 66:4165-4176

Newton RC, Manning CE (2003) Activity coefficient and polymerization of aqueous silica at 800 °C, 12 kbar, from solubility measurements on SiO_2-buffering mineral assemblages. Contrib Mineral Petrol 146:135-143

Newton RC, Manning CE (2005) Solubility of anhydrite, $CaSO_4$, in NaCl-H_2O solutions at high pressures and temperatures: applications to fluid-rock interaction. J Petrol 46:701-716

Newton RC, Manning CE (2006) Solubilities of corundum, wollastonite and quartz in H_2O-NaCl solutions at 800 °C and 10 kbar: Interaction of simple minerals with brines at high pressure and temperature. Geochim Cosmochim Acta 70:5571-5582

Newton RC, Manning CE (2007) Solubility of grossular, $Ca_3Al_2Si_3O_{12}$, in H_2O-NaCl solutions at 800 °C and 10 kbar, and the stability of garnet in the system $CaSiO_3$-Al_2O_3-H_2O-NaCl. Geochim Cosmochim Acta 71:5191-5202

Newton RC, Manning CE (2008a) Solubility of corundum in the system Al_2O_3-SiO_2-H_2O-NaCl at 800 °C and 10 kbar. Chem Geol 249:250-261

Newton RC, Manning CE (2008b) Thermodynamics of SiO_2-H_2O fluid near the upper critical end point from quartz solubility measurements at 10 kbar. Earth Planet Sci Lett 274:241-249

Newton RC, Manning CE (2010) Role of saline fluids in deep-crustal and upper-mantle metasomatism: insights from experimental studies. Geofluids 10:58-72

Oelkers EH, Helgeson HC (1991) Calculation of activity coefficients and degrees of formation of neutral ion pairs in supercritical electrolyte solutions. Geochim Cosmochim Acta 55:1235-1251

Pan D, Spanu L, Harrison B, Sverjensky DA, Galli G (2013) The dielectric constant of water under extreme conditions and transport of carbonates in the deep Earth. Proc Natl Acad Sci USA 110:6646-6650

Pitzer KS (1977) A thermodynamic model for aqueous solutions of liquid-like density. Rev Mineral 17:97-142

Pitzer KS (1979) Theory: ion interaction approach. *In*: Activity Coefficients in Electrolyte Solutions. Pytkowitz RM (ed) CRC Press, Boca Raton, p 157-208

Pitzer KS (1983) Dielectric constant of water at very high temperature and pressure. Proc Natl Acad Sci USA 80:4575-4576

Plyasunov AV, Shock EL (2001) Correlation strategy for determining the parameters of the revised Helgeson-Kirkham-Flowers model for aqueous nonelectrolytes. Geochim Cosmochim Acta 65:3879-3900

Pokrovskii VA, Helgeson HC (1995) Thermodynamic properties of aqueous species and the solubilities of minerals at high pressures and temperatures: the system Al_2O_3-H_2O-NaCl. Am J Sci 295:1255-1342

Pokrovskii VA, Helgeson HC (1997) Thermodynamic properties of aqueous species and the solubilities of minerals at high pressures and temperatures: the system Al_2O_3-H_2O-KOH. Chem Geol 137:221-242

Quist AS (1970) The ionization constant of water to 800° and 4000 bars. J Phys Chem 74:3396-3402

Quist AS, Marshall WL (1968a) Electrical conductances of aqueous sodium chloride solutions from 0 to 800° and pressures to 4000 bars. J Phys Chem 68:684-703

Quist AS, Marshall WL (1968b) Ionization equilibria in ammonia-water solutions to 700 °C and to 4000 bars pressure. J Phys Chem 72:3122-3128

Saul A, Wagner W (1989) A fundamental equation for water covering the range from the melting line to 1273 K at pressures up to 25000 MPa. J Phys Chem Ref Data 18:1537-1564

Shock EL, Helgeson HC (1988) Calculation of the thermodynamic and transport properties of aqueous species at high pressures and temperatures: correlation algorithms for ionic species and equation of state predictions to 5 kb and 1000 °C. Geochim Cosmochim Acta 52:2009-2036

Shock EL, Helgeson HC (1990) Calculation of the thermodynamic and transport properties of aqueous species at high pressures and temperatures: Standard partial molal properties of organic species. Geochim Cosmochim Acta 54:915-945

Shock EL, Helgeson HC, Sverjensky DA (1989) Calculation of the thermodynamic and transport properties of aqueous species at high pressures and temperatures: standard partial molal properties of inorganic neutral species. Geochim Cosmochim Acta 53:2157-2183

Shock EL, Oelkers EH, Johnson JW, Sverjensky DA, Helgeson HC (1992) Calculation of the thermodynamic and transport properties of aqueous species at high pressures and temperatures: Effective electrostatic radii to 1000 °C and 5 kb. J Chem Soc Faraday Trans 88:803-826

Shock EL, Sassani DC, Willis M, Sverjensky DA (1997) Inorganic species in geologic fluids: correlations among standard molal thermodynamic properties of aqueous ions and hydroxide complexes. Geochim Cosmochim Acta 61:907-950

Sverjensky DA, Shock EL, Helgeson HC (1997) Prediction of the thermodynamic properties of aqueous metal complexes to 1000 °C and 5 kb. Geochim Cosmochim Acta 61:1359-1412

Sweeton FH, Mesmer RE, Baes CF (1974) Acidity measurements at elevated temperatures. VII. Dissociation of water. J Solution Chem 3:191-214

Syracuse EM, van Keken PE, Abers GA (2010) The global range of subduction zone thermal models. Phys Earth Planet Interior 183:73-90

Tanger JC, IV, Helgeson HC (1988) Calculation of the thermodynamic and transport properties of aqueous species at high pressures and temperatures: revised equations of state for the standard partial molal preperties of ions and electrolytes. Am J Sci 288:19-98

Touret JLR (1985) Fluid regime in southern Norway: the record of fluid inclusions. *In*: The Deep Proterozoic Crust in the North Atlantic Provinces. Tobi AC, Touret JLR (eds) Reidel, Dordecht, p 517-549

Tropper P, Manning CE (2007a) The solubility of corundum in H_2O at high pressure and temperature and its implications for Al mobility in the deep crust and upper mantle. Chem Geol 240:54-60

Tropper P, Manning CE (2007b) The solubility of fluorite in H_2O and H_2O-NaCl at high pressure and temperature. Chem Geol 242:299-306

Tropper P, Manning CE, Harlov DE (2011) Solubility of $CePO_4$ monazite and YPO_4 xenotime in H_2O and H_2O-NaCl at 800 °C and 1 GPa: Implications for REE and Y transport during high-grade metamorphism. Chem Geol 282:58-66

Vernon RH (1979) Formation of late sillimanite by hydrogen metasomatism (base-leaching) in some high-grade gneisses. Lithos 12:143-152

Wagner W, Pruß A (2002) The IAPWS formulation 1995 for the thermodynamic properties of ordinary water substance for general and scientific use. J Phys Chem Ref Data 31:387-535

Walther JV, Helgeson HC (1977) Calculation of the thermodynamic properties of aqueous silica and the solubility of quartz and its polymorphs at high pressures and temperatures. Am J Sci 277:1315-1351

Wilke M, Schmidt C, Dubrail J, Appel K, Borchert M, Kvashnina K, Manning CE (2012) Zircon solubility and zirconium complexation in H_2O-Na_2O-SiO_2-Al_2O_3 fluids at high pressure and temperature. Earth Planet Sci Lett 349:15-25

Wohlers A, Manning CE (2009) Solubility of corundum in aqueous KOH solutions at 700 °C and 1 GPa. Chem Geol 262:310-317

Wohlers A, Manning CE (2013) Solubility of K-feldspar, muscovite and corundum in H_2O, with and without quartz at 700 °C and 1 GPa: Implications for high-pressure fluid-mineral interaction in model pelitic and granitic systems. Geochimica et Cosmochimica Acta (submitted)

Wohlers A, Manning CE, Thompson AB (2011) Experimental investigation of the solubility of albite and jadeite in H_2O, with paragonite plus quartz at 500 and 600 °C, and 1-2.25 GPa. Geochim Cosmochim Acta 75:2924-2939

Wykes JL, Newton RC, Manning CE (2008) Solubility of andradite, $Ca_3Fe_2Si_3O_{12}$, in a 10 mol% NaCl solution at 800 °C and 10 kbar: Implications for the metasomatic origin of grandite garnet in calc-silicate granulites. Am Mineral 93:886-892

Zaraisky GP (1994) The influence of acidic fluoride and chloride solutions on the geochemical behaviour of Al, Si and W. *In*: Fluids in the Crust: Equilibrium and Transport Properties. Shmulovich KI, Yardley BWD, Gonchar CG (eds) Chapman and Hall, London, p 139-162

Zhang Y.G, Frantz JD (2000) Enstatite-forsterite-water equilibria at elevated temperatures and pressures. Am Mineral 85:918-925

Zotov N, Keppler H (2000) In-situ Raman spectra of dissolved silica species in aqueous fluids to 900 °C and 14 kbar. Am Mineral 85:600-604

Zotov N, Keppler H (2002) Silica speciation in aqueous fluids at high pressures and high temperatures. Chem Geol 184:71-82

Reviews in Mineralogy & Geochemistry
Vol. 76 pp. 165-218, 2013
Copyright © Mineralogical Society of America

6

Speciation and Transport of Metals and Metalloids in Geological Vapors

Gleb S. Pokrovski[1*], Anastassia Y. Borisova[1,2], Andrey Y. Bychkov[2]

[1] Géosciences Environnement Toulouse
GET-UMR5563, Observatoire Midi-Pyrénées
Université de Toulouse
CNRS-IRD-OMP, 14 Av. E. Belin
F-31400 Toulouse, France

[2] Geological Department
Moscow State University
Leninskie Gory, Moscow
119991 Moscow, Russia

**gleb.pokrovski@get.obs-mip.fr; glebounet@gmail.com*

INTRODUCTION

Geological aqueous fluids operate in a wide range of temperatures (from 0 to 1000 °C) and depths (from Earth surface to ~10s km), over which the physical-chemical properties of water and water-salt-gas systems and, consequently, their capacities to dissolve minerals and to transport chemical elements are very different. The principal types of geological fluids are illustrated in Figure 1, showing the domains of the liquid, vapor, and supercritical fluid phases in the water phase diagram as a function of temperatures (*T*) and pressures (*P*) typical of Earth's crust. Understanding the impact of these different fluid phases on geological processes requires knowledge of mineral solubility and metal speciation and partitioning among the different fluid phases. The degree of this knowledge also significantly varies across this *T-P* range, as roughly illustrated by the three fields identified in Figure 1. In the domain of moderate-temperature aqueous solutions (light-gray field, labeled 1) a large amount of data exists about the nature and stability of major metal complexes, and thermodynamic models have been developed over ~50 years for predicting ore mineral solubilities. By contrast, it is only recently that new insights were obtained into the speciation and transport of economic metals in low-density vapor and fluid phases typical of hydrothermal-magmatic deposits (white field, labeled 2 in Fig. 1), but a number of questions still remain concerning the role of the vapor phase in metal transfers. Similarly, our current knowledge is still insufficient in the domain of high-pressure fluids typical of subduction zones (dark-gray field, labeled 3 in Fig. 1), for which very little is known about the effect of the major ligands like chloride, sulfur, carbon or silica on metal mobility. These lacks hamper our understanding of the geological impact of all these fluids in the continuity of metal and volatile transfers through Earth's entire crust.

Because the density of these aqueous phases varies over several orders of magnitude across the *T-P* range of terrestrial processes, it is convenient to consider the different types of aqueous fluid phases in terms of this parameter. In this article, we use the term "vapor" in a wider sense than it is usually employed by chemists; here it refers to a volatile fluid phase which is produced by magma degassing and/or fluid boiling over a wide *T* range (~100-1000 °C) and whose density is lower that the critical density of the given fluid composition. The term "liquid" is used for an aqueous, commonly salt-bearing, solution whose density is greater than its critical density.

1529-6466/13/0076-0006$10.00 http://dx.doi.org/10.2138/rmg.2013.76.6

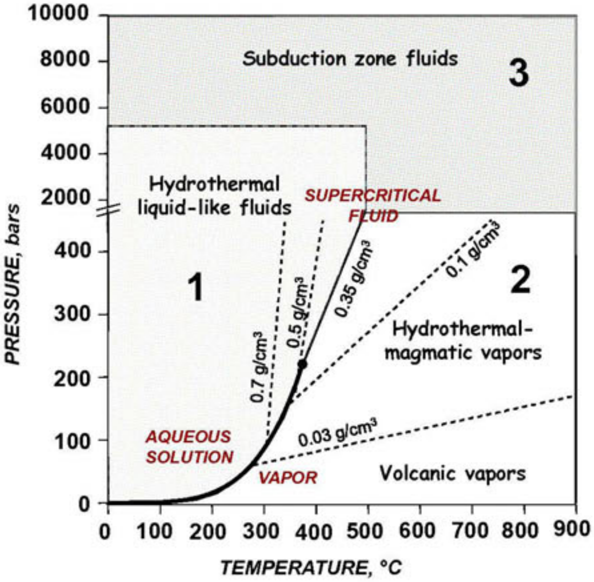

Figure 1. High-temperature part of the water phase diagram showing the domains of the different aqueous phases (liquid, vapor *sensu stricto*, and supercritical fluid) and three major types of geological fluids according to their *T*-*P*-density parameters and the degree of our knowledge of metal speciation and solubility as discussed in the Introduction.

Typical density ranges at magmatic-hydrothermal conditions on Earth are ~0.001-0.35 g/cm^3 and 0.35-1.0 g/cm^3 for vapor and liquid phases, respectively. Vapor-like terrestrial fluids may be divided into two sub-types, which mostly differ from one another by their density: volcanic vapors and hydrothermal-magmatic vapors (Fig. 1). Although there is a continuity between these vapor types in their geological *T*-*P*-depth contexts in Earth's crust, our physical-chemical knowledge of these fluids is not continuous and the available experimental and thermodynamic approaches used for their study are different, as well as the capacity of these vapors to carry and fractionate chemical elements.

If the large capacity to carry salts and metals has long been recognized for aqueous liquid-like solutions, the role of vapor in the transport of metals has been ignored owing to the fundamental assumption that, with the exception of mercury, metals and metalloids are not sufficiently concentrated in the vapor phase, and the main geological impact of magmatic and volcanic vapors is to transport volatile constituents such as water, carbon, sulfur, and chloride. As a result, until recently geological models of ore deposits assumed that metals concentrate in the dense liquid phase and boiling just promotes the partitioning of volatiles (e.g., H_2, H_2S, CO_2) from the aqueous solution to the vapor, resulting in changes of pH, redox potential, ligand concentration and, consequently, mineral solubility in the liquid phase. Recent advances in both high-*T* experimental techniques and micro-analytical tools for the study of natural fluid inclusions have substantially changed this classical point of view. In particular, a new major insight into the role of the vapor-like fluids in metal mobilization and fractionation has been provided in the past 10-15 years by measurements of major and trace element concentrations in coexisting high-density liquid (dominanly H_2O-NaCl-KCl) and low-density vapor (dominantly H_2O-HCl-H_2S±CO_2) inclusions in quartz from a variety of magmatic-hydrothermal Cu-Au-Sn-Mo-W deposits. Analyses of these inclusions, formed at *T* of 300-800 °C and *P* of 100-

1000 bars, show spectacular enrichments in Cu, Au, and, in some cases As, Sb and B, of the vapor phase compared to other metals (e.g., Zn, Fe, Ag, Mn, W, Sn, Pb), which preferentially concentrate in the dense chloride-rich solutions. Vapor separation may thus allow the selective transport of some metals, even those that are commonly believed to be nonvolatile, and is likely to provide a major contribution for both the formation of ore deposits and hydrothermal-volcanic metal fluxes into the atmosphere and biosphere. These findings can now be compared with recent laboratory experiments and physical-chemical models in water-salt-sulfur systems of vapor-brine-silicate melt partitioning and the vapor-phase solubility of minerals, allowing more accurate and systematic constraints on the major physical-chemical factors that control metal vapor-phase transport. These discoveries of the past 15 years of significant vapor-phase transport capacities for metals and metalloids are a major motivation for this review.

In this contribution, we overview the recent experimental data and thermodynamic models of the chemical speciation of metals and metalloids and the solubility of their solid phases in vapor-like fluid phases ranging from low-density volcanic gases to supercritical fluids operating at magmatic-hydrothermal conditions. We compare these data and models with the natural metal content in vapor-like phases from different geological settings to evaluate the role of these fluids in the metal transfer and formation of economic magmatic-hydrothermal ore deposits. Finally, we outline the remaining gaps and potential future directions in the research on geological vapor-like fluids.

SPECIATION, THERMODYNAMICS, AND PARTITIONING OF METALS AND METALLOIDS IN GEOLOGICAL VAPORS

Volcanic vapors

Volcanic vapors are characterized by low pressures (close to 1 bar) in a wide range of temperatures (~100-1000 °C) and are composed of ~90% of water with 0.*n* to *n*% of CO_2, H_2, HCl, H_2S and SO_2 as major components. As such, their composition strongly resembles that of dilute salt-poor hydrothermal fluids. Volcanic and fumarole vapors provide the most obvious demonstration of the geological role of vapor phases in transporting chemical elements. This type of fluid phase is briefly discussed below.

Brief outline of sublimate mineralogy and fumarole metal contents. Extensive work on volcanic gases and fumarole discharges, condensates and sublimates since the mid-20th century suggests selective vapor transport of many metals and metalloids (e.g., Symonds et al. 1987; Symonds and Reed 1993; Hedenquist et al. 1994; Hedenquist 1995; Taran et al. 1995, 2001; Pokrovski et al. 2002b). Numerous studies of their sublimation mineralogy and fumarole contents are available from many active volcanoes in the world (e.g., Hedenquist 1995; Williams-Jones and Heinrich 2005; references cited). Both naturally formed sublimates and incrustation at fumaroles' outlets to the surface (e.g., Naboko 1964; Stoiber and Rose 1974) and those formed in meter-long silica tubes inserted into fumaroles (e.g., Le Guern and Bernard 1982) unambiguously demonstrate that a volcanic vapor phase transports a plethora of major, minor and trace elements, which quantitatively precipitate on cooling. Apart from common components such as native sulfur, silicates, iron sulfides and oxides, and arsenic sulfides, volcanic sublimates were reported to contain different base and precious metal sulfide and oxide phases ubiquitous in economic magmatic-hydrothermal ores (e.g., chalcopyrite, molybdenite, wolframite, cassiterite), metal (oxy)chlorides and sulfates (e.g., $PbCl_2$, CuCl, $PbSO_4$), more exotic minerals concentrating trace elements (e.g., $Mo_3O_8{\cdot}nH_2O$, Bi-Cd-In sulfosalts, ReS_2, $CuAlAsO_5$), native metals (e.g., Si, Cu, Ti, Pb, Bi) and metallic gold and platinoids (e.g., Naboko 1964; Symonds et al. 1987, 1992; Symonds and Reed 1993; Taran et al. 2000; Yudovskaya et al. 2006). There is systematic temperature zonation in element precipitation, with minerals having high melting/sublimation temperatures and low volatility (i.e., the vapor pressure of the gas species in equilibrium with the condensed phase) precipitating at higher *T* (typically 700-900 °C; e.g., iron oxides, silicates, tungstanates) and those having low melting temperature and high volatility and solubility, and thus saturating at the lower *T* end (typically 100-300 °C; e.g., As and Pb sulfides, native sulfur). Although this zonation in different volcanic settings may be quite variable and depend on the geochemical and petrologic specificity of the magmatic system, fluid sources (magmatic vs. meteoric), and major volatile gas composition (e.g., H_2S, SO_2, HCl, HF), the main trend is driven by a combination of the temperature and volatility of the stable solid phase itself, which are the key physical-chemical parameters governing metal transport by volcanic gases, and they determine the so-called "geochemical volatility of elements" during degassing of magmas (Rubin 1997; Saunders and Brueseke 2012). More generally, sublimation mineralogy also roughly follows the condensation sequence of elements during planetary formation where temperature variations are the major variable (e.g., Cameron 1962; Wood and Hashimoto 1993).

Additional insight into volcanic vapor transport of metals is provided by direct analyses of the metal contents in fumarole condensates, whose compilations have been done in numerous previous studies for most active volcanoes in the world (e.g., Symonds et al. 1992; Taran et al. 1995, 2000; Williams-Jones et al. 2002; Williams-Jones and Heinrich 2005; references cited). In many studies, element abundances in condensates, sublimates or incrustations are expressed as an enrichment factor compared to magma, EF_i, which is the ratio of the element *i* concentration to that of a reference element (usually Mg or Ti) in the sample to the corresponding ratio in the magma: $EF_i = (C_i/C_{Mg})_{sample}/(C_i/C_{Mg})_{magma}$ (e.g., Zoller et al. 1983; Symonds et al. 1987). Because Mg and Ti concentrations are extremely low in the vapor phase compared to magmas, it follows that most metals and metalloids have enrichment factors as defined above attaining 5 to 7 orders of magnitude in gas condensates (e.g., Symonds et al. 1987; Taran et al. 1995). However, such an expression of metal volatility might be misleading as to the absolute gas-phase capacities to transport metals. In fact, despite large variations in some cases, the majority of volcanic gas and fumarole vapor samples show absolute concentrations typically less than a few ppm for base metals such as Zn, Pb, Cu, Sn, Mo, Ag or As, and less than a few ppb for Au, Pt or Re (e.g., Hedenquist et al. 1994; Hedenquist 1995; Williams-Jones and Heinrich 2005; and references therein). With a few exceptions of the most volatile elements (e.g., Hg, Cd, Se, Re), these concentrations are lower than or comparable to the mean crustal abundance of the corresponding metal (Rudnic and Gao 2003), and to its tenors in magmas from the same volcanic area. Such concentrations correspond to absolute gas/magma partition coefficients ($K_i = C_{i,gas}/C_{i,magma}$) close to or lower than 1 for most metals of economic interest with few exceptions, as exemplified in Figure 2. This figure shows that major metals (e.g., Fe, Al, Ti; Mg) are definitely not enriched in volcanic vapors, the volatility of base metals (e.g., Zn, Sn, Mo, Pb) is rather low, resulting in their enrichment of the magma by a factor of 10 to 1000, metalloids (As, B), and chalcophile metals (Ag, Au, Pt) have on average a similar preference for magma and volcanic gas, and only a few trace metals/metalloids (Re, Se, Hg-not shown) are capable of moderately enriching the gas phase (K_i ~ 10). It follows from this analysis that in the majority of cases, a volcanic vapor phase generated by shallow degassing of magma is unlikely to be capable of concentrating and transporting most metals on a large scale to form an economic ore deposit or significant geochemical anomaly. Thus modern active volcanoes can only be representative of embryonic porphyry-type magmatic-hydrothermal Cu-Au deposits, and volcanic acitivity (e.g., large caldera-forming eruptions) generally has a negative effect on the mineralization potential (e.g., Audétat and Simon 2012; references cited).

Gas-phase speciation of metals and thermodynamic modeling. One of the first attempts to apply thermodynamics to a magmatic vapor phase was that of Krauskopf (1957, 1964), who attempted to calculate the equilibrium between principal metal oxide and sulfide minerals and their ideal gas species oxides, native elements, chlorides and sulfides as a function of

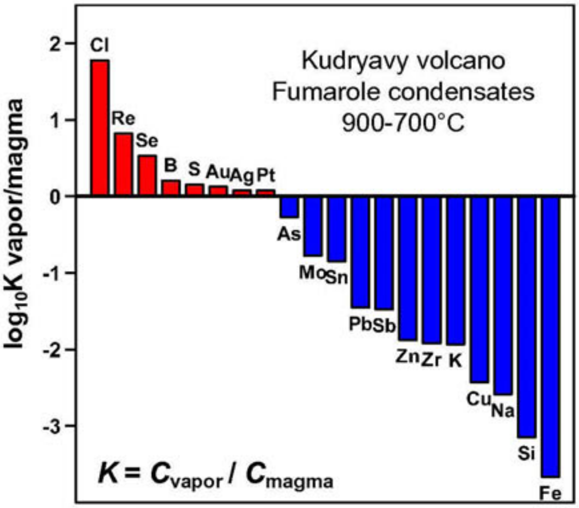

Figure 2. Vapor/magma partitioning coefficients for selected chemical elements from analyses of fumarole condensates and associated lavas or rocks from Kudryavy volcano, Kuril Islands, Russia according to the data from Taran et al. (1995).

gas-phase composition, and concluded that vapor is unlikely to be responsible for formation of large ore deposits and massive metal transport except probably for Hg, As and Sb. Since then, gas-phase transport and precipitation of many metals and metalloids have been a subject of extensive thermodynamic modeling based on gas-sublimate chemical equilibria in water-free systems at 1 bar pressure (e.g., Symonds et al. 1987, 1992; Symonds and Reed 1993; Tkachenko et al. 1999; Churakov et al. 2000; Taran et al. 2000, 2001; Pokrovski et al. 2002b; references cited) and using chloride, sulfide, oxide, oxy-chloride, hydride, and native metal gaseous species whose thermodynamic properties are available in large databases (e.g., JANAF - Chase 1998; IVTANTHERMO – Belov et al. 1999; GASTHERM - Symonds and Reed 1993; Pankratz 1982; Pankratz et al. 1987; Barin 1995). The most common methods for studying the composition and thermodynamic properties of gas species at low total pressures (less than a few bars) are measurements of the vapor pressure of a species in equilibrium with a solid phase as a function of temperature using static or dynamic (flow-through) cells that allow recovering of the condensed vapor or coupling with a high-temperature mass-spectrometer (e.g., Glemser and Wendlandt 1963; Hashimoto 1992; Meschter et al. 2013). Analyzing the solid phase solubility vs. T yields the enthalpy and entropy of the solid-gas reaction; these data coupled with the corresponding properties of the solid phase allow derivation of the enthalpy, Gibbs free energy, and entropy of the dominant gas species. In addition, the entropy and heat capacity as a function of T may also be accurately calculated by statistical mechanics approaches for ideal gas molecules and using their geometry and vibrational and rotational frequencies either from spectroscopic measurements or calculations of force constants of chemical bonds using quantum-chemistry methods (e.g., Lewis and Randall 1965; Chase 1998).

An example of species distribution calculation for arsenic in a volcanic gas is shown in Figure 3. The available thermodynamic data roughly reproduce the sublimation sequences as a function of temperature, particularly for volatile elements, as found in quartz tubes. The agreement is less good for dissolved metal concentrations in fumarole vapors. Although the variations are large, depending on the element, temperature and natural setting, the predicted gas-phase concentrations, assuming an equilibrium with a corresponding sublimate phase, are

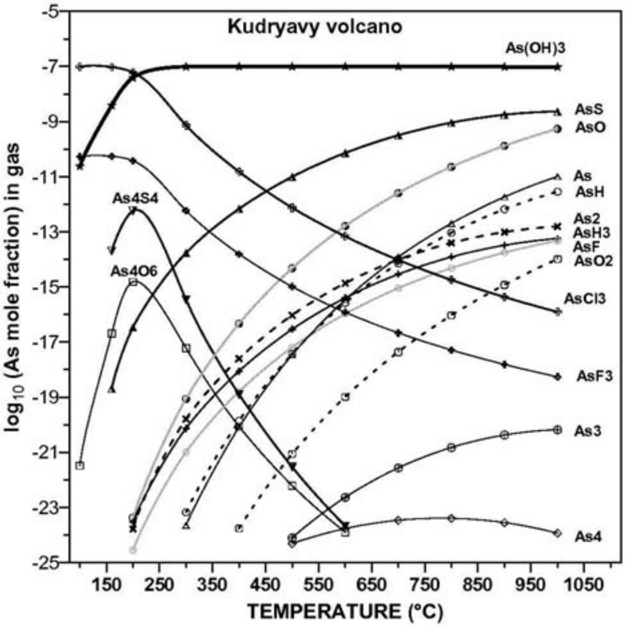

Figure 3. Calculated distribution of As gaseous species (expressed in logarithms of As mole fractions in the gas) as a function of temperature at atmospheric pressure in a cooling magmatic gas from Kudryavy volcano, Kuril Islands. The following initial gas composition, typical of high-temperature fumaroles of Kudryavy volcano, was adopted at 900 °C (in mol %): $H_2O = 94.5$, $CO_2 = 2.0$, $H_2 = 1.0$, $SO_2 = 1.5$, $H_2S = 0.5$, $HCl = 0.5$, $HF = 0.03$, and $As = 10^{-5}$ (Taran et al. 1995). Thermodynamic properties of anhydrous As gas species were taken from Belov et al. (1999), those of $As(OH)_{3(g)}$ from Pokrovski et al. (2002b). It can be seen that $As(OH)_{3(g)}$ is by far the dominant As species at temperatures above 200 °C (modified from Pokrovski et al. 2002b).

generally up to several orders of magnitude less than those measured, for both rock-forming non-volatile elements such as Mg, Al, Si, Ti, Cr (e.g., Symonds et al. 1987, 1992) and many trace metals such as Mo, W, Au, REE, PGE (e.g., Taran et al. 1995, 2000; Crocket 2000; Yudovskaya et al. 2006; Gilbert and Williams-Jones 2008). This discrepancy may be due to many factors such as (Symonds and Reed 1993; Taran et al. 1995) a) difficulties related to sampling of fumarole condensates, in particular a contamination by rock particles, b) poor constraints of the redox potential of the gas, c) kinetic issues during sublimate precipitation such as formation of thermodynamically metastable and thus more volatile phases, and d) lack of thermodynamic data for some important gas metal species. The last factor may be particularly critical for metals having a large chemical affinity for water and OH ligands. For example, experimental studies reveal that hydroxide species of many metals and metalloids ($Si(OH)_4$, $Al(OH)_3$, $B(OH)_3$, H_2MoO_4, H_2WO_4, $As(OH)_3$; e.g., Glemser and Wendlandt 1963; Bernard et al. 1990; Hashimoto 1992; Pokrovski et al. 2002b; Meschter et al. 2013), which are not systematically integrated in the common thermodynamic databases above, are extremely stable at high temperatures and water pressures far less than 1 bar and thus dominate the speciation of these elements in most volcanic gases (see Fig. 3). Thus, it seems very likely that gas-phase hydrolysis and hydration similar to those in an aqueous solution (e.g., Baes and Mesmer 1976) and dense vapor-like phase (see below) play an important role in the speciation and transport of these and other (e.g., REE, Sb, Zr, Re) metals and metalloids in volcanic gases. Their quantitative modeling requires acquisition of thermodynamic data for such important gaseous species.

Hydrothermal-magmatic vapors

Vapors forming by boiling or unmixing of hydrothermal-magmatic fluids upon their ascent and decompression in the crust at a few kilometers of depth are similar to volcanic gases in major component composition, i.e., generally H_2O-dominated (≥ 70-90 wt%) with a few to 10s wt% of CO_2, and a few wt% of chloride (HCl and alkali chlorides), and sulfur (H_2S and SO_2), and lesser amounts of other gases such as CH_4, H_2, Ar, or HF (Hedenquist and Lowernstern 1994; Giggenbach 1997). Despite these similarities in chemistry, their metal contents, as measured in fluid inclusions trapped by gangue minerals in hydrothermal deposits or sampled from drill holes in active geothermal areas, are typically 2 to 5 orders of magnitude higher than those in the vapor from the majority of volcanic fumaroles. The main difference between the surficial volcanic vapors and hydrothermal vapors at elevated pressure is the density, which increases by a factor of ~100 from the surface (ρ_{vapor}~0.001 g/cm^3 at <10 bar) to a few kilometers depth (ρ_{vapor}~0.01-0.4 g/cm^3 at 100-1000 bar; Kestin et al. 1984). Density (or water pressure) appears to be the major parameter affecting mineral solubility in the vapor phase at hydrothermal conditions. It is a driving force of enhanced hydration and hydrolysis of metals similar to aqueous liquid and supercritical fluid, as is shown below. Our interpretation of metal solubility, speciation and partitioning in hydrothermal vapor, both from nature and the laboratory, is largely based on the robust knowledge of metal speciation in the dense aqueous liquid and supercritical fluid (Fig. 1), which will be briefly outlined first.

Speciation of metals and metalloids in aqueous solution. Thanks to numerous experimental studies carried out since the 1960's-1970's, a large amount of data has been produced about the nature and stability of major aqueous species of many metals and metalloids in hydrothermal solution; they have been a subject of numerous reviews (Brimhall and Crerar 1987; Zotov et al. 1995; Seward and Barnes 1997; Wood and Samson 1998; Akinfiev and Zotov 2001; Kouzmanov and Pokrovski 2012; Pokrovski et al. 2013a; this volume; references cited). Most of these data were obtained using solubility methods in hydrothermal batch or flow-through reactors allowing sampling or quenching of the fluid phase equilibrated, at a given T and P, with a stable mineral phase, and analyzing the bulk metal concentration as a function of ligand concentrations, pH, oxygen or sulfur fugacity (see Liebscher 2007; this volume for detailed reviews of experimental techniques). Some more recent works employed *in situ* spectroscopic (mostly UV-Vis and X-ray absorption), and potentiometric methods (see Oelkers et al. 2009; this volume for an overview). The obtained data are integrated into thermodynamic equations, such as the Helgeson-Kirkham-Flowers (HKF) equation of state (Helgeson et al. 1981; Tanger and Helgeson 1988; Shock et al. 1997; Sverjensky et al. 1997), the density model (Anderson et al. 1991), or the electrostatic model (Ryzhenko 1981), enabling predictions of thermodynamic properties of aqueous metal complexes and solubility of minerals over a range of temperatures and pressures, typically to 600 °C and 5 kbar for fluid of densities above 0.4-0.5 g/cm^3, and salinities up to ~10 mol of NaCl equivalent per kg of fluid (~50-60 wt%). The resulting thermodynamic databases (e.g., SUPCRT; Johnson et al. 1992), coupled with user-friendly computer codes, allow equilibrium calculations of mineral solubility, phase relationships, and chemical speciation in fluid-mineral systems (see Oelkers et al. 2009 for a recent review).

These achievements allow the major types of aqueous metal complexes to be identified below ~500 °C in a typical liquid-like (density > 0.4 g/cm^3) hydrothermal fluid containing alkali chloride salts and sulfur as sulfide and/or sulfate (Fig. 4; see also Wood and Samson 1998; Kouzmanov and Pokrovski 2012 for more quantitative assessment of the stabilities and solubilities of major complexes of economic metals). In the majority of geological settings in which such fluids operate, metalloids such as As, Sb, Bi, Si, and B form uncharged hydroxide species (e.g., Manning 1994; Pokrovski et al. 1996, 2006; Zotov et al. 2003; Nikolaeva 2009; Tooth et al. 2013). Molybdenum and W are likely to exist as oxy-hydroxide anions and ion pairs with Na and K (Zotov et al. 1995; Wood and Samson 2000; Minubaeva and Seward 2010), but

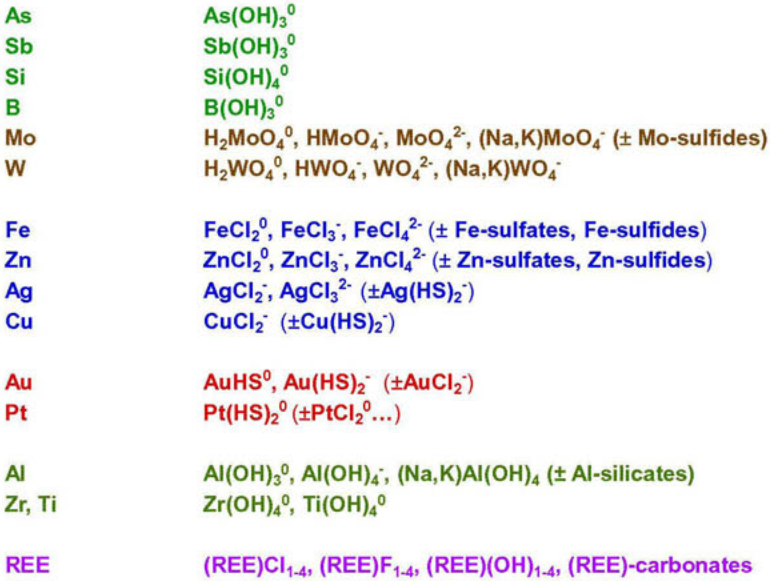

As	**$As(OH)_3^0$**
Sb	**$Sb(OH)_3^0$**
Si	**$Si(OH)_4^0$**
B	**$B(OH)_3^0$**
Mo	**$H_2MoO_4^0$, $HMoO_4^-$, MoO_4^{2-}, $(Na,K)MoO_4^-$ (± Mo-sulfides)**
W	**$H_2WO_4^0$, HWO_4^-, WO_4^{2-}, $(Na,K)WO_4^-$**
Fe	**$FeCl_2^0$, $FeCl_3^-$, $FeCl_4^{2-}$ (± Fe-sulfates, Fe-sulfides)**
Zn	**$ZnCl_2^0$, $ZnCl_3^-$, $ZnCl_4^{2-}$ (± Zn-sulfates, Zn-sulfides)**
Ag	**$AgCl_2^-$, $AgCl_3^{2-}$ (±$Ag(HS)_2^-$)**
Cu	**$CuCl_2^-$ (±$Cu(HS)_2^-$)**
Au	**$AuHS^0$, $Au(HS)_2^-$ (±$AuCl_2^-$)**
Pt	**$Pt(HS)_2^0$ (±$PtCl_2^0$…)**
Al	**$Al(OH)_3^0$, $Al(OH)_4^-$, $(Na,K)Al(OH)_4$ (± Al-silicates)**
Zr, Ti	**$Zr(OH)_4^0$, $Ti(OH)_4^0$**
REE	**$(REE)Cl_{1\text{-}4}$, $(REE)F_{1\text{-}4}$, $(REE)(OH)_{1\text{-}4}$, (REE)-carbonates**

Figure 4. Metal speciation in a typical hydrothermal fluid at $T \leq 500$ °C and $\rho \geq 0.4$ g/cm^3 in the H_2O-NaCl-KCl-HCl-H_2S-SO_4 system, according to available experimental and thermodynamic studies cited in the text.

the stability of sulfide complexes is insufficiently known at $T > 100$ °C (e.g., Rickard and Luther 2006; Zhang et al. 2012). The speciation of base and associated metals such as Cu, Fe, Zn, Pb, Cd, and Ag is largely dominated by chloride complexes (Brimhall and Crerar 1987; Wood and Samson 1998; Akinfiev and Zotov 2001; Pokrovski et al. 2013b), probably with the rare exception of some concentrated sulfate brines and low-temperature H_2S-rich waters, in which these metals may also form sulfate and sulfide complexes, respectively (e.g., Wood and Samson 1998; Rickard and Luther 2006). Gold and Pt form predominantly sulfide and/or chloride complexes depending on temperature, pH, and Cl and S contents (e.g., Sassani and Shock 1998; Xiong and Wood 2000; Pokrovski et al. 2013a). High field strength elements like Al, Ga, Zr, Hf, Ti, Cr form, depending on pH, charged or neutral hydroxide species that are usually very weakly soluble in hydrothermal fluids (Bénézeth et al. 1997; Tagirov and Schott 2001; Knauss et al. 2001). Rare Earth Elements (REE) may form hydroxide, chloride, fluoride or carbonate species depending on pH and the availability of these ligands in the fluid (e.g., Wood 1990; Haas et al. 1995; Williams-Jones et al. 2012). The exact composition (i.e., the number of ligands in the dominant complex and its electric charge) and stability (i.e., the thermodynamic stability constant) of some of these species (e.g., Fe, Zn and Cd chlorides, Bazarkina et al. 2010; Saunier et al. 2011; Pokrovski et al. 2013b; Mo and W oxy-hydroxides and Na/K ion pairs vs. oxy-chlorides and sulfides, Zhang et al. 2012; REE chlorides vs. fluorides, Williams-Jones et al. 2012) are still a matter of debate, mostly because of a lack of data. This general picture of metal-ligand affinities is consistent with the fundamental soft-hard classification of elements (e.g., Pearson 1963) and allows a first-order estimation of metal solubility and precipitation mechanisms (e.g., Crerar et al. 1985; Spycher and Reed 1989; Barnes 1997; Heinrich 2005; Kouzmanov and Pokrovski 2012; references cited).

Another fundamental property of aqueous metal cations and their complexes revealed by *in situ* spectroscopic studies (X-ray absorption, X-ray and neutron diffraction, Raman and NMR spectroscopy) and molecular modeling approaches is strong solvation by surrounding water molecules forming more or less well defined hydration spheres around the metal cation (e.g., see Magini et al. 1988; Ohtaki and Radnai 1993; Seward and Driesner 2004; Sherman 2010; Driesner 2013, this volume). The first shell coordination of many metal cations is well defined, and typically varies from 2 to 10 water molecules; it is similar to metal coordination geometry in its hydrated salts. Loose and more distant (metal-oxygen distances > ~3 Å) shells of water molecules around a metal cation are often not explicitely detected by spectroscopic techniques or molecular modeling approaches. This hydration is the fundamental cause of metal salt solubilities in water. Metal-ligand complexation in solution is also intimately linked to hydration: to form an inner-sphere complex, a ligand (e.g., Cl^-, HS^-, or F^-) substitutes for a water molecule in the nearest coordination sphere of the metal. Details of the structure of hydrated cations and their complexes with chloride, hydroxide and sulfide and their first-shell coordination changes with temperature and pressure are known for many metals and metalloids in dense aqueous solutions (Driesner 2013, this volume). It seems very likely that similar hydration and complexation mechanisms also control metal solubility, partitioning, and molecular structures in the hydrothermal vapor phase, as discussed below.

Hydration model for solid-phase solubility in vapor. Previous studies in unsaturated water vapor (i.e., at pressures below the vapor-liquid saturation curve of water or H_2O-salt solution) of salts and silica solubilities (e.g., Morey and Hesselgesser 1951; Pitzer and Pabalan 1986; Alekhin and Vakulenko 1987; references cited) and more recent works on solubility of native Au (Archibald et al. 2001; Zezin et al. 2007, 2011), CuCl (Archibald et al. 2002), AgCl (Migdisov et al. 1999; Migdisov and Williams-Jones 2013), SnO_2 (Migdisov and Williams-Jones 2005), and MoO_3 (Rempel et al. 2006) demonstrate that the dominant control of metal solubility is water pressure. Most of these measurements were conducted by sampling or quenching techniques in hydrothermal reactors, and analyzing the total metal content in the condensate as a function of water pressure, ligand content, and redox potential. They show that, at water pressures of a few hundred bars, the solubility of a metal-bearing solid phase such as oxide, chloride or native metal is many orders of magnitude higher compared to the volatility of this solid in a dry H_2O-free system, which may be described by anhydrous oxide, chloride or metal ideal gas species like those in volcanic vapors (see above). The enhanced solubility in the presence of water was interpreted by stoichiometric solid-gas reactions, for example:

$$\mathrm{AgCl_{(s)}} + n\,\mathrm{H_2O_{(g)}} = \mathrm{AgCl{\cdot}}n\mathrm{H_2O_{(g)}} \tag{1a}$$

$$\mathrm{CuCl_{(s)}} + n\,\mathrm{H_2O_{(g)}} = \mathrm{CuCl{\cdot}}n\mathrm{H_2O_{(g)}} \tag{1b}$$

$$\mathrm{MoO_{3(s)}} + n\,\mathrm{H_2O_{(g)}} = \mathrm{MoO_3{\cdot}}n\mathrm{H_2O_{(g)}} \tag{1c}$$

$$\mathrm{Au_{(s)}} + \mathrm{HCl_{(g)}} + n\,\mathrm{H_2O_{(g)}} = \mathrm{AuCl{\cdot}}n\mathrm{H_2O_{(g)}} + 0.5\,\mathrm{H_{2(g)}} \tag{1d}$$

$$\mathrm{Au_{(s)}} + \mathrm{H_2S_{(g)}} + n\,\mathrm{H_2O_{(g)}} = \mathrm{AuS{\cdot}}n\mathrm{H_2O_{(g)}} + 0.5\,\mathrm{H_{2(g)}} \tag{1e}$$

where n is the apparent hydration number, which is determined from the analysis of the metal dissolved concentration in the vapor phase in equilibrium with its solid phase as a function of water pressure or fugacity; in logarithmic coordinates it corresponds to the tangent of the slope of a plot of dissolved metal fugacity $f_{\mathrm{Ag_{(vapor)}}}$ vs. water fugacity $f_{\mathrm{H_2O}}$ (in bars), in the vapor with constant concentrations of other volatiles (HCl, H_2S, H_2), for example (Fig. 5A,C):

$$n = \left(\frac{\partial \log f_{\mathrm{Ag_{(vapor)}}} - V^{\circ}_{\mathrm{AgCl_{(s)}}}(P-1)/RT}{\partial \log f_{\mathrm{H_2O}}} \right)_{T, f_{\mathrm{HCl}}, f_{\mathrm{H_2S}}, f_{\mathrm{H_2}}} \tag{1f}$$

where P is the total pressure, T is the temperature in Kelvin, R is the universal gas constant, V° is the molal volume of the solid phase, $V^{\circ}_{\mathrm{AgCl(s)}}(P-1)/RT$ is the Pointing pressure correction (Sandler 1999) of the fugacity of silver vapor species in equilibrium with $AgCl_{(s)}$ (which does not exceed a few % of the value of the metal species fugacity at total pressures below 200

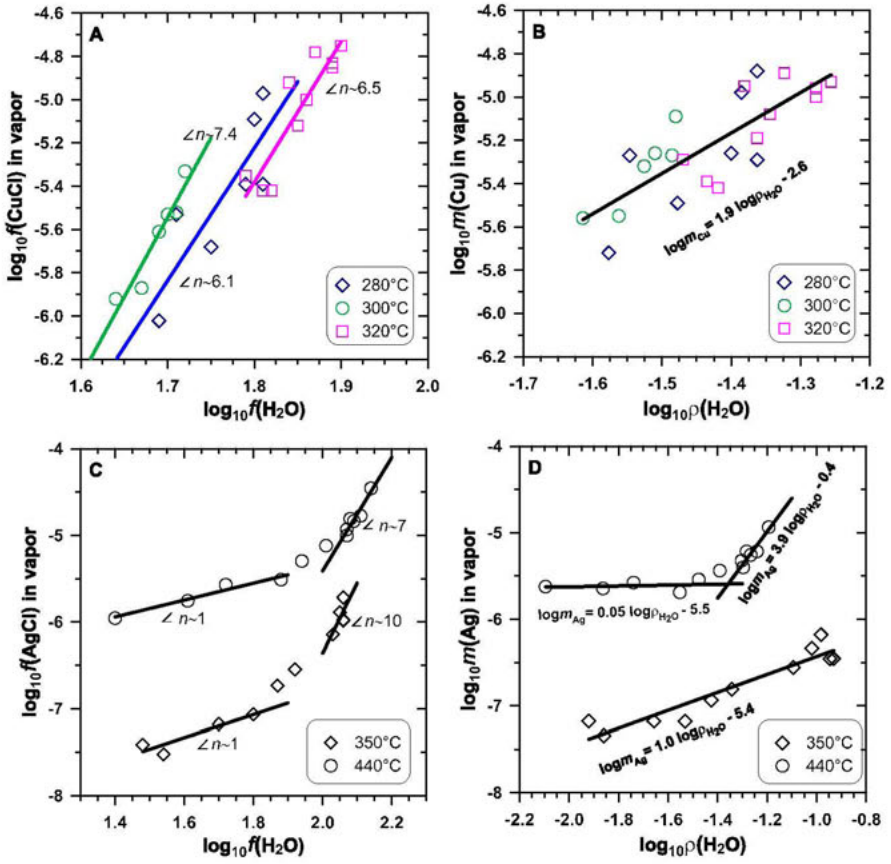

Figure 5. Comparison of the hydration model and density model for solubility of $CuCl_{(s)}$ and $AgCl_{(s)}$ in water vapor. Experimental data points are from Archibald et al. (2002) and Migdisov and Williams-Jones (2013) for Cu and Ag, respectively. Note small but non-systematic changes with temperature of the average hydration number (n, which is the tangent of the slope in this plot according to equation 1b) for the dominant $CuCl\cdot nH_2O$ species in the narrow H_2O fugacity range studied (A). Alternatively, all data points, expressed in Cu molality (mol Cu/kg H_2O), independently of T, may be described within the data scatter by a single linear equation (4b) involving the water density (B). For $AgCl_{(s)}$ whose solubility was studied in a wider H_2O pressure range, there are large changes in hydration number with increasing pressure, whose interpretation requires a large number of hydrated species (C). Alternatively, all data points at 350 °C may be fitted by a single straight line vs. water density according to equation (4b), but at 440 °C they reveal at least two different dependencies on water density (D), which may be due to changes in the nature of Ag species in the vapor from hydrated AgCl to $AgCl_2^-$ or $HAgCl_2$ in the supercritical domain.

bars), and $f_{Ag_{(vapor)}} = X_{Ag_{(vapor)}} P_{H_2O} \; _{H_2O}$, where$\gamma X_{Ag_{(vapor)}}$ is the mole fraction of dissolved silver in the vapor, P_{H_2O} is water vapor pressure, which is close to the total pressure (in bars), and γ_{H_2O} is the fugacity coefficient of the dissolved Ag hydrated species, which was assumed to be equal to that of water in those studies. Equation (1f) is based on classical gas-phase thermodynamics and mass action law of stoichiometric hydration reactions like those in (1a) to (1e); its detailed derivation is given in Williams-Jones and Heinrich (2005). Figure 5 shows an example of the hydration approach applied to the solubility of $CuCl_{(s)}$ and $AgCl_{(s)}$ in unsaturated water vapor.

Apparent hydration numbers obtained in such a way, however, vary between 0 and ~15, depending on the species, T, and P; in most cases, they increase systematically with pressure

(Migdisov and Williams-Jones 2013; references therein). Large changes in hydration number were reported by these authors over a rather limited *T* (~300-350 °C) and P_{H_2O} (~20-200 bar) range (e.g., $AuCl{\cdot}nH_2O$, $n = 3$ to 5; $MoO_3{\cdot}nH_2O$, $n = 2$ to 4; $CuCl{\cdot}nH_2O$, $n = 6$ to 8; Archibald et al. 2001, 2002; Rempel et al. 2006). More recently, Migdisov and Williams-Jones (2013) extended solubility measurements of $AgCl_{(s)}$ in water vapor over a larger *T*-*P* range (to 440 °C and ~250 bar) and reported an exponential increase of $AgCl_{(s)}$ solubility with increasing *P*, which corresponds to hydration numbers higher than 10 at the highest pressure investigated (Fig. 5C). They analyzed these data using 14 stepwise hydrated species, from $AgCl{\cdot}H_2O$ to $AgCl{\cdot}14H_2O$ and derived their Gibbs free energies as a function of *T* and *P*. However, it should be noted that large uncertainties are intrinsic to the determination of *n* values in the coordinates $f_{Ag_{(vapor)}}$-f_{H_2O}; they strongly increase with increasing the slope of the solubility curve. Moreover, the number of experimental data points of $AgCl_{(s)}$ solubility (see Fig. 5) is comparable to and at some temperatures lower than the number of hydrated species used for their description, so that it is uncertain whether such stepwise hydration does occur in the vapor. Furthermore, the large hydration numbers derived from the classical thermodynamic equations above may appear ambiguous from a molecular structure view; such large numbers correspond to rather distant outer-sphere water molecules around the metal which can neither be constrained by available spectroscopic techniques (e.g., XAS, NMR, XRD), most of which are only sensitive to the nearest coordination sphere around the metal in the fluid phase, nor by molecular dynamics modeling, which does not detect discrete water molecules or well-defined hydration shells beyond the first shell around the metal ion even in dense aqueous solution (e.g., Sherman 2010; Pokrovski et al. 2013b).

Similarly, by analyzing the tangent of the slope in a plot of metal solubility versus HCl, H_2 or H_2S fugacity at a fixed P_{H_2O} for reactions like:

$$Au_{(s)} + m\ HCl_{(g)} + n\ H_2O_{(g)} = AuCl_m{\cdot}nH_2O_{(g)} + 0.5m\ H_{2(g)} \quad (2a)$$

$$Au_{(s)} + m\ H_2S_{(g)} = AuS{\cdot}(m-1)H_2S_{(g)} + H_{2(g)} \quad (2b)$$

one can derive the apparent ligation number, *m*, (i.e., the number of HCl or S ligands in the dominant species) and the metal valence state, *s*:

$$m = \left(\frac{\partial \log f_{Au_{(vapor)}}}{\partial \log f_{H_2S}} \right)_{T, f_{H_2O}, f_{H_2}} \quad (2c)$$

$$s = 2\left(\frac{\partial \log f_{Au_{(vapor)}}}{\partial \log f_{H_2}} \right)_{T, f_{H_2O}, f_{H_2S}} \quad (2d)$$

The coefficient 2 in Equation (2d) is because H_2 formation or consumption involves two electrons. The derived ligation numbers for metals are systematically smaller than the hydration numbers above and do not vary significantly over the investigated ligand concentration range; for example, in the HCl-bearing vapors they are close to ~1 for Au, Cu and Ag, suggesting the dominant presence of monochloride vapor species CuCl, AgCl and AuCl hydrated in a variable extent by water molecules (Migdisov et al. 1999; Archibald et al. 2001, 2002); and are close to 3 for Au in the H_2S-bearing system (Zezin et al. 2007). However, because of the data scatter and limited *T*-*P* and ligand concentration ranges covered so far by the available data, exact ligation numbers are also subjected to significant uncertainties. For example, Reactions (1e) and (2b) require Au redox state to be +2 ($s = 2$) and coordination number 3 ($n = 2$, $m = 3$) in the species formed. This contradicts the dominant Au redox state of +1 and typical coordination numbers of 2 in fluids and minerals at hydrothermal conditions (e.g., Seward 1989; Stefánsson and Seward 2004; Pokrovski et al. 2009a,b, 2013a; cited references), reflecting the general difficulties of precise derivation of metal speciation from bulk solubility data only. Another limitation of the hydration model is the impossibility of constraining the degree of polymerization of a gaseous species based on the analysis of solubility data in the vapor phase; for example, the formation of a copper chloride trimer, $Cu_3Cl_3 \cdot nH_2O$ (Archibald et al. 2002), yields the identical Cu solubility dependence vs. f_{H_2O} or f_{HCl} as that for the $CuCl \cdot nH_2O$ monomer described by Reaction (1b).

In summary, despite the limitations of the hydration model discussed above, these important studies confirm three fundamental controls on vapor-phase transport of metals: a) in the hydrothermal vapor phase, metals form complexes with the same ligands as in aqueous solution (chloride, sulfide, or hydroxide); b) in contrast to the aqueous solution or hypersaline liquid, the major vapor species are uncharged (at least in unsaturated vapor below the water critical point), in agreement with the low dielectric constant of the vapor favoring ion association and neutral species stability; and c) as in aqueous solutions, the metal complexes are solvated by water molecules; the higher the pressure the more metal that can be dissolved in the vapor phase in equilibrium with a metal-bearing solid or melt. The relatively narrow *T-P* range of available measurements and large uncertainties intrinsic to the elevated hydration numbers changing for a given species make practical application of these results difficult to conditions of natural hydrothermal-magmatic vapor phases. As was emphasized by the authors themselves (Migdisov and Williams-Jones 2013), although hydration can enhance the solubility of metals by orders of magnitude, concentrations of Cu, Au, Sn, and Mo determined in the laboratory, even at the highest hydration numbers or those extrapolated to higher *T* and *P*, are typically ~3 to 4 orders of magnitude lower than those measured in vapor inclusions from hydrothermal-magmatic deposits (see below and Kouzmanov and Pokrovski 2012; references cited). This discrepancy means that metals form species in the natural hydrothermal-magmatic vapor phase other than in the laboratory experiments discussed above and/or extrapolations to higher *T-P* using this hydration approach are not accurate enough. Another difficulty when extrapolating to the solubility data of natural systems on simple chlorides and oxides used in laboratory measurements above is that in most cases these phases are too soluble to be stable in high-*T* hydrothermal settings in which sulfide minerals are the solubility-controlling phases for most base and precious metals.

Model of solid-phase solubilities and vapor-liquid distribution based on ideal gas species. Another model, alternative to the hydration approach, may be applied for species that exist in an ideal gas state similar to that in H_2O-poor low density volcanic gases. This model mostly concerns volatile non-electrolytes (gases and organic molecules) and some metalloids (B, Si, As, Mo) that exist as neutral oxy-hydroxide species over a wide range of water pressures (see above). The model is based on the knowledge of thermodynamic properties of ideal gas species; it has been successfully applied for describing vapor-liquid equilibria of gases, volatile organic compounds and a few metalloids (Plyasunov and Shock 2003; Plyasunov 2011a,b, 2012). Combining these thermodynamic properties with fugacity coefficients as a function of *T* and *P* allows calculating solubilities of oxides in steam and vapor-liquid partitioning. For example, for the dissolution reaction at given *T* and *P*:

$$SiO_{2(s)} + n\ H_2O_{(g)} = SiO_2 \cdot n(H_2O)_{(g)} \tag{3a}$$

Its equilibrium constant is described as

$$\ln K^{\circ}(T) = \ln \frac{X_2 \cdot (P/P^{\circ})\varphi_2^{\infty}}{(f_1)^n} - \frac{V(SiO_{2(s)}) \cdot (P - P^{\circ})}{RT} \tag{3b}$$

where X_2 is the mole fraction of the dissolved metal in the vapor phase, f_1 is the fugacity of pure water, $n = 2$ for silica, φ_2^{∞} is the fugacity coefficient of the dissolved species at infinite dilution in water vapor, V is the molal volume of the solid phase, and P° is the standard pressure (1 bar). The values of $K^{\circ}(T)$ can be calculated from the thermodynamic properties of Reaction (3a) constituents at the standard pressure. The fugacity coefficients of the dissolved species at higher water pressures are estimated using the following equation based on the virial equation of state:

$$\ln\varphi_2^{\infty} = \frac{2B_{12}}{V_1} \quad \ln\frac{PV_1}{RT} \tag{3c}$$

where B_{12} is the second mixed virial coefficient for the gas-phase interaction between the dissolved hydroxide or hydrated oxide species and water, and V_1 stands for the molal volume of pure water. The coefficient B_{12} is approximated using the relationship $B_{12} \approx k\ B_{11}$, where B_{11} is the second virial coefficient of water, which is well known (Harvey and Lemmon 2004), and k is equal to the number of hydroxide groups or water molecules in the dissolved oxide or hydroxide species. This approach has been used for describing silica and boric acid solubilities and vapor-liquid partitioning coefficients using the thermodynamic properties of their main gaseous forms $Si(OH)_4$ and $B(OH)_3$ (Plyasunov 2011a,b, 2012). Although the method is quite accurate and straightforward thermodynamically, it is only applicable to species that exist in both water-poor and water-rich vapors and for which thermodynamic properties are available in the ideal gaseous state. This is not the case for most metals whose vapor-phase speciation and hydration degree change significantly with increasing water pressure (or density).

Density model for mineral solubility in water vapor. In view of the large variations of apparent hydration numbers in metal-bearing species and changes in their ligation numbers over the large *T-P* range of natural systems, it is appropriate to consider alternative approaches that relate solubility to vapor-phase density. Such approaches do not require the knowledge of exact chemical species in the vapor or fluid phase (which may be multiple and hydrated in variable degree depending on P_{H_2O}); they use the two major and easily accessible macroscopic parameters of the fluid and vapor phases, which are temperature and density. The combined effect of T and steam density on the solubility of oxide and silicate minerals was observed more than 60 years ago (e.g., Morey and Hesselgesser 1951), but it is only since the 1980's that it has been applied in a systematic way to describe the dissociation constants of water, acids, and bases in aqueous solution and mineral solubilities over a large T-range (e.g., Marshall and Franck 1981; Mesmer et al. 1988; Anderson et al. 1991; references therein), using equations involving T and ρ_{H_2O}:

$$\log K = A + \frac{B}{T} + \frac{C}{T^2} + \frac{D}{T^3} + \left(E + \frac{F}{T} + \frac{G}{T^2}\right)\log\rho_{H_2O} \tag{4a}$$

where K is a reaction constant (or dissolved element concentration in the case of mineral dissolution); A, B, C, D, E, F and G are T-P-independent constants; T is temperature in Kelvin; and ρ_{H_2O} is the water density. Depending of the available *T-P* data range of experimental data, simplified equations derived from Equation (4a) may be used to describe the solubility of minerals in aqueous fluids:

$$\log K = A + E\log\rho_{H_2O} \tag{4b}$$

$$\log K = A + \frac{B}{T} + E\log\rho_{H_2O} \tag{4c}$$

$$\log K = A + \frac{B}{T} + \frac{F\log\rho_{H_2O}}{T} \tag{4d}$$

Such equations were very efficient for describing quartz solubility (e.g., Morey 1957; Fournier and Potter 1982; Manning 1994) and other silicate minerals (Dolejs and Manning 2010) in supercritical fluid over a very wide hydrothermal-magmatic *T-P* range, from hydrothermal steams to subduction-zone fluids, and other metalloid and metal oxides (e.g., GeO_2, Pokrovski et al. 2005b; CuO, Palmer et al. 2004a), over more limited *T-P* windows.

Because these models have significant predictive power, they may be applied for describing solid solubilities in HCl-bearing water vapor, as shown in Figure 5(b,d) for $CuCl_{(s)}$ and $AgCl_{(s)}$. It can be seen that $CuCl_{(s)}$ solubility measured by Archibald et al. (2002) from 280 to 320 °C and in a limited P range (50-100 bars) is matched by Equation (4b) over the whole set of data and independently of temperature. The same equation performs well for $AgCl_{(s)}$ solubility at 350 °C between 30 and 170 bars, measured by Migdisov and Williams-Jones (2013). Such simple relationships point out that Cu and Ag speciation (and likely 1st shell coordination) in the vapor phase remains constant over the studied T-P range, with CuCl and AgCl complexes hydrated by a variable number of water molecules. In contrast, their data for Ag at supercritical temperatures (400 °C - not shown, and 440 °C - Fig. 5D) reveal at least two different dependencies of water density described by Equation (4b). This may imply significant changes of Ag speciation or coordination with increasing P_{H_2O} (and density) at these elevated temperatures, with formation of different Ag species, such as $HAgCl_2$, also evoked at magmatic temperatures in HCl-bearing water vapors (Simon et al. 2008; Migdisov and Williams-Jones 2013) or reduction of Ag first-shell coordination with increasing temperature, similar to that observed in dense aqueous solutions for Ag and other transition metals (Crerar et al. 1985; Bazarkina et al. 2010; Pokrovski et al. 2013b). Thus the density model may potentially allow identifying speciation changes in the vapor phase; however more data in a wider T-P-density range are required for most metals to make it as predictive as for the dense aqueous solutions and supercritical fluids. Similar density models are accurate enough for describing the vapor-liquid fractionation of various metals, as will be shown below.

Fluid density control on vapor-liquid partitioning of metals in S-free systems. Vapor-liquid equilibria and partitioning of alkaline and alkaline earth metal chlorides (LiCl, NaCl, KCl, $CaCl_2$, $MgCl_2$, $SrCl_2$), halogens (HCl and HBr), sulfate (H_2SO_4, $NaHSO_4$) and ammonia have been a subject of considerable experimental and modeling efforts; most of these data were summarized in the excellent compilation of Liebscher (2007). To date, the best known system is no doubt H_2O-NaCl, whose *PVTX* properties in two- and three-phase regions are accurately described over a wide T-P range (see Driesner and Heinrich 2007; references therein). Until recently little effort has been devoted, in contrast, to trace and economic metal and metalloid partitioning in vapor-liquid systems for which only scarce data were available until the 2000's (e.g., Martynova 1964 and references therein; Bischoff and Rosenbauer 1987; Kukuljan et al. 1999).

New insight into the vapor transport of economic metals like Au, Cu, Ag, Fe, Zn, Mo, Pt, REE has recently been offered by direct measurements of vapor-liquid partition coefficients of metals in model two-phase salt-water systems (H_2O-NaCl/KCl-HCl) analogous to brine- and vapor-like fluid inclusions from magmatic-hydrothermal Cu-Au-Mo-Sn deposits at temperatures from ~300 to 500 °C and pressures from P_{sat} to ~500 bar (Shmulovich et al. 2002; Pokrovski et al. 2005a, 2008a,b; Pokrovski 2010; Rempel et al. 2009, 2012). Vapor-liquid partitioning of alkali trace metals (Li, Rb, Cs) and metalloids (B, As, Si) was recently examined in water-salt systems pertinent to boiling sub-seafloor geothermal systems, and epithermal metal deposits (e.g., Pokrovski et al. 2002b, Liebscher et al. 2005; Foustoukos and Seyfried 2007a,b). These measurements were performed using constant-volume or flexible-cell hydrothermal reactors allowing sampling of the vapor and liquid phases.

All these works demonstrate that the vapor-liquid distribution of elements obeys simple relationships involving the densities of the coexisting vapor and liquid phases. Figure 6 shows that on a logarithmic scale the partition coefficient of each metal, $K_{vapor/liquid}$, which is the ratio of metal mass concentrations in the coexisting phases, C_{vapor}/C_{liquid}, is linearly proportional to the ratio between the vapor and liquid densities ($\rho_{vapor}/\rho_{liquid}$), which are well known in the H_2O-NaCl system (e.g., Driesner and Heinrich 2007):

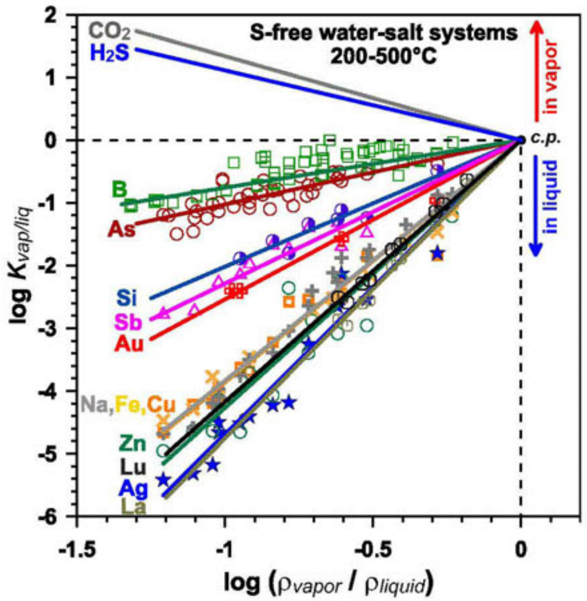

Figure 6. Vapor-liquid partition coefficients, $\log K_{\text{vap/liq}} = \log (m_{\text{vapor}}/m_{\text{liquid}})$, where m is the number of moles of the element per 1 kg of fluid in the corresponding phase, of different metals and metalloids at two-phase equilibrium in the system H_2O + NaCl ± KCl ± HCl; at ~200 to 600 °C as a function of the vapor-to-liquid density ratio. Symbols stand for experimental data from the following sources: B – Styrikovich et al. (1960), Kukuljan et al. (1999), Liebscher et al. (2005), Foustoukos and Seyfried (2007b); As^{III} – Pokrovski et al. (2002a, 2005a); Si, Na, Zn, Fe^{II}, Cu^{I}, Ag^{I} and Au^{I} – Pokrovski et al. (2005a); Sb^{III} – Pokrovski et al. (2005a, 2008b); Lu and La – Shmulovich et al. (2002). Limited data for Mo^{VI} (Rempel et al. 2009) and Pb (Pokrovski et al. 2008b) plot close to As/B and Zn/Fe/Cu, respectively (omitted for clarity). Data for Cu (not shown for clarity) from Rempel et al. (2012) plot close to those in this figure at 400 °C, but at 350 °C and 450°C exhibit large scatter, up to 2 orders of magnitude of $K_{\text{vap/liq}}$ values at similar vapor/liquid density ratios, and are generally 1-3 orders of magnitude higher than those shown here; these discrepancies are likely due to experimental difficulties related to sampling and analyses of below-ppm level Cu concentrations in their experiments (see discussion in Rempel et al. 2012). Lines for metals and metalloids represent the regression through origin (i.e., critical point, c.p.) of the experimental data for each element using the equation $\log K = n \log(\rho_{\text{vapor}}/\rho_{\text{liquid}})$, where n is an empirical coefficient for each metal (Eqn. 5, see text). For comparison, lines for gases CO_2 and H_2S are linear regressions of $\log K$ values calculated using the corresponding Henry constants between 150 and 350 °C at P_{sat} from the SUPCRT database (Jonhson et al. 1992).

$$\log K_{\text{vapor/liquid}} = n \log \frac{\rho_{\text{vapor}}}{\rho_{\text{liquid}}} \tag{5}$$

where n is the empirical regression coefficient for each metal, which reflects the extent of vapor-phase hydration, species volatility, and metal speciation in the liquid phase (see below). All lines tend to converge to the critical point of the system where the concentrations are identical in both phases and the partition coefficient is, by definition, equal to one.

Such "ray diagrams" have long been known for the partitioning of salts and acids between vapor and aqueous solution (e.g., Styrikovich et al. 1955; Alvarez et al. 1994). They stem from classical thermodynamics and statistical mechanics, showing that the hydration energy of a solute evolves linearly with the solvent density (Bischoff et al 1986; Harvey and Levelt Sengers 1990; Alvarez et al. 1994; Palmer et al. 2004b). In S-free water-salt systems, where the speciation of metals and metalloids is dominated either by hydroxide or chloride complexes (Fig. 4), and where no large changes in speciation over the investigated *T-P*-salinity range occur, any significant deviation from a linear trend with an origin at the critical point should be regarded as an experimental/analytical artifact (e.g., Pokrovski 2010).

The relationships in Figure 6 confirm the validity of this model for a variety of metals and metalloids in a wide temperature range. They support the findings in unsaturated vapor systems (see above) and demonstrate that water-solute interaction (i.e., hydration) is a key factor controlling metal vapor-phase solubility and vapor-liquid partitioning. The following trend of element volatility in a two-phase water-salt system in the order of decreasing their $K_{\text{vapor/liquid}}$ values may be established on the basis of available experimental data: $B \approx As^{III} \approx Mo^{VI} > Si \approx Sb^{III} \approx Au^{I} > Cu^{I} \approx Fe^{II} \approx Na \approx K \geq Zn > Ag \approx Cd \approx$ REE. Metalloids that form neutral hydroxide species both in the vapor and liquid (Pokrovski et al. 2002b) are distinctly more volatile than most metals forming charged chloride complexes in the liquid phase (Fig. 4). Gold that forms predominantly $AuCl_2^-$ in the S-free salt-bearing liquid phase (Pokrovski et al. 2009a,b, 2013a) appears to be the most volatile of economic metals investigated so far, as indicated by the few available experimental data points (Pokrovski et al. 2005a). The least volatile metals are Ag, Cd (not shown), and REE^{III}; their low volatility is likely due to the enhanced stability of their charged chloride complexes in salt-rich liquids (Bazarkina et al. 2010; Pokrovski et al. 2013b). The exact nature and stoichiometry of metal chloride species in the vapor phase remain unclear. Rare available data on the stabilities and hydration numbers (*n*) of $AuCl{\cdot}nH_2O$, $CuCl{\cdot}nH_2O$, and $AgCl{\cdot}nH_2O$, derived from experiments at $P_{H_2O} <$ ~200 bar discussed above (Migdisov et al. 1999; Archibald et al. 2001, 2002; Migdisov and Williams-Jones 2013), predict Au, Cu and Ag concentrations in the saturated vapor phase of water-salt systems up to several orders of magnitude lower than the experimental data shown in Figure 6, and the metal content in vapor-like inclusions from magmatic-hydrothremal deposits (see below). This discrepancy indicates that a) apparent hydration numbers of such vapor species (see Eqns. 1a-e) are likely to increase with increasing pressure or density making it difficult accurate predictions at pressures above those covered by the experiments (Migdisov and Williams-Jones 2013), and/or b) the dominant species of these metals in the vapor phase over the large density range of water-salt systems are probably not simple uncharged mono-chlorides. With the pressure rise and the vapor density approaching that of the liquid, resulting in an increase of chloride content of the vapor phase and its dielectric constant, it may be expected that the vapor would contain chloride species of higher ligation numbers, similar to those in the coexisting liquid (Fig. 4).

Whatever the exact species stoichiometry for metals in the vapor phase, it can be seen in Figure 6 that, contrary to As and B (±Mo, not shown) whose $K_{\text{vapor/liquid}}$ values approach one, gold, copper and other economic metals are unable to enrich the vapor phase relative to the coexisting liquid. All of them are concentrated in the liquid by a factor of 10 to 1000 at conditions typical of vapor-brine separation in porphyry and related systems at temperatures to at least 500 °C. For comparison, gases (CO_2, H_2, H_2S) and volatile acids (HCl) systematically display vapor-liquid distribution in favor of the vapor phase, which may also be roughly described by Equation (5) sufficiently for most practical geochemical purposes (Fig. 6); a more detailed account of gas partitioning is beyond the scope of the present paper. The patterns of Figure 6 coupled with the knowledge of liquid-phase speciation of metals (Fig. 4) allow the following qualitative controls on vapor-liquid fractionation to be identified: a) because the strength and extent of hydration of a solute are a primary function of the aqueous fluid density, which are lower in the vapor compared to the coexisting liquid, the stronger the hydration the less metal partitions into the vapor phase, thus preferring the dense aqueous solution to the vapor; b) charged complexes, which are far stronger hydrated than their neutral counterparts, are less volatile; c) most metals and metalloids form mononuclear species in the vapor phase similarly to their main complexes in aqueous solution, as demonstrated by the independence of $K_{\text{vapor/liquid}}$ values of total dissolved concentration; and d) the distribution of the ligand itself between vapor and liquid also influences metal partitioning, e.g., the increase of salt concentration in the liquid with increasing the vapor/liquid density contrast lowers the vapor partitioning of metals, forming charged chloride complexes; in contrast, the increase of volatile content of the vapor (H_2S, HCl) will favor the volatility of elements forming neutral chloride and sulfide complexes. The effects of HCl, fluid acidity, and sulfur on vapor-liquid partitioning are discussed below.

Effect of HCl on vapor-liquid partitioning. Hydrochloric acid is an important constituent of natural vapors. Its effect on vapor-liquid partitioning has been examined in detail for As^{III} (Pokrovski et al. 2002b, 2005a), Sb^{III} (Pokrovski et al. 2005a, 2008b), and Cu, Zn, Fe and Ag (Pokrovski et al. 2005a) in H_2O-NaCl-HCl systems at 350-400 °C. It can be seen in Figure 7 that the partitioning coefficients of arsenic are independent of the HCl vapor phase content (up to at least 0.2 moles HCl per kg of vapor), which is typical of natural systems and in agreement with the large stability of $As(OH)_3$, both in vapor and liquid (Pokrovski et al. 2002b). The partition of Zn, Cu, Fe, Ag (and Au - not shown) is also independent of HCl, suggesting that their speciation, dominated by chloride complexes, is likely to be similar in both phases. Antimony partitioning is not affected by the presence of a moderate HCl content (< 0.1 wt% HCl in vapor), but at higher HCl concentrations Sb is enriched in the vapor, consistent with the formation of volatile (hydroxy)chloride species as shown by *in situ* X-ray absorption spectroscopy (XAS) in vapor-brine systems (Pokrovski et al. 2008b). Consequently, the vapor-liquid fractionation patterns for Sb, which are sensitive to HCl content, may be indicative of the acidity and chlorinity conditions in a magmatic-hydrothermal system. Thus As/Sb ratios in coexisting brine and vapor-like inclusions may be used as an indicator of pH and HCl content of during fluid unmixing and boiling in natural systems (e.g., Pokrovski et al. 2008b).

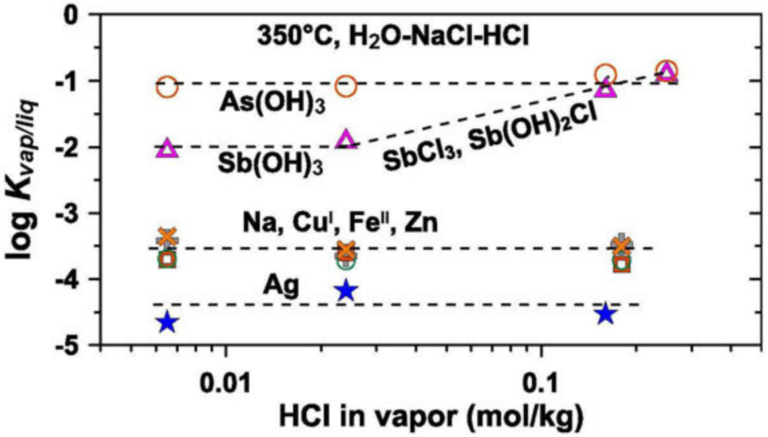

Figure 7. The effect of HCl on the vapor-liquid partitioning coefficients of metals and metalloids in the H_2O-NaCl-HCl system at 350 °C (modified from Pokrovski et al. 2005a).

Effect of liquid-phase metal speciation on vapor-liquid partitioning. The vapor-liquid distribution patterns of metals and metalloids discussed above suggest that the identity and stability of their dominant species in the liquid phase should influence their partitioning in the vapor. For example, a change in pH of the liquid phase leading to deprotonation of neutral hydroxide complexes of metalloids will result in a decrease of vapor-liquid partitioning because of the lower volatility of the formed charged anions. This is illustrated in Figure 8 showing that vapor-liquid partition coefficients of arsenious acid measured as a function of the liquid phase pH at 350 °C (Pokrovski et al. 2002b) closely follow the fraction of the neutral $As(OH)_3$ species

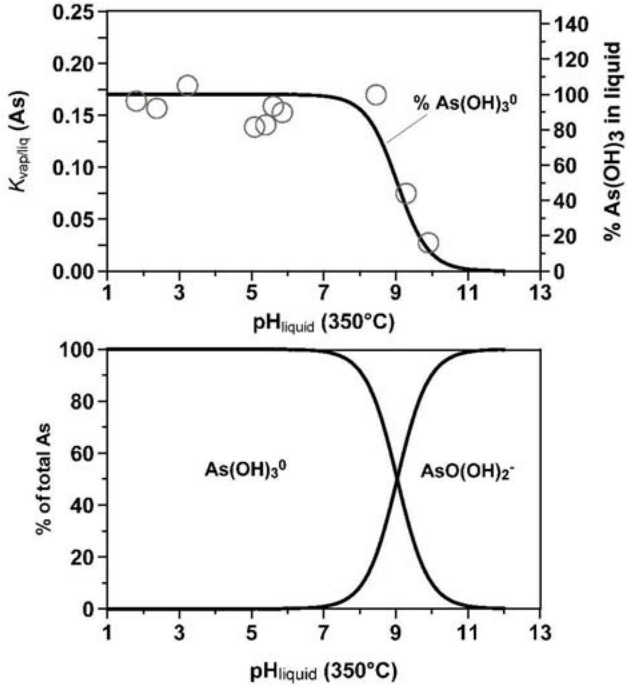

Figure 8. The effect of liquid-phase pH on As^{III} vapor/liquid partition coefficient ($K_{vap/liq}$) at 350 °C and P_{sat} (upper graph). The symbols represent average values from experiments reported by Pokrovski et al. (2002b); the solid curve shows the percentage (with respect to total dissolved As) of the aqueous $As(OH)_3$ species in solution. The calculated distribution of As hydroxide species in solution as a function of pH at an ionic strength of 0.1 is shown in the lower graph. With increasing pH, the measured $K_{vap/liq}$ values closely follow the amount of neutral $As(OH)_3$ in solution, demonstrating that charged aqueous species ($AsO(OH)_2^-$) insignificantly contribute to arsenic volatility (modified from Pokrovski et al. 2002b).

in the liquid, which is constant at $pH < 9$ but decreases at a higher pH due to the formation of its dissociated counterpart, $AsO(OH)_2^-$. Similar behavior was observed for other metalloids like Si, B, and also Mo, forming neutral oxy-hydroxide species in aqueous solution (Fig. 4), which deprotonate at an alkaline pH (Styrikovich et al. 1959; Martynova et al. 1964; Rempel et al. 2009). Analogous trends hold for Au and probably Cu sulfide species (see below and Pokrovski et al. 2008a). Very recent experimental data on Ga oxy-hydroxide (α-GaOOH) solubility in vapor phase as a function of water pressure and HCl concentration (Nekrasov and Bychkov 2011; Nekrasov et al. 2013), coupled with the knowledge of Ga speciation in the liquid phase as a function of pH (Bénézeth et al. 1997, Pokrovski et al. 2002a) suggest that a maximum value of the vapor-liquid partitioning coefficient of Ga is at a pH around 4 at 150° and 200 °C, corresponding to the predominance of the neutral $Ga(OH)_3$ complex in the liquid and vapor. Such dependencies for species of very different nature (hydroxide, sulfide or chloride) clearly demonstrate that, with all other parameters being equal, the extent of vapor enrichment by a chemical element is largely determined by the fraction of its uncharged form in the liquid.

Vapor-liquid partitioning of metals in sulfur-free systems at magmatic conditions. At temperatures of 600-800 °C, corresponding to last stages of silicic melt crystallization and fluid degassing in porphyry systems, limited experimental data were recently obtained using the method of synthetic fluid inclusions trapped in quartz for Au, Cu, Zn, Ag, and Fe in S-free systems containing Na, K, and Fe chloride saline liquids, silicate melts, and H_2O-HCl vapor phases (e.g., Simon and Ripley 2011; Kouzmanov and Pokrovski 2012; Pokrovski et al. 2013a for details). In contrast to the vapor-liquid systems below 500 °C discussed above, the interpretation of these data in terms of different metal species in vapor and liquid phases is not possible at present owing to the paucity of data, limited *T-P*-composition range of measurements, and the absence of robust thermodynamic models for metals in magmatic fluids.

The available vapor/liquid partition coefficients roughly follow density relationships similar to those established for lower-temperature hydrothermal conditions (Fig. 6), although with absolute vapor-hypersaline liquid partition coefficients somewhat higher than below 500 °C for similar vapor/liquid density ratios (Fig. 9). The difference, however, rarely exceeds an order of magnitude and may be explained by the increasing fraction of neutral, and thus more volatile, chloride species in the hypersaline liquid with increasing temperature (e.g., Pokrovski et al. 2008a) and/or possible formation of oxychloride or hydrogen-chloride species in the magmatic vapor phase (e.g., Simon et al. 2005). Both phenomena are due to the reinforcement of electrostatic interactions in aqueous complexes with increasing temperature and a decreasing dielectric constant of the solvent. This enhances the stability of uncharged species and strengthens chemical bonds with hard ligands (e.g., O/OH vs. Cl). Even at temperatures as high

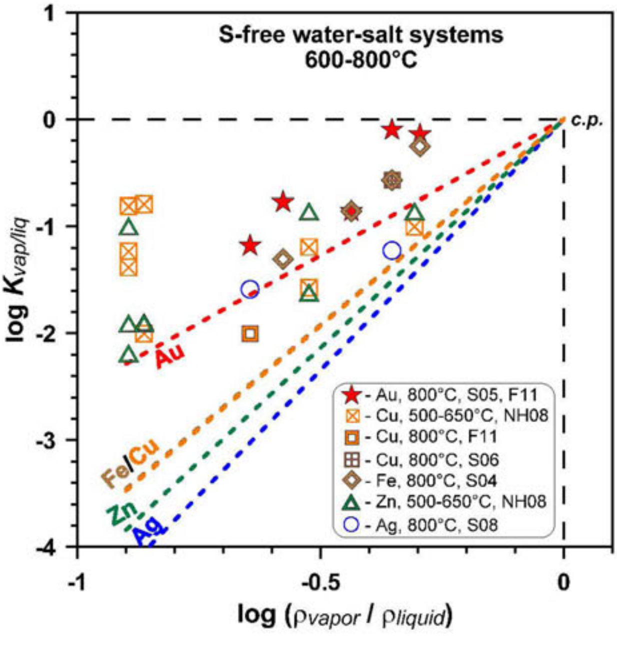

Figure 9. Vapor-liquid partition coefficients, log $K_{vap/liq}$ = log (m_{vapor}/m_{liquid}), of Au, Cu, Fe, Zn, and Ag in the two-phase system $H_2O+NaCl\pm KCl\pm HCl$ at magmatic temperatures (600-800 °C) as a function of the vapor-to-liquid density ratio. Symbols stand for experimental data from the following sources: NH08 - Nagaseki and Hayachi (2008), S04 – Simon et al. (2004), S05 - Simon et al. (2005), S06 – Simon et al. (2006), S08 – Simon et al. (2008), F11 – Frank et al. (2011). The dashed straight lines through the critical point (c.p.) for the indicated elements represent the density-model predictions in S-free systems based on data below 500 °C (Pokrovski et al. 2005a, 2008a). With the exception of a few non-systematic outliers, most high-temperature data follow, within errors, a roughly linear log*K* vs. log($\rho_{vapor}/\rho_{liquid}$) dependence with an origin at the critical point, similar to that established at hydrothermal temperatures; the somewhat higher *K* values likely reflect the increasing fraction of neutral, and thus more volatile, metal chloride species with increasing temperature and/or possible formation of new oxy-chloride and hydrogen-chloride species in magmatic vapor phase.

as 800 °C, all principal porphyry-deposit metals (Au, Cu, Fe) are enriched in the liquid phase compared to the vapor (Fig. 9). Note that both vapor and liquid densities change in regular and predictable fashion that may be reasonably approximated by the best known H_2O-NaCl system (Driesner and Heinrich 2007) for natural vapor and hypersaline liquid compositions dominated by Na, K, and Fe chlorides. Consequently, these simple density trends provide an efficient and practical way of predicting vapor-liquid fractionation over the range of magmatic-hydrothermal conditions, with an uncertainty within one order of magnitude.

The presence of CO_2, which has a weak capacity for direct binding to most base and chalcophile metals, will affect the fluid properties mainly by enlarging the degree of immiscibility between the vapor and liquid, further enhancing the density contrast between these two phases. This should lead to a larger contrast in the vapor-liquid distribution for most metals with further enrichment in the dense liquid phase. The effect of sulfur, which may selectively bind some metals, appears to be different.

Effect of sulfur on vapor-liquid partitioning. Experimental data for S-free systems agree with observations on natural coexisting liquid and vapor inclusions for all metals and metalloids, except Au and Cu, which show systematic enrichment in the natural vapor phase (see below, Fig. 16). The most plausible explanation for Au and Cu enrichment in the vapor phase is the formation of volatile species with sulfur (Heinrich et al. 1999), the second most important ligand after chloride. The effect of reduced sulfur on vapor-liquid partitioning has recently been investigated experimentally, both at hydrothermal (Pokrovski et al. 2008a; Rempel et al. 2012) and magmatic (Simon et al. 2006; Nagaseki and Hayachi 2008; Frank et al. 2011; Lerchbaumer and Audétat 2012) conditions.

At temperatures of 350 to 500 °C, experiments in hydrothermal reactor with sampling show that with the addition of 1 to 2 wt% of S to the water-salt system at acidic-to-neutral pH, equilibrium Cu and Au partition coefficients ($K_{\text{vapor/liquid}}$) increase by one to two orders of magnitude (Fig. 10), attaining values in favor of the vapor for Au (K_{Au} up to 7 at acidic conditions), whereas the volatility of Ag, Zn, Fe, and Pb is almost unaffected (Pokrovski et al. 2008a). Platinum exhibits partitioning similar to Au, largely in favor of the vapor phase (K_{Pt}~10; however no experimental data in S-free systems are available for comparison).

At higher temperatures (600-800 °C), synthetic fluid inclusion studies also demonstrate an increase in K values for Cu in the presence of S, but exhibit large discrepancies. For example, Lerchbaumer and Audétat (2012) reported K_{Cu} values two orders of magnitude lower than those of Nagaseki and Hayashi (2008) in the same H_2O-NaCl-S system and similar T-P, with H_2S concentrations up to 5 to 10 wt% in the vapor phase (K_{Cu} ~0.1 vs. 10; Fig. 10). Lerchbaumer and Audétat (2012) criticized the Nagaseki and Hayashi (2008) measurements by suggesting heterogeneous entrapment of copper sulfide particles in the latter study. Other experimental studies, both at hydrothermal (Pokrovski et al. 2008a; Rempel et al. 2012) and magmatic (Simon et al. 2006; Frank et al. 2011) temperatures, report vapor/liquid partitioning coefficients for Cu between ~0.1 and ~0.5 at dissolved S contents up to 1 to 2 wt%, typical for porphyry systems (Seo et al. 2009). Although these K_{Cu} values are systematically less than one (with the exception of the study by Nagaseki and Hayashi 2008), they are up to an order of magnitude higher than in S-free systems for the same conditions and data source (Fig. 9).

Although the exact nature and stoichiometry of Au, Pt, and Cu complexes in the vapor phase remain unconstrained, it is likely that these metals form neutral hydrogen-sulfide complexes, probably similar to those in the liquid phase. For example, recent *in situ* XAS measurements in moderate density (0.3-0.5 g/cm^3) supercritical fluids (Pokrovski et al. 2009b) and molecular dynamics simulations (Lui et al. 2011) indicate that $Au(HS)H_2S^0$ may form in acidic S-rich ($H_2S > 0.1$ m) fluids and, by inference, vapors. This species has two sulfur ligands bound to the Au atom in a linear geometry and does not show detectable water molecules in the inner and outer coordination spheres of Au. Because weak hydration in aqueous solution means

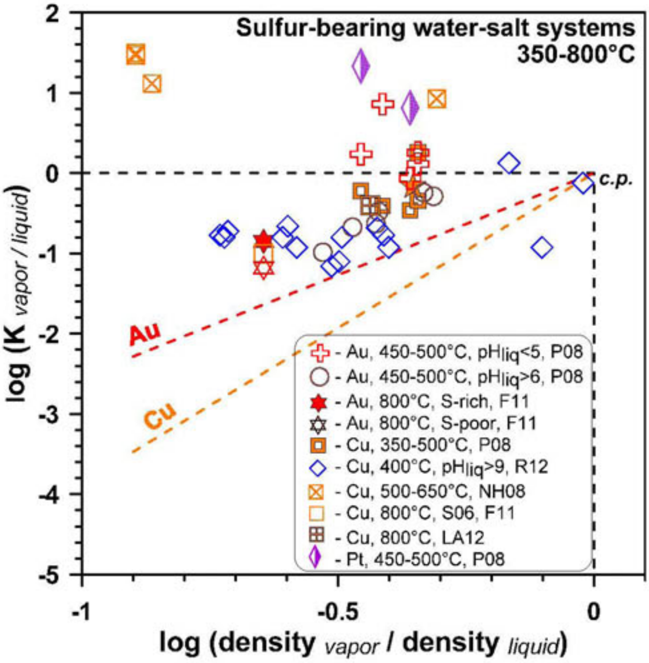

Figure 10. The effect of sulfur on vapor-liquid partition coefficients, log $K_{\text{vapor/liquid}}$ = log ($m_{\text{vapor}}/m_{\text{liquid}}$) of Au, Cu and Pt in model two-phase salt-water sulfur-rich systems (H_2O-NaCl-KCl-HCl-$FeCl_2$-S-NaHS-pyrrhotite-bornite), 400-800 °C, and 1-10 wt% sulfur in the vapor. Symbols stand for experimental data from the following sources: P08 – Pokrovski et al. (2008b), NH08 – Nagaseki and Hayachi (2008), S06 – Simon et al. (2006), F11 – Frank et al. (2011), LA12 – Lerchbaumer and Audétat (2012), R12 – Rempel et al. (2012). Partitioning of Zn, Fe and Ag (not shown) is not affected within errors by the presence of sulfur (Pokrovski et al. 2008a; Simon et al. 2008). For comparison, the dashed straight lines through the critical point (c.p.) for Cu and Au represent the density-model predictions from Pokrovski et al. (2005a) in the S-free system. At temperatures of magmatic-hydrothermal transition (600-800 °C) and sulfur contents of a few wt%, with the expection of a single study (NH08), the effect of sulfur on Cu and Au vapor-liquid partitioning is weak in front of the large errors that affect the data (c.f. Fig. 9 in S-free systems). In contrast, at hydrothermal temperatures (400-500 °C) at acidic pH Au partitions preferentially into the vapor, with $K_{\text{vapor/liquid}}$ ~1 to 10, whereas at neutral-to-basic pH the effect of sulfur is much weaker, consistent with the change of Au liquid-phase speciation at pH > ~5 from neutral $AuHS^0$ and/or $Au(HS)H_2S^0$ to negatively charged $Au(HS)_2^-$ (see text). The effect of reduced sulfur of metal partitioning at $T \leq 350$ °C is more difficult to evaluate at present because of the large data scatter due to experimental difficulties which stem from the low solubility of metal sulfides at such moderate temperatures (Pokrovski et al. 2008a; Rempel et al. 2012).

enhanced volatility in the vapor, such species might have a partitioning similar to that of gases (e.g., H_2S, CO_2), which enrich the vapor phase with a decrease of the vapor/liquid density ratio (e.g., Fig. 6). At elevated H_2S contents in the vapor (10s-100s bars), gaseous sulfide species of Au, Cu and Ag solvated by H_2S molecules in a variable extent such as $AuS{\cdot}nH_2S$, $Cu_2S{\cdot}nH_2S$, $Ag_2S{\cdot}nH_2S$ have also been proposed on the basis of metal sulfide solubility measurement in high-pressure H_2S gas below 350-400 °C (Zezin et al. 2007; Bychkov and Nikolaeva 2013), but their extrapolation to conditions of vapor-liquid unmixing in porphyry-like systems remains uncertain. Regardless the exact species stoichiometry and structure, the higher volatility of Au and Pt compared to Cu is consistent with the far greater stability of Au and Pt hydrogen sulfide species in an aqueous solution. The low volatility of Zn, Fe, and Ag is a direct consequence of the larger stability of their chloride vs. sulfide complexes in aqueous solutions (Fig. 4).

Another important factor controlling the vapor-liquid distribution of Au, and probably Cu, in S-rich systems is the fluid acidity. Because a neutral species in solution generally has a far greater volatility than its charged counterpart (see Fig. 8, and Pokrovski et al. 2002b, 2008a), Au is expected to be more volatile in S-rich systems under acidic conditions where $AuHS^0$ and, probably, $Au(HS)H_2S^0$ are more abundant in the liquid phase. At pH > ~5-6, at which $Au(HS)_2^-$ is dominant in solution (Stefánsson and Seward 2004; Pokrovski et al. 2009b), Au $K_{vapor/liquid}$ values are systematically lower than 1 (Pokrovski et al. 2008a). It can be seen in Figure 10 that at similar H_2S concentrations in the system (~0.5 wt% S), Au vapor-liquid partitioning coefficients in cases where the liquid phase pH is < 5 are systematically higher than those where the liquid-phase pH ≥ 6, reflecting the change of the dominant Au species in the liquid. At more alkaline pH (>7-8), deprotonation of H_2S to HS^- (pK_{diss} ~7) further lowers the H_2S abundance in the vapor because of the enhanced partitioning of the charged HS^- into the liquid. This will favor Au enrichment in the liquid phase. Thus, vapor-liquid unmixing of a neutral-to-basic fluid, in which $Au(HS)_2^-$ and $Cu(HS)_2^-$ are dominant, will not be favorable for Au and Cu transport by the vapor phase.

The effect of CO_2 on vapor-liquid partitioning of S-bound metals remains experimentally unconstrained. The data for CO_2-free systems discussed above suggest that partitioning of volatile Au- and Pt-bearing sulfide complexes into the vapor phase might be enhanced in the presence of CO_2, due to a) an increase in the density contrast between liquid and vapor and resulting partitioning of H_2S into the vapor, and b) specific solvation of neutral non-polar molecules, such as $Au(HS)H_2S^0$ complexes, by non-polar CO_2 (Pokrovski et al. 2008a). The selective solvation capacities of supercritical CO_2 are widely used in chemical engineering for synthesis and purification of organo-metallic and organic compounds at moderate temperatures (e.g., Erkey 2000; Bruner 2004). This effect of CO_2 awaits experimental confirmation for conditions pertinent to natural systems.

Vapor-brine-supercritical fluid-silicate melt partitioning in experimental and natural systems

This section is devoted to an overview of experimental and natural data on metal and metalloid partitioning between different fluid types (supercritical fluid, brine and vapor) and hydrous silicate (mostly silicic) melts at crustal conditions (typically, 600-1000 °C, 500-5000 bars). Such data are essential for evaluating the metal and fluid sources for hydrothermal deposits, and for establishing fundamental analogies with the vapor-liquid partitioning trends discussed above. The available data are presented in terms of fluid-melt distribution coefficient, $K_{fluid/melt} = C_{fluid}/C_{melt}$, where C_{fluid} and C_{melt} are concentrations of the element in fluid and melt, respectively. They are plotted in Figure 11 and represent the range of published data for different elements. Experimental data concern model fluid-melt systems and were obtained by fluid quench and synthetic fluid inclusion techniques using cold-seal reactors (Fig. 11A), whereas natural data are from coexisting fluid and melt inclusion assemblages from magmatic minerals and silicate glasses (Fig. 11B). Both types of samples are analysed in most cases by laser ablation-inductively coupled plasma mass spectrometry (LA-ICPMS). Distinction is made between brine and vapor phases in cases where they were distinguished in a publication; in other cases the term 'supercritical fluid' (both vapor-like and brine-like) is employed. Five groups of elements, metalloids (B, As, Sb), molybdenum, and chalcophile (Cu, Ag, Au, Pt), base (Fe, Zn, Pb), and lithophile (Na, K, REE) metals are considered below.

Metalloids: B, As, Sb. This group of elements shows experimental and natural fluid-melt partitioning coefficients typically between ~0.1 and ~10 (Fig. 11A). The observed variations are likely related to differences in the silicic melt composition, and the presence of volatile components in the fluid phase such as HCl, sulfur, and carbon dioxide, depending on the element. Boron behavior in experimental fluid-melt systems was investigated by Pichavant (1981), London et al. (1988), Webster et al. (1989), and Schatz et al. (2004) at 500-800 °C

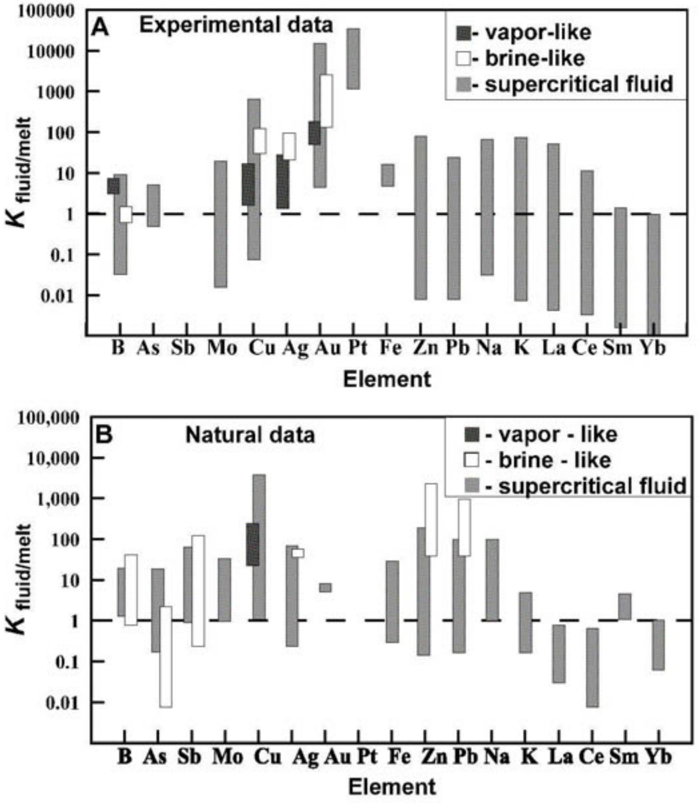

Figure 11. Partition coefficients between the different types of magmatic fluids (vapor, brine, and supercritical fluid) and coexisting silicate melts ($K_{\text{fluid/melt}} = C_{\text{fluid}}/C_{\text{melt}}$, where C_{fluid} and C_{melt} are concentrations of the element in the indicated phase) for selected elements according to available experimental (A) and natural (B) data. Experimental data are from: B: Pichavant 1981; London et al. 1988; Webster et al. 1989; Keppler 1996; Schatz et al. 2004; As: Simon et al. 2007; Mo and Cu: Khitarov et al. 1982; Candela and Holland 1984; Urabe 1985; Manning and Pichavant 1988; Keppler and Wyllie 1991; Williams et al. 1995; Chevychelov and Chevychelova 1997; Bai and Koster van Groos 1999; Schäfer et al. 1999; Simon et al. 2006; Frank et al. 2011; Ag: Simon et al. 2008; Au: Hanley et al. 2005; Simon et al. 2005, 2007; Frank et al. 2011; Pt: Hanley et al. 2005; Fe: London et al. 1988; Zn and Pb: Holland 1972; Khitarov et al. 1982; Urabe 1985, 1987; London et al. 1988; Keppler 1996; Chevychelov and Chevychelova 1997; Na, K, La, Ce, Sm, Yb: Holland 1972; Flynn and Burnham 1978; Khitarov et al. 1982; London et al. 1988; Webster et al. 1989; Keppler 1996; Bai and Koster van Groos 1999; Schäfer et al. 1999; Reed et al. 2000. Natural data are from: B, As and Sb: Audétat et al. 2008; Zajacz et al. 2008; Audétat 2010; Borisova et al. 2012; Lerchbaumer and Audétat 2013; Mo, Fe, Na, K, La, Sm and Yb: Zajacz et al. 2008; Lerchbaumer and Audétat 2013; Cu: Lowenstern 1993; Zajacz et al. 2008; Vikent'ev et al. 2012; Audétat et al. 2008; Audétat 2010; Lerchbaumer and Audétat 2013; Ag, Zn and Pb: Audétat et al. 2008; Zajacz et al. 2008; Audétat 2010; Borisova et al. 2012; Vikent'ev et al. 2012; Lerchbaumer and Audétat 2013; Au: Vikent'ev et al. 2012; Ce: Zajacz et al. 2008; Vikent'ev et al. 2012. The vertical bars outline the range of data points for each element for the different fluid types.

and 1-2 kbar. These data show that $K_{\text{fluid/melt}}$ values cluster around 1 in some studies or show a slight preference to the vapor in others; in all cases they are independent of the salt content of the fluid. Arsenic partitioning between aqueous fluid and granitic melt at 800 °C and 1.2 kbar is also found to be independent of salt content and only weakly dependent on H_2S at redox conditions of the NNO (nickel-nickel oxide) buffer (Simon et al. 2007). Fluid-melt partitioning of B and As is controlled by the dominant presence of neutral hydroxide complexes in silicate melt, as shown by Raman (Veksler et al. 2002) and X-ray absorption (Borisova et al. 2010) spectroscopy, which are similar to the major $B(OH)_3$ and $As(OH)_3$ species in hydrothermal fluids and vapors (see above). Natural data on both metalloids are in good agreement with the experiments, demonstrating $K_{\text{fluid/melt}}$ values around 1 (Fig. 11B) as shown by analyses of coexisting granitic and pegmatitic melt and fluid inclusions in quartz (Audétat and Pettke 2003; Zajacz at al. 2008; Borisova et al. 2012; Lerchbaumer and Audétat 2013). For Sb, in contrast, Borisova et al. (2012) reported elevated K values (40-285) for Ehrenfriedersdorf pegmatite, which are consistent with the formation of volatile oxy-chloride and chloride complexes, similar to those at hydrothermal conditions (Pokrovski et al. 2006). Such high natural K values for Sb would be indicative of elevated HCl concentrations in this pegmatite system, according to the pH/Cl indicator proposed by Pokrovski et al. (2008b).

Molybdenum. This element has been a subject of significant experimental efforts since the 1980's in model granitic-like systems similar to those hosting the major part of Mo magmatic-hydrothermal deposits (Khitarov et al. 1982; Candela and Holland 1984; Chevychelov and Chevychelova 1997; Keppler and Wyllie 1991; Schäfer et al. 1999; Bai and Koster van Groos 1999). As for As and B, Mo fluid/melt partitioning was found to be only weakly dependent on Cl and F concentration in the fluid (Candela and Holland 1984) or even decrease with an increase in HCl (Keppler and Wyllie 1991). This may indicate the formation in magmatic fluid and vapor of molybdate anions whose solubility decreases with increasing pH, similar to those in lower temperature aqueous fluids (Fig. 4; Kouzmanov and Pokrovski 2012). Molybdenum preference for the aqueous fluid increases with the pressure rise (Chevychelov and Chevychelova 1997; Schäfer et al. 1999; Bai and Koster van Groos 1999), consistent with the increasing affinity of Mo for water vapor at hydrothermal conditions (e.g., Rempel et al. 2006, see above). Several studies reported an increased Mo partitioning into carbonate-rich fluids (Khitarov et al. 1982; Bai and Koster van Groos 1999); whether Mo forms direct carbonate complexes or this enrichment is a result of changes in pH and consequent deprotonation of Mo oxy-hydroxide species (Fig. 4), remains to be understood. The melt structure may also influence Mo partitioning, so that both increasing SiO_2 content and decreasing the ASI index of the melt (Al/(Na+K+2Ca), mol%) increase Mo $K_{\text{fluid/melt}}$ values (Chevychelov and Chevychelova 1997; Bai and Koster van Groos 1999). The effect of sulfur on Mo partitioning is likely to favor Mo enrichment of the fluid or vapor phase (Khitarov et al. 1982; Tingle and Fenn 1984; Manning and Pichavant 1988). The local atomic structure around Mo in quenched silicate glasses was studied using X-ray absorption spectroscopy (Farges et al. 2006). The spectra are consistent with molybdate-like moieties ($Mo^{VI}O_4^{2-}$) in S-free glasses at variable redox conditions (from quartz-fayalite-magnetite, QFM-1, to atmospheric oxygen buffer) and with thio-oxo species like $Mo^{(IV,V,VI)}O_nS_n$ (n = 1, 2, 3) in reduced (from iron-wustite, IW-1, to QFM-1) S-bearing glasses. At high sulfur fugacities, these thio-oxo-molybdate species are progressively substituted by purely sulfide species of four- and six-fold coordination ($Mo^{IV}S_4^{4-}$ or $Mo^{IV}S_6^{8-}$). The presence of H_2O and halogens favors higher coordination of Mo in these species without direct evidence for the presence of O and Cl atoms in the nearest coordination sphere of Mo in S-rich glasses. In contrast, no clear influence of H_2O was observed on the local structure of Mo in the hydrous silicate glasses under S-poor and oxidizing conditions. However, following the intrinsic limitations of EXAFS spectra, which are little sensitive to light atoms like H or distant atomic shells, the complex charge, and protonation and hydration degree could not be established. Natural data on Mo fluid/melt partitioning (Zajacz et al. 2008; Lerchbaumer and Audétat 2013) show on average equal preference of Mo for fluid and melt despite significant scatter, and the absence of any dependence on salt content of the fluid, which is consistent with the dominant presence of Mo^{VI} oxy-hydroxide species.

Chalcophile elements (Cu, Ag, Au, Pt). Both natural and experimental data shown in Figure 11 demonstrate a strong affinity of these metals to aqueous fluid, with $K_{\text{fluid/melt}}$ values from 1 to 10,000 depending on the element and conditions. The chloride and, to a lesser extent, sulfur content of the fluid are the major parameters governing the partitioning of these metals, but other factors such as silicic melt composition (ASI, SiO_2 content) and carbonate concentration were also reported in a few studies. These factors are secondary compared to those of Cl and S; for example, carbonate presence in the system increases by 2-3 times Cu $K_{fluid/melt}$ values compared to a CO_2-free system, whereas increasing the (Na + K)/Al ratio or decreasing ASI index in silicic melt results in a decrease of Cu $K_{fluid/melt}$ partitioning in Cl-bearing systems (e.g., Bai and Koster van Groos 1999).

All available experimental studies show that Cu partitioning into the fluid phase is greatly enhanced in the presence of chloride (NaCl/KCl and HCl) in the system, and that $K_{fluid/melt}$ values are directly proportional to Cl fluid concentration (Khitarov et al. 1982; Candela and Holland 1984; Keppler and Wyllie 1991; Williams et al. 1995; Bai and Koster van Groos 1999; Simon et al. 2005; Frank et al. 2011). Consequently, in vapor-brine-melt systems, Cu brine-melt partitioning is systematically higher than vapor-melt (Fig. 11), consistent with the vapor/brine distribution of copper discussed above (Fig. 9) and the high Cu affinity for chloride in natural fluids at high temperature (Berry et al. 2009). The effect of sulfur is less pronounced; for example, only a moderate increase in Cu $K_{fluid/melt}$ values (by a factor of 2) was observed by Khitarov et al. (1982) for S contents up to 1 wt% and oxygen partial pressures of 10^{-5}-$10^{-3.5}$ bar at 700-900 °C, and Simon et al. (2006) reported a 5-fold increase in Cu $K_{fluid/melt}$ values at H_2S concentrations of a few wt% at redox conditions of NNO compared to a S-free system. Again, even in H_2S-rich systems, Cu vapor/melt is lower than brine/melt partitioning, yielding a vapor/brine distribution lower than 1 at magmatic temperatures (Figs. 10, 11). In natural systems, analyses of Cu-rich low-density fluid bubbles, trapped in melt inclusions in quartz of silicic volcanic rocks from the 1912 Valley of Ten Thousand Smokes, Alaska (Lowenstern 1993) and in CO_2-dominated vapor bubbles from quartz phenocrysts of rhyolites from Pantelleria, Sicily (Lowenstern et al. 1991), show $K_{vapor/melt}$ values for Cu of 100 to 1000. Rare natural data on Cu partitioning between fluids and silicic melts in granitic-pegmatite (Zajacz et al. 2008) and magmatic-hydrothermal (Audétat and Pettke 2003; Vikent'ev et al. 2012) systems agree with the range of experimentally measured values in laboratory NaCl-bearing systems (Fig. 11).

Gold, similarly to Cu, strongly prefers the aqueous phase to silicate melt with $K_{fluid/melt}$ values above 10 (Fig. 11). The effect of HCl on Au brine/melt partitioning in a water-haplogranitic melt system (800 °C 1.0-1.5 kbar, NNO) was found to be negligible at < 1 wt% HCl (K_{Au} is constant and close to ~40), but to increase at higher HCl contents (K_{Au} attains ~830 at 4 wt% HCl), probably indicating the formation of AuCl or Au(HCl)Cl complexes (Frank et al. 2002). Data on Au partitioning in less acidic conditions, in a S-free system composed of haplogranite melt, magnetite, metallic Au, and NaCl-KCl aqueous brine and vapor (800 °C, 1.1-1.5 kbar, NNO), also suggest formation of Au^I chloride complexes (e.g., $AuCl_2^-$ or Au(HCl)Cl), displaying a somewhat lower vapor/melt (8-72) than brine/melt (56-100) partition coefficients, both types of values increasing with the pressure increase (Simon et al. 2005). Much higher fluid/melt partition coefficients (up to 10,000) were found by Hanley et al. (2005) for Au and Pt between highly saline (20-70 wt% NaCl equivalent) S-free fluid and peraluminous melt at NNO redox and 1-2.6 wt% HCl (1.5 kbar and 600-800 °C). However, that pilot study on Pt suggests a lack of equilibrium in most experiments, resulting in a large data dispersion. The observed in that work partitioning of Au and Pt in favor of the fluid is nevertheless highest among the metals (Fig. 11A).

The effect of sulfur on Au partitioning remains insufficiently constrained and is likely hidden by the dominant control of chloride. For example, identical, within errors, $K_{vapor/melt}$ values for Au (between 12 and 15) were obtained in a vapor+haplogranitic melt+magnetite system with and without pyrrhotite (800 °C, 1.2 kbar, NNO, Simon et al. 2007). Higher $K_{vapor/melt}$ values, up to 100, were measured in systems richer in sulfur in the presence of (Cu, Fe)S intermediate solid solutions at similar *T-P*; however, in the presence of brine, Au always preferred this phase over the vapor (Frank et al. 2011). Zajacz et al. (2010, 2012b) suggested, on the basis of gold solubility measurements, that Au speciation both in vapor and melt in H_2O-S-Cl-bearing systems at magmatic conditions, is controlled by AuCl , AuHS, and (K/Na)AuS complexes. Fluid–melt (mafic to intermediate) partition coefficients for Au are systematically higher than for Cu, likely due to formation of these and, potentially, other species with sulfur ligands. Other recent studies evoked the degree of silicate melt polymerization and FeO activity (which determines the sulfur activity) in controlling Au solubility in hydrous melts (e.g., Botcharnikov et al. 2011; Jégo and Pichavant 2012; Zajacz et al. 2013). The only available natural data on gold partitioning between vapor-like fluid and rhyolite melt in the Uzel'ginskoe magmatic-hydrothermal Cu-Zn sulfide ore field from the Urals ($K_{\text{fluid/melt}}$ ~8, at $\text{NaCl}_{\text{equiv}}$ 1.2-6.2 wt%, Vikent'ev et al. 2012) agree with the minimal values measured in experimental NaCl-bearing systems (Simon et al. 2005, 2007).

In contrast to Cu and Au, Ag partitions much more weakly into the vapor phase in fluid-melt systems according to rare experimental data (Simon et al. 2008), with $K_{\text{vapor/melt}}$ 10-100 times lower than for Cu or Au in similar conditions (Simon et al. 2005, 2006). A lower Ag than Au and Cu preference for the fluid phase has also been observed in natural fluid/melt inclusions from granitic (Zajacz et al. 2009) and magmatic-hydrothermal (Vikent'ev et al. 2012) systems. Silver fluid/melt partitioning lower than 1 (at 5 wt% $\text{NaCl}_{\text{equiv}}$, 700-720 °C, 1.0-1.2 kbar) has been reported by Audétat and Pettke (2003) for the Rio del Medio barren granite (New Mexico), and slightly above 1 (K_{Ag} ~ 2-5) for the Treasure Mountain Dome (Colorado) and the Stronghold granite (Arisona). In contrast, strong partitioning of Ag into the brine-like fluid relative to hydrous peraluminous melt (K_{Ag} = 46) was found for a natural rare-metal pegmatite (Borisova et al. 2012). This is in line with the large stability of Ag chloride complexes in the dense saline phase over a range of temperatures (Pokrovski et al. 2013b). The fluid/melt partition data for Au, Cu, and Ag follow the same order as in vapor-liquid systems at lower temperatures (< 600 °C), showing that Au and Cu are more volatile than Ag (see above, and Fig. 6 and 7). However, Cu enrichment of the fluid phase might be due to post-entrapment modifications of the fluid and melt inclusions (see below and Lerchbaumer and Audétat 2013). Nevertheless, all three elements show a marked preference for a high-salinity liquid rather than for vapor or melt in magmatic conditions.

***Base metals* (*Zn, Fe, Pb*).** The limited natural and experimental data shown in Figure 11 display a moderate affinity of these metals for aqueous fluid vs. silicate melt. The observed variations in fluid/melt partitioning are related to salt concentration in the fluid and, in a lesser extent, to the silicic melt composition (ASI index). The chloride content of the fluid is a primary control on base metal partitioning (Holland 1972; Khitarov et al. 1982; Urabe 1985), owing to the dominant formation of chloride complexes in both the liquid and vapor phases (see above). An increase in the ASI index also tends to increase $K_{\text{fluid/melt}}$ for these elements, probably because of the stronger solubility of these metals in alkaline melts (Urabe 1985). For Fe^{2+}, however, no significant differences in the local environment in the melt were observed between hydrous and dry haplogranite (lower ASI) and haplotonalitic (higher ASI) systems (Wilke et al. 2006). The silica content in the melt seems to exert some effect as well; for example, $K_{\text{fluid/melt}}$ for Pb and Zn differ by a factor of 2 to 4 for different silicic melts with a slight preference of Pb and Zn for granodioritic melt (Chevychelov and Chevychelova 1997). In Cl-free systems, the effect of carbonate ($NaHCO_3$, at 700-900 °C and 2 kbar; Khitarov et al. 1982) is to increase by 3-7 times the $K_{\text{fluid/melt}}$ values, both for Zn and Pb, compared to a CO_2-free system. Fluid acidity plays a major role in Zn and Pb enrichment of the fluid phase, as shown by fluid/melt partitioning experiments in NaCl-HCl-H_2O systems at 800 °C and 1.6-5.0 kbar (Urabe 1987), which is in line with the enhanced solubility of Pb and Zn phases in acidic hydrothermal fluids at lower temperatures (e.g., Kouzmanov and Pokrovski 2012). Absolute fluid-melt distribution coefficients of Zn and Pb were found to be between 1 and 10 for experimental systems containing granitic melt and 1 molal chloride aqueous fluid at 750-850 °C, 1-2 kbar, and redox conditions of NNO; these values are typically 5 to 10 times lower than for Cu in the same conditions (Chevychelov et al. 2005).

Natural data from granitic and pegmatite quartz-hosted inclusions (Zajacz et al. 2008) show a positive correlation between the partition coefficients of Pb, Zn, and Fe and chlorinity of the aqueous fluid. These data do not display any influence of oxygen fugacity or melt composition on the partitioning. Another recent set of natural data on coexisting brines and pegmatite melts (Borisova et al. 2012) reports $K_{\text{brine/melt}}$ values of Zn and Pb in the range 50-1800 for peraluminous pegmatite-like melts, which are partly higher than or partly overlap with Zajacz et al.'s (2008) data for peralkaline to peraluminous melts for which no distinction was made between brine-like and vapor-like fluids. Relatively low Zn and Pb fluid/melt partitioning (below 20 at 5 wt% $NaCl_{\text{equiv}}$, 700-720 °C, 1.0-1.2 kbar) was reported by Audétat and Pettke (2003) in the Rio del Medio granite (New Mexico) and by Lerchbaumer and Audétat (2013) for different granite-hosted Mo deposits in the US and Norway. Single-phase, vapor-rich, and hypersaline liquid inclusions from giant porphyry Cu-Au(-Mo) deposits at Bingham, El Teniente, Bajo de la Alumbrera, Questa, and Butte show a characteristic Zn/Pb ratio, ranging from 1 to 6 in the order of the listed deposits, which is constant for a given deposit and is not affected by phase separation of the input magmatic fluid or Cu-Au-Mo precipitation in the porphyry environment (Kouzmanov and Pokrovski 2012), thus implying differences in the Zn/Pb ratio of the parental magmas and/or particularities of fluid degassing in the different settings. The use of the Zn/Pb ratio as a new potential tracer of magma composition and fluid-melt separation processes requires more systematic experimental data on melt-fluid partitioning in different conditions.

Alkali metals (Na, K) and Rare Earth Elements (La, Ce, Sm, Yb). These lithophile elements have often been measured together in experimental and natural studies and, consequently, are considered together here. Chloride is no doubt a key parameter affecting their fluid/melt partitioning. Experimentally measured Na and K partitioning is on average around 1; it increases with increasing Cl^- or HCl ligand concentration (Urabe 1985; Bai and Koster van Groos 1999; Reed et al. 2000), prefers the aqueous fluid phase and extracts Na and K from the melt due to both partial formation of ion pairs and charge balance constraints for these major cations and the chloride anion. A large effect of chloride in a lithophile element (K, Rb, Sr, Ba) enrichment of NaCl/KCl aqueous fluids has also been observed at $T > 1000$ °C and $P \geq 3$ kbar (Keppler 1996). According to natural data (Zajacz et al. 2008), Na generally partitions more strongly than K into an aqueous fluid (Fig. 11B), which is in agreement with the lower solubility of K-bearing than Na-bearing aluminosilicates, resulting in a large increase of Na/K ratios in most hydrothermal fluids with decreasing temperature (e.g., Giggenbach 1988).

The extent of fluid/melt partitioning of REE is also directly proportional to the chloride content of the fluid, suggesting the formation of stable chloride complexes, likely $REECl_3$, in the fluid phase (Flynn and Burnham 1978; Webster et al. 1989; Bai and Koster van Groos 1999; Zajacz et al. 2009). Some of these and other works have also revealed an effect of the melt composition (ASI index) and degree of depolymerization; an increase in both parameters favors REE partitioning into the fluid phase (e.g., Flynn and Burnham 1978; Veksler et al. 2002). The fluoride content may also affect REE partitioning (Veksler et al. 2002); however, the generally strong chemical affinity of F for REE in the fluid phase may be neutralized by the preferential partitioning of F into silicate melt such that the overall impact on REE fluid/melt partitioning is small. The absolute values of $K_{\text{fluid/melt}}$ of REE, both from experimental and natural samples, are generally lower than 1, demonstrating their preference for silicate melts. The relatively low fluid-phase mobility of REE is consistent with the scarcity of hydrothermal *sensu stricto* REE deposits (Chakhmouradian and Wall 2012). Rare available natural data on REE partitioning between vapor-like fluid and rhyolite melt in the Uzel'ginskoe magmatic-hydrothermal Cu-Zn sulfide ore field in the Urals ($K_{\text{vapor/melt}} \sim 0.01$ for Ce and 0.06 for Nd, Vikent'ev et al. 2012) agree with the experimentally measured values in NaCl-poor bearing systems (Fig. 11; Flynn and Burnham 1978; Webster et al. 1989; Bai and Koster van Groos 1999; Reed et al. 2000). These data suggest that REE prefer saline aqueous fluids compared to vapor. This is also in agreement with the very low volatility of REE in vapor-liquid systems at lower temperatures (Fig. 6). Consequently their vapor-phase transport is not expected to play a significant role over the whole range of magmatic-hydrothermal processes.

ROLE OF THE VAPOR-LIKE FLUIDS IN METAL AND METALLOID TRANSPORT IN NATURAL SYSTEMS AND THE FORMATION OF ORE DEPOSITS

Low-temperature boiling geothermal systems

Geothermal systems in active volcanic areas represent a relatively accessible example of processes that hot geothermal fluids undergo when rising to the surface, such as vapor-liquid separation, boiling, and vapor-phase transport of chemical elements. A geothermal system includes a heat source, supplied by magmatic intrusions or hot volcanic rocks, a groundwater reservoir, and a discharge zone (White et al. 1971; White 1973). For many systems there is also a boiling zone where liquid and steam coexist and a vapor-dominated zone where steam is separated from the liquid (White 1973). Both zones contain a high-enthalpy (2000-3000 kJ/kg; Arnórsson et al. 2006) vapor phase capable of supplying a large quantity of heat when it condenses to liquid that may be used for producing geothermal energy, which is the main reason of economic interest in these systems. The composition of liquid water and steam has been extensively studied (e.g., Ellis 1979; Henley and Ellis 1983; D'Amore and Pruess 1986; Arnórsson et al. 2007). Deep hydrothermal fluids, so-called primary waters, in most geothermal areas are typically neutral and of low salinity (up to ~0.*n* wt% NaCl, Giggenbach 1995) due to a large contribution from diluted meteoric waters; however, elevated salinities (up to 5 wt% NaCl equivalent) are observed in some coastal areas influenced by the presence of seawater (Arnórsson et al. 1978). The composition of thermal springs at the surface is more variable and may be dominated by chloride, sulfate or carbonate. Some geothermal systems exhibit a zonation in water composition, with chloride-dominated in the central parts and sulfate- and/or carbonate-dominated at the periphery. This variability is mainly controlled by the three following factors: a) mixing between vapor condensates, deep saline fluids, and surface waters; b) surface evaporation; and c) H_2S oxidation to sulfate by atmospheric oxygen. The two latter processes lead to H_2SO_4 concentrated solutions (pH up to ~ 0) in mud pools and intensive leaching of wall rocks (e.g., Browne and Ellis 1970). The gas phase chemistry has been studied in detail (Giggenbach 1980, 1987, 1995; Krupp and Seward 1990; Arnórsson et al. 2007; Taran 2009; Zelenski and Taran 2011; references cited); it is largely dominated by water vapor ($\geq$ 90%), with moderate amounts of CO_2 (few wt%), H_2S (up to ~0.1 wt%), and trace amounts of other gases (H_2, NH_3, CH_4, Ar). Processes such as boiling, mixing, and conductive cooling and their effects on major element vapor and liquid composition and mineral precipitation have been extensively modeled in different geothermal areas (Giggenbach 1984; Fournier 1989; Spycher and Reed 1989; Hedenquist 1991; Migdisov and Bychkov 1998). In contrast, fewer data are available about metal and metalloid concentrations in geothermal vapors and their vapor-liquid partitioning. In this section we overview these data for geothermal wells and surface fumaroles and compare them with the experimental and theoretical results discussed above.

Geothermal wells. Two-phase well discharges (liquid and vapor) provide information about condensate composition and vapor-liquid partitioning of elements. Sampling techniques and the different types of steam separators allowing extraction of liquid and vapor phases from wet steam wells were discussed in detail in Arnórsson et al. (2006). Extensive studies of steam and liquid from geothermal wells have been conducted in the world's major geothermal areas such as Italy (Möller et al. 2003), Iceland (Giroud 2008), Kamtchatka (Nikolaeva and Bychkov 2007; Nikolaeva 2009), New Zealand (Glover 1988), and the US (Smith et al. 1987) for gases and major elements; however, less attention has been devoted to metals and metalloids. A detailed methodological work on the vapor-liquid fractionation of boron in different types and regimes of wet-steam wells and at different temperatures has recently been conducted for the Mutnovsky geothermal area by Nikolaeva and Bychkov (2007). Comparisons of the sampled vapor and liquid quantities with theoretical estimations based on adiabatic boiling suggest that vapor-liquid separation occurs at greater temperatures and depth before arriving at the steam separator. Consequently, only a part of the vapor-liquid mixture may be captured by the separator. Thus most of such vapor and liquid samples are likely to be a product of a non-representative steam-liquid mixture and are unlikely to correspond to natural vapor-liquid separation at the well's depth and temperature (Arnórsson and Stefánsson 2005a,b).

Nevertheless, steam and liquid water sampling of wells may serve as a field analog of laboratory experiments on vapor-liquid partitioning, provided care has been taken to reduce or correct for the contamination of the vapor by liquid droplets that contain much higher metal and metalloid concentrations. The degree of steam contamination is usually estimated by analyzing it for Na or K (Arnórsson et al. 2006; Nikolaeva 2009), which are not volatile at moderate temperatures (e.g., Fig. 6). Because these and other metals largely partition into the liquid phase under such conditions, ($K_{\text{vapor/liquid}} < 10^{-5}$ at $T < 300$ °C), even very minor contamination by the liquid phase (typically a few % of the mass of the condensate) is sufficient to completely obscure the vapor-phase contribution for such metals. Consequently, in most cases unambiguous estimation of steam concentrations is only possible for relatively volatile elements, such as B and As, whose equilibrium $K_{\text{vapor/liquid}}$ values are much higher (~0.001-0.1, Fig. 6). These analyses indicate that, despite a large scatter, steam/liquid partition coefficients for both metalloids show a reasonable correspondence with equilibrium values, except for a few outliers (Fig. 12A). A similar agreement between average steam-liquid distribution coefficients and equilibrium values is observed for arsenic despite a significant data scatter (Fig. 12B).

Fewer data are available for trace and weakly soluble metals because of a) the vapor-liquid separation artifacts discussed above, b) a possible contamination of vapor and liquid samples by well tubing, separators, and sampling materials made of steel, copper, brass, rubber, all containing lots of trace metals, and c) issues related to sample preservation and analyses or ultra-trace elements. An example reflecting in part these issues is a study of vapor-liquid partitioning of REE between vapor and liquid as sampled at 120 °C and 2 bars from geothermal wells in the Larderello-Travale geothermal field, Tuscany, Central Italy (Möller et al. 2003). Vapor-liquid distribution coefficients of REE and Y found in that study ranged between 0.02 and 0.5; they did not show correlations with the major element composition of the steam (CO_2, Cl, B). When corrected for vapor contamination by liquid using Na, these values remained several orders of magnitude higher than those predicted using the density model based on REE chloride vapor-liquid partitioning measured in the laboratory in salt-water systems at T 300-400 °C (Fig. 6; Shmulovich et al. 2002). The apparent elevated REE partitioning into the steam at Larderello may either be related to geothermal wells sampling issues listed above or reflect the existence in the vapor phase of REE complexes more volatile than chlorides, such as uncharged hydroxides (e.g., $REE(OH)_3$ or REEO(OH), Möller et al. 2003). The latter hypothesis awaits experimental confirmation.

Surface thermal springs. Sampling of vapor and liquid phases in such settings is also subject to many difficulties related to low metal concentrations, vapor contamination by liquid, and partial vapor condensation. If precautions against these issues are taken and clean materials (e.g., cleaned Teflon or polypropylene) are used for sampling, accurate results may be obtained for a range of trace metals and metalloids. For example, a design shown in Figure 13 (Arnórsson et al. 2006; Nikolaeva and Bychkov 2007; Nikolaeva 2009; references therein) allows ef-

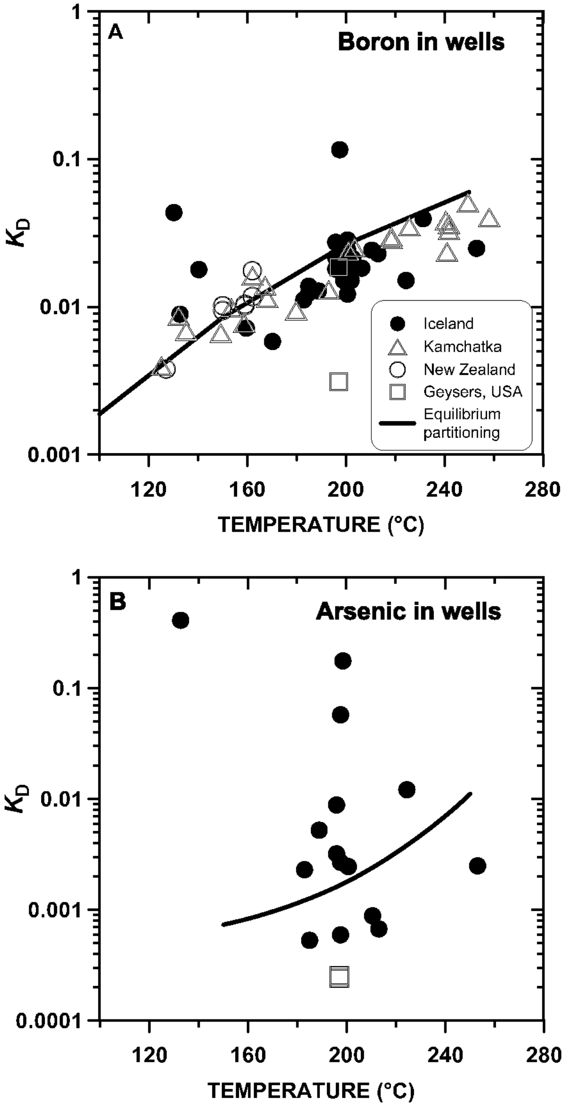

Figure 12. Boron and arsenic steam-liquid distribution coefficients ($K_D = C_{vapor}/C_{liquid}$) as a function of temperature from wet steam wells. Data from Iceland (Giroud 2008), Kamchatka (Nikolaeva and Bychkov 2007), New Zealand (Glover 1988) and Geysers, USA (Smith et al. 1987). The solid lines indicate equilibrium vapor-liquid partitioning of both elements according to Nikolaeva (2009) (boric acid) and Pokrovski et al. (2002b) (arsenous acid).

ficient separation of a major part of liquid-phase droplets (≥ 50 μm), and sampling of vapor in a clean environment. Nevertheless, contamination by micrometric droplets and analytical difficulties for trace elements (below the ppb level) may not be completely excluded. This sampling device was recently used in a systematic study of vapor-liquid partitioning of boron and arsenic, which are relatively abundant in surface springs of Kamtchatka (Nikolaeva and Bychkov 2007). It was found that both boron and arsenic exhibit vapor-liquid distribution coefficients for most data points between 0.001 and 1 with a rough average value in the 0.01-0.1 range (Fig. 14). This is about two orders of magnitude higher than the equilibrium values at $T < 100$ °C for boric and arsenic acids, which are believed to be the major B and As forms in such conditions (Pokrovski et al. 2002b; Nikolaeva 2009). Because of the paucity of volatile components capable of forming other complexes with boron and arsenic (e.g., fluorides, chlorides, sulfides) in the steam and water, it is more likely that the vapor sampled at and below 100 °C lacks equilibrium with the liquid water at the surface. This vapor would thus not be produced by liquid-phase boiling and separation at the surface, but it would originate from deeper and hotter parts of the system. Such H_2O-undersaturated vapor, carrying higher element concentrations than that produced by surface boiling and emanation, may rapidly ascend to the surface without reaching equilibrium with the colder liquid waters. This lack of equilibrium is in agreement with the presence of vapor-dominated deeper horizons in the Mutnovsky volcano area; it may also be the case in other places. This explanation is confirmed by estimations, using equilibrium vapor-liquid distribution coefficients for B at $T > 100$-150 °C (shown by the solid curve in Fig. 12A), of the depth and temperature of the vapor generation, which are in good agreement with other gas and fluid geothermometers (quartz solubility, Na/K ratio, H_2 content, Nikolaeva and Bychkov 2007).

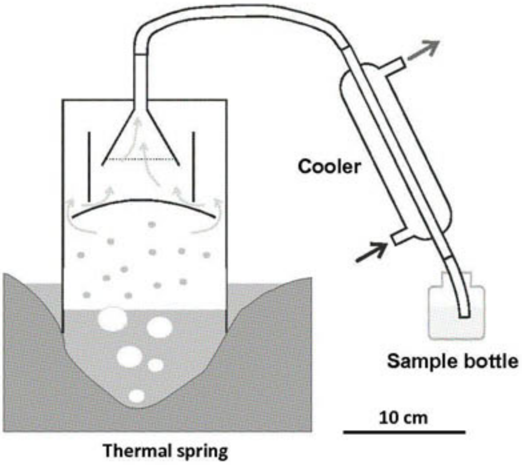

Figure 13. A typical device used for vapor-phase sampling of surface springs (according to Arnórsson et al. 2006; Nikolaeva and Bychkov 2007).

In other geothermal settings, high volatilities of some metalloids may also be due to the formation of particular compounds. This is likely the case of arsenic in gases and air around the low-temperature ($T < 60$ °C) geothermal springs of Yellowstone National Park in the US (Planer-Friedrich et al. 2006). Arsenic gas-phase speciation was determined using specific adsorption of As gaseous forms on solid-phase micro-fibers, followed by gas chromatography extraction and analyses by mass spectrometry. Different As methyl-chloride species such as $(CH_3)_2AsCl$, $(CH_3)_3As$, $(CH_3)_2AsSCH_3$, and CH_3AsCl_2 were detected; they predominate over major inorganic forms ($As(OH)_3$) and are responsible for high As concentrations of air or gas, up to 200 mg/m^3. Such species are likely to be produced via thermophile bacterial activity in hot springs. The effect of microorganisms on the volatility of metals and metalloids is one of the unexplored areas of research on the vapor phase in geothermal areas. However, it is unlikely that bacterial activity contributes significantly to element volatility at temperatures above 90 °C.

Published and accessible reports of vapor-phase content and vapor-liquid partitioning of trace metals and metalloids other than B and As in surface geothermal sources are rare and the sampling methods are not sufficiently detailed, with few exceptions (e.g., Giroud 2008; Nikolaeva 2009). In one of the recent works (Nikolaeva 2009), a large spectrum of elements were systematically analyzed in vapor condensates and coexisting waters in springs from different geothermal systems of Kamtchatka (Uzon Caldera, Geyser Valley, Karymsky, and Mutnovsky volcanoes). The measured range of vapor-liquid distribution coefficients ($K_D = C_{vapor}/C_{liquid}$) for selected elements is shown in Figure 15. Alkaline, alkaline-earth, and lanthanide metals exhibit partitioning coefficients between 0.0001 and 0.1, which are much higher than equilibrium values predicted using the density model based on laboratory measurements ($K_{vapor/liquid} < 10^{-6}$ at 100 °C, see Fig. 6). This discrepancy may be due to a contamination of the vapor by liquid droplets and/or analytical issues of sample storage and quantification of below-

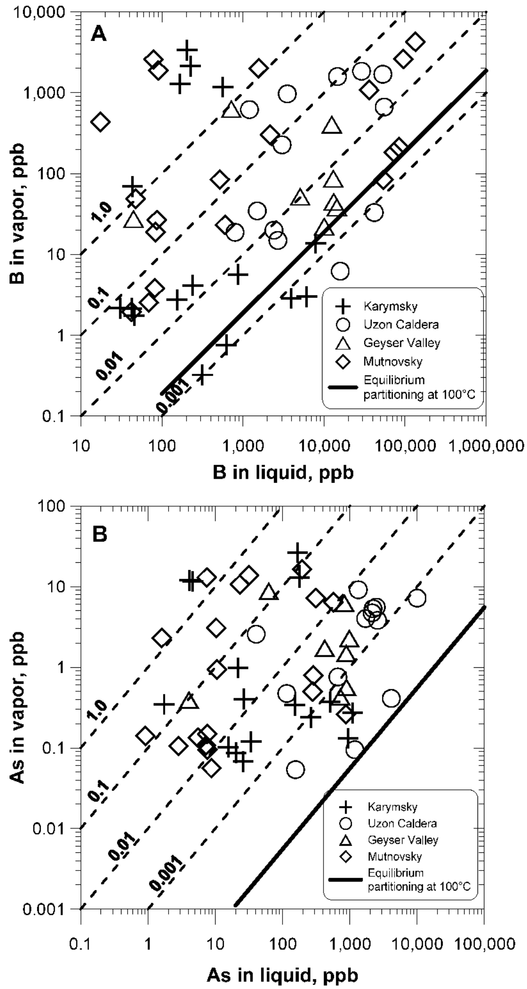

Figure 14. Boron and arsenic concentrations (in parts per billion, ppb) in the coexisting vapor and liquid phase from surface springs in the geothermal fields of Kamtchatka indicated in the legend, according to data from Nikolaeva (2009). The solid line corresponds to equilibrium vapor-liquid partitioning at 100 °C according to Nikolaeva (2009) for boric acid, and Pokrovski et al. (2002b) for arsenous acid, whereas dashed lines with corresponding values indicate vapor-liquid distribution coefficients.

ppb-level concentrations. Metals and metalloids, such as Cu, La, W, Ga, As, and Sb, show average K_D values around 0.01 with large variations, attaining ~5 orders of magnitude. This may be due to partial contamination, analytical issues and the presence of yet unknown volatile forms for some elements. The highest average (K_D~0.1) and maximum (K_D up to ~10s in favor of the vapor) are typical of Cd, Pb, and B, which are relatively common elements in high-temperature volcanic fumarole condensates and sublimates (see above). The K_D values above 1 cannot be explained by liquid-droplet contamination and thus are likely due to the ascent of non-equilibrium hot and deep vapor phases containing higher elemental concentrations, or the presence of some still unknown volatile forms (e.g., for Cd and Pb). Note that the absolute metal concentrations in both liquid and vapor phases in low-T surface springs are generally very small (0.0n to 10s ppb), implying that such very low-density vapors have a low capacity for massively transporting metals compared to deep high T-P magmatic hydrothermal systems, which will be discussed below.

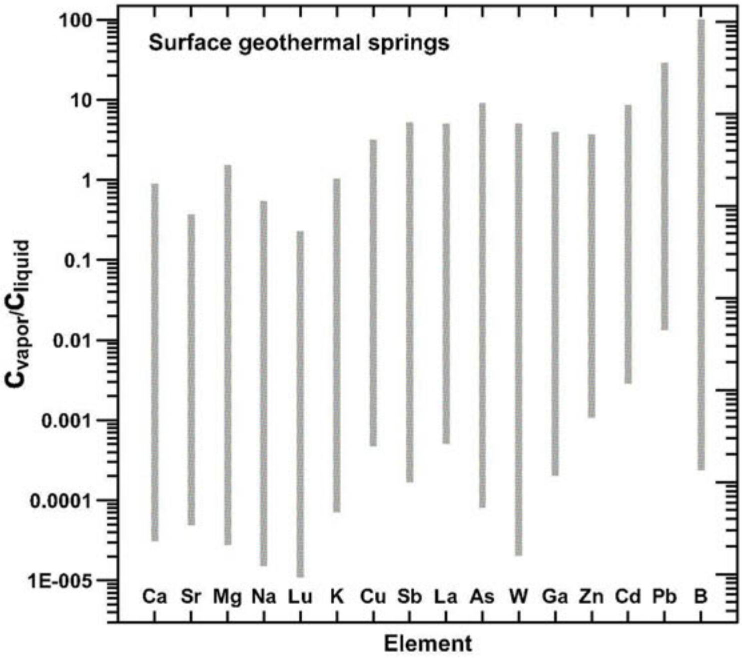

Figure 15. Partition coefficients between the vapor and liquid phase ($K_D = C_{vapor}/C_{liquid}$) in surface geothermal springs of Kamtchatka (Karymsky, Mutnovsky, Uzon Caldera and Geyser Valley) for selected metals and metalloids, according to Nikolaeva (2009). The vertical gray bars outline the range of datapoints for each element.

Magmatic-hydrothermal systems

The experimental and thermodynamic data overviewed above provide a foundation for interpreting the geological role of the vapor phase in metal transport and ore precipitation in the crust. The rapidly growing analytical database of economic metal concentrations acquired since the last ~15 years, mainly using LA-ICPMS analyses of fluid inclusions from different types of magmatic-hydrothermal deposits, together with improved knowledge of vapor-phase speciation and vapor-liquid fractionation of metals discussed above, allows a direct comparison of natural vapor-liquid fractionation patterns with experimental data and thermodynamic predictions. In this section, we focus on abundant fluid inclusion data from porphyry Cu-Au-Mo and associated skarn and epithermal deposits that host a major part of these metal resources on Earth (Sillitoe 2010). Detailed discussions on magma and fluid evolution, fluid inclusion types, metal and mineral zonation, and ore formation mechanisms in these settings have been provided in recent reviews (e.g., Heinrich 2007; Sillitoe 2010; Simon and Ripley 2011; Richards 2011; Audétat and Simon 2012; Kouzmanov and Pokrovski 2012; Pokrovski et al. 2013a; references cited).

Natural vapor-liquid partitioning of sulfur and metals and comparison with experimental data. Vapor-rich and hypersaline-liquid inclusions commonly coexist in quartz and quartz-sulfide stockwork veins in porphyry deposits, forming trails of inclusions which homogenize at similar temperatures (Roedder 1984; references cited). Such fluid inclusion assemblages result from unmixing of homogeneous single-phase magmatic fluid upon its ascent, cooling and decompression, and are formed by simultaneous entrapment of single vapor or hypersaline liquid inclusions along healed fractures (Roedder 1971; Henley and McNabb 1978; Heinrich 2007). Whereas the large metal transporting capacities of the liquid-like inclusions have long been appreciated (e.g., Williams-Jones and Heinrich 2005), the presence of metals in low-density salt-poor vapor was long overlooked due to the lack of robust analytical data. Results of PIXE, LA-ICP-MS, and, recently, SR-XRF analyses of vapor-liquid fluid inclusion assemblages demonstrate that: a) significant element fractionation between hypersaline liquid and vapor is widespread in magmatic-hydrothermal systems, regardless of pressure and temperature, and b) the vapor phase has the ability to transport high concentrations of some metals at pressures above ~100 bar (Heinrich et al. 1992, 1999; Audétat et al. 1998; Cauzid et al. 2007; Seo et al. 2009).

Figure 16 summarizes recently published data on coexisting hypersaline liquid and vapor-rich inclusions formed in porphyry and skarn environments compiled by Kouzmanov and Pokrovski (2012). The data are reported as distribution coefficients, $K_{\text{metal}} = C_{\text{vapor}}/C_{\text{liquid}}$, where C refers to the concentration (in ppm) of the metal in each of the two phases, vapor or liquid. It can be seen that S, Cu, and As have average partitioning coefficients around 1, but the overall magnitude of this partitioning varies strongly between different datasets, especially for Cu (K_{Cu} ranges from ≤0.1 to 100). Gold, where detectable, shows a clear preference for the vapor phase, with K_{Au} up to ~50. Note that absolute concentrations in the vapor phase attain values of ≥10,000 and ≥10 ppm, respectively, for Cu and Au, which is about two to four orders of magnitude higher than their average crustal abundances. Metals such as Bi and Ag have values between 0.1 and ~1, with a few exceptions where they are slightly enriched in the vapor phase. Metals such as Fe, Zn, and Pb, together with Na (and K - not shown) are clearly concentrated in the Cl-rich hypersaline liquid, with typical $K_{\text{vapor/liquid}}$ values between 0.01 and 0.1.

This trend of metal volatility is in semi-quantitative agreement with the experimental measurements of vapor-liquid partitioning in model salt-gas-water systems and density models discussed above for most metals except copper and, to a lesser extent, gold. Experimental $K_{\text{vapor/liquid}}$ values for Cu in a wide range of T (400-800 °C) and sulfur content (up to few wt%) typical of porphyry deposits never exceed 1 in all studies except that of Nagaseki and Hayachi (2008); the highest experimentally measured $K_{\text{vapor/liquid}}$ values for Au do not exceed 10 (see Fig. 10 and corresponding discussion). Until recently, the discrepancy between natural fluid inclusion data and the majority of laboratory experiments for Cu has not received a sound explanation; hypotheses evoked the formation of some volatile sulfur-chloride-hydroxide species not observed in experiments or very high sulfur concentrations (~10s wt%) that enhance Cu partitioning in the vapor phase (e.g., Pokrovski et al. 2008a). Similarly, the stronger partitioning of Au in magmatic vapor phases in nature compared to the rare experiments was explained by salting out effects on neutral Au hydrogen sulfide species in salt-rich liquids or by formation of other stable vapor species, probably with SO_2, which is abundant in porphyry-like systems, but was not thoroughly investigated experimentally (Pokrovski et al. 2008a, 2009b). Although these hypotheses still await verification by future experimental work, in 2012-2013 new experimental and analytical data on fluid inclusions suggested a quite different explanation, which is discussed below.

Post-entrapment modifications of natural vapor-like inclusions. A plausible explanation of the anomalously elevated Cu content in natural vapor-like inclusions was recently offered by measurements on sulfur-rich natural and synthetic fluid inclusions in quartz re-equilibrated with different fluid compositions at 600-800 °C and 700-1300 bar (Lerchbaumer and Audétat 2012). These data revealed rapid diffusion of the Cu^+ ion through the quartz, leading to large post-entrapment changes in Cu concentration in the inclusion. The requirements for the substantial diffusional gain of Cu are a) a change in pH in the surrounding fluid from highly acidic to more neutral, and b) the presence of significant amounts of sulfur (H_2S±SO_2) in the pre-existing vapor-like inclusions. Such requirements are fulfilled in nature when a magmatic-hydrothermal fluid or vapor ascends, cools down, loses sulfur through precipitation of pyrite and chalcopyrite, oxidation or dilution, and is neutralized through interactions with alkali aluminosilicate rocks. In contrast, the S-rich fluid entrapped in quartz develops, during its cooling, significant acidity due to both precipitation of Cu and Fe sulfides and the breakdown of SO_2 in a closed system according to the following reactions:

$$CuCl_2^{-} + FeCl_2^{0} + 2H_2S = CuFeS_{2(s)} \quad 3H^{+} + \quad 0.5H_2 \quad 4Cl^{-} \qquad (6a)$$

$$4SO_2 \quad 4H_2O = H_2S \quad 3HSO_4 \quad 3H \qquad (6b$$

The large gradient in H^+ concentrations between the highly acidic S-rich internal fluid and neutral S-poor external fluid leads to coupled H^+ outward and Cu^+ (±Na, Li) inward diffusion according to the reaction:

$$Cu^{+}{}_{external} + H^{+}{}_{inclusion} = Cu^{+}{}_{inclusion} + H^{+}{}_{external} \qquad (6c)$$

Although Cu^+ is a minor Cu-bearing species in the fluid or vapor phase compared to the dominant Cu chloride, this cation has an elevated diffusion coefficient through channels along the *c*-axis of quartz similar to that of H^+ (and Na^+ and Li^+) (Lerchbaumer and Audétat 2012; references cited). The process goes on until all reduced sulfur in the inclusion is consumed by precipitation with Cu^+ coming from outside. This results in Cu/S ratios close to 2, similar to those in chalcopyrite in many natural vapor inclusions (Seo et al. 2009; Kouzmanov and Pokrovski 2012), confirming the control by Reactions (6a-c). Thus, the elevated copper (and probably silver) content in many quartz-hosted vapor-like inclusions from porphyry deposits (Fig. 16) and also melt inclusions from rhyolites (Kamenetsky and Danyushevsky 2005) might be a post-entrapment modification, the extent of which depends on the thermal history of the host quartz and the chemical evolution of the external fluid and silicate melt. In contrast, Au and base metals like Zn, Fe or Pb are likely not be affected by such diffusion processes (Lerchbaumer and Audétat 2012).

Previous experimental studies in S-free systems also support these conclusions. Zajacz et al. (2008) imposed strong chemical gradients using concentrated HCl external solutions to test post-entrapment modifications of fluid and melt inclusions in quartz for a large number of elements including alkaline and alkaline earth elements, Cu and Ag, and found that only cations with a charge of +1 and a radius equal to or smaller than 1.0 Å (Li^+, Cu^+ , Na^+, Ag^+) diffused through quartz, whereas those having higher electric charges and/or larger radii (e.g., K, Rb, Cs) do not diffuse significantly, or not at least during the time (duration < 10 days) and temperatures (500-720 °C) of the experiment. Because Au^+ is similar in size to K^+ (~1.4 Å) it would not be expected to diffuse fast enough to create significant post-entrapment enrichment or depletion.

More recently, Seo and Heinrich (2013) analysed, using LA-ICPMS, coeval vapor and brine inclusions trapped in coexisting topaz, garnet, and quartz from Mole Granite (Australia) and showed that in contrast to all other metals and sulfur whose concentrations are identical in quartz- and topaz/garnet-hosted inclusions, Cu concentrations in vapor-like inclusions in quartz are 1-2 two orders of magnitude higher than in coeval inclusions in topaz and garnet. Since the structure of these silicate minerals does not allow rapid diffusion of cations compared to quartz, these findings nicely confirm the recent experiments discussed above. Seo and Heinrich (2013) developed a simple thermodynamic model based on the Reaction (6c) whose Gibbs free energy is the driving force of Cu^+ diffusion into quartz to compensate for the outward diffusion of H^+ from the inclusion-hosted acid fluid. These authors also suggest that Au^+ diffusion, if it does occur, is expected to be in the opposite direction, i.e., out of the inclusion, so that Au concentrations analysed in natural high-T vapor-like inclusions from magmatic-hydrothermal deposits might be correct or at least represent minimal estimates. These new results allow a better estimation of the effect of the vapor phase in Cu-Au deposit formation, which is briefly outlined below.

Role of the vapor phase in metal transport and ore formation. The experimental data and thermodynamic considerations presented here, together with the growing body of natural

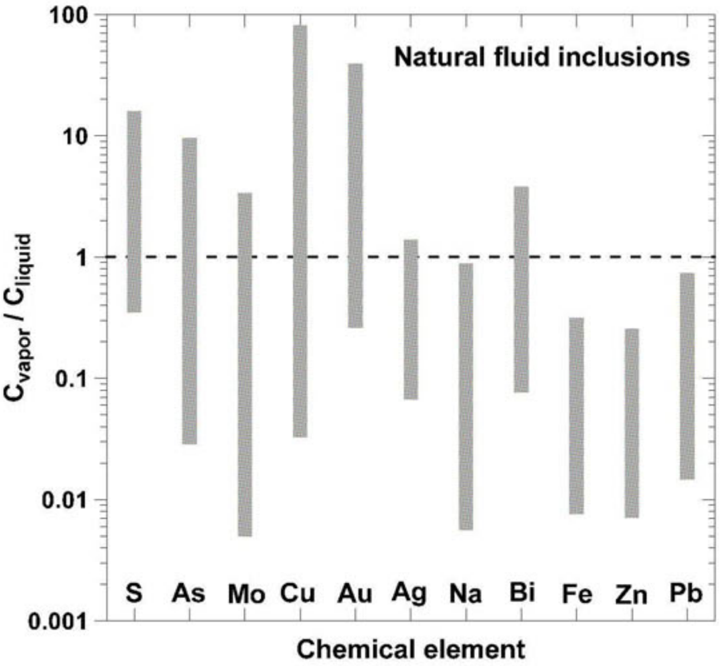

Figure 16. Vapor-liquid partition coefficient ($K = C_{vapor}/C_{liquid}$) of sulfur and selected metals and metalloids from analyses of coexisting vapor and hypersaline liquid inclusions in boiling assemblages in quartz from porphyry Cu-Au-Mo and related deposits, obtained by *in situ* laser ablation ICPMS (modified from Kouzmanov and Pokrovski 2012). Data from Heinrich et al. (1999), Ulrich et al. (1999, 2002), Pettke et al. (2001), Audétat and Pettke (2003), Kehayov et al. (2003), Baker et al. (2004), Williams-Jones and Heinrich (2005), Klemm et al. (2007, 2008), and Seo et al. (2009, 2012). Note that the enhanced partitioning of Cu into the vapor phase (K up to ~100) is likely to be a post-entrapment artifact due to Cu diffusion through quartz (see text and Lerchbaumer and Audétat 2012; Seo and Heinrich 2013, for details). The vertical gray bars outline the range of datapoints for each element.

data from melt, fluid, vapor, and brine inclusions in minerals unambiguously attest that the vapor phase is able to extract and transport significant amounts of metals sufficient to form an economic deposit. However, the amplitude of this transport is very different depending on the *T*-*P*-depth conditions and magmatic fluid evolution paths. Details of fluid properties and evolution in a salt-water system and their effect on metal ore formation in porphyry, epithermal and related environments have been amply discussed in recent reviews (e.g., Williams-Jones and Heinrich 2005; Heinrich 2007; Richards 2011; Kouzmanov and Pokrovski 2012; references cited). Here we will briefly summarize the major differences in the role of the vapor phase in metal behavior in the high *T*-*P* regime (typically above the critical point of water, $T >$ ~350-400 °C, $P >$ ~200-300 bars), which is best represented by porphyry Cu-Au-Mo and orogenic Au deposits, and in the moderate *T*-*P* regime (typically between 150 and 350 °C and $P < 200$ bars), which is typical of epithermal Cu-Au-Ag deposits. Boiling near-surface geotherms, which operate at even lower T ($\leq$ ~100 °C), were discussed in the previous section.

During their evolution in the crust, magmatic, hydrothermal or metamorphic fluids undergo five major processes that cause metal redistribution and deposition: decompression, phase separation (or boiling), cooling, interaction with rocks, and mixing with external waters (Heinrich 2007; Kouzmanov and Pokrovski 2012). These processes are interconnected and one may override or act in parallel with another. Elevated fluid/melt partition coefficients for most economic base and precious metals discussed above ($K_{fluid/melt}$ ~ typically above 10-100, Fig. 11) and those of the major volatiles H_2O, S, Cl ($K_{fluid/melt}$ values for Cl and S are up to 300, depending on melt composition, volatile contents, pressure, temperature and oxygen fugacity; Métrich and Rutherford 1992; Webster 1992a,b; Scaillet et al. 1998; Zajacz et al. 2012a) indicate that an aqueous saline fluid degassed from a silicate magma containing a few wt% of H_2O at depth of a few km will be able to extract more than half of the total Au, Cu, Ag, Zn, Pb, and Mo amount of the magma (Fig. 17). Although the role of magmatic Fe-Cu sulfide phases and melts, which are known to concentrate Cu, Au, Pt and Ag, is still a matter of debate (see Audétat and Simon 2012 for a recent review), it was assumed here for simplicity that silicic magma is undersaturated with sulfide, so that the extent of fluid-silicate melt partitioning should exert a dominant control at this stage of porphyry deposit formation. The generation of a low-density supercritical fluid and/or a vapor phase occurs mostly during fluid *decompression*, i.e., a pressure decrease, both affecting the transport capacities of the homogeneous supercritical fluid itself and inducing *phase separation* with generation of vapor and liquid phases of contrasting densities. These two main phenomena will be briefly considered here; a detailed account of the other processes of fluid evolution, mostly concerning liquid-like fluids (e.g., cooling, fluid-rock interactions, and fluid mixing), has been discussed in recent reviews (Heinrich 2007; Richards 2011; Kouzmanov and Pokrovski 2012; Pokrovski et al. 2013a).

Decompression. All ascending fluids, magmatic and otherwise, undergo a pressure decrease. Although the most direct result of this is *phase separation* (see next subsection) and adiabatic temperature decline, a pressure decrease in a *single-phase* fluid may also affect mineral

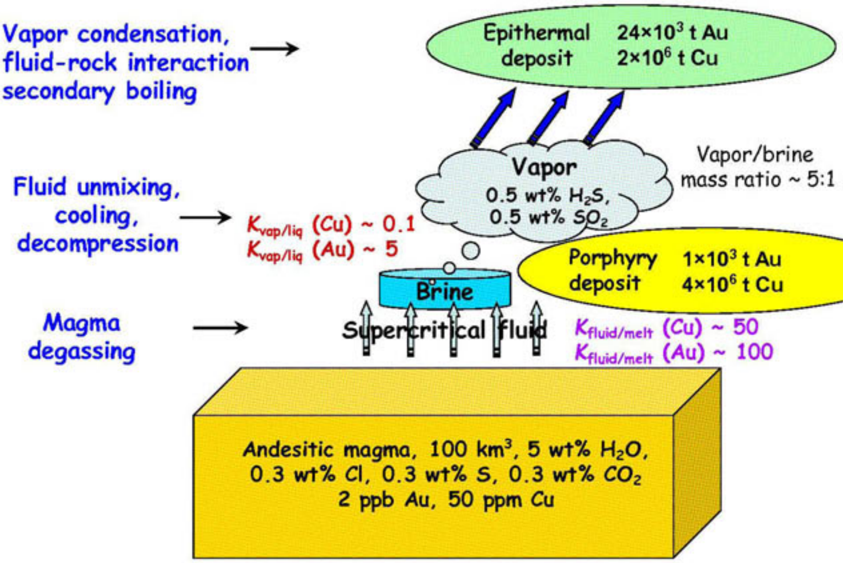
Vapor condensation, fluid-rock interaction secondary boiling
Epithermal deposit
24×10³ t Au
2×10⁶ t Cu
Vapor
0.5 wt% H₂S,
0.5 wt% SO₂
Vapor/brine mass ratio ~ 5:1
Fluid unmixing, cooling, decompression
K_vap/liq (Cu) ~ 0.1
K_vap/liq (Au) ~ 5
Porphyry deposit
1×10³ t Au
4×10⁶ t Cu
Brine
Magma degassing
Supercritical fluid
K_fluid/melt (Cu) ~ 50
K_fluid/melt (Au) ~ 100
Andesitic magma, 100 km³, 5 wt% H₂O,
0.3 wt% Cl, 0.3 wt% S, 0.3 wt% CO₂
2 ppb Au, 50 ppm Cu

Figure 17. Diagram showing the key processes of porphyry-epithermal deposit formation with an emphasis on the actions of the vapor phase: supercritical S- and metal-enriched fluid degassing from an andesitic magma undersaturated with Fe(Cu) sulfide phases, its subsequent separation into the dominant vapor and hypersaline liquid, porphyry Cu(-Au) deposit formation upon fluid decompression and cooling and vapor-liquid unmixing, vapor-phase Au (and Cu) transport to shallower environments, and epithermal Au(-Cu) deposit formation upon vapor-phase condensation, water-rock interaction, further cooling and/or boiling (see text for details). Also indicated are typical vapor-liquid and fluid-melt partition coefficients of Cu and Au at these conditions and the maximam amounts of Cu and Au than may be deposited in porphyry and epithermal environments provided 100% efficiency in precipitation mecanisms.

solubility. However, the quantification of the *P* effect on solubilities of sulfide minerals is difficult because of lack of experimental data, particularly in low-density vapor and supercritical fluids. Large datasets and predictive models (e.g., HKF or density model, see above) are only available for quartz, which shows a sharp decrease in solubility with decreasing *P* at a given *T* (e.g., Fournier 1999; Manning 1994; Kouzmanov and Pokrovski 2012), consistent with the drop in fluid density as discussed in previous sections. Similarly, a decrease in temperature (typically from ~500 °C to 350 °C) at a given pressure (typically < 800 bar) causing the fluid density increase yields retrograde quartz solubility. This enhances rock permeability by quartz dissolution with a temperature decrease, allowing sulfide metal deposition in the newly created vein and pore space. A typical example is the Bingham Canyon porphyry Cu-Au deposit where Cu deposition occurred by cooling and decompression in a narrow *T-P* interval (425-350 °C, 200-140 bar) coupled with retrograde quartz solubility (Landtwing et al. 2005). Pressure is also suggested to have an influence on Cu vs. Au distribution in porphyry deposits, as shown in a recent compilation of Cu/Au ratios for 50 porphyry-style Cu-Au±Mo deposits which display a large variation in the values, from 10^3 to 10^6, correlating with the depth and pressure of ore deposition (Murakami et al. 2010). Thus deep-seated deposits are expected to be deficient in Au and enriched in Cu. This was explained by earlier precipitation of chalcopyrite relative to gold; the latter is stabilized in the form of sulfide complexes and may be transported upward by the vapor-like phase to lower pressure conditions. However, because the pressure and temperature decrease and associated changes in fluid acidity, redox, and sulfur speciation all occur together, it is challenging to identify the contribution of pressure itself on metal distribution.

Phase separation. Another key process leading to generation of a vapor phase is immiscibility, which is caused by a pressure decrease as the fluid ascends toward the surface; this phenomenon is recorded by coexisting liquid- and vapor-rich fluid inclusions (e.g., Kouzmanov and Pokrovski 2012; references therein). In deep high *T-P* environments typical of porphyry deposits, phase separation results in condensation of a minor amount of hypersaline liquid from the dominant low-salinity vapor phase, whereas in the epithermal environment, phase separation occurs by boiling of the dominant aqueous liquid via generation of vapor bubbles (Heinrich 2007; Richards 2011). The effect of phase separation on metal transport and deposition in these two cases is different. According to natural fluid inclusions, phase separation in porphyry deposits at high *T-P* results in a contrasting fractionation of ore-forming elements, with Au and Cu enriched in the vapor phase compared to Fe, Zn, Pb, and Ag (Fig. 16). Until recently, this enrichment was believed to be a prerequisite for the generation of fluids that could form epithermal Au-Cu deposits, with contraction of the vapor to an acidic S-bearing liquid capable of transporting Cu and Au at relatively low temperatures (Heinrich 2005). Such conditions may be met in high-sulfidation Cu-Au deposits (Hedenquist et al. 1993, 1998; Heinrich et al. 2004) and Carlin Au deposits (e.g., Muntean et al. 2011), which are spatially associated with underlying porphyry deposits and magmatic intrusions, providing a source of vapor. However, the recent experimental and analytical discoveries of post-entrapment Cu enrichment in natural fluid inclusions (Lerchbaumer and Audétat 2012; Seo and Heinrich 2013, see above) have modified these ore deposit models for copper. On the basis of experimental data discussed above, the most reasonable $K_{\text{vapor/liquid}}$ values for Cu would be around 0.1 for typical vapor-liquid immiscibility conditions in porphyry systems (Lerchbaumer and Audétat 2012). This value, combined with typical vapor/brine mass ratios between ~4 and 9 in most porphyry systems (e.g., Hedenquist et al. 1998; Landtwing et al. 2010; Lerchbaumer and Audétat 2012), implies that the brine phase will likely carry copper amounts larger than those in the vapor phase. These results support the early models suggesting that the major medium concentrating Cu at porphyry depths (~1-3 km) is hypersaline liquid generated by phase separation (e.g., Henley and McNabb 1978; Bodnar 1995; Beane and Bodnar 1995). Consequently, brine-vapor separation in porphyry deposits does not cause selective Cu transfer to the vapor as has been thought for the last 10 years (e.g., Heinrich et al. 1999; Seo et al. 2009; references therein), but is more likely to promote Cu ore deposition via decompression, unmixing and cooling of the two fluid phases (Seo and Heinrich 2013). In contrast, gold, which is definitely more volatile than Cu in hydrothermal S-rich vapor phases as shown by experiments (Pokrovski et al. 2008a) and is likely not being affected by post-entrapments artifacts (Zajacz et al. 2009; Seo and Heinrich 2013), may be selectively transported by the vapor phase. For example, adopting a reasonable average value of 5 for the $K_{\text{vapor/liquid}}$ coefficient of Au in a S-rich acidic porphyry environment, the vapor phase formed upon unmixing of the ascending magmatic fluid will concentrate more than 90% of the total Au. Thus, these differences in Au and Cu distribution may also explain the Au/Cu zonations in porphyry deposits, as discussed in the previous subsection. Figure 17 qualitatively summarizes general tendencies in Au and Cu distribution in melt-fluid and vapor-brine systems typical of porphyry and epithermal environments. It can be seen in this figure that despite the differences in partitioning amongst the metals, in addition to Au which is largely transported by the vapor phase, this phase is also able to carry absolute amounts of Cu (and also Fe, Ag, Zn, and Pb) sufficient to form an economic epithermal deposit provided that there are focused fluid fluxes and efficient geochemical gradients inducing precipitation.

The effect of phase separation in the porphyry environment on the behavior of Mo is less evident. Limited fluid-inclusion analyses (Fig. 16; Seo et al. 2009, 2012) and laboratory experiments on the vapor-liquid distribution of molybdic acid in S-free systems (Rempel et al. 2009) suggest that a significant portion of the Mo may also be in the vapor phase. In contrast to Cu and Au, however, a S-rich vapor phase is expected to precipitate all Mo when it cools and condenses, because of extremely low MoS_2 solubility at $T < 400$ °C, whereas Au and Cu are sufficiently soluble in the condensed liquid under such conditions (see Kouzmanov and Pokrovski 2012 for an overview of metal solubilities in dense fluid phases from porphyry systems). However, in both high-sulfidation and low-sulfidation epithermal systems, Mo can be locally abundant (up to ~0.1 wt %), thus implying existence of other, not yet studied, complexes, capable of transporting Mo at conditions relevant to epithermal environment.

Many orogenic gold deposits (see reviews of Mikucki 1998; Groves et al. 2003; Heinrich 2007) extending over the whole depth of the continental crust in a wide T range, typically from 600 to 300 °C, also show evidence of phase separation of early aquo-carbonic fluids poor in salt but rich in H_2S as recorded by fluid inclusions (e.g., Yardley et al. 1993). Gold deposition in such settings is believed to occur via sulfidation reactions of the S-rich fluid with Fe-bearing rocks and/or by a process similar to fluid boiling in shallow epithermal systems (see below) that may extend to much greater depths (up to 10 km) because of the greater CO_2 content (10s wt%) that favors unmixing with formation of a CO_2- and H_2S-rich vapor phase and a high-density aqueous liquid. The mechanism of Au precipitation would be the breakdown of Au hydrogen sulfide complexes in the liquid phase due to the loss of H_2S into the vapor (Drummond and Ohmoto 1985; Heinrich 2007). These ore formation models, however, are based on the assumption that Au and other metals are not soluble in CO_2-rich vapors, a hypothesis that lacks any experimental confirmation.

In low-temperature (< 300-350 °C) and pressure (< 100-200 bar) epithermal environments, the density of the vapor phase is too low (< 0.1 g/cm^3) for significant partitioning of any metal into the vapor phase (Fig. 6). The main effect of boiling a liquid under such conditions is removal of H_2S and CO_2 into the vapor. This leads to the breakdown of Au hydrogen sulfide complexes in the liquid phase and results in gold precipitation in veins of bonanza ore zones as shown by both natural observations (e.g., Saunders and Schoenly 1995; Simmons et al. 2005) and thermodynamic modeling (Seward 1989; Spycher and Reed 1989; Cooke and McPhail 2001; Ronacher et al. 2004). The efficiency of the vapor removal strongly depends on the permeability of the system. Focused fluid flow and efficient Au deposition induced by boiling were suggested to be two key factors for formation of large Au epithermal deposits, based on studies of active geothermal systems (e.g., Simmons and Browne 2007). In addition, boiling results in the liquid becoming more alkaline (pH increase) mainly due to a loss of H_2S and CO_2, which in turn may lead to precipitation of galena, sphalerite, chalcopyrite, pyrite, and argentite. The pH increase also leads to precipitation of bladed calcite and adularia, which are useful indicators of boiling zones in epithermal Au exploration (Simmons et al. 2005; Heinrich 2007). Boiling at temperatures below 300 °C is likely to be responsible for Au, Ag, and associated base metal sulfide deposition in low-sulfidation epithermal deposits (e.g., André-Mayer et al. 2002). Recent thermo-mechanical models of the effect of earthquakes on gold-quartz vein formation suggest that faults opening during seismic events result in large fluid pressure drops owing to the creation of empty space, which in turn yields rapid and efficient quartz, gold, and other metal precipitation via so called 'flash vaporization' of the fluid (Weatherley and Henley 2013). For example, the boiling of a CO_2-bearing fluid at ~250 °C induced by faulting events in the El Callao mining district (Venezuela) was likely to yield common precipitation of Au and As-bearing pyrite (Velàsquez et al. 2013).

MAJOR CONCLUSIONS

The key points of this review are the following:

1) Geological vapor-like phases are ubiquitous in the shallow crust (typically down to a few km depth), but may extend to deeper levels (to ~10 km) in the presence of large fractions of volatiles (like CO_2 and CH_4) in the fluid. Their formation and evolution in the crust are driven by the properties of the water-salt-gas systems that allow for vapor-liquid unmixing phenomena in a wide *T*-*P* range. The major manifestations of such phases are volcanoes and boiling geothermal springs at Earth's surface, and magmatic-hydrothermal deposits of metals of economic interest at depth. The vapor-like crustal fluids are essentially aqueous, but may also contain in some cases large fractions (~*n* to 10*n* wt%) of volatiles (CO_2, HCl, H_2S, SO_2, CH_4) and moderate concentrations of salt (NaCl, KCl). Recent analytical, experimental, and theoretical advances have allowed a growing appreciation of the role of vapor-like fluids in the behavior of metals and metalloids and formation of ore deposits.

2) The key physical-chemical phenomenon controlling element solubilities and transport by the vapor phase is hydration, which is directly proportional to the fluid density or pressure. Simple thermodynamic models involving these well-known parameters allow semi-empirical descriptions of mineral solubilities and vapor-liquid partitioning of many chemical elements for most geological purposes. The denser the aqueous vapor, the more metal it can transport. Thus, low-pressure low-density volcanic gases and geothermal steams have lower capacities of concentrating most metals than the silicate melts from which they originate. In contrast, in magmatic-hydrothermal systems at moderate depth, a denser vapor generated by phase separation of magmatic or metamorphic fluids is able to transport large amounts of metals.

3) Metals and metalloids form complexes in the vapor phase with the same major ligands, water/OH, chloride and sulfur, as in the dense aqueous solution or supercritical fluid phase, but their exact stoichiometry and electrical charge may differ. In the H_2O+NaCl/KCl±S±Cl systems at hydrothermal conditions, the majority of metals and metalloids partition in favor of the saline liquid, with metalloids (B, As, Si, Sb, Mo) being more volatile than most economic metals (Au, Cu, Fe, Ag, REE). However, selective enrichment in the vapor phase vs. liquid is possible in the presence of significant amounts of HCl for Sb, and of sulfur ($H_2S \pm SO_2$) for Au, Pt and, partly, Cu. Another factor governing metal vapor-liquid distribution in such systems is the metal speciation in the liquid phase, which depends on pH and ligand concentration. Uncharged hydroxide, chloride, and sulfide metal complexes in the liquid phase are generally far more volatile than their charged counterparts.

4) Most laboratory experiments on vapor-brine-silicate melt partitioning are in reasonable agreement with natural fluid and melt inclusion data from magmatic and pegmatite systems

and associated hydrothermal deposits for all metalloids and most base metals except Cu, which shows systematically enhanced partitioning into the vapor phase in natural fluid inclusions. Recent experimental and analytical studies reveal preferential diffusion of Cu^+ (and possibly Ag^+) from the external fluid or silicate melt into S-rich vapor-like inclusions after entrapment in host-quartz, leading to artificial Cu enrichments, whereas such artifacts do not significantly affect other metals. These findings suggest a reconsideration of recent models emphasizing enhanced vapor-phase transport for Cu in high-temperature porphyry systems, and a return to classical older models suggesting that the supercritical fluid and brine are the main medium for Cu in such systems. Natural fluid inclusion data for Au and Mo also show in some cases fluid-phase contents and vapor-liquid partition coefficients higher than rare available experimental data, likely suggesting the existence of yet unknown dissolved species for these metals.

5) Vapor-melt and fluid-melt partitioning coefficients for most base and precious metals ($K_{\text{fluid/melt}}$ ~ typically between 10 and 100), as shown by experimental and natural data, are largely in favor of the fluid phase, thus allowing efficient extraction of most metals into the degassing aqueous fluid phase. During the fluid ascent, decompression, and unmixing in porphyry environments, most metals including Cu will concentrate in the brine phase and (partly) precipitate in response to vapor-liquid separation and cooling, whereas a major part of Au may be entrained by the S-rich vapor phase to shallower epithermal deposits. This vapor will still be able also to carry sufficient concentrations of Cu (and also Fe, Zn and Pb) to form a potentially economic epithermal deposit when it condenses into an aqueous liquid, cools down, mixes with external waters, interacts with rocks and/or boils.

6) In shallow epithermal settings and geothermal fields, the metal-transporting capacities of the low-density vapor phase are very low, and the main medium for metals and metalloids is the aqueous solution. Boiling and vapor generation in such systems mostly result in partitioning of volatile components (HCl, H_2S, CO_2, H_2) and a consequent decrease in acidity and ligand concentration and increase in redox potential in the liquid phase, all these factors being favorable for precious and base metal precipitation.

REMAINING GAPS AND NEAR-FUTURE CHALLENGES

This review has also highlighted the fact that, in spite of significant progress in understanding the composition and properties of geological metal-transporting vapors at elevated temperatures, much remains to be done. The research on vapor-like fluids is facing a number of analytical, experimental, and theoretical challenges, some of which are briefly outlined below.

Analytical challenges

A number of analytical challenges for fluid inclusions, which are the only direct witnesses of natural vapor-like fluids, remain to be addressed. If metal concentrations are now be routinely analyzed in fluid and melt inclusions in hydrothermal and magmatic minerals and glasses at levels of a few ppm by modern LA-ICPMS machines (e.g., Seo et al. 2009; Pettke et al. 2012; Borisova and Gouy 2013), the situation is different for chlorine and sulfur which are the primary elements controlling the transport and partitioning of base and precious metals in magmatic-hydrothermal systems. In general, sulfur remains one of the most poorly quantified major fluid components. Only a few studies have measured the S content in individual fluid inclusions using LA-ICPMS (Guillong et al. 2008; Seo et al. 2009, 2011; Catchpole et al. 2011, 2013). Such total sulfur analyses should be coupled with *in situ* spectroscopic determination of the abundances of different sulfur species using *in situ* micro-Raman spectroscopy (e.g., Giuliani et al. 2003; Jacquemet et al. 2012), and X-ray absorption and emission spectroscopy (e.g., Métrich et al. 2009; Mori et al. 2010). New developments of microanalytical techniques based on standardless protocols for XAS (e.g., Cauzid et al. 2006) and LA-ICPMS (Borisova and Gouy 2013) should allow more accurate analyses of metals in water-poor, CO_2- and CH_4-rich vapor inclusions and gas bubbles, which are currently poorly quantified owing to a lack of internal standardization (e.g., Hanley and Gladney 2011).

A better account of possible fluid and melt inclusion post-entrapment modifications due to selective metal diffusion through the host mineral (e.g., Kamenetsky and Danyushevsky 2005; Zajacz et al. 2008; Lerchbaumer and Audétat 2012; Seo and Heinrich 2013) is also essential for robust interpretation of Au, Cu, and Ag concentrations in the vapor inclusions. Analyses of fluid inclusions in gangue and sulfide minerals other than quartz (e.g., Simmons et al. 1988; Wilkinson et al. 2009; Kouzmanov et al. 2010) should better constrain such possible artifacts and verify the broadly accepted paradigm in ore deposit research that gangue (quartz, calcite) and associated ore (metal sulfides) minerals are cogenetic.

More attention should be given to examining metal ratios in melt-brine-vapor systems, which may be sensitive to some factors such as HCl content (e.g., As/Sb, Pokrovski et al. 2008b) or melt composition and fluid-melt separation conditions (e.g., Zn/Pb, Kouzmanov and Pokrovski 2012), and thus constitute potential geochemical traces.

Another analytical challenge is the use of non-traditional stable isotopes of metals and metalloids as tracers of fluid and vapor sources and phase separation processes. Although much has been done for understanding the fractionation of light isotopes of H, O, C and S in vapor-liquid systems (e.g., Liebscher 2007; references cited), very few data are available for metals and metalloids like Cu, Fe, Zn, Mo, Ge in natural and laboratory mineral-fluid-vapor systems, and there are no quantitative models for these small, typically less than a few per mil, fractionations owing to a lack of laboratory calibrations at controlled conditions.

Experimental challenges

The analytical issues discussed above should advance in parallel with speciation and solubility experiments in model laboratory systems under controlled conditions that nature does not offer. The behavior of many economically valuable metals and metalloids in the vapor phases and vapor-liquid-melt systems is still poorly known owing to the lack of experimental data on their speciation and partitioning. This particularly concerns Au, Pt, and Mo in high T-P magmatic-hydrothermal systems, but also trace metals of high technological value such as Ge, Ga, Re, for which vapor-phase transport may potentially be important (e.g., Nekrasov et al. 2013).

For most chalcophile and precious metals, sulfur is the key agent controlling their fluid-phase transport and precipitation as sulfide minerals. If in volcanic vapors, H_2S and SO_2 are no doubt the major sulfur species at close-to-atmospheric pressure over a wide T-range, sulfur speciation in denser aqueous vapors, fluids, and silicate melts may be quite different, and the thermodynamic properties of ideal gas sulfur species cannot be used in modeling such systems. For example, the recent discovery of a polysulfide sulfur form, the trisulfur ion S_3^-, which is stable in aqueous liquids and supercritical fluids above ~300 °C and over a wide P range (Pokrovski and Dubrovinsky 2011; Pokrovski and Dubessy 2012; Jacquemet et al. 2012), might change the current interpretations of both sulfur behavior and degassing and its control on metals in S-rich fluids and vapors of porphyry Cu(-Au-Mo) and orogenic Au deposits. *In situ* spectroscopic approaches (e.g., Raman) are necessary to better constrain the stability domain of S_3^- and other intermediate sulfur forms (e.g., other polysulfides, SO_2, and sulfites) and their partitioning in vapor-liquid-melt systems that cannot be fully quantified using quenched natural and laboratory samples. Solubility and spectroscopy (e.g., XAS) experiments in systems where such sulfur species are abundant should allow quantifying their effect on the speciation, transport, and partitioning of Au and other sulfur-loving metals such as Cu, Mo, and Pt.

Another essential experimental need is to better understand the effect of CO_2 on metal transport and partitioning. Our present understanding of its effect in hydrothermal systems is based on a fundamental assumption that metals are not soluble enough to allow their transport in CO_2-rich phases and that the main role of CO_2 is to enhance vapor-liquid immiscibility and to modify the pH of the liquid phase during boiling. However, recent studies (e.g., Pokrovski et al. 2008a; Hanley and Gladney 2011) evoked the possibility of enhanced transport of Cu, Au, Pd, and Ni by CO_2-rich fluids or vapors, but there is no sound physical-chemical interpretation of this potentially important phenomenon because of a lack of experimental data on ore metal solubility and vapor-liquid partitioning in CO_2-rich fluid systems under magmatic-hydrothermal conditions.

With the improvement of micro-beam laser, X-ray, IR, and UV sources and progress in high *T-P* optical cell design (e.g., diamond-anvil cell, this volume; piston cells, Testemale et al. 2005; capillary cells, Chou et al. 2008) it has now become possible to investigate multiphase melt-fluid-vapor systems *in situ* using Raman, XAS or UV spectroscopy and to measure both metal total concentration in the different phases and its molecular structure. If lots of data on metal speciation and solubility exist now for high-density aqueous solutions (e.g., see reviews of Seward and Driesner 2004; Oelkers et al. 2009; this volume), only a few studies have attempted to investigate vapor-like fluids and vapor-brine or fluid-melt systems (e.g., Pokrovski et al. 2002b, 2008b; Veksler et al. 2002; Wilke et al. 2006; Berry et al. 2009; Etschmann et al. 2010). Such spectroscopic approaches are expected to provide a key complement to 'classical' bulk solubility/partitioning measurements using chemical reactor or synthetic fluid inclusion techniques.

Modeling challenges

A major theoretical challenge in our understanding of the geological role of vapor-like fluids is interpretation of experimental data on the solubility/partitioning and metal speciation in the framework of physical-chemical equations of state enabling predictions over the wide range of conditions of crustal fluids, from aqueous solutions to hypersaline brines and a low-density vapor phase. At present, there is a gap in our ability to predict metal behavior in multiphase systems between, on the one hand, the liquid and dense supercritical fluid phase ($\rho >$ 0.4-0.5 g/cm^3), for which robust thermodynamic models (e.g., HKF or density model) are available, and, on the other hand, the low-density under-saturated vapor ($\rho <$ ~0.01 g/cm^3) for which ideal gas thermodynamics may be applied with reasonable accuracy. In between lies a large domain of hydrothermal-magmatic vapors of moderate density in which metal speciation is still poorly known, and current models (e.g., hydration, density models, see above) require more experimental data to reach an accuracy comparable to that for a high-density solution or a low-density gas phase. Integration of such data in user-friendly databases and computer codes (e.g., Oelkers et al. 2009) will enable thermodynamic and kinetic modeling of mineral-fluid-vapor systems.

In the 2000's, molecular modeling approaches based on quantum chemistry and molecular dynamics have given new insights into the atomic structure and hydration energy of ore metal complexes (e.g., Au, Cu, Ag, Zn, Cd, Sb), helping to interpret spectroscopic and solubility data and to make choices among possible speciation models to describe experimental data (e.g., Sherman 2010; Liu et al. 2011; Pokrovski et al. 2009a,b, 2013b). Such approaches, though still in the beginning stages, are expected to provide a direct link between the molecular properties of the vapor-phase species and their thermodynamic stability and solubility.

Another advance of the beginning of the 21th century is the growing application of physical hydrology approaches based on heat distribution and fluid flow models and permeability changes, which have allowed integrated reactive transport models of fluid paths, pressure and temperature evolution, unmixing and boiling, and three-dimensional ore distribution and shape (e.g., Driesner and Geiger 2007; Ingebritsen and Appold 2012; Weis et al. 2012; Weatherley and Henley 2013). However, the chemistry of fluid-rock interactions, mineral solubility, and chemical element speciation in the fluid and vapor phase are not yet quantitatively and systematically accounted for in these models, in particular for metals. Integration of both chemistry and physics in the same conceptual model of ore deposit formation would thus be another major computational challenge and would contribute to our fundamental understanding of the geological role of vapor phases in metal ore deposit formation and to improving ore exploration and extraction.

ACKNOWLEDGMENTS

This work was supported by the Agence Nationale de la Recherche (grant SOUMET - ANR 2011 Blanc SIMI 5-6/009-01 to G.S.P), the University of Toulouse (grant CO2MET to G.S.P.), and by the Russian Science Foundation (RFBR grants 10-05-00254 to A. Y. Borisova, and 12-05-00957a to A. Y. Bychkov). We are grateful to Andri Stefánsson for inviting us to write this contribution, for his patience while waiting for the manuscript, and his efficient editorial handling. We thank Terry Lacy and an anonymous reviewer for their comments that greatly improved this paper. We are indebted to Jodi J. Rosso, Series Editor, for her invaluable assistance in the manuscript editing and proofing. Tatiana Pokrovski is acknowledged for her assistance in the manuscript preparation, Yuri Taran for discussions on volcanic gas chemistry, and Vladimir Naumov for discussions on fluid-melt partitioning.

REFERENCES

Akinfiev NN, Zotov AV (2001) Thermodynamic description of chloride, hydrosulphide, and hydroxide complexes of Ag(I), Cu(I), and Au(I) at temperatures of 25-500 °C and pressures of 1-2000 bar. Geochem Int 39:990-1006

Alekhin YV, Vakulenko AG (1988) Thermodynamic properties and solubility of NaCl in water vapour at 300-500 °C up to 300 bar. Geochem Int 25(5):97-110

Alvarez J, Corti HR, Fernandez-Prini R, Japas ML (1994) Distribution of solutes between coexisting steam and water. Geochim Cosmochim Acta 58:2789-2798

Anderson GM, Castet S, Schott J, Mesmer RE (1991) The density model for estimation of thermodynamic parameters of reactions at high temperature and pressure. Geochim Cosmochim Acta 55:1769-1779

André-Mayer A-S, Leroy J L, Bailly L, Chauvet A, Marcoux E, Grancea L, Llosa F, Rosas J (2002) Boiling and vertical mineralization zoning: A case study from the Apacheta low-sulfidation epithermal gold-silver deposit, southern Peru. Miner Deposita 37:452-464

Archibald SM, Migdisov AA, Williams-Jones AE (2001) The stability of Au-chloride complexes in water vapor at elevated temperatures and pressures. Geochim Cosmochim Acta 65:4413-4423

Archibald SM, Migdisov AA, Williams-Jones AE (2002) An experimental study of the stability of copper chloride complexes in water vapor at elevated temperatures and pressures: Geochim Cosmochim Acta 66:1611-1619

Arnórsson S, Stefánsson A (2005a) Wet-steam well discharges. I. Sampling and calculation of total discharge compositions. Proceedings World Geothermal Congress, Antalya, Turkey 0870

Arnórsson S, Stefánsson A (2005b) Wet-steam well discharges. II. Assessment of aquifer fluid compositions. Proceedings of World Geothermal Congress, Antalya, Turkey 0896

Arnórsson S, Grönvold K, Sigurdsson S (1978) Aquifer chemistry of four high temperature geothermal systems in Iceland. Geochim Cosmochim Acta 42:523-536

Arnórsson S, Bjarnason JO, Giroud N, Gunnarsson I, Stefánsson A (2006) Sampling and analysis of geothermal fluids. Geofluids 6:203-216

Arnórsson S, Stefánsson A, Bjarnason JÖ (2007) Fluid-fluid interaction in geothermal systems. Rev Mineral Geochem 65:259-312

Audétat A (2010) Source and evolution of molybdenum in the porphyry Mo(-Nb) deposit at Cave Peak, Texas. J Petrol 51:1739-1760

Audétat A, Pettke T (2003) The magmatic–hydrothermal evolution of two barren granites: A melt and fluid inclusion study of the Rito del Medio and Canada Pinabete plutons in northern New Mexico (USA). Geochim Cosmochim Acta 67:97-121

Audétat A, Simon AC (2012) Magmatic controls on porphyry copper deposits. Soc Econ Geol Spec Pub 16:573-618

Audétat A, Günther D, Heinrich CA (1998) Formation of a magmatic–hydrothermal ore deposit: Insights with LA-ICP-MS analysis of fluid inclusions. Science 279:2091-2094

Audétat A, Pettke T, Heinrich CA, Bodnar RJ (2008) The composition of magmatic-hydrothermal fluids in barren and mineralized intrusions. Econ Geol 103:877-908

Baes CF Jr, Mesmer RE (1976) The Hydrolysis of Cations. Wiley

Bai TB, Koster van Groos AF (1999) The distribution of Na, K, Rb, Sr, Al, Ge, Cu, W, Mo, La and Ce between granitic melts and coexisting aqueous fluids. Geochim Cosmochim Acta 63:1117-1131

Baker T, Van Achterberg E, Ryan C, Lang JR (2004) Composition and evolution of ore fluids in a magmatic–hydrothermal skarn deposit. Geology 32:117-120

Barin I (1995) Thermochemical Data of Pure Substances. Third Edition, VHC

Barnes HL (ed) (1997) Geochemistry of Hydrothermal Ore Deposits. Wiley, New York

Bazarkina EF, Pokrovski GS, Zotov AV, Hazemann J-L (2010) Structure and stability of cadmium chloride complexes in hydrothermal fluids. Chem Geol 276:1-17

Beane RE, Bodnar RJ (1995) Hydrothermal fluids and hydrothermal alteration in porphyry copper deposits. Arizona Geol Soc Digest 20:83-93

Belov GV, Iorish VS, Yungman VS (1999) IVTANTHERMO for Windows – database on thermodynamic properties and related software. Calphad 23:173-180

Bénézeth P, Diakonov II, Pokrovski GS, Dandurand J-L, Schott J, Khodakovsky IL (1997) Gallium speciation in aqueous solution: Experimental study and modelling. Part II. Solubility of α-GaOOH in acidic solutions from 150 to 250 °C and hydrolysis constants of gallium (III) to 300 °C. Geochim Cosmochim Acta 61:1345-1357

Bernard A, Symonds RB, Rose WI Jr (1990) Volatile transport and deposition of Mo, W, and Re in high temperature magmatic fluids. Appl Geochem 5: 317-326

Berry AJ, Harris AC, Kamenetsky VS, Newville M, Sutton SR (2009). The speciation of copper in natural fluid inclusions at temperatures up to 700 °C. Chem Geol 259:2-7

Bischoff JL, Rosenbauer RJ (1987) Phase separation in seafloor geothermal systems: an experimental study of the effects on metal transport. Am J Sci 287:953-978

Bischoff JL, Rosenbauer RJ, Pitzer KS (1986) The system NaCl-H_2O: relations of vapor-liquid near the critical temperature of water and of vapor-liquid-halite from 300 to 500 °C. Geochim Cosmochim Acta 50:1437-1444

Bodnar RJ (1995) Fluid-inclusion evidence for a magmatic source for metals in porphyry copper deposits. Mineral Ass Canada Short Course Ser 23:139-152

Borisova AY, Gouy S (2013) A new method for quantifying elemental concentrations in natural and synthetic fluid inclusions and bubbles. Am Miner (submitted)

Borisova AY, Pokrovski GS, Pichavant M, Freydier R, Candaudap F (2010) Arsenic enrichment in hydrous peraluminous melts: Insights from femtosecond laser ablation-inductively coupled plasma-quadrupole mass spectrometry, and *in situ* X-ray absorption fine structure spectroscopy. Am Mineral 95:1095-1104

Borisova AY, Thomas R, Salvi S, Candaudap F, Lanzanova A, Chmeleff J (2012) Tin and associated metal and metalloid geochemistry by femtosecond LA-ICP-QMS microanalysis of pegmatite-leucogranite inclusions: new evidence for melt-melt-fluid immiscibility. Mineral Mag 76:91-113

Botcharnikov RE, Linnen RL, Wilke M, Holtz F, Jugo PJ, Berndt J (2011). High gold concentrations in sulphide-bearing magma under oxidizing conditions. Nature Geosci 4:112–115

Brimhall GH, Crerar DA (1987) Ore fluids: Magmatic to supergene. Rev Mineral 17:235-321

Browne PRL, Ellis AJ (1970) The Ohaki-Broadlands hydrothermal area, New Zealand: Mineralogy and related geochemistry. Am J Sci 269:97-131

Bruner G (ed) (2004) Supercritical Fluids as Solvents and Reaction Media. Elsevier

Bychkov AY, Nikolaeva IY (2013) Experimental study of the transport of chalcophile metals in gaseous hydrogen sulfide. Geochem Int 51:413-416

Cameron AGW (1962) The formation of the sun and planets. Icarus 1:13-69

Candela PA, Holland HD (1984) The partitioning of copper and molybdenum between silicate melts and aqueous fluids. Geochim Cosmochim Acta 48:373-380

Catchpole H, Kouzmanov K, Fontboté L, Guillong M, Heinrich CA (2011) Fluid evolution in zoned Cordilleran polymetallic veins - Insights from microthermometry and LA-ICP-MS of fluid inclusions. Chem Geol 281:293-304

Catchpole H, Kouzmanov K, Putlitz B, Fontboté L, Seo JH (2013) Fluid evolution of porphyry-related zoned base metal mineralization in the Morococha district, Peru. Econ Geol (in review)

Cauzid J, Philippot P, Martinez-Criado G, Ménez B, Labouré S (2007) Contrasting Cu-complexing behaviour in vapour and liquid fluid inclusions from the Yankee Lode tin deposit, Mole Granite, Australia. Chem Geol 246:39-54

Chakhmouradian AR, Wall F (2012) Rare earth elements: Minerals, mines, magnets (and more). Elements 8:333-340

Chase MW Jr (1998) NIST-JANAF Thermochemical Tables, 4th ed. J Phys Chem Ref Data, Monograph No. 9

Chevychelov VY, Chevychelova TK (1997) Partitioning of Pb, Zn, W, Mo, Cl and major elements between aqueous fluid and melt in the systems granodiorite (granite leucogranite) – H_2O-NaCl-HCl. Neues Jahr Mineral Abh 172:101-115

Chevychelov VY, Zaraisky GP, Borisovskii SE, Borkov DA (2005) Effect of melt composition and temperature on the partitioning of Ta, Nb, Mn, and F between granitic (alkaline) melt and fluorine-bearing aqueous fluid: fractionation of Ta and Nb and conditions of ore formation in rare-metal granites. Petrology 13:305-321 (In Russian)

Chou I-M, Song Y, Burruss RC (2008) A new method for synthesizing fluid inclusions in fused silica capillaries containing organic and inorganic material. Geochim Cosmochim Acta 72:5217-5231

Churakov SV, Tkachenko SI, Korzhinskii MA, Bocharnikov RE, Shmulovich KI (2000) Evolution of composition of high-temperature fumarolic gases from Kudryavy volcano, Iturup, Kuril Islands: The thermodynamic modeling. Geochem Int 38:436-451

Cooke DR, McPhail DC (2001) Epithermal Au-Ag-Te mineralization, Acupan, Baguio district, Philippines: Numerical simulations of mineral deposition. Econ Geol 96:109-131

Crerar D, Wood S, Brantley S (1985) Chemical controls on solubility of ore-forming minerals in hydrothermal solutions. Can Mineral 23:333-352

Crocket JH (2000) PGE in fresh basalt, hydrothermal alteration products, and volcanic incrustations of Kilauea volcano Hawaii. Geochim Cosmochim Acta 64:1791-1807

D'Amore F, Pruess K (1986) Correlations between steam saturation, fluid composition and well decline in vapor-dominated reservoirs. Geothermics 15:167-183

Driesner T (2013) The molecular-scale fundament of geothermal fluid thermodynamics. Rev Mineral Geochem 76:1-33

Driesner T, Geiger S (2007) Numerical simulation of multiphase fluid flow in hydrothermal systems. Rev Mineral Geochem 65:187-212

Driesner T, Heinrich CA (2007) The system H_2O–NaCl. Part I: Correlation formulae for phase relations in temperature–pressure–composition space from 0 to 1000 °C, 0 to 5000 bar, and 0 to 1 X_{NaCl}. Geochim Cosmochim Acta 71:4880-4901

Drummond SE, Ohmoto H (1985) Chemical evolution and mineral deposition in boiling hydrothermal systems. Econ Geol 80:126-147

Ellis AJ (1979) Explored geothermal systems. *In*: Geochemistry of Hydrothermal Ore Deposits. Barnes HL (ed) John Wiley and Sons, New York, p 632-683

Erkey C (2000) Supercritical carbon dioxide extraction of metals from aqueous solutions: a review. J Supercrit Fluids 17:259-287

Etschmann BE, Liu W, Testemale D, Müller H, Rae NA, Proux O, Hazemann J-L, Brugger J (2010) An *in situ* XAS study of copper(I) transport as hydrosulfide complexes in hydrothermal solutions (25-592 °C, 180-600 bar): Speciation and solubility in vapor and liquid phases. Geochim Cosmochim Acta 74:4723-4739

Farges F, Siewert R, Ponader CW, Brown GE, Pichavant M, Behrens H (2006) Structural environment around molybdenum in silicate glasses and melts: II. Effect of temperature, pressure, H_2O, halogens and sulfur. Can Mineral 44:755-773

Flynn RT, Burnham CW (1978) An experimental determination of rare earth partition coefficients between a chloride containing vapor phase and silicate melts. Geochim Cosmochim Acta 42:685-701

Fournier RO (1989) Geochemistry and dynamics of the Yellowstone National Park hydrothermal system. Ann Rev Earth Planet Sci 17:13-53

Fournier RO (1999) Hydrothermal processes related to movement of fluid from plastic into brittle rock in the magmatic-epithermal environment. Econ Geol 94:1193-1211

Fournier RO, Potter RW,II (1982) An equation correlating the solubility of quartz in water from 25° to 900°C at pressures up to 10,000 bars. Geochim Cosmochim Acta 46:1969-1973

Foustoukos DI, Seyfried WE (2007a) Quartz solubility in the two-phase and critical region of the NaCl-KCl-H_2O system: Implications for submarine hydrothermal vent systems at 9°50'N East Pacific Rise. Geochim Cosmochim Acta 71:186-201

Foustoukos DI, Seyfried WE (2007b) Trace element partitioning between vapor, brine and halite under extreme phase separation conditions. Geochim Cosmochim Acta 71:2056-2071

Frank MR, Candela PA, Piccoli PM, Glascock D (2002) Gold solubility, speciation and partitioning as a function of HCl in the brine-silicate melt-metallic gold system at 800 °C and 100 MPa. Geochim Cosmochim Acta 66:3719-3732

Frank MR, Simon AC, Pettke T, Candela PA, Piccoli PM (2011) Gold and copper partitioning in magmatic-hydrothermal systems at 800 °C and 100 MPa. Geochim Cosmochim Acta 75:2470-2482

Giggenbach WF (1980) Geothermal gas equilibria. Geochim Cosmochim Acta 44:2021-2032

Giggenbach WF (1984) Mass transfer in hydrothermal alteration systems—A conceptual approach. Geochim Cosmochim Acta 48:2693-2711

Giggenbach WF (1987) Redox processes governing the chemistry of fumarolic gas discharges from White Island, New Zealand. Appl Geochem 2:143-161

Giggenbach WF (1988) Geothermal solute equilibria. Derivation of Na-K-Mg-Ca geoindicators. Geochim Cosmochim Acta 52:2749-2765

Giggenbach WF (1995) Variations in the chemical and isotopic composition of fluids discharged from the Taupo Volcanic Zone, New Zealand. J Volcanol Geotherm Res 68:89-116

Giggenbach WF (1997) The origin and evolution of fluids in magmatic-hydrothermal systems. *In:* Geochemistry of Hydrothermal Ore Deposits, 3rd edition. Barnes HL (ed) New York, John Wiley & Sons, p 737-796

Gilbert CD, Williams-Jones AE (2008) Vapour transport of rare earth elements (REE) in volcanic gas: Evidence from encrustations at Oldoinyo Lengai. J Volcanol Geotherm Res 176:519-528

Giroud N (2008) A chemical study of arsenic, boron and gases in high-temperature geothermal fluids in Iceland. PhD thesis, University of Iceland, Reykjavik

Giuliani G, Dubessy J, Banks D, Vinh HQ, Lhomme T, Pironon J, Garnier V, Trinh PT, Long PV, Ohnenstetter D, Schwarz D (2003) CO_2-H_2S-COS-S_8-AlO(OH)-bearing fluid inclusions in ruby from marble-hosted deposits in Luc Yen area, North Vietnam. Chem Geol 194:167-185

Glemser O, Wendlandt HG (1963) Gaseous hydroxides. *In*: Advances in Inorganic Chemistry and Radiochemistry. Vol. 5. Emeléus HJ, Sharpe AG (eds) VCHS, p 215-258

Glover RB (1988) Boron distribution between liquid and vapour in geothermal fluids. Proc 10th New Zealand Geothermal Workshop, p 223-227

Groves DI, Goldfarb RJ, Robert F, Hart CJR (2003) Gold deposits in metamorphic belts: Overview of current understanding, outstanding problems, future research, and exploration significance. Econ Geol 98:1-29

Guillong M, Latkoczy C, Seo JH, Günther D, Heinrich CA (2008) Determination of sulfur in fluid inclusions by laser ablation ICP-MS. J Anal Atom Spectrom 23:15811589

Haas JR, Shock EL, Sassani DC (1995) Rare earth elements in hydrothermal systems: Astimates of standard partial molal thermodynamic properties of aqueous complexes of the rare earth elements at high temperatures and pressures. Geochim Cosmochim Acta 59:4329-4350

Hanley JJ, Gladney ER (2011) The presence of carbonic-dominant volatiles during the crystallization of sulfide-bearing mafic pegmatites in the North Roby zone, Lac des Iles Complex, Ontario. Econ Geol 106:33-54

Hanley JJ, Pettke T, Mungall JE, Spooner ETC (2005) The solubility of platinum and gold in NaCl brines at 1.5 kbar, 600 to 800 °C: A laser ablation ICP-MS pilot study of synthetic fluid inclusions. Geochim Cosmochim Acta 69:2593-2611

Harvey AH, Lemmon EW (2004) Correlation for the second virial coefficient of water. J Phys Chem Ref Data 33:369-376

Harvey AH, Levelt Sengers JMH (1990) Correlation of the aqueous Henry's constants from 0 °C to the critical point. AIChE J 36:539-546

Hashimoto A (1992) The effect of H_2O gas on volatilities of planet-forming major elements: I. Experimental determination of the thermodynamic properties of Ca-, Al-, and Si-hydroxide gas molecules and its application to the solar nebula. Geochim Cosmochim Acta 56:511-532

Hedenquist JW (1991) Boiling and dilution in the shallow portion of the Waiotapu geothermal system, New Zealand. Geochim Cosmochim Acta 55:2753-2765

Hedenquist JW (1995) The ascent of magmatic fluid: Discharge versus mineralization. Mineral Assoc Canada Short Course Ser 23:263-289

Hedenquist JW, Lowenstern JB (1994) The role of magmas in the formation of hydrothermal ore deposits. Nature 370:519–527

Hedenquist JW, Simmons SF, Giggenbach WF, Eldridge CS (1993) White Island, New Zealand, volcanic-hydrothermal system represents the geochemical environment of high-sulfidation Cu and Au ore deposition. Geology 21:731-734

Hedenquist JW, Aoki M, Shinohara H (1994) Flux of volatiles and ore-forming metals from the magmatic-hydrothermal system of Satsuma Iwojima volcano. Geology 22:585-588

Hedenquist JW, Arribas A Jr., Reynolds TJ (1998) Evolution of an intrusion-centered hydrothermal system: Far Southeast-Lepanto porphyry and epithermal Cu-Au deposits, Philippines. Econ Geol 93:373-404

Heinrich CA (2005) The physical and chemical evolution of low-salinity magmatic fluids at the porphyry to epithermal transition: A thermodynamic study. Miner Deposita 39:864-889

Heinrich CA (2007) Fluid–fluid interactions in magmatic-hydrothermal ore formation. Rev Mineral Geochem 65:363-387

Heinrich CA, Ryan CG, Mernagh TP, Eadington PJ (1992) Segregation of ore metals between magmatic brine and vapor - a fluid inclusion study using PIXE microanalysis. Econ Geol 87:1566-1583

Heinrich CA, Günther D, Audédat A, Ulrich T, Frischknecht R (1999) Metal fractionation between magmatic brine and vapour, and the link between porphyry-style and epithermal Cu-Au deposits. Geology 27:755-758

Heinrich CA, Driesner T, Stefánsson A, Seward TM (2004) Magmatic vapor contraction and the transport of gold from porphyry to epithermal ore deposits. Geology 39:761-764

Helgeson HC, Kirkham DH, Flowers GC (1981) Theoretical prediction of the thermodynamic behavior of aqueous electrolytes at high pressures and temperatures: IV. Calculation of activity coefficients, osmotic coefficients, and apparent molal and standard and relative partial molal properties to 600 °C and 5 kb. Am J Sci 291:1249-1516

Henley RW, Ellis AJ (1983) Geothermal systems ancient and modern: A geochemical review. Earth Sci Rev 19:1-50

Henley RW, McNabb A (1978) Magmatic vapor plumes and ground-water interaction in porphyry copper emplacement. Econ Geol 73:1-20

Holland HD (1972) Granites, solutions and base metal deposits. Econ Geol 67:281-301

Ingebritsen SE, Appold MS (2012) The physical hydrology of ore deposits. Econ Geol 107:559-584

Jacquemet N, Guillaume D, Zwick A, Pokrovski GS (2012) *In situ* Raman spectroscopy identification of the S_3^- ion in gold-bearing fluids from synthetic fluid inclusions. Geo-Raman X, Nancy, France. J Conf Abst, 207-208

Jégo S, Pichavant M (2012) Gold solubility in arc magmas: Experimental determination of the effect of sulfur at 1000 °C and 0.4 GPa. Geochim Cosmochim Acta 84:560-592

Johnson JW, Oelkers EH, Helgeson HC (1992) SUPCRT92: A software package for calculating the standard molal thermodynamic properties of minerals, gases, aqueous species, and reactions from 1 to 5000 bar and 0 to 1000 °C. Comp Geosci 18:899-947

Kamenetsky VS, Danyushevsky LV (2005) Metals in quartz-hosted melt inclusions: Natural facts and experimental artifacts. Am Mineral 90:1674-1678

Kehayov R, Bogdanov K, Fanger L, von Quadt A, Pettke T, Heinrich CA (2003) The fluid chemical evolution of the Elatiste porphyry Cu-Au-PGE deposit, Bulgaria. *In*: Mineral Exploration and Sustainable Development. Eliopoulos DG (ed) Rotterdam, Millpress, p 1173-1176

Keppler H (1996) Constraints from partitioning experiments on the composition of subduction-zone fluids. Nature 380:237-240

Keppler H, Wyllie PJ (1991) Partitioning of Cu, Sn, Mo, W, U, and Th between melt and aqueous fluid in the systems haplogranite-H_2O-HCl and haplogranite-H_2O-HF. Contrib Mineral Petrol 109:139-150

Kestin J, Sengers JV, Kamgar-Parsi B, Levelt-Sengers JMH (1984) Thermophysical properties of fluid H_2O. J Phys Chem Ref 13:175-183

Khitarov NI, Malinin SD, Lebedev EB, Shibieva NP (1982) Partition of Zn, Cu, Pb and Mo between the fluid phase and silicate melt of granitic composition under high-temperature and pressure. Geokhimiya 8:1094-1107

Klemm LM, Pettke T, Heinrich CA, Campos E (2007) Hydrothermal evolution of the El Teniente deposit, Chile: Porphyry Cu-Mo ore deposition from low-salinity magmatic fluids. Econ Geol 102:1021-1045

Klemm LM, Pettke T, Heinrich CA (2008) Fluid and source magma evolution of the Questa porphyry Mo deposit, New Mexico, USA. Miner Deposita 43:533-552

Knauss KG, Dibley MJ, Bourcier WL, Shaw HF (2001) Ti(IV) hydrolysis constants derived from rutile solubility measurements made from 100 to 300 °C. Appl Geochem 16:1115-1128

Kouzmanov K, Pokrovski GS (2012) Hydrothermal controls on metal distribution in Cu(-Au-Mo) porphyry systems. Soc Econ Geol Spec Pub 16: 573-618

Kouzmanov K, Pettke T, Heinrich CA (2010) Direct analysis of ore-precipitating fluids: combined IR microscopy and LA-ICP-MS study of fluid inclusions in opaque ore minerals. Econ Geol 105:351-373

Krauskopf KB (1957) The heavy metal content of magmatic vapor at 600 °C. Econ Geol 52:786-807

Krauskopf KB (1964) The possible role of volatile metal compounds in ore genesis. Econ Geol 59:22-45

Krupp RE, Seward TM (1990) Transport and deposition of metals in the Rotokawa geothermal system, New Zealand. Miner Deposita 25:73-81

Kukuljan JA, Alvarez JL, Fernández-Prini R (1999) Distribution of $B(OH)_3$ between water and steam at high temperatures. J Chem Thermodyn 31:1511-1521

Landtwing MR, Pettke T, Halter WE, Heinrich CA, Redmond PB, Einaudi MT, Kunze K (2005) Copper deposition during quartz dissolution by cooling magmatic-hydrothermal fluids: The Bingham porphyry. Earth Planet Sci Lett 235:229-243

Landtwing MR, Furrer C, Redmond PB, Pettke T, Guillong M, Heinrich CA (2010) The Bingham Canyon porphyry Cu–Mo–Au deposit III. Zoned copper–gold ore deposition by magmatic vapor expansion. Econ Geol 105:91-118

Le Guern F, Bernard A (1982) A new method for sampling and analyzing volcanic sublimates - Application to Merapi volcano, Java. J Volcanol Geotherm Res 12:133-146

Lerchbaumer L, Audétat A (2012) High Cu concentrations in vapor-type fluid inclusions: An artifact? Geochim Cosmochim Acta 88:255-274

Lerchbaumer L, Audétat A (2013) The metal content of silicate melts and aqueous fluids in subeconomically Mo mineralized granites: Implications for porphyry Mo genesis. Econ Geol 108:987-1013

Lewis GN, Randall M (1965) Thermodynamics. 2nd edition, International Student Edition, Mexico

Liebscher A (2007) Experimental studies in model fluid systems. Rev Mineral Geochem 65:15-47

Liebscher A, Meixner A, Romer RL, Heinrich W (2005) Liquid-vapor fractionation of boron and boron isotopes: Experimental calibration at 400 °C/23 MPa to 450 °C/42 MPa. Geochim Cosmochim Acta 69:5693-5704

Liu X, Lu X, Wang R, Zhou H, Xu S (2011) Speciation of gold in hydrosulphide-rich ore-forming fluids: Insights from first-principles molecular dynamics simulations. Geochim Cosmochim Acta 75:185-194

London D, Hervig RL, Morgan GB (1988) Melt-vapor solubilities and elemental partitioning in peraluminous granite-pegmatite systems: experimental results with Macusani glass at 200 MPa. Contrib Mineral Petrol 99:360-373

Lowenstern JB (1993) Evidence for a copper-bearing fluid in magma erupted at the Valley of Ten Thousand Smokes, Alaska. Contrib Mineral Petrol 114:409-421

Lowenstern JB, Mahood GA, Rivers ML, Sutton SR (1991) Evidence for extreme partitioning of copper into a magmatic vapor phase. Science 252:1405-1409

Magini M, Licheri G, Paschina G, Piccaluga G, Pinna G (1988) X-ray diffraction of ions in aqueous solutions: Hydration and complex formation. CRC Press, Boca Raton, Florida

Manning CE (1994) The solubility of quartz in H_2O in the lower crust and upper mantle. Geochim Cosmochim Acta 58:4831-4839

Manning DAC, Pichavant M (1988) Volatiles and their bearing on the behavior of metals in granitic systems. *In*: Recent Advances in the Geology of Granite-Related Mineral Deposits. Special Vol 39. Taylor RP, Strong DF (eds) Can Inst Mineral Metall, p 13-24

Marshall WM, Franck EU (1981) Ion product of water substance, 0-1000 °C, 1-10,000 bars, new international formulation and its background. J Phys Chem Ref Data 10:295-304

Martynova OI (1964) Some questions on the solubility of low-volatile inorganic compounds in water steam at high temperatures and pressures. Zh Fiz Khim 38:1065-1076 (in Russian)

Meschter PJ, Opila EJ, Jacobson NS (2013) Water vapor–mediated volatilization of high-temperature materials. Ann Rev Mat Res 43, doi: 10.1146/annurev-matsci-071312-121636

Mesmer RE, Marshall WL, Palmer DA, Simonson JM, Holmes HF (1988) Thermodynamics of aqueous association and ionization reactions at high temperatures and pressures. J Solution Chem 17:699-718

Métrich N, Rutherford MJ (1992) Experimental study of chlorine behavior in hydrous silicic melts. Geochim Cosmochim Acta 56:607-616

Métrich N, Berry AJ, O'Neill HStC, Susini J (2009) The oxidation state of sulfur in synthetic and natural glasses determined by X-ray absorption spectroscopy. Geochim Cosmochim Acta 73:2382-2399

Migdisov AA, Bychkov AY (1998) The behavior of metals and sulfur during the formation of hydrothermal mercury-antimony-arsenic mineralization, Uzon Caldera, Kamchatka, Russia. J Volcanol Geotherm Res 84:153-171

Migdisov AA, Williams-Jones AE (2005) An experimental study of cassiterite solubility in HCl-bearing water vapour at temperatures up to 350 °C. Implications for tin ore formation. Chem Geol 217:29-40

Migdisov AA, Williams-Jones AE (2013) A predictive model for metal transport of silver chloride by aqueous vapor in ore-forming magmatic-hydrothermal systems. Geochim Cosmochim Acta 104:123-135

Migdisov AA, Williams-Jones AE, Suleimenov OM (1999) Solubility of chlorargyrite (AgCl) in water vapor at elevated temperatures and pressures. Geochim Cosmochim Acta 63:3817-3827

Mikucki EJ (1998) Hydrothermal transport and depositional processes in Archean lode-gold systems: A review. Ore Geol Rev 13:307-321

Minubayeva Z, Seward TM (2010) Molybdic acid ionization under hydrothermal conditions to 300 °C. Geochim Cosmochim Acta 74:4365-4374

Möller P, Dulski P, Morteani G (2003) Partitioning of rare earth elements, yttrium, and some major elements among source rocks, liquid and vapor of Larderello-Travale Geothermal Field, Tuscany (Central Italy). Geochim Cosmochim Acta 67:171-183

Morey GW (1957) The solubility of solids in gases. Econ Geol 52:225-251

Morey GW, Hesselgesser JM (1951) The solubility of some minerals in superheated steam at high temperatures. Econ Geol 46:821-835

Mori R, Paris E, Giuli G, Eeckhout SG, Kavcic M, Zitnik M, Bucar K, Pettersson LGM, Glatzel P (2010) Sulfur-metal orbital hybridization in sulfur-bearing compounds studied by X-ray emission spectroscopy. Inorg Chem 49:6468-6473

Muntean JL, Cline JS, Simon AC, Longo AA (2011) Magmatic-hydrothermal origin of Nevada's Carlin-type gold deposits: Nature Geosci 4:122-127

Murakami H, Seo JH, Heinrich CA (2010). The relation between Cu/Au ratio and formation depth of porphyry-style Cu-Au±Mo deposits. Miner Deposita 45:11-21

Naboko SI (1964) Contemporary volcanoes and gas hydrothermal activity. Geologiya SSSR 31:323-387 (in Russian)

Nagaseki H, Hayashi KI (2008) Experimental study of the behavior of copper and zinc in a boiling hydrothermal system. Geology 36:27-30

Nekrasov SY, Bychkov AY (2011) Experimental study of Ga and Al oxide solubility in gas-vapor mixture at 200 °C. Geochem Int 49:90-94

Nekrasov SY, Migdisov AA, Williams-Jones AE, Bychkov AY (2013) An experimental study of the solubility of Gallium(III) oxide in HCl-bearing water vapour. Geochim Cosmochim Acta (in press)

Nikolaeva IY (2009) Experimental study of transportation forms of boron in low-and medium-temperature hydrothermal process. PhD thesis, Lomonosov Moscow State University, Moscow (in Russian)

Nikolaeva IY, Bychkov AY (2007) Boron gas-liquid distribution in hydrothermal springs of Mutnovski volcano (Kamchatka). Vest KRAUC 9:3-13 (in Russian)

Oelkers EH, Bénézeth P, Pokrovski GS (2009) Thermodynamic databases for water-rock interaction. Rev Mineral Geochem 70:1-46

Ohtaki H, Radnai T (1993) Structure and dynamics of hydrated ions. Chem Rev 93:1157-1204

Palmer DA, Bénézeth P, Simonson JM (2004a) The solubility of copper oxides around the water/steam cycle. Power Plant Chem 6:81-88

Palmer DA, Simonson JM, Jensen JP (2004b) Partitioning of electrolytes to steam and their solubilities in steam. *In*: Aqueous Systems at Elevated Temperatures and Pressures. Palmer DA, Fernàndez-Prini R, Harvey AH (eds.) New York, Elsevier, p 409-439

Pankratz LB (1982) Thermodynamic Properties of Elements and Oxides. Bureau of Mines, Bulletin # 672

Pankratz LB, Mah AD, Watson SW (1987) Thermodynamic Properties of Sulfides. Bureau of Mines, Bulletin # 689

Pearson RG (1963) Hard and soft acid and bases. J Am Chem Soc 85:3533-3539

Pettke T, Halter WE, Driesner T, von Quadt A, Heinrich CA (2001) The porphyry to epithermal link: Preliminary fluid chemical results from the Apuseni Mountains, Romania, and Famatina, Argentina. *In*: 11th Annual V. M. Goldschmidt Conference, Abstract 3537, LPI Contribution No. 1088, Lunar and Planetary institute, Houston (CD-ROM)

Pettke T, Oberli F, Audétat A, Guillong M, Simon AS, Hanley JJ, Klemm LM (2012) Recent developments in element concentration and isotope ratio analysis of individual fluid inclusions by laser ablation single and multiple collector ICP-MS. Ore Geol Rev 44:10-38

Pichavant M (1981) An experimental study of the effect of boron on a water saturated haplogranite at 1 Kbar vapor pressure. Contrib Mineral Petrol 76:430-439

Pitzer KS, Pabalan RT (1986) Thermodynamics of NaCl in steam. Geochim Cosmochim Acta 50:1445-1454

Planer-Friedrich B, Lehr C, Matschullat J, Merkel BJ, Nordstrom DK, Sandstrom MW (2006) Speciation of volatile arsenic at geothermal features in Yellowstone National Park. Geochim Cosmochim Acta 70:2480-2491

Plyasunov AV (2011a) Thermodynamic properties of H_4SiO_4 in the ideal gas state as evaluated from experimental data. Geochim Cosmochim Acta 75:3853-3865

Plyasunov AV (2011b) Thermodynamics of $B(OH)_3$ in the vapor phase of water: Vapor-liquid and Henry's constants, fugacity and second cross virial coefficients. Fluid Phase Equilib 305:212-218

Plyasunov AV (2012) Thermodynamics of $Si(OH)_4$ in the vapor phase of water: Henry's and vapor-liquid distribution constants, fugacity and cross virial coefficients. Geochim Cosmochim Acta 77:215-231

Plyasunov AV, Shock EL (2003) Prediction of the vapor-liquid distribution constants for volatile nonelectrolytes in water up to its critical temperature. Geochim Cosmochim Acta 67:4981-5009

Pokrovski GS (2010) Enhanced vapor-phase transport of tin in hydrothermal systems or experimental artifacts? J Volcanol Geotherm Res 194:63-66

Pokrovski GS, Gout R, Zotov A, Schott J, Harrichoury JC (1996) Thermodynamic properties and stoichiometry of the arsenic(III) hydroxide complexes at hydrothermal conditions. Geochim Cosmochim Acta 60:737-749

Pokrovski GS, Schott J, Hazemann J-L, Farges F, Pokrovsky OS (2002a) An X-ray Absorption Fine Structure and Nuclear Magnetic Resonance spectroscopy study of gallium-silica complexes in aqueous solution. Geochim Cosmochim Acta 66:4203-4322

Pokrovski GS, Zakirov IV, Roux J, Testemale D, Hazemann J-L, Bychkov AY, Golikova GV (2002b) Experimental study of arsenic speciation in vapor phase to 500 °C: Implications for As transport and fractionation in low-density crustal fluids and volcanic gases. Geochim Cosmochim Acta 66:3453-3480

Pokrovski GS, Roux J, Harrichoury J-C (2005a) Fluid density control on vapor-liquid partitioning of metals in hydrothermal systems. Geology 33:657-660

Pokrovski GS, Roux J, Hazemann J-L, Testemale D (2005b) An X-ray absorption spectroscopy study of argutite solubility and germanium aqueous speciation in hydrothermal fluids to 500 °C and 400 bar. Chem Geol 217:127-145

Pokrovski GS, Borisova AY, Roux J, Hazemann JL, Petlang A, Tella M, Testemale D (2006) Antimony speciation in saline hydrothermal fluids: A combined X-ray absorption fine structure spectroscopy and solubility study. Geochim Cosmochim Acta 70:4196-4214

Pokrovski GS, Borisova AY, Harrichoury J-C (2008a) The effect of sulfur on vapor-liquid fractionation of metals in hydrothermal systems. Earth Planet Sci Lett 266:345-362

Pokrovski GS, Roux J, Hazemann JL, Borisova AY, Gonchar AA, Lemeshko MP (2008b) *In situ* X-ray absorption spectroscopy measurement of vapor-brine fractionation of antimony at hydrothermal conditions. Mineral Mag 72:667-681

Pokrovski GS, Tagirov BR, Schott J, Bazarkina EF, Hazemann J-L, Proux O (2009a) An *in situ* X-ray absorption spectroscopy study of gold-chloride complexing in hydrothermal fluids. Chem Geol 259:17-29

Pokrovski GS, Tagirov BR, Schott J, Hazemann J-L, Proux O (2009b) A new view on gold speciation in sulfur-bearing hydrothermal fluids from *in situ* X-ray absorption spectroscopy and quantum-chemical modelling. Geochim Cosmochim Acta 73:5406-5427

Pokrovski GS, Dubrovinsky LS (2011) The S_3^- ion is stable in geological fluids at elevated temperatures and pressures. Science 331:1052-1054

Pokrovski GS, Dubessy J (2012) *In situ* Raman spectroscopy reveals new sulfur forms in high-temperature geological fluids. GeoRaman X, Nancy, France. J Conference Abstracts, p. 77-78

Pokrovski GS, Akinfiev AA, Borisova AY, Zotov AV, Kouzmanov K (2013a) Gold speciation and transport in geological fluids: Insights from experiments and physical-chemical modeling. *In*: Gold-Transporting Hydrothermal Fluids in the Earth's Crust. Geological Society of London Special Publication (in press)

Pokrovski GS, Roux J, Ferlat G, Seitsonen A, Vuilleumier R, Hazemann J-L (2013b) Silver in saline hydrothermal fluids from *in situ* X-ray absorption spectroscopy and first-principles molecular dynamics. Geochim Cosmochim Acta 106:501-523

Reed MJ, Candela PA, Piccoli PM (2000) The distribution of rare earth elements between monzogranitic melt and the aqueous volatile phase in experimental investigations at 800 °C and 200 MPa. Contrib Mineral Petrol 140:251-262

Rempel KU, Williams-Jones EE, Migdisov AA (2006) The solubility of molybdenum in water vapour at elevated temperatures and pressures: Implications for ore genesis. Geochim Cosmochim Acta 70:687-696

Rempel KU, Williams-Jones EE, Migdisov AA (2009) The partitioning of molybdenum (VI) between aqueous liquid and vapour at temperatures up to 370 °C. Geochim Cosmochim Acta 73:3381-3392

Rempel KU, Liebscher A, Meixner A, Romer RL, Heinrich W (2012) An experimental study of the elemental and isotopic fractionation of copper between aqueous vapour and liquid to 450 °C and 400 bar in the CuCl-NaCl-H_2O and CuCl-NaHS-NaCl-H_2O systems. Geochim Cosmochim Acta 94:199-216

Richards JP (2011) Magmatic to hydrothermal metal fluxes in convergent and collided margins. Ore Geol Rev 40:1-26

Rickard D, Luther III GW (2006) Metal sulfide complexes and clusters. Rev Mineral Geochem 61:421-504

Roedder E (1971) Fluid inclusion studies on the porphyry-type ore deposits at Bingham, Utah, Butte, Montana, and Climax, Colorado. Econ Geol 66:98-120

Roedder E (1984) Fluid inclusions. Rev Mineral 12:1-646

Ronacher E, Richards JP, Reed MH, Bray CJ, Spooner ETC, Adams PD (2004) Characteristics and evolution of the hydrothermal fluid in the North zone high-grade area, Porgera gold deposit, Papua New Guinea. Econ Geol 99:843-867

Rubin K (1997) Degassing of metals and metalloids from erupting seamount and mid-ocean ridge volcanoes: Observations and predictions. Geochim Cosmochim Acta 61:3525-3542

Rudnick RL, Gao S (2003) Composition of the continental crust. Treatise on Geochemistry 3:1-64

Ryzhenko BN (1981) Equilibria in Hydrothermal Solutions. Moscow, Nauka (in Russian)

Sandler SI (1999) Chemical and Engineering Thermodynamics, 3rd ed. Wiley & Sons

Sassani DC, Shock EL (1998) Solubility and transport of platinum-group elements in supercritical fluids: Summary and estimates of thermodynamic properties of ruthenium, rhodium, palladium, and platinum solids, aqueous ions, and complexes to 1000 °C and 5 kbar. Geochim Cosmochim Acta 62:2643-2671

Saunders JA, Brueseke ME (2012) Volatility of Se and Te during subduction-related distillation and the geochemistry of epithermal ores of the Western United States. Econ Geol 107:165-172

Saunders JA, Schoenly PA (1995) Boiling, colloid nucleation and aggregation, and the genesis of bonanza Au-Ag ores of the Sleeper deposit, Nevada. Miner Deposita 30:199-210

Saunier G, Pokrovski GS, Poitrasson F (2011) First experimental determination of iron isotope fractionation between hematite and aqueous solution at hydrothermal conditions. Geochim Cosmochim Acta 75:662-6654

Scaillet B, Clemente B, Evans BW, Pichavant M (1998) Redox control of sulfur degassing in silicic magmas. J Geophys Res Solid Earth 103:23937-23949

Schäfer B, Frischknecht R, Günther D, Dingwell DB (1999) Determination of trace-element partitioning between fluid and melt LA-ICP-MS analysis of synthetic fluid inclusions in glass. Eur J Mineral 11:415-426

Schatz OJ, Dolejš D, Stix J, Williams-Jones AE, Layne GD (2004) Partitioning of boron among melt, brine and vapor in the system haplogranite-H_2O-NaCl at 800 °C and 100MPa. Chem Geol 210:135-147

Seo JH, Heinrich CA (2013) Selective copper diffusion into quartz-hosted vapor inclusions: Evidence from other host minerals, driving forces, and consequences for Cu-Au ore formation. Geochim Cosmochim Acta 113:60-69

Seo JH, Guillong M, Heinrich CA (2009) The role of sulfur in the formation of magmatic-hydrothermal copper-gold deposits. Earth Planet Sci Lett 282:323–328

Seo JH, Guillong M, Aerts M, Zajacz Z, Heinrich CA (2011) Microanalysis of S, Cl, and Br in fluid inclusions by LA-ICP-MS. Chem Geol 284:35-44

Seo JH, Guillong M, Heinrich CA (2012) Separation of molybdenum and copper in porphyry deposits: the roles of sulfur, redox, and pH in ore mineral deposition at Bingham Canyon. Econ Geol 107:333-356

Seward TM (1989) The hydrothermal chemistry of gold and its implications for ore formation: Boiling and conductive cooling as examples. Econ Geol Monogr 6:398-404

Seward TM, Barnes HL (1997) Metal transport by hydrothermal ore fluids. *In*: Geochemistry of Hydrothermal Ore Deposits, 3rd ed. Barnes HL (ed) New York, Wiley and Sons, p 435-486

Seward TM, Driesner T (2004) Hydrothermal solution structure: experiments and computer simulations. *In*: Aqueous Systems at Elevated Temperatures and Pressures: Physical Chemistry in Water, Steam and Hydrothermal Solutions. Palmer DA, Fernändez-Prini R, Harvey AH (eds) Elsevier Ltd., p 149-182

Sherman DM (2010) Metal complexation and ion association in hydrothermal fluids: insights from quantum chemistry and molecular dynamics. Geofluids 10:41-57

Shmulovich K, Heinrich W, Möller P, Dulski P (2002) Experimental determination of REE fractionation between liquid and vapour in the systems NaCl-H_2O and $CaCl_2$-H_2O up to 450 °C. Contrib Mineral Petrol 44:257-273

Shock EL, Sassani DC, Willis M, Sverjensky DA (1997) Inorganic species in geologic fluids: Correlations among standard molal thermodynamic properties of aqueous ions and hydroxide complexes. Geochim Cosmochim Acta 61:907-950

Sillitoe RH (2010) Porphyry copper systems. Econ Geol 105:3-41

Simmons SF, Browne PRL (2007) Hydrothremal minerals and precious metals in the Broadlands-Ohaaki geothermal system: Implications for understanding low-sulfidation epithermal deposits. Econ Geol 95:971-999

Simmons SF, Gemmell JB, Sawkins FJ (1988) The Santo Niño silver-lead-zinc vein, Fresnillo, Mexico: Part II. Physical and chemical nature of ore-forming solutions. Econ Geol 83:1619-1641

Simmons SF, White NC, John DA (2005) Geological characteristics of epithermal precious and base metal deposits. Econ Geol 100th Anniv Vol 100:485-522

Simon AC, Ripley EM (2011) The role of magmatic sulfur in the formation of ore deposits. Rev Mineral Geochem 73:513-578

Simon AC, Frank MR, Pettke T, Candela PA, Piccoli PM, Heinrich CA (2005). Gold partitioning in melt-vapor-brine systems. Geochim Cosmochim Acta 69:3321-3335

Simon AC, Pettke T, Candela PA, Piccoli PM, Heinrich CA (2006) Copper partitioning in a melt-vapor-brine-magnetite-pyrrhotite assemblage. Geochim Cosmochim Acta 70:5583-5600

Simon AC, Pettke T, Candela PA, Piccoli PM, Heinrich CA (2007) The partitioning behavior of As and Au in S-free and S-bearing magmatic assemblages. Geochim Cosmochim Acta 71:1764-1782

Simon AC, Pettke T, Pettke T, Candela PA, Piccoli PM, Heinrich CA (2008) The partitioning behavior of silver in vapor-brine-rhyolite melt assemblages. Geochim Cosmochim Acta 72:1638-1659

Smith CL, Ficklin WH, Thompson JM (1987) Concentrations of arsenic, antimony, and boron in steam and steam condensate at the Geysers, California. J Volcanol Geotherm Res 32:329-341

Spycher NF, Reed MH (1989) Evolution of a Broadlands-type epithermal ore fluid along alternative P-T paths: Implications for the transport and deposition of base, precious and volatile metals. Econ Geol 84:328-359

Stefánsson A, Seward TM (2004) Gold(I) complexing in aqueous sulphide solutions to 500 °C at 500 bar. Geochim Cosmochim Acta 68:4121-4143

Stoiber RE, Rose WI Jr. (1974) Fumarole incrustations at active Central American volcanoes. Geochim Cosmochim Acta 38:495-510

Styrikovich MA, Khaibullin IK, Tshvirashvili DG (1955) A study of salt solubility in high-pressure water steam. Doklady AN SSSR 100:1123-1126

Styrikovich MA, Martynova OI, Khaibullin IK, Mingulina EI (1959) Some features of the transfer of weak inorganic acids into the saturated vapor. Teploenergetika 9:50-56 (in Russian)

Styrikovich MA, Tshvirashvili DG, Hebieridze DP (1960) A study of the solubility of boric acid in saturated water vapor. Dokl AN SSSR 134: 615-617 (in Russian)

Sverjensky DA, Shock EL, Helgeson HC (1997) Prediction of the thermodynamic properties of aqueous metal complexes to 1000 °C and 5 kb. Geochim Cosmochim Acta 61:1359-1412

Symonds RB, Rose WI, Reed MH., Lichte FE, Finnegan DL (1987) Volatilization, transport and sublimation of metallic and non-metallic elements in high-temperature gases at Merapi Volcano, Indonesia. Geochim Cosmochim Acta 51:2083-2101

Symonds RB, Reed MH, Rose WI (1992) Origin, speciation, and fluxes of trace-element gases at Augustine volcano, Alaska: Insights into magma degassing and fumarolic processes. Geochim Cosmochim Acta 56:633-657

Symonds RB, Reed MH (1993) Calculation of multicomponent chemical equilibria in gas-solid-liquid systems: Calculation methods, thermochemical data, and applications to studies of high-temperature volcanic gases with examples from Mount St Helens. Am J Sci 293:758-864

Tagirov B, Schott J (2001) Aluminum speciation in crustal fluid revisited. Geochim Cosmochim Acta 61:4267-4280

Tanger JC, Helgeson HC (1988) Calculation of the thermodynamic and transport properties of aqueous species at high pressures and temperatures: Revised equations of state for the standard partial molal properties of ions and electrolytes. Am J Sci 288:19-98

Taran YA (2009) Geochemistry of volcanic and hydrothermal fluids and volatile budget of the Kamchatka–Kuril subduction zone. Geochim Cosmochim Acta 73:1067-1094

Taran YA, Hedenquist JW, Korzhinsky MA, Tkachenko SI, Shmulovich KI (1995) Geochemistry of magmatic gases from Kudryavy volcano, Iturup, Kuril Islands. Geochim Cosmochim Acta 59:1749-1761

Taran YA, Bernard A, Gavilanes J-C, Africano F (2000) Native gold in mineral precipitates from high-temperature volcanic gases of Colima volcano, Mexico. Appl Geochem 15:337-346

Taran YA, Bernard A, Gavilanes J-C, Lunezheva E, Cortés A, Armienta MA (2001) Chemistry and mineralogy of high-temperature gas discharges from Colima volcano, Mexico. Implications for magmatic gas-atmosphere interaction. J Volcanol Geotherm Res 108:245-264

Testemale D, Argoud R, Geaymond O, Hazemann J-L (2005) High pressure/high temperature cell for x-ray absorption and scattering techniques. Rev Sci Instrum 76: 043905-043909

Tingle TN, Fenn PM (1984) Transport and concentration of molybdenum in granite and molybdenite systems: Effect of fluorine and sulfur. Geology 12:156-158

Tkachenko SI, Porter RP, Korzinsky MA, van Bergen MD, Shmulovich KI, Schteinberg GS (1999) Investigation of processes of ore and mineral formation from hogh-temperature fumarole gases at Kudryavy volcano, Iturup, Kurils Islands. Geokhimia 4:410-422 (in Russian)

Tooth B, Etschmann B, Pokrovski GS, Testemale D, Hazemann J-L, Grundler PV, Brugger J (2013) Bismuth speciation in hydrothermal fluids: An X-ray absorption spectroscopy and solubility study. Geochim Cosmochim Acta 101:156-172

Ulrich T, Günther D, Heinrich CA (1999) Gold concentrations of magmatic brines and the metal budget of porphyry copper deposits. Nature 399:676-679

Ulrich T, Günther D, Heinrich CA (2002) Evolution of a porphyry Cu-Au deposit, based on LA-ICP-MS analysis of fluid inclusions: Bajo de la Alumbrera, Argentina. Econ Geol 97:1889-1920

Urabe T (1985) Aluminous granite as a source magma of hydrothermal ore deposits: An experimental study. Econ Geol 80:148-157

Urabe T (1987) The effect of pressure on the partitioning ratios of lead and zinc between vapor and rhyolite melts. Econ Geol 82:1049-1052

Veksler I, Thomas R, Schmidt C (2002) Experimental evidence of three coexisting immiscible fluids in synthetic granitic pegmatite. Am Mineral 87:775-779

Velásquez G, Béziat D, Salvi S, Siebenaller L, Borisova AY, Pokrovski GS, de Parseval P (2013) Formation and deformation of pyrite and implications for gold mineralization at the El Callao mining district, Venezuela. Econ Geol (in press)

Vikent'ev IV, Borisova AY, Karpukhina VS, Naumov VB, Ryabchikov ID (2012) Direct data on the ore potential of acid magmas of the Uzel'ginskoe ore field (Southern Urals, Russia). Dokl Earth Sci 443:401-405

Weatherley DK, Henley RW (2013) Flash vaporization during earthquakes evidenced by gold deposits. Nature Geosci 6:294-298

Webster JD (1992a) Fluid-melt interactions involving Cl-rich granites: Experimental study from 2 to 8 kbar. Geochim Cosmochim Acta 56: 659-678

Webster JD (1992b) Water solubility and chlorine partitioning in Cl-rich granitic systems: Effects of melt composition at 2 kbar and 800 °C. Geochim Cosmochim Acta 56: 679-687

Webster JD, Holloway JR, Hervig RL (1989) Partitioning of lithophile trace elements between H_2O and H_2O+CO_2 fluid and topaz rhyolite melt. Econ Geol 84:116-134

Weis P, Driesner T, Heinrich CA (2012) Porphyry-copper ore shells form at stable pressure-temperature fronts within dynamic fluid plumes. Science 338:1613-1616

White DE (1973) Characteristics of geothermal resources *In*: Geothermal Energy. Pernger P, Otte C (ed) Stanford Univ Press p 69-95

White DE, Muffler LJP, Truesdell AH (1971) Vapor-dominated hydrothermal systems compared with hot-water systems. Econ Geol 66:75-97

Wilke M, Schmidt C, Farges F, Malavergne V, Gautron L, Simionovici A, Hahn M, Petit P-E (2006) Structural environment of iron in hydrous aluminosilicate glass and melt - Evidence from X-ray absorption spectroscopy. Chem Geol 229:144-161

Wilkinson JJ, Stoffell B, Wilkinson CC, Jeffries TE, Appold MS (2009) Anomalously metal-rich fluids form hydrothermal ore deposits. Science 323:764-767

Williams TJ, Candela PA, Piccoli PM (1995) The partitioning of copper between silicate melts and two-phase aqueous fluids: An experimental investigation at 1 kbar, 800 °C, and 0.5 kbar, 850 °C. Contrib Miner Petrol 121:388-399

Williams-Jones AE, Heinrich CA (2005) Vapor transport of metals and the formation of magmatic-hydrothermal ore deposits. Econ Geol 100:1287-1312

Williams-Jones AE, Migdisov AA, Archibald SM, Xiao Z (2002) Vapor-transport of ore metals. *In:* Water-Rock Interactions, Ore Deposits, and Environmental Geochemistry. A Tribute to David A. Crerar. Hellmann R, Wood SA (eds) Geochem Soc Spec Pub 7:279-306

Williams-Jones AE, Migdisov AA, Samson IM (2012) Hydrothremal mobilization of rare earth elements – a tale of "Ceria" and "Ittria". Elements 8:355-360

Wood JA, Hashimoto A (1993) Mineral equilibrium in fractionated nebular systems. Geochim Cosmochim Acta 57:2377-2388

Wood SA (1990) The aqueous geochemistry of rare-earth elements and yttrium. 2. Theoretical predictions of speciation in hydrothermal solutions to 350 °C at saturation water vapour pressure. Chem Geol 88:99-125

Wood SA, Samson IM (1998) Solubility of ore minerals and complexation of ore metals in hydrothermal solutions. Rev Econ Geol 10:33-80

Wood SA, Samson IM (2000) The hydrothermal geochemistry of tungsten in granitoid environments: I. Relative solubilities of ferberite and scheelite as a function of T, P, pH and m_{NaCl}. Econ Geol 95:143-182

Xiong Y, Wood SA (2000) Experimental quantification of hydrothermal solubility of platinum-group elements with special reference to porphyry copper environments. Miner Petrol 68:1-28

Yardley BWD, Banks DA, Bottrell SH, Diamond LW (1993) Post-metamorphic gold quartz veins from NW Italy –The composition and origin of the fluid. Mineral Mag 57:407-422

Yudovskaya MA, Distler VV, Chaplygin IV, Mokhov AV, Trubkin NV, Gorbacheva SA (2006) Gaseous transport and deposition of gold in magmatic fluid: Evidence from the active Kudryavy volcano, Kurile Islands. Miner Deposita 40:828-848

Zajacz Z, Halter WE, Pettke T, Guillong M (2008) Determination of fluid/melt partition coefficients by LA-ICPMS analysis of co-existing fluid and silicate melt inclusions: Controls on element partitioning. Geochim Cosmochim Acta 72:2169-2197

Zajacz Z, Hanley JJ, Heinrich CA, Halter WE, Guillong M (2009) Diffusive reequilibration of quartz-hosted silicate melt and fluid inclusions: Are all metal concentrations unmodified? Geochim Cosmochim Acta 73:3013-3027

Zajacz Z, Seo JH, Candela PA, Piccoli PM, Heinrich CA (2010). Alkali metals control the release of gold from volatile-rich magmas. Earth Planet Sci Lett 297:50-56

Zajacz Z, Candela PA, Piccoli PM, Sanchez-Valle C (2012a) The partitioning of sulfur and chlorine between andesite melts and magmatic volatiles and the exchange coefficient of major cations. Geochim Cosmochim Acta 89:81-101

Zajacz Z, Candela PA, Piccoli PM, Wälle M, Sanchez-Valle C (2012b) Gold and copper in volatile saturated mafic to intermediate magmas: Solubilities, partitioning, and implications for ore deposit formation. Geochim Cosmochim Acta 91:140-159

Zajacz Z, Candela PA, Piccoli PM, Sanchez-Valle C, Wälle M (2013) Solubility and partitioning behavior of Au, Cu, Ag and reduced S in magmas. Geochim Cosmochim Acta 112:288-304

Zelenski M, Taran Y (2011) Geochemistry of volcanic and hydrothermal gases of Mutnovsky volcano, Kamchatka: Evidence for mantle, slab and atmosphere contributions to fluids of a typical arc volcano. Bull Volcanol 73:373-394

Zezin DY, Migdisov AA, Williams-Jones AE (2007) The solubility of gold in hydrogen sulfide gas: An experimental study. Geochim Cosmochim Acta 71:3070-3081

Zezin DY, Migdisov AA, Williams-Jones AE (2011) The solubility of gold in H_2O-H_2S vapor at elevated temperatures and pressures. Geochim Cosmochim Acta 75:5140-5153

Zhang L, Audétat A, Dolejs D (2012) Solubility of molybdenite (MoS_2) in aqueous fluids at 600-800 °C, 200 MPa: a synthetic fluid inclusions study. Geochim Cosmochim Acta 77:175-185

Zoller WH, Parrington JR, Phelan Kotra JM (1983) Iridium enrichment in airborne particles from Kilauea volcano, January 1983. Science 222:1118-1121

Zotov AV, Kudrin AV, Levin KA, Shikina ND, Var'yash LN (1995) Experimental studies of the solubility and complexing of selected ore elements (Au, Ag, Cu, Mo, As, Sb, Hg) in aqueous solutions. *In*: Fluids in the Crust. Equilibrium and Transport Properties. Shmulovich KI, Yardley BWD, Gonchar GG (eds) Chapman & Hall, London, p 95-138

Zotov AV, Shikina ND, Akinfiev NN (2003) Thermodynamic properties of the Sb(III) hydroxide complex $Sb(OH)_3(aq)$ at hydrothermal conditions. Geochim Cosmochim Acta 67:1821-1836

Reviews in Mineralogy & Geochemistry
Vol. 76 pp. 219-263, 2013
Copyright © Mineralogical Society of America

Solution Calorimetry Under Hydrothermal Conditions

Peter Tremaine and Hugues Arcis

Department of Chemistry
University of Guelph
50 Stone Road East
Guelph, Ontario, N1G 2W1, Canada

tremaine@uoguelph.ca *harcis@uoguelph.ca*

Dedicated to Prof. R. H. Wood on the Occasion of His 80th Birthday

INTRODUCTION

The first quantitative studies of the thermodynamics of hydrothermal solutions were made in 1903 by A.A. Noyes and W.D. Coolidge (1903), who used the change in conductance associated with ionization to measure the ionization constants of water and aqueous acids and bases up to about 300 °C at steam saturation. The need to develop nuclear reactor coolant chemistry in the 1950's led national laboratories in several countries to develop new experimental methods for measuring solubility products, equilibrium constants and activity coefficients under the corrosive conditions encountered at elevated temperatures. Complementary studies by geochemists investigating geothermal systems and ore body formation have led to additional experimental techniques suitable for near critical and supercritical conditions (See, for example: Palmer et al. 2004; Mesmer et al. 1997; Ulmer and Barnes 1983). Modern methods include potentiometric titrations, conductivity, solubility, UV-visible Raman and infrared spectroscopy, X-Ray absorption spectroscopy (XAS), neutron scattering, and the calorimetric methods that are the subject of this review. These methods are all important to hydrothermal geochemistry and industrial chemistry because they yield thermodynamic parameters and structural information about the aqueous reactions associated with specific systems under study. However, it is simply not practical, or even possible, to measure the properties of all the thermodynamic and kinetic parameters that control important hydrothermal processes.

This problem has been addressed by the development of thermodynamic databases and geochemical modeling codes, which can be used to predict the stability of mineral assemblages, vapor-liquid equilibria, and the effects of solubility and redox reactions on mass transport as a function of pressure and temperature under hydrothermal conditions (See, for example: Anderko et al. 2002; Oelkers et al. 2009). Indeed, the emergence of process simulation software, based on multi-component, multi-phase chemical equilibrium models, as a tool for interpreting metamorphic systems, chemical process design, and environmental studies, is one of the great successes of 20th century science. It is not generally recognized that the thermodynamic data for many of the most important aqueous species under hydrothermal conditions are *extrapolations*, based on values at 25 °C. The predictive models on which these extrapolations are based, such as the well-known Helegon-Kirkham-Flowers-Tanger model (Tanger and Helgeson 1988; Shock et al. 1992) are all derived from the results of solution calorimetry.

The 1970's ushered in a revolution in development of flow calorimetric methods to the study of hydrothermal solutions, spurred on by the invention of the Picker calorimeter at

1529-6466/13/0076-0007$05.00 http://dx.doi.org/10.2138/rmg.2013.76.7

the University of Sherbrooke (Picker et al. 1971), and the availability of small-scale low-cost equipment for high-pressure liquid chromatography suitable for providing the high-precision pumps and pressure control required for high-temperature solution calorimetry. The key parameter for developing predictive models for aqueous species is the *standard partial molar heat capacity*, C°_{p}, which provides a means of extrapolating values from the very large thermodynamic databases at 25 °C and 1 bar, to elevated temperatures and pressures. In the early 1960's, experimental values for the standard partial molar heat capacities were known for fewer than 10 species, and only at 25 °C. By the 1980's, values had been measured for hundreds of species, at temperatures as high as 400 °C. The advances in solution calorimetry that led to these developments are described nicely in the recent monograph edited by Wilheim and Letcher (2010).

Our purpose in this chapter is to provide a brief review of the history and application of solution calorimetry for hydrothermal systems, and to present a practical discussion of modern instruments and the experimental methods used to provide accurate data. We have attempted to present the material at a level that will allow geochemical modelers and other users of calorimetric data to develop the insights needed to evaluate the strengths and limitations of the data in the literature, and to assist experimentalists in identifying new model systems that merit the time and effort required to make these very difficult quantitative measurements. The review is also aimed at experimental geochemists and applied chemists from other fields who consider adding hydrothermal calorimetry to their programs as a research tool.

The first section of this chapter provides a short review of the underlying chemical thermodynamics, at a level similar to that described by Atkins and De Paula (2009), Anderson (2005) or Pitzer (1995). The second section describes the Helgeson-Kirkham-Flowers-Tanger model and other "equations of state" used to predict equilibrium constants and the standard-state properties of ions and non-electrolytes under hydrothermal conditions. The next three sections describe the operating principles of vibrating-tube densitometers, heat-capacity calorimeters and heat-of-mixing calorimeters, including a brief history and a few examples of their application. We conclude with a discussion of the current state of the art and some scientific challenges to be addressed.

THERMODYNAMIC RELATIONS

Equations for the temperature and pressure dependence of Gibbs energies and equilibrium constants

Chemical reactions are driven by changes in Gibbs free energy. In aqueous solutions, the change in Gibbs energy is related to concentrations by the expression which defines the standard Gibbs energy of reaction, ΔG°, in terms of the *chemical equilibrium constant*, *K*,

$$\Delta G^{\circ} -= \; RT \ln K \qquad (1)$$

where *T* is the absolute temperature in Kelvin, and *R* is the ideal gas constant. Using the ionization of a simple acid as an example,

$$\mathrm{HA_{(aq)}} \rightleftarrows \mathrm{H^{+}{}_{(aq)}} + \mathrm{A^{-}{}_{(aq)}} \qquad (2)$$

the equilibrium constant is written as

$$K = \frac{a_{\mathrm{H^{+}}} \cdot a_{\mathrm{A^{-}}}}{a_{\mathrm{HA}}} \qquad (3)$$

where $a_{\mathrm{A-}}$, $a_{\mathrm{HA},}$ and $a_{\mathrm{H+}}$ are activities in molality units. Molalities ($\mathrm{mol{\cdot}kg^{-1}}$) are used instead of molarities ($\mathrm{mol{\cdot}L^{-1}}$) because they are not affected by the thermal expansion or contraction of water with temperature and pressure. The conversion of equilibrium constants and other thermodynamic properties that describe temperature and pressure effects on the molality scale with those based on molarity and mole fraction units is described by Hepler (1981).

The equilibrium constant refers to infinitely dilute solutions in the hypothetical 1 mol·kg^{-1} standard state, and thus is not a function of ionic strength (Pitzer 1995; Anderson 2005; Atkins and De Paula 2009). The *equilibrium quotient* is defined as

$$Q = \frac{m_{\mathrm{H}^+} \cdot m_{\mathrm{A}^-}}{m_{\mathrm{HA}}} \tag{4}$$

where $m_{\mathrm{A}-}$, $m_{\mathrm{H}+}$ and m_{HA} are molalities of the species $\mathrm{A}^-_{(\mathrm{aq})}$, $\mathrm{H}^+_{(\mathrm{aq})}$ and $\mathrm{HA}_{(\mathrm{aq})}$, respectively. The ratio between molalities and activities of solutes is defined as the activity coefficient, $\gamma = a/m$, so that

$$\ln K = \ln Q \quad \ln\left(+ \frac{\gamma_{\mathrm{H}^+} \cdot \gamma_{\mathrm{A}^-}}{\gamma_{\mathrm{HA}}} \right) \tag{5}$$

where $\gamma_{\mathrm{A}-}$, $\gamma_{\mathrm{H}+}$, and γ_{HA} are activity coefficients of $\mathrm{A}^-_{(\mathrm{aq})}$, $\mathrm{H}^+_{(\mathrm{aq})}$ and $\mathrm{HA}_{(\mathrm{aq})}$, respectively. Since the last term in the above equation vanishes as ionic strength approaches zero, log$K$ is usually obtained from the experimentally determined log Q values by extrapolation to infinite dilution.

The temperature and pressure dependence of $\Delta G°$ is derived from the two basic thermodynamic equations, $\Delta G° = \Delta H° - T\Delta S°$ and $dG° = V°dP - S°dT$. Adding $\Delta S° = (\partial \Delta G/\partial T)_P$, $\Delta C_P^\circ = T(\partial \Delta S/\partial T)_P$ and $\Delta V° = (\partial \Delta G/\partial P)_T$, into the exact differential for Gibbs energy yields the expression

$$\Delta G^\circ_{T,P} = \Delta G^\circ_{T_\mathrm{r},P_\mathrm{r}} - \Delta S^\circ_{T_\mathrm{r},P_\mathrm{r}}\left(T - T_\mathrm{r}\right) + \int_{T_\mathrm{r}}^{T} \Delta C_P^\circ dT - T\int_{T_\mathrm{r}}^{T} \frac{\Delta C_P^\circ}{T} dT + \int_{P_\mathrm{r}}^{P} \Delta V_T^\circ dP \tag{6}$$

which can be integrated from the standard reference conditions, T_r = 25 °C = 298.15 K and P_r = 1 bar to the conditions of interest (T, P). Because the vapor pressure of water exceeds 1 bar above 100 °C, the integration can be done first as a function of temperature at constant pressure (1 bar), then as a function of pressure at constant temperature, as in Equation (6). An alternative is to increase the pressure at 25 °C, then to integrate from 25 °C to the temperature of interest at constant pressure P. At steam saturation and temperatures below 250 °C, water is quite incompressible and the pressure effects on the C_P° and $V°$ terms are often ignored.

For equilibrium constants, the expression consistent with Equations (1) and (6) is:

$$\log K_{T,P} = \log K^\circ_{T_\mathrm{r},P_\mathrm{r}} \quad + \frac{1}{2.303R} \quad \Delta H^\circ_{T_\mathrm{r},P_\mathrm{r}} \left(\frac{1}{T} \quad \frac{1}{T_\mathrm{r}} \right)$$
$$+ \int \frac{\Delta C_P^\circ}{T} dT - \frac{1}{T}\int \Delta C_P^\circ dT - \int \Delta V_T^\circ dP \tag{7}$$

and the standard molar enthalpy of reaction, $\Delta H°$, varies with temperature according to the relationship $(\partial \Delta H°/\partial T)_P = \Delta C_P^\circ$. Empirical and semi-empirical expressions for ΔC_P° and $\Delta V°$ can be used in Equations (6) and (7), to represent the temperature- and pressure-dependence of experimental values for $\Delta G°$ and log$K$. Alternatively, if ΔC_P° and $\Delta V°$ are known as a function of temperature, Equations (6) and (7) can be used to calculate $\Delta G°$ or log$K$ vs. T and P (Mesmer et al. 1988; Pitzer 1995; Tremaine et al. 2004).

Solvation effects

Theoretical and semi-empirical models used to predict the temperature- and pressure-dependence of thermodynamic functions are usually based on the simple conceptual model for ionic hydration proposed by Frank and Evans (1945) and shown in Figure 1. The ion is considered to be surrounded by two hydration shells. For small ions, shown in Figure 1, the first hydration sphere consists of tightly held waters held in place by ion-dipole interactions and, possibly, covalent bonds. For large ions, and non-polar non-electrolytes, the first hydration shell is thought to be a clathrate-like cage, which forms around the solute because water-water hydrogen bonding is stronger than the solute-water interactions. In both cases, the second hydration shell forms through hydrogen bonding of water molecules that link those in the first hydration shell to molecules in bulk water. The hydrogen-bonded waters in second hydration shell may have a higher or lower entropy than those in bulk water (sometimes called "structure-makers" or "structure breakers").

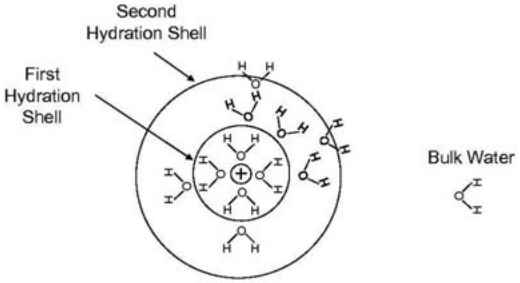

Figure 1. A schematic of the first and second hydration shells that surround a cation. Long-range interactions with the dipoles of bulk water are described by the Born equation.

Most semi-empirical models for the thermodynamic properties of aqueous solutes are derived from thought-experiments of the type shown in Figure 2. In these thought-experiments, the motion of ion in the gas-phase ion is stopped; it is transferred into a motionless cavity in the water; the ion is allowed to perturb the water surrounding the cavity; and then the "hydrated" ion and the cavity that surrounds it are allowed to move about in the bulk water. In the discussion that follows, the process of transferring the ion in its standard state from the gas phase to the aqueous phase is called "*solvation*." The changes the ion causes to take place in the water surrounding it are called "*hydration*."

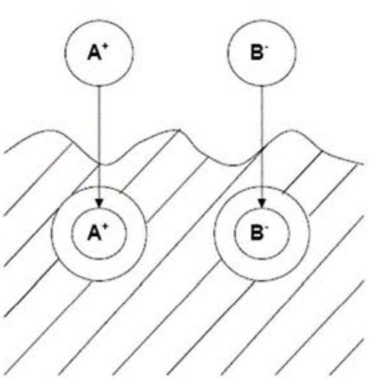

Figure 2. The solvation of ion pairs and electrolytes in water. Elevated temperatures favor ion-pairing and long-range solvent polarization as described by the Born equation due to the higher compressibility. The primary hydration shell is often approximated by a cavity radius that is larger than the crystallographic radius of the ion.

The solvation process for transferring a species from the ideal gas standard state to the hypothetical one molal standard state is described by the expressions:

$$\begin{aligned}\Delta_{solv}G^{\circ} &= \Delta_{solv}H^{\circ} - T\Delta_{solv}S^{\circ} \\ &= \Delta_{solv}U^{\circ} + P\Delta_{solv}V^{\circ} - T\Delta_{solv}S^{\circ}\end{aligned} \tag{8}$$

and

$$\Delta_{solv}G^{\circ} = \Delta_{solv}G^{\circ}_{hydr} + \Delta_{solv}G^{\circ}_{pol} + \Delta_{solv}G^{\circ}_{std\,state} \tag{9}$$

where $\Delta_{solv}G^{\circ}_{hydr}$ is the Gibbs energy of creating the cavity in the water, including short-range hydrogen bonding effects described by Frank and Evans (1945); $\Delta_{solv}G^{\circ}_{pol}$ is the long-range polarization effect (i.e., long-range interactions between the ion and the dipoles in bulk water); $\Delta_{solv}G^{\circ}_{std\,state} = RT\ln(V_g/V_l)$ is the correction for the different volumes of the two standard states. At ambient temperatures, bulk liquid water consists of long-range hydrogen-bonded networks, roughly tetrahedral, that extend, on a time-averaged basis, to three or more nearest neighbors, with a considerable degree of thermal motion and inter-penetration of the tetrahedra (Ben-Naim 1980, 1987; Ohtaki and Radnai 1993; Svishchev and Kusalik 1995). The model for $\Delta_{solv}G^{\circ}_{hydr}$ is derived by considering the effects of hydrogen bonding in the first and second shells relative to bulk water. Strong ion-water interactions in the first hydration shell are typically associated with negative values of $\Delta_{solv}U^{\circ}_{hydr}$, $\Delta_{solv}S^{\circ}_{hydr}$, and $\Delta_{solv}V^{\circ}_{hydr}$. Strong hydrogen bonds in the second shell are associated with negative values of $\Delta_{solv}U^{\circ}_{hydr}$ and $\Delta_{solv}S^{\circ}_{hydr}$ and positive values of $\Delta_{solv}V^{\circ}_{hydr}$. Increasing temperatures favor larger values of $\Delta_{solv}S^{\circ}_{hydr}$ and increasing pressures favor smaller values of $_{solv}\ _{hydr}$. The long-range ion-water interactions are described by the Born equation, discussed below.

The thermodynamic properties of ions and non-electrolytes at elevated temperatures and pressures have been discussed by Mesmer et al. (1988, 1991) and others (See, for example Levelt-Sengers 1991; Fernandez Prini et al. 1992). As the temperature is raised along the saturation pressure curve, long-range hydrogen-bonding breaks down and water becomes more compressible until, at the critical temperature and pressure, the compressibility of water becomes infinite. Raising the temperature causes the equilibrium of ionization reactions to shift in the direction that favors smaller volumes ($P\Delta V^{\circ} < 0$) and greater entropies ($T\Delta S^{\circ} > 0$). At ambient temperatures, short-range and long-range interactions around the ionized and neutral acids and bases are species-specific so that $\Delta_{solv}G^{\circ}$ can shift in either a positive or negative direction with modest increases in temperature and pressure, depending on the number of hydrogen-bond acceptors and donors, the charge, and the size and shape of the species in question. At temperatures above about 200 °C, the short-range ion-water interactions shown in Figure 1 persist, however, long-range solute-water interactions begin to dominate as a result of the decreased hydrogen bonding in water itself and the resulting increase in the compressibility of liquid water. Ions attract more and more water around them as the temperature is raised towards the critical point, resulting in a net decrease in their standard partial molar volume and a decrease in entropy. Neutral molecules repel water more effectively through hydrophobic interactions, resulting in a net increase in both their standard partial molar volumes and entropies. An example is shown in Figure 3, which plots the standard partial molar volumes of morpholine and its chloride salt, morpholinium chloride up to 300 °C (Tremaine et al. 1997). Both effects approach infinity at the critical point of water. The result is that we can draw the following general conclusions:

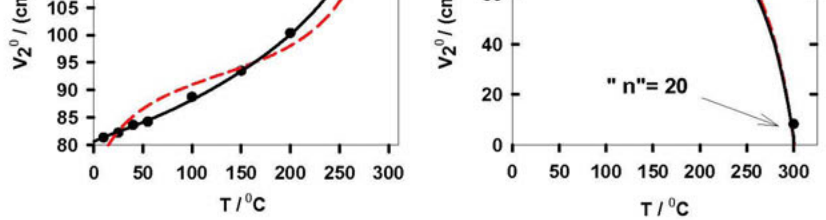

Figure 3. Experimental standard partial molar volumes of morpholine and morpholinium chloride at 101 bar as a function of temperature, with hydration numbers calculated from the density model. Fits of the density model and Helgeson-Kirkham-Flowers-Tanger model are shown as solid and dashed lines, respectively. [Used by permission of ACS, from Tremaine et al. (1997) *J Phys Chem*, Vol. 101, Figs. 8 and 9, p 416.]

- At temperatures above about 250 °C along the steam-saturation-pressure curve, increasingly long-range ion-water interactions causes the chemical potential of most ions to decrease
- At temperatures above about 250 °C along the steam-saturation-pressure curve, increasingly hydrophobic solute-water interactions causes the chemical potential of most neutral species to decrease
- At temperatures below 100 °C, hydration effects are species-specific.
- Solutes in the range $100\ ^\circ\mathrm{C} < T < 250\ ^\circ\mathrm{C}$ display intermediate behavior.

The temperature dependence of standard partial molar properties

During the past 100 years, accurate values of standard molar Gibbs energies and enthalpies of formation, $\Delta_f G^\circ_{T_r,P_r}$ and $\Delta_f H^\circ_{T_r,P_r}$, have been measured under ambient conditions for a very large number of aqueous ions and non electrolytes. In addition to developing methods for direct *measurements* of equilibrium constants under hydrothermal solutions, modern research has focused on measuring, or estimating, values for the standard partial molar properties, C_P° and $V^\circ_{T_r,P_r}$ as a means of *extrapolating* tabulated thermodynamic parameters for aqueous species at 25 °C and 1 bar, to elevated temperatures and pressures.

As is evident from the preceding discussion, long-range solute-solvent interactions dominate at elevated temperatures, due to the large thermal expansivity α_1 and isothermal compressibility κ_1 of the solvent associated with classical near-critical conditions. This effect causes C_P° and V° to approach $-\infty$ at the critical point when ion-water long-range polarization interactions dominate, and $+\infty$ at the critical point for non-electrolytes when hydrophobic effects are the dominant contributors. The limiting near-critical behavior is described by the dimensionless, generalized Krichevski parameter, A_{12} (Levelt Sengers 1991). Standard partial molar volumes V°, are expressed in terms of A_{12} by the relationship:

$$A_{12} = \frac{V_2^\circ}{\kappa_1 RT} \lim_{n_2 \to 0} \left(\frac{\partial (PV/RT)}{\partial n_2} \right)_{T,V,n_1} \tag{10}$$

in which A_{12} is a smooth, continuous and finite function, even at the critical point. The sign of A_{12} is determined by the nature of the solute-water interactions. The "infinity" is due to the compressibility of the solvent, κ_1. Here, n_2 is the number of moles of solute. The subscript "1" is always reserved for the solvent, water. Short-range hydrophobic and hydrophilic hydration effects dominate near ambient conditions. Typical behavior for V° is plotted in Figure 4.

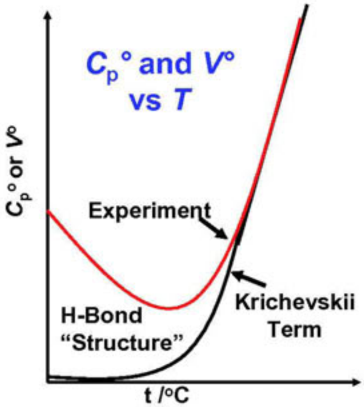

Figure 4. Typical behavior of the standard partial molar volume or heat capacity of a non-electrolyte at steam saturation pressures, showing high-temperature limiting behavior described by the Krichevskii equation as the critical point is approached. Near ambient temperatures, short-range hydration effects associated with hydrogen-bonding "structure" become much more important. These are typically described by empirical terms in the density model, the HKF model and other "equations of state" for standard partial molar properties.

O'Connell, Wood and their co-workers (O'Connell et al. 1996; Plyasunov et al. 2000a,b; Sedlbauer et al. 2000; Myers at al. 2002; Plyasunov and Shock 2004) have developed equations of state for aqueous electrolytes and non-electrolytes using terms based on the Krichevski parameter and other terms that dominate at low temperature to describe short-range hydration effects. A similar approach has been used by Helgeson and his coworkers (Helgeson et al. 1981; Tanger and Helgeson 1988; Shock et al. 1992) who used the Born equation to describe long-range ion-solvent polarization. These equations are constructed so that they have a simple physically-correct model for the limiting near-critical behavior of C_p° and V° which dominates at high temperature, and a purely empirical function for short range hydration effects which can be determined by measuring values for C_p° and V° under near-ambient conditions. However, the challenges in measuring C_p° and V° are formidable, even under ambient conditions.

"EQUATIONS OF STATE" FOR STANDARD PARTIAL MOLAR PROPERTIES

The "density" model

Franck (1956, 1961) observed that the ionization constants K of many aqueous species at elevated temperatures and pressures act as linear functions of density of water ρ_1, when $\log K$ is plotted against $\log \rho_1$ over a very wide range. Based on this observation, Marshall and Franck (1981) developed the "density" model to represent the ionization constant K_w of water at temperatures up to 1000 °C and at pressures up to 10 kbar. This has been used for representing K of general ionization reactions by Mesmer et al. (1988):

$$\log K = \left(a + \frac{b}{T} + \frac{c}{T^2} + \frac{d}{T^3}\right) + k \log \rho \tag{11}$$

$$k = \left(e + \frac{f}{T} + \frac{g}{T^2}\right) \tag{12}$$

where a, b, c, d, e, f, and g are adjustable parameters; and ρ_1 is the density of water. The first term, which dominates at low temperature, is associated with the short-range hydration term in Equation (9) and the "intrinsic" thermodynamic properties of the molecule itself. The "density" term, which dominates at high temperatures, is associated with the long-range polarization and standard state terms.

The Gibbs energy of ionization ΔG° is related to K by Equation (1):

$$\Delta G^\circ = -2.303RT\left[\underbrace{\left(a + \frac{b}{T} + \frac{c}{T^2} + \frac{d}{T^3}\right)}_{\text{Short-range hydration}} + \underbrace{\left(e + \frac{f}{T} + \frac{g}{T^2}\right)\log \rho_1}_{\text{Long-range polarization}}\right] \tag{13}$$

Other thermodynamic quantities can be derived from above equations. The enthalpy of ionization ΔH° can be obtained from the identity:

$$\left(\frac{\partial}{\partial T}\frac{\Delta G^\circ}{T}\right)_P = -\frac{\Delta H^\circ}{T^2} \tag{14}$$

to yield:

$$\Delta H^\circ = -2.303R\left(b + \frac{2c}{T} + \frac{3d}{T^2} + \left(f + \frac{2g}{T}\right)\log \rho_1\right) - RT^2 k\alpha_1 \tag{15}$$

where $\alpha_1 = -(1/\rho_1)(\partial\rho_1/\partial T)_P$ is the thermal expansion coefficient of water; and k is the fitted function given in Equation (12).

Similarly, the entropy of ionization ΔS°, the standard partial molar heat capacity of ionization $\Delta_r C_P^\circ$, and the standard partial molar volume of ionization ΔV° can be derived from ΔG° using standard thermodynamic identities (Mesmer et al. 1988) so that:

$$\Delta S^\circ = 2.303R\left(a \quad \frac{c}{T^2} \quad \frac{2d}{T^3} - \left(e \; \frac{g}{T^2}\right)\log \;{}_1\right) \quad RTk\,\rho_1 \quad - \quad \alpha \tag{16}$$

$$\Delta C_P^\circ = \; 2.303R\left[\;\frac{2c}{T^2} \quad \frac{6d}{T^3} \quad \left(\frac{2g}{T^2}\right)\log \;{}_1\right] \tag{17}$$

$$-R\alpha_d\left(2eT - \frac{2g}{T}\right) - RT^2 k\left(\frac{\partial\alpha_1}{\partial T}\right)_P$$

$$\Delta V^\circ \; = \; -RT\cdot k\cdot \kappa_1 \tag{18}$$

Here $\kappa_1 = (1/\rho_1)(\partial\rho_1/\partial P)_T$ is the compressibility of water.

Equation (11) can be further simplified over a restricted region, and the simplified form has fewer parameters (Anderson et al. 1991). More complex versions have been adopted to describe ΔV° accurately at low temperatures (Clarke and Tremaine 1999). The behavior of $\log K$, ΔS°, ΔC_P°, and ΔV° for the ionization of several weak acids and bases over a wide range of temperature and pressure, can be interpreted according to the density model (Mesmer et al. 1988). The functions for ΔC_P°, and ΔV° clearly show the very large electrostriction effects, which arise from the ability of ions to attract increasing numbers of water molecules as the compressibility of water increases under near critical conditions.

Experimental ionization and association constants have been measured under supercritical conditions, primarily using the conductivity, EMF, described by Mesmer et al. (1991), and by the heat capacity and density methods described below. At low temperatures, the thermodynamic stability of different species is controlled by the complex interplay of hydrogen-bonding effects. Above about 100 °C, reactions are increasingly driven by the entropy changes associated with the hydrophilic and hydrophobic effects associated with long-range polarization of the solvent.

For several aqueous systems, both ionization constants and functions for ΔC_P°, and ΔV° have been independently measured. As an example to illustrate the usefulness of Equation (13), Tremaine et al. (1997) have used the experimental values of V° for morpholine and the morpholinium ion shown in Figure 3, and values of C_P° obtained below 55 °C, to estimate ΔC_P° for the morpholine ionization equilibrium at high temperatures using the semi-empirical HKF model. Combining these contributions with that from the first term in Equation (13), yields $\log K = -4.843$ at 300 °C, which is in an excellent agreement with the values (-4.79 ± 0.06) and (-4.69 ± 0.06) measured in KCl media by Mesmer and Hitch (1977), and in sodium trifluoromethanesulfonate ($NaCF_3SO_3$) by Ridley et al. (2000), respectively.

The Helgeson-Kirkham-Flowers-Tanger model

Helgeson and his co-workers (Helgeson et al. 1981; Tanger and Helgeson 1988; Shock et al. 1992) have developed an equation of state, based on the Born equation for ionic hydration which is widely used by geochemists. Briefly, the Helgeson-Kirkham-Flowers (HKF) model consists of expressions for standard partial heat capacity and volume functions in Equation (7), and assumes that the standard molar Gibbs energy and enthalpy of formation of each species at 298.15 K and 0.1 MPa are known properties.

In this model, the standard molar properties of aqueous ions Y° are considered to have two contributions: an electrostatic term based on the Born equation ${}_{\mathrm{Born}}$, and a non-electrostatic term Y_n°. These correspond to the low- and high-temperature terms in Equation (13), $Y_n^\circ \approx Y_{intr}^\circ + \Delta Y_{hydr}^\circ + \Delta Y_{std\ state}^\circ$ and $\Delta Y_{\mathrm{Born}}^\circ \approx \Delta Y_{pol}^\circ$

$$Y^\circ = Y_n^\circ + \Delta Y_{\mathrm{Born}}^\circ \tag{19}$$

The Born equation describes the Gibbs energy of ionic hydration, i.e., the transfer of an ion from the ideal gas to water, by representing the ion as a charged conducting sphere and water as a continuous dielectric medium without molecular structure as illustrated in Figure 2. The Born equation takes the form

$$\Delta G_{\mathrm{Born}}^\circ = \omega_{\mathrm{Born}}\left(1 - \frac{1}{\varepsilon_{\mathrm{r}}}\right) \tag{20}$$

where ε_{r} is the solvent dielectric constant; ω_{Born} is a term that includes the ionic charge Z, ionic radius r_{e}, permittivity of free space ε_{o}, and Avogadro's number N_{A}.

$$\omega_{\mathrm{Born}} = \frac{N_A (Ze)^2}{8\pi\varepsilon_{\mathrm{o}} r_{\mathrm{e}}} \tag{21}$$

The primary hydration sphere of most ions varies only slightly with temperature (Seward and Driesner 2004). The Helgeson-Kirkham-Flowers (HKF) model treats this by employing an *effective* ionic radius, where r_{e} is a simple linear function of crystallographic radius r_x and charge Z, $r_{\mathrm{e}} = r_x + 0.94|Z|$ for cations and $r_{\mathrm{e}} = r_x$ for anions. The revised HKF model (Tanger and Helgeson 1988; Shock et al. 1992) also considered r_{e} to be a function of T and P above 300 °C. The appropriate temperature and pressure derivatives of $\Delta G_{\mathrm{Born}}^\circ$ yield expressions for $\Delta C_{P,\mathrm{Born}}^\circ$ and $\Delta V_{\mathrm{Born}}^\circ$ in terms of the same parameters.

The non-electrostatic term Y°_n accounts for three contributions: (i) the intrinsic gas phase property of the solute, (ii) the change arising from the difference in standard states between the gas phase and solution, and (iii) short-range hydration effects (Fernandez-Prini et al. 1992). In the HKF treatment, Y_n° is used as an empirical fitting equation with the following form:

$$V^\circ = a_1 + a_2\left(\frac{1}{\Psi + P}\right) + \left[a_3 + a_4\left(\frac{1}{\Psi + P}\right)\right]\left(\frac{1}{T - \Theta}\right) + V_{\mathrm{Born}}^\circ \tag{22}$$

Here Θ is a solvent parameter equal to 228 K, which corresponds to temperature at which supercooled liquid water undergoes anomalous behavior (Angell 1982; Debenedetti 1998; Mishima and Stanley 1998); Ψ is a similar solvent parameter equal to 2600 bars; and a_1, a_2, a_3, and a_4 are temperature- and pressure-independent, but species-dependent, fitting parameters.

The non-electrostatic contribution $\Delta C_{P,n}^\circ$ can be represented by a temperature dependent function similar to that used for V°. The pressure dependence of $\Delta C_{P,n}^\circ$ can be derived from the V° expression based on the thermodynamic identity $(\partial C_P/\partial P)_T = -T(\partial^2 V/\partial T^2)_P$ to yield the following expression for the entire standard partial molar heat capacity:

$$C_P^\circ = c_1 + c_2\left(\frac{1}{T - \Theta}\right)^2 - 2T\left(\frac{1}{T - \Theta}\right)^3\left[a_3\left(P - P_{\mathrm{r}}\right) + a_4 \ln\left(\frac{\Psi + P}{\Psi + P_{\mathrm{r}}}\right)\right] + C_{P,\mathrm{Born}}^\circ \tag{23}$$

Here c_1 and c_2 are temperature- and pressure-independent, but species-dependent, parameters; Θ is again a parameter with the value of 228 K; P_{r} is the reference pressure (1 bar); and a_3 and a_4 are determined by the fits to V° from Equation (22).

Standard partial molar volumes and heat capacities of aqueous ions and electrolytes typically exhibit an inverted U-shape as a function of temperature in Figure 5 (Hovey and

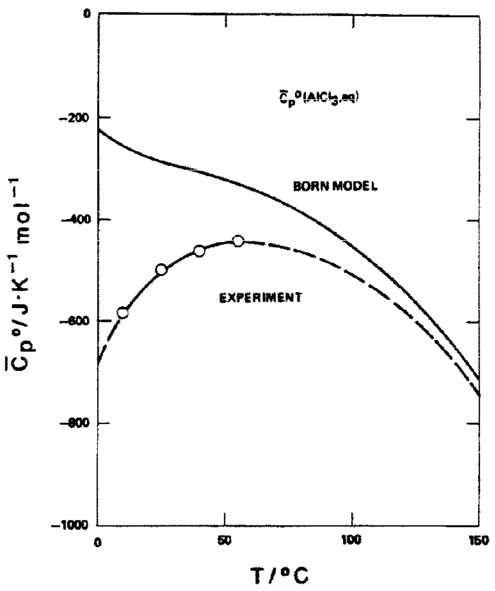

Figure 5. Experimental standard partial molar hear capacities for $AlCl_{3(aq)}$ from 10 to 55 °C. The dashed line is the HKF extrapolation to elevated temperatures. The solid line is the contribution of the Born term, and the difference is the contribution of the empirical coefficients that account for low-temperature hydrogen-bonding "structural" effects. [Used by permission of Elsevier, from Hovey and Tremaine (1986) *Geochim Cosmochim Acta*, Vol. 50, Fig. 2, p 458.]

Tremaine 1986). This is consistent with the singular temperatures of water at –45 °C (228 K) and 373 °C (647 K, the critical temperature) where second-derivative thermodynamic parameters approach +∞. The parameters in the revised HKF model have been selected so that the electrostatic contribution dominates at high temperatures where the Born model is most satisfactory, and the non-electrostatic contribution to V^o and C_p^o dominates at low temperatures. The revised HKF model has been used widely for the extrapolation of low temperature standard partial molar properties of aqueous ions and electrolytes to elevated temperatures and pressures.

The revised HKF model has also been used by Shock and Helgeson (1990) for the prediction of the standard partial molar properties of *neutral* aqueous organic species up to 1000 °C and 5 kbar. It was fitted to the available experimental data for neutral aqueous organic species at elevated temperatures and pressures, as shown in Figure 3. The fitted parameters were then used to develop correlations with other low temperature thermodynamic constants. In contrast to the positive $\Delta C_{p,\mathrm{Born}}^o$ and $\Delta V_{\mathrm{Born}}^o$ for aqueous ions and electrolytes, as required by theory, the fitted Born terms for neutral species can be either positive or negative. According to Equation (21), negative values of $\Delta C_{p,\mathrm{Born}}^o$ and $\Delta V_{\mathrm{Born}}^o$ correspond to negative values of ω_e, so that Z_e, the effective charge, is an imaginary number. Clearly, the expression for the electrostatic contribution has no physical meaning, and the validity of the revised HKF model for neutral species is questionable. The predictive capability stated in the paper is also limited by the rather sparse experimental data available at the time the correlations were derived.

THERMODYNAMICS OF SOLUTION CALORIMETRY

Standard partial molar heat capacities and volumes

Standard partial molar heat capacities and volumes are most commonly determined by measuring the heat capacity and volume of aqueous solutions relative to water, in order to determine the corresponding apparent molar properties, Y_ϕ as a function of mole fraction or molality. Apparent molar properties record the total effect of the solute on the solution, per mole added:

$$Y_{\phi} = \frac{Y_{(\mathrm{soln})} - Y_{(\mathrm{solvent})}}{n_{\mathrm{solute}}} \tag{24}$$

The concentration dependence of Y_ϕ yields the partial molar property,

$$\overline{Y_2} = \left(\frac{\partial Y}{\partial n_2}\right)_{n_1,T,P} \;;\quad Y_{\phi} + n_2\left(\frac{\partial Y_{\phi}}{\partial n_2}\right)_{n_1,T,P} \tag{25}$$

from which:

$$\overline{Y_2} = Y_{\phi} \quad m\!\!+_{2}\left(\frac{\partial Y_{\phi}}{\partial m_2}\right)_{T,P} \tag{26}$$

The standard partial molar heat capacity and volume are determined from the limiting values at infinite dilution:

$$Y_2^{\circ} = \lim_{x_2 \to 0} \overline{Y_2} \quad \lim_{m_2 \to 0} \overline{Y_2}\!\!= \quad \lim_{m_2 \to 0} Y_{\phi,2} \qquad = \tag{27}$$

The experimental challenge is that accurate extrapolations to determine C_P° and V° require measurements of the apparent molar properties, $C_{P\phi}$ and V_{ϕ}, at concentrations low enough to allow extrapolations to infinite dilution with an extended Debye Hückel equation. A 0.1 mol·kg^{-1} solution contains only 0.1 mol solute in 55.516 mol water, so that values of the difference in volume ($V_{\mathrm{soln}} - V_1$) and heat capacity ($C_{P,\mathrm{soln}} - C_{P,1}$) are less than 1 percent, where the subscript "1" refers to the solvent, water. In order to measure $C_{P\phi}$ and V_ϕ accurately, the density and heat capacity relative to water must be determined to an accuracy of ± 0.00001 cm^3 g^{-1} and ± 0.00001 J g^{-1}, respectively. Until the invention of the vibrating-tube densimeter (Kratky et al. 1969; Picker et al. 1974) and the Picker microcalorimeter (Picker et al. 1971), such measurements were painfully difficult, and only possible near ambient conditions.

Standard partial molar enthalpies and heats of mixing

Heat of mixing is defined as the energy that accompanies the mixing process of initially separated pure components at constant temperature and pressure. Because the process is isobaric $Q = \Delta H$ and so the heat of mixing is equal to the enthalpy of mixing. The molar heat of mixing $\Delta_{\mathrm{mix}}H_{\mathrm{m}}$ commonly expressed in J mol^{-1} (for one mole of mixture) is defined as:

$$\Delta_{\mathrm{mix}}H_{\mathrm{m}} = \frac{H - \sum_{i=1}^{N} n_i H_{i,\mathrm{m}}^{\bullet}}{n_t} \tag{28}$$

where H is the enthalpy of mixture; $H_{i,\mathrm{m}}^{\bullet}$ is the molar enthalpy of a pure component i; and n_{t} is the total number of moles present in the system.

The excess molar enthalpy is the difference between the molar enthalpy of the mixture H_{m} and that of an ideal mixture $H_{\mathrm{m}}^{\mathrm{id}}$,

$$H_{\mathrm{m}}^{\mathrm{E}} = H_{\mathrm{m}} \quad H_{\mathrm{m}}^{\mathrm{id}}- \tag{29}$$

where:

$$H_{\mathrm{m}}^{\mathrm{id}} = \frac{\sum_{i=1}^{N} n_i H_{i,\mathrm{m}}^{\bullet}}{n_t} \tag{30}$$

Finally, it is possible to relate excess molar enthalpy to the molar enthalpy of mixing, but care needs to be taken in considering which standard state convention should be used.

Enthalpies of mixing use either the symmetric Raoult's law (mole fraction) standard state, or the Henry's law hypothetical one molal standard state for the solute, depending on the system studied and its application. The symmetric Raoult's Law convention is generally used for mixtures where the quantities of the constituents in the system are comparable. In this case, the standard state for each component i is the pure liquid so that $\gamma_i \rightarrow 1$ when $x_i \rightarrow 1$:

$$\lim_{x_i \rightarrow 1} \overline{H_i} = H^{\bullet}_{i,m} \tag{31}$$

leading to:

$$H^{\mathrm{E}}_{\mathrm{m}} = \sum_{i=1}^{N} x_i \overline{H_i} - \sum_{i=1}^{N} x_i H^{\bullet}_{i,m} = \Delta_{\mathrm{mix}} H_{\mathrm{m}} \tag{32}$$

The asymmetric convention is generally used when considering solutes in a solvent. In that case the chosen standard state for a component i in smaller quantity compared to the solvent denoted by 1 is the infinite dilute Henry's Law standard state, with $\gamma_i \rightarrow 1$ when $x_i \rightarrow 0$. For the solvent the pure liquid Raoult's Law standard state is used, with $\gamma_1 \rightarrow 1$ when $x_1 \rightarrow 1$. Equation (31) applies for the solvent and, for the solute, we have:

$$\lim_{x_i \rightarrow 0} \overline{H_i} = H^{\circ}_{i,m} \tag{33}$$

For the solute, in the Henry's Law reference state, Equation (33) takes the form:

$$H^{\mathrm{E}}_{\mathrm{m}} = \Delta_{\mathrm{mix}} H_{\mathrm{m}} - \sum_{i=1}^{N} x_i \left(H^{\circ}_{i,m} - H^{\bullet}_{i,m} \right) \tag{34}$$

Expressions for converting excess enthalpies and other thermodynamic functions from excess properties defined by the Raoult's law standard state, and the apparent molar properties defined by the hypothetical one-molal standard state, discussed below, are given by Desnoyers and Perron (1997).

Excess properties

Activity coefficient models. The excess properties of electrolyte solutions are described by various forms of the extended Debye-Hückel equation. The most straightforward is a simple Taylor series expansion of the limiting law,

$$\log \gamma_{\pm} = -A_{\gamma} I^{1/2} + B_{\gamma} I + C_{\gamma} I^{3/2} + \ldots \tag{35}$$

in which $\gamma_{\pm}$ is the mean activity coefficient of a solution containing molality m_i of each ionic species of charge z_i. I is the ionic strength:

$$I = m_{\pm} = \frac{1}{2} \sum_i m_i z_i \tag{36}$$

and the term $A_{\gamma} I$ is the theoretical Debye-Hückel limiting slope. $B_{\gamma} I$, $C_{\gamma} I^{3/2}$ and higher order terms are used as adjustable parameters. The appropriate temperature and pressure derivatives of this expression (Pitzer 1995) yield the corresponding expressions for the excess enthalpy, L_{ϕ}; apparent molar heat capacity, $C_{P,\phi}$; and apparent molar volume, V_{ϕ}:

$$\Delta_{react} H = \Delta_{react} H^{\circ} + \Delta_{dil} H \tag{37}$$

$$\text{where } \Delta_{dil} H = -L_{\phi} = +A_L I^{1/2} + B_L I + C_L I^{3/2} + \ldots$$

$$C_{P,\phi} = C_P^{\circ} + A_J I^{1/2} + B_J I + C_J I^{3/2} + \ldots$$

$$V_{\phi} = V^{\circ} + A_V I^{1/2} + B_V I + C_V I^{3/2}$$

The Debye-Hückel limiting slope A_γ as defined by Pitzer (1995) for *apparent* molar properties, differs from older definitions for *partial* molar properties by a factor of 3/2. For example at 25 °C and 1 bar the new Debye Hückel parameter for enthalpy is $A_L^{NEW}/RT = (2/3)\times[A_L^{OLD}/RT] = (2/3)\times 1.1773 = 0.7849$. Values for the Debye-Hückel limiting slopes, based on Hill's (1990) equation of state for water, have been compiled by Archer and Wang (1990). These form the basis of an accurate equation of state for the $NaCl_{(aq)}$ system over a very wide range of temperature and pressure (Archer 1992), which is widely used for calibration of densitometers and heat-capacity calorimeters. NIST has released more up-to-date values for the Debye-Hückel slopes, based on the dielectric constant expression of Fernandez et al. (1997) and the equation of state for water by Wagner and Pruß (2002). Unfortunately, there is no corresponding equation of state for $NaCl_{(aq)}$. As a result the equations of state by Hill (1990), Archer and Wang (1990) and Archer (1992) continue to be used in calorimetric studies due to their internal consistency.

Taylor expansions based on an extended form of the limiting law, yield more complex expressions for the apparent molar properties (Millero 1979; Pitzer 1995), but these require fewer adjustable parameters to fit a given set of ionic-strength dependent data; for example:

$$\log\gamma_{\pm} = -\omega A_\gamma \frac{I^{1/2}}{1+I^{1/2}} + B_\gamma I + C_\gamma I^{3/2} + \dots \tag{38}$$

The corresponding expressions for the apparent molar properties are given below:

$$L_\phi = \frac{3}{2}\omega A_L\left(\frac{1}{\Lambda} - \frac{\sigma}{3}\right)I^{1/2} + B_L I + C_L I^{3/2} + \dots \tag{39}$$

$$C_{P,\phi} = C_P^\circ + \frac{3}{2}\omega A_J\left(\frac{1}{\Lambda} - \frac{\sigma}{3}\right)I^{1/2} + B_J I + C_J I^{3/2} + \dots$$

$$V_\phi = V^\circ + \frac{3}{2}\omega A_V\left(\frac{1}{\Lambda} - \frac{\sigma}{3}\right)I^{1/2} + B_V I + C_V I^{3/2} + \dots$$

Where

$$\Lambda = 1 + I^{1/2}; \qquad \sigma = \frac{3\left(\Lambda - 1/\Lambda - 2\ln\Lambda\right)}{I^{3/2}} \tag{40}$$

Modern treatments of calorimetric measurements to high concentrations frequently use the Pitzer ion-interaction model (Pitzer 1973, 1991, 1995), especially when the results from several complementary experimental methods are simultaneously regressed into a comprehensive model for the temperature and pressure dependence of excess properties (Pitzer 1995). The Pitzer equations for single electrolyte solutions are given below:

$$\log\gamma_{\pm} = \left|z_A z_B\right| f^\gamma + m\left(2\frac{\nu_A\nu_B}{\nu}\right)B_{AB}^\gamma + m^2\left[2\frac{\left(\nu_A\nu_B\right)^{3/2}}{\nu}\right]C_{AB}^\gamma \tag{41}$$

where:

$$-f^\gamma = A_\phi\left[\frac{I^{1/2}}{\left(1+bI^{1/2}\right)} + \frac{2}{b}\ln\left(1 + bI^{1/2}\right)\right]$$

$$B_{AB}^\gamma = B_{AB} + B_{AB}^\phi \quad \text{and} \quad C_{AB}^L = \frac{3}{2}C_{AB}^\phi$$

Here, z_A, z_B are the ionic charges; ν_A, ν_B the stoichiometric coefficients; and $b = 1.2$ mol·kg^{-1} is the Pitzer parameter. The B terms depend on ionic strength and are usually fitted to experimental data using two to three adjustable parameters (Wang et al. 1997, 1998; Oakes et al. 1998). Apparent molar properties can then be derived in the following forms:

$$L_\phi = \nu \left|z_A \cdot z_B\right| \left(\frac{A_L}{2b}\right) \ln\left(1 + b I^{1/2}\right) - 2\nu_A \nu_B RT^2 \left[m B^L_{AB} + m^2 \left(\nu_A \nu_B\right) C^L_{AB}\right] \tag{42}$$

$$C_{P,\phi} = C_P^\circ + \nu \left|z_A \cdot z_B\right| \left(\frac{A_J}{2b}\right) \ln\left(1 + b I^{1/2}\right) - 2\nu_A \nu_B RT^2 \left[m B^J_{AB} + m^2 \left(\nu_A \nu_B\right) C^J_{AB}\right]$$

$$V_\phi = V^\circ + \nu \left|z_A \cdot z_B\right| \left(\frac{A_V}{2b}\right) \ln\left(1 + b I^{1/2}\right) - 2\nu_A \nu_B RT^2 \left[m B^V_{AB} + m^2 \left(\nu_A \nu_B\right) C^V_{AB}\right]$$

where:

$$B^L_{AB} = \left(\frac{\partial B_{AB}}{\partial T}\right)_{P,I} \quad \text{and} \quad C^L_{AB} = \frac{\left|z_A \cdot z_B\right|^{1/2}}{2} \left(\frac{\partial C^\phi_{AB}}{\partial T}\right)_P$$

$$B^J_{AB} = \left(\frac{\partial^2 B_{AB}}{\partial T^2}\right)_{P,I} + \frac{2}{T}\left(\frac{\partial B_{AB}}{\partial T}\right)_{P,I} \quad \text{and} \quad C^J_{AB} = \left(\frac{\partial^2 C^\phi_{AB}}{\partial T^2}\right)_P + \frac{2}{T}\left(\frac{\partial C^\phi_{AB}}{\partial T}\right)_P \tag{43}$$

$$B^V_{AB} = \left(\frac{\partial B_{AB}}{\partial p}\right)_{T,I} \quad \text{and} \quad C^V_{AB} = \frac{\left|z_A \cdot z_B\right|^{1/2}}{2} \left(\frac{\partial C^\phi_{AB}}{\partial p}\right)_T$$

Apparent molar properties of mixtures. The apparent molar properties of mixtures are defined by the expression:

$$Y_{\phi,\text{mixture}} = \frac{Y_{(\text{soln})} - Y_{(\text{solvent})}}{\sum\limits_{i=2,3..} n_{\text{solute},i}} \tag{44}$$

For a multi-component salt system, on the molality scale, this is usually expressed as:

$$Y_\phi^{\text{Exp}} = \frac{M_{\text{Total}}}{\rho_{\text{soln}}} - \frac{10^3\left(\rho_{\text{soln}} - \rho_1\right)}{\rho_{\text{soln}} \rho_1 m_{\text{Total}}} \tag{45}$$

For a two-salt system, the "total" molar mass and "total" molality are given by:

$$M_{\text{Total}} = \frac{\left(m_2 M_2 + m_3 M_3\right)}{\left(m_2 + m_3\right)}, \quad \text{and } m_{\text{Total}} = m_2 + m_3 \tag{46}$$

where component "1" is usually reserved for the solvent.

Young's rule (Young and Smith 1954; Millero 1971, 1979, 2001) states that, at constant temperature, the apparent molar properties of a mixture may be approximated by summing the apparent molar properties of the single-salt solutions at the ionic strength of the mixture:

$$Y_\phi^{\text{Exp}}(I) = \frac{m_2}{m_{\text{Total}}} Y_{\phi,2}(I) + \frac{m_3}{m_{\text{Total}}} Y_{\phi,3}(I) + \ldots. \tag{47}$$

Experience has shown that this is a reasonably accurate assumption for moderately dilute solutions sharing a common anion or cation. Apparent molar heat capacities are a special case, since the temperature increment required to make the measurement shifts the chemical equilibrium. This "chemical relaxation effect" must be subtracted before Young's rule can be applied. For a two component solute, the expression is:

$$C_{P,\phi}^{\text{Exp}}(I) = \frac{m_2}{m_2 + m_3} C_{P,\phi,2}(I) + \frac{m_3}{m_2 + m_3} C_{P,\phi,3}(I) + C_{P,\phi}^{\text{Relax}} \tag{48}$$

In the simplest case, for ion association and neglecting the enthalpy of dilution,

$$C_{P,\phi}^{\mathrm{Relax}} = -\alpha \frac{(\Delta_r H^\circ)^2}{(RT^2)} \tag{49}$$

where α is the degree of association and $\Delta_r H^\circ$ is the standard molar enthalpy of the association reaction (Woolley and Hepler 1977). General methods for calculating the chemical relaxation effect have been reported by Mains et al. (1984). Finally, we note that the Pitzer Ion Interaction Model (Pitzer 1973, 1991, 1995) and the Bromley Interaction Model (Bromley 1973) have been widely used to describe the thermodynamics of complex mixtures up to very high concentrations. These are described thoroughly in several papers and monographs (see, for example: Pitzer 1991, 1995; Stumm and Morgan 1996). They are beyond the scope of this chapter.

DENSIMETRY

Vibrating-tube densimeters

The measurement of apparent molar volumes of aqueous solutes underwent a revolution with the invention of the vibrating-tube densimeter by Kratky et al. (1969), and its development by Picker et al. (1974) and others. The operating principle is based on accurate measurements of the *changes* in the resonant frequency of a vibrating tube, due to the difference in the tube's mass as the contents are changed from a calibration gas or solvent, to water, to the aqueous solution of interest. A typical design for a high-temperature densimeter (Albert and Wood 1984; Xiao et al. 1997) is shown in Figure 6. In the low-temperature design, the insulated tube carries current, and lies between the poles of an electromagnet within a vacuum chamber. In the high temperature design, two insulated rods, connected to the control circuit by fine silver wires, are attached to the vibrating tube by insulating cement and lie between the poles of a permanent magnet. One rod carries an AC current which drives the vibration at the resonant frequency through a phase-lock loop. The second rod is connected to the frequency counter and acts as a passive frequency sensor which carries AC current induced by its movement through the magnetic field. The reciprocal of the resonant frequency ω is the period, τ, which has a linear relation to density according to the relationship:

$$\rho_{\mathrm{soln}} - \rho_1 = k_{\mathrm{Instr}}\left(\tau^2 - \tau_1^2\right); \text{ where } \tau = \frac{1}{\omega} \tag{50}$$

The term k_{Instr} is a calibration constant and the subscript 1 denotes the solvent. The calibration constant is determined from measurements with water and nitrogen; water and a 1.0 mol·kg^{-1} standard solution of aqueous NaCl; or water and isotopically pure D_2O, using the self-consistent equations of state reported by Hill (1990); Archer (1992) and, for D_2O, Hill et al. (1982), Kestin et al. (1984) and Kestin and Sengers (1986).

For studies near ambient temperatures, the most sensitive commercial instrument for thermochemical applications is the DMA 5000, manufactured by Anton Paar Ltd., which is capable of relative density measurements from 0 to 90 °C, to a precision of $\pm 2\times10^{-6}$ g·cm^{-3}.

Vibrating tube densimeters are an attractive option for studying hydrothermal systems because there is no vapor space and hence the pressure can be controlled independently of temperature using modern liquid chromatography pumps and backpressure regulators. The principal challenge is to control the temperature to ± 0.05 °C or better, over a time period of several hours required for multiple injections of calibration standards and solution samples. This was accomplished in the first such instrument by Albert and Wood (1984) using a nested set of evacuated chambers, each with independent temperature control. A similar design by

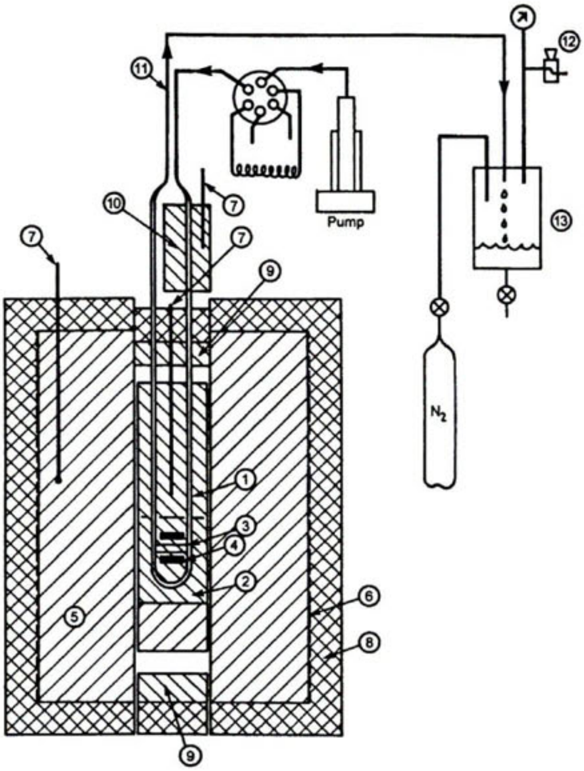

Figure 6. Vibrating-tube densimeter and a typical sample injection system. 1, U-shaped vibrating tube; 2, densimeter cell body; 3, Inconel rods for sensing and driver current; 4, permanent magnet; 5, brass oven; 6, insulated heating wire; 7, RTD; 8, thermal insulator; 9, brass heat shield; 10, brass preheater; 11, heat exchanger; 12; back pressure regulator; 13, receiver vessel. [Used by permission of Elsevier, from Xiao et al. (1997) *J Chem Thermodyn*, Vol. 29, Fig. 1, p 263.]

Corti et al. (1990) uses a massive brass block instead of the vacuum chambers. In both cases the heater coils must be wound symmetrically forward and backward so that no magnetic field is generated. These instruments, operate from ~50 °C to 450 °C and 325 °C, respectively, with a precision of $\pm 2\times10^{-5}$ g·cm^{-3} (Corti et al. 1990; Xiao et al. 1997). The brass oven is simpler to construct, with a shorter resident time suitable for samples that thermally decompose, but is more limited in its temperature range.

A typical injection system is shown in Figure 6. Briefly, the system consists of a liquid chromatography pump and sample injection loop upstream of the densimeter, followed by a backpressure regulator. The pump controls the flow rate, typically 0.2 to 2 cm^3·min^{-1}, and the back-pressure regulator controls the pressure. Often a second liquid loop, located downstream of the oven but before the backpressure regulator, is used to sample the solutions *after* they leave the densimeter to ensure that no thermal decomposition took place. Accurately calibrated transducers are required before and after the densimeter cell to ensure that there is no pressure drop. This is especially important at temperatures above 250 °C, where the solvent compressibility effects become important. Care must be taken to deoxygenate the feed-water when using platinum tubes with chloride, ammonia, or other ligands that may form Pt(IV) complexes at elevated temperatures, since severe corrosion may result. For oxidizing conditions, titanium alloys are suitable.

A suitable phase-lock loop is essential to the successful construction of a vibrating tube densimeter, since the signals are very weak. Improvements on the original design of the electronics have been reported by Wood et al. (1989). Several new designs for the densimeter itself have also been reported to extend its temperature range, simplicity, and/or ease of use (Hakin et al. 1998; Hynek et al. 1997, 1999; Majer et al. 1999). In addition to measuring apparent molar volumes, vibrating tube densimeters can be used to measure bubble-points of multi-component solutions (Crovetto et al. 1991).

As an example, Bulemela and Tremaine (2008) have used the densimeter shown in Figure 7 to determine apparent molar volumes of dilute aqueous solutions of several thermally stable alkanolamines at temperatures from 150 °C to 325 °C and pressures as high as 150 bar. The results were corrected for the ionization and used to obtain the standard partial molar volumes, V_2°. Values of V_2° for monoethanolamine (MEA), diethanolamine (DEA), triethanolamine (TEA) and 2-diethylethanolamine (2-DEEA) are plotted in Figure 7. Similar studies on a wide range of organic solutes have been carried out by Criss and Wood (1996), Majer's group in Clermont Ferrand (Censky et al 2007) and Hnědkovský's groups in Prague (Simurka et al. 2011) The application of such results for modeling the chemistry of pH-control agents in thermal and nuclear power stations, and in developing functional group-additivity models for organic solutes is briefly described in the Discussion Section as a current area of investigation.

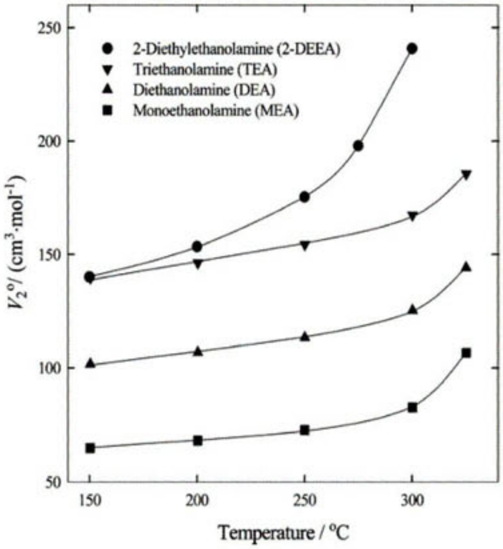

Figure 7. Standard partial molar volumes, of monoethanolamine (MEA), diethanolamine (DEA), triethanolamine (TEA), and 2-diethylethanolamine (2-DEEA) plotted as a function of temperature. [Used by permission of ACS, from Bulemela and Tremaine (2008) *J Phys Chem*, Vol. 112, Fig. 2, p 5630.]

HEAT-CAPACITY CALORIMETRY

Pioneering studies

The design features of modern calorimeters have been presented by a number of authors (See, for example: Wilhelm and Letcher 2010; and references cited therein). Briefly, there are four basic types of calorimeters. *Adiabatic* calorimeters use batch cells, surrounded by extremely efficient thermal shields, and measure the heat capacity of the cell plus its contents by measuring the power required to heat the cell under conditions where no heat flow takes place between the cell and its surroundings. *Isoperibol* calorimeters measure the heat released by a reaction or phase transition, by measuring the temperature rise of a well-insulated cell, and correcting for the (small) heat transfer to the surroundings as the reaction takes place. Isothermal calorimeters are based on two design concepts. *Power-compensated isothermal* *calorimeters* measure the power required to maintain a constant temperature as a reaction proceeds, against a constant cooling load. *Heat-flux* or *Calvet isothermal calorimeters* use a sensitive thermopile or Peltier device to measure the heat flow from the reaction chamber into a large heat sink that surrounds the cell, designed so that the temperature rise of the cell relative to the surroundings is extremely small.

The experimental challenges to measuring apparent molar heat capacities by conventional calorimetric methods are formidable. The first challenge is to achieve the necessary precision of $\pm\ 10^{-5}\ \mathrm{J{\cdot}g^{-1}}$ required to study molalities down to 0.1 $\mathrm{mol{\cdot}kg^{-1}}$. This requires the most sensitive adiabatic calorimeter, with thin-walled glass vessels. Pioneering studies by Ackermann (Ackermann 1957; Ruterjans et al. 1969) used this approach. Extending adiabatic calorimetric studies to hydrothermal conditions requires thick-walled vessels, which lowers the sensitivity. A second challenge arises from the heat effects associated with the vapor pressure of water, which become significant above about 50 °C. (See for example Zhang et al. 2002).

An alternative approach, developed by Cobble and his coworkers (Criss and Cobble 1964; Cobble 1966; and references cited therein), is the so-called "integral heat of solution" method, where an isoperibol calorimeter was used to measure the heat of solution of crystalline salts, A^+B^-, as a function of temperature. The enthalpies of solution, $\Delta_{\mathrm{sol}}H_T$, were then used to calculate the apparent molar heat capacity of the aqueous solutes from the relationship,

$$\Delta C_{P,T}(AB)=\left(\frac{\partial \Delta H_T(AB)}{\partial T}\right)\ \text{€}_{P,\phi,T}(AB)\quad C_{\overline{P},T}(AB,solid) \tag{51}$$

Since the heat capacities and enthalpies of formation of solids are accurately known, this method yields both the standard partial molar heat capacity $C^{\circ}_{P,T}$ and the enthalpy of formation $\Delta_f H^{\circ}$ of the aqueous solute as a function of temperature, although the values of $C_{P,\phi}$ are less accurate than those from direct measurements using the modern methods described below. An advantage of the integral heat of solution approach is that enthalpies of solution can be measured at concentrations below $10^{-3}\ \mathrm{mol{\cdot}kg^{-1}}$.

The Picker flow microcalorimeter

Principles of operation. The modern era of hydrothermal solution thermodynamics began with the invention of the Picker heat-capacity microcalorimeter at the University of Sherbrooke (Picker et al. 1971; Desnoyers et al. 1976) and its extension to hydrothermal conditions by R.H. Wood at the University of Delaware (Smith-Magowan and Wood 1981). Like the vibrating tube densimeter the instrument measures the *difference* in properties between the solution of interest and pure water. A schematic of the design is shown in Figure 8. The Picker calorimeter is a twin-cell flow instrument with a number of insightful, indeed rather clever, innovations. Its' operating principle is based on measuring the *difference* between the heat capacities of two parallel cells, configured so that flow rate uncertainties and temperature fluctuations cancel.

Briefly, all calorimeters measure the heat capacity by determining the heat, Q, required to raise the temperature of a gram of solution by ΔT. In a tubular flow calorimeter this is expressed as

$$C_P=\frac{Q}{\Delta T}\quad\frac{\mathcal{P}}{f_m\Delta T} \tag{52}$$

where, $\mathcal{P}$ is the heater power and f_m is the mass flow rate. In the Picker, twin-cell design, the inlet tubes are in close proximity to one another, thermostatted by the same temperature-controlled fluid, so that the inlet temperatures are identical. The power applied to Tube 1 (the "sample" cell) is adjusted to maintain the same temperature increment as Tube 2 (the "reference" cell). Since the values of ΔT are identical, the ratio of heat capacities of the fluids in the two cells is given by the ratio of heater power and mass flow rates:

$$\frac{C_{P_1}}{C_{P_2}} = \frac{\left(\dfrac{\mathcal{P}_1}{f_{m_1}}\right)}{\left(\dfrac{\mathcal{P}_2}{f_{m_2}}\right)} = \frac{\mathcal{P}_1}{\mathcal{P}_2}\,\frac{f_{m_2}}{f_{m_1}} \quad . \tag{53}$$

The power ratio, $\mathcal{P}_1/\mathcal{P}_2$ can be accurately measured, but flow-rate control to ±10^{-5} is problematic. Picker's genius was to join the two cells by a long length of tubing, the "delay line", shown in Figure 8. The instrument is zeroed by adjusting W_1/W_2 with water through the two cells, then the solution of interest is introduced and the measurement taken when sample is in cell 1 and water in cell 2, with the interface moving through the delay line.

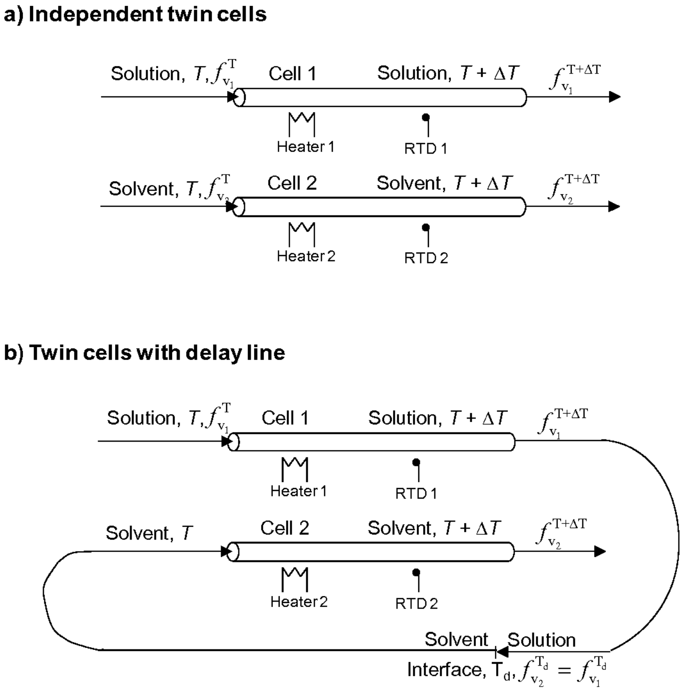
a) Independent twin cells
Solution, $T, f_{V_1}^{T}$
Cell 1
Solution, $T + \Delta T$
$f_{V_1}^{T+\Delta T}$
Heater 1
RTD 1
Solvent, $T, f_{V_2}^{T}$
Cell 2
Solvent, $T + \Delta T$
$f_{V_2}^{T+\Delta T}$
Heater 2
RTD 2
b) Twin cells with delay line
Solution, $T, f_{V_1}^{T}$
Cell 1
Solution, $T + \Delta T$
$f_{V_1}^{T+\Delta T}$
Heater 1
RTD 1
Solvent, T
Cell 2
Solvent, $T + \Delta T$
$f_{V_2}^{T+\Delta T}$
Heater 2
RTD 2
Solvent
Solution
Interface, $T_d, f_{V_2}^{T_d} = f_{V_1}^{T_d}$

Figure 8. The conceptual design of the Picker flow heat-capacity microcalorimeter.

At interface between the two fluids in the delay line volumetric flow rates must be equal,

$$f_{V_1} = f_{V_2} \tag{54}$$

Mass flow is related to f_V by the fliud's density

$$f_{\mathrm{m}} = f_V \cdot \rho \tag{55}$$

where f_m and f_V are respectively the mass and volume flow rate , so that the ratio of mass flow rates is given by the density ratio at the at the temperature of the delay line, T_{delay}:

$$\frac{f_{m_2}}{f_{m_1}} = \frac{f_{V_1,T_{\mathrm{delay}}}}{f_{V_2,T_{\mathrm{delay}}}} \frac{\rho_{2,T_{\mathrm{delay}}}}{\rho_{1,T_{\mathrm{delay}}}} = \frac{\rho_{2,T_{\mathrm{delay}}}}{\rho_{1,T_{\mathrm{delay}}}} \tag{56}$$

and

$$\frac{C_{P_1,T}}{C_{P_2,T}} = \frac{\mathcal{P}_1}{\mathcal{P}_2} \frac{\rho_{2,T_{\mathrm{d}}}}{\rho_{1,T_{\mathrm{d}}}} \tag{57}$$

Experimental measurements usually report the heat-capacity/density ratio corresponding to the power increment in the sample cell, $\Delta\mathcal{P}/\mathcal{P} = (\mathcal{P}_1 - \mathcal{P}_2)/\mathcal{P}_2$:

$$\left[\frac{C_{P_1,T} \cdot \rho_{1,T_{\mathrm{d}}}}{C_{P_2,T} \cdot \rho_{2,T_{\mathrm{d}}}} - 1\right] = \frac{\mathcal{P}_1}{\mathcal{P}_2} - 1 = \frac{\Delta\mathcal{P}}{\mathcal{P}_2} \tag{58}$$

Densities, which must also be known to very high precision, are usually determined by measuring relative densities, $(\rho - \rho_1)$ in a vibrating tube densimeter, then calculating ρ from Hill's (1990) equation of state for water.

For almost two decades, Picker calorimeters were manufactured by Patrick Picker through his own company, Sodev, and a number are still in operation. In operating these instruments, we note that the values of $C_{P\phi}$ are obtained at the mean temperature $T_{\mathrm{Bath}} + \Delta T/2$, and that density measurements should be at the mean temperature, not the calorimeter bath temperature. The tubular cells are insulated from one-another and their surroundings by a vacuum. Desnoyers et al. (1976) have shown that the heat- capacity/density ratios must be corrected for heat leaks, using chemical standards, usually 1 mol·kg^{-1} NaCl. The heat-leak correction factor, F, is typically less than 1%.

High-temperature heat-capacity flow calorimeters. In 1981, Smith-Magowan and Wood reported the first practical design for a calorimeter capable of measuring apparent molar heat capacities at temperatures up to and above the critical point of water. The design is based on the Picker flow concept, with the flow rate provided by a liquid chromatography pump upstream of the instrument, a back-pressure regulator to control pressure, and HPLC sample injection loops similar to those for the injection system for the densimeter as shown in Figure 9. A key element in the design is that the delay-line is thermostatted at 25 °C so that, from Equation (56), the high-temperature specific heat capacity ratio can be calculated from room-temperature solution densities. The design has been improved several times, most recently by Hnědkovský et al. (2002). At present we are aware of two operating instruments worldwide, those at Clermont-Ferrand and the Institute of Chemical Technology in Prague. The instruments are calibrated by injecting water and standard solutions of $NaCl_{(aq)}$, using values for their densities and specific heat capacities from the equations of state by Hill (1990) and Archer (1992), respectively. An alternative calibration approach was reported by Carter and Wood (1991), in which a precise high-pressure syringe pump is used to increase the flow rate into the reference cell relative to the sample cell, by an accurately known increment.

The experimental results from these instruments have been ground-breaking, in that they have provided "hard" experimental data for a whole series of electrolytes and non-electrolyte systems that have been used as model systems for developing the "HKF" model and other equations of state used to extrapolate standard partial molar properties from ambient thermodynamic data. As an example, we show the results for reported by Biggerstaff et al. (1985, 1988), Biggerstaff and Wood (1988) and White et al. (1988) for the apparent molar heat capacities of $Ar_{(aq)}$ and $NaCl_{(aq)}$ at 322 bar and temperatures from 330 to 480 °C, plotted in Figure 10, respectively. These results span the subcritical and supercritical regions of these phase solutions at a pressure above the critical pressure of 221 bar. The plots of

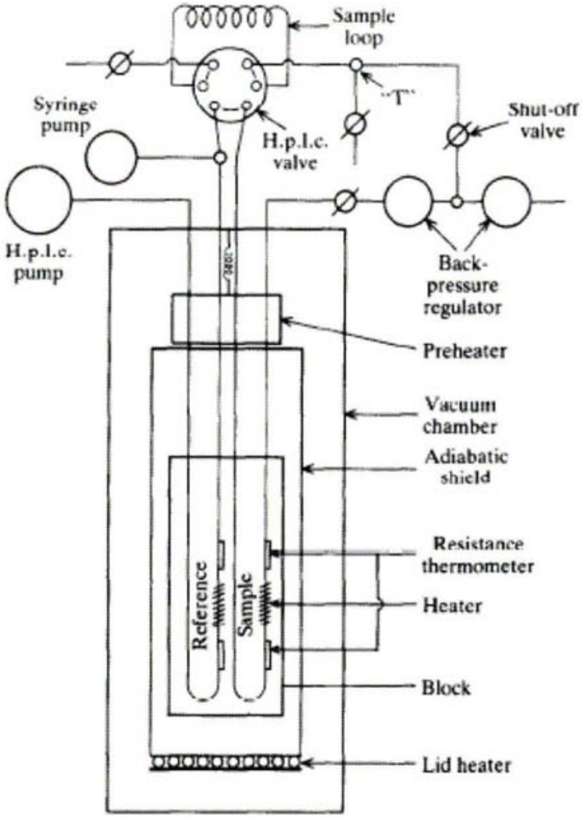
Sample loop
"T"
Syringe pump
H.p.l.c. valve
Shut-off valve
H.p.l.c. pump
Back-pressure regulator
Preheater
Vacuum chamber
Adiabatic shield
Resistance thermometer
Heater
Block
Lid heater
Reference
Sample

Figure 9. A schematic diagram of the high-temperature differential flow heat-capacity calorimeter developed by R.H. Wood and his co-workers. The 6-port HPLC valve is used for sample injection, with the dotted lines giving the flow connections in the sample loading position. Rotating the valve by 120° puts it in the sample measuring position, so that the water from the pump pushes the sample through the calorimeter tubing, first into cell 1, then through the delay line into cell 2. [Used by permission of Elsevier, from White et al. (1988) *J Chem Thermodyn*, Vol. 20, Fig. 1, p 160.]

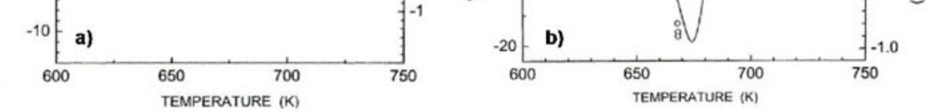

Figure 10. (a) Apparent molar heat capacities of aqueous argon a pressure of $P = 322$ bar. The solid curve is the expansivity of water $(\partial^2\rho/\partial T^2)_P$. [Used by permission of Elsevier, from Palmer et al. (2004) Aqueous Systems at Elevated Temperatures and Pressures, Fig. 2.17, p 56.]. (b) Apparent molar heat capacities of aqueous NaCl at a pressure of $P = 322$ bar. The dashed curve is the expansivity of water $(\partial^2\rho/\partial T^2)_P$. [Used by permission of Elsevier, from Palmer et al. (2004) *Aqueous Systems at Elevated Temperatures and Pressures*, Fig. 2.19, p 61.]

$C_{P,\phi}$ for aqueous argon show the behavior expected for a hydrophobic solute with a positive Krischevskii parameter, i.e. a solute that lowers the critical temperature of water. The values of $C_{P,\phi}(\mathrm{Ar_{(aq)}})$ deviate to large negative values as T_c is approached, then swing to large positive values as the temperature is increased above T_c. The values of $C_{P,\phi}(\mathrm{NaCl_{(aq)}})$ show the inverse behavior, typical of a hydrophilic ionic system. These effects are consistent with both the density model (Mesmer et al. 1988) and the Born equation (Helgeson et al. 1981), and are qualitatively predicted by classic cubic equations of state.

As a second example, Figure 11 is a plot of the standard partial molar heat capacity for the amino acid proline, up to the limit of its thermal stability (Clarke et al. 2000). The plots for $C_P^{\circ}(\mathrm{proline_{(aq)}})$ and $V^{\circ}(\mathrm{proline_{(aq)}})$ increase to a maximum value at ~125 °C, then decrease towards increasingly negative values with increasing temperature, much like ionic solutes. The pressure dependence of C_P° and V° are also typical of ionic solutes. The reason is that amino acids are zwitterions, and the solvation of dipoles can be described by a higher-order form of the Born equation:

$$\Delta_{\mathrm{solv}}G^{\circ}_{\mathrm{Dipole}} = \frac{-\mu^2 N_A}{4\pi\varepsilon_0 r_e^{3}}\left(\frac{\varepsilon_r - 1}{2\varepsilon_r + 1}\right) \tag{59}$$

were μ is the dipole moment, ε_r is the static dielectric constant, and the other terms are identical to those in the Born equation, Equation (59). Calculations using low-temperature heat capacity measurements and correlations based on neutral organic solutes by Amend and Helgeson (1997b) had predicted that values of C_P° and V° would display positive Krichevskii behavior, rather than the negative behavior that was observed.

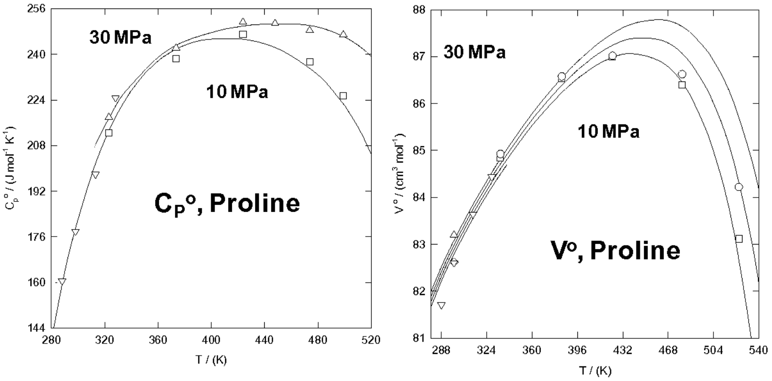

Figure 11. Standard partial molar properties of amino acids. [Used by permission of ACS, from Clarke and Tremaine (1999), J Phys Chem B, Vol. 103, Fig. 10, p 5140 and from Clarke et al. (2000) *J Phys Chem B*, Vol. 104, Fig. 7, p 11788.]

Twin-cell differential scanning nanocalorimeters and Calvet calorimeters

The Privalov differential heat-capacity nanocalorimeter. In 1995, Peter Privalov's group reported a new twin cell differential scanning nanocalorimeter, specifically designed to measure the very small enthalpies associated with biological reactions (Privalov et al. 1995). A commercial calorimeter based on this design was sold by the Calorimetry Sciences Corp. as the CSC Nano DSC III, and now by TA Instruments Ltd. as the TA Nano DSC. The nanocalorimeter incorporates fixed cells, shown in Figure 12, to avoid changes in thermal response due to cell placement. The cells are connected by thin tubes to a small reservoir at the

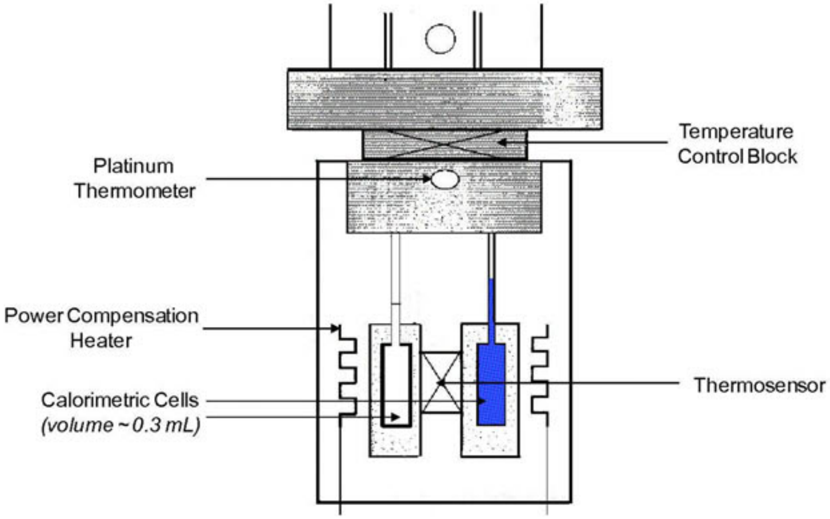

Figure 12. The conceptual design of the Privalov fixed-cell nano differential scanning calorimeter with its two fixed cylinder cells: one filled with a reference solution the second one with the sample solution. The temperature control block contains heating and cooling Peltier elements connected to a high-precision temperature controller.

top of the instrument. The reference cell is loaded with water, the sample cell with the solution of interest. The temperature is then scanned from ~ 5 °C to temperatures as high as 140 °C, under a pressure of 3 to 6 bars. Water and solution are allowed to expand into and out of the reservoirs so that the two cells are always completely full of fluid.

Earle Woolley's group at Brigham Young University has shown that the Nano DSC can be used to measure accurate apparent molar heat capacities with a sensitivity equal to, or better than, the commercial Sodev Picker calorimeter and with a wider temperature range (Woolley 1997, 2007). Because the masses of solution and water change with temperature during each scan, the nanocalorimeter measures differences in the heat-capacity density product between the sample cell and reference cell. The difference in heating power is given by the expression:

$$\Delta\mathcal{P} = \mathcal{P}_1 \quad \mathcal{P}_2 \quad \left(\epsilon_{P,1,T} \quad {}_{1,\mathrm{T}} \cdot \rho C_{P,\overline{2,T}} \quad {}_{2,\mathrm{T}}\right)\left[\rho\frac{r}{k_{\mathrm{Instr}}(r,T,P)}\right] \tag{60}$$

where $r = (dT/dt)$ is the heating rate in °C/s, and k_{Instr} is a calibration constant that depends on temperature, pressure and heating rate. In Woolley's method, the instrument is calibrated by multiple heating and cooling scans with water in both the sample and reference cells, then again with a standard solution of $\mathrm{NaCl}_{(\mathrm{aq})}$ in the sample cell. These are followed by runs with samples, typically 8 to 10 heating and cooling scans per sample, followed by another calibration with $\mathrm{NaCl}_{(\mathrm{aq})}$ and water to determine the drift in k_{Instr} with time. Each set of 10 runs takes about 12 hours. Heating and cooling runs are analyzed separately to determine the values of specific heat-capacity density product of sample relative to water the sample cell:

$$\Delta\mathcal{P}(\mathrm{Soln}) - \Delta\mathcal{P}(\mathrm{H_2O}) =$$

$$\left[C_{P,1,T}(\mathrm{Soln})\cdot\rho_{1,T}(\mathrm{Soln}) - C_{P,1,T}(\mathrm{H_2O})\cdot\rho_{1,T}(\mathrm{H_2O})\right]\left[\frac{r}{k_{\mathrm{Instr}}(r,T,P)}\right] \tag{61}$$

from which,

$$C_{P,1,T}(\mathrm{Soln}) = \frac{k_{\mathrm{Instr}}(r,T,P)}{r\cdot\rho_T(\mathrm{Soln})}\left[\Delta\mathcal{P}(\mathrm{Soln})-\Delta\mathcal{P}(\mathrm{H_2O})\right]+\left[\frac{C_{P,T}(\mathrm{H_2O})\cdot\rho_T(\mathrm{H_2O})}{\rho_T(\mathrm{Soln})}\right] \qquad (62)$$

The solution densities are typically measured with an Anton Paar DMA 5000, which operates up to 90 °C, then extrapolated to higher temperatures if necessary. Details of the calibration procedure are given by Ballerat-Busserolles et al. (2000). A thorough review of the application of this technique to a wide variety of aqueous solutes has been presented by Woolley (2007).

High-temperature twin-cell Calvet calorimeters. In 1991, Jean-Pierre Grolier's group at Blaise Pascal University reported the use of a Setaram C-80 twin-cell Setaram Calvet calorimeter for measuring relative heat capacities of aqueous solutions relative to water (Coxam et al. 1991). The concept pre-dated the Privalov calorimeter, described above, and the operating principle is identical. Briefly, Calvet calorimeters use a thermopile composed of a large number of thermocouple junctions that surround each cell compartment to measure the difference in heat flow to and from the two cells as the temperature of the surroundings is raised. The cylindrical high-pressure cells contain water and the solution of interest, which expand out of the cells into a small pressure-vessel reservoir as the temperature is raised. The original study by Coxam et al. (1991) reported specific heat capacities for $NaCl_{(aq)}$ from 0.1 to

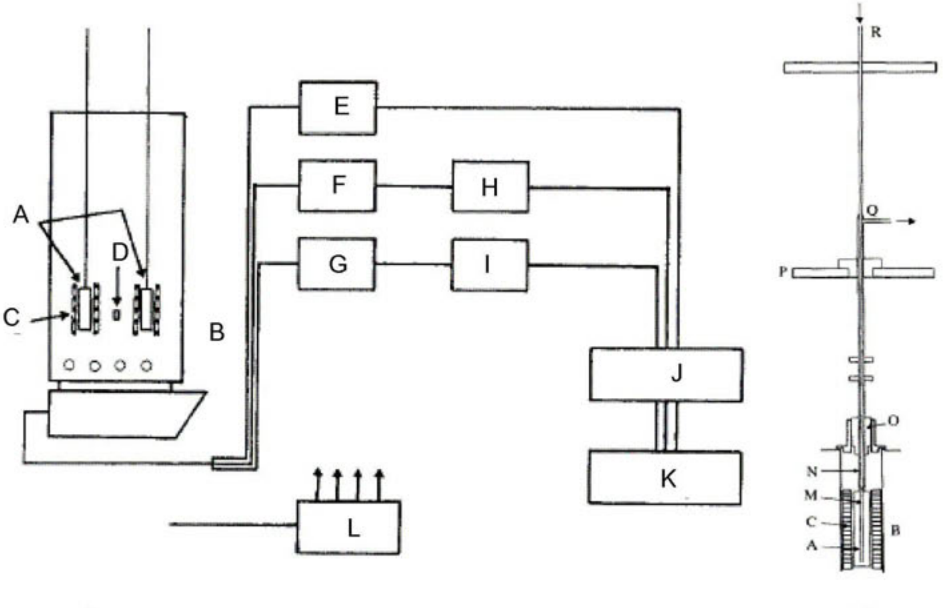

Figure 13. (a) Schematic diagram of the arrangement of the C-80 calorimeter: A, sample and reference cells; B, Setaram C-80 calorimetric block; C, thermopiles; D, temperature detector (Pt, 100f~); E, temperature-control programmer; F, security temperature unit; G, calorimeter-signal amplifier; H, digital display; I, digital voltmeter; J, RS-232 interface; K, computer; L, electric supply. [Used by permission of Elsevier, from Coxam et al. (1991) *J Chem Thermodyn*, Vol. 23, Fig. 1, p 1077.]. (b) Schematic of the Coxam's high pressure heat capacity cell after placement in the C-80 Calvet calorimeter: (A) calorimeter cell; (B) calorimeter block; (C) thermopile; (M) inner filling tube; (O) aluminum thermal guards; (P) calorimeter lid; (Q) Tee junction for overflow; (R) filling tube. [Used by permission of Elsevier, from Coxam et al. (1991) *J Chem Thermodyn*, Vol. 23, Fig. 2, p 1078.]

2 mol·kg^{-1} up to 250 °C. Schematics of the Setaram C-80 and the cell design by Coxam et al. are shown in Figure 13.

This approach has been refined, and used more recently by Glen Hefter's laboratory in Murdoch University to measure specific heat capacities and $C_{P,\phi}$ for $NaOH_{(aq)}$ and sodium aluminate ($NaAl(OH)_{4(aq)}$) at 50 to 300 °C with concentrations from 0.5 to 8 mol·kg^{-1} (Schrödle et al. 2008, 2010). The principal advantage of the method is that it uses a commercial instrument, with cells that can be constructed by a skilled machine shop from Hastelloy or titanium alloys, using HPLC tubing, fittings and valves. It is very suitable for quantitative studies on highly concentrated solutions, but is limited to concentrations above ~0.5 mol·kg^{-1}. A disadvantage, relative to custom-made Wood differential flow calorimeters is the lower sensitivity, and the need for a high-temperature densimeter to determine relative densities for each solution sample at the experimental temperatures and pressures.

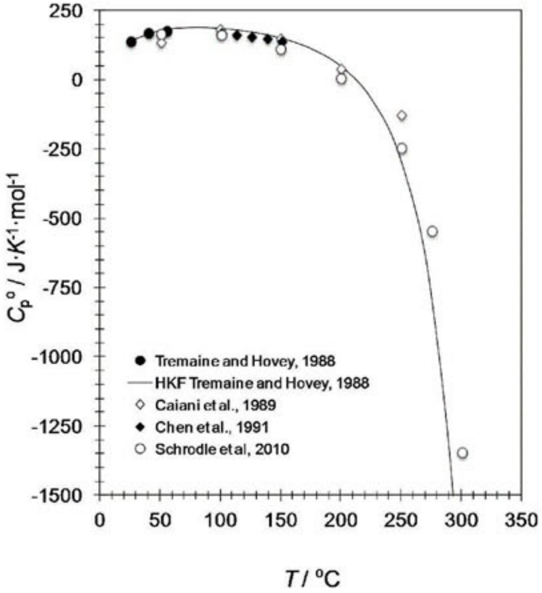

Figure 14. Comparison of standard partial molar heat capacities of sodium aluminate, C_P° [$NaAl(OH)_{4(aq)}$] at steam saturation from (●) Hovey et al. 1988; (◇) Caiani et al. 1989; (◆) Chen et al. 1991 and (○) Schrödle et al. 2010.

Figure 14 is a plot of C_P° (Al(OH$_4^-$) at steam saturation, showing results from Schrödle et al. (2010) obtained using this calorimeter, compared to values obtained by using a Picker calorimeter (Hovey et al. 1988), a Wood-type flow differential calorimeter (Caiani et al. 1989) and integral heats of solution (Chen et al. 1991). The measurements are challenging because they require an excess of NaOH to avoid precipitation, then subtraction the contribution of the excess base using Young's Rule to calculate $C_{P\phi}(NaAl(OH)_4^-)$.

Integral heat of solution measurements

Recently Cobble and his co-worker Essmaiil Djamali published a series of papers reporting apparent enthalpies of solutions and apparent molar heat capacities derived from them using the "integral heat of solution" method at temperatures up to 325 °C at steam-saturation pressures (See, for example, Djamali et al. 2009 and Djamali and Cobble 2009a,b,c). The measurements were done over the course of many years, in a custom-made high pressure isoperibol calorimeter reported by Djamali et al. (2010) and shown in Figure 15. The novelty of the instrument is its large sample volume, 865 cm^3, and the ability to break ampoules containing the solid inside the vessel, with stirring. The large size allows the heat of solution of crystalline salts to be made isothermally at concentrations as dilute as 10^{-3} mol·kg^{-1}. While similar measurements can be made in a Setaram C-80, the small size of the vessels (~ 8 cm^3) makes ampoule breaking a challenge and limits the measurements to concentrations above 10^{-2} mol·kg^{-1}.

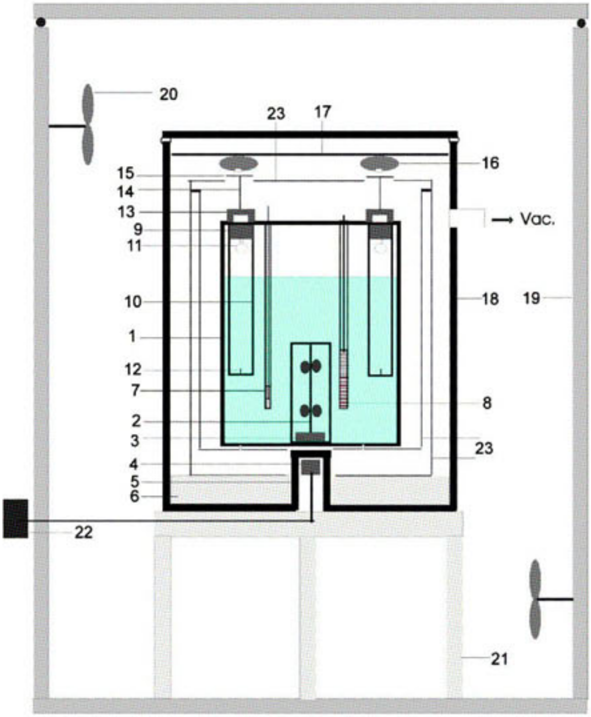

Figure 15. The schematic diagram of high temperature calorimeter: 1, the bomb; 2, stirring paddles; 3, titanium-encased magnetic housing; 4, rotating magnet; 5, rotating magnetic housing; 6, insulator support; 7, thermister well with thermister in Ga-8% Sn alloy; 8, heater well with calibration heater in Ga-8% Sn alloy; 9, sample holder; 10, guide rail; 11, quartz sample bulb; 12, sharp pin; 13, permanent magnet; 14, permanent magnet extension; 15, metal plate of high permeability; 16, electromagnet; 17, electromagnet holder; 18, vacuum jacket; 19, air thermostat; 20, air circulation fan; 21, vacuum jacket support; 22, electrical motor; 23, radiation shields. [Used by permission of AIP, from Djamali et al. (2010) *Rev Sci Instrum*, Vol. 81, Fig. 1, p 075105-2.]

The ability to measure $\Delta_{sol}H_T$, and the resulting values of $C_{P,\phi}$ at low concentrations is important because ion pairing is significant at temperatures above 250 °C, and many electrolytes are only sparingly soluble under these conditions. One example of results from their measurements is new values for the standard partial molar heat capacities of fully ionized $HCl_{(aq)}$, $NaCl_{(aq)}$ and $NaOH_{(aq)}$ up to 325 °C at steam saturation, that remove the effects of ion-pairing (Djamali and Cobble 2009a,b) by providing an improved extrapolation to zero ionic strength. A second example is recent papers by Djamali and Cobble (2009b); and Djamali et al. (2009) that report the first values of C_P° for three divalent ions, $Ba^{2+}_{(aq)}$, $Co^{2+}_{(aq)}$ and $Cu^{2+}_{(aq)}$; and one trivalent metal ion, $Gd^{3+}_{(aq)}$ at temperatures up to 325 °C. The standard partial molar heat capacities of these 2:1 electrolytes are plotted in Figure 16.

The advantage of Cobble's calorimeter over the Wood differential flow calorimeters is that it allows measurements at an order-of-magnitude lower concentration. The disadvantage is the uncertainties in $C_{P,\phi}$ arising from the need to calculate $(\partial\Delta_{sol}H_T/\partial T)_P$ and the corrections required to compensate for heat effects due to the volume change and osmotic pressure change associated with the dissolution of the salt.

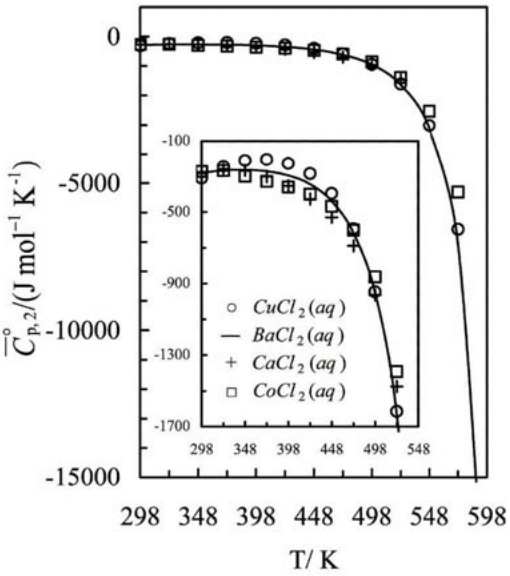

Figure 16. Standard state partial molal heat capacities of some representative 2:1 electrolytes at P_{sat}. [Used by permission of ACS, from Djamali et al. (2009) *J Phys Chem B*, Vol. 113, Fig. 3, p 2408.]

HEAT OF MIXING CALORIMETRY

Pioneering instruments

Heat of mixing calorimeters for ambient conditions. Flow calorimetry appeared in the late 1960's, spurred by the development of accurate stepping motors and high precision syringe and peristaltic pumps. Flow methods are attractive because they minimize the time required to load and clean the vessels; and they avoid the long equilibration times, presence of a gas phase and surface adsorption effects, which inherent features of batch calorimetric methods. The first reported application of flow technology to calorimetric measurements was by Priestley et al. (1965), who used an isoperibol design which measured the temperature difference at the outlet of the mixing chamber relative to the mean temperature of the two incoming liquids. His instrument was used to measure the enthalpies of formation of a series of metal complexes with EDTA. In the late 1960's, Stoesser and Gill (1967) and Monk and Wadsö (1968) reported independent designs for twin-cell heat-flux calorimeters. The twin cell design uses a reference cell, identical to the mixing cell but either without flow, or with flow of the mixed liquid, to cancel non-ideal heat flux behavior. In 1969, Picker et al. published novel designs two heat-of-mixing micro-calorimeters. The first was an adiabatic instrument that measured the temperature increment occurring during the mixing process relative to the inlet temperature of the two liquids. The second design was for a flow calorimeter capable of running under adiabatic or isothermal conditions to study both liquid- and gas phase reactions. Both instruments were so sensitive that they were able to reach steady states within 1 min, so that the flow rates of the mixing fluids could be varied continuously in order to obtain heats of mixing over the entire composition range.

Principles of operation for isothermal calorimeters. The underlying operating principle of isothermal calorimeters is based on heating or cooling the reaction vessel to balance the heat liberated or consumed by the mixing reaction. In order to maintain the reaction zone at a constant temperature the energy output is adjusted with a controlled heater to balance the energy arising from the chemical reaction plus the energy removed by a constant heat-leak path. The enthalpy is directly obtained from the power $\Delta\mathcal{P}$ (mW) required to maintain the temperature of the calorimeter constant and the molar flow-rate f_n (mol·s^{-1}) of the solution. Positive values ($\Delta\mathcal{P} > 0$) correspond to endothermic processes and negative values ($\Delta\mathcal{P} > 0$ correspond to an exothermic processes. The mixture composition is controlled by molar flow-rate of the fluids into the mixing chamber of the calorimeter. Most often, fluids are injected into the calorimeter by using pumps. The molar flow-rate of the mixture is derived from the volumetric flow-rate of the fluids in each pump and their corresponding densities. The molar enthalpy of mixing, $\Delta_{mix}H_m$, expressed as J·mol^{-1}, is then derived from the calorimetric signal using the molar flow rate of the fluids (mol·s^{-1}) and the power $\Delta\mathcal{P}$ (mW):

$$\Delta_{\mathrm{mix}}H_{\mathrm{m}} = \frac{\Delta P}{f_n} \tag{63}$$

The expression for Calvet calorimeters is similar,

$$\Delta_{\mathrm{mix}}H_{\mathrm{m}} = \frac{\Delta S}{f_n} = \frac{S_{mix} - S_{baseline}}{f_n} \tag{64}$$

where S_{mix} is the differential heat flux between the mixing cell and the reference cell during the mixing reaction, expressed as power, and $S_{baseline}$ is the differential heat flux recorded as a baseline at the same flow rate using a reference liquid, often one of the pure fluids.

For binary mixtures, the molar flow rate of the fluids 1 and 2 ($\mathrm{mol{\cdot}s^{-1}}$) is obtained from the volumetric flow rate, the density and the molar mass of both fluids:

$$f_n = \frac{\rho_1}{M_1} f_{V,1} + \frac{\rho_2}{M_2} f_{V,2} = x_1 \quad x_2 \tag{65}$$

Here, $f_{V,1}$, ρ_1, M_1 and $f_{V,2}$, ρ_2, M_2 are the volumetric flow rate ($\mathrm{cm^3{\cdot}s^{-1}}$), the density ($\mathrm{g{\cdot}cm^{-3}}$) and the molar mass ($\mathrm{g{\cdot}mol^{-1}}$) of fluids 1 and fluid 2, respectively. Fluid densities at the temperature and pressure of the reservoir and pumps (i.e. pressure of the system for a syringe pump and atmospheric pressure for an isocratic pump) can be measured or calculated with appropriate equations of state. The NIST program "REFPROP" provides accurate *PVT* data for H_2O, CO_2, and several other solvents.

The composition of a 2-component solution is obtained from the expressions:

$$x_2 = \frac{\frac{\rho_2}{M_2} \cdot f_{V,2}}{\frac{\rho_1}{M_1} \cdot f_{V,1} + \frac{\rho_2}{M_2} \cdot f_{V,2}} \tag{66}$$

$$m = \frac{1000 \cdot \rho_2 \cdot f_{v,2}}{M_2 \cdot \rho_1 \cdot f_{v,1}} \tag{67}$$

One further advantage of these instruments is that, by varying the ratio of injection rates from the two pumps, it is possible to detect phase vapor-liquid and gas-liquid phase separation, and to conduct enthalpic titrations. In favorable cases, the enthalpic titrations can yield simultaneous values for equilibrium constants and enthalpies of reaction.

Heat of mixing calorimeters for elevated pressures and temperatures. The first heat-of mixing flow calorimeters for measurements at high pressure and temperature were reported by Messikomer and Wood (1975) at the University of Delaware and by Christensen at his co-workers at Brigham Young University (Christensen et al. 1976, 1981; See also, Ott 1997). Messikomer and Wood's instrument was a heat-flux flow calorimeter, capable of measuring accurate values for the heat of dilution of $NaCl_{(aq)}$ and osmotic coefficients derived from them, up to 100 °C. The calorimeter was made of four major parts: a flow line fed by syringe pumps; a mixing cell composed of 5-stage heat exchanger equipped with calibration heaters; a heat sink lined with thermopiles which surrounded the mixing cell and linked to a acquisition data system; and an air bath temperature controller. An improved design, reported by Mayrath and Wood (1982) has been used to determine heats of dilution for $NaCl_{(aq)}$, sulfate salts and some hydrophobic electrolytes (Mayrath and Wood 1982, 1983a,b). Although the design was not pursued, it demonstrated many of the concepts used in subsequent high-temperature heat-capacity and heat-of-mixing calorimeters.

Approximately one year later, Christensen et al. (1976) reported the design of an isothermal high-pressure calorimeter capable of operating from 0 to 80 °C and pressures up to 400 bar. Briefly the calorimeter consisted of a tubular reaction vessel in contact with a Peltier thermoelectric cooler to remove energy generated from the mixing reaction and a heating unit which was used to maintain the mixing cell at constant temperature. The module containing the calorimeter was immersed in a constant temperature water bath to control the temperature. Fluids were injected into the vessel with a high-pressure HPLC syringe pump, and a backpressure regulator, located downstream of the calorimeter, controlled the pressure. Although limited to temperatures below 100 °C, this instrument was widely used to study the properties of aqueous CO_2-amine mixtures, and CO_2 mixtures with various organic solvents, used to remove acid gases in the oil and gas industry (Ott 1997). The BYU instrument was commercialized, first by Tronac, then by Calorimetry Sciences Corp., and an improved version of this design is now available from TA Instruments.

Heat-of mixing flow calorimeters for measurements at high pressure and temperature are based on three approaches. First, several power-compensated, isothermal, flow heat-of-mixing instruments for hydrothermal conditions have been derived from the BYU design concept, discussed above. A second approach, pioneered by Busey et al. (1984) at Oak Ridge National Laboratories, is based on the use of commercial Setaram Calvet calorimeters which can accommodate custom-made heat-of-mixing cells. Finally, the isoperibol heat-of-solution calorimeter constructed by Cobble's group can be used for heat of dilution and heat-of-reaction experiments. Details of each approach are discussed in the following sections.

Power-compensated isothermal flow heat of mixing calorimeters

BYU calorimeters with air baths. In the 1980's, the calorimetry group at Brigham Young University (BYU) developed a series of isothermal flow calorimeters capable of measuring heats of reaction from 100 to 500 °C at pressures from 1 to 400 bar. The basic design consists of a tubular mixing cell, located in a vacuum container surrounded by a system of concentric thermal shields whose temperatures are independently controlled. The entire system is placed inside an air-bath to prevent any heat loss due to convection or conduction.

The design of the mixing cell design is shown in Figure 17. It consists of two inlet tubes coiled around an isothermal cylinder made of copper because of its very high thermal conductivity. The two fluids to be mixed come together at a T-junction at the top of the cylinder and exit though a single, larger diameter tube which acts as a mixing chamber. The tube must be in perfect

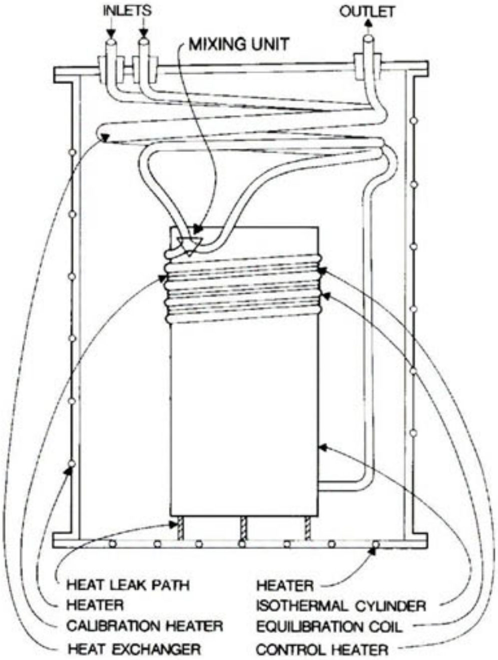

Figure 17. Reaction vessel of the BYU isothermal flow calorimeter. [Used by permission of Elsevier, from Christensen et al. (1986) *Thermochim Acta*, Vol. 99, Fig. 2, p 162.]

thermal contact with the isothermal cylinder, and long enough to make sure that all the heat of reaction will be sensed by the thermopiles for the range of enthalpies, reactions kinetics and flow rates that will be encountered. In the BYU design, the "mixing chamber" is coiled around the isothermal cylinder together with both a calibration heater and a control heater. The purpose of the calibration heater is to check the efficiency of the mixing cell arrangement, while the control heater helps to maintain the isothermal cylinder at constant temperature. Another original design feature is the use of a controlled heat-leak path instead of using a Peltier device to remove energy from the reaction zone (Christensen and Izatt 1984). To achieve this, the bottom of the cylinder is supported by 3 nickel plated brass bolts that act as the heat leak path. The size and number of bolts is designed to produce a heat leak rate of ~ 1 $J \cdot s^{-1}$ for a temperature difference of $\Delta T = 1$ °C between the bottom of the cylinder and the bottom of the reaction vessel (see Fig. 17). The temperature of the reaction vessel is controlled to ± 0.0005 °C. The heat leak is then accurately controlled by adjusting the temperature difference between the bottom of the isothermal cylinder and the bottom of the vessel that supports the brass bolts. Before entering the mixing chamber the fluids are brought to the desired temperature by wrapping the inlet tubing around each of the thermal shields (Christensen et al. 1981, 1984, 1986; Oscarson et al. 1991). The final inlet temperature adjustment is realized by a counter current heat exchanger located inside the reaction vessel where the inlet tubes are in thermal contact with the exit tube from the mixing chamber.

As noted above, the reaction vessel itself is located inside an insulated container inside the innermost thermal shield. It is important to note that the temperature of the each of the different zones of the calorimeter (separated by the thermal shields) is adjusted to create a 10 °C temperature difference between the reaction vessel and the outer shield. This ensures a conduction temperature gradient sufficient to provide the heat path leak. The fluids are injected in the mixing cell with high-pressure pumps and a back-pressure regulator located at the end of the flow line controls the pressure of the system.

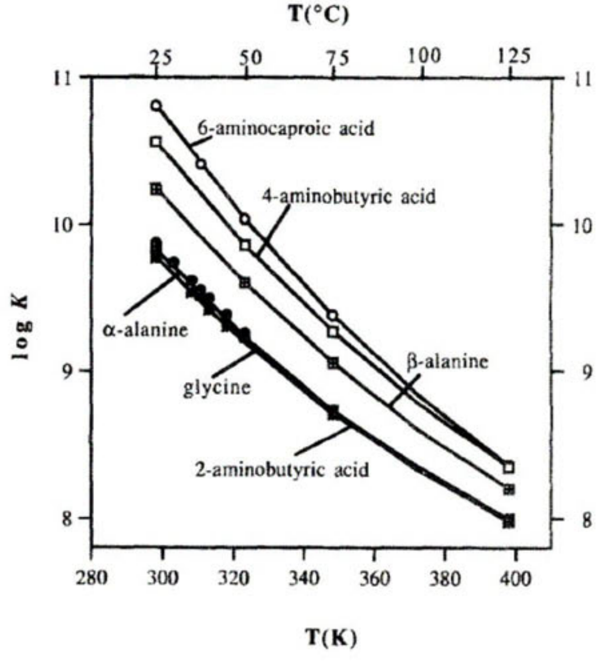

Figure 18. Plot of log K values for the protonation reactions for glycine, α-alanine, β-alanine, 2-aminobutyricacid, 4-aminobutyricacid and 6-aminocaproicacid as a function of temperature. [Used by permission of Springer, from Gillepsie et al. (1995) *J Solution Chem*, Vol. 24, Fig. 4, p 1243.]

A large number of systems have been studied using isothermal calorimeters of this design. Among those we can cite Ott et al. (1986) who measured very accurate and reproducible excess molar enthalpy of mixing for the system {water + ethanol} at 25 °C up to 150 bar, and Gillespie et al. (1995) who obtained accurate values for the enthalpies of ionization of amino acids, and their equilibrium constants up to 125 °C, plotted in Figure 18. Chen et al. (1996) upgraded the material of construction by using platinum-rhodium alloy tubing, and used their instrument to study reactions under extreme conditions. The new calorimeter was able to measure enthalpies of dilution of aqueous sodium hydroxide solutions (~ 0.5 m) up to 300 °C and 93 bar, and sodium chloride solutions (~ 0.5 m) up to 350 °C and 176 bar.

BYU calorimeter with eutectic molten salt bath for near-critical conditions. The BYU air bath calorimeters, described above, contained the heat-of-mixing unit within concentric cans, each accurately controlled at a different temperature. Although this configuration led to significant temperature gradients, these effects could be controlled with baseline corrections up to about 300 °C. but became increasingly large at higher temperatures. To address these issues, Fuangswasdi et al. (2001) developed a new isothermal flow calorimeter for measuring heats of mixing at temperatures as high as 380 °C, and pressures up to 500 bar. The principal innovations of this design are immersion of the reaction vessel and associated tubing in a eutectic salt bath, and the use of a thermoelectric cooler instead of nickel bolts as the heat-leak path. These changes made it possible to maintain the reaction zone at a constant temperature under conditions approaching the critical point of water. The advantages of the new calorimeter over the air-bath instruments developed at BYU are simplification of the design, making it easier to maintain the equipment, reduction of the temperature gradients so that baseline corrections are minimized, and ability to make reliable measurements above 350 °C. The calorimeter yields results for the heat of mixing of sodium chloride solutions and water at 300 and 350°C that were in good agreement with experimental values by Chen et al. (1996) in an air-bath instrument, and were within 10% of results by Busey at al. (1984).

Flow heat of mixing cells in Calvet calorimeters

Oak Ridge National Laboratory flow calorimeter. In the mid 1980's, Dick Busey at Oak Ridge National Laboratory (Busey et al. 1984) designed a new flow-heat-of-mixing cell for use in a commercial Setaram HT1000 Calvet calorimeter. The HT 1000 is a twin-cell heat-flux calorimeter, similar in concept to the Setaram C-80 described above. The principle differences are that the HT 1000 is a massive, fixed-base instrument, with higher sensitivity and a much wider range of operating temperatures (ambient to 1000 °C). The two tubular heat-sensing chambers are intended to accommodate calorimeter cells with a variety of designs. The lower parts of the two chambers are surrounded by 450-junction thermopiles that measure the differential heat flux between sample and reference cells. The upper parts of the two chambers are insulated from the sensing areas below them, but thermostatted to the same temperature.

Two identical, tubular heat-of-mixing flow cells were constructed, one for the sample chamber and one for the reference chamber. Each cell has an upper portion, designed to achieve thermal equilibrium of the two incoming streams of fluid, and a lower mixing chamber, constructed so that it is in good thermal contact with the sensing elements of the calorimeter. These are able to measure enthalpies of mixing or dilution at temperatures 425 °C and pressures up to 500 bar. The beauty of designing heat-of-mixing cells for use in a commercial instrument is that it shifts the emphasis from developing a complex calorimeter to the design of a suitable high-pressure, high-temperature cell.

The Busey et al. (1984) cell design is shown in Figure 19. The inlet for each cell consists of two lengths of platinum rhodium tubing, one for each liquid, surrounded by heat exchanger, all in tight thermal contact with a stainless-steel confinement cylinder, which sits in the well of the calorimeter. The confinement cylinder is broken in two parts: an upper one containing the heat exchanger and the lower one containing the mixing chamber. Just between the two parts of the confinement cylinder there is a small transition zone where the two inlet tubes are reduced to capillary size and are wound as a pair around the 4-hole insulator tube shown in Figure 19, in order to reduce conduction of heat from the mixing zone to the block via the

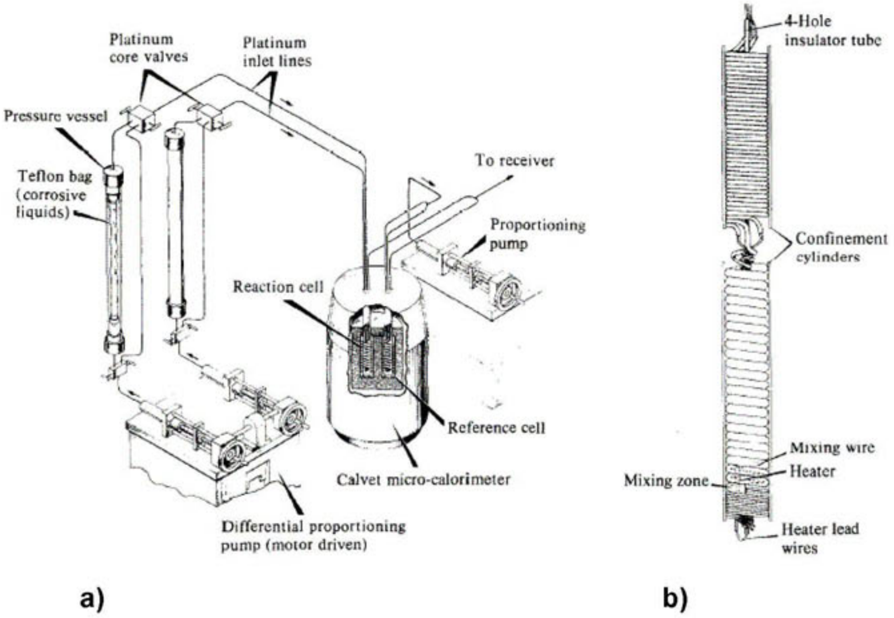
Platinum core valves
Platinum inlet lines
Pressure vessel
Teflon bag (corrosive liquids)
To receiver
Proportioning pump
Reaction cell
Reference cell
Calvet micro-calorimeter
Differential proportioning pump (motor driven)
a)
4-Hole insulator tube
Confinement cylinders
Mixing wire
Heater
Mixing zone
Heater lead wires
b)

Figure 19. (a) Schematic drawing of the Busey's heat-flow and liquid-flow calorimetric apparatus. [Used by permission of Elsevier, from Busey et al. (1984) *J Chem Thermodyn*, Vol. 16, Fig. 1, p 345.] (b) One of the two duplicate heat exchangers placed within a Calvet microcalorimeter. Overall dimensions are 1.676 cm o.d. x 18 cm in length. [Used by permission of Elsevier, from Busey et al. (1984) *J Chem Thermodyn*, Vol. 16, Fig. 2, p 346.]

inlet lines and the upper heat exchanger. The capillary-sized inlet tubes then carry their fluids vertically down the center of the lower compartment to the base of the cell. When they reach the bottom of the cell, the inlet tubes are first coiled in spirals to make perfect contact with the inner wall of the confinement cylinder and then they are gold-soldered together into a common larger diameter tube that serves as a mixing chamber. The mixing chamber tube is coiled into a spiral in very tight contact with the inner wall of the lower confinement cylinder so that it can transfer the heat of mixing to the thermopile of the calorimeter. A spiral of thin platinum wire is placed inside the "mixing zone" just after the junction of the two inlet tubes to facilitate the mixing of the two reacting liquids. After giving up its heat and leaving the lower confinement cylinder with the fully mixed fluid, the tube is coiled together with the two inlet tubes in the upper confinement cylinder as a heat exchanger, to ensure that the temperature of the incoming fluids matches that of the heat of mixing cell. The mixed liquid then passed on to the two inlet tubes of an identical cell in the reference chamber of the Calvet calorimeter. A ceramic-encased platinum resistance thermometer is located just before the beginning of the "mixing zone" of each cell to provide electrical calibration purpose.

The two fluids are injected into the flow line by high-pressure syringe pumps. The usual procedure for operating such pumps is to use them only with water. The corrosive sample liquids are contained in liquid chromatography injection loops, or in Teflon bags located in small pressure vessels as part of the injection system. Turning a valve then allows water from the pumps to push the liquids out of the injection loop or Teflon bags into the calorimeter. The solutions need to be purged of all traces of oxygen when ligands such as halides or amines are present, in order to avoid corrosion from the formation of Pt(IV) complexes. If the Teflon bag system is used, oxygen must also be purged from the water from the pump that pushes against the bags, since oxygen has been found to diffuse through the Teflon. Before the solutions enter the cells, they are brought to a temperature close to the working temperature of the calorimeter by a pre-heater, which was described in the original paper.

With this calorimeter Holmes et al. (1987) were able to measure enthalpies of dilution of aqueous HCl at concentrations as high as 15.6 mol·kg^{-1}, and temperatures and pressure up to 375 °C and 400 bar (see Fig. 20).

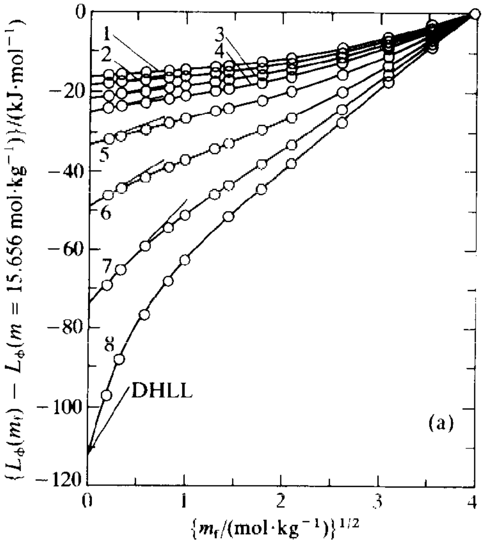

Figure 20. The enthalpy of dilution of HCl(aq) plotted as the apparent relative molar enthalpy L_ϕ, at the final molality m_f relative to L_ϕ at an initial molality m_i = 15.656 mol·kg^{-1}: 1 298.64 K and 7.0 MPa; 2. 320.77 K and 7.0 MPa; 3, 348.00 K and 7.0 MPa; 4, 373.65 K and 7.0 MPa; 5, 422.96 K and 7.0 MPa; 6, 472.98 K and 13.9 MPa; 7, 524.90 K and 20.6 MPa; 8, 571.50 K and 32.5 MPa. [Used by permission of Elsevier, from Holmes et al. (1987) *J Chem Thermodyn*, Vol. 19, Fig. 1, p 870.]

Université Blaise Pascal flow calorimeter. Over the past two decades, a series of isothermal heat of mixing cells, similar in concept to that of Busey et al. (1984), have been developed at the Université Blaise Pascal in France for use in the Setaram C-80 Calvet calorimeter (Mathonat et al. 1994; Koschel et al. 2006; Arcis et al. 2011). The sensing thermopiles and twin cell compartments of C-80 calorimeter are similar to those of the HT 1000, but there is no temperature controlled upper block to act as a pre-heater for the incoming fluids. To address this issue, Mathonat et al. (1994) designed the cell (see Fig. 21) and injection system. The lower portion of the cell containing the mixing chamber is very similar to that of Busey, except that it lacks an electrical calibration heater. Briefly, the inlet tubes that transport the fluids are connected to one another in a small chamber at the bottom of the cell, shown as "M" in Figure 21, which is silver-soldered to a tubular mixing chamber. The quantitative mixing of the fluids occurs in this 2.8 m long mixing chamber, coiled in good thermal contact with the inner wall of a confinement cylinder (18.7 mm i.d., 80 mm height) that sits in the well of the calorimeter. The upper part of the cell uses a set of four pre-heaters to bring the fluids to the exact working temperature of the calorimeter, before mixing takes place. Two of the pre-heaters are located just above the calorimetric sensing block, within the body of the calorimeter. These consist of counter-current heat exchangers, in which the inlet and outlet tubing is coiled on the outer surface of a copper cylinder (Arcis et al. 2011). The first two pre-heaters consist of cylindrical copper rods, in which the inlet and outlet tubing are tightly fitted in grooves inside the pre-heater cylinder. All pre-heaters are thermo-regulated by heating cartridges and a platinum resistance thermometer connected to a P.I.D. controller. The fluids {liquid + liquid} or {gas + liquid} are injected into the mixing unit by two Isco high-pressure syringe pumps regulated at constant temperature in order to ensure a constant mass flow rate. The flow-rate stability for {gas + liquid} mixing can be improved by inserting a large (1 L) pressure vessel downstream of the calorimeter and upstream of the back-pressure regulator (Arcis et al. 2007).

As can be seen in Figure 22, Mathonat et al. (1994) demonstrated the performance of their instrument by comparing the excess enthalpies for the system {water + ethanol} with the very

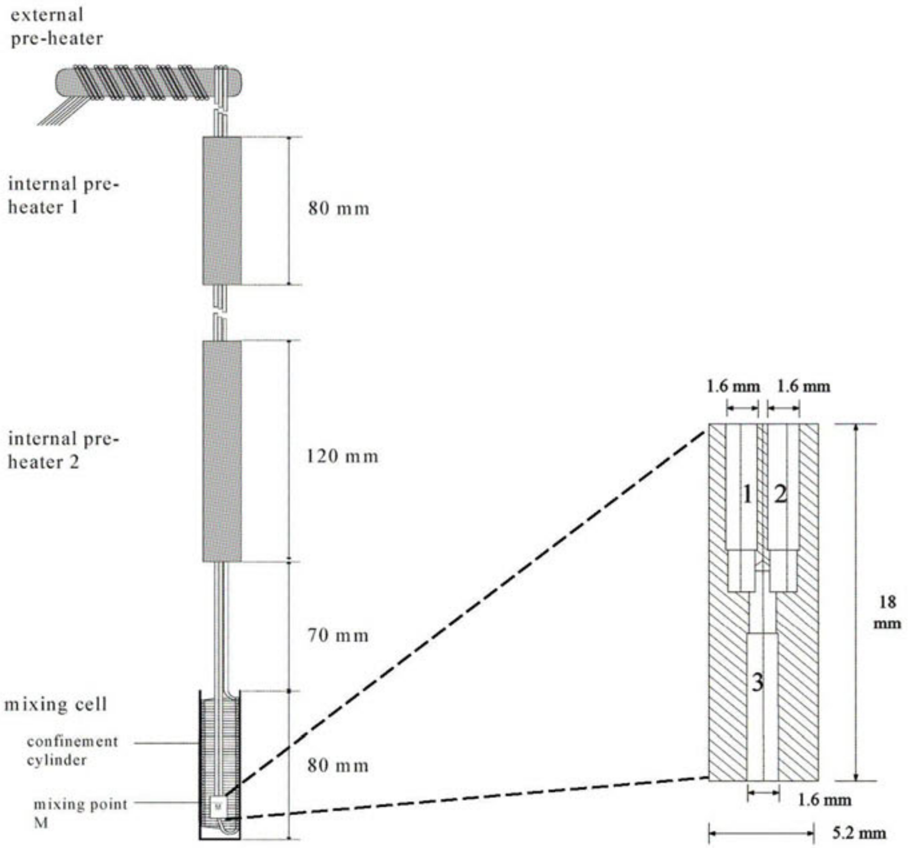

Figure 21. Mixing unit designed by Clermont-Ferrand group. [Used by permission of ACS, from Koschel et al. (2007) *Ind Eng Chem Res*, Vol. 46, Figs. 2 and 3, p 1424.]

accurate data of Ott et al. (1987). Most of the experimental data reported by Clermont-Ferrand group using this calorimeter has been focused on aqueous amines and other solvent systems relevant to the capture and sequestration of greenhouse gases (Mathonat et al. 1997; Koschel et al. 2006; Arcis et al. 2007, 2011, 2012a,b).

Steam-gas mixtures

Wormald and Colling (1983) developed a new isothermal flow mixing calorimeter capable of measuring excess enthalpy of gas mixtures up to 425 °C and 250 bar. Briefly, thermometers fixed on the inlet and outlet tubing (just before and after the mixing point) read the temperature, and a heater located beside the mixing point is used to adjust the temperature difference caused by the mixing process to zero. In order to reduce the time response of the calorimeter, its walls are made of light-weight thin-walled stainless steel only able to support a maximum pressure of 1 MPa. The trick used here to prevent any leaks or rupture of the thin-walled tubing is to mount the calorimeter inside a pressure vessel, and adjust the pressure inside the vessel with inert gas to be the same as the pressure inside the calorimeter. If the fluid for study is in its liquid state at room temperature it is introduced with a high-pressure chromatography pump at a controlled flow rate and then vaporized by a flash boiler heated in a fluidized-alumina bath.

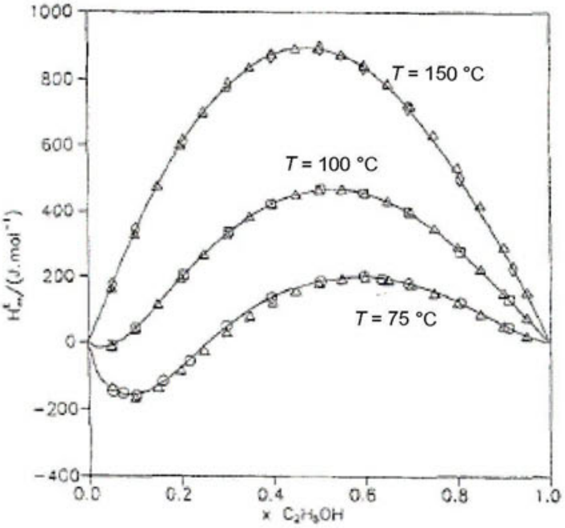

Figure 22. Molar enthalpy of mixing, H^E_m, for $\{x\ C_2H_5OH + (1\text{-}x)\ H_2O\}$ at $P = 50$ bar from Mathonat et al. (1994) at $T = 75$ °C (○), 100 °C (□), 150 °C (◇) and from Ott et al. (1987) at the same temperatures (△). [Used by permission of Springer, from Mathonat et al. (1994) *J Solution Chem*, Vol. 23, Fig. 3, p 1171.]

If the fluid is in its gas state, it is introduced directly from its tank reservoir. A heat-exchange coil wrapped around the pressure vessel allows the water vapor to reach the experimental temperature before being mixed with the gas or vapor under investigation. The flow rate control of the gas is done using a needle valve located at the end of the flow line. For that purpose, after the mixing process has occurred the fluid (in a liquid state at room temperature) is separated from the other fluid (gas at room temperature) by condensation and trapped into a reservoir. The gas is redirected toward the needle valve, thereby permitting the operator to adjust the flow rate. Before the start of an experiment the flow line needs to be purged and pressurized with the gas selected for study (if it is not combustible) or with nitrogen. We note that the use of modern temperature-regulated high-pressure syringe pumps would simplify the injection procedure. Wormald and his co-workers have reported measurements on 28 mixtures containing steam using this calorimeter (Wormald and Colling 1983; Wormald and Lancaster 1989; Wormald 2000; and references cited therein). As an example, excess enthalpies for the system $\{H_2O + C_6H_{14}\}$ are plotted in Figure 23.

Calibration of isothermal heat-of-mixing calorimeters

Calibration of isothermal heat-of-mixing calorimeters may be done by electrical calibration or through the use of chemical standards. For the Setaram C 80 and other Calvet calorimeters using batch heat-of-mixing cells, the calibration is often done by measuring the heats of fusion of NIST standard metals during well-defined heating and cooling cycles. Although electrical calibration is always desirable, batch cells for isothermal heat-of-solution, heat of dilution and titration experiments can be calibrated by the measuring heat of solution of standard reference materials or the titration of standard acid or base reference materials. Calibrations should be done at regular time intervals dictated by the type of experiment being done. For experiments involving flow cells the calibration should be done before and after each series of measurements at each temperature. Since a series of measurements may take days, additional calibration points may be desirable. If the design of the flow cell includes a calibration heater, it is preferable to do an electrical calibration. If not a chemical calibration can be done with a reference system as such as {water + ethanol} (Ott et al. 1986, 1987) or an acid-base neutralization reaction, using NIST standard reference materials.

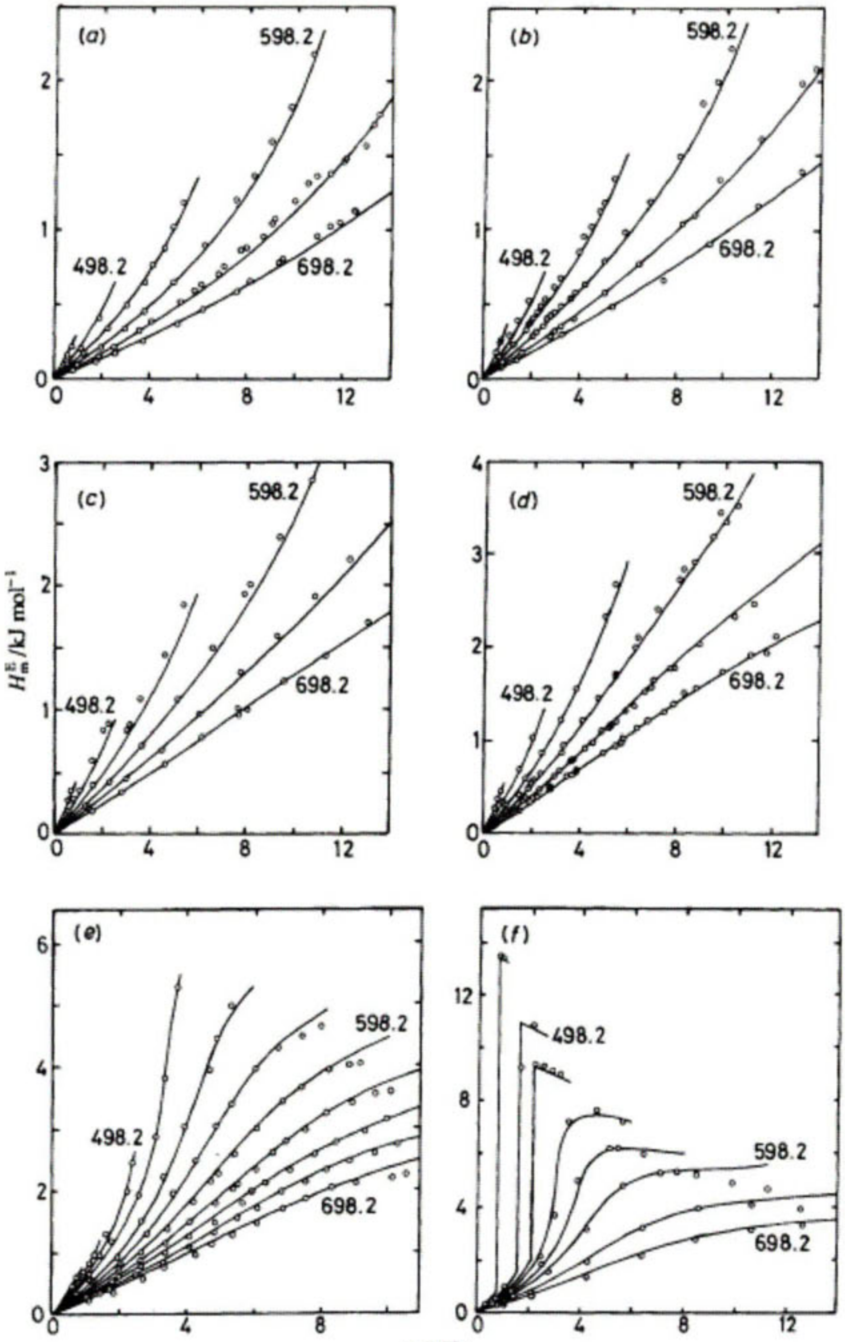

Figure 23. Enthalpy of mixing, H^E_m, for $\{0.5\ H_2O + 0.5\ C_nH_{2n+2}\}$ for $n = 2$-7 as a function of pressure from $T = 175$ °C to $T = 425$ °C. (a) $n = 2$, (b) $n = 3$, (c) $n = 4$, (d) $n = 5$, (e) $n = 6$, (f) $n = 7$. [Used by permission of RSC, from Wormald and Landcaster (1989) *J Chem Soc Faraday Trans 1*, Vol. 85, Fig. 2, p 1321.]

DISCUSSION

Current state-of-the-art for hydrothermal solution calorimetry

The 1980's and 1990's were a golden age for the development of modern high temperature calorimeters and densimeters. The invention of the vibrating tube densimeter and the Picker calorimeter in the 1970's led to the large data base of standard molar heat capacities and volumes at temperatures in the range 10 to 55 °C, from which the parameters for most of the species in the HKF model and other equations of state were derived (Shock et al. 1992; Sedlbauer et al. 2000; etc.). The development of the high-temperature differential flow heat capacity calorimeter and densimeter by Wood's group at Delaware; the flow heat-of-mixing isothermal calorimeter at BYU (Ott 1997); and the many high precision instruments for conductivity, calorimetry, isopiestic studies and EMF measurements invented at Oak Ridge National Laboratories (Mesmer et al. 1997) provided data up to about 300 °C for enough species that modelers could develop the pragmatic expressions for the temperature and pressure dependence of standard partial molar properties that form the core of most databases for hydrothermal systems. (See, for example: Valyashko 2008; Oelkers et al. 2009).

The success of these instruments is based on several factors. First is the availability of modern liquid chromatographic pumps, backpressure regulators valves, fittings and tubing that made the evolution from large stirred batch systems to small-scale exquisitely-crafted flow systems possible. Second is the realization that success lies in measuring the *difference* in the properties of solutions relative to water directly, so that systematic errors in temperature control, flow rate or instrumental parameters cancel one another. Third, is the hard-won understanding, based on experience, that high temperature aqueous solutions are so extremely corrosive that the materials of construction for all wetted surfaces must *always* be matched to the chemical system being studied. Finally, there is now a whole series of clever designs for injection systems, insulators, seals, heat exchangers, and calibration devices. There were never more than a dozen instruments of each type capable of reaching temperatures above 250 °C. Many of these are at risk, because of changes in priorities of national laboratories and university faculty retirements. The challenge will be to retain and build on the art and design experience required to construct the next generation of instruments for quantitative studies under hydrothermal conditions.

Data compilations

Oelkers et al. (2009) have provided a comprehensive review of modern "equations of state" for standard partial molar properties, and the data bases that are in current use for geochemical and industrial calculations. In general, data for hydrothermal conditions are based on accurate experimental data near ambient conditions and various correlation methods obtained by regressing fitted parameters from the HKF model for the few systems for which experimental data do exist at temperatures above 100 °C (See, for example: Plyasunov and Shock 2001b). Correlation algorithms now exist for predicting Krichevskii parameters for some species (Plyasunov and Shock 2001a, 2004). These correlations provide a useful guide to experimentalist in two ways. First, a careful reading of the source of the tabulated data yields insights in identifying solute species, or classes of solutes, that merit the time, effort and cost of quantitative experimental measurements under extreme conditions. Second, the estimated thermodynamic data can be used in chemical equilibrium models to select optimum experimental conditions.

Some current areas for investigation

A disadvantage of all types of differential heat-capacity calorimeters, is that they are limited to molalities above about 0.05 mol·kg^{-1}, and that they measure the apparent molar heat capacity, $C_{P\phi}^{\mathrm{Exp}}$, of bulk solutions. As a result, they cannot be used to determine the properties of species that are only sparingly soluble, or species that are only stable in solutions that contain an excess of supporting electrolyte, acid, or base. Many of the obvious simple electrolytes have been studied by Wood and his co-workers, and some of those that remain face challenges due to ion-pairing or solubility limits.

Because of these constraints, there is a serious lack of experimental data at elevated temperatures for metal complexes and ion-pairs. Heat of solution calorimeters and heat-of-mixing measurements have the potential to provide results for these systems, since they can operate at concentrations, as low as 10^{-3} mol·kg^{-1}, in the presence of high concentrations of acid, base or ligands. Moreover, no corrections are required for chemical relaxation effects in flow-heat-of-mixing studies, since the measurements are isothermal. The recent papers by Cobble and Djamali, cited above, using the integral heat of solution method, and some of the studies at BYU by Oscarson, Izatt and their co-workers provide examples of the potential of this approach. The principle challenge is to identify the equilibrium speciation. Ideally, an *in situ* spectroscopic or pH probe should be used. These are few, if any, calorimeters that provide the capability for high-quality enthalpy measurements *and* quantitative spectroscopic studies under hydrothermal conditions. The next-best approach is to undertake parallel spectroscopic and calorimetric studies on the identical solutions using separate instruments.

There is also a growing body of experimental data for organic solutes in high temperature water (See, for example, Plyasunov and Shock 2001a; Plyasunova et al. 2004). These have been used to derive "equations of state" for the standard partial molar volumes and heat capacities suitable for a number of organic systems (Shock and Helgeson 1990; Shock 1995; Sedlbauer et al. 2000; Plyasunov et al. 2000a,b; Plyasunov and Shock 2001a). We particularly note that Hnedkovsky's group is carrying out a program of systematic measurements to determine C_p° and V° for a large number of organic species. In making such measurements it is important to sample solutions after the calorimeter or densimeter to ensure that no thermal decomposition has taken place.

We note that experimental values for the standard partial molar properties of simple neutral gaseous species have been determined for only a handful of systems up to near-critical conditions. These include argon ethylene and xenon (Biggerstaff et al. 1988) and CH_4, CO_2, H_2S, and NH_3 (Hnědkovský and Wood RH 1997; Hnědkovský et al. 1996). These measurements are difficult because of the challenges of preparing solutions with accurately known concentrations for dissolved gases that are sparingly soluble except under high-pressure conditions. The HKF correlation parameters used by geochemists to estimate values for neutral species were derived from these few systems (Shock and Helgeson 1990). Clearly, there is a need for more data.

One important application of these instruments is for developing expressions to predict the standard partial molar properties of organic solutes based on their structure. For example, the apparent molar volumes of the thermally stable alkanolamines at temperatures plotted in Figure 7 have been used with literature results for alcohols, carboxylic acids and hydroxycarboxylic acids to calculate the standard partial molar volume contributions of the functional groups >CH-, $>CH_2$, $-CH_3$, -OH, -COOH, -O-, >N-, >NH, $-NH_2$, $-COO^-Na^+$, $-NH_3^+Cl^-$, $>NH_2^+Cl^-$ and $>NH^+Cl^-$, over the range (150 °C $\le T \le$ 325 °C). Expressions derived from these results allow predictions of the standard partial molar volume of aqueous organic solutes composed of these groups at temperatures up to ~310 °C and pressures of 10 - 20 MPa, to within a precision of ± 5 cm^3·mol^{-1}. This work follows earlier studies that have been carried out for both standard partial molar heat capacities and standard partial molar volumes up to 250 °C by Criss and Wood (1996), and others. Data such as these form the basis for several models for the thermodynamic properties of organic solutes in high-temperature water, based on functional group additivity models (Amend and Helgeson 1997a; Yezdimer et al. 2000; Sedlbauer et al. 2002; Lin and Sandler 2000, 2002).

CONCLUDING REMARKS

The brief outline presented here demonstrates the incredible progress that has been made over the past 30 years, in developing calorimeters for measuring accurate thermodynamic parameters for aqueous systems up to and above the critical point of water. Many of these instruments are custom-made, using a combinations of HPLC pumps, valves and fittings; exotic materials such as gold, platinum, sapphire and diamond; corrosion-resistant alloys; accurate temperature control; dedication; know-how; and experience. There is a need to expand these methods into the range from ~250 °C into the supercritical region, where measurements are sparse, and to examine some of the challenging species, noted in the discussion above. The challenge is that these measurements are demanding, and long-term, stable funding is required to support a successful program. A second issue is that specialized calorimeter labs require access to spectroscopic tools, capable of operating under the same pressure-temperature-concentration regime, to determine the speciation in the solutions under investigation. Our experience in Canada, and in other countries, has been that the government agencies that support university research cannot provide the long-term funding as a program in basic research. Success requires insight by the experimentalist in selecting benchmark systems for study, that have potential to provide *both* key data needed to advance basic understanding, *and* data or understanding required by a funding partner to address an industry-wide problem. With a careful selection of target systems for study, the right instruments and the right collaborators, the scientific payout is enormous.

ACKNOWLEDGMENTS

The authors express deep gratitude to Prof. Robert H. Wood, Professor Emeritus, University of Delaware, for his many contributions to the field of hydrothermal chemistry, for providing our research group with the benefit of his extensive experience in calorimetry and conductivity measurements, and for many fruitful discussions. We are grateful to the National Science and Engineering Research Council of Canada (NSERC), the University Network of Excellence in Nuclear Engineering (UNENE), Atomic Energy of Canada Ltd. (AECL), Ontario Power Generation Ltd. (OPG), Bruce Power Ltd. and the CANDU Owners Group (COG), for contributing strong funding support and insightful technical advice over the past two decades. PD Dr. Thomas Driesner (ETH Zurich) provided insightful comments on the manuscript. Funds from an NSERC Strategic Research Grant supported the preparation of this review paper.

REFERENCES

Ackerman T (1957) Hydration of H^+ and OH^- ions in water from heat capacity measurements. Discuss Faraday Soc 24:180-193

Albert HJ, Wood RH (1984) High-precision flow densimeter for fluids at high temperatures to 700 K and pressures to 40 MPa. Rev Sci Instrum 55:589-593

Amend JP, Helgeson HC (1997a) Group additivity equations of state for calculating the standard molal thermodynamic properties of aqueous organic species at elevated temperatures and pressures. Geochim Cosmochim Acta 61:11-46

Amend JP, Helgeson HC (1997b) Calculation of the standard molal thermodynamic properties of aqueous biomolecules at elevated temperatures and pressures. Part 1.1-α-amino acids. J Chem Soc Faraday Trans 93:1927-1941

Anderko A, Wang P, Rafal M (2002). Electrolyte solutions: from thermodynamic and transport property models to the simulation of industrial processes. Fluid Phase Equilib 194-197:123-142

Anderson G (2005) Thermodynamics of Natural Systems, 2nd Edition. Cambridge University Press. Cambridge

Anderson GM, Castet S, Schott J, Mesmer RE (1991) The density model for estimation of thermodynamic parameters of reactions at high temperatures and pressures. Geochim Cosmochim Acta 55:1769-1779

Angell CA (1982) Supercooled water. *In*: Water a Comprehensive Treaties. Vol. 7. Frank F (ed) Plenum Press, New York and London, p 1-82

Archer DG (1992) Thermodynamic properties of the NaCl + H_2O system II: thermodynamic properties of NaCl(aq), NaCl·$2H_2O$(cr), and phase equilibria. J Phys Chem Ref Data 21:793-829

Archer DG, Wang P (1990) The dielectric constant of water and Debye-Hückel limiting slopes. J Phys Chem Ref Data 19:371-411

Arcis H, Rodier L, Coxam J-Y (2007) Enthalpy of solution of CO_2 in aqueous solutions of 2-amino-2-methyl-1-propanol. J Chem Thermodyn 39:878–887

Arcis H, Ballerat-Busserolles K, Rodier L, Coxam J-Y (2011) Enthalpy of solution of carbon dioxide in aqueous solutions of monoethanolamine at temperatures of 322.5 K and 372.9 K and pressures up to 5 MPa. J Chem Eng Data 56:3351–3362

Arcis H, Ballerat-Busserolles K, Rodier L, Coxam J-Y (2012a) Measurement and modeling of enthalpy of solution of carbon dioxide in aqueous solutions of diethanolamine at temperatures of (322.5 and 372.9) K and pressures up to 3 MPa. J Chem Eng Data 57:840–855

Arcis H, Ballerat-Busserolles K, Rodier L, Coxam J-Y (2012b) Measurement and modeling of enthalpy of solution of carbon dioxide in aqueous solutions of tri-ethanolamine at temperatures of 322.5 K and 372.9 K and pressures up to 5 MPa. J Chem Eng Data 57:3587–3597

Atkins P, De Paula J (2010) Physical Chemistry, 9th Edition. Freeman, New York

Ballerat-Busserolles K, Origula ML, Woolley EM (2000) Calibration of a fixed-cell temperature scanning calorimeter to measure precise solution heat capacities from 275 to 398 K at 0.35 MPa, Thermochim Acta 347:3-7

Ben-Naim A (1980) Hydrophobic Interactions. Plenum Press, New York

Ben-Naim A (1987) Solvation Thermodynamics. Plenum Press, New York

Biggerstaff DR, Wood RH (1988) Apparent molar volumes of aqueous argon, ethylene and xenon from 300 to 715 K. J Phys Chem 92:1988-1994

Biggerstaff DR, White DE, Wood RH (1985) Heat capacities of aqueous argon from 306 K to 578 K. J Phys Chem 89:4378-4381

Biggerstaff DR, White DE, Wood RH (1988) Apparent molar heat capacities of aqueous argon, ethylene, and xenon at temperatures up to 720 K and pressures to 33 MPa. J Phys Chem 92:1994-2000

Bromley LA (1973). Thermodynamic properties of strong electrolytes in aqueous solutions. AIChE 19:313-320

Bulemela E, Tremaine PR (2008) Standard partial molar volumes of some aqueous alkanolamines and alkoxyamines at temperatures up to 325 °C: Functional group additivity in polar organic solutes under hydrothermal conditions. J Phys Chem 112:5626-5645

Busey RH, Holmes HF, Mesmer RE (1984) The enthalpy of dilution of aqueous sodium chloride to 673 K using a new heat-flow and liquid-flow microcalorimeter. Excess thermodynamic properties and their pressure coefficients. J Chem Thermodyn 16:343-312

Caiani P, Conti G, Gianni P, Matteoli E (1989) Apparent molar heat capacity and relative enthalpy of aqueous sodium hydroxoaluminate between 323 and 523 K. J Solution Chem 18:447-461

Carter RW, Wood RH (1991) Calibration and sample measurement techniques for flow heat capacity calorimeters. J Chem Thermodyn 23:1037-1056

Censky M, Sedlbauer J, Majer V, Ruzicka V (2007) Standard partial molal properties of aqueous alkylphenols and alkylanilines over a wide range of temperatures and pressures. Geochim Cosmochim Acta 71:580-603

Chen Q, Xu Y, Hepler LG (1991) Calorimetric study of the digestion of gibbsite, $A1(OH)_3$(cr), and thermodynamics of aqueous aluminate ion, $A1(OH)_4^-$(aq), Can J Chem 69:1685-1690

Chen X, Oscarson JL, Cao H, Gillespie SE, Izatt RM (1996) A new flow calorimeter designed for operation to 450 °C and 50 MPa. Thermochim Acta 285:11-23

Christensen JJ, Izatt RM (1984) An isothermal flow calorimeter designed for high temperature, high pressure operation. Thermochim Acta 73:117-129

Christensen JJ, Hansen LD, Eatough DJ, Izatt RM, Hart RM (1976) Isothermal high pressure flow calorimeter. Rev Sci Instrum 47:730-734

Christensen JJ, Hansen LD, Izatt RM, Eatough, DJ, Hart RM (1981) Isothermal, isobaric, elevated temperature, high-pressure, flow calorimeter. Rev Sci Instrum 52:1226-1231

Christensen JJ, Brown PR, Izatt RM (1986) An isothermal flow calorimeter for high temperature aqueous solutions. Thermochim Acta 99:159-168

Clarke RG, Tremaine PR (1999) Amino acids under hydrothermal conditions: apparent molar volumes of α-alanine, β-alanine and proline at temperatures from 298 to 523 K and pressures up to 20.0 MPa. J Phys Chem B 103:5131-5137

Clarke RG, Hnědkovský L, Tremaine PR, Majer V (2000) Amino acids under hydrothermal conditions: apparent heat capacities of α-alanine, β-alanine, glycine and proline at temperatures from 298 to 500 K and pressures up to 30.0 MPa. J Phys Chem B 104:11781-11793

Cobble JW (1966) High-temperature aqueous solutions. Science 152:1479–1485

Corti HR, Fernandez-Prini R, Svarc F (1990) Densities and partial molar volumes of aqueous solutions of lithium, sodium, and potassium hydroxides up to 250 °C. J Solution Chem 19:793-809

Coxam J-Y, Quint JR, Grolier J-PE (1991) Modification of a C-80 Setaram calorimeter for measuring heat capacities of liquids at temperatures up to 548 K and pressures up to 20 MPa. J Chem Thermodyn 23:1075-1083

Criss CM, Cobble JW (1964) The thermodynamic properties of high temperature aqueous solutions. IV. Entropies of the ions up to 200 °C and the correspondence principle J Am Chem Soc 86:5385-5390

Criss CM, Wood RH (1996) Apparent molar volumes of aqueous solutions of some organic solutes at the pressure 28 MPa and temperatures to 598 K J Chem Thermodyn 28:723-741

Crovetto R, Wood RH (1991) New detection method for determining phase boundaries. Fluid Phase Equilibr 65:253-261

Debenedetti PG (1998) One substance - two liquids? Nature 396:127-129

Desnoyers JE, Perron G (1997) Treatment of excess thermodynamic quantities for liquid mixtures. J Solution Chem 26:749-755

Desnoyers JE, de Visser C, Perron G, Picker P (1976) Reexamination of the heat capacities obtained by flow microcalorimetry, recommendation for the use of a chemical standard. J Solution Chem 5:605-616

Djamali E, Cobble JW (2009a) High dilution calorimetric determination of the standard state thermodynamic differences between the properties of H^+(aq) and Na^+(aq) up to 598.15 K. J Chem Thermodyn 41:1284-1291

Djamali E, Cobble JW (2009b) Thermodynamic properties of aqueous gadolinium perrhenate and gadolinium chloride from high dilution calorimetry at extreme temperatures and pressures. J Phys Chem B 113:2409-2413

Djamali E, Cobble JW (2009c) Standard state thermodynamic properties of completely ionized aqueous Sodium sulfate using high dilution calorimetry up to 598.15 K paper. J Phys Chem B 113:11688-11695

Djamali E, Chen K, Murray Jr RC, Turner PJ, Cobble JW (2009) Standard state thermodynamic properties of Ba^{2+}(aq), Co^{2+}(aq), and Cu^{2+}(aq) up to 598.15 K, and temperature effect on ligand field. J Phys Chem B 113:2404-2408

Djamali E, Turner PJ, Murray Jr RC, Cobble JW (2010) A high-temperature high-pressure calorimeter for determining heats of solution up to 623 K. Rev Sci Instrum 81:075105-1-075105-6

Fernandez DP, Goodwin ARH, Lemmon EW, Levelt-Sengers JMH, Williams RC (1997) A formulation for the static permittivity of water and steam at temperatures from 238 to 873 K at pressures up to 1200 MPa, including derivatives and Debye-Hückel coefficients. J Phys Chem Ref Data 26:1125-1166

Fernandez-Prini RJ, Corti HR, Japas ML (1992) High-Temperature Aqueous Solutions: Thermodynamic Properties. CRC Press, Boca Raton

Franck EU (1956) Hochverdichteter wasserdampf II.lonendissociation von KC1 in H_2O bis 750 °C. Z Phys Chem 8:107-126

Franck EU (1961) Uberkritisches wasser als electrolytisches losungsmittel. Angew Chem 73:309-322

Frank HS, Evans MW (1945) Free volume and entropy in condensed systems III. Entropy in binary liquid mixtures; partial molal entropy in dilute solutions; structure and thermodynamics in aqueous electrolytes. J Chem Phys 13:507-532

Fuangswasdi S, Oscarson J, Zhou L, Izatt RM (2001) A new flow calorimeter using a eutectic molten salt as the temperature control medium. Thermochim Acta 373:13-22

Gillespie SE, Oscarson JL, Izatt RM, Wang P, Renuncio JAR, Pando C (1995) Thermodynamic quantities for the protonation of amino acid amino groups from 323.15 to 398.15 K. J Solution Chem 24:1219-1247

Hakin AW, Daisley DC, Delgado L, Liu JL, Marriott RA, Tompkins G (1998) Volumetric properties of glycine in water at elevated temperatures and pressures measured with a new optically driven vibrating tube densimeter. J Chem Thermodyn 30:583-606

Helgeson HC, Kirkham DH, Flowers GC (1981) Theoretical predictions of the thermodynamic behavior of aqueous electrolytes at high-pressures and temperatures: IV. Calculation of activity coefficients, osmotic coefficients, and apparent molar and standard and relative partial molar properties to 600 °C and 5 kb. Am J Sci 281:1249-1516

Hepler LG (1981) Correct calculation of $\Delta H°$, $\Delta C_P°$, and $\Delta V°$ from temperature and pressure dependences of equilibrium constants: the importance of thermal expansion and compressibility of the solvent. Thermochim Acta 50:69-72

Hill PG (1990) A Unified fundamental equation for the thermodynamic properties of H_2O. J Phys Chem Ref Data 19:1233-1274

Hill PG, MacMillan RDC, Lee V (1982) A fundamental equation of state for heavy water. J Phys Chem Ref Data 11:1-14

Hnědkovský L, Wood RH (1997) Apparent molar heat capacities of aqueous solutions of CH_4, CO_2, H_2S, and NH_3 from 304 K to 704 K and pressures at 28 MPa. J Chem Thermodyn 29:731-747

Hnědkovský L, Wood RH, Majer V. (1996) Volumes of aqueous solutions of CH_4, CO_2, H_2S and NH_3 at temperatures from 298.15 K to 705 K and pressures to 35 MPa. J Chem Thermodyn 29:731-747

Hnědkovský L, Hynek V, Majer V, Wood RH (2002) A new version of differential flow heat capacity calorimeter; tests of heat loss corrections and heat capacities of aqueous NaCl from T = 300 K to T = 623 K. J Chem Thermodyn 34:755-782

Holmes HF, Busey RH, Simonson JM, Mesmer RE, Archer DG, Wood RH (1987) The enthalpy of dilution of HCl(aq) to 648 K and 40 MPa thermodynamic properties. J Chem Thermodyn 19:863–890

Hovey JK, Tremaine PR (1986) Thermodynamics of aqueous aluminum: Standard partial molar heat capacities of Al^{3+} from 10 to 55°C. Geochim Cosmochim Acta 50:453-459

Hovey JK, Hepler LG, Tremaine PR (1988) Thermodynamics of aqueous aluminate Ion: Standard partial molar heat capacities and volumes of $Al(OH)_4^-(aq)$ from 10 to 55 °C. J Phys Chem 92:1323-1332

Hynek V, Hnědkovský L, Cibulka I (1997) A new design of a vibrating-tube densimeter and partial molar volumes of phenol (aq) at temperatures from 298 K to 573 K. J Chem Thermodyn 29:1237-1252

Hynek V, Degrange S, Polednicek M, Majer V, Quint J, Grolier J-PE (1999) Combined flow-mixing power-compensation calorimeter and vibrating tube densimeter for measurements at superambient condition. J Solution Chem 28:631-636

Kestin J, Sengers JV. (1986) New formulations for the thermodynamic properties of light and heavy water. J Phys Chem Ref Data 15:305-320

Kestin J, Sengers JV, Kamgar-Parsi B, Levelt-Sengers JMH (1984) Thermophysical properties of fluid D_2O. J Phys Chem Ref Data 13:601-609

Koschel D, Coxam JY, Rodier L, Majer V. (2006) Enthalpy and solubility data of CO_2 in water and NaCl(aq) at conditions of interest for geological sequestration. Fluid Phase Equilib 247:107-120

Koschel D, Coxam JY, Majer V. (2007) Enthalpy and solubility data of H_2S in water at conditions of interest for geological sequestration. Ind Eng Chem Res 46:1421-1430

Kratky O, Leopold H, Stabinger H (1969) Determination of density of liquids and gases to an accuracy of 10^{-6} g/cm^3. Z Angew Phys 27:273-277

Levelt-Sengers JMH (1991) Thermodynamics of solutions near the solvent's critical point. *In*: Supercritical Fluid Technology: Reviews in Modern Theory and Applications. Bruno TJ, Ely JF (eds). CRC Press: Boca Raton, FL, p 1-56

Lin ST, Sandler SI (2000) Multipole corrections to account for structure and proximity effects in group contribution methods: octanol-water partition coefficients. J Phys Chem A 104:7099-7105

Lin ST, Sandler SI (2002) Henry's law constant of organic compounds in water from a group contribution model with multipole corrections. Chem Eng Sci 57:2727-2733

Mains GJ, Larson JW, Hepler LG (1984) General thermodynamic analysis of the contributions of temperature-dependent chemical equilibria to heat capacities of ideal gases and ideal associated solutions. J Phys Chem 88:1257-1261

Majer V, Crovetto R, Wood RH (1999) A new version of the vibrating-tube flow densitometer for measurements at temperatures up to 730 K. J Chem Thermodyn 23:333-344

Marshall WL, Franck EU (1981) Ion product of water substance, 0-1000°C, 1-10,000 Bars: New international formulation and its background. J Phys Chem Ref Data 10:295-304

Mathonat C, Hynek V, Majer V, Grolier J-PE (1994) Measurements of excess enthalpies at high temperature and pressure using a new type of mixing unit. J Solution Chem 23:1161-1182

Mathonat C, Majer V, Mather AE, Grolier J-PE (1997) Enthalpies of absorption and solubility of CO2 in aqueous solutions of methyldiethanolamine. Fluid Phase Equilib 140:171-182

Mayrath JE, Wood RH (1982) Enthalpy of dilution of aqueous sodium chloride at 349.15 to 472.95 K measured with a flow calorimeter. J Chem Thermodyn 14:15-26

Mayrath JE, Wood RH (1983a) Enthalpies of dilution of aqueous solutions of two hydrophobic solutes: t-butanol bromide and tetra-n-butylammonium, at 346.15 to 423.65 K. J Chem Thermodyn 15:625-632

Mayrath JE, Wood RH (1983b) Enthalpy of dilution of aqueous solutions of Na_2SO_4, K_2SO_4, and $MgSO_4$, at 373.15 and 423.65 K and of $MgCl_2$, at 373.15, 423.65, and 472.95 K. J Chem Eng Data 28:56-59

Mesmer RE, Hitch BF (1977) Base strength of amines at high temperatures. Ionization of cyclohexylamine and morpholine. J Solution Chem 6:251-261

Mesmer RE, Marshall WL, Palmer DA, Simonson JM, Holmes HF (1988) Thermodynamics of aqueous association and ionization reactions at high temperatures and pressures. J Solution Chem 17:699-718

Mesmer RE, Palmer DA, Simonson JM (1991) Ion association at high temperatures and pressures. *In*: Activity Coefficients in Electrolyte Solutions, 2nd Edition. Pitzer KS (ed) CRC Press, Boca Raton FL, p 491-529

Mesmer RE, Palmer DA, Simonson JM, Holmes HF, Ho PC, Wesolowski DJ, Gruszkiewicz MS (1997) Experimental studies in high temperature aqueous chemistry at Oak Ridge National Laboratory. Pure Appl Chem 69:905-914

Messikomer EE, Wood RH (1975) The enthalpy of dilution of aqueous sodium chloride at 298.15 to 373.15 K, measured with a flow calorimeter. J Chem Thermodyn 7:119-130

Millero FJ (1971) The molal volumes of electrolytes. Chem Rev 71:147-176

Millero FJ (1979) A review on partial molal compressibility, volume, expansibility, enthalpy, and heat capacity of electrolyte aqueous solutions and seawater. *In*: Activity Coefficients in Electrolyte Solutions. Vol. 2. Pytkowicz M (ed) CRC Press, Boca Raton FL, p 63-151

Millero FJ (2001) Physical Chemistry of Natural Waters. Wiley Interscience, New York. 654 pp

Mishima O, Stanley EH (1998) The relationship between liquid, supercooled and glassy water. Nature 396:329-335

Monk P, Wadsö I (1968) A flow micro reaction calorimeter. Acta Chem Scand 22:1842-1852

Myers JA, Sandler SI, Wood RH (2002) An equation of state for electrolyte solutions covering wide ranges of temperature, pressure, and composition. Ind Eng Chem Res 41:3282-3297

Noyes AA, Coolidge WD (1903) The electrical conductivity of aqueous solutions at high temperatures; I. Description of the apparatus. Results with NaCl and KCl up to 306 °C. Z Phys Chem 46:323-378

O'Connell JP, Sharygin AV, Wood RH (1996) Infinite dilution partial molar volumes of aqueous solutes over wide ranges of conditions. Ind Eng Chem Res 35:2808-2812

Oakes CS, Pitzer KS, Sterner SM (1998) The system NaCl-$CaCl_2$-H_2O: Part 3. Heats of dilution and mixing at 373 to 573 K and 21.5 MPa using a new high-temperature, flow-through calorimeter. Geochim Cosmochim Acta 62:1133-1146

Oelkers EH, Bénézeth P, Pokrovski GS (2009) Thermodynamic databases for water-rock interaction. Rev Mineral Geochem 70:1-46

Ohtaki H, Radnai T (1993) Structure and dynamics of hydrated ions. Chem Rev 93:1157-1204

Oscarson JL, Chen X, Gillespie SE, Izatt RM (1991) An isothermal flow calorimeter for high-temperature basic solutions. Thermochim Acta 185:51-61

Ott JB (1997) Forty years of calorimetery at Brigham Young University. Thermochim Acta 300:255-281

Ott JB, Stouffer CE, Cornett GV, Woodfield BF, Wirthlin RC, Christensen JJ (1986) Excess enthalpies for (ethanol + water) at 298.15 K and pressures of 0.4, 5,10, and 15 MPa. J Chem Thermodyn 18:1-12

Ott JB, Stouffer CE, Cornett GV, Woodfield BF, Che Guanquan, Christensen JJ (1987) Excess enthalpies for (ethanol + water) at 398.15, 423.15, 448.15, and 473.15 K and at pressures of 5 and 15 MPa. Recommendations for choosing (ethanol + water) as an H_m^E reference mixture. J Chem Thermodyn 19:337-348

Palmer DA, Fernandez-Prini R, Harvey AH (eds) (2004) Aqueous Systems at Elevated Temperatures and Pressures: Physical Chemistry in Water, Steam and Aqueous Solutions. Elsevier Academic Press, Amsterdam

Picker P, Jolicoeur C, Desnoyers JE (1969) Steady state and composition scanning differential flow microcalorimeters. J Chem Thermodyn 1:469-483

Picker P, Leduc PA, Philip PR, Desnosers JE (1971) Heat capacity of solutions by flow microcalorimetry. J Chem Thermodyn 3:631-642

Picker P, Tremblay E, Jolicoeur C (1974) A high precision digital readout flow densimeter for liquids. J Sol Chem 3:377-384

Pitzer KS (1973) Thermodynamics of electrolytes. I. Theoretical basis and general equations. J Phys Chem 77:268-277

Pitzer KS (1991) Ion interaction approach: theory and data correlation. *In:* Activity Coefficients in Electrolyte Solutions. 2nd Edition. CRC Press, Boca Raton FL, p 75-153

Pitzer KS (1995) Thermodynamics, 3rd Edition. McGraw-Hill, New York

Plyasunov AV, Shock EL (2001a) Estimation of the Krichevskii parameter for aqueous nonelectrolytes. J Supercrit Fluids 20:91-103

Plyasunov AV, Shock EL (2001b) Correlation strategy for determining the parameters of the revised Helgeson-Kirkham-Flowers model for aqueous nonelectrolytes. Geochim Cosmochim Acta 65:3879-3900

Plyasunov AV, Shock EL (2004) Prediction of the Krichevskii parameter for volatile nonelectrolytes in water. Fluid Phase Equilibr 222–223:19-24

Plyasunov AV, O'Connell JP, Wood RH (2000a) Infinite dilution partial molar properties of aqueous solutions of nonelectrolytes. I. Equations for partial molar volumes at infinite dilution and standard thermodynamic functions of hydration of volatile nonelectrolytes over wide ranges of conditions. Geochim Cosmochim Acta 64:495-512

Plyasunov AV, O'Connell JP, Wood RH, Shock EL (2000b) Infinite dilution partial molar properties of aqueous solutions of nonelectrolytes. II. Equations for the standard thermodynamic functions of hydration of volatile nonelectrolytes over wide ranges of conditions including the subcritical Temperatures. Geochim Cosmochim Acta 64:2779-2795

Plyasunova NV, Plyasunov AV, Shock EL (2004) Database of thermodynamic properties for aqueous organic compounds. Int J Thermophys 25:351- 360

Priestley PT, Sebborn WS, Selman RFW (1965) Continuous-flow enthalpimetry. Analyst 90:589-593

Privalov G, Kavina V, Freire E, Privalov PL (1995) Precise scanning calorimeter for studying thermal properties of biological macromolecules in dilute solution. Anal Biochem 232:79-85

REFPROP: Equations of State for Pure and Binary Fluids. NIST Standard Reference Database 22, 8.0

Ridley MK, Xiao C, Palmer DA, Wesolowski DJ (2000) Thermodynamic properties of the ionization of morpholine as a function of temperature and ionic strength. J Chem Eng Data 45:502-507

Ruterjans H, Schreiner F, Sage U, Ackermann T (1969), Apparent molal heat capacities of aqueous solutions of alkali halides and alkylammonium salts. J Phys Chem 73:986-994

Schrödle S, Königsberger E, May PM, Hefter G (2008) Heat capacities of aqueous solutions of sodium hydroxide and water ionization up to 300°C at 10 MPa. Geochim Cosmochim Acta 72:3124-3138

Schrödle S, Königsberger E, May PM, Hefter G (2010) Heat capacities of aqueous sodium hydroxide/aluminate mixtures and prediction of the solubility constant of boehmite up to 300°C. Geochim Cosmochim Acta 74:2368-2379

Sedlbauer J, O'Connell JP, Wood RH (2000) A new equation of state for correlation and prediction of standard molal thermodynamic properties of aqueous species at high temperatures and pressures. Chem Geol 163:43-63

Sedlbauer J, Bergin G, Majer V. (2002) Group contribution method for Henry's law constant of aqueous hydrocarbons. AIChE J 48:2936-2959

Seward T Driesner TM (2004) Hydrothermal solution structure: experiments and computer simulations. *In*: Aqueous Systems at Elevated Temperatures and Pressures: Physical Chemistry in Water, Steam and Hydrothermal Solutions. Palmer DA, Fernandez-Prini R, Harvey AH (eds) Elsevier Academic Press, Amsterdam, p 149-182

Shock EL (1995) Organic acids in hydrothermal solutions: standard molal thermodynamic properties of carboxylic acids and estimates of dissociation constants at high temperatures and pressures. Am J Sci 295:496-580

Shock EL, Helgeson HC (1990) Calculation of the thermodynamic and transport properties of aqueous species at high pressures and temperatures: Standard partial molal properties of organic species. Geochim Cosmochim Acta 54:915-945

Shock EL, Helgeson HC, Sverjensky DA (1989) Calculation of the thermodynamic and transport properties of aqueous species at high pressures and temperatures: Standard partial molal properties of inorganic neutral species. Geochim Cosmochim Acta 53:2157-2183

Shock EL, Oelkers EH, Johnson JW, Sverjensky DA, Helgeson HC (1992) Calculation of the thermodynamic properties of aqueous species at high pressures and temperatures: Effective electrostatic radii, dissociation constants, and standard partial molal properties to 1000 °C and 5 kb. J Chem Soc Faraday Trans 88:803-826

Simurka L, Cibulka I, Hnědkovský L (2011) Partial molar volumes of selected aliphatic alcohols at infinite dilution in water at temperatures T = (278 to 573) K and pressures up to 30 MPa. J Chem Eng Data 56:4564-4576

Smith-Magowan D, Wood RH (1981). Heat capacity of aqueous sodium chloride from 320 to 600 K measured with a new flow calorimeter. J Chem Thermodyn 13:1047-1073

Stoesser PR, Gill SJ (1967) Precision flow-microcalorimeter. Rev Sci Instrum 38:422-425

Stumm W, Morgan JJ (1996) Water Chemistry. Wiley, New York

Svishchev IM, Kusalik PG (1995) Spatial structure in liquid water under normal and critical conditions. *In*: Physical Chemistry of Aqueous Systems: Meeting the needs of Industry. Proceedings of the 12th International Conference on the Properties of Water and Steam. White HJ Jr, Sengers JV, Neumann DB, Bellows JC (eds) Begell House, New York, p 222-228

Tanger JC, Helgeson HC (1988) Calculation of the thermodynamic and transport properties of aqueous species at high pressures and temperatures: Revised equations of state for the standard partial molal properties of ions and electrolytes. Am J Sci 288:19-98

Tremaine PR, Shvedov D, Xiao C (1997) Thermodynamic properties of aqueous morpholine and morpholinium chloride at temperatures from 10 to 300 °C: Apparent molar volume, heat capacities, and temperature dependence of ionization. J Phys Chem 101:409-419

Tremaine PR, Zhang K, Bénézeth P, Xiao C (2004) Ionization of acids and bases under hydrothermal conditions. *In*: Aqueous Systems at Elevated Temperatures and Pressures: Physical Chemistry in Water, Steam and Hydrothermal Solutions. Palmer DA, Fernandez-Prini R, Harvey AH (eds). Elsevier Academic Press, Amsterdam, p 441-492

Ulmer GC, Barnes HL (1987) Hydrothermal Experimental Techniques. John Wiley & Sons, New York

Valyashko V. (2008) Hydrothermal Properties of Materials. John Wiley & Sons, Ltd., New York

Wagner W, Pruß A (2002) The IAPWS formulation 1995 for the thermodynamic properties of ordinary water substance for general and scientific use. J Phys Chem Ref Data 31:387-5353

Wang P, Oakes CS, Pitzer KS (1997) Thermodynamics of aqueous mixtures of magnesium chloride with sodium chloride from 298.15 to 573.15 K. New measurements of the enthalpies of mixing and of dilution. J Chem Eng Data 42:1101-1110

Wang P, Oakes CS, Pitzer KS (1998) Thermodynamics of the system $MgCl_2$–NaCl–H_2O to 573 K: New measurements of heat of mixing and heat of dilution. Int J Thermophys 19:739-748

White DE, Wood RH, Biggerstaff DR (1988) Heat capacities of 0.0150 mol·kg^{-1} NaCl(aq) from 604 K to 718 K. J Chem Thermodyn 20:159-168

Wilhelm E, Letcher TM (2010) Heat Capacities: Liquids, Solutions and Vapors. RSC Publishing, Cambridge, 516 pp

Wood RH, Buzzard CW, Majer V, Inglese A (1989) A phase-locked loop for driving vibrating tube densimeters. Rev Sci Instrum 60:493-494

Woolley EM (1997) Use of a fixed-cell, power-compensation, differential-output, temperature-scanning calorimeter to measure heat capacities of NaCl(aq) at temperatures from 283.15K to 393.15 K at the pressure 0.3 MPa. J Chem Thermodyn 29:1377-1385

Woolley EM (2007) A new tool for an old job: Using fixed cell scanning calorimetry to investigate dilute aqueous solutions. J Chem Thermodyn 39:1300-1317

Woolley EM, Hepler LG (1977) Heat capacities of weak electrolytes and ion association reactions: method and application to aqueous $MgSO_4$ and HIO_3 at 298 K. Can J Chem 55:158-163

Wormald CJ (2000) Excess enthalpies of steam + non-electrolyte mixtures. Experimental measurements and predictive methods. *In*: Steam, Water, and Hydrothermal Systems: Physics and Chemistry Meeting the Needs of Industry. Tremaine PR, Hill PG, Irish DE, Balakrishnan PV (eds). NRC Press Ottawa, p 355-364

Wormald CJ, Colling CN (1983) Excess enthalpies for (water + mitrogen) (g) up to 398.2 K and 12.6 MPa. J Chem Thermodyn 15:725-737

Wormald CJ, Lancaster NM (1989) A cubic equation of state for mixtures containing steam. J Chem Soc Faraday Trans 85:1315-1326

Xiao C, Bianchi H, Tremaine PR (1997) Excess molar volumes and densities of (methanol + water) at temperatures between 323 K and 573 K and pressures of 7.0 MPa and 13.5 MPa. J Chem Thermodyn 29:261-286

Yezdimer EM, Sedlbauer J, Wood RH (2000) Predictions of thermodynamic properties at infinite dilution of aqueous organic species at high temperatures via functional group additivity. Chem Geol 164:259-280

Young TF, Smith MB (1954) Thermodynamic properties of electrolytes in aqueous solution. J Phys Chem 58:716-724

Zhang K, Hawrylak B, Palepu R, Tremaine PR (2002) Thermodynamics of aqueous amines: Excess molar heat capacities, volumes and expansibilities of [methyl-diethanolamine (MDEA) + water] and [2-amino-2-methyl-1-propanol (AMP) + water] mixtures. J Chem Thermodyn 34:679-710

Reviews in Mineralogy & Geochemistry
Vol. 76 pp. 265-309, 2013
Copyright © Mineralogical Society of America

8

Structure and Thermodynamics of Subduction Zone Fluids from Spectroscopic Studies

Carmen Sanchez-Valle

Institute for Geochemistry and Petrology
Department of Earth Sciences ERDW
ETH Zurich
CH-8092 Zurich, Switzerland

carmen.sanchez@erdw.ethz.ch

INTRODUCTION

Fluids[1] in subduction zones have been a subject of growing interest for at least the last 20 years. Subduction zones are the major places on Earth for mass transfer, element recycling and chemical differentiation through magmatic processes in which fluids released from the slab play a central role. Hydrous subduction zone magmas are essential in the formation of numerous types of hydrothermal ore deposits and are the driving force behind magmatic-hydrothermal and geothermal systems in volcanic arcs. It is widely recognized that the characteristic geochemical signature of arc magmas results from the metasomatism of the magma source by a slab-derived flux (McCulloch and Gamble 1991; Elliott 2003). Large uncertainties remain however concerning the chemical composition and nature of the slab flux (aqueous fluid, hydrous melt or supercritical fluid?) and, ultimately, about the mechanisms of mass transfer from the slab to the mantle wedge. Correlating inputs and outputs in subduction zones to quantitatively estimate mass transfer and element recycling relies on thermodynamic modeling of fluid-rock interactions at pressure-temperature above 5 GPa and 1500 K (Manning 2004a). Key constraints on these models are the phase relations, mineral solubility, the behavior of trace elements (partition coefficients) and the physico-chemical and thermodynamic properties of high-pressure fluids at relevant conditions. Unfortunately, quantitative information on fluid properties at relevant P-T conditions are in most cases not available due to experimental difficulties associated with the non-quenchable character of fluid phases. New experimental designs, especially those using laser or synchrotron-based spectroscopic techniques combined with high temperature diamond anvil cells (Basset et al. 1993), are now opening the possibility for monitoring *in situ* the chemical composition of fluid phases and for the determination of structural parameters and thermodynamic quantities.

In this chapter, I review recent progress in determining the thermodynamic properties and molecular-scale structure of high-pressure aqueous fluids based on spectroscopic studies using diamond anvil cells. Some of the topics of this chapter are expanding fields of study, and the goal is not only to provide an overview of the achievements, but more importantly, to identify future research directions. After a short introduction to the chemistry of subduction zone fluids, the chapter examines the structure and speciation of major and two key group of trace elements, High Field Strength Elements (HFSE) and Rare Earth Elements (REE),

---

[1] "Fluid" is a general term that denotes any mobile phase such as liquid, vapor, gases, or melts and is introduced because the meaningful distinction of these different fluid types at ambient conditions becomes obsolete at high pressures and temperatures where transitions between the various types are often gradational.

1529-6466/13/0076-0008$05.00 http://dx.doi.org/10.2138/rmg.2013.76.8

in subduction zone fluids as determined from Raman and X-ray absorption (XAS) studies under pressure. Complemented by insights provided by emerging theoretical methods, the results will be used to discuss briefly the mobilization and transport of HFSE and REE during subduction. The second part of the chapter addresses the lack and limitations of experimental data and equations of state for the density and thermodynamic properties of aqueous fluids at the *P-T* conditions of fluid processes in subduction zones. The application of sound velocity measurements in the diamond anvil cell by Brillouin scattering spectroscopy to determine the density and equation of state of high-pressure fluids is discussed next. The chapter concludes with a discussion of insights into the physical chemistry of aqueous species in high-pressure fluids (> 0.5 GPa) that start to emerge from the growing number of volumetric studies.

CHEMISTRY AND STRUCTURE OF SUBDUCTION ZONE FLUIDS

Chemistry of subduction zone fluids

At the high-pressure and high-temperature conditions of the Earth's lower crusts and upper mantle water-rich fluids gain the capacity to dissolve significant amounts of rock components. The extent of mass transfer and element fractionation in subduction zones is determined by this reactivity of the fluids with rock-forming minerals and their ability to mobilize major and trace elements. Insights into the compositional evolution of deep fluids have been obtained from analysis of a limited number of natural fluids samples, including rare pore fluid samples from accretionary margins and fluid inclusions preserved in high-pressure rocks, or through experimental studies at relevant pressures and temperatures. Reviews by Manning (2004a, 2013, this volume) and Hermann et al. (2006) provide a comprehensive discussion on the chemistry of subduction zone fluids, with extensive details on constraints from natural rocks. A brief overview of the most important aspects of fluid chemistry is outlined in the following.

Mineral solubility in aqueous fluids/hydrous melts and trace element partitioning between phases have received much experimental attention over the past two decades. The combined results from quench experiments (e.g., Manning 1994, 2007; Keppler 1996; Newton and Manning 2003, 2008a,b; Kessel et al. et al. 2005a,b; Spandler et al. 2007; Antignano and Manning 2008) and diamond anvil cell approaches (Sanchez-Valle et al. 2003; Schmidt and Rickers 2003; Bureau et al. 2007; Manning et al. 2008; Wilke et al. 2012) form the basis for major advancements in the development of thermodynamic models that are able to predict the properties of aqueous species and the composition of fluids in complex systems at subduction zone *P-T* conditions (e.g., Newton and Manning 2008a; Dolejs and Manning 2010; Hunt and Manning 2012; Dolejs 2013, this volume).

Direct samples of subduction zone fluids are scarce and have been restricted to shallow depths (< 25 km). Pore fluids from dehydration events in Costa Rica (< 15 km depth, 373-423 K) and the Mariana subduction zone (15-25 km depth) have chlorinities below that of seawater. Total dissolved solids (TDS) are low (28 g/kg H_2O) and dominated by Na and Cl, with low Si (0.032 to 0.084 millimol/ kg H_2O) and little amounts of other alkali and alkali earth metals (e.g., Silver et al. 2000; Tryon et al. 2010). Deeper fluid samples (25-60 km depth), preserved as fluid inclusions in exhumed mafic rocks (Fu et al. 2001; Gao and Klemd 2001), typically show an increase in the TDS up to 75 g/kg H_2O and salinities of 1-7 wt% NaCl, although passive solute enrichment due to water loss cannot be ruled out. The fluids in eclogite-facies are dominantly aqueous in composition and provide direct evidence for the release of H_2O-rich fluids by the breakdown of hydrous minerals in the slab. This is consistent with thermodynamic modeling of mineral solubility data (Manning 1998) and experimental studies of the composition of fluids equilibrated with subducted sediments (Spandler et al. 2007). Estimated TDS at the blueschist to eclogite transition are less than 48 g/kg H_2O TDS (~ 5 wt% dissolved solutes of which > 75% SiO_2 and ~15% Na_2O+Al_2O_3) at ~ 850 K and 1.5-2.5 GPa (50-70 km depth) but are notably richer in silica and Al compared to lower pressure fluids. Fluids released by the slab at the eclogite facies are thus diluted and mainly composed of Si-Al-Na. They contain only moderate loads of Large Ion Lithophile Elements (LILE), Sr and Pb, and do not carry significant amounts of Light REE LREE, U and Th that can, therefore, be retained in the subducting slab to greater depth into sub-arc regions. This observation implies that most of the trace element budget of the slab may be preserved during major metamorphic dehydration events and that other slab fluxes are required for element recycling in subduction zones (Spandler et al. 2007). Hydrous melts produced by fluid-mediated slab melting are able to transfer larger amounts of trace elements from the slab to the mantle wedge (Hermann et al. 2006).

The mutual solubilities of water and silicate melts increase with increasing pressure and temperature, and their compositional and structural differences vanish above the second critical end point, leaving a single-phase supercritical fluid (see Hack et al. 2007 for a recent review). Direct evidence for the miscibility between the two phases was first provided by Shen and Keppler (1997) in the albite ($NaAlSi_3O_8$)-water system from diamond anvil cell experiments, and later reported for a range of simple silicate-water systems (Bureau and Keppler 1999) and $NaAlSi_3O_8$-$H_2O \pm Na_2O \pm B_2O_3 \pm F_2O$ (Sowerby and Keppler 2002). Miscibility in high-pressure aqueous fluids and melts such as those released by subducting slabs and percolating through the overlying mantle wedge has recently been reviewed (Poli and Schmidt 2002; Manning 2004a; Hermann et al. 2006; Hack et al. 2007 and references cited). A survey of the available experimental data indicates that second critical end point in felsic systems occurs at 2.5-3.5 GPa and around 973 K but there remains significant controversy about its location in mafic and ultramafic systems (Stalder et al. 2000; Kessel et al. 2005b; Mibe et al. 2011). Intermediate (supercritical) fluids may have enhanced capacity for mass transport (Kessel et al. 2005a) but their significance in natural systems along *P-T* trajectories for slab subduction paths remains debated (Manning 2004a; Hermann et al. 2006; Hack et al. 2007). They are expected to occur only in a narrow temperature interval (50-100 K), where a significant increase in the solute load in the fluid is observed (> 30 wt% dissolved solutes; Manning 2004a; Hermann et al. 2006).

The mechanism leading to miscibility of aqueous fluids and silicate melts controls the compositional evolution and physico-chemical properties of subduction zone fluids, even in relatively dilute systems (Manning 2004a,b). It has been demonstrated that the increase in silica concentration in the fluid is accommodated by progressive polymerization of species in the fluid, i.e., an increase in Si-O-Si bonding (Fig. 1). Silica clusters will also incorporate Al, alkalis (Na and K), and, ultimately, trace elements (Manning 2004a). As proposed by Manning (2004a), a supercritical fluid can thus evolve from pure H_2O to hydrous melt as dissolved components are incorporated; i.e., solute speciation changes from hydrated ions or molecules to small clusters that are the precursors for the polymerized network of a hydrous silicate liquid. The following section reviews spectroscopic evidence for polymeric species in aluminosilicate systems and their stability in deep fluids.

Polymerization of silicate components in high-pressure fluids

Aqueous silica polymerization. The dissolution of quartz in water at near neutral pH conditions leads to the formation of dissolved orthosilicic acid monomer, H_4SiO_4, following the reaction:

$$SiO_{2(cr)} + 2H_2O_{(aq)} \leftrightarrow H_4SiO_{4(aq)} \qquad (1)$$

The enhanced solubility of quartz with increasing pressure and temperature (Manning 1994; Hunt and Manning 2012 and references cited) results from extensive polymerization of H_4SiO_4 units to form pyrosilicic acid dimers, $H_6Si_2O_7$, according to the reaction:

$$2H_4SiO_4 \leftrightarrow H_6Si_2O_7 + H_2O \qquad (2)$$

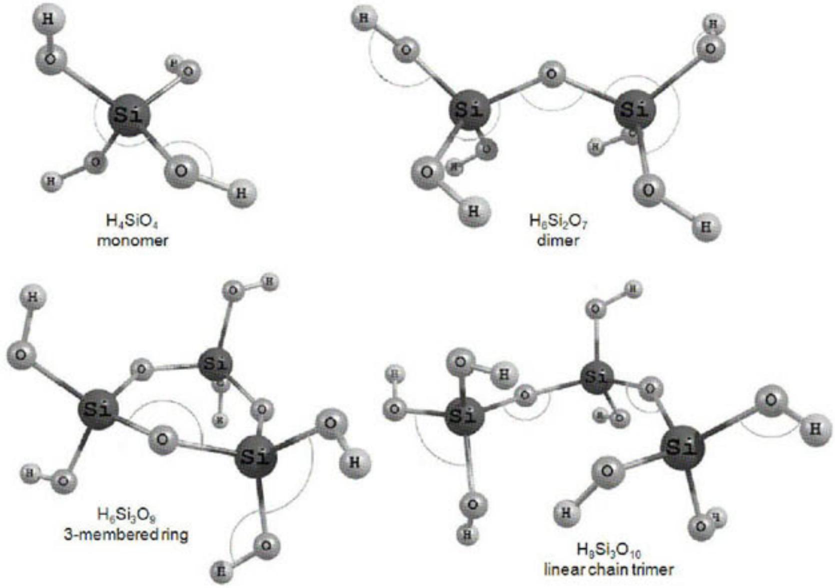

Figure 1. Structure of the main aqueous silica species in subduction zone fluids. [Used with permission of Elsevier from Hunt et al. (2011) *Chemical Geology*, Vol. 283, p. 161-170, Fig. 1.]

Silica polymers have been identified in SiO_2-bearing solutions at low pressure and temperature by using different spectroscopic methods, including Raman and NMR spectroscopy (Zotov and Keppler 2000, 2002 and references cited). Spectroscopic evidence for the polymerization of silica in high-pressure aqueous fluids was first provided by Mysen (1998) who identified $H_6Si_2O_7$ dimers and $H_6Si_3O_9/H_8Si_3O_{10}$ trimers (Fig. 1) in fluids equilibrated with SiO_2-K_2O-H_2O melts by using Raman spectroscopy in hydrothermal diamond anvil cells.

Thermodynamic analyses of polymerization reactions in high-pressure water-rich fluids from direct Raman studies under pressure have so far only been conducted in the SiO_2-H_2O system. One of the main difficulties in the extension of this approach to more complex systems is the uncertainty in the assignment of observed vibrational bands to specific silica species and structural subunits (Fig. 2). *Ab initio* calculated frequencies of dissolved silicate species provide a theoretical basis for the assignment of the experimental spectral features (Sykes and Kubicki 1996; Tossell 1999, 2005; Zotov and Keppler 2000; Mibe et al. 2008; Hunt et al. 2011). Table 1 displays a compilation of the experimental and theoretical vibrational frequencies for the main species formed in aqueous fluids, hydrous melts and supercritical fluids in alkali-aluminosilicate systems.

Zotov and Keppler (2000, 2002) investigated the speciation of silica in quartz saturated aqueous fluids to 1.4 GPa and 173 K by Raman spectroscopy in hydrothermal diamond anvil cells. At 0.5 GPa, H_4SiO_4 monomers are the dominant species in the investigated T range, while $H_6Si_2O_7$ dimers dominate the speciation of dissolved silica above 1073 K at 1.2 GPa. The concentration of H_4SiO_4 and $H_6Si_2O_7$ species in the fluid at various temperature and pressure conditions (Fig. 3) was derived from the integral intensity of the 780 cm^{-1} and 630 cm^{-1} Raman bands respectively (Table 1), corrected by the corresponding scattering cross-sections. The speciation data were used to determine the equilibrium constant of Reaction (2):

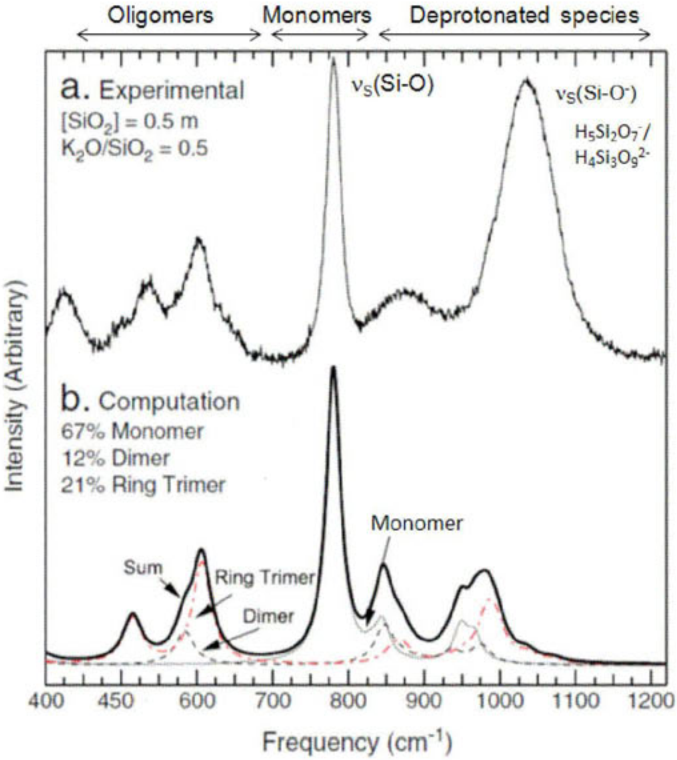

Figure 2. Silica polymers formed in K_2O-SiO_2 aqueous solution ([Si] = 0.5 *m*, $K_2O/SiO_2 = 0.5$) identified by Raman spectroscopy and theoretical calculations of Raman spectra with variable proportions of silica species: 67% monomer, 12% dimer, and 21% ring trimer at room conditions (see Fig. 1). Deprotonated monomers and oligomers (850-1125 cm^{-1}) are abundant due to the high alkalinity (pH = 12.42) of the solutions. [Used with permission of Elsevier from Hunt et al. (2011) *Chemical Geology*, Vol. 283, p. 161-170, Fig. 7.]

$$K_{(m)\text{-}(d)} = \frac{a_{H_6Si_2O_7}\, a_{H_2O}}{a^2_{H_4SiO_4}} \tag{3}$$

The results indicate that an isobaric increase in temperature at pressure above 0.5 GPa favors the formation of dimers, although the effect is more pronounced at higher pressure (Fig. 4). The calculated enthalpy ΔH and the entropy ΔS of the polymerization Reaction (2) are $\Delta H = 12.6 \pm 1.3$ kJ mol^{-1} and $\Delta S = 40.7 \pm 1.3$ J mol^{-1} K^{-1} at 0.5 GPa, and $\Delta H = 77.7 \pm 5.3$ kJ mol^{-1} and $\Delta S = 123.7 \pm 10.2$ J mol^{-1} K^{-1} at 1.2 GPa, respectively.

Measurements of total dissolved aqueous silica in equilibrium with silica-buffering mineral assemblages were used by Newton and Manning (2003) to provide additional constraints on the thermodynamic properties of polymerized silica aqueous solutions. Introducing an activity model based on a standard state convention of unit activity of the hypothetical pure monomer solution at the *P* and *T* of interest, the equilibrium constant for Reaction (2) was determined as:

$$K_{(m)\text{-}(d)} = \frac{X_{(d)}}{X^2_{(m)}} \;\; \frac{(1-\gamma_{Si})}{2\gamma^2_{Si}X_{Si}} \tag{4}$$

where $X_{(m)}$ and $X_{(d)}$ are the mole fraction of the silica monomer and dimer in solution; X_{Si} and

Table 1. Chemical species in silicate-bearing aqueous fluids, hydrous silicate melts and supercritical fluids and their principal Raman bands determined from experimental and theoretical studies.

Species	Raman frequency (cm^{-1})		Band assignment	*Ref*#
	Exp.	***Cal.***		
		SiO_2 – H_2O system		
H_4SiO_4 (Mo)	785 600	783/788	ν_s(Si-O)	[1 ; 2,3]
$H_3SiO_4^-$ (Mo)	781	694	ν_s(Si-O)	[4 ; 5]
	1020	1141	ν_s(Si-O^-)	[4 ; 5]
$H_2SiO_4^{2-}$ (Mo)	772	611	ν_s(Si-O)	[4 ; 5]
	925	928	ν_s(Si-O^-)	[4 ; 5]
$H_6Si_2O_7$ (D)	630	631/620	In plane δ_s(Si-O-Si), ν(Si-BO), ν_s(Si-O_H)	[1; 2,3]
	920	916	ν_s(Si-O_H)	[1 ; 2]
	225	—	δ(O-Si-O)	[1 ; -]
$H_6Si_3O_9$ (3R)	—	629/633	ν_s(Si-O-Si)	[- ; 3,4]
$H_8Si_3O_{11}$ (L)	—	588	ν_s(Si-O-Si)	[- ; 4]
$H_8Si_4O_{12}$ (4R)	—	490	ν_s(Si-O-Si)	[- ; 8]
		SiO_2 – Al_2O_3 – H_2O system		
$Al(OH)_4^-$	620	616	ν(Al-OH_2)	[4 ; 6]
$Al(OH)_3H_2O$	—	439	ν(Al-O)	[- ; 6]
$H_6Al_2O_7^{2-}$ (D)	545	—	δ(Al-O-Al)	[4 ; -]
$H_6SiAlO_7^-$ (D)	575	585	ν(T-O), δ(Si-O-Al)	[7 ; 7]
$H_4SiAlO_7^{3-}$ (D)	574	—	ν(T-O), δ(Si-O-Al)	[4 ; -]
$H_6Si_2AlO_9^-$ (3R)	575	574	ν(T-O-T)	[7 ; 8]
$H_8Si_3AlO_{12}^-$ (4R)	480	488	ν(T-O-T)	[7 ; 8]
		$KAlSi_3O_8$ – H_2O system		
KH_3SiO_4 (Mo)	750-765	748	ν(Si-O)	[7 ; 7]
$KAl(OH)_4$	—	619	ν(Al-O)	[- ; 7]
$H_2K\,AlO_3$	—	691	ν(Al-O)	[- ; 7]

Notes:

Mo = monomer; D = dimer; 3R = 3-membered ring, L = linear; 4R = 4-membered ring; ν = stretching vibration; δ = bending vibration; O_H = terminal oxygen; O^- = deprotonated oxygen species; Sub-index *s* refers to symmetric vibrations. Exp, experimental; Calc, calculated data; T = Si, Al

#First set of references refers to experimental frequencies, the second denotes the source of the calculated frequencies: [exp ; calc]

References: [1] Zotov and Keppler (2002); [2] Zotov and Keppler (2000); [3] Tossell (2005); [4] Gout et al. (2000); [5] Hunt et al. (2011); [6] Tossell (1999); [7] Mibe et al. (2008); [8] Sykes and Kubicki (1996)

$\gamma_{Si} = X_{(m)}/X_{Si}$, are the mole fraction and activity coefficient of total dissolved silica. At 1073 K and 1.2 GPa, they reported $K_{(m)\text{-}(d)} = 155$ (Fig. 4), in agreement with Zotov and Keppler (2002). Their results indicate that 70% of the dissolved silica occurs as dimers at 1073 K and 1.2 GPa. When approaching the hydrous melting of quartz, more polymerized species may also form in solution and ring trimers $H_6Si_3O_9$ (Fig. 1) are assumed to dominate under these conditions (Newton and Manning 2008a; Manning et al. 2010). Deprotonated monomers (e.g., $H_3SiO_4^-$ and $H_2SiO_4^{2-}$) and oligomers ($H_5Si_2O_7^-$ and $H_4Si_3O_9^{2-}$) (Table 1 and Fig. 2) are only observed in very alkaline solutions (pH > 11.5) (Gout et al. 2000; Hunt et al. 2011) and are not expected to play an important role in near-neutral subduction zone fluids.

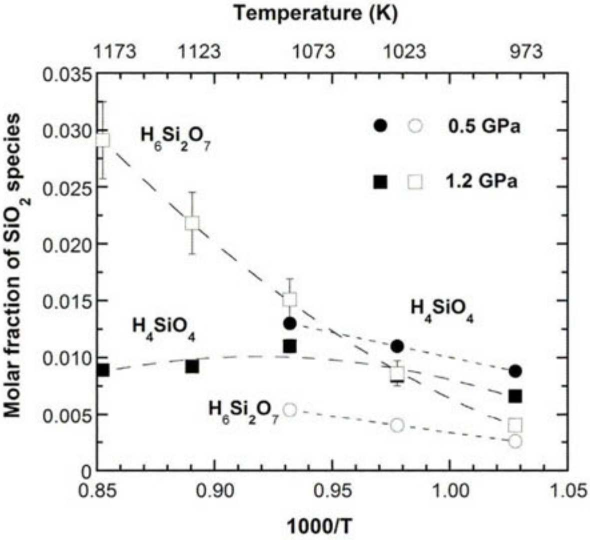

Figure 3. Molar fraction of dissolved SiO_2 species in quartz-saturated SiO_2-H_2O fluids ($xH_2O + xH_4SiO_4 + xH_6Si_2O_7 = 1$) as a function of temperature at 0.5 GPa and 1.2 GPa (data from Zotov and Keppler 2002). The concentration of H_6SiO_7 dimers increases isobarically with increasing temperature and the effect is more pronounced at 1.2 GPa, where dimers dominate the speciation of dissolved silica above 1073 K. At 0.5 GPa, H_4SiO_4 aqueous monomers are dominant in the investigated temperature range.

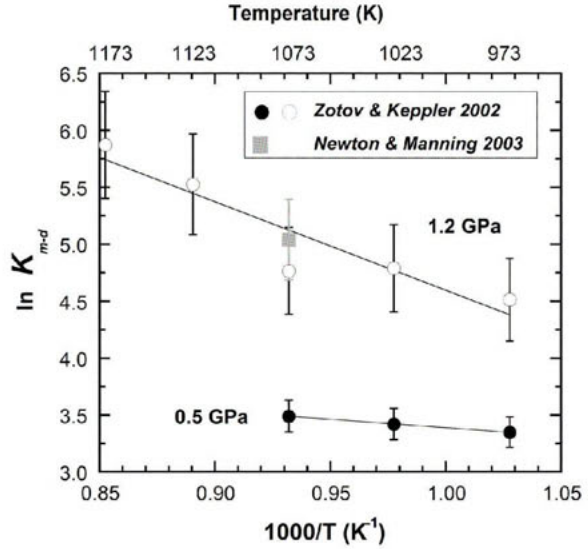

Figure 4. Temperature and pressure dependence of the equilibrium constant $K_{(m)\text{-}(d)}$ for the dimer formation Reaction (2). Full and empty circles are data determined from *in situ* monitoring of dissolved silica species by Raman spectroscopy (Zotov and Keppler 2002). The gray square represents $\ln K_{(m)\text{-}(d)}$ calculated from the activity coefficient model for aqueous silica derived from SiO_2 solubility measurements in equilibrium with silica-buffering mineral assemblages at 1073 K and 1.2 GPa (Newton and Manning 2003). Both pressure and temperature favor the formation of dimers in the aqueous fluid in equilibrium with quartz, although the effect of pressure is stronger. Lines are linear fits to the data.

Polymerization of alkali aluminosilicate components. Strong support for complexation among alkali aluminosilicate (Si ± Al ± Na) components in high-pressure fluids is provided by the enhanced solubility of quartz and corundum in the presence of aluminosilicate or alkali-aluminosilicate minerals at crustal and upper mantle conditions (e.g., Manning 2007; Newton and Manning 2008b; Manning et al. 2010). However, the formation and stability of Si ± Al ± Na complexes at high-pressure and high temperature conditions has only been investigated in a few reconnaissance studies (Mysen 1998; Mibe et al. 2008).

The solubility of corundum Al_2O_3 in water increases by a factor of ten from ambient conditions to 973 K and 1 GPa (Manning 2007), suggesting the formation of polynuclear Al clusters (e.g., $H_6Al_2O_8$) in the fluid. However, so far there is no spectroscopic evidence for such species in high-temperature-pressure fluids. Deprotonated adimers $H_6Al_2O_6^{2-}$ (Table 1) have been identified in concentrated Al-bearing solutions by room temperature Raman studies (Gout et al. 2000) although they are only stable at very high pH values (> 12). The enhanced solubility of Al in aqueous fluids equilibrated with Al_2O_3 + kyanite assemblages (Manning 2007) suggest the incorporation of Al in Si species through the pH-dependent reactions:

$$Al^{3+} + H_4SiO_4 \leftrightarrow H_3AlSiO_4^{2+} + H^+ \quad (pH < 2) \tag{5}$$

$$Al(OH)_4^- + H_4SiO_4 \leftrightarrow H_6AlSiO_7^- + H_2O \quad (pH > 4.5) \tag{6}$$

Potentiometric studies (Pokrovski et al. 1996; Salvi et al. 1998) indicate that the stability of Al-Si complexes (Reactions 5 and 6) increases with temperature up to 573 K at vapor saturation pressures. More recently, Mibe et al. (2008) identified $H_6AlSiO_7^-$ species in supercritical fluids in the system $KAlSi_3O_8 - H_2O$ at 2.1 GPa and 1073-1173 K, showing that the stability of Al-Si complexes persists to upper mantle conditions.

Poynuclear Si-Al-alkali (namely Na and K) species may form in more complex systems upon addition of dissolved alkali species as shown by the enhanced solubility of Al_2O_3 in SiO_2 + NaCl fluids (Newton and Manning 2008b) and of SiO_2 in presence of albite + paragonite assemblages (Manning et al. 2010). However, direct spectroscopic evidence for these species is still missing. In the Raman studies of Mibe et al. (2008), only KH_3SiO_4 monomers were unambiguously identified in aqueous fluids in the $KAlSi_3O_8$–H_2O system while to extensive overlapping between vibrational bands prevented the characterization of more complex species predicted by *ab initio* calculations of the Raman spectra (Table 1).

Polymeric aqueous alkali-aluminosilicate species are, therefore, important structural units in subduction-zone fluids that promote critical mixing between H_2O-rich fluids and silicate melt at crustal and upper mantle conditions. In addition to enhancing the solubility of major minerals and mineral assemblages, Si-Al-Na polymeric species play an important role in the dissolution of trace elements, with important consequences for mass transfer and the geochemical cycle of trace element. In the next sections, the role of polymeric species in the mobilization and transport of HFSE trace elements by subduction zone fluid is discussed based on recent experimental studies.

CONTROLS ON TRACE ELEMENT SPECIATION IN SUBDUCTION ZONE FLUIDS

The speciation of trace elements in high-pressure fluids plays a critical role in determining their mobility and transport in subduction-related magmatic-hydrothermal processes. Although the atomic-scale mechanisms controlling these processes still remain poorly understood, they likely result from a complex interplay between pressure, temperature, the properties of the water solvent, association/dissociation of dissolved solutes and available ligands (namely Cl, F), as well as the extent of Si-Al-Na polymerization in high-pressure silicate-rich fluids.

Changes in these parameters trigger strong variations in element mobility and transport in crustal/upper mantle settings (e.g., Seward 1981; Harvey and Friend 2004; Manning 2004a) as will be illustrated from the results of the experimental studies discussed below.

The dissolution of mineral components in water-rich fluids is controlled by the ability of water to hydrate species in solution (Marcus 1985). The solvent properties of water depend on the density, pH, structure of hydrogen bond network and dipole moments (i.e., dielectric constant ε) that evolve upon increasing pressure and temperature with depth. The progressive disruption of the hydrogen bond network in water from ambient to supercritical conditions (Kalinichev 2001; Seward and Driesner 2004) leads to a decrease in the dielectric constant of water (Pitzer 1983; Wasserman et al. 1995; Fernandez et al. 1997; Pan et al. 2013) that has important implications for the hydrations of ions (Marcus 1985, 2009). The decrease of the dielectric constant of water, ε, with increasing temperature reduces solvent's ability to shield the ions in solution and the electrostatic ion-ion interactions in the fluid are enhanced (Marcus 1985). This process promotes ion association in high temperature fluids, favoring ion pairing or complexation with available ligands (Seward 1981; Seward and Driesner 2004). However, pressure will have an opposite effect on ion hydration and association in water. At constant temperature, an increase in pressure leads to the strengthening of the hydration shell around the ions, thus favoring dissociated solutes in high-pressure fluids.

The bulk fluid composition, and particularly the extent of polymerization of the silicate components, is a primary control on the speciation of trace elements in high-pressure silicate bearing aqueous fluids. This is illustrated by the enhanced solubility of refractory trace elements such as Zr^{4+} or Ti^{4+} in fluids containing dissolved silicates compared to pure H_2O (Audetat and Keppler 2005; Tropper and Manning 2005; Antignano and Manning 2008; Manning et al. 2008; Wilke et al. 2012), through the formation of stable complexes with polymeric Si-Al-Na species in high-pressure fluid (Wilke et al. 2012; Louvel et al. 2013). The coordination chemistry involving polymerized silicate species thus governs the mobility and transport of key trace elements from the slab to the mantle wedge. A better understanding of the atomic-scale mechanism that controls the formation and stability of these complexes in high-pressure fluids is necessary to evaluate mass transfer and element recycling in subduction zones.

STUDIES ON TRACE ELEMENT SPECIATION IN SUBDUCTION ZONE FLUIDS BY X-RAY ABSORPTION SPECTROSCOPY

While the speciation of a large number of trace elements in hydrothermal fluids has been investigated at low pressures and temperatures (typically at < 0.1 GPa to 773 K), high-pressure studies using fluid compositions directly relevant for deeper subduction zones are rare. Much of the speciation work has focused on the stability of ore metal complexes in dilute halogen-bearing solutions with the aim of understanding the genesis and chemical controls of hydrothermal ore deposition (Pokrovski et al. 2013, and references cited). However, understanding mass transfer processes in subduction zones requires a better knowledge of trace element speciation in silicate-bearing aqueous fluids, hydrous silicate melts and supercritical fluids that are better proxies for deep subduction zone fluids as discussed above (Manning 2004a; Hermann et al. 2006).

Current knowledge about trace element speciation in dry or hydrous silicate melts primarily comes from a large number of studies by X-ray absorption spectroscopy (XAS) conducted on silicate glasses and melts at room pressures (e.g., Brown et al. 1995). Over the last decade, a growing but still small number of studies have addressed the speciation of selected trace elements at pressure, temperature and fluid compositions more relevant to subduction zone processes by combining XAS and externally heated diamond anvil cells. The principles of X-ray absorption spectroscopy will be only briefly outlined below as introductory and advanced level books and review papers about the topic are available (e.g., Crozier et al. 1988; Brown et al. 1995; Als-Niels and McMorrow 2001; Bunker 2010). Instead, details of the XAS analysis at high-pressure conditions are described, focusing on illustrating major advancements on the characterization of low atomic number trace elements in dilute fluids under high-pressure–high-temperature conditions in diamond anvil cells (Figs. 5-6).

X-ray absorption spectroscopy (XAS)

XAS is one of the most informative probes of the local structural environment and chemical state of the selected element in condensed or vapor phases. XAS is performed by scanning the energy range corresponding to the K or L-absorption edge (i.e., energy of core-level electrons) of the selected element using a synchrotron X-ray beam. The transitions of the photo-electron to higher bound-state energy levels or the backscattering of the photo-electron from the atoms surrounding the absorbing atom give rise to modulations of the X-ray absorption coefficient. Analyses of the fine structure of the absorption coefficients as a function of X-ray energy provide information on the chemical state and structural environment of the absorbing atom. Two different regions can be distinguished in the X-ray absorption spectra, although the division is purely conventional and reflects the different theoretical approaches used: 1) X-ray absorption near-edge structure (XANES), that corresponds to the region just below and up to 0.1 or 0.15 keV above the absorption edge (Figs. 7-8). The XANES part of the spectrum is sensitive to the electronic structure of the absorbing element, which changes with valence state (i.e., oxidation state) as well as with the structural arrangement and type of surrounding atoms. 2) Extended X-ray absorption fine structure (EXAFS), the fine structure occurring at energies further above the edge, extending from ca. 0.1 to 1 keV or further. The EXAFS part of the spectrum provides quantitative information on the distances between the absorbing atom and neighboring atoms as well as the number of surrounding atoms and their nature in the coordination shell.

XAS measurements are conducted in transmission or fluorescence mode. In transmission, changes of the beam intensity after passing thorough sample are monitored. This approach requires optimized thickness and is preferred for concentrated samples, i.e., when the element of interest is a major component in the system. In dilute system (for example, trace elements in fluids), monitoring the X-ray fluorescence emitted by the atoms is the preferred technique. In fluorescence mode, the x-ray signal emitted by the sample contains the contribution of elastically (Rayleigh) and inelastically (Compton) scattered X-rays in addition to the fluorescence signal. While fluorescence emission is isotropic, the scattering contribution is not, due to the polarization of the synchrotron X-ray. Scattering will be minimized at 90 degrees to the incident beam in the horizontal plane, thus increasing the sensitivity of the XAS analysis (Als-Niels and McMorrow 2001; Bunker 2010 for details).

XAS measurements in high-pressure fluids

Since the pioneer high-pressure XAS measurements by Ingalls et al. (1981), a number of studies have been performed on aqueous systems both at subcritical and supercritical conditions (e.g., Fulton et al. 1996; Seward et al. 1996; Bassett et al. 2000a, 2005; Pokrovski et al. 2013). High-pressure-temperature cells have been conceived for XAS analysis but most of the measurements have been restricted to pressure-temperature conditions close to the liquid-vapor coexistence curve (e.g., Mosselmans et al. 1996; Seward et al. 1996; Sherman et al. 2000 and references cited), or to conditions typically below 0.05-0.1 GPa at 773 K (e.g., Fulton et al. 1996; Hoffmann et al. 2000; Pokrovski et al. 2013 and references cited) in dilute hydrothermal solutions.

Diamond anvil cells (Bassett et al. 1993) are better adapted for studying ion speciation at the pressures, temperatures (> 0.5 GPa and > 1000 K), and fluid compositions relevant to processes in subduction zones. However, the standard design of the diamond anvil cell has two major limitations for XAS analysis. First, the typical 2 mm thickness of the diamond windows limits the analysis of dilute systems in transmission to relatively heavy elements having X-ray energies above 11 keV (~As K-edge) (Fig. 5). Second, the impossibility of accessing the samples through the metallic gasket that confines the highly reactive fluids precludes collection of XAS in fluorescence mode in the optimal 90 degrees geometry, where the sensitivity of the analysis is maximal and the detection limits are lowest (Fig. 6).

Several modification of the diamond anvil design have been devised to overcome the limitations outlined above. To minimize the attenuation of X-rays due to absorption in transmission measurements, Bassett et al. (2000a) employed diamond anvils with a laser-milled hole ("holy diamonds") to decrease the path length of the transmitted X-ray beam through the diamond down to ~0.15 to 0.20 mm (Fig. 6A). This modification translates into an increase in the transmission by up to a factor of two at the As K-edge (Fig. 5) and permits XAS analysis from hydrothermal solutions in transmission mode at the K-edge of first row transition metals (e.g., Zn). Alternatively, Sanchez-Valle et al. (2004) showed that a reduction of the thickness of the diamond window by a factor of two (Fig. 5) decreases the attenuation due to absorption and widens the optical opening of the cell, thus permitting the collection of the fluorescence signal at 15°-30° from the incident beam (Fig. 6A to 6D). This configuration does not jeopardize the strength of the diamonds and extends the XAS analysis to higher

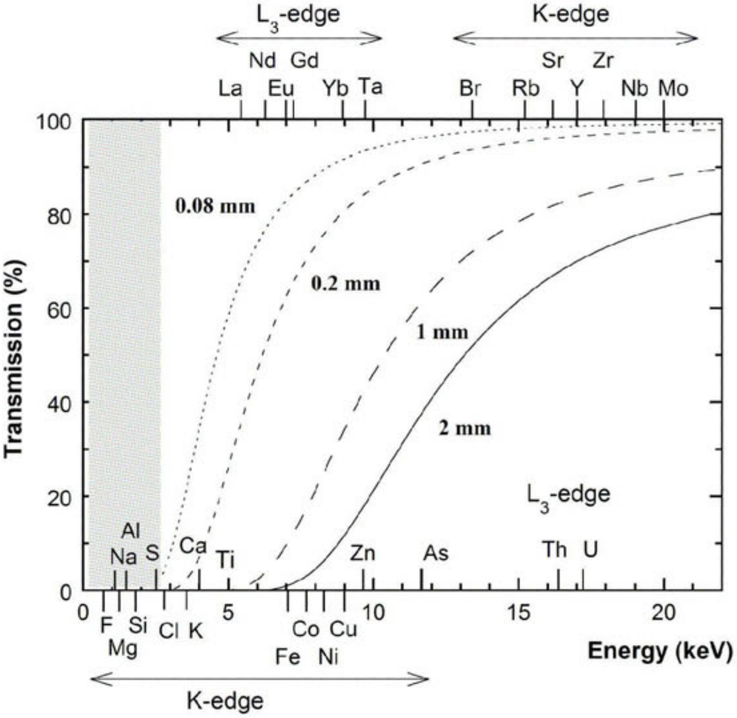

Figure 5. Transmission (in %) of X-rays as a function of energy through diamond windows of various thickness used in diamond anvil cells for XAS studies on hydrothermal fluids. The energies corresponding to the absorption edges (K or L_3) of selected trace elements and other relevant elements in fluid processes in subduction zones are indicated. The gray shaded area indicates the opacity range of diamond anvil cells for X-rays. The absorption edges of major elements in subduction zone fluids (Si, Al, Na) and relevant ligands (S, Cl, F) are below 3 keV, thus precluding speciation studies by XAS at high *P-T* conditions in diamond anvil cells.

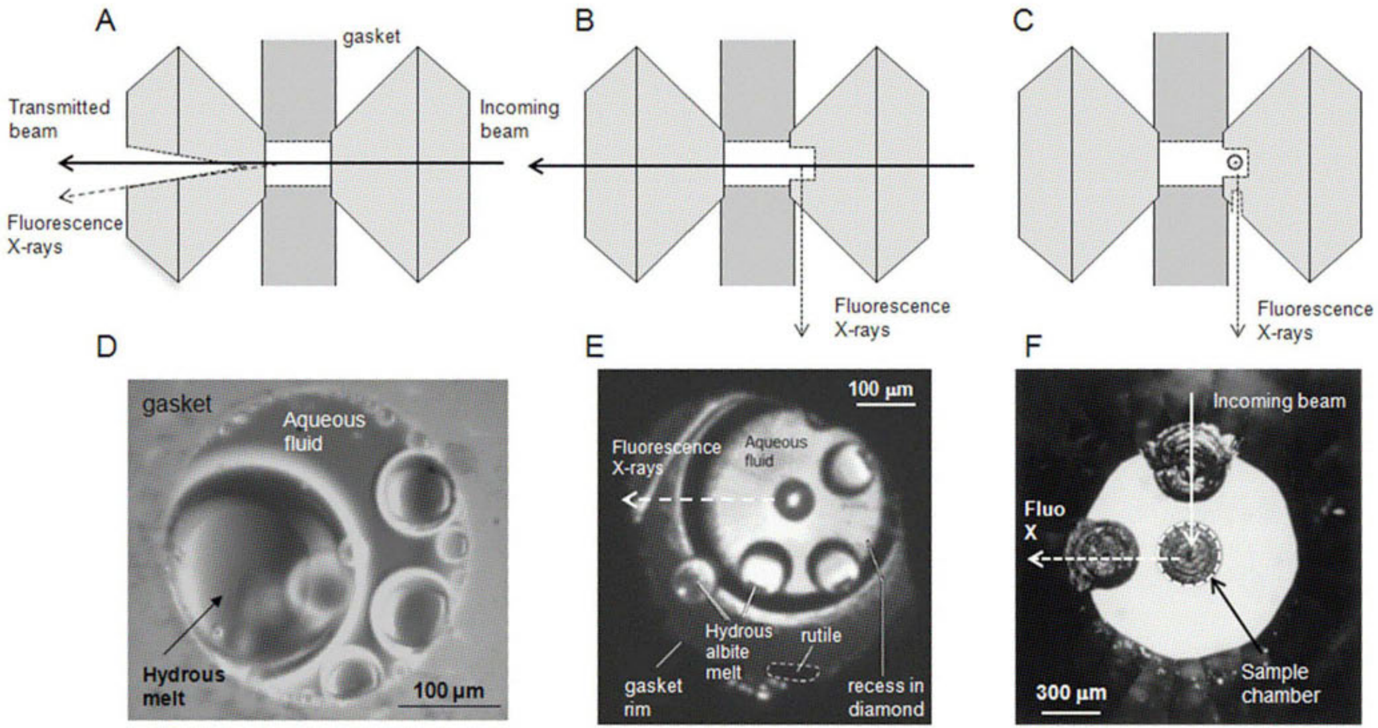
A
gasket
Transmitted beam
Incoming beam
Fluorescence X-rays
B
Fluorescence X-rays
C
Fluorescence X-rays
D
gasket
Aqueous fluid
Hydrous melt
100 µm
E
100 µm
Fluorescence X-rays
Aqueous fluid
Hydrous albite melt
rutile
gasket rim
recess in diamond
F
Incoming beam
Fluo X
300 µm
Sample chamber

Figure 6. (A-C) Schematic representation of the different collection geometries and modified diamond anvils used for XAS analysis of hydrothermal fluids in the diamond anvil cell. In C, the incoming beam arrives perpendicular to the plane of the figure at 90° from the outgoing fluorescence beam. (D-F) Microphotographs showing the sample chamber arrangement in the corresponding collection geometries. (D) Hydrous haplogranitic melt globules coexisting with an aqueous fluid at 1073 K and 2 GPa. (E) Hydrous albite melt globules coexisting in the sample cavity (300 µm diameter, ~50 µm depth) milled in the center of the diamond culet {Used with permission of Elsevier from Manning et al. (2008), *Earth Planet Sci Lett*, Vol. 272, p. 730-737, Fig. 1.]. (F) Details of the laser-milled diamonds for fluorescence XAS analysis of low Z elements. In addition to the sample cavity drilled in the culet (as in picture E), two grooves are milled at 90°. The incoming X-ray beam arrives through the top groove and the fluorescence signal emitted by the sample reaches the detector through the other groove, after passing out only through ~0.08 mm diamond to minimize the attenuation of the signal [Used with permission of Oldenbourg Wissenschaftsverlag GmbH from Bassett et al. (2000b) *Z Kristallogr*, Vol. 215, p. 711-717.]

pressures, albeit with a significant reduction in the sensibility of the analysis and limited access to energy edges below 10 keV (Louvel et al. 2013).

Further modifications of the diamond anvil design were introduced by Bassett et al. (2000b) and Schmidt and Rickers (2003) for XAS collection in fluorescence mode at 90 deg from the incoming beam, thereby increasing the sensitivity of the analysis (i.e., lowering the detection limits). Schmidt and Rickers (2003) employed diamonds with a laser-milled recess (~0.035 mm depth) in the center of the culet (Fig. 6B). Only the sample portion contained in the recess is probed (Fig. 6E). Before reaching the detector, the path through the diamond anvil still induces significant attenuation of the fluorescence X-rays and XAS studies have only been performed above the Fe K-edge (Wilke et al. 2006, 2012). Bassett et al. (2000b) extended the XAS analysis under pressure to lower energy edges by employing a more sophisticated configuration in which the diamonds have two additional laser-milled grooves oriented at 90° from each other as illustrated in Figure 6F. The grooves provide access for the incident and fluorescence X-ray with a minimum of diamond (~ 0.08 mm) in the path, significantly enhancing the transmission of the fluorescence signal as seen in Figure 5. This new design of diamond anvils enabled the study of the local structure around REE (5.8-8.9 keV) in diluted solutions (e.g., 0.06 *m* $GdCl_3$) up to 773 K and 0.52 GPa (Mayanovic et al. 2007a), and hold potential for studies below the Ti^{4+} K-edge (Fig. 5).

The developments described above have opened new possibilities to investigate directly the structural environment of a wider range of geochemically relevant elements at pressure-temperature conditions corresponding to fluid processes in the crust and shallow upper mantle, including subduction zones. An important experimental limitation of XAS for high-pressure speciation studies in the diamond anvil cell, however, is the difficulty of probing the local environment of elements with atomic numbers below that of Ti^{4+} (Fig. 5). Unfortunately, this includes the geochemically important elements Ca, Mg and K, as well as the major components in subduction zone fluids, Si, Al, Na, and major ligands, such as S, Cl or F, whose absorption edges fall below 3 keV (Fig. 5).

SPECIATION OF TRACE ELEMENTS IN SUBDUCTION ZONE FLUIDS

Studies of the speciation of trace elements in subduction zone fluids have mainly focused on HFSE and REE as major groups of geochemical tracers. An overview of the major trends on the speciation of representative trace elements of these groups is provided to further discuss implications for their mobilization and fractionation in subduction-related processes.

Speciation of High Field Strength Elements (HFSE)

Interest in understanding the speciation of HFSE in subduction zone fluids stems from their unique role as tracers of mass and heat transfer in subduction zones and the need to understand the processes that cause the characteristic HFSE depletion in arc magmas to constraint the conditions of formation.

***Zirconium* (Zr^{4+}).** Among the HFSE, Zr^{4+} has received the most of attention in terms of speciation studies in high-pressure aqueous fluids and hydrous silicate melts that are simplified analogs for fluids produced by the dehydration and melting of subducting slabs. Wilke et al. (2012) and Louvel et al. (2013) investigated the effect of fluid composition and pH on the speciation of Zr^{4+} at pressure and temperature conditions up to 1073 K and 2.4 GPa. Both studies demonstrated a strong compositional dependence of the speciation of Zr^{4+} in high-pressure fluids.

Figure 7 shows examples of XANES spectra of Zr-bearing aqueous fluids and hydrous melts at various pressures and temperatures, together with selected reference crystalline compounds. The spectra display noticeable differences in the shape and position of the absorption edge

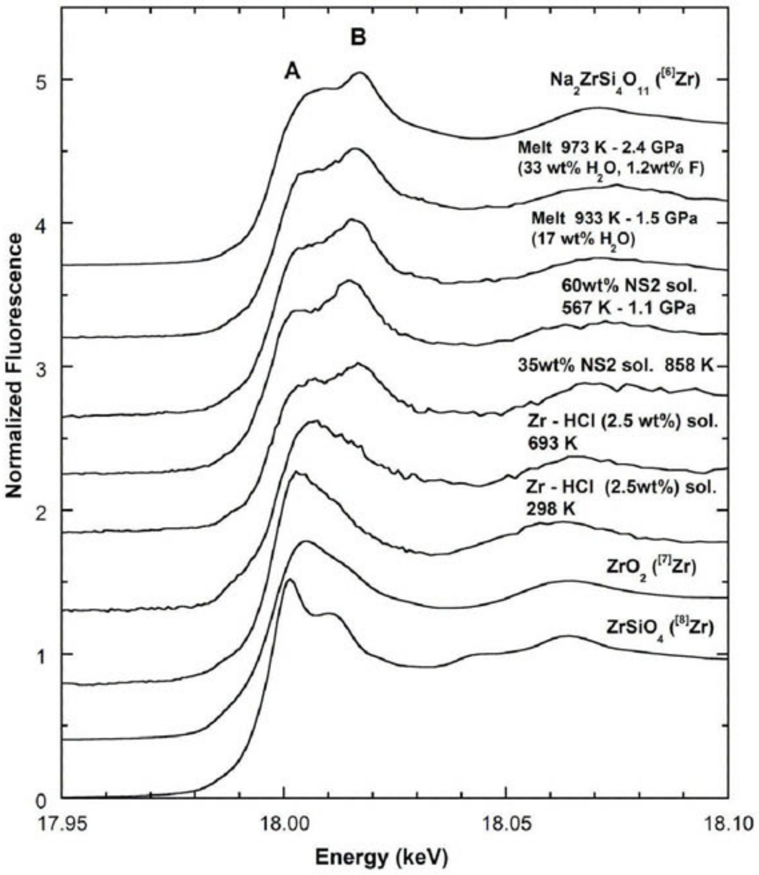

Figure 7. Normalized Zr^{4+} K-edge XANES spectra acquired *in situ* in Cl-bearing (referred to as Zr-HCl 2.5 wt% sol.), $Na_2Si_2O_5$-bearing aqueous fluids (NS2 sol.) and hydrous haplogranite melts (± fluorine) at various pressures and temperatures. Amounts of HCl, NS2 in the fluids, and H_2O and fluorine in the haplogranite melt are given in wt%. Spectra of reference crystalline compounds at ambient conditions, vlasovite ($Na_2ZrSi_4O_{11}$, $^{[6]}Zr$), baddeleyite (ZrO_2, $^{[7]}Zr$) and zircon ($ZrSiO_4$, $^{[8]}Zr$), are shown for comparison (redrawn from Louvel et al. 2013).

crest, which splits into two components (A and B) with variable relative intensities depending on Zr^{4+} coordination. In crystalline compounds with 8-fold Zr^{4+} coordination by oxygen (ZrO_8 sites, hereafter referred to as $^{[8]}Z$) such as zircon $ZrSiO_4$, feature A displays maximal intensity whereas feature B dominates the absorption edge in samples with 6-fold Zr^{4+} coordination (ZrO_6 sites) such as $NaZrSi_2O_{11}$ (vlasovite). In ZrO_2 (baddaleyite) with 7-fold Zr^{4+} coordination (ZrO_7 sites, $^{[7]}Zr$) the absorption crest is much broader but feature A displays maximal intensity. The contribution of next-nearest neighbors (Si and/or Na for zircon and vlasovite, and Zr for baddaleyite) to the shape of the Zr^{4+} absorption edge in the model has been shown by *ab initio* XANES calculations (Louvel et al. 2013).

The XANES spectra are very sensitive to Zr^{4+} local structure and can be thus used as a first proxy for the local coordination of Zr^{4+} in high-pressure aqueous fluids and hydrous silicate melts (Fig. 7). In low-pH aqueous fluids (2.5 wt% HCl), the spectra display very similar features to those of baddaleyite ($^{[7]}Zr$) and $ZrOCl_2{\cdot}8H_2O$ ($^{[8]}Zr$) (not shown, see Wilke et al.

2012), consistent with the presence of the $[Zr(H_2O)_8]^{4+}$ aqua ions in dilute fluids (Messner et al. 2011). *Ab initio* XANES calculations $^{[8]}Zr$ clusters as found in $ZrSiO_4$ and $ZrOCl_2{\cdot}8H_2O$ (distances Zr–O = 2.13-2.27 Å) and of the $[Zr(H_2O)_8]^{4+}$ aqua ion (distances Zr–O = 2.20 Å and Zr–H = 2.89 Å, Messner et al. 2011) reproduce well the main features of the experimental spectra (Fig. 8A), further supporting the speciation model (Fig. 9A). The larger width and asymmetry of the experimental absorption crest is consistent with disorder in the first hydration shell of Zr^{4+} aqua ions. Zirconium speciation appears to be rather insensitive to the pH in dilute aqueous solutions. The $[Zr(H_2O)_8]^{4+}$ aqua ion is stable in sulfur- and/or Cl-bearing fluids at neutral to acidic conditions (Kanazhevskii et al. 2006; Wilke et al. 2012; Louvel et al. 2013). A decrease in the hydration number to 7 was reported in high pH solutions with 6 wt% dissolved NaOH (Wilke et al. 2012).

The addition of dissolved alkali-silicate components to the aqueous fluid induces strong changes in the speciation of Zr^{4+}, as recorded by changes in the shape of the XANES spectra (Fig. 7). Changes are consistent with a reduction in the Zr^{4+} coordination number from 8 to 6 and with the incorporation of Si and Na ions into the second coordination shell (Fig. 9B) to form ZrO_6-Si/Na clusters similar to those observed in $Na_2ZrSi_4O_{11}$ (vlasovite) (Louvel et al. 2013) and Zr-bearing silicate glasses (Farges et al. 1991; Louvel et al. 2013). Zircono alkali-silicate ZrO_6-Si/Na clusters are thus energetically more favorable than $[Zr(H_2O)_8]^{4+}$ aqua ions in silicate-bearing high-pressure aqueous fluids. Wilke et al. (2012) observed the formation of Zr-O-Si/Na complexes in fluids containing about 18 wt% dissolved silicates (17 wt% $Na_2Si_3O_7$ + 1 wt% Al_2O_3) but the minimal concentration for the onset of complexation has not been constrained. The incorporation of Zr^{4+} into polymerized domains in the fluid is a favorable mechanism for the enhanced solubility of $ZrSiO_4$ in silicate-bearing aqueous fluids

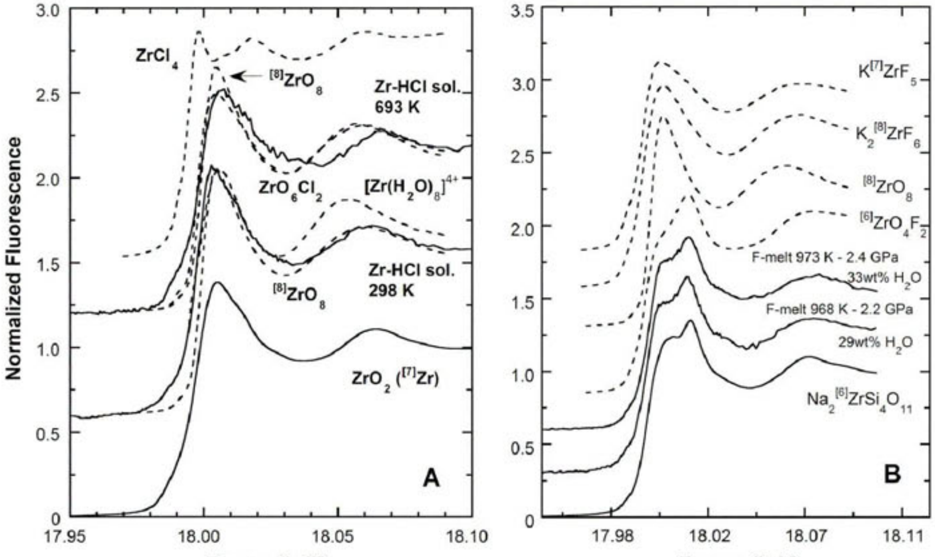

Figure 8. Complexation of Zr^{4+} with halogens in subduction zone fluids. (A) Experimental Zr^{4+} K-edge XANES spectra collected on Zr-HCl (2.5 wt% HCl) aqueous solutions at 298 and 693 K (black lines) vs. *ab initio* calculated XANES spectra (dashed lines) of various $ZrO_{8-x}Cl_x$ clusters (with $x = 0, 2$), $[Zr(H_2O)_8]^{4+}$ aqua ion and $^{[8]}ZrCl_4$. (B) Experimental XANES spectra on F-bearing hydrous silicate melts (black lines) vs. *ab initio* calculated XANES spectra of various ZrO_x, ZrF_y and ZrO_xF_y clusters (redrawn from Louvel et al. 2013).

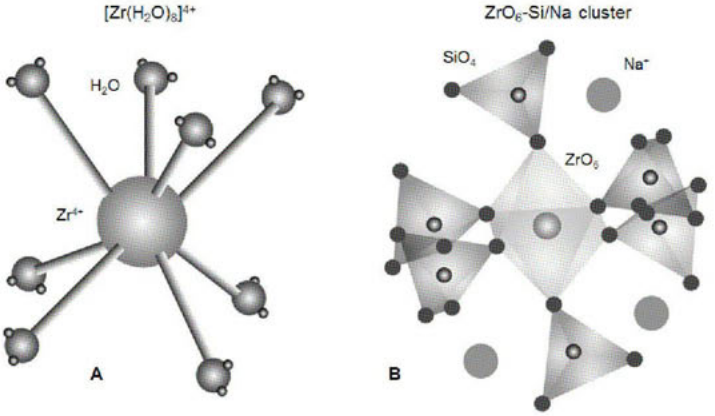

Figure 9. Structure of Zr^{4+} aqua ion $[Zr(H_2O)_8]^{4+}$ (A) and alkali-zirconosilicate complexes (B) as identified from XAS studies on model subduction zone fluids. $[Zr(H_2O)_8]^{4+}$ dominates Zr^{4+} speciation in dilute aqueous fluids; ZrO_6-Si/Na cluster are observed in silicate-bearing aqueous fluids, hydrous silicate melts and supercritical fluids. Cluster parameters obtained from EXAFS data analysis (Louvel et al. 2013) are: distance Zr-O= 2.09 ± 0.04 Å, and Zr-Si/Na distance of 3.66 ± 0.06 Å.

(Wilke et al. 2012). These complexes also dominate Zr^{4+} speciation in high-pressure F-free and F-bearing hydrous haplogranite melts (15.5-33 wt% dissolved H_2O) and they are stable at crustal and upper mantle conditions.

The occurrence of Al^{3+} in substitution of Si^{4+} in the ZrO_6-Si/Na cluster (Fig. 9B) has not been resolved from the available EXAFS data, that yield similar Zr^{4+} coordination numbers and inter-atomic distances for cluster in $Na_2Si_2O_5$-bearing fluids (without Al^{3+}) and in hydrous haplogranite melt (with Al^{3+}) (Louvel et al. 2013). However, the negative correlation between zircon solubility and Al_2O_3 content of the fluid reported by Wilke et al. (2012) further suggest that Al^{3+} is not incorporated to the ZrO_6-Si/Na cluster.

In Cl-bearing high temperature, dilute fluids (Fig. 8A), the chlorination of Zr^{4+} is not extensive and, at most, two Cl^- ions replace the water ligands in the first coordination shell. This conclusion was drawn from a comparison of the experimental spectra with *ab initio* calculations of the XANES spectra of $ZrO_{8-x}Cl_x$ clusters (Louvel et al. 2013). In more concentrated HCl-bearing aqueous fluids (16 wt% HCl) equilibrated with quartz, an increase in the extent of chlorination was reported by Wilke et al. (2012), with $[Zr(H_2O)_4Cl_3]^+$ being the dominant species in these conditions.

Whether Zr (and other HFSE) forms stable complexes with fluorine in silicate melts has been a matter of debate over the last 20 years and remains unclear in light of the high-pressure XAS data of Louvel et al. (2013) (Fig. 8B). The increase in the solubility of HFSE minerals with increasing F^- content in granitic melts reported by Keppler (1993) was explained by the depolymerization of the silicate network due to the reaction of F^- with Al^{3+} to form AlF_6^{-3} complexes. This mechanism increases the number of non-bridging oxygen (NBO) that favor the dissolution of Zr^{4+} in the melt. Alternatively, Keppler (1993) suggested direct complexation between Zr^{4+} and F^- in the melt to explain the enhanced solubility. XAS studies by Farges (1996) in F-bearing silicate glasses did not show clear evidence for fluorine first neighbors around Zr^{4+}, although the author concluded that the EXAFS analysis could discriminate between Zr–O and Zr–F bonds if complexation is extensive. However, the XANES data reported in Figure 7 show strong similarities between F-free and F-bearing hydrous haplogranite melts, and structural parameters derived from the EXAFS data analysis remain indistinguishable within errors (Louvel et al. 2013). Moreover, the *ab initio* XANES spectra calculated for various Zr-oxyfluoride clusters (ZrO_x, ZrF_x and ZrO_xF_y) (Fig. 8B) further suggest the limitations of XAS analysis to identify Zr-F complexes at low (~1.2 wt%) fluorine concentrations, even though they cannot not be ruled out.

Niobium (Nb^{5+}) and Tantalum (Ta^{5+}). Mayanovic and co-workers (2007b, 2013) investigated the speciation of Nb^{5+} in hydrous silicate melts and that of Ta^{5+} in hydrous haplogranite silicate melts and coexisting aqueous fluids at high-pressure. Their XANES data on high-pressure hydrous silicate melts are consistent with the occurrence of Nb^{5+} and Ta^{5+} in regular metal-O_6 moieties that share corners with SiO_4 tetrahedral units, similar to the Zr^{4+} complex shown in Figure 9B and similar to those reported in Nb-bearing glasses of peralkaline to peraluminous compositions (Piilonen et al. 2006). TaO_6-Si/Na clusters also dominate the speciation of Ta^{5+} in aqueous fluids (Mayanovic et al. 2013) and most likely that of Nb^{5+}, although spectroscopic support is not available.

Titanium (Ti^{4+}). XAS studies of the speciation of Ti^{4+} in subduction zone fluids are not available because measurements remain challenging in dilute systems at the low energies of the Ti^{4+} K-edge (Fig. 5). Some information about the plausible speciation Ti^{4+} in subduction zone fluids has been derived from theoretical (van Sijl et al. 2010) and Raman spectroscopy studies (Mysen 2012) and available information for Ti^{4+}speciation in silicate glasses/melts.

An increase in Ti^{4+} hydration number in water from 5-fold at ambient conditions to 6-fold at 1000 K and 3.6 GPa as the density of the solvent increases was reported by van Sijl et al. (2010). In alkali-rich aluminosilicate glasses and melts, Ti^{4+} is mainly found as 5-fold coordinated Ti-O-(Si/Na/Al) clusters (Farges et al. 1996; Farges and Brown 1997) with oxygen in square-prismatic configuration (i.e., 1 Ti=O bond of 1.7 Å and 4 Ti–O bonds of 1.95 Å). Larger proportions of 6- and 4-fold coordinated Ti^{4+} are identified in less polymerized (basaltic and trachytic) and more polymerized (rhyolites and tektites) compositions, respectively (Farges and Brown 1997). Based on these observation and on TiO_2 rutile solubility data in albite- and nepheline-bearing aqueous fluids, Antignano and Manning (2008) proposed that $NaOTi(OH)_4^-$ species with 5-fold coordination of Ti^{4+} are energetically favorable in these fluids. Alternatively, Hayden and Manning (2011) suggested tetrahedral coordination of Ti^{4+} in the fluid due to the possibility of substituting Ti^{4+} by 4-fold coordinated Al^{3+} and Si^{4+} in Si-Al-Na clusters formed in aqueous solutions (Manning 2004a,b, 2007; Newton and Manning 2008b; Mibe et al. 2008). Investigations of Ti^{4+} complexation in coexisting hydrous silicate melts and aqueous fluids in the Na_2O-Al_2O_3-SiO_2-H_2O-TiO_2 system to 1173 K and 2.2 GPa by Raman and FTIR spectroscopy (Mysen 2012) indicate 4- or 5-fold coordination with oxygen in $Q^0{}_{Ti}(Na)$ units (see below). The solubility mechanism of rutile in melts, silicate-bearing aqueous fluids and supercritical fluids inferred from the spectroscopic data is described by the reaction:

$$4Q^1{}_{Si}(Na) + 4H_2O \leftrightarrow 4Q^0{}_{Si}(HNa) + Q^0{}_{Ti}(Na) \tag{7}$$

where Q refers to the oxygen coordination polyhedral around the central cations indicated by subscripts denote and superscripts denote the number of bridging oxygens; the symbol in parentheses is the type of cation that forms bonds with non-bridging oxygen in the Q-species.

As noted by Mayanovic et al. (2013), the picture that emerges from the studies on Zr^{4+}, Ta^{5+}, Nb^{5+} and Ti^{4+} is that highly charged cations coordinate with Q-species in units with preferred symmetry (6-, 5-, 4-fold) in the fluid, and that the local structure is preserved upon cooling from a highly depolymerized silicate-rich aqueous fluid into a polymerized hydrous silicate melt and finally into highly polymerized silicate glasses.

Speciation of Rare Earth Elements (REE)

Experimental studies of the speciation of REE (i.e., lanthanides and Y) at moderate pressures (typically vapor saturation) in hydrothermal fluids (e.g., Wood 1990; Gammons et al. 2002; Migdisov et al. 2009 and references cited) have been motivated by the need to better understand the mobility and transport of REE at shallow depths and the chemical controls on REE hydrothermal ore deposition (Taylor and Fryer 1982; Williams-Jones et al. 2000). Only a few studies have addressed the speciation of REE at higher pressures relevant to subduction zones and the speciation in more complex silicate-bearing aqueous fluids remains largely unknown.

Advances in understanding the speciation of trivalent REE ions (Nd^{3+}, Yb^{3+}, Eu^{3+}, La^{3+}, Gd^{3+}) in hydrothermal solutions at higher pressures resulted from a series of XAS studies conducted to 773 K and 0.52 GPa by Anderson et al. (2002) and Mayanovic et al. (2002, 2007a,b, 2009). In Cl-free aqueous solutions, the EXAFS analyses show evidence for a contraction of the REE-O distance in the aqua ion $[REE(H_2O)_\delta]^{3+}$ (with $\delta = 9$ for Nd^{3+}, Eu^{3+}, Gd^{3+} and La^{3+}, and $\delta = 8$ for Yb^{3+} and the uniform reduction of the first hydration shell water molecules from room temperature to 773 K (Fig. 10A). The number of hydration water molecules decreases moderately from 9.0 ± 0.5 to 7.0 ± 0.4 in Gd^{3+} (Mayanovic et al. 2007a), while a more dramatic reduction of the H_2O ligands from 8.3 ± 0.5 to 5.1 ± 0.3 is observed (Fig. 10) for Yb^{3+} over the same pressure-temperature range (Mayanovic et al. 2009). The extent of dehydration with temperature is element-dependent and reflects the stability of the aqua REE ions: $[Gd(H_2O)_9]^{3+} > [Nd(H_2O)_9]^{3+} > [Eu(H_2O)_9]^{3+} > [Yb(H_2O)_8]^{3+}$. The stability trend is consistent with the "tetrad effect" for REE complexes in aqueous solvents that originates from differences in the occupancy of the 4f electronic levels across the lanthanide series (Nugent 1970; Kawabe 1992).

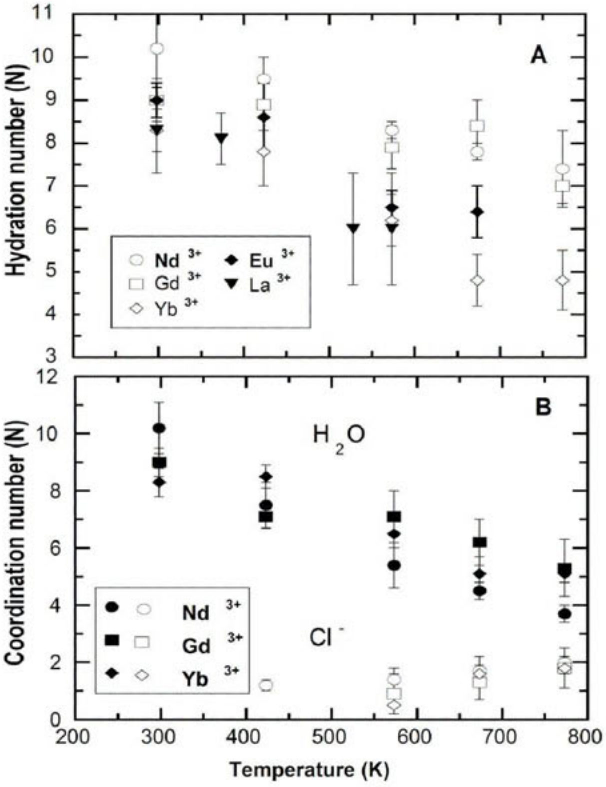

Figure 10. (A) Hydration number for REE^{3+} in chloride-free solutions and (B) average H_2O and chloride ligands in the coordination shell of REE in low pH chlorinated aqueous solutions under pressure to 773 K. Stepwise inner-shell chloroaqua complexes $[REE(H_2O)_{\delta-n}Cl_n]^{+3-n}$ (with $\delta = 9$, 8,7 for Nd^{3+}, Gd^{3+} and Yb^{3+}) form in chlorinated solutions above 423 K. The higher chlorination number of Nd^{3+} compared to Yb^{3+} or Gd^{3+} indicates higher stability of LREE-chloro over HREE-chloro complexes (B). Data source: Nd^{3+} (Mayanovic et al. 2009); Gd^{3+} (Mayanovic et al. 2007); Yb^{3+} (Mayanovic et al. 2002).

Experiments conducted in low pH chlorinated fluids show a progressive replacement of first shell H_2O ligands by Cl^- ions in the coordination shell as temperature increases (Figs. 10 and 11), consistent with the stepwise formation of complexes of the type $[REE(H_2O)_{\delta-n}Cl_n]^{+3-n}$ following the reaction:

$$[REE(H_2O)_{(d)}]^{3+} + nCl^- \leftrightarrow [REE(H_2O)_{\delta-n}Cl_n]^{+3-n} + nH_2O \tag{8}$$

where $\delta = 9$, 8 and 7 for Nd^{3+}, Gd^{3+} and Yb^{3+}, respectively, and n ranges from 0 to 3 (Mayanovic et al. 2002, 2007a, 2009). In a 0.05 *m* $NdCl_3$ solution, the number of water ligands decreases from 7.5±0.8 to 3.7±0.3 while the Cl^- number increases from 1.2±0.2 to 2.0±0.2 from 423 to 773 K (Mayanovic et al. 2009). Figure 11 depicts the structure of $Yb(H_2O)_5Cl_2^+$ chloroaqua complex identified by XAS as the dominant Yb^{3+} species in low pH chlorinated hydrothermal solutions from 573 to 772 K up to 0.52 GPa. The experimental datasets for Nd^{3+}, Gd^{3+} and Yb^{3+} allow comparing the relative stability of REE^{3+} chloroaqua complexes in the system (Fig. 10). Nd^{3+} displays increased association with chloride and thereby greater chloride complex stability in comparison with Yb^{3+} or Gd^{3+} under hydrothermal conditions. The results of Mayanovic and co-workers indicate greater stability of LREE chloride complexes than HREE chloride complexes in low pH hydrothermal fluids, in agreement with studies at lower pressures (Gammons et al. 2002; Migdisov et al. 2009) and earlier theoretical calculations (Wood 1990).

The progressive dehydration and contraction of the hydration shell with increasing temperature are common features experimentally observed in the local structure of various ions in hydrothermal solutions (e.g., Ag, Sr, Zn, Fe), including at much moderated pressures (e.g., Seward et al. 1996, 1999; Mayanovic et al. 2003). The relaxation of the hydration shell is a consequence of the depression of ion-solvent interactions and concomitant enhancement of long-range electrostatic ion-ion interactions in the fluid that facilitate the incorporation of Cl ligands in the first coordination shell (Figs. 10-11).

Constraints on REE^{3+} speciation at higher pressure and temperature have been provided by the *ab initio* calculations of van Sijl et al. (2009) who examined the energetics of REE^{3+}

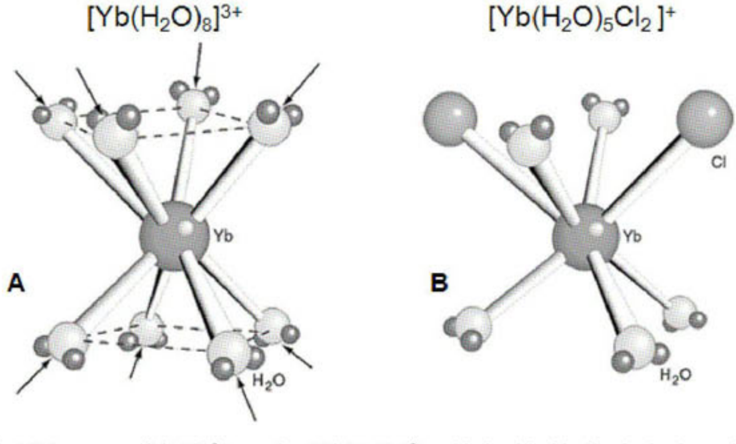

Figure 11. (A) Structure of the Yb^{3+} aqua ion $[Yb(H_2O)_8]^{3+}$ stable in chloride-free hydrothermal solutions to 423 K and (B) stepwise Yb^{3+} chloroaqua complex $[Yb(H_2O)_5Cl_2]^+$ dominant in low pH chloride-bearing aqueous solutions at 773 K. The arrows indicate the contraction of the H_2O molecules towards the Yb^{3+} aqua ion with temperature, which is accompanied by a reduction in the hydration number from 8 at 298 K to 5 at 773 K in chloride-free fluids [Redrawn with permission of the American Chemical Society after Mayanovic et al. (2002) *J Phys Chem A*, Vol. 106, p 6591-6599, Fig 8.]

hydration and complexation with Cl^- and F^- ligands at pressures in excess of 2.5 GPa at 1000 K, with more direct implications for the mobilization and transport of REEs in deeper parts of subduction zones. An increase in temperature and dielectric constant ε of the fluid with depth along typical subduction geotherms (e.g., SW Japan, Peacock and Wang 1999) results in an increase in the hydration free energy of aqua REE ions $[REE(H_2O)_{8,9}]^{3+}$: large hydration numbers become less favorable with increasing temperature, consistent with the experimental observations (Fig. 10). More interestingly, the simulations indicate that with an increase in water density beyond the range experimentally investigated, the extent of dehydration is similar for all lanthanides. This observation has important consequences for the fractionation between LREE and HREE by high-pressure fluids that will be discussed below. Additionally, the data of van Sijl et al. (2009) show that REE complexation with fluoride is energetically more favorable than with chloride, a conclusion also reached from solubility studies conducted at much lower pressures (Migdisov et al. 2009).

MOBILIZATION AND FRACTIONATION OF TRACE ELEMENTS IN SUBDUCTION ZONES

High Field Strength Elements (HFSE)

The occurrence of rutile and zircon in veins in ultra-high-pressure metamorphic rocks exhumed from subduction zones (e.g., Rubatto and Hermann 2003; Gao et al. 2007) and the experimental studies of mineral solubility cited above provide evidence for the efficient mobilization of "refractory" HFSE in subduction zones by water-rich fluids. Therefore, melting of the slab would not be necessary to recycle them in subduction settings. The speciation studies discussed above identify HFSE-O-Si/Na complexes in aqueous fluids as a favorable mechanism for the mobilization and transport of "immobile" HFSE during fluid-rock interactions in the lower crust/upper mantle. The effectiveness of HFSE uptake and transport in subduction zones are mainly controlled by the nature and composition of the mobile agent.

A high alkali/Al will favor the formation of HFSE-O-Si/Na species that may be efficient agents for the large-scale transport of HFSE (Wilke et al. 2012). The concentration of dissolved silicates required for the effective mobilization of HFSE by slab derived fluids can be roughly estimated based on a series of TiO_2 solubility measurements as a function of fluid composition reported by Hayden and Manning (2011). Concentrations above 20 wt% of dissolved silicate are at the threshold for the enhanced rutile solubility in aqueous fluids, consistent with the spectroscopic evidence for HFSE-O-Si/Na complexation (Wilke et al. 2012; Louvel et al. 2013). This estimate implies that the relatively dilute fluids expelled at shallow depths (<5 wt% dissolved solutes) with less than do not provide the most favorable environment to mobilize and transport HFSE in subduction zones.

Enhanced mineral solubility with pressure and temperature is accompanied by a significant increase of polymerization of dissolved alkali aluminosilicate components in the aqueous fluids even at sub-solidus or subcritical conditions (Manning et al. 2010). High-pressure solute-rich aqueous fluids (20-30 wt% dissolved silicates), or supercritical fluids (> 30-60 wt% dissolved silicates) if the subduction path intersects the temperature-pressure conditions of the critical curves (Hack et al. 2007), will favor the extraction of HFSE from the slab. However, the lower density and viscosity of silicate-bearing aqueous fluids compared to supercritical phases (Hack and Thompson 2011) will facilitate upward migration and percolation from the top of the slab to the mantle wedge and thus will be more efficient for HFSE transport in subduction zones despite their lower HFSE load.

The picture that is emerging from the arguments discussed above is that the depletion in HFSE that characterizes arc magmas (McCulloch and Gamble 1991) cannot be explained by

HFSE segregation into refractory and non-soluble accessory phases in the slab (Kelemen et al. 1990; Rudnick et al. 2000; Rubatto and Hermann 2003). Slab-derived aqueous fluids likely undergo major compositional changes while migrating through the mantle wedge that result in a loss of HFSE on their path to the source of arc magmas. Hydration reactions in the mantle wedge consumes the slab-derived fluids and likely induce changes in silica activity and/or Na/Al concentrations in the fluid that could affect the stability of HFSE-O-Si/Na complexes, eventually leading to precipitation of the slab-derived solute in the hydrated mantle adjacent to the top of the slab (Manning 2004a; Hack and Thompson 2011). Although HFSE could be remobilized by dehydration-hydration or dissolution-crystallization processes in the mantle wedge, it is likely that the hydrated peridotites at the top of the slab are ultimately recycled down to the transition zone with the subducting slab, preventing HFSE from reaching the source of arc magmas.

Mobilization of REE and LREE/HREE fractionation

Although the speciation studies discussed above are limited to dilute halogen-bearing fluids, they exercise some constraints on the mobilization of REE and the role of ligands on the LREE/HREE fractionation by subduction zone fluids. An interesting results with important consequences for the fractionation between LREE and HREE by high-pressure fluids was derived from the theoretical speciation studies of van Sijl et al. (2009). While LREE form more stable complexes with water than HREE (Yb^{3+}) below 0.5 GPa, at upper mantle conditions (2.5 GPa, 1000 K) the decrease in the extent of hydration of REE occurs at an equal rate for all REE. Based on this observation, changes in water density at the conditions of the slab surface will not affect the fractionation between LREE and HREE (van Sijl et al. 2009), and therefore, other ligands (namely Cl^-, F^-, CO_3^{2-} or SO_4^{2-}) may play an important role in the mobilization and selective fractionation of REE at depth. The higher stability of LREE chloride complexes relative to HREE chloride complexes observed below 0.5 GPa (Fig. 10) will be consistent with an enrichment in LREE in chlorinated aqueous fluids released at shallow depths. Whether the complex stability trend (LREE > HREE) persists at higher depths or a more uniform behavior as observed in water is to be expected, remains unclear and would require further studies. Additional constraints on the effect of other ligands such as F^-, CO_3^{2-} or SO_4^{2-} that form stronger complexes with REE than Cl^-, and the role of polymerized silicate units on the mobilization and fractionation of REE at high-pressure requires further investigation to establish the link between slab fluids and the characteristic REE spectrum of arc magmas.

PRESSURE-VOLUME-TEMPERATURE-COMPOSITION (*PVTx*) RELATIONS AND THERMODYNAMIC PROPERTIES OF AQUEOUS FLUIDS

Modeling fluid-mineral interactions to quantify mass transfer in high-pressure settings requires knowledge of the volumetric, thermodynamic, and transport properties of aqueous fluids over wide ranges of temperature, pressure and compositions. Both equations of state (EoS) and experimental data for the *PTVx* properties of aqueous fluids are available, but rarely encompass the pressure-temperature and compositions relevant for fluid processes in subduction zones. Theoretical and experimental limitations to extend the range of validity of EoS to high pressures are briefly discussed below.

Equations of state (EoS) for aqueous fluids

A thorough review of the most commonly employed EoS in geochemistry and petrology for pure fluids (e.g., H_2O, CO_2, CH_4, …) and mixtures including salt components (namely NaCl) was presented recently by Gottschalk (2007). It is noticed however that a number of these EoS have been calibrated to available volumetric data from experimental studies, typically obtained in a very limited range of pressures (< 0.5-1 GPa) (see below). The extension of these EoS to conditions relevant for fluid processes in the upper mantle have relied on extrapolations in pressure over very large ranges using empirical methods and/or constraints from molecular dynamic simulations (e.g., Holland and Powell 1991; Pitzer and Sterner 1994; Wagner and Pruß 2002). Large discrepancies are often observed between the thermodynamic properties derived from these different formulations. Equations of state for silicate-bearing water-rich fluids are virtually nonexistent, although correlations based on ideal mixing between hydrous melts and water properties have been developed to predict their density (Hack and Thompson 2011).

Molecular dynamic (MD) simulations have been applied to construct EoS for molecular fluids and their mixtures over a broad range of pressure and temperature conditions (e.g., Brodholt and Wood 1993a,b; Zhang and Duan 2005; see Gottschalk 2007 for additional references). The validity of the different interaction potentials employed in the MD simulation (Kalinichev 2001) is, however, difficult to assess due to the lack of high-pressure experimental data to test the theoretical predictions. A common test of validity for the theoretical EoS is their ability to reproduce the experimental reaction boundaries for some well characterized phase transformations involving fluid phases (e.g., Brodholdt and Wood 1993a). The application of MD simulations to explore the *PVT* properties of saline solutions has so far been limited to pressures below 0.5 GPa for the lack of experimental data to compare them to (Brodholt 1998). Experimental data on the *PVT* EoS of fluids would therefore be helpful to test and refine intermolecular/inter-atomic potentials in the fluid, which in turn provide a theoretical foundation for a more robust extrapolation of the data beyond the experimental *P-T* range of calibration.

Experimental studies of *PVTx* properties in aqueous systems

Several experimental techniques have been applied to determine the *PVTx* properties of aqueous systems at pressure-temperature conditions relevant for hydrothermal processes in crustal and shallow upper mantle setting. Data on the volumetric properties of geologically relevant pure fluids and mixtures (e.g., H_2O-NaCl, H_2O-CO_2, H_2O-NaCl-CO_2, H_2O-CO_2-CH_4, etc.) have been measured extensively at pressures below 0.5 GPa. Experimental data are much scarcer above this pressure due to experimental limitations. The main experimental methods, their pressure-temperature range of applicability, and the main datasets are discussed. Additional details can be found in the cited original references. Although shock wave methods provide a means to determine the *PVT* properties of fluids at extreme pressure and temperatures, they have been intentionally excluded from this discussion due to imprecise temperature estimations and limited application to compositions other that pure water (e.g., Lyzenga et al. 1982).

***Vibrating tube densimetry* (*VTD*).** This technique provide density measurements with high accuracy, typically better than 0.1%, based on correlations between the density of the fluid and the vibration period of a U-shaped tube that forms the core of the VTD (Albert and Wood 1984; Blencoe et al. 1996). Density data for binary chlorinated aqueous solutions (e.g., Majer et al. 1988, 1991: Simonson et al. 1994; Oakes et al. 1995), CO_2-H_2O, CH_4-CO_2 mixtures (Seitz and Blencoe 1996, 1999) have been obtained using this approach. Typical operation pressures are below 0.04 GPa at 700 K, although modifications of the tube material and wall thickness have extended the range of the density measurements up to 0.1 GPa (Seitz and Blencoe 1996, 1999).

Constant and variable volume piezometers. A number of piezometers have been developed to determine the *PVT* properties of hydrothermal fluids at *P-T* conditions typically below 773 K and 0.3 GPa (e.g., NaCl-H_2O solutions, Urusova et al. 1975 and Bischoff and Rosenbauer 1985; CO_2-H_2O, Takenouchi and Kennedy 1964). A detailed description of these devices and relevant data for hydrothermal solutions can be found in Corti and Abdulagatov

(2008). Specific volume measurements in water up to 0.9 GPa and 1173 K were conducted by Burnham et al. (1969) using a bellow densimeter in an internally heated argon-pressurized vessels (Holloway 1971). The extension of the experiments to higher pressures is limited by the need to used solid pressure media for further compression, which reduces the reliability of the volume measurements.

Synthetic fluid inclusion technique. Synthetic fluid inclusions provide a elegant technique to determining the *PVT* properties of geological fluids (Bodnar and Sterner 1987; Bodnar 1995) without the need to determine precise volumes at the temperature and pressure of interest. Rather, the volumetric properties of fluids of known composition entrapped in fractured grains of host minerals (chiefly quartz) are inferred from optical determination of phase transitions by microthermometry (Roedder 1984), assuming isochoric behavior of the inclusion. Bodnar and co-workers have provided extensive data on the phases relations and *PVTx* properties of aqueous fluids in the NaCl-H_2O (Bodnar et al. 1985; Knight and Bodnar 1989; Bodnar 1995), CO_2-H_2O (Sterner and Bodnar 1991), and CH_4-H_2O (Lin and Bodnar 2010) binaries, and ternary NaCl-H_2O-CO_2 systems (Schmidt et al. 1995; Schmidt and Bodnar 2000) over a broad range of compositions up to 0.6 GPa and 1000 K. Major shortcomings for the extension of this method to higher pressures and temperatures are the enhanced solubility of quartz and considerable deviations of the inclusion from isochoric behavior due to the thermal expansion and compressibility of the quartz host (Bodnar and Sterner 1987). To overcome these limitations, Brodholt and Wood (1994) introduced the use of corundum as the host mineral as it has a higher strength and ensures isochoric quench paths. Brodholt and Wood (1994) extended the volumetric studies on water to 2.5 GPa and 1873 K and later, Frost and Wood (1997) determined the *PVT* properties of H_2O-CO_2 fluids at 0.94-1.94 GPa and up to 1373 K. The volumetric determinations based on homogenization of two fluids (liquid-vapor) by microthermometry limits however the applicability to densities below 1 $g{\cdot}cm^{-3}$. Withers et al. (2000) introduced the use of ^1H MAS NMR to determine the density of water trapped in corundum inclusions at 1.4-4 GPa and 973-1373 K (> 1 $g{\cdot}cm^{-3}$). To my knowledge, no attempts have been made to extend the high-pressure synthetic fluid inclusion approach to other aqueous compositions.

Methods based on sound velocity measurements. The speed of sound in a material is a thermodynamic property directly related to its density (see details for fluids in Friend 2001). Since the early 1950, sound velocity measurements have been performed in water and aqueous electrolytes using a variety of pressure cells and ultrasonic methods to calibrate equations of state (e.g., Holton 1951; Wilson 1959; Heydemann and Houck 1969 for water, Millero et al. 1987 and references cited for saline solutions). Typical operation conditions are below 1.2 GPa and 500 K. The extension of this method above 500 K is limited by the reactivity of the fluid sample with the buffer rods/transducer assembly. An alternative approach to measure sound velocities at conditions where physical contact with the sample is difficult consist in using a fully optical method based in the inelastic scattering of light, such as Brillouin scattering spectroscopy or impulsive stimulated scattering (ISS). Because these methods only require optical access to the sample and can be applied to small volumes, they can readily be combined with diamond anvil cells to extend the measurements to a higher pressure-temperature regime, only limited by the strength of the diamonds themselves.

EQUATIONS OF STATE OF FLUIDS FROM SOUND VELOCITY MEASUREMENTS BY BRILLOUIN SPECTROSCOPY

Brilloun spectroscopy is based on the inelastic scattering of optical waves (i.e., photons) by propagating thermally excited acoustic waves (i.e., acoustic phonons) in condensed or vapor phases. The Brillouin scattering effect was theoretically predicted by Brilloun (1922) and Mandelstam[2] (1926) and experimentally confirmed by E. Gross (1930). The development of laser sources in the sixties brought a dramatic revival of interest in the applications of Brillouin scattering to investigate the properties of materials and in particular, the dynamics of liquids (e.g., Cummins and Gammon 1966; Mountain 1966; Figgins 1970). In the Earth Sciences, applications of Brillouin spectroscopy were pioneered by Weidner (Weidner et al. 1975) who adapted the technique to determine the elastic properties of single crystals. Over the last three decades, Brillouin scattering measurements in combination with diamond anvil cells have extensively been applied to investigate the elastic properties of materials, including geologically relevant phases, at very high pressures and temperatures (Grimsditch 2001; Bass 2007; Polian et al. 2010). An introduction to the principles of Brillouin scattering spectroscopy and to the application in conjunction with diamond anvil cells to determine the density and equations of state of fluids under pressure is presented below.

Principles of Brillouin scattering spectroscopy

The random thermal motion of molecules in a material produces local fluctuations of the density that can be described as a superposition of sound waves (i.e., thermal phonons) that propagate in all directions. The sound waves generate a strain field in the material that results in periodic modulations of the dielectric constant ε and of the refractive index n ($n = \sqrt{\varepsilon}$) that can scatter (elastically or inelastically) incident light (elasto-optical scattering). Brillouin (inelastic) scattering can be seen as a Bragg's reflection of the incident light wave by the moving diffraction grating created by the propagating thermal phonons (Fig. 12A). After phonon-photon interaction, the light inelastically (Brillouin) scattered by the sample is Doppler shifted in frequency with respect to the incident light. The frequency shift $\Delta\nu_i$ (so called Brillouin shift), is proportional to the velocity ($\mathcal{V}_i$) of the propagating phonon (sound wave) through the relationship:

$$\mathcal{V}_i = \left(\frac{\Delta\nu_i}{\nu_0}\right)\left(\frac{c}{2n\sin(\theta/2)}\right) = \frac{\lambda_0 \Delta\nu_i}{2n\sin(\theta/2)} \tag{9}$$

where the subscript i refers to compressional (i = P) or shear (i = S) waves in the material, c, ν_0 and λ_0 are the velocity, frequency and the wavelength of the incident light, n the refractive index of the material and θ is the scattering angle inside the sample (Fig. 12A). This relation is derived by applying the Bragg law and the conservation of momentum to the phonon-photon interaction (Fig. 12A). Details of the mathematical analysis are beyond the scope here but can be found elsewhere (e.g., Figgings 1970; Grimsditch 2001; Polian et al. 2010). The scattering process gives rise to two shifted Brillouin lines ($\pm\,\Delta\nu_i$) that corresponds to the case where energy is taken or given to the phonon (i.e., Stokes or anti-Stokes interaction). Classically, this is seen as a Doppler shift from advancing sound waves (higher frequency lines, anti-Stokes) or receding sound waves (lower frequency, Stokes) (Fig. 12).

Brillouin spectra are characterized by the central Rayleigh (quasi-elastic) line and the symmetrically shifted Brillouin (inelastic) doublet, whose frequency shift ($\Delta\nu_i$) typically falls in the GHz to tens of GHz (< few cm^{-1}) range (Figs. 12 and 13) . In anisotropic crystalline solids, three pairs of Brillouin lines corresponding to the compression and the two mutually orthogonal polarizations of the shear wave ($\mathcal{V}_{\text{SH}}$ and $\mathcal{V}_{\text{SV}}$). In glasses and isotropic crystalline materials, which withstand shear stresses, both compressional $\mathcal{V}_{\text{P}}$ and shear $\mathcal{V}_{\text{S}}$ wave propagates and two pairs of Brillouin shifted lines are observed in the scattered light spectrum.

---

[2] Leonid Mandelstam predicted the fine structure splitting of the Rayleigh (quasi-elastic) scattering as early as 1918, but only reported the discovery in 1926 (Mandelstam, L.I. (1926) "Light Scattering by Inhomogeneous Media". *Zh. Russ. Fiz-Khim. Ova. 58, 381*). The Brillouin scattering effect is also called Brillouin-Mandelstam scattering (BMS) to recognize the latter's contribution.

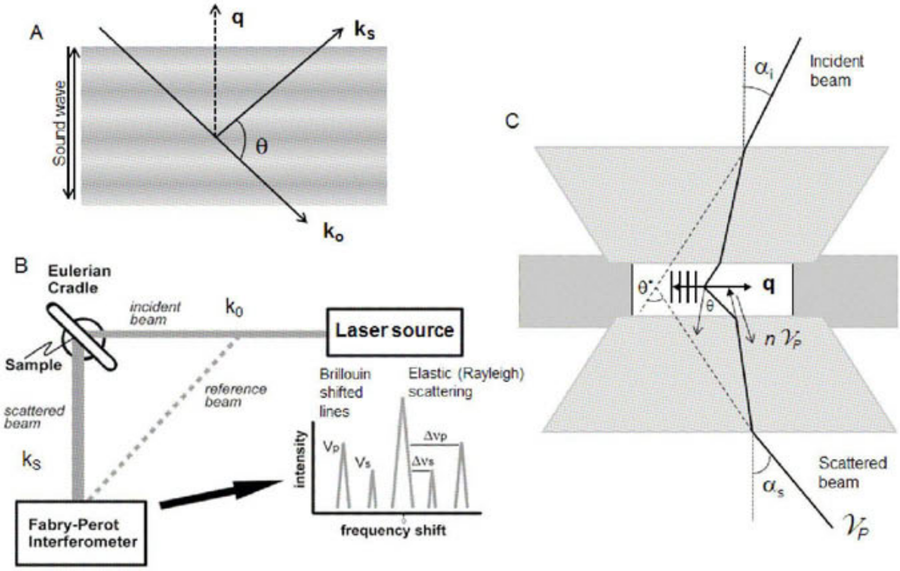
A
q
k_S
Sound wave
θ
k_o
C
α_i
Incident beam
θ*
θ
q
$n\mathcal{V}_P$
α_s
Scattered beam
$\mathcal{V}_P$
B
Eulerian Cradle
incident beam
k_0
Laser source
Sample
reference beam
scattered beam
k_S
Brillouin shifted lines
Elastic (Rayleigh) scattering
intensity
Vp
Vs
Δvp
Δvs
frequency shift
Fabry-Perot Interferometer

Figure 12. A) Representation of the scattering process as a Bragg reflection of the incident light (with wave-vector $\mathbf{k_0}$) by modulations of the refractive index n produced by thermally excited sound waves (wave-vector $\mathbf{q}$, phonons). By the conservation of momentum ($\mathbf{q} = \mathbf{k_0} - \mathbf{k_S}$), the modulus of the phonon vector is defined as $|\mathbf{q}| \approx 2n|\mathbf{k_0}|\sin(\theta/2)$, where θ is the angle between the incident ($\mathbf{k_0}$) and scattered light ($\mathbf{k_S}$). B) Schematic setup for Brillouin scattering measurements. C) Platelet scattering geometry in the diamond anvil cell. Phonons ($\mathbf{q}$) propagating parallel to the faces of the diamonds are probed. α_i and α_S are respectively the angle between the incident and scattered beams and the normal to the diamond surface. θ is the scattering angle inside the sample (as in A) and θ^* is the external scattering angle, i.e., angle between the incident and scattered light outside the sample. $\mathcal{V}_P$ is the velocity of the compressional in platelet geometry, and $n\mathcal{V}_P$ refers to a backscattered signal arising from the light partially reflected from the output diamond anvil and acts as a second excitation source.

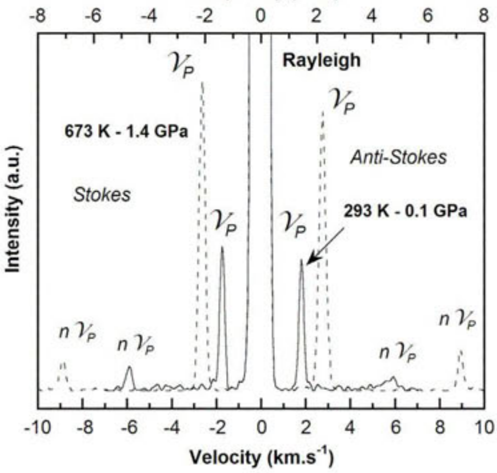

Figure 13. Brillouin spectra of 1 molal NaCl solutions (5.5 wt% NaCl) at various *P-T*. The central unshifted component corresponds to the quasi-elastic (Rayleigh) scattering; the shifted components arise from inelastic (Brillouin) scattering. The compressional wave velocities $\mathcal{V}_P$ and $n\mathcal{V}_P$, where n is the refractive index of the fluid, are labeled. The frequency (GHz) (top scale) converts into velocities (km/s) (bottom scale) through Equation (10), with external scattering angle $\theta^* = 50°$ (i.e., angle between incident and scattered light) and incident laser wavelength $\lambda_0 = 532.1$ nm.

In simple liquids (such as H_2O, CO_2, CH_4) and in aqueous solutions at ambient and moderates pressures or at high temperature, only compressional V_P waves propagate and one pair of Brillouin shifted lines is observed (Fig. 13). Dispersion or acoustic absorption processes are negligible in these fluids and the frequencies lie below the relaxation frequency ($\nu_R = 2\pi\tau^{-1}$ where τ is the relaxation period, Figgins 1970) associated with perturbation of the structural or chemical equilibria. In these conditions, the measured acoustic velocities can directly be related to the equation of state as presented below (Abramson et al. 1999; Friend 2001). Typical Brilloun spectra collected in 1 *m* NaCl solution at various pressures and temperatures are shown in Figure 13.

For comparison, Raman scattering is another case of inelastic scattering of light by thermal vibrations. There, light scattering is produced by optical phonons due to vibrational and rotational transitions in single molecules, and whose frequencies typically range from THz to tens of THz (100-4000 cm^{-1}). The spectral analysis of such different frequency ranges thus requires completely different types of spectrometers and the information provided is also substantially different. While Brillouin spectroscopy provides information about the elasticity of materials, Raman spectroscopy fingerprints ionic or molecular groups in the material.

Brillouin spectroscopy, as Raman spectroscopy, does not excite vibrations in the probed system but relies on the naturally occurring thermal motion of the atoms. The scattered intensity is extremely small, only about 10^{-6} of the incident intensity, thus resulting in time consuming measurements, particularly in materials that displays low elastic-optic coupling. An alternative approach to sound velocity measurements consists in exciting the natural thermal vibrations by a pump laser to amplify the diffraction grating (Fig. 12A) during the measurements. This method, known as Impulsive Stimulated Scattering (ISS) (or stimulated Brillouin scattering) is also applied to determine the equations of state of geological fluids (Wiryana et al. 1998; Abramson et al. 1999, 2001; Abramson and Brown 2004) and the results are summarized here together with results from classical Brillouin scattering.

Brillouin spectroscopy of fluids under pressure

Brillouin scattering measurements are performed by illuminating the sample by a focused visible (typically 514.5 or 532.1 nm wavelengths) laser beam and analyzing the scattered light (Fig. 12B). The subtle shift of the photon frequency in Brillouin spectroscopy (0.1 to 100 GHz, < 5 cm^{-1}) compared to the frequency of the probing laser light (typically 10^5 GHz) requires high resolution interferometers to be resolved. Modern Brillouin scattering setups operate on the basis of the six-pass tandem Fabry-Pérot interferometer devised by Sandercock (1982) to achieve the resolution required to discriminate the (quasi)elastic and inelastic contributions in the spectra (Fig. 13). The accessible frequency range can be estimated from the values of the instrumental resolution and of the scattering geometry. For the measurements, the sample is mounted in a Eulerian cradle to precisely control the scattering geometry of the experiment, i.e., the scattering angle, θ, as this is critical for an accurate determination of the phonon velocities (see Eqns. 9-10). Details of the experimental setups for Brillouin scattering can be found elsewhere (e.g., Sinogeikin et al. 2006; Murakami et al. 2008: Sanchez-Valle et al. 2010).

Brillouin scattering measurements in the diamond anvil cell are most commonly performed using symmetric scattering geometry, also called "platelet" geometry (Fig. 12C). The geometrical requirement for the samples is to have parallel faces, which in the case of fluids is defined by the parallel faces of the diamond anvils. In this configuration, light is scattered by thermal phonons propagating parallel to the sample surface and the modulus of the phonon vector is given by $|\mathbf{q}| = 2nk\sin\theta$ (Fig. 12), where θ is the scattering angle inside the sample. Applying Snell's law to the different interfaces encountered by the beam (Fig. 12), the refractive index *n* of the sample cancels out and the phonon vector is given by $|\mathbf{q}| = 2k\sin(\theta^*/2)$, where θ^* is the external scattering angle, i.e., the angle between the incident and scattered light outside the sample (see Whitfield et al. 1976 for the details). This geometry thus makes it possible to obtain the velocities $\mathcal{V}_i$ directly from the measured frequency shift $\Delta\nu_i$ by applying the relationship:

$$\mathcal{V}_i = \frac{\lambda_0 \Delta\nu_i}{2\sin(\theta^* / 2)} \tag{10}$$

where other symbols have the same meaning as in Equation (9). The platelet/symmetric scattering geometry, introduced by Whitfield et al. (1976), is thus the preferred configuration for measurements under extreme conditions as the typically unknown changes of the refractive index of the sample with pressure and temperature need not be known.

An additional advantage of using the platelet geometry for measurements in the diamond anvil cell is that it makes it possible to obtain simultaneously the velocity of the compressional wave $\mathcal{V}_P$ and the backscattered (180°) signal $n\mathcal{V}_P$, that arises from using the light reflected in the diamond surface as a second probe of the fluid (Fig. 12C). In an isotropic medium, the measured Brillouin shifts in platelet ($\Delta\nu_{\theta^*}$) and in backscattering ($\Delta\nu_{180°}$) geometry (Fig. 13) can be combined to determine the refractive index n as:

$$n = \left(\frac{\Delta\nu_{180°}}{\Delta\nu_{\theta^*}}\right) \sin\left(\frac{\theta^*}{2}\right) \tag{11}$$

where θ^* is the scattering angle in platelet geometry. This offers a method for obtaining the refractive index of the fluid, a macroscopic property that provides direct information on the polarizability of the solvent molecules and on the microscopic scale interactions between them. This information is relevant for the refinement of interaction potentials of the solvent, particularly those that include polarization effects (e.g., Kalinichev 2001), and for the development of models for ion solvation and solute-solute interactions in high-pressure aqueous fluids.

Sound velocity measurements in aqueous fluids are ideally performed as a function of pressure along isotherms to simplify the data analysis and to obtain independent equations of states from the measured sound velocities (see below). The variations with pressure and temperature of the sound velocities in 1 *m* NaCl aqueous solution along various isotherms up to 4.5 GPa and 673 K are illustrated in Figure 14. Sound velocities increase monotonously with pressure along each isotherm but the temperature dependence remains typically moderate compared to the pressure dependence.

Determination of density from measured sound velocities

The density $\rho(P,T,x)$ of the fluid and the measured sound velocities $\mathcal{V}_P(P,T,x)$ are related through the thermodynamic relationships:

$$\left(\frac{\partial\rho}{\partial P}\right)_T = \frac{1}{\mathcal{V}_P^2} + \frac{T \cdot \alpha_P^2}{C_P} \tag{12}$$

$$\alpha_P = -\frac{1}{\rho}\left(\frac{\partial\rho}{\partial T}\right)_P \tag{13}$$

$$\left(\frac{\partial C_P}{\partial P}\right)_T = -T \cdot \left(\frac{\partial^2 v_{sp}}{\partial T^2}\right)_P = -\frac{T}{\rho}\left[\alpha_P^2 + \left(\frac{\partial\alpha_P}{\partial T}\right)_P\right] \tag{14}$$

where α_P is the coefficient of thermal expansion, C_P the specific heat capacity and v_{sp} is the specific volume of the fluid. The density is inverted from the measured velocities $\mathcal{V}_P$ (Fig. 14) by recursive integration of Equations (12-14) (e.g., Wiryana et al. 1998; Abramson and Brown 2004; Mantegazzi et al. 2012). The inversion of the data requires knowledge of the density

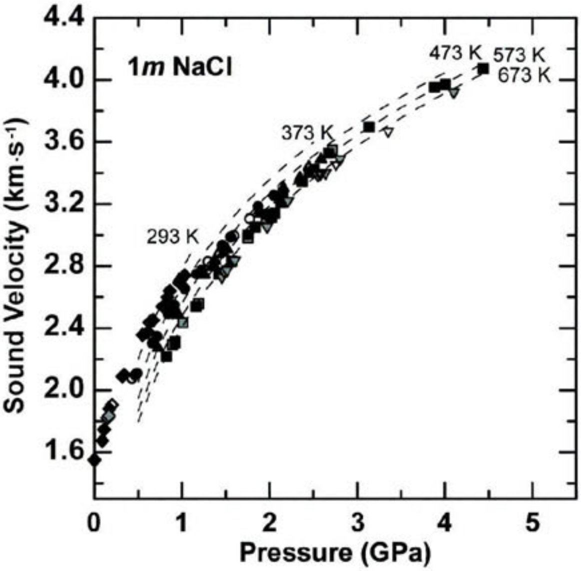

Figure 14. Sound velocities measured in 1 *m* NaCl solution as a function of pressure along various isotherms from 293 to 673 K. Dashed lines are sound velocities calculated from the equation of state constructed from the data. Deviations are smaller than 1% and within the experimental errors in the velocities (after Mantegazzi et al. 2013).

and heat capacity C_P at an arbitrary initial pressure, selected depending on the experimental sound velocity data and available thermodynamic data for the aqueous fluid of interest. Typical experimental errors of 1% in measured velocities at high-P-T result in uncertainties below 0.4% in the inverted densities. Errors on derived thermodynamic properties, including thermal expansion α_P, heat capacity C_P and isothermal and adiabatic compressibilites (β_T and β_S), do not typically exceed 5%.

PHYSICO-CHEMISTRY OF AQUEOUS FLUIDS AT ELEVATED PRESSURES (> 0.5 GPa)

Applications of sound velocity measurements at high pressure to determine the density and thermodynamic properties of geologically relevant aqueous fluids under pressure are still limited but under development. The expanding volumetric data for aqueous solutions at pressures in excess 0.5 GPa serve as a test of validity for available EoS of aqueous fluids, and offer access to unexplored aspect of the behavior of aqueous species in high-pressure fluids, i.e., the evolution of partial molar volumes, solute-solvent interactions or water-salt mixing. This information provides the foundation for the extension of thermodynamic models for aqueous species beyond their current range of validity (< 0.5 GPa). Some of these aspects are reviewed below.

Volumetric properties of high-pressure aqueous fluids (> 0.5 GPa)

Water, as the main component in natural fluids, has received the most of attention in term of sound velocity measurements to extend the pressure-range of the experimental equations of state. Wiryana et al. (1998) and Abramson and Brown (2004) by ISS, and Sanchez-Valle et al. (2013) by Brillouin scattering spectroscopy, extended the available density data (< 1 GPa) to pressures in excess of 7 GPa at 673 K. Overall, the results are in mutual agreement and indicate that the IAPWS-95 EoS (Wagner and Pruß 2002) underestimates H_2O density by less than 0.7% at 6 GPa at 673 K (Fig. 15). However, the accuracy of the IAPWS-95 to predict the thermodynamic properties of water decreases rapidly when extrapolated beyond 4 GPa at relatively moderated temperatures: the IAPWS-95 underestimates the heat capacity C_P by about 10% and overestimates the thermal expansion by about 20% at 7 GPa and 673 K (Sanchez-Valle et al. 2013). Note that Asahara et al. (2010) provided additional constraints on the equation of state of water from sound velocity measurements along the ice melting curve to 25 GPa and 900 K in a laser heated diamond anvil cell but the available data did not allow to obtain independently an EoS (i.e., by integration of Eqns. 12 to 14). As advised by the authors, the density and derived thermodynamic data should be assessed further before being applied to correct available EoS or for the refinement of theoretical inter-atomic potential of water under elevated P-T conditions.

Abramson and Brown (2004) used their EoS for water to test the volumetric data derived from fluid inclusion FI studies conducted to 3 GPa and 973-1873 K (Brodholt and Wood 1993a; Withers et al. 2000). Densities obtained from the FI data are generally 5% lower than predicted from the experimental equation of state, likely due to the non-isochoric behavior of the corundum host and fluid leaking. Based on this observation, Abramson and Brown (2004) reinterpreted the FI data and concluded that the highest measured density in the FI should be taken as a lower bound for the true density of the fluid.

Investigations of the volumetric properties of water-salt systems have primarily focused on aqueous electrolyte solutions, including sulfate-, carbonate- and NaCl-bearing aqueous solutions, that are important components in deep natural fluids (Fig. 15). Abramson et al. (1999, 2001) were first to report the density of salt-water fluids from sound velocity measurements in

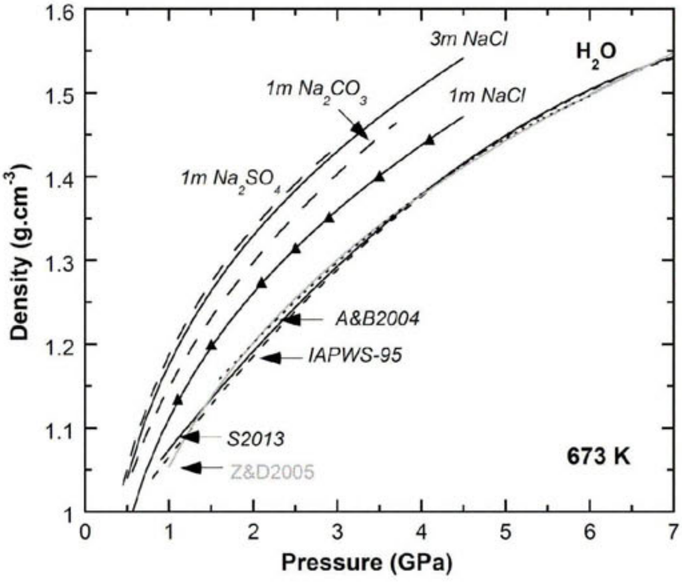

Figure 15. Density of H_2O and aqueous salt solutions as a function of pressure at 673 K. Symbols are selected densities for 1 m NaCl solution obtained from the inverstion of the sound velocitiy data reported in Figure 14 using Equations (12)-(14). Lines are denisities calculated from equations of state of H_2O: Wagner and Pruß (2002), IAPWS-95; Abramson and Brown (2004), A&B2004; Sanchez-Valle et al. (2013), S2013; Zhang and Duan (2005), Z&D2005; data for salt solutions are from Mantegazzi (2012) and Mantegazzi et al. (2013).

0.1 *m* and 0.5 *m* aqueous Na_2SO_4 solutions up to 573 K and 3 GPa. Extending this early work, Mantegazzi et al. (2012) measured the density of 1 *m* Na_2SO_4 solutions up to 773 K and 3 GPa and proposed an empirical EoS that represents volume with deviations less than 0.4% in the investigated *P-T* range. The first volumetric data for binary NaCl-H_2O fluids at pressures above 0.5 GPa were recently reported by Mantegazzi et al. (2013) from sound velocity measurements on 1 *m* and 3 *m* NaCl aqueous solutions to 673 K and 4.5 GPa. An empirical equation of state (EoS) for NaCl-H_2O fluids was generated by combining the data with literature data for H_2O (Wagner and Pruß 2002; Sanchez-Valle et al. 2013), and used for extrapolation of thermodynamic properties to 1073 K and 4.8 *m* NaCl, 0.5-4.5 GPa. The extended equation of state predicts the volumetric properties of NaCl fluids with an uncertainty smaller than 3% at 4.5 GPa and 1073 K, spanning the conditions for major dehydration events in subduction zones. Predicted densities are in good agreement with available data (up to 0.5 GPa) in the range of overlapping (e.g., Hilbert 1979; Bodnar 1985; Anderko and Pitzer 1993; Driesner 2007). Finally, densities and thermodynamic properties of oxidized carbon-bearing aqueous fluids (Na_2CO_3- and $NaHCO_3$-bearing fluids) to 673 K and 3 GPa have been reported by Mantegazzi (2012) (Fig. 16). Applications to predict the speciation of oxidized carbon in high-pressure aqueous fluids based on partial molar volumes of dissolved carbon species are under way.

Attempts to extend the work to fluid compositions other than water and simple salt solutions under pressure have been rather limited. Only reconnaissance experiments have been conducted on H_2O-CO_2 fluids (with 95 mol% H_2O) to 535 K and 3 GPa (Qin et al. 2010) and additional work will be necessary to implement a thermodynamic model for CO_2-bearig fluids at high *P-T*. Experiments by Tkachev et al. (2005) on concentrated sodium disilicate (Na_2O-$2SiO_2$) aqueous solutions (18 wt% Na_2O and 36 wt% SiO_2) up to 475 K and 4 GPa are the only one study on Al-Si bearing fluids representative of more polymerized aqueous fluids in subduction zones. The detection of shear wave components in their Brillouin spectra at all investigated *P-T* conditions indicates however that the fluid is not relaxed and therefore, the velocity data cannot be directly interpreted in terms of the equation of state (see above):

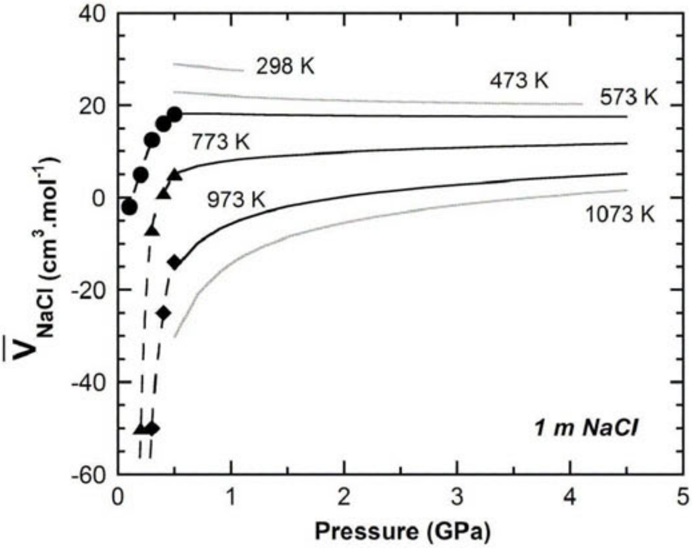

Figure 16. Partial molar volume of NaCl in 1 *m* NaCl aqueous solution as a function of pressure at various temperatures. Solid lines are derived from the experimentally constrained EoS of Mantegazzi et al. (2013). Symbols are low pressure data from Bodnar (1985). Dashed lines are guidelines only.

reported densities should thus be taken only as approximating the actual density of alkali-silica aqueous solutions at high pressures. With a careful choice of compositions and *P-T* conditions to ensure relaxation of the fluid at the conditions of the measurements, there are *a priori* no fundamental limitations to extend this approach to determine the volumetric properties and equations of state of more complex silicate-bearing aqueous solutions at conditions relevant for the lower crust and upper mantle.

Solute-solvent interactions in salt solutions under pressure

Solute-solute and solute-solvent interactions in aqueous fluids are a key control on the association/dissociation and hydration of ions, and ultimately on the solubility of minerals in high-pressure-high-temperature aqueous fluids. Direct information on solute-solute and solute-solvent interactions can be obtained from the partial molar volumes of the components in solution.

Partial molar volumes of salts in aqueous solution are derived from the volumetric data (Fig. 15) as:

$$\overline{V}_i = \left(\frac{\partial V_m}{\partial n_i}\right)_{P,T,n} = -V_m \quad X_{\mathrm{H_2O}} \left(\frac{\partial V_m}{\partial X_{\mathrm{H_2O}}}\right)_{P,T} \tag{15}$$

where n_i are the moles of component i (e.g., NaCl, Na_2CO_3, $NaHCO_3$ or Na_2SO_4) and V_m is the average molar volume of the aqueous mixture (cm^3/mol for 1 mol of the solution) calculated as:

$$V_m(T,P) = \frac{M_{\mathrm{H_2O}\text{-}i}(X_{\mathrm{H_2O}})}{\rho(T,P,X_{\mathrm{H_2O}})} \tag{16}$$

where $M_{\mathrm{H_2O}\text{-}i}(X_{\mathrm{H_2O}})$ is the molar mass of the H_2O-i mixture as a function of the concentration, and $\rho(T,P,X_{\mathrm{H_2O}})$ is the density calculated from the equations of state presented above. The partial molar volumes of NaCl in 1 *m* NaCl solution calculated from the EoS of Mantegazzi et al. (2013) are in good agreement with low pressure data (< 0.5 GPa) from fluid inclusion studies (Bodnar 1985) in the range of overlapping (Fig. 16). Taken together, the $\overline{V}_{NaCl}$ remains positive at temperatures below 473 K at all investigated pressures and display a minor pressure dependence from 0.5-1 to 4.5 GPa. At higher temperatures, $\overline{V}_{NaCl}$ are large and negative at low pressure (< 0.5-1 GPa) but increase rapidly upon compression along each isotherm, before displaying a more reduced pressure dependence.

At infinite dilution, where ion-ion interactions are absent, the partial molar volume of the ion or electrolyte $\overline{V}_i^{\infty}$ $(n_i \rightarrow 0)$ is of fundamental interest since it is directly related to solute-solvent interactions in the fluid. A reliable extrapolation of volumetric properties of aqueous electrolytes using the Debye-Hückel limiting law (e.g., Hilbert 1979; Corti and Abdulagatov 2008) to determine $\overline{V}_i^{\infty}$ at high pressures (> 0.5 GPa) requires experimental volumetric data at various low concentrations (< 0.1 *m*) that is not available for NaCl solutions at present (Mantegazzi et al. 2013). Abramson et al. (2001) and Mantegazzi (2012) reported volumetric data for Na_2SO_4, Na_2CO_3 and $NaHCO_3$ salt solutions at various concentrations down to 0.1 *m* that were used to derive partial molar volumes at infinite dilution. The results are shown as a function of pressure to 4.5 GPa along various isotherms together with low pressure data for NaCl aqueous solutions (Hilbert 1979; Rogers and Pitzer 1982) in Figure 17.

At infinite dilution, where ion-ion interactions are absent, the partial molar volume of an electrolyte is the result of two volume contributions:

$$\overline{V}_i^{\infty} = V_{i,\mathrm{int}} \quad V_{i,\mathrm{el\overset{+}{e}c}} \tag{17}$$

where $V_{i,int}$ refers to the intrinsic volume of the electrolyte i in solution, and $V_{i,\mathrm{elec}}$ is the

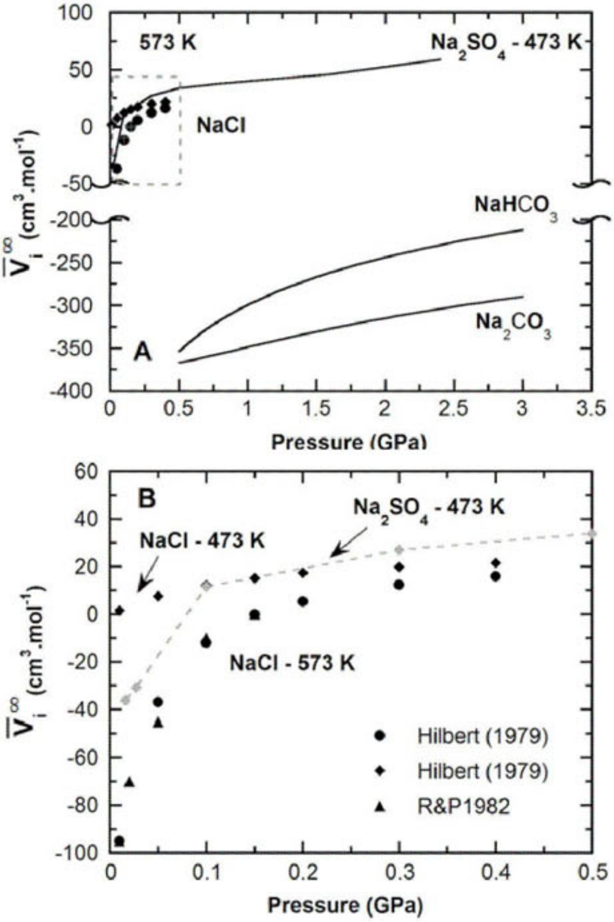

Figure 17. (A) Pressure dependence of the partial molar volume at infinite dilution of various salts in water at 573 K. (B) Details of the low pressure portion of the diagram (< 0. 5 GPa). Data source: Na_2CO_3 and $NaHCO_3$ (Mantegazzi 2012); NaCl (Hilbert 1979; Rogers and Pitzer 1982). Data for Na_2SO_4 is only available at 473 K (Abramson et al. 2001).

electrostriction volume due to ion hydration and ion-solvent interactions. The intrinsic volume is the *P-T* independent hard sphere volume characteristic of each ion or electrolyte, while the electrostriction volume arises from the locally denser packing of solvent molecules caused by the electric field of the ions in solution that attracts the surrounding water molecules. The electrostrictive volume is therefore negative when the water structure in the hydration shell around the ion locally increases the density and depends on the compressibility and dielectric constant ε of the solvent (see Marcus 2011, and references cited for details). At high temperature and low pressures, when the hydrogen bond structure of uncompressed water is more open and void spaces in the solvent larger (Marcus 2011), the electrostrictive contribution predominates and results in large negative values of $\overline{V}^{\infty}_{\mathrm{Na_2SO_4}}$ and $\overline{V}^{\infty}_{\mathrm{NaCl}}$ (Fig. 17B). Indeed, Abramson et al. (1999) showed that low pressures below 0.03 GPa (Fig. 17B), the pressure dependence of $\overline{V}^{\infty}_{\mathrm{Na_2SO_4}}$ is directly correlated to the pressure dependence of the dielectric constant ε of the solvent ($\partial\varepsilon^{-1}/\partial P$), hence controlled by ion-solvent interactions. The $\overline{V}^{\infty}_{i}$ of NaCl and Na_2SO_4

become less negative upon compression and eventually positive: the electrostriction term is less dominant because electrostriction is likely less effective on the more compacted structure of compressed water. At high pressure, the $\overline{V}_i^{\infty}$ is dominated by the intrinsic volume term, and the incompressibility of ions results in a reduced pressure dependence. The contrasting behavior of the $\overline{V}_i^{\infty}$ of various salts in high-pressure solutions reflects differences in ion-solvent interactions related to the specificity of ions (Fig. 17), including differences in the intrinsic volume, shape or polarity (Marcus 2011). In contrast with dissolved Na_2SO_4, where $\overline{V}^{\infty}_{Na_2SO_4}$ becomes positive above 0.27 GPa, the $\overline{V}^{\infty}_{Na_2CO_3}$ and $\overline{V}^{\infty}_{NaHCO_3}$ display very large negative values over the entire pressure range.

Fugacity and activity of water in high-pressure salt solutions

Solute-solvent interactions in aqueous solutions result in non-ideal thermodynamic properties that affect mineral reactions involving fluid phases at high pressure. The non-ideality in the properties are reflected by changes in the fugacity f and activity a of water upon addition of dissolved salts or non-polar solutes (CO_2, CH_4, etc.). Equations of state and experimental studies of devolatilization reactions under pressure have been used to derive the fugaticity and activity of fluids at high pressure and temperature (e.g., Kerrick and Jacobs 1981; Holland and Powell 1991; Pitzer and Sterner 1994; Aranovich and Newton 1996, 1999).

Mantegazzi et al. (2013) evaluated the effect of dissolved NaCl in the fugacity and activity of water at high pressures from their experimental EoS for NaCl-H_2O fluids. The results are reported in Figures 18 to 20. The fugacity of pure H_2O was obtained as:

$$\int_{P_0}^{P} V_i^0 dP = RT\ln(f_i^0) \quad RT\ln(f^{0}_{i,P_0}{}^{-}) \tag{18}$$

where R is the gas constant, T the temperature, V_i^0 and f_i^0 are respectively the molar volume of pure H_2O and its fugacity at a given P, and f^0_{i,P_0} is the fugacity of pure H_2O at the reference state pressure P_0. The fugacity of water in the H_2O-NaCl aqueous solution, f_i, is defined as:

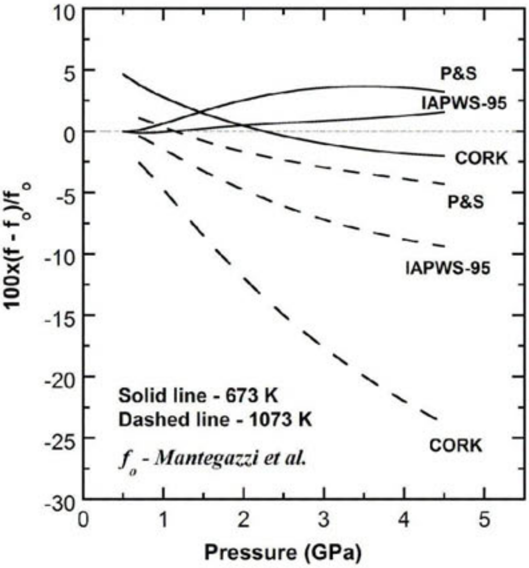

Figure 18. Deviations (in %) between the water fugacity predicted by several EoS and the experimentally constrained EoS (f_0) for NaCl-H_2O fluids (0-4.28 molal NaCl) of Mantegazzi et al. (2013) to 4.5 GPa along isotherms at 673 K (solid lines) and 1073 K (dashed lines). P&S, Pitzer and Sterner (1994); IAPWS-95, Wagner and Pruß (2002); CORK, Holland and Powell (1991).

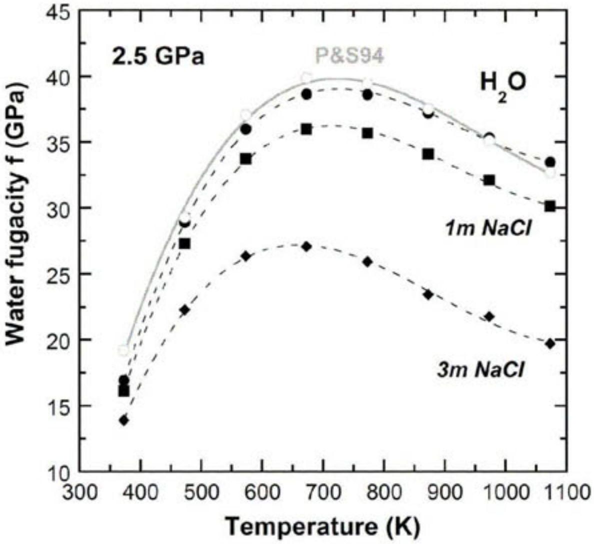

Figure 19. Effect of temperature and NaCl concentration in the fugacity of water at 2.5 GPa. At constant *P-T*, the fugacity of water fugacity decreases with increasing NaCl concentration. Full symbols: Mantegazzi et al. (2013); gray: Pitzer and Sterner (1994). Lines are guidelines only.

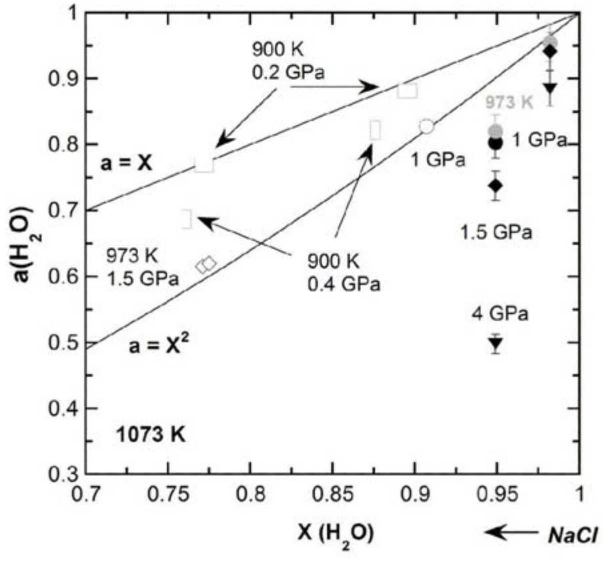

Figure 20. Activity of water a_{H_2O} in NaCl aqueous solutions vs. water mole fraction X_{H_2O} at 1073 K (unless indicated differently) and various pressures. Full symbols: Mantegazzi et al. (2013); gray circles denotes data at 973 K; empty symbols: data from Aranovich and Newton (1996) at the indicated *P-T*. Pressure decreases the activity of water and the effect is more pronounced with increasing NaCl concentration in the fluid. Solid lines correspond to ideal ($a_{H_2O} = X_{H_2O}$) and non-ideal ($a_{H_2O} = X_{H_2O}^2$) mixing between NaCl and H_2O in NaCl aqueous solutions.

$$RT\ln(f_i) = \int_{P_0}^{P} \overline{V}_i dP + RT\ln(f_{i,P_0}) \cong \int_{P_0}^{P} \overline{V}_i dP + RT\ln(X_i) + RT\ln(f^0_{i,P_0}) \tag{19}$$

where $\overline{V}_i$ and X_i are the partial molar volume and the mole fraction of H_2O in the mixture respectively, and f^0_{i,P_0} has the same meaning as in Equation (18). The nearly-equal sign (≅) in Equation (19) stems from the assumption of ideal behavior of the components at the reference pressure P_0, following the Lewis-Randall fugacity rule: $f_{i,P_0} \cong X_i \cdot f^0_{i,P_0}$. Taking the fugacity of pure water at the reference pressure $P_0 = 0.5$ GPa (f^0_{i,P_0}) from the IAPWS-95 EoS, the partial molar volume $\overline{V}_i$ is obtained from the NaCl-H_2O EoS using the relationship:

$$\overline{V}_{i=H_2O} = \left(\frac{\partial V_m}{\partial n_i}\right)_{P,T,n} = V_m + (1 - X_{H_2O}) \left(\frac{\partial V_m}{\partial X_{H_2O}}\right)_{P,T} \tag{20}$$

where V_m is the molar volume of the aqueous mixture as defined in Equation (16).

A comparison between the fugacity of pure water derived from the experimental EoS of Mantegazzi et al. (2013) and results from EoS for water widely used among geochemists and petrologists to determine phase equilibria involving fluid phases are reported in Figure 18. Differences with the EoS of Pitzer and Sterner (1994) and the extrapolations of the IAPWS-95 EoS (Wagner and Pruß 2002) are smaller than 2%, but negative deviations larger than 5% are observed with the Compensated Redlich-Kwong (CORK) EoS (Holland and Powell 1991). At 1073 K, the EoS of Pitzer and Sterner (1994) shows the best agreement with the experimentally derived EoS whereas the deviations of the CORK EoS continuously increase with pressure, reaching differences of up to 25% at 4.5 GPa. A critical evaluation and assessment of the different equations of state is provided by their ability to reproduce experimentally-determined mineral-fluid equilibria. The equations of state were tested by using the antigorite dehydration reaction in subducted slabs: antigorite = forsterite + enstatite + fluid (Fig. 21). Better agreement was found between the experimental antigorite breakdown reaction boundaries (Ulmer and Trommsdorf 1995) and those calculated using the fugacities of Mantegazzi et al. (2013) than with the CORK EoS (Holland and Powell 1991). This observation indicates that the experimentally-based EoS is more reliable in the calculation of water fugacities and phase equilibria involving fluid phases than previous formulations, particularly in the high-pressure range.

The effect of dissolved NaCl on the fugacity of water is illustrated in Figure 19. At constant P-T, the fugacity of water decreases with increasing NaCl concentration in the fluid. Note that the maximum in the fugacity at 2.5 GPa shifts towards lower temperatures when the concentration of NaCl increases to 3 molal, likely due to a larger disruption of the hydrogen bond structure of water with increasing NaCl concentration (Leberman and Soper 1995).

The data reported in Figure 19 can be used to obtain the activity of water a_{H_2O} in salt solutions by applying the relationship:

$$RT\ln(a_{H_2O}) = \int_{P_0}^{P} \overline{V}_{H_2O} dP - \int_{P_0}^{P} V^0_{H_2O} dP + RT\ln(X_{H_2O}) = RT\ln(f_{H_2O}) - RT\ln(f^0_{H_2O}) \tag{21}$$

Where f_{H_2O} and $\overline{V}_{H_2O}$ are respectively the fugacity and the partial molar volume of H_2O in the mixture, $f^0_{H_2O}$ and $V^0_{H_2O}$ the fugacity and molar volume of pure H_2O at the same P-T conditions, and X_{H_2O} is the molar fraction of H_2O in the mixture. The activity-concentration data for water in NaCl aqueous solutions (X_{H_2O} = 0.989 and 0.949) at selected pressures and 1073 K derived from the equation of state of Mantegazzi et al. (2013) are displayed in Figure 19. Pressure decreases the activity of water ($a_{H_2O} < X_{H_2O}$) and deviations from ideality ($a_{H_2O} = X_{H_2O}$) are more pronounced with increasing NaCl concentration in the fluid (Fig. 19).

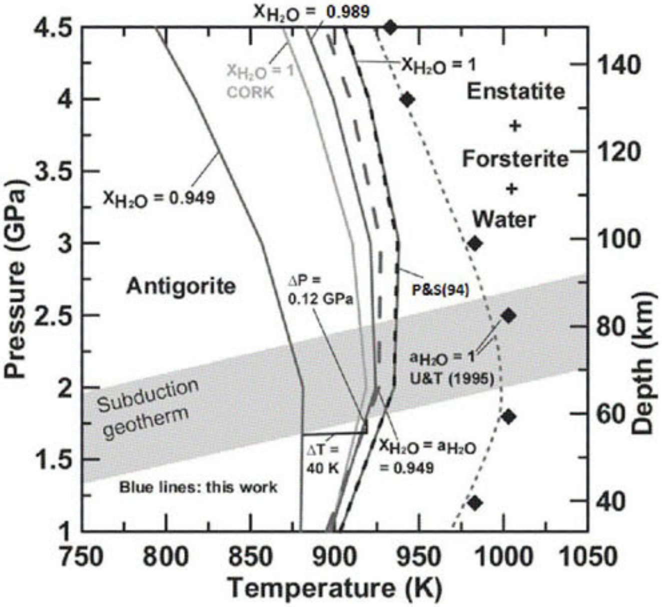

Figure 21. Dehydration boundaries of antigorite as a function of pressure, temperature and water mole fraction (X_{H_2O}). Black solid lines are calculated for different X_{H_2O} (=1, 0.989, 0.949) from the EoS for NaCl-H_2O fluids of Mantegazzi et al. (2013); black short-dashed from the EoS of Pitzer and Sterner (1994) for pure H_2O ($X_{H_2O} = 1$); grey solid line from the CORK EoS (Holland and Powell 1991) for pure H_2O ($X_{H_2O} = 1$). The black long-dashed line shows the reaction boundary calculated assuming ideal mixing between water and NaCl in a 3 *m* NaCl fluids, $a_{H_2O} = 0.949$. The diamonds and dotted line represent the experimental boundaries for the dehydration of antigorite determined in quenched samples by Ulmer and Trommsdorff (1995) in a close system ($a_{H_2O} = 1$, U&T1995). A typical subduction geotherm is shown.

The decrease in water activity with pressure is consistent with results inferred from the depression of the brucite-periclase equibilibria in more concentrated salt solutions ($X_{H_2O} = 0.8$) at pressures from 0.2 GPa to 1.5 GPa and 1073 K. Franz (1982) obtained three reversed brackets at 900-930 K and 0.2 GPa and salinities of $X_{H_2O} = 0.8$ and reported ideal behavior of NaCl and water at these conditions. Shmulovich et al. (1982) reported a decrease of the activity of water relative to the 0.2 GPa data from experiments conducted at 0.4 GPa for two different fluid compositions ($X_{H_2O} = 0.84$ and 0.74). This trend was further confirmed in detailed experiments conducted by Aranovich and Newton (1996) at 873-1173 K and 0.2-1.5 GPa. At the highest pressure investigated, a_{H_2O} is well approximated by $a_{H_2O} = X^2_{H_2O}$ (Fig. 20).

The nearly ideal behavior of salt solutions at low pressures, even at elevated NaCl concentrations, is consistent with the high association between Na and Cl ions into neutral $NaCl^0$ pairs in high-temperature aqueous solutions below 0.2 GPa, as inferred from electrical conductivity measurements by Quist and Marshall (1968). Pressure-induced dissociation of NaCl ion pairs in the fluid above 0.4 GPa (Quist and Marshall 1968) further decreases the activity of water. Based on the diminished activity of water in concentrated salt solutions, Newton and Manning (2002, 2005) suggested that they behave as hydrous salt melts consisting of water and completely dissociated NaCl.

Even at much lower NaCl concentrations, the data of Mantegazzi et al. (2013) indicate significant non-ideality in mixing at high pressure, with implications for the location of dehydration reactions in subducting slabs as show in Figure 21. Along a normal subduction geotherm, for instance, the assumption of ideal mixing in 3 *m* NaCl solution ($X_{H_2O} = 0.949$) shifts the antigorite breakdown boundaries to greater depths by ca. 4 km ($\Delta T = 40$ K, $\Delta P = 0.12$ GPa). This observation indicates that, as the amount of dissolved NaCl in slab derived fluids decreases with depth due to the incompatible character of Na and Cl ions, the activity of water increases in the fluid (Fig. 20) and an increase of the depth at which the dehydration reaction take place is expected (Fig. 21). More generally, the progressive changes in water activity due to the decrease in salt concentration will continuously propagate the location of the dehydration reaction boundaries towards higher depths.

CONCLUDING REMARKS AND OUTLOOK

Significant progress has been made over the last decade in understanding the chemical and physical properties of water-rich fluids at pressures in excess of 0.5 GPa. This chapter has provided an overview of major developments in diamond anvil cell approaches to characterize fluid properties *in situ* at subduction zone conditions. Most progress has been made in understanding the structure of silicate-rich aqueous fluids and intermediate (supercritical) fluids and their role in the mobilization and transport of key trace elements that witness mass transfer and recycling in subduction-related magmatic hydrothermal processes. The handful of speciation studies discussed in this chapter have provided a comprehensive picture of the effect of chloride and dissolved silicates on the mobilization and transport of HFSE and REE. However, additional studies are needed to assess the role of other ligands (e.g., F^-, CO_3^{2-}, SO_4^{2-}) or melt compositions, such as carbonatite and carbonated silicates, on the mobilization and transport of trace elements at subduction zone conditions. Finally, the speciation of trace elements in solvents other than pure water, such as H_2O-CO_2 fluids at crustal/upper mantle conditions should be addressed in order to elucidate the mass transfer mechanisms in subduction zones.

Progress made in the development of experimentally constrained—although still empirical—equations of state for water and salt solutions open the path for expanding the thermodynamic databases for aqueous species above 0.5 GPa (e.g., Helgeson-Kirkham-Flowers HKF model, Helgeson et al. 1981) to assist in the modeling of fluid-rock interaction and mass transfer processes in the lower crust/upper mantle. Although limited so far to aqueous salt solutions and pure molecular systems, Brillouin scattering studies combined with diamond anvil cells hold great promise for extending the investigations to more complex systems, including silicate-bearing aqueous fluids, H_2O-CO_2 mixtures or ternary systems for a more representative description of fluid properties and processes in subduction zones. Major efforts are needed, however, to integrate the expanding high-pressure volumetric data into theoretically based EoS with capacity for extrapolation to pressure-temperature regions well beyond the range of available experimental data. Refinement of potentials that govern the intermolecular interactions under pressure from the volumetric data should set the baseline for the development of more robust computational EoS from molecular dynamic simulations.

Computational simulations have provided unprecedented insight into the structure of H_2O and ion hydration, geometry and structure in dilute fluids over the last 15 years (Driesner 2013, this volume). Improvement in codes and computational power have allowed to extend the theoretical approaches to the speciation of major (silica species) and trace elements in more complex silicate-bearing fluids. Combination of experimental and theoretical approaches holds promise for major advancements into the geochemistry of high-pressure fluids in subduction zones in the next decade.

ACKNOWLEDGMENTS

I am grateful to Andri Stéfansson, Thomas Driesner and Pascale Bénézeth for the invitation to contribute to this volume. I wish to thank D. Mantegazzi, M. Louvel, W. Malfait and T. Driesner for collaborations that made this work possible. Careful reviews by T. Driesner helped to improve an early version of the manuscript. This study was supported in part by the Swiss National Science Foundation, the ETHIIRA program of ETH Zurich and the European Synchrotron Radiation Facility (ESRF).

REFERENCES

Abramson EH, Brown JM (2004) Equation of state of water based on speeds of sound measured in the diamond-anvil cell. Geochim Cosmochim Acta 68:1827-1835

Abramson EH, Brown JM, Slutsky LJ (1999) Applications of impulsive stimulated scattering in the earth and planetary sciences. Ann Rev Phys Chem 50:279-313

Abramson EH, Brown JM, Slutsky LJ, Wiryana S (2001) Measuring speed of sound and thermal diffusivity in the diamond-anvil cell. Int J Thermophys 22:405-414

Albert HJ, Wood RH (1984) High-precision flow densimeter for fluids at temperatures to 700 K and pressures to 40 MPa. Rev Sci Instrum 55:589-594

Als-Nielsen J, McMorrow D (2001) Elements of Modern X-ray Physics. John Wiley & Sons

Anderko A, Pitzer KS (1993) Equation-of-state representation of phase-equilibria and volumetric properties of the system NaCl-H_2O above 573 K. Geochim Cosmochim Acta 57:1657-1680

Anderson AJ, Jayanetti S, Mayanovic RA, Bassett WA, Chou I-M (2002) X-ray spectroscopic investigations of fluids in the hydrothermal diamond anvil cell: the hydration structure of aqueous La^{3+} up to 300 °C and 1600 bars. Am Mineral 87:262-268

Antignano A, Manning CE (2008) Rutile solubility in H_2O, H_2O-SiO_2, and H_2O-$NaAlSi_3O_8$ fluids at 0.7-2.0 GPa and 700-1000 degrees C: Implications for mobility of nominally insoluble elements. Chem Geol 255:283-293

Aranovich LY, Newton RC (1996) H_2O activity in concentrated NaCl solutions at high pressures and temperatures measured by the brucite-periclase equilibrium. Contrib Mineral Petrol 125:200-212

Aranovich LY, Newton RC (1999) Experimental determination of CO_2-H_2O activity-composition relations at 600-1000 °C and 6-14 kbar by reversed decarbonation and dehydration reactions. Am Mineral 84:1319-1332

Asahara Y, Murakami M, Ohishi Y, Hirao N, Hirose K (2010) Sound velocity measurement in liquid water up to 25 GPa and 900 K: Implications for densities of water at lower mantle conditions. Earth Planet Sci Lett 289: 479-485

Audétat A, Keppler H. (2005) Solubility of rutile in subduction zone fluids, as determined by experiments in the hydrothermal diamond anvil cell. Earth Planet Sci Lett 232:393-402

Bass JD (2007) Mineral Physics: Techniques for measuring high P/T elasticity. *In*: Treatise of Geophysics. Price GD and Schubert J (eds.) Elsevier, p 269-292

Bassett WA, Anderson AJ, Mayanovic RA, Chou I-M (2000a) Hydrothermal diamond anvil cell for XAFS studies of first-row transition elements in aqueous solution up to supercritical conditions. Chem Geol 167:3-10

Bassett WA, Anderson AJ, Mayanovic RA, Chou I-M (2000b) Modified hydrothermal diamond anvil cells for XAFS analyses of elements with low energy absorption edges in aqueous solutions at sub- and supercritical conditions. Z Kristallogr 215:711-717

Bassett WA, Chou I-M, Anderson AJ, Mayanovic R (2005) Aqueous chemistry in the diamond anvil cell up to and beyond the critical point of water. *In*: Chemistry at Extreme Conditions. Riad Manaa M (ed) Elsevier, p 223-240

Bassett WA, Shen AH, Bucknum M, Chou I-M (1993) A new diamond anvil cell for hydrothermal studies to 2.5 GPa and from −190 °C to 1200 °C. Rev Sci Instrum 64:2340-2345

Bischoff JL, Rosenbauer RJ (1985) An empirical-equation of state for hydrothermal seawater (3.2% NaCl). Am J Sci 285:725-763

Blencoe JG, Drummond SE, Seitz JC, Nesbitt BE (1996) A vibrating-tube densimeter for fluids at high pressures and temperatures. Int J Thermophys 17:179-190

Bodnar RJ (1985) Pressure–volume–temperature-composition (PVTX) properties of the system water–sodium-chloride at elevated temperatures and pressures. PhD Dissertation. Pennsylvania State University

Bodnar RJ (1995) Experimental determination of the PVTX properties of aqueous solutions at elevated temperatures and pressures using synthetic fluid inclusions: H_2O-NaCl as an example. Pure Appl Chem 67:873-880

Bodnar RJ, Burnham CW, Sterner SM (1985) Synthetic fluid inclusions in natural quartz. III. Determination of phase equilibrium properties in the system H_2O-NaCl to 1000 °C and 1500 bars. Geochim Cosmochim Acta 49:1861-1873

Bodnar RJ, Sterner SM (1987) Synthetic fluid inclusions. *In:* Hydrothermal Experimental Techniques. Ulmer GC, Barnes HL (eds) Wiley, p 423-457

Brillouin L (1922) Diffusion de la lumiere et des rayonnes X par un corps transparent homogene; influence de l'agitation thermique. Ann Phys (Paris) 17:88-122 (in French)

Brodholt J (1998) Molecular dynamics simulations of aqueous NaCl solutions at high pressures and temperatures. Chem Geol 151:11-19

Brodholt J, Wood BJ (1993a) Simulations of the structure and thermodynamic properties of water at high pressures and temperatures. J Geophys Res 98:519-536

Brodholt J, Wood BJ (1993b) Molecular-dynamics simulations of the properties of CO_2-H_2O mixtures at high-pressures and temperatures. Am Mineral 78:558-564

Brodholt J, Wood BJ (1994) Measurements of the PVT properties of water to 25 kbars and 1600 °C. Geochim Cosmochim Acta 58:2143-2148

Brown GE, Farges F, Calas G (1995) X-ray scattering and X-ray spectroscopy studies of silicate melts. Rev Mineral 32: 317-410

Bunker G (2010) Introduction to XAFS-A practical guide to X-ray absorption fine structure spectroscopy. Cambridge Press

Bureau H, Keppler H (1999) Complete miscibility between silicate melts and hydrous fluids in the upper mantle: experimental evidence and geochemical implications. Earth Planet Sci Lett 165:187-196

Bureau H, Ménez B, Malavergne V, Somogyi A, Simionovici A, Massare D, Khodja H, Daudin L, Gallien JP, Shaw C, Bonnin-Mosbah M (2007) In situ mapping of high-pressure fluids using hydrothermal diamond anvil cells. High Press Res 27:1-13

Burnham CW, Holloway JR, Davis NF (1969) The specific volume of water in the range 1000 to 8900 bars, 20 °C to 900 °C. Am J Sci 267A:70-95

Corti HR, Abdulagatov IM (2008) PVTx properties of hydrothermal systems. *In*: Hydrothermal Experimental Data. Valyashko VM (ed) John Wiley & Sons, p 135-193

Crozier ED, Rehr JJ, Ingalls R (1988) Amorphous and liquid systems. *In*: X-ray Absorption, Principles, Applications, Techniques of EXAFS, SEXAFS and XANES. Koningsberger DC, Prins R (eds) Wiley p 373-442

Cummins HZ, Gammon RW (1966) Rayleigh and Brillouin scatting in liquids: the Landau-Placzek ratio. J Chem Phys 44:2785 (1-12)

Dolejs D (2013) Thermodynamics of aqueous species at high temperatures and pressures: equations of state and transport theory. Rev Mineral Geochem 76:35-79

Dolejs D, Manning CE (2010) Thermodynamic model for mineral solubility in aqueous fluids: theory, calibration and application to model fluid-flow systems. Geofluids 10:20-40

Driesner T (2007) The system H_2O-NaCl. Part II: Correlations for molar volume, enthalpy, and isobaric heat capacity from 0 to 1000 degrees C, 1 to 5000 bar, and 0 to 1 X-NaCl. Geochim Cosmochim Acta 71:4902-4919

Driesner T (2013) The molecular-scale fundament of geothermal fluid thermodynamics. Rev Mineral Geochem 76:5-33

Elliott TR (2003) Tracers of the slab. *In*: Inside the Subduction Factory. Geophysical Monograph 138. Eiler J (ed) American Geophysical Union, Washington, p 23-45

Farges F (1996) Does Zr-F "complexation" occur in magmas? Chem Geol 127:253-268

Farges F, Brown GE (1997) Coordination chemistry of titanium(IV) in silicate glasses and melts. 4. XANES studies of synthetic and natural volcanic glasses and tektites at ambient temperature and pressure. Geochim Cosmochim Acta 61:1863-1870

Farges F, Brown GE, Navrotsky A, Gan H, Rehr JJ (1996) Coordination chemistry of Ti(IV) in silicate glasses and melts. 3. Glasses and melts from ambient to high temperatures. Geochim Cosmochim Acta 60:3055-3065

Farges F, Ponader CW, Brown GE (1991) Structural environments of incompatible elements in silicate glass melt systems. 1. Zirconium at trace levels. Geochim Cosmochim Acta 55:1563-1574

Fernandez DP, Goodwin ARH, Lemmon EW, Levelt-Sengers JMH, Williams RC (1997) A formulation for the static permittivity of water and steam at temperatures from 238 K to 873 K at pressures up to 1200 MPa, including derivatives and Debye-Hückel coefficients. J Phys Chem Ref Data 26:1125-1166

Figgins R (1970) Inelastic light scattering in liquids: Brillouin scattering. Contemp Phys 12:283-297

Franz G (1982) The brucite-periclase equilibrium at reduced H_2O activities: some information about the system H_2O–NaCl. Am J Sci 282:1325-1339

Friend DG (2001) Speed of sound as a thermodynamic property of fluids. *In*: Modern Acoustical Techniques for the Measurement of Mechanical Properties. Experimental Methods in Physical Sciences. Vol. 39. Levy M, Bass HE, Stern R (eds) Academic Press, p 237-306

Frost DJ, Wood BJ (1997) Experimental measurements of the properties of H_2O-CO_2 mixtures at high pressures and temperatures. Geochim Cosmochim Acta 61:3301-3309

Fu B, Touret JLR, Zheng YF (2001) Fluid inclusions in coesite-bearing eclogites and jadeite quartzite at Shuanghe, Dabie Shan (China). J Metamorph Geol 19:529-545

Fulton JL, Pfund DM, Wallen SL, Newville M, Stern EA, Ma Y (1996) Rubidium ion hydration in ambient and supercritical water. J Phys Chem 105: 2161-2166

Gammons CH, Wood SA, Youning L (2002) Complexation of the rare earth elements with aqueous chloride at 200 °C and 300 °C and saturated water vapor pressure. *In*: Water-Rock Interactions, Ore Deposits, and Environmental Geochemistry: A Tribute to David A. Crerar. Special Publication **7**. The Geochemical Society.

Gao J, Klemd R (2001) Primary fluids entrapped at blueschist to eclogite transition: evidence from the Tianshan meta subduction complex in northwest China. Contrib Mineral Petrol 142:1-14

Gao J, John T, Klemd R, Xiong X M (2007) Mobilization of Ti-Nb-Ta during subduction: Evidence from rutile-bearing dehydration segregations and veins hosted in eclogite, Tianshan, NW China. Geochim Cosmochim Acta 71:4974-4996

Gottschalk M (2007) Equations of state for complex fluids. Rev Mineral Geochem 65:49-97

Gout R, Pokrovski GS, Schott J, Zwick A (2000) Raman spectroscopic study of aluminum silicate complexes at 20 °C in basic solutions. J Sol Chem 29:1173-1186

Grimsditch M (2001) Brillouin scattering. *In*: Handbook of Elastic Properties of Solids, Liquids, and Gases. Vol 1. Dynamic Methods for Measuring the Elastic Properties of Solids. Levy M, Bass HE, Stern RR, Keppens V (eds) Academic Press, p 331-347

Gross E (1930) Change of wave-length of light due to elastic heat waves at scattering in liquids. Nature 126:400-404

Hack A, Thompson AB (2011) Density and viscosity of hydrous magmas and related fluids and their role in subduction zone processes. J Petrol 52:1333-1362

Hack AC, Thompson AB, Aerts M (2007) Phase relations involving hydrous silicate melts, aqueous fluids and minerals. Rev Mineral Geochim 65:129-185

Harvey AH, Friend DG (2004) Physical properties of water. *In*: Physical Chemistry in Water, Steam and Hydrothermal Solutions. Palmer DA, Fernandez-Prini R, Harvey AH (eds), Elsevier, p 1-27

Hayden LA, Manning CE (2011) Rutile solubility in supercritical $NaAlSi_3O_8$–H_2O fluids. Chem Geol 28:74-81

Helgeson HC, Kirkham DH, Flowers GC (1981) Theoretical prediction of the thermodynamic behavior of aqueous electrolytes at high pressures and temperatures: IV. Calculations of activity coefficients, osmotic coefficients, and apparent molal and standard and relative partial molal properties to 600 °C and 5 kbar. Am J Sci 281:1241-1516

Hermann J, Spandler C, Hack A, Korsakov AV (2006) Aqueous fluids and hydrous melts in high pressure and ultra-high pressure rocks: Implications for element transfer in subduction zones. Lithos 92:399-417

Heydemann PIM, Houck JC (1969) Self-consistent ultrasonic methods for the determinations of the equation of state of liquids at very high pressures. J Appl Phys 40:1609-1613

Hilbert R (1979) PVT-Daten von Wasser und von wässrigen Natriumchlorid-Lösungen. PhD Dissertaion, Universität Karlsruhe

Hoffmann MM, Darab JG, Heald SM, Yonker CR, Fulton JL (2000) New experimental developments for *in situ* XAFS studies of chemical reactions under hydrothermal conditions. Chem Geol 167:89-103

Holland T, Powell R (1991) A Compensated-Redlich-Kwong (CORK) Equation for volumes and fugacities of CO_2 and H_2O in the range 1 bar to 50 kbar and 100-1600 °C. Contrib Mineral Petrol 109:265-273

Holloway JR (1971) Internally heated pressure vessels. *In:* Research Techniques for High Pressure and High Temperature. Ulmer GC (ed) Springer-Verlag, p 217-258

Holton G (1951) Ultrasonic propagation in liquids under high pressures: velocity measurements on water. J Appl Phys 22:1407-1413

Hunt JD, Kavner A, Schauble EA, Snyder D, Manning CE (2011) Polymerization of aqueous silica in H_2O-K_2O solutions at 25-200 °C and 1 bar to 20 kbar. Chem Geol 283:161-170

Hunt JD, Manning CE (2012)A thermodynamic model for the system SiO_2-H_2O near the upper critical end point based on quartz solubility experiments at 500-1100 °C and 5-20 kbar. Geochim Cosmochim Acta 86:196-213

Ingalls R, Tranquada JM, Whitmore JE, Crozier ED (1981) X-ray absorption spectroscopy at high pressures. *In:* Physics of solids under high pressure: proceedings of the International Symposium on the Physics of Solids under High Pressure, Bad Honnef, Germany, August 10-14, 1981. Schilling JS, Shelton RN (eds) North-Holland Pub. Co., p 67-72

Kalinichev AG (2001) Molecular simulations of liquid and supercritical water: thermodynamics, structure, hydrogen bonding. Rev Mineral Geochem 42:83-129

Kanazhevskii VV, Shmachkova VP, Kotsarenko NS, Kolomiichuk VN, Kochubei DI (2006) Changes in the zirconium local surrounding on ligand substitution in solutions. J Struct Chem 47:860-868

Kawabe I (1992) Lanthanide tetrad effect in Ln^{3+} ionic radii and the refined spin-pairing energy theory. Geochem J 26:309-335

Kelemen PB, Johnson KTM, Kinzler RJ, Irving AJ (1990) High field strength element depletions in arc basalts due to mantle-magma interactions. Nature 345:521-524

Keppler H (1993) Influence of fluorine on the enrichment of high-field strength trace-elements in granitic-rocks. Contrib Mineral Petrol 114:479-488

Keppler H (1996) Constraints from partitioning experiments on the composition of subduction-zone fluids. Nature 380:724-727

Kerrick DM, Jacobs GK (1991) A modified Redlich-Kwong equation of state for H_2O, CO_2 and H_2O-CO_2 mixtures at elevated pressures and temperatures. Am J Sci 281:735-767

Kessel R, Schmidt MW, Ulmer P, Pettke T (2005a) Trace element signature of subduction-zone fluids, melts and supercritical liquids at 120-180 km depth. Nature 437:724-727

Kessel R, Ulmer P, Pettke T, Schmidt MW, Thompson AB (2005b) The water-basalt system at 4 to 6 GPa: phase relations and second critical endpoint in a K-free eclogite at 700 to 1400 C. Earth Planet Sci Lett 237:873-892

Knight CL, Bodnar RJ (1989) Synthetic fluid inclusions. IX. Critical PVTX properties of NaCl-H_2O solutions. Geochim Cosmochim Acta 53:3-8

Leberman R, Soper AK (1995) Effect of high-salt concentrations on water structure. Nature 378:364-366

Lin F, Bodnar RJ (2010) Synthetic fluid inclusions XVIII: Experimental determination of the PVTX properties of H_2O–CH_4 to 500 °C, 3 kbar and $XCH_4 < 4$ mol%. Geochim Cosmochim Acta 74:3260-3272

Louvel M, Sanchez-Valle C, Malfait WJ, Testemale D, Hazemann J-L (2013) Zr complexation in high pressure aqueous fluids and silicate melts and implications for HFSE mobilization in subduction zones. Geochim Cosmochim Acta 104:281-299

Lyzenga GA, Ahrens TJ, Nellis WJ, Mitchell AC (1982) The temperature of shock-compressed water. J Chem Phys 76:6282-6286

Majer V, Gates JA, Inglese A, Wood RH (1988) Volumetric properties of aqueous NaCl solutions from 0.0025 to 5.0 mol/kg^{-1}, 323 to 600 K, and 0.1 to 40 MPa. J Chem Thermodyn 20, 949

Majer V, Hui L, Crovetto R, Wood RH (1991) Volumetric properties of aqueous 1-1 electrolyte solutions near and above the critical temperature of water I. Densities and apparent molar volumes of NaCl(aq) from 0.0025 to 3.1 mol/kg^{-1}, 604.4 to 725.5 K, and 18.5 to 38.0 MPa. J Chem Thermodyn 23:213-225

Mandelstam LI (1926) Light scattering by inhomogeneous media. Zh Russ Fiz-Khim Ova 58:381-391

Manning CE (1994) The solubility of quartz in H_2O in the lower crust and upper mantle. Geochim Cosmochim Acta 58:4831-4839

Manning CE (1998) Fluid composition at the blueschist - eclogite transition in the model system Na_2O-MgO-Al_2O_3-SiO_2-H_2O-HCl. Schweiz Mineral Petrogr Mitt 78:225-242

Manning CE (2004a) The chemistry of subduction-zone fluids. Earth Planet Sci Lett 223:1-16

Manning CE (2004b) Polymeric silicate complexing in aqueous fluids at high pressure and temperature, and its implications for water–rock interaction. *In*: Water–Rock Interaction. Proceedings of the 11th International Symposium on Water-rock Interactions. Wanty RB, Seal II RR (eds) London, p 45–49

Manning CE (2007) Solubility of corundum plus kyanite in H_2O at 700 °C and 10 kbar: evidence for Al-Si complexing at high pressure and temperature. Geofluids 7:258-269

Manning CE (2013) Thermodynamic modeling of fluid-rock interaction at mid-crustal to upper-mantle conditions. Rev Mineral Geochem 76:135-164

Manning CE, Antignano A, Lin HA (2010) Premelting polymerization of crustal and mantle fluids, as indicated by solubility of albite + paragonite + quartz in H_2O at 1 GPa and 350-620 °C. Earth Planet Sci Lett 292:325-336

Manning CE, Wilke M, Schmidt C, Cauzid J (2008) Rutile solubility in albite-H_2O and $Na_2Si_3O_7$-H_2O at high temperatures and pressures by in-situ synchrotron radiation micro-XRF. Earth Planet Sci Lett 272:730-737

Mantegazzi D (2012) PVTx properties of saline aqueous fluids from acoustic velocity measurements by Brillouin scattering spectroscopy. PhD Dissertation, ETH Zurich

Mantegazzi D, Sanchez-Valle C, Driesner T (2013) Thermodynamic properties of aqueous NaCl solutions to 1073 K and 4.5 GPa, and implications for dehydration reactions in subducting slabs. Geochim Cosmochim Acta, doi: 10.1016/j.gca.2013.07.015

Mantegazzi D, Sanchez-Valle C, Reusser E, Driesner T (2012) Thermodynamic properties of sodium sulfate aqueous solutions to 773 K and 3 GPa derived from acoustic velocity measurements in the diamond anvil cell. J Chem Phys 137:224501 (1-8)

Marcus Y (1985) Ion Solvation. Chichester, New York, Wiley

Marcus Y (2009) Effect of ions on the structure of water: structure making and structure breaking. Rev Chem 109, 1346-1370

Marcus Y (2011) Electrostriction in electrolyte solutions. Chem Rev 111:2761-2783

Mayanovic RA, Jayanetti S, Anderson AJ, Bassett WA, Chou I-M (2003) Relaxation of the structure of simple metal ion complexes in aqueous solutions at up to supercritical conditions. J Chem Phys 118:719-727

Mayanovic RA, Anderson AJ, Bassett WA, Chou I-M (2007a) On the formation and structure of rare-earth element complexes in aqueous solutions under hydrothermal conditions with new data on gadolinium aqua and chloro complexes. Chem Geol 239:266-283

Mayanovic RA, Anderson AJ, Bassett WA, Chou I-M (2007b) Spectroscopic studies of Eu/HNO_3 aqueous solutions at high temperatures and pressures and Nb-bearing silicate melt phases coexisting with hydrothermal fluids by improved mounting of a modified hydrothermal diamond anvil cell. Rev Sci Instrum 78:053904 (1-9)

Mayanovic RA, Anderson AJ, Bassett WA, Chou I-M (2009) The structure and stability of aqueous rare-earth elements in hydrothermal fluids: New results on neodymium(III) aqua and chloroaqua complexes in aqueous solutions to 500 °C and 520 MPa. Chem Geol 259:30-38

Mayanovic RA, Jayanetti S, Anderson AJ, Bassett WA, Chou I-M (2002) The structure of Yb^{3+} aquo ion and chloro complexes in aqueous solutions at up to 500 °C and 270 MPa. J Phys Chem A 106:6591-6599

Mayanovic RA, Yan H, Anderson AJ, Solferino G (2013) Investigation of the structural environment of Ta in a silicate glass and water system under high P–T conditions. J Non-Cryst Solids 368:71-78

McCulloch M, Gamble A (1991) Geochemical and geodynamical constraints on subduction zone magmatism. Earth Planet Sci Lett 102:358-374

Messner CB, Hofer TS, Randolf BR, Rode BM (2011) Structure and dynamics of the Zr^{4+} ion in water. Phys Chem Chem Phys 13:224-229

Mibe K, Kawamoto T, KN Matsukage NK, FeiY, Ono S (2011) Slab melting versus slab dehydration in subduction-zone magmatism. Proc Natl Acad Sci 108:8177-8182

Mibe K, Chou I-M, Bassett WA (2008) *In situ* Raman spectroscopic investigation of the structure of subduction-zone fluids. J Geophys Res 113, B04208

Migdisov AA, Williams-Jones AE, Wagner T (2009) An experimental study of the solubility and speciation of the Rare Earth Elements (III) in fluoride- and chloride-bearing aqueous solutions at temperatures up to 300 degrees C. Geochim Cosmochim Acta 73:7087-7109

Millero FJ, Vinokurova F, Fernandez M, Hershey JP (1987) PVT properties of concentrated electrolytes. 6. The speed of sound and apparent molal compressibilities of NaCl, Na_2SO_4, $MgCl_2$, and $MgSO_4$ solutions from 0 °C to 100 °C. J Solution Chem 16:269-284

Mosselmans JFW, Schofield PF, Charnock JM, Garner CD, Patrick RAD, Vaughan DJ (1996) X-ray absorption studies of metal complexes in aqueous solution at elevated temperatures. Chem Geol 127:339-350

Mountain RD (1966) Thermal relaxation and Brillouin scattering in liquids. J Res Nat Bur Stand.-A. Phys Chem 70A:207-220

Murakami M, Asahara Y, Ohishi Y, Hirao N, Hirose K (2008) Development of in situ Brillouin spectroscopy at high pressure and high temperature with synchrotron radiation and infrared laser heating system: Application to the Earth's deep interior. Phys Earth Planet Sc 174:282-291

Mysen (1998) Interactions between aqueous fluids and silicate melt in the pressure and temperatures regime of the Earth's crust and upper mantle. Neues Jahrb Mineral Abh 172:227-244

Mysen B (2012) High-pressure and high-temperature titanium solution mechanisms in silicate-saturated aqueous fluids and hydrous silicate melts. Am Mineral 87:1241-1251

Newton RC, Manning CE (2002) Experimental determination of calcite solubility in H_2O–NaCl solutions at deep crust/upper mantle pressure and temperatures: implications for metasomatic processes in shear zones. Am Mineral 87:1401-1409

Newton RC, Manning CE (2003) Activity coefficient and polymerization of aqueous silica at 800 °C, 12 kbar, from solubility measurements on SiO_2-buffering mineral assemblages. Contrib Mineral Petrol 146:135-143

Newton RC, Manning CE (2005) Solubility of anhydrite, $CaSO_4 \cdot H_2O$, in NaCl-H_2O solutions high pressures and temperatures: applications to fluid-rock interactions. J Petrol 46:701-716

Newton RC, Manning CE (2008a) Thermodynamics of SiO_2-H_2O fluid near the upper critical end point from quartz solubility measurements at 10 kbar. Earth Planet Sci Lett 274:241-249

Newton RC, Manning CE (2008b) Solubility of corundum in the system Al_2O_3–SiO_2–H_2O–NaCl at 800 °C and 10 kbar. Chem Geol 249:250-261

Nugent LJ (1970) Theory of the tetrad effect in the lanthanide(III) and actinide(III) series. J Inorg Nucl Chem 32:3485-3491

Oakes CS, Simonson JM, Bodnar RJ (1995) Apparent molar volumes of aqueous calcium chloride to 250°C, 400 bars, and molalities of 0.242 to 6.150. J Solution Chem 24, 897-916

Pan D, Spanu L, Harrison B, Sverjensky DA, Galli G (2013) Dielectric properties of water under extreme conditions and transport of carbonates in the deep Earth. Proc Natl Acad Sci USA 110:6646-6650

Peacock SM, Wang K (1999) Seismic consequences of warm versus cool subduction metamorphism: examples from Southwest and Northeast Japan. Science 286:937-939

Piilonen PC, Farges F, Linnen RL, Brown GE, Pawlak M, Pratt A (2006) Structural environment of Nb^{5+} in dry and fluid-rich (H_2O, F) silicate glasses: A combined XANES and EXAFS study. Can Mineral 44:775-794

Pitzer (1983) Dielectric constant of water at very high temperature and pressure. Proc Natl Acad Sci 80:4575-4576

Pitzer KS, Sterner SM (1994) Equations of state valid continuously from zero to extreme pressures for H_2O and CO_2. J Chem Phys 101:3111-3116

Pokrovski GS, Borisova AY, Bychkov AY. (2013) Speciation and transport of metals and metalloids in geological vapors. Rev Mineral Geochem 76:165-218

Pokrovski GS, Schott J, Harrichoury JC, Sergeyev AS (1996) The stability of aluminum silicate complexes in acidic solutions from 25 to 150 °C. Geochim Cosmochim Acta 60:2495-2501

Poli S, Schmidt MW (2002) Petrology of subducted slabs. Annu Rev Earth Planet Sci 30:207-235

Polian A, Simon P, Pages O (2010) Optical spectroscopy methods and high-pressure–high-temperature studies. *In:* Thermodynamic Properties of Solids. Chaplot SL, Mittal R, Choudhury N (eds) Wiley-VHC, p 223-286

Qin J, Li M, Li J, Chen R, Duan Z, Zhou Q, Li F, Cui Q (2010) High temperatures and high pressures Brillouin scattering studies of liquid H_2O+CO_2 mixtures. J Chem Phys 133:154513-154513-6

Quist AS, Marshall WL (1968) Electrical conductance of aqueous sodium chloride solutions from 0 to 800 °C at pressures up to 4000 bars. J Phys Chem 72:684-703

Roedder E (1984) Fluid Inclusions. Rev Mineral 12:1-644

Rogers PSZ, Pitzer KS (1982) Volumetric properties of aqueous sodium chloride solutions. J Chem Phys Ref Data 11:15-81 (1982)

Rubatto D, Hermann J (2003) Zircon formation during fluid circulation in eclogites (Monviso, Western Alps): Implications for Zr and Hf budget in subduction zones. Geochim Cosmochim Acta 67:2173-2187

Rudnick RL, Barth M, Horn I, McDonough WF (2000) Rutile-bearing refractory eclogites: Missing link between continents and depleted mantle. Science 287:278-281

Salvi S, Pokrovski GS, Schott J (1998) Experimental investigation of aluminum–silica aqueous complexing at 300 °C. Chem Geol 151:51-67

Sanchez-Valle C, Chio C-H, Gatta GD (2010) Elasticity of pollucite: a zeolite with potential applications to the storage of radioactive Cs. J Appl Phys 108:093509

Sanchez-Valle C, Daniel I, Martinez I, Simionovici A, Reynard B (2004) Progress in quantitative analyses of high P-T fluids using *in situ* Synchrotron X-ray fluorescence spectroscopy. J Phys Condens Matt 16:S1197-S1206

Sanchez-Valle C, Mantegazzi D, Bass JD, Reusser E (2013) Equation of state, refractive index and polarizability of compressed water to 7 GPa and 673 K. J Phys Chem 138:054505 (1-9)

Sanchez-Valle C, Martinez I, Daniel I, Philippot P, Bohic S, Simionovici A (2003) Dissolution of strontianite at high P-T conditions: an *in situ* Synchrotron X-ray fluorescence study. Am Mineral 88:978-985

Sandercock JR (1982) Trends in Brillouin-scattering - studies of opaque materials, supported films, and central modes. *In*: Light Scattering in Solids. III. Recent Results. Cardona M, Guntherodt G (eds) Springer-Verlag, p 51-173

Schmidt C, Bodnar RJ (2000) Synthetic fluid inclusions. XVI. PVTX properties in the system H_2O-NaC-CO_2 at elevated temperatures, pressures, and salinities. Geochim Cosmochim Acta 64:3853-3869

Schmidt C, Rickers K (2003) In-situ determination of mineral solubilities in fluids using a hydrothermal diamond-anvil cell and SR-XRF: solubility of AgCl in water. Am Mineral 88:288-292

Schmidt C, Rosso, KM, Bodnar RJ (1995) Synthetic fluid inclusions. XIII. Experimental determination PVT properties in the system H_2O + 40 wt% NaCl + 5 mol% CO_2 at elevated temperature and pressure. Geochim Cosmochim Acta 59:3953-3959

Seitz JC, Blencoe JG (1996) Volumetric properties for $\{(1-x)CO_2+xCH_4\}$, $\{(1-x)CO_2+xN_2\}$ and $\{(1-x)CH_4+xN_2\}$ at the pressures (19.94, 29.94, 39.94, 59.93, 79.93, and 99.93) MPa and the temperature 673.15 K. J Chem Thermodyn 28:1207-1213

Seitz JC, Blencoe JG (1999) The CO_2–H_2O system. Experimental determination of volumetric properties at 400 °C, 10-100 MPa. Geochim Cosmochim Acta 63:1559-1569

Seward TM (1981) Metal complex formation in aqueous solutions at elevated temperatures and pressures. *In*: Chemistry and Geochemistry of Solutions at High Temperatures and Pressures. Pergamon Press. Phys Chem Earth 13-14:113-132

Seward TM, Driesner T (2004) Hydrothermal solution structure: experiments and computer simulations. *In:* Physical Chemistry in Water, Steam and Hydrothermal Solutions. Palmer DA, Fernandez-Prini R, Harvey AH (eds) Elsevier Amsterdam, p 149-182

Seward TM, Henderson CMB, Charnock JM, Dobson BR (1996) An X-ray absorption (EXAFS) spectroscopic study of aquated Ag^+ in hydrothermal solutions to 350 °C. Geochim Cosmochim Acta 60:2273-2282

Seward TM, Henderson CMB, Charnock JM, Driesner T (1999) An EXAFS study of solvation and ion pairing in aqueous strontium solutions to 300 °C. Geochim Cosmochim Acta 63:2409-2418

Shen AH, Keppler H (1997) Direct observation of complete miscibility in the albite-H_2O system. Nature 385:710-712

Sherman DM, Ragnarsdottir KV, Oelkers EH, Collins CR (2000) Speciation of tin (Sn^{2+} and Sn^{4+}) in aqueous Cl solutions from 25 °C to 350 °C: an in situ EXAFS study. Chem Geol 167:169-176

Shmulovich KI, Shmonov VM, Zharikov VA (1982) The thermodynamics of supercritical fluid systems. *In*: Advances in Physical Geochemistry. Saxena SK (ed) Springer, p 173-190

Silver E, Kastne rM, Fisher A, Morris J,. McIntosh K, Saffer D (2000) Fluid flow paths in the middle America Trench and Costa Rica margin. Geology 28: 679-682

Simonson JM, Oakes, CS, and Bodnar, RJ (1994) Densities of NaCl(aq) to the temperature 523 K at pressures to 40 MPa measured with a new vibrating-tube densitometer. J Chem Thermodyn 26:345-356

Sinogeikin SV, Bass JD, Prakapenka V, Lakshtanov DL, Shen G, Sanchez-Valle C, Rivers M (2006) A Brillouin spectrometer interfaced with synchrotron radiation for simultaneous X-ray density and acoustic velocity measurements. Rev Sci Instrum 77:103905

Sowerby JR, Kepller (2002) The effect of fluorine, boron and excess sodium on the critical curve in the albite-H_2O system. Contrib Mineral Petrol 143:32-37

Spandler C, Mavrogenes JA, Hermann J (2007) Experimental constraints on element mobility from subducted sediments using high P synthetic fluid/melt inclusions. Chem Geol 239:228-249

Stalder R, Ulmer P, Thompson AB, Gunther D (2000) High pressure fluids in the system MgO-SiO_2-H_2O under upper mantle conditions. Contrib Mineral Petrol 140:607-618

Sterner SM, Bodnar RJ (1991) Synthetic fluid inclusions. X. Experimental determination of P-V-T-X properties in the CO_2-H_2O system to 6 kb and 700°C. Am J Sci 291:1-54

Sykes D, Kubicki JD (1996) Four-membered rings in silica and aluminosilicate glasses. Am Mineral 81:265-272

Takenouchi S, Kennedy GC (1964) Binary system H_2O-CO_2 at high temperatures + pressures. Am J Sci 262:1055-1074

Taylor RP, Fryer BJ (1982) Rare earth element geochemistry as an aid to interpreting hydrothermal ore deposits. *In:* Metallization Associated with Acid Magmatism, Volume 6. Evans AM (ed) Wiley, New York, p 357-365

Tkachev SN, Manghnani MH, Williams Q, Ming LC (2005) Compressibility of hydrated and anhydrous Na_2O-$2SiO_2$ liquid and also glass to 8 GPa using Brillouin scattering. J Geophys Res 110:7201-7213

Tossell JA (1999) Theoretical studies on aluminate and sodium aluminate species in models for aqueous solution: $Al(OH)_3$, $Al(OH)_4^-$ and $NaAl(OH)_4$. Am Mineral 84:1641-1649

Tossell JA (2005) Theoretical study on the dimerization of $Si(OH)_4$ in aqueous solution and its dependence on temperature and dielectric constant. Geochim Cosmochim Acta 69:283-291

Tropper P, Manning CE (2005) Very low solubility of rutile in H_2O at high pressure and temperature, and its implications for Ti mobility in subduction zones. Am Mineral 90:502-505

Tryon MD, Wheat CG, Hilton DR (2010) Fluid sources and pathways of the Costa Rica erosional convergent margin. Geochem Geophys Geosyst 11:Q04S22, doi: 10.1029/2009GC002818

Ulmer P, Trommsdorf V. (1995) Serpentine stability to mantle depths and subduction-related magmatism. Science 268:858-661

Urusova MA (1975) Volume properties of aqueous solutions of sodium chloride at elevated temperatures and pressures. Russ J Inorg Chem 20:1717-1721

van Sijl J, Allan NL, Davies G, van Westrenen W (2009) Molecular modelling of rare earth element complexation in subduction zone fluids. Geochim Cosmochim Acta 73:3934-3947

van Sijl J, Allan NL, Davies G, van Westrenen W (2010) Titanium in subduction zone fluids: First insights from ab initio molecular metadynamics simulations. Geochim Cosmochim Acta_74:2797-2810

Wagner W, Pruß A (2002) The IAPWS formulation 1995 for the thermodynamic properties of ordinary water substance for general and scientific use. J Phys Chem Ref Data 31:387-535

Wasserman E, Wood B, Brodholt J (1995) The static dielectric-constant of water at pressures up to 20 kbar and temperatures to 1273 K - experiment, simulations, and empirical equations. Geochim Cosmochim Acta 59:1-6

Weidner D, Swyler K, Carleton H (1975) Elasticity of microcrystals. Geophys Res Lett 2:189-192

Whitfield CH, Brody EH, Bassett WA (1976) Elastic-moduli of NaCl by Brillouin-scattering at high-pressure in a diamond anvil cell. Rev Sci Instrum 47:942-947

Wilke M, Schmidt C, Dubrail J, Appel K, Borchert M, Kvashnina K, Manning CE (2012) Zircon solubility and zirconium complexation in H_2O+Na_2O+SiO_2±Al_2O_3 fluids at high pressure and temperature. Earth Planet Sci Lett 349-350:15-25

Wilke M, Schmidt C, Farges F, Malavergne, V, Gautron L, Simionvici A, Hahn M, Petit P-E (2006) Structural environment of iron in hydrous aluminosilicate glass and melt-evidence from X-ray absorption stpectroscopy. Chem Geol 229:144-161

Williams-Jones AE, Samson IM, Olivo GR (2000) The genesis of hydrothermal fluorite-REE deposits in the Gallinas Mountains, New Mexico. Econ Geol 95:327-342

Wilson WD (1959) Speed of sound in distilled water as a function of temperature and pressure. J Acoust Soc Am 31:1067-1072

Wiryana S, Slutsky LJ, Brown JM (1998) The equation of state of water to 200 degrees C and 3.5 GPa: model potentials and the experimental pressure scale. Earth Planet Sci Lett 163:123-130

Withers AC, Kohn SC, Brooker R, Wood BJ (2000) A new method for determining the P-V-T properties of high-density H_2O using NMR: Results at 1.4-4.0 GPa and 700-1100 °C. Geochim Cosmochim Acta 64:1051-1057

Wood SA (1990) The aqueous geochemistry of the rare-earth elements and yttrium. Part 2. Theoretical predictions of speciation of hydrothermal solutions to 350 °C at saturated water vapor pressure. Chem Geol 88:99-125

Zhang Z, Duan Z (2005) Prediction of the PVT properties of water over wide range of temperature and pressures from molecular dynamics simulations. Phys Earth Planet Interiors 149:335-354

Zotov N, Keppler H (2000) *In situ* Raman spectra of dissolved silica species in aqueous fluids to 900 C and 14 kbar. Am Mineral 85:600-604

Zotov N, Keppler H (2002) Silica speciation in aqueous fluids at high pressures and high temperatures. Chem Geol 184:71-82

Reviews in Mineralogy & Geochemistry
Vol. 76 pp. 311-350, 2013
Copyright © Mineralogical Society of America

9

Thermodynamics of Organic Transformations in Hydrothermal Fluids

Everett L. Shock[1,2], Peter Canovas[1], Ziming Yang[2], Grayson Boyer[2], Kristin Johnson[2], Kirtland Robinson[2], Kristopher Fecteau[2], Todd Windman[2], Alysia Cox[1]

GEOPIG
[1]School of Earth & Space Exploration
[2]Department of Chemistry & Biochemistry
Arizona State University
Tempe, Arizona 85287, U.S.A.

Everett.Shock@asu.edu

MESSAGES FROM NATURE

Hydrothermal fluids obtain organic compounds through diverse pathways. In submarine systems organic compounds are already dissolved in seawater that is heated and transformed into hydrothermal fluids through water-rock reactions. Microbes inhabiting hydrothermal systems produce metabolites that enter the fluids, and cells can be carried into the reaction zones by circulating fluids and pyrolyzed. Analogous sources of organic compounds can be anticipated in continental systems with the possible addition of novel plant- and soil-derived organic compounds from the surface. In addition, hydrothermal systems possess large potentials for abiotic organic synthesis that may add a novel suite of compounds. When sedimentary rocks are present, ancient biogenic organic matter can be mobilized or transformed by hot fluids. These transformations accompany the generation of petroleum, coal, and other fossil fuels, suggesting that expectations for hydrothermal transformations can be built on those that occur in sedimentary basins. Likewise, some types of ore deposition are accompanied by transformations of organic compounds, and metal-organic complexes may be involved in enhancing the transport of metals in ore-forming and other crustal fluids. With these thoughts in mind, this review starts with an inventory of the types of organic compounds found in hydrothermal systems and some ways that hydrothermal organic compounds are transformed.

ORGANIC INVENTORY OF HYDROTHERMAL FLUIDS

Methane can be generated biotically and abiotically from organic or inorganic reactants, and since it lacks a carbon-carbon bond, some researchers would not consider it to be an organic compound. Nevertheless, more data exist for methane in hydrothermal fluids than for any organic compound that fits the definition. Methane has been quantified in continental and submarine hydrothermal fluids, fumarolic gases associated with hydrothermal systems, oil-field brines, deep fluids in sedimentary basins and igneous basement rocks, fluids associated with active serpentinization, and fluid inclusions in minerals from ore deposits, sedimentary basins, and deep crustal settings (recent examples include: Sherwood-Loller et al. 2002; Tassi et al. 2003, 2005a,b, 2007, 2012a,b,c; Potter et al. 2004; Fiebig et al. 2004, 2007, 2009, Cruse and Seewald 2006, 2010; Ikorsky and Avedisyan 2007; Taran et al. 2010; Cinti et al. 2011; Nivin 2011; McLin et al. 2012; Magro et al. 2013). Typical abundances in submarine hy-

1529-6466/13/0076-0009$05.00 http://dx.doi.org/10.2138/rmg.2013.76.9

drothermal fluids from unsedimented basalt-hosted mid-ocean ridge settings are <0.5 millimolal, but up to 2.5 millimolal in systems hosted in ultramafic rocks (McCollom 2008; Shock and Canovas 2010). Hydrothermal fluids in submarine systems buried beneath sediments can contain an order of magnitude more methane than ultramafic-hosted fluids, or more (Charlou et al. 1998, 2002, 2010; Douville et al. 2002; Melchert et al. 2008; Proskurowski et al. 2008; Fabri et al. 2011; Konn et al. 2011). The consequences for the thermodynamic activities of aqueous methane ($CH_{4(aq)}$) when submarine hydrothermal fluids mix with seawater are illustrated in Figure 1. The highest temperature for each curve in this figure corresponds to the activity of $CH_{4(aq)}$ in each individual end-member hydrothermal fluid (Shock and Canovas 2010). Note that the spread of $CH_{4(aq)}$ activities in this selection of end-member submarine hydrothermal fluids spans four orders of magnitude.

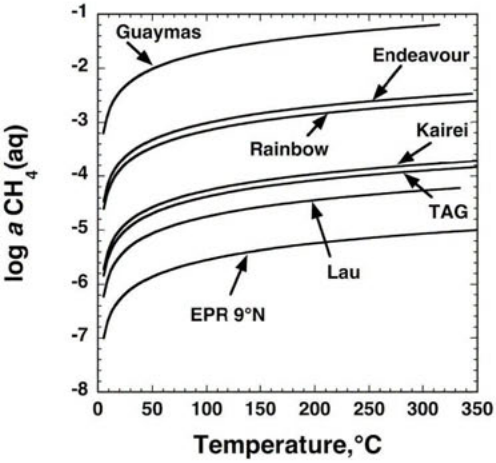

Figure 1. Calculated activities of aqueous methane resulting from mixing of submarine hydrothermal fluids with seawater (modified after Shock and Canovas 2010). The high temperature ends of the curves start at the temperature of each submarine fluid. Samples represent basalt-hosted (EPR 9°N, TAG, Kairei), back-arc (Lau), ultramafic-hosted (Rainbow) and sediment-affected (Endeavor) or covered (Guaymas) systems.

At continental hydrothermal settings, using Yellowstone as a reference point, methane is often detected in gases at <1 mol% on an H_2O-free basis (Mazor and Wasserburg 1965; Gunter and Musgrave 1966; White et al. 1971; Thompson and Hutchinson 1981; Werner and Brantley 2003; Werner et al. 2008; Bergfeld et al. 2011; Chiodini et al. 2012). Bergfeld et al. (2011) report methane abundances as high as 8.2 mol% at Washburn Hot Springs in Yellowstone, where Allen and Day (1935) report methane concentrations up to 15 mol%. Reports from hydrothermal and fumarolic systems at volcanoes in Italy, Greece, the Philippines, Taiwan, Chile, El Salvador, and Mexico are typically < 0.3 mol% (Capaccioni et al. 2001; Tassi et al. 2003, 2005a,b, 2007, 2012a,b,c; Fiebig et al. 2004, 2007; Yang 2008; Magro et al. 2013).

In many sites of active serpentinization where high concentrations of dissolved H_2 were measured (up to 16 millimolal), methane abundances are also elevated, reaching concentrations as high as 2.5 millimolal, as documented at submarine sites including Lost City (Kelley et al. 2001, Proskurowski et al. 2006, 2008), Rainbow (Charlou et al. 2002), Logatchev 1 (Charlou et al. 2002, Proskurowski et al. 2006), Logatchev 2, Ashadze 1 and 2 (Charlou et al. 2010), and Nibelungen (Melchert et al. 2008), as well as Conical Seamount and South Chamorro Seamount in the Mariana Forearc (Mottl et al. 2003), and at continental ophiolites including Samail (Neil and Stanger 1983), Tablelands (Szponar et al. 2012), Gruppo di Voltri (Cipolli et al. 2004), Zambales (Abrajano et al. 1988), Chimaera and Tekirova (Hosgormez et al. 2008; Etiope et al. 2011), The Cedars (Morrill et al. 2013), and Socorro Island (Taran et al. 2010). The consistent observation that abundant methane concentrations can be found in serpentinizing systems suggests that methane generation is inherent to this geochemical process.

Light hydrocarbons (C_{2+}) are often quantified in many of the same samples that yield methane data, and typically have a much lower abundance than methane leading to ratios of C_1/C_{2+} from < 100 to > 4000 in submarine hydrothermal fluids (see review by McCollom 2008).

Interpretations can be complex though as exemplified by the Main Endeavour Field, which is an unsedimented hydrothermal system on the Juan De Fuca ridge that displays characteristics of being influenced by hydrothermal fluids that have interacted with sediments. Compared to other unsedimented ridges, it has higher concentrations of methane and total ammonia (Lilley et al. 1993) with prominent concentrations of C_1–C_3 alkanes, alkenes, benzene and toluene (Cruse and Seewald 2010). Curiously, similarly high ratios of C_1/C_{2+} are found in emanations from seafloor gas hydrates (Lapham et al. 2013).

Light hydrocarbons were observed only rarely in early studies from Yellowstone, because in most cases stripping of the gas stream of carbon dioxide (typically the most abundant gas besides water vapor) is necessary to concentrate the trace gases for analysis. Using this approach, hydrocarbons as large as butane were first analyzed in Yellowstone samples in the 1970's (Gunter 1978). Both *n*-butane and *iso*-butane were present in comparable amounts and ethane, ethene and propene were also detected, but alkynes were below detection. The amounts of each of the alkanes were inversely correlated with carbon number in a pattern reminiscent of natural gas. Related methods have enabled a recent flood of research into light hydrocarbons associated with volcanic fumaroles and hydrothermal fluids (Darling 1998a,b; Capaccioni and Mangani 2001; Capaccioni et al. 2001, 2004; Tassi et al. 2003, 2005a,b, 2007, 2009, 2010c, 2012b,c; Gherardi et al. 2005; Schwandner et al. 2013). As discussed below, these data are being combined with thermodynamic calculations to estimate deep subsurface temperatures and oxidation states.

Headspace solid phase microextraction can be a useful technique for investigating less volatile organic compounds in volcanic gases or dissolved in hydrothermal fluids, expanding beyond the suite of extremely volatile hydrocarbons associated with the gas phase of volcanic and hydrothermal systems (Mangani et al. 2004; Schwandner et al. 2004, 2013; Tassi et al. 2009, 2010a,b). These methods were applied to water samples from Italian hot springs along with analysis of the aqueous organic compounds (Di Gioia et al. 2006). Headspace analysis yielded a handful of alcohols, phenols, and esters. Analysis of redissolved lyophyllized (freeze-dried) residues of water samples revealed the presence of aliphatic acids, alcohols, and alkanes with even-numbered carbon-chain lengths between 12 and 20. This distribution is highly suggestive of being derived from algae, which were observed in the springs. A selection of Spanish thermal features having source temperatures in the range of 45-66 °C were analyzed for their dissolved organic carbon composition via gas chromatography-mass spectrometry (Gonzalez-Barreiro et al. 2009). A variety of sample preparation techniques were explored, including liquid-liquid extraction, solid phase extraction via a flow-through cartridge with a sorbent resin, and solid phase microextraction, and tuned for specific groups of compounds by selecting appropriate solvents or solid-phase materials. The combined results demonstrated that the springs were diverse in their organic functionality; among the functional groups detected were amines, amides, esters, ketones/aldehydes, carboxylic acids, alcohols, aliphatic and cyclic alkanes, and aromatic compounds. Microorganisms are cited as being responsible for many of the compounds, as well as the redox transformations needed to yield the variety of functional groups. Interpretation of both of these studies is complicated by the fact that water samples were not filtered prior to sample extraction, thus the signal of organic compounds directly extracted from planktonic microbes are likely contributing to, or even dominating, the suite of organic compounds detected and possibly masking the truly dissolved organic carbon.

Larger hydrocarbons are also occasionally reported in submarine hydrothermal fluids. At 13°N on the East Pacific Rise (EPR), nonvolatile hydrocarbons from high temperature vent fluids were found to be between 57 and 100 times more abundant in dissolved and particulate forms, respectively, than ambient bottom seawater (ABS), and warm fluids issuing from an adjacent fissure had levels 400 times that of ABS (Brault et al. 1988). Hydrothermal vent fluids from the Rainbow field on the Mid-Atlantic Ridge (MAR) are reported to contain C_9–C_{14} *n*-alkanes, C_9–C_{13} branched alkanes, C_9–C_{11} cycloalkanes, C_7–C_{12} monoaromatic hydrocarbons, naphthalene and methyl-naphthalene, C_{13}–C_{16} polycyclic aromatic hydrocarbons (PAHs; fluorene, phenanthrene, pyrene) and $C_{9:0}$–$C_{18:0}$ *n*-carboxylic acids (Holm and Charlou 2001; Konn et al. 2009, 2012). Experiments by Konn et al. (2011) on the hydrothermal degradation of *Pyrococcus abyssi* biomass offer evidence that a portion of the aliphatic hydrocarbons present in hydrothermal fluids at the Rainbow vent field may be abiogenic. Aromatic hydrocarbons and *n*-carboxylic acids though, may have a biogenic origin, with aromatic hydrocarbons and linear fatty acids being derived from thermogenic alteration of material from the subseafloor biosphere.

A variety of aromatic compounds were detected via liquid-liquid extraction of water samples from thermal wells in the Pannonian basin in Hungary (Kárpati et al. 1999; Varsanyi et al. 2002; Fekete et al. 2009). Among the compounds identified are alkylbenzenes, naphthalenes, indenes, fluorenes, biphenyls, and a variety of PAHs and heterocyclic compounds. Phenols were not detected in all samples, which the authors suggest is related to either the lack of terrestrially-derived humic substances or insufficient maturity of the kerogen in the sediments. In general, aromatic compounds appear at temperatures >80 °C, phenols at >90 °C, and organic acids at the hottest temperatures.

High concentrations of organic acids are reported in sedimentary basin fluids associated with coal and petroleum at concentrations up to 10,000 ppm (see compilations by Helgeson et al. 1993; Shock 1994, 1995). Their relative abundances were used to examine aqueous organic reaction paths in high-temperature/pressure fluids (Shock 1988, 1989, 1994; Helgeson et al. 1993; Seewald 2001; McCollom and Seewald 2003a; 2003b), as well as microbial transformations at lower temperatures (Manning 1997). In fact, the initial proposal that organic compounds reach states of metastable equilibrium in high-temperature geologic fluids emerged from analysis of acetic and propanoic acid concentrations in oil-field brines (Shock 1988, 1989).

Total concentrations of formic acid (both protonated and deprotonated forms) were measured in samples from geochemically diverse hot spring locations across Yellowstone (Windman et al. 2007). Formic acid concentrations ranged from below detection to approximately 500 ppb with the highest concentrations occurring in the more acidic (pH 2-3) samples, though there was no distinct pH dependence (see Fig. 2). Thermodynamic calculations using these measured formic acid concentrations in conjunction with analytical data for inorganic solutes demonstrate that formic acid oxidation is generally quite favorable, whereas formic acid reduction to methane is thermodynamically disfavored in many instances. These calculations suggest that aqueous reactions involving organic compounds are thermodynamically poised toward oxidation, especially when hot spring fluids, which are relatively reduced overall, reach the surface and encounter oxygen from the atmosphere. It follows that other organic compounds in more reduced oxidation states than that of formic acid (+2) exist even further from equilibrium.

Organic acids are also detected in submarine hydrothermal fluids (Konn et al. 2009; Lang et al. 2010). Formate and acetate concentrations are reported for fluids from the ultramafic-hosted Lost City hydrothermal field by Lang et al. (2010), who showed that end-member hydrothermal fluids are greatly enriched in these acids compared to local bottom seawater. These results are summarized in Figure 3, which shows the negative correlation of acid anion concentrations with increasing Mg abundance indicative of seawater contributions to the samples. Lang et al. (2010) argue for an abiotic source for the formate, consistent with isotopic data, and conclude that much of the acetate derives from microbial metabolism. Konn et al. (2009) report the identification of C_8 to C_{18} carboxylic acids in samples from Lost City and Rainbow hydrothermal fluids, and suggest biotic origins for these compounds, which is plausible given the presence of long-chain acids as microbial membrane components.

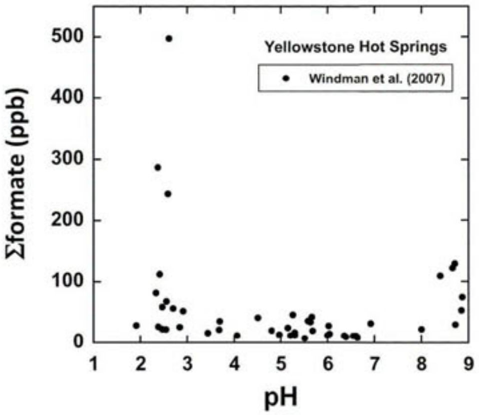

Figure 2. Total formate ($HCOO^-$ + $HCOOH$) concentrations reported in Yellowstone hot springs plotted against the pH of each hot spring.

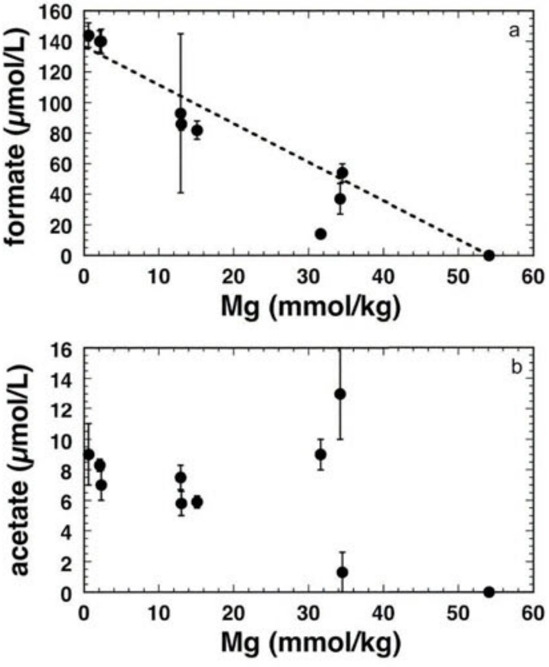

Figure 3. Concentrations of total formate and total acetate in fluids sampled at the Lost City submarine hydrothermal field, plotted against the total magnesium content of the fluids (modified after Lang et al. 2010). Extrapolation toward zero magnesium yields estimates of formate content of the hydrothermal fluids. Acetate data are more ambiguous.

HYDROTHERMAL ORGANIC TRANSFORMATION PROCESSES

Formation of petroleum in most deep sedimentary basins involves processes of macromolecular kerogen and bitumen reaction at elevated temperatures and pressures, where lower-molecular-weight petroleum products are produced through covalent bond cleavage and organic functional-group transformations. In many geologic settings aqueous solutions attend these transformations, although traditional models of petroleum generation downplay the involvement of H_2O as a reactant or product (see Manning et al. 2013). The conventional explanation for petroleum formation holds that when kerogen is subjected to increasing temperatures and pressures that exceed the "oil window," it is transformed into various petroleum products (Tissot and Welte 1984). These changes are commonly depicted on Van Krevelen diagrams that show changes in H/C and O/C ratios of kerogens, such as that in Figure 4. Various types of

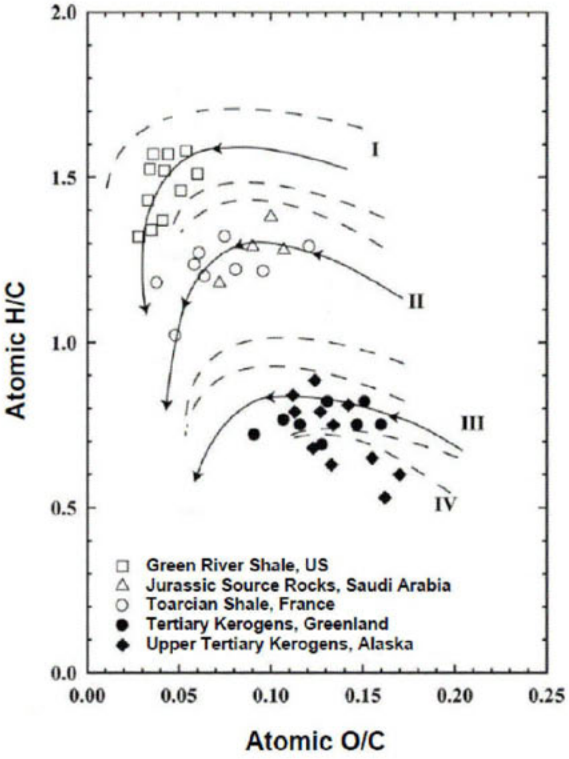

Figure 4. A Van Krevelen diagram showing compositions of kerogens in terms of their atomic ratios of hydrogen to carbon and oxygen to carbon. The symbols represent analytical data from natural samples; solid curves show trajectories of compositional change in three types of kerogen during diagenesis of sediments and subsequent burial and maturation when gas and oil are produced (modified after Helgeson et al. 2009).

kerogen begin with different H/C and O/C ratios, but their paths converge through the stages of maturation. In the conventional view, the decreasing trend of H/C and O/C ratios indicate that kerogen transformation involves both the elimination of carbonyl and carboxyl groups (both contain C=O that is present in ketones and acids), and the removal of hydrogen via C-H bond breaking, cyclization and aromatization of hydrocarbons. In other words, these alteration processes are associated with oxidation/reduction reactions.

Theoretical calculations and computer experiments allow a thermodynamic analysis of these transformations by characterizing the chemical interaction of kerogens and crude oils with their surrounding aqueous environments (Helgeson 1991; Helgeson et al. 1993, 2009). Under the hypotheses that 1) oil generation in source rocks is an inevitable and irreversible process of oxidation and reduction, and 2) that reactant kerogen and water, together with petroleum and $CO_{2(g)}$ products are driven toward metastable equilibrium with each other, Helgeson et al. (2009) applied group additivity algorithms and the thermodynamic properties of kerogen and petroleum in a series of calculations and simulations. Their models confirmed that a drive toward metastable equilibrium among the products (petroleum, oxidized kerogen, water, and CO_2 gas) of incongruent melting of immature kerogen is responsible for petroleum formation in source rocks.

Evidence from experimental studies of specific organic compounds suggest that reaction pathways linking the two most abundant groups in sedimentary basins, i.e., alkanes in petroleum and carboxylic acids in co-existing oil-field brines, include oxidation/reduction and hydration/dehydration at oil reservoir conditions (Fig. 5, Seewald 2003). The reactants and products in the stepwise reactions were shown to approach metastable equilibrium states through

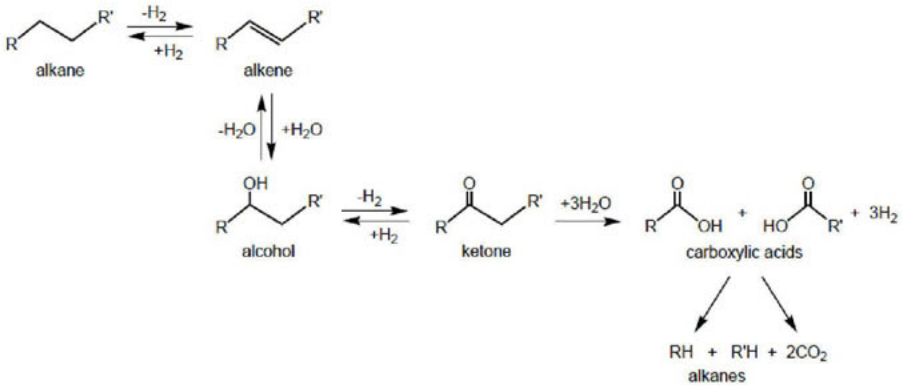

Figure 5. Reaction pathways proposed by Seewald (2001a, 2003) among alkanes, alkenes, alcohols, alkenones (ketones) and carboxylic acids through hydration/dehydration and oxidation/reduction reactions in sedimentary basins fluids associated with petroleum.

hydrothermal experiments (Seewald 1994, 2001a,b; McCollom and Seewald 2003a,b). The kinetic barriers for these organic transformation reactions at ambient conditions are overcome by the increase of temperature, allowing the petroleum products, such as aliphatic alkanes and natural gas, to reach thermodynamically favorable, low-energy states in sedimentary basins.

Nonvolatile hydrocarbons from submarine hydrothermal fluids might also originate from thermal decomposition of organic matter, in this case transported into the high temperature reaction zones of the systems by circulating fluids or derived from the flushing of organic compounds out of the walls of chimney structures prior to venting. Most of the organic compounds are accompanied by biomarkers and membrane fatty acids (Simoneit et al. 1990) and thus probably have biological origins (McCollom 2008). This helps explain the enhanced concentrations of hydrocarbons in high temperature vent fluids relative to ABS at EPR 13°N reported by Brault et al. (1988). Further analyses confirmed trace amounts of biomarker compounds, as well as linear hydrocarbons of C_{35} or larger. The particulate fraction had observable fatty acids as well. Comita et al. (1984) observed that sterols, triacylglycerols, and wax esters comprised more than 90% of the lipid fraction in vent fluids at EPR 21°N. Aliphatic hydrocarbons were the minority in the lipid class comprising $< 3\%$. The major components typically centered around $C_{19\text{-}20}$ with *n*-alkanes dominating this compound class (Comita et al. 1984).

Suspended particulate matter was also studied at and around submarine hydrothermal systems. Comita et al. (1984) used *in situ* filtration of hydrothermal fluid at EPR 21°N, 106°W to sample suspended particulate matter within tens of meters from active vents over a 2-40 °C range. Particulate organic carbon in warm waters influenced by diffuse vents was five times more abundant than in ABS and had a ten-fold higher lipid concentration. Investigations of organic carbon compounds at diffuse flow sites at EPR 13°N, 105°W revealed elevated levels of amino acids associated with clusters of *Alvinellinae* worms (Alberic 1986), as well as suspended particulate fatty acids that were at concentrations 15-25 times higher in the 10 °C diffuse venting fluid than in ambient seawater (Brault et al. 1984; Daumas et al. 1988). Monosaturated $C_{16:1}$ and $C_{18:1}$ hydrocarbons were at higher abundances in the near-vent particles than in material further from vents, allowing the interpretation that the near-vent particles were less degraded. However, branched-chain C_{15} and C_{17} acids were not significantly enriched in near-vent samples, which may indicate a lesser contribution from bacteria-rich particulate matter.

Organic compounds can also accumulate in sediments surrounding hydrothermal vents. Shulga et al. (2010) analyzed *n*-alkanes in hydrothermal deposits at the MAR Broken Spur site and found that the majority fell between C_{14} and C_{35} and had abundances between 0.007 to 0.016 mg/g. Based on the composition of the *n*-alkanes, these researchers concluded that there were nearly equal contributions from abiogenic thermocatalytic and biogenic sources in the samples. At the Trans-Atlantic Geotraverse (TAG) hydrothermal field (MAR 26°N), Brault and Simoneit (1989) analyzed three sulfide-rich samples and found minor amounts of volatile-rich hydrothermal petroleum with *n*-alkanes ranging from C_{11} to C_{22}. An aromatic fraction containing naphthalene and phenanthrene, as well as their alkyl homologs and aromatic compounds, was interpreted as supporting a hydrothermal origin for these trace organic fractions (Brault and Simoneit 1989; Simoneit et al. 1990).

Sulfide chimneys and metaliferous sediments from plumes at EPR and MAR have concentrations of nonvolatile organic compounds in the range of tens of mg/g (Brault et al. 1984, 1988, 1989; Simoneit et al. 1990, 2004; Glynn et al. 2006). Branched and linear alkanes, fatty acids, PAHs, and various biomarkers were identified from these sites, as well as a large unresolved complex mixture of unidentifiable compounds. Pyrolysates from sedimentary detrital organic matter can be found in trace levels at sites along the EPR (Brault et al. 1988). There is also a large number of organic compounds from microbial organisms found in fluids, chimneys, and sediments that have yet to be understood in terms of distribution, composition, and abundance, but techniques such as two-dimensional gas chromatography may aid in the resolution of samples with complex mixtures (Brault et al. 1989; Simoneit 1990; Takai et al. 2001; Schrenk et al. 2003; Glynn et al. 2006; Kormas et al. 2006; Ventura et al. 2012).

Oxidation/reduction reactions involving organic compounds are suspected to occur in the genesis of several types of ore deposits (reviews include Landais and Gize 1997; Gize 1999; and Greenwood et al. 2013). In particular, the donation of electrons from organic compounds to sulfate is observed in roll-front uranium deposits, as well as base-metal sulfide deposits (Machel 1989). Uranium deposits are typically found in continental fluvial arkosic sandstones or in organic-rich shales (Landais 1996), and reduced zones that contain organic matter are often associated with uranium minerals (Hofmann 1993). The reduction of U^{VI} to U^{IV} coupled to the oxidation of organic matter represented by

$$2(\mathrm{RH}) + \mathrm{UO_2}^{2+} \rightarrow 2\mathrm{R} + 2\mathrm{H}^+ + \mathrm{UO_2} \tag{1}$$

where R represents the main C-bearing portion of the organic compound, was experimentally demonstrated (Andreyev and Chumachenko 1964; Landais 1996). As indicated in this reaction, the reduction of uranyl ions to uraninite requires the oxidation of carbon in the organic product relative to the organic reactant. This can be accomplished in many ways, including the development of double bonds, the transformation of alkanes to alkenes or alcohols to ketones, cyclization of alkanes, and the aromatization of cyclic alkane groups. Progress of this overall process may help explain the trend toward more polar (and therefore more oxidized) as opposed to saturated (more reduced) compositions of organic compounds from chloroform extracts of various uranium deposits (Fig. 6).

There is a long-established association between base-metal ore deposits and organic compounds, including the Mississippi Valley Type (MVT) deposits hosted in paleozoic sediments in North America. An ore formation model involving reduction of sulfate and precipitation of metal sulfides from brines containing base metals complexed with chloride seems consistent with compositions of most MVT deposits (Sverjensky 1986). An alternative mechanism of metal transport as complexes with organic ligands has been widely discussed in the literature (Barnes 1979; Giordano and Barnes 1981; Giordano 1985, 2002; Sverjensky 1986; Shock 1998, 2000; Prapaipong et al. 1999). In addition, oxidation of organic compounds in MVT deposits shows evidence of biodegradation and is thought to reflect sulfur oxidation

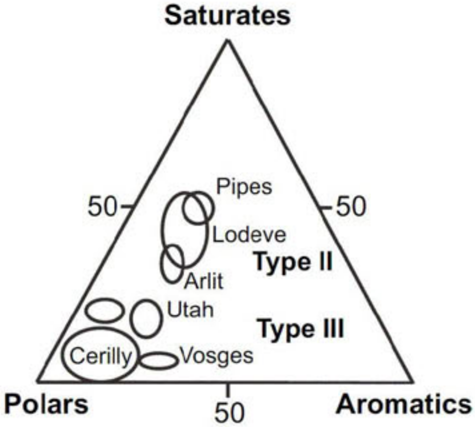

Figure 6. Composition of chloroform extracts from different uranium deposits. 'Polars' and 'Aromatics' are more oxidized than 'Saturates'. Pipes- breccia pipes, Grand Canyon Area, Arizona , Lodeve- Lodeve, France. Arlit- Arlit-Akouta, Niger. Utah- Temple Mountain, Utah. Vosges- Vosges, France. Cerilly- black shales, Cerilly, France. Type II and III refer to types of kerogen, see Figure 5 (modified after Landais 1996).

to sulfate (Gize 1999). In Australia, the paleoproterozoic McArthur River, or "Here's Your Chance" pyritic shale member within the Barney Creek Formation hosts a large Pb/Zn/Ag deposit that resulted from the interactions of a hot metal-rich brine with the Barney Creek sediments and organic matter during or after deposition (Williford et al. 2011). Extracts of hydrocarbons from the Barney Creek Formation show an elevated abundance of isoprenoid compounds and most had a saturation to aromatic ratio of greater than 1 (Summons et al. 1988). The copper and silver deposits found in the Permian Kupferschiefer shale in Germany and Poland are also thought to have a link to organic matter incorporated in sediments deposited under anoxic conditions and subjected to secondary oxidation by fluids moving through underlying red beds (Püttmann et al. 1988, 1989, 1990, 1991). Two possible reaction schemes suggested by Püttmann et al. (1989) are shown in Figure 7. The loss of aliphatic hydrocarbons and the sulfidation of aromatic hydrocarbons document the oxidation of organic matter coupled to the deposition of copper and silver ores (Püttmann et al. 1988). Oxidation of the Kupferschiefer deposits is accompanied by aromatic and organosulfur compounds thought to reflect the generation of sulfur and polysulfides during sulfide oxidation (Gize 1999).

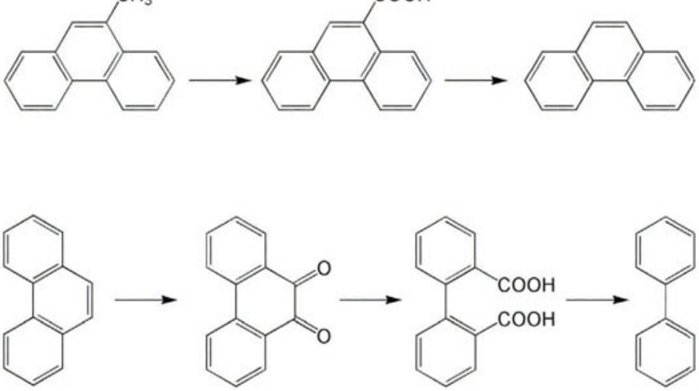

Figure 7. Two reactions schemes showing oxidation and decarboxylation or organic compounds found associated with base metal ore deposits: 1-methylphenanthrene through the carboxylic acid to phenanthrene, and phenanthrene through phenanthrenequinone and biphenyl diacid to biphenyl (modified after Püttmann et al. 1989; with structures corrected).

Native copper deposits in the Proterozoic Nonesuch Formation, of Michigan, comprised of lacustrine shales and siltstones, are thought to have formed by the precipitation of metals from a migrating, heated fluid coupled to the oxidation of organic matter (Ho et al. 1990). The total organic carbon content of mineralized and unmineralized units was found to be similar, suggesting organic carbon conservation during the ore-forming process. An example of how organic compounds can be oxidized during pyrite reduction is illustrated by the conversion of alkanes to aromatic compounds (in this case, cyclohexane C_6H_{12} to benzene C_6H_6; Ho and Mauk 1996).

$$C_6H_{12} + 12CuCl_2^- + 3FeS_2 \rightarrow 6Cu_2S + 3Fe^{2+} + 6H^+ + 24Cl^- + C_6H_6 \qquad (2)$$

Note that in this reaction the organic oxidation reaction is coupled to the reduction of sulfur from the −1 oxidation state in pyrite (FeS_2) to the −2 oxidation state in chalcocite (Cu_2S), and that the oxidation state of copper is unaffected. Nevertheless, the reduction of pyrite coupled with organic oxidation triggers the accumulation of copper from solution as chalcocite.

Ore deposits in the Great Basin of western North America have been associated with organic carbon for over half a century (Joralemon 1951; Radtke and Scheiner 1970; Ilchik et al. 1986; Hulen and Collister 1999; Large et al. 2011). At the Carlin ore deposit, characterized by Silurian thin-bedded siliceous, argillaceous, dolomitic limestones and siliceous limestones with acid hydrothermal solution deposition of gold ores, three types of organic compounds were found, including activated carbon, high molecular weight hydrocarbons and humic acids (Radtke and Scheiner 1970). The amount and chemical state of gold deposited in the carbonaceous limestone is mainly controlled by the relative amounts and types of carbonaceous matter present, although temperature, pH and changes in oxidation state are all involved (Radtke and Scheiner 1970). At the Alligator Ridge ore deposits, hosted in middle Paleozoic carbonate rocks with gold mineralization primarily in the Devonian-Mississippian Pilot Shale, the maturity of the organic matter increased owing to hydrothermal activity (Ilchick et al. 1986). Although Large et al. (2011) suggest carbonaceous sedimentary rocks as sources for gold and arsenic in Carlin-type and sediment-hosted gold deposits, specific reactions relating the transformations of organic matter to gold deposition processes have yet to be fully articulated.

THERMODYNAMIC EXPLANATIONS

Insights about the driving forces behind the transformations of organic compounds that occur in the Earth at elevated temperatures and pressures can be gained by evaluating relative stabilities of aqueous organic compounds with thermodynamic calculations. The main advantage of this approach is that thermodynamic data are derived from laboratory experiments on pure compounds and their mixtures and solutions, all of which is *independent* of observations made from nature, or from experiments designed to explore organic compound reactivity. Therefore, thermodynamic calculations supply a means of testing hypotheses derived from observations, and can spur efforts to take new views of natural systems. In this section we focus on oxidation/reduction and hydration/dehydration reactions, but start with a consideration of solubility relations.

Hydrocarbon dissolution

Everyday experience at ambient conditions with hydrocarbons and other organic compounds leaves the impression that many of these compounds are not particularly soluble in water. However, things change as temperature increases. Take for example the change with temperature of the equilibrium constant for the reaction

$$CH_{4(g)} \rightleftarrows CH_{4(aq)} \qquad (3)$$

shown in Figure 8a. Symbols in this figure are calculated from various experimental studies, and the curve is obtained using data and parameters for $CH_{4(aq)}$ from Plyasunov and Shock (2001) with those for $CH_{4(g)}$ from Helgeson et al. (1998) to calculate the standard Gibbs energy ($\Delta_r G^\circ$) of Reaction (3) which yields the equilibrium constant (K) via

$$2.303RT \log K = -\Delta_r G^\circ \tag{4}$$

where R represents the gas constant and T stands for temperature (in K). As shown in Figure 8a, starting at low temperatures, log K for Reaction (3) becomes more negative as temperature increases at pressures corresponding to the boiling curve of H_2O (P_{SAT}). This behavior is common for gas solubility reactions, including CO_2, O_2, N_2 and H_2S, and is consistent with everyday experience of carbonated beverages losing their carbonation more easily at high than at low temperatures. But, our everyday experience with aqueous solutions rarely exceeds 100 °C, and it turns out that extrapolating the decreasing solubility between 0° and 100 °C on up in temperature would lead to colossally inaccurate estimates. The equilibrium constant for Reaction (3), like those for other gases, shows a minimum in temperature, and increases dramatically along the boiling curve for H_2O as shown in Figure 8a. At all temperatures above about 200 °C the equilibrium constant for Reaction (3) is more positive than the room temperature value, and at 350 °C is about an order of magnitude greater. This suggests that the equilibrium concentration of methane in solution is likely to be greater in hydrothermal fluids than in surface waters. Of course it must be kept in mind that

$$K = \frac{a\mathrm{CH}_{4(aq)}}{fCH_{4(g)}} = \frac{\gamma\mathrm{CH}_{4(aq)}\, m\mathrm{CH}_{4(aq)}}{\phi\mathrm{CH}_{4(g)}\, p\mathrm{CH}_{4(g)}} \tag{5}$$

where a, m, and γ, stand for the activity, molality, and activity coefficient of (in this case) aqueous methane, and f, p and ϕ designate the fugacity, partial pressure, and fugacity coefficient of methane gas. Care must be taken to evaluate partial pressures, fugacity coefficients and activity coefficients if molalities are to be determined from values of K. Nevertheless, in the case that these other parameters are roughly constant or offsetting, changes in molality can be inferred from changes in K. Given the magnitude of those changes as shown in Figure 8, it makes sense that hydrothermal fluids that reach the Earth's surface can contain dissolved methane abundances far in excess of values expected for other surface waters. And, at the elevated pressures of hydrothermal systems, dissolved methane concentrations can be considerably higher than values observed in hot springs.

Changes in log K for some other hydrocarbon dissolution reactions are also shown in Figure 8, again using data and parameters for the aqueous species from Plyasunov and Shock (2001) and for the pure hydrocarbons (liquid or gas) from Helgeson et al. (1998). The ranges of the log K axes are the same for all the plots in this figure, which makes it possible to compare directly potential differences in solubilities. The reactions represented in this figure are

ethene: $C_2H_{4(g)} \rightleftarrows C_2H_{4(aq)}$ (6)
benzene: $C_6H_{6(l)} \rightleftarrows C_6H_{6(aq)}$ (7)
cyclohexane: $C_6H_{12(l)} \rightleftarrows C_6H_{12(aq)}$ (8)
n-hexane: $C_6H_{14(l)} \rightleftarrows C_6H_{14(aq)}$ (9)
toluene: $C_6H_5CH_{3(l)} \rightleftarrows C_6H_5CH_{3(aq)}$ (10)

Note that log K for ethene (Reaction 6, Fig. 8b) is always slightly more positive than that for methane, but that the magnitudes of the changes with temperature are quite similar. In contrast, benzene (Fig. 8c, Reaction 7) shows more positive log K values at low temperatures, minimizing at about room temperature, but also a greater increase in the magnitude of log K with increasing temperature than methane or ethene. Likewise, log K values for cyclohexane

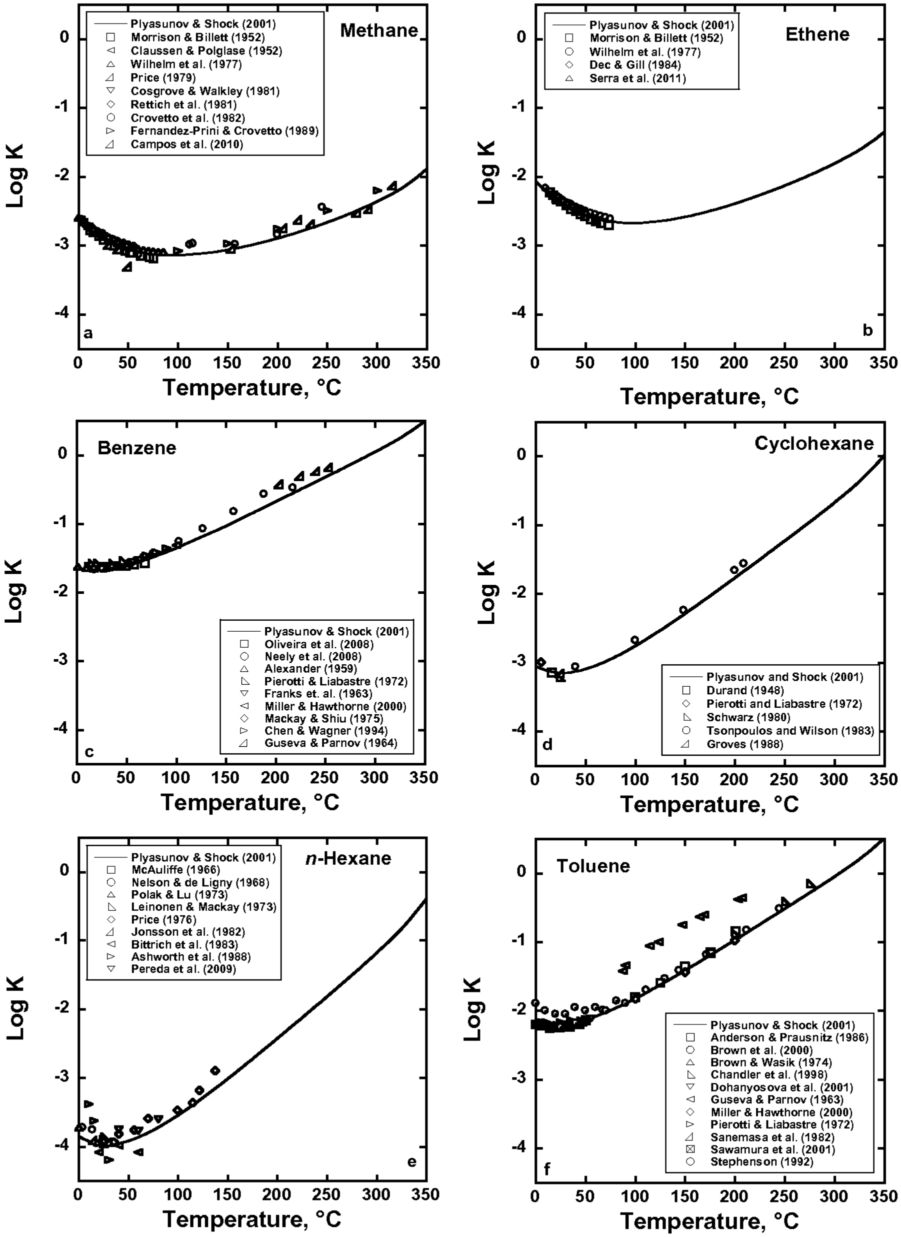

Figure 8. Equilibrium constants for hydrocarbon dissolution Reactions (3 and 6-10). Symbols represent experimental data from the sources indicated, and curves are calculated using thermodynamic data and equations of state for pure hydrocarbons (gases and liquids) from Helgeson et al. (1998) and from Plyasunov and Shock (2001) for aqueous solutes. In both theoretical studies, many other types of experimental data and theoretical constraints were considered in addition to the equilibrium constants shown in these figures.

(Fig. 8d, Reaction 8), *n*-hexane (Fig. 8e, Reaction 9) and toluene (Fig. 8f, Reaction 10) show minima near room temperatures and dramatic increases with increasing temperature. Differences in the behavior of alkanes are revealed by comparing the plots in Figures 8a and 8e for methane and *n*-hexane, which show that the more negative the log *K* values are at low temperatures the greater the increase in log *K* will be with increasing temperature. Results for the three 6-carbon compounds in Figure 8 allow a comparison among the relative behavior of alkanes, cycloalkanes, and aromatics. At room temperature, benzene has the most positive log *K* value, so it would be the most soluble—all else being the same—and *n*-hexane would be the least soluble. As temperature increases from 0° to 350 °C at P_{SAT}, the equilibrium constant for benzene (Reaction 7) increases by about two orders of magnitude, while that for cyclohexane (Reaction 8) increases by about three orders of magnitude and that for n-hexane (Reaction 9) increases by about three and a half orders of magnitude. As a result, log *K* values converge as temperature increases. These three values span a range of about 2.2 log *K* units at 25 °C, and only about 1 unit at 350 °C. In fact, hydrocarbons, including crude oil, become completely miscible in water at higher temperatures and pressures (Price 1991).

Hydration/dehydration

Hydration and dehydration reactions involving minerals are familiar to geochemists and petrologists who study weathering, diagenesis, hydrothermal alteration, and metamorphism. Weathering, diagenesis and alteration produce hydrous minerals including clays and micas from anhydrous phases like feldspars and pyroxenes, and when clay minerals and other hydrous phases are buried, heated, and metamorphosed they can dehydrate. Likewise, organic compounds show evidence of hydration/dehydration reactions in geochemical processes. As an example, it is common for alcohols to dehydrate to form alkenes according to overall reactions such as

$$CH_3CH_2OH_{(aq)} \rightleftarrows C_2H_{4(aq)} + H_2O \tag{11}$$

in which ethanol (CH_3CH_2OH) dehydrates to form ethene (or ethene hydrates to form ethanol). The equilibrium constant for this reaction is given by

$$K = \frac{aC_2H_{4(aq)}\, aH_2O}{aCH_3CH_2OH_{(aq)}} \tag{12}$$

which can be rearranged in its logarithmic form to yield

$$\log\left(\frac{aC_2H_{4(aq)}}{aCH_3CH_2OH_{(aq)}}\right) = \log K \quad \log aH_2O \tag{13}$$

Unless the ionic strength of the fluid is significantly higher than that of seawater, it can be assumed that $aH_2O \approx 1$ (aH_2O values in mixtures of submarine hydrothermal fluids and seawater are calculated to fall between 0.977 and 0.989 depending on mid-ocean ridge location, Shock and Canovas 2010). In this case, the activity ratio of the alkene to the alcohol is equivalent to the equilibrium constant, and equilibrium constants of this type are quite sensitive to temperature as shown in Figure 9 for dehydration of ethanol through 1-octanol to the corresponding alkenes (all equilibrium constants for reactions involving aqueous organic compounds used throughout the rest of this chapter were calculated with thermodynamic data, equations, and parameters from Shock et al. 1989, Shock and Helgeson 1990, Schulte and Shock 1993, and Shock 1995). Note that these equilibria shift by 3 to 5 orders of magnitude in favor of the alkenes as temperature increases from 0° to 350 °C at P_{SAT}. These shifts represent considerable thermodynamic drives for dehydration as temperature increases, or hydration as temperature drops. As discussed in the next section, the potential for oxidation of alkanes to alkenes at redox states influenced by mineral assemblages increases with increasing

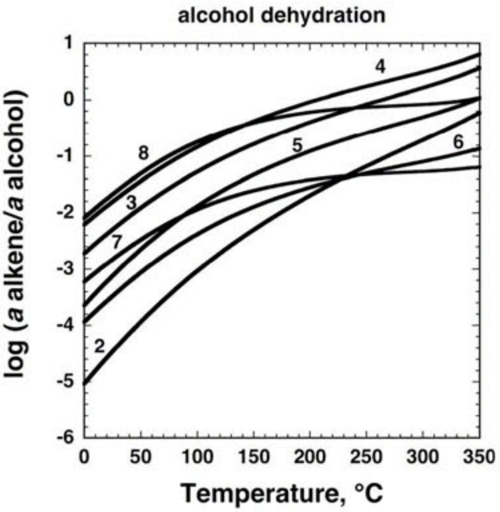

Figure 9. Calculated metastable equilibrium ratios of alkenes to alcohols as functions of temperature at P_{SAT}, and the assumption that $aH_2O = 1$, calculated with data, equations, and parameters provided by Shock and Helgeson (1990). Numbers refer to the number of carbons in both alkene and alcohol (e.g., 2 stands for Reaction 11 between ethene and ethanol). Increasing ratios of alkene to alcohol show that the dehydration reaction is increasingly favored as temperature increases. The dispersion of curves on this plot may enable predictions about which alcohols to expect in geologic settings, but may also result from uncertainties in thermodynamic data.

temperature, which sets up the possibility of competition between the rates of reduction and hydration of alkenes as fluids cool. If these rates were well understood it might be possible to obtain cooling rates from relative abundances of alcohols and alkanes from the same alkene sources.

Oxidation/reduction

As summarized above, numerous lines of evidence indicate that oxidation-reduction (redox) reactions are common among organic compounds in geologic systems and during geochemical processes. One of the simplest redox reactions among aqueous organic compounds is between alkanes and alkenes, illustrated by the reaction between ethane and ethene given by

$$C_2H_{6(aq)} \rightleftarrows C_2H_{4(aq)} + H_{2(aq)} \tag{14}$$

This reaction was studied experimentally by Seewald (1994) who showed that it is reversible at hydrothermal conditions, which inspired some of the latest developments described in section III. The equilibrium constant for this reaction is given by

$$K = \frac{aC_2H_{4(aq)}\ aH_{2(aq)}}{aC_2H_{6(aq)}} \tag{15}$$

which can be rearranged in its logarithmic form to yield

$$\log aH_{2(aq)} = \log K - \log\left(\frac{aC_2H_{4(aq)}}{aC_2H_{6(aq)}}\right) \tag{16}$$

If we choose to set the activities of the aqueous hydrocarbons equal to each other, then the ratio equals one, and the corresponding equilibrium activity of aqueous hydrogen can be evaluated from values of log K as shown by the dashed curve labeled 2 in Figure 10 for Reaction (14), as well as analogous reactions for 3-carbon through 8-carbon alkanes and alkenes. Note that the dashed curves for the larger hydrocarbon pairs plot nearly on top of one another.

Also shown in Figure 10 are three curves indicating values of the activity of $H_{2(aq)}$ in equilibrium with iron-bearing mineral assemblages:

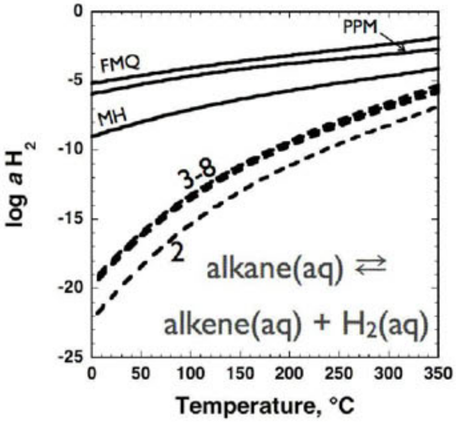

Figure 10. Equilibrium values of $H_{2(aq)}$ activity consistent with equal activities of alkanes and alkenes (dashed curves, numbers refer to number of carbon atoms in the alkane and alkene; e.g., 2 corresponds to Reaction 14; 4 through 8 refer to reactions involving 1-alkenes) or iron-bearing mineral assemblages (solid curves, Reactions 17-19) as functions of temperature at P_{SAT}. Equilibrium constants were evaluated with data, equations, and parameters from Helgeson et al. (1978) and Shock and Helgeson (1990). Note that the reaction between ethane and ethene falls at somewhat lower equilibrium $H_{2(aq)}$ activities than the other reactions shown, all of which roughly coincide.

magnetite-hematite (MH) $$2Fe_3O_4 + H_2O \rightleftarrows 3Fe_2O_3 + H_{2(aq)} \quad (17)$$

pyrrhotite-pyrite-magnetite (PPM) $$\tfrac{3}{2}FeS + H_2O \rightleftarrows \tfrac{3}{4}FeS_2 + \tfrac{1}{4}Fe_3O_4 + H_{2(aq)} \quad (18)$$

fayalite-magnetite-quartz (FMQ) $$\tfrac{3}{2}Fe_2SiO_4 + H_2O \rightleftarrows Fe_3O_4 + \tfrac{3}{2}SiO_2 + H_{2(aq)} \quad (19)$$

Fayalite (Fe_2SiO_4) contains only Fe^{II}, hematite (Fe_2O_3) contains only Fe^{III}, and magnetite (Fe_3O_4) contains both Fe^{II} and Fe^{III}. It follows that fayalite is stable at and above the upper curve, hematite at and below the lower curve, and magnetite at and between the upper and lower curves. Pyrrhotite (FeS) is stable at and above the middle curve, and pyrite (FeS_2) is stable at and below the middle curve. Unlike these phase-boundary curves for the mineral assemblages, which determine regions of the diagram where minerals occur or are excluded at equilibrium, the dashed curves for pairs of aqueous hydrocarbons show where their activities are equal. At equilibrium there would be activities of aqueous alkenes and alkanes at all points on the figure. Above the dashed curves the equilibrium activity ratio would favor the alkane, while below alkene activities would exceed those of the corresponding alkanes. Evidently the observation that alkanes are far more abundant than alkenes in geologic systems is consistent with their relative stabilities at redox conditions common to many types of rocks.

Reactions like (14) can also be used to test whether metastable equilibria among organic compounds occur in natural systems. One utility of demonstrating metastable equilibrium for alkane-alkene reactions is that measured ratios can be combined with equilibrium constants calculated from thermodynamic data to evaluate $H_{2(aq)}$ activities, as evident in Equation (16). Activities of $H_{2(aq)}$ can be used as indicators of the of the redox state of subsurface environments and deep regions of hydrothermal systems. Another way that metastable equilibria can be used is to combine measurements of alkanes, alkenes and $H_{2(aq)}$ to solve for temperatures. Spurred by experimental evidence that reactions like (14) are reversible at hydrothermal temperatures and pressures, and that the ratio of ethene to ethane attains metastable equilibrium values (Seewald 1994), Cruse and Seewald (2006, 2010) used alkene/alkane/H_2 equilibria to estimate values of temperature attained deep in reaction zones of submarine hydrothermal systems as shown in Figure 11.

Many processes that generate alkanes from organic matter, or alkanes from other alkanes, also involve oxidation/reduction. As an example, consider the production of methane from ethane via

$$C_2H_{6(aq)} + H_{2(aq)} \rightleftarrows 2CH_{4(aq)} \quad (20)$$

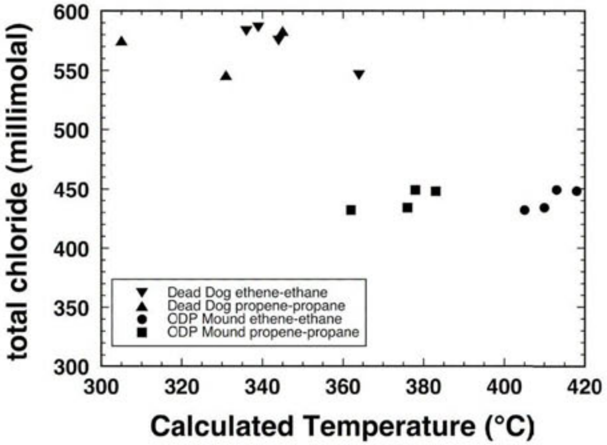

Figure 11. Symbols show chloride concentrations plotted against temperatures calculated assuming metastable equilibrium among alkanes, alkenes, and hydrogen measured in submarine hydrothermal fluids from Middle Valley on the Juan De Fuca Ridge (modified after Cruse and Seewald 2006).

The carbon in methane (−4) is more reduced than that in ethane (−3), requiring the addition of H_2 to balance the reaction, and making this an oxidation/reduction process. The equilibrium constant for this reaction is given by

$$K = \frac{(a\mathrm{CH}_{4(\mathrm{aq})})^2}{a\mathrm{C}_2\mathrm{H}_{6(\mathrm{aq})}\ a\mathrm{H}_{2(\mathrm{aq})}} \tag{21}$$

and is plotted as log K in Figure 12a. The logarithmic form of this expression can be rearranged to give

$$\log a\mathrm{CH}_{4(\mathrm{aq})} = \frac{1}{2}\left[\log K + \log a\mathrm{H}_{2(\mathrm{aq})} + \log a\mathrm{C}_2\mathrm{H}_{6(\mathrm{aq})}\right] \tag{22}$$

which allows calculation of aqueous methane activities in metastable equilibrium with aqueous ethane activities at $H_{2(aq)}$ activities set by mineral assemblages. Results of this type are plotted in Figure 12b, where it can be seen that methane prevails over ethane at redox conditions consistent with mineral assemblages regardless of temperature at P_{SAT}. Also shown in Figure 12b are conditions where the activity of aqueous ethane exceeds that of aqueous methane, or, in other words, conditions where the polymerization of methane to ethane is thermodynamically favored. It can be seen that polymerization, which involves the oxidation of carbon, is favorable only at conditions in the stability range of hematite, which means that no reduced iron would be present. This trend continues as the carbon-chain length of aqueous alkanes increases as shown in Figure 13, where it can be seen that butane activities would exceed those of ethane, and octane activities would exceed those of butane only at highly oxidized conditions. The relative stabilities among aqueous alkanes, when compared with oxidation states set by common mineral assemblages, help to explain why methane is the most abundant alkane in most hydrothermal fluids, and why other alkanes typically decrease dramatically in abundance.

One variation on this theme is the recognition that methane, ethane, and propane appear to reach metastable equilibrium states relative to the reaction

$$2\mathrm{C}_2\mathrm{H}_{6(g)} = \mathrm{C}_3\mathrm{H}_{8(g)} + \mathrm{CH}_{4(g)} \tag{23}$$

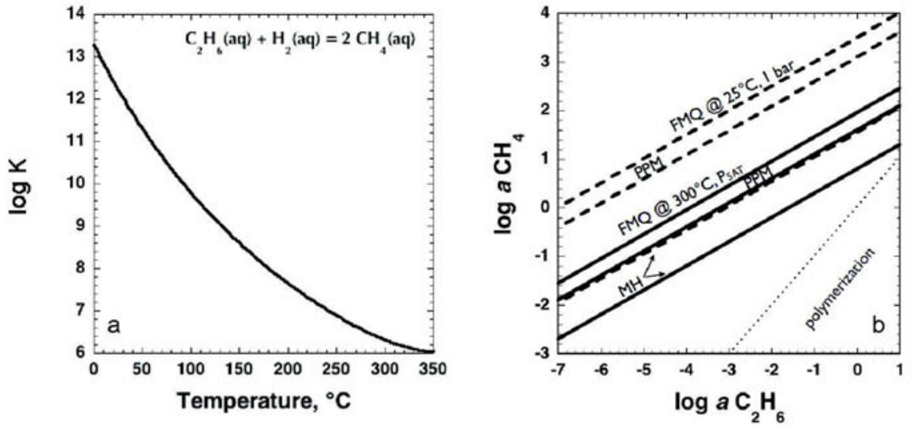

Figure 12. a) The equilibrium constant for Reaction (20) as a function of temperature at P_{SAT} showing a 7 order of magnitude shift, which suggests that methane becomes increasingly stable as temperature decreases. This is borne out in b) where activities of aqueous methane are plotted against those of aqueous ethane. The dotted line shows equal activities and conditions below and to the right of this line would favor polymerization of methane to form ethane. Metastable equilibrium ratios of methane to ethane at $H_{2(aq)}$ activities set by iron-bearing mineral assemblages (Reactions 17-19) at 25 °C and 1 bar (dashed) and 300 °C and P_{SAT} (solid) fall on the side of the diagram where methane is dominant. Thermodynamic calculations conducted with data, equations and parameters from Shock and Helgeson (1990) and Helgeson et al. (1978).

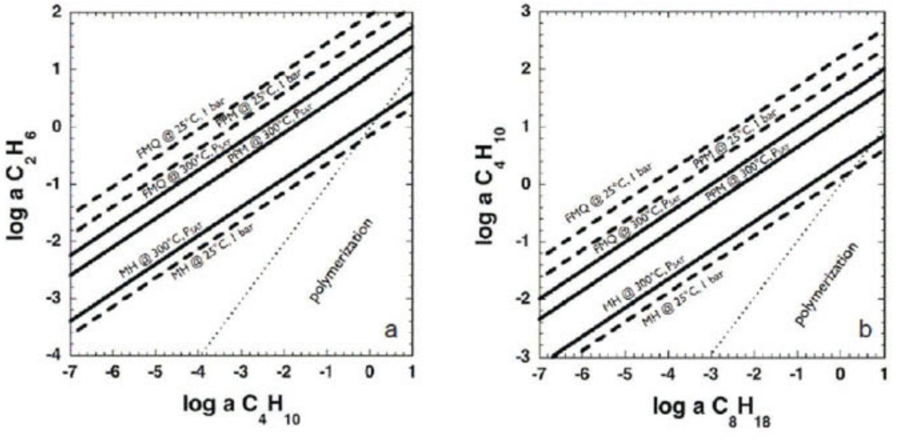

Figure 13. Plots like that in Figure 12b for the reactions a) $C_4H_{10(aq)} + H_{2(aq)} = 2\ C_2H_{6(aq)}$, and b) $C_8H_{18(aq)} + H_{2(aq)} = 2\ C_4H_{10(aq)}$. Solid and dashed lines as in Figure 12b, dotted lines show equal activities of pairs of aqueous alkanes in each case. These plots illustrate that most oxidation states of common iron-bearing mineral assemblages favor reduction reactions in which larger aqueous alkanes react to form smaller aqueous alkanes. Conditions at which this trend is reversed, labeled "polymerization," require conditions to be at or more oxidized than those set by the equilibrium coexistence of magnetite and hematite. Thermodynamic calculations conducted with data, equations, and parameters from Shock and Helgeson (1990) and Helgeson et al. (1978).

which was studied in volcanic gases by Capaccioni and Mangani (2001) and Tassi et al. (2007). The latter authors show that data from El Salvador geothermal systems produce tightly constrained temperature estimates if equilibrium with Reaction (23) is assumed, as shown in Figure 14. Although they did not obtain such tight temperature constraints, Capaccioni and Mangani (2001) showed that partial pressures of methane, ethane, and propane from the

Campi Fliegri in Italy could be used to estimate temporal and spatial changes in temperatures, and combined their results with data for alkane/alkene pairs and metastable equilibrium assumptions. Whether the aqueous version of Reaction (23) reveals evidence of further metastable equilibria in hydrothermal systems awaits appropriate samples. Meanwhile, the plots in Figure 15 provide estimates of how such equilibria are influenced by temperature.

Relative stabilities

The idea of relative stabilities among aqueous organic compounds can be expanded to examine why certain compounds are the dominant forms of organic carbon in natural hydrothermal fluids at elevated temperatures and pressures. Three examples are depicted in Figure 16.

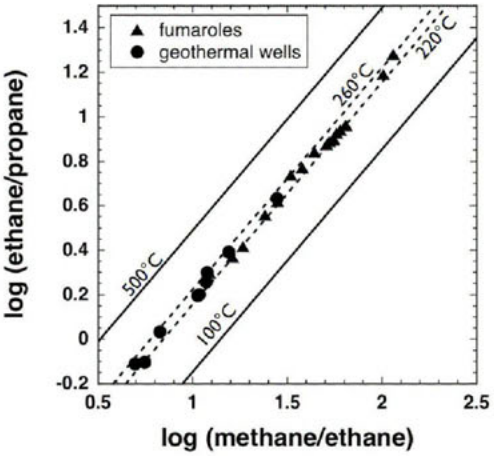

Figure 14. Logarithmic plot of the molar ratios of ethane to propane to that of methane to ethane in gases from fumaroles (triangles) and geothermal wells (circles) from the Berlin and Ahuachapan-Chipilapa geothermal fields in El Salvador (on a H_2O-free basis; modified after Tassi et al. 2007). Solid and dashed lines show temperatures calculated by the original authors assuming equilibrium with respect to Reaction (23). The tight clustering of calculated temperatures suggests metastable equilibrium among propane, ethane and methane in these natural systems.

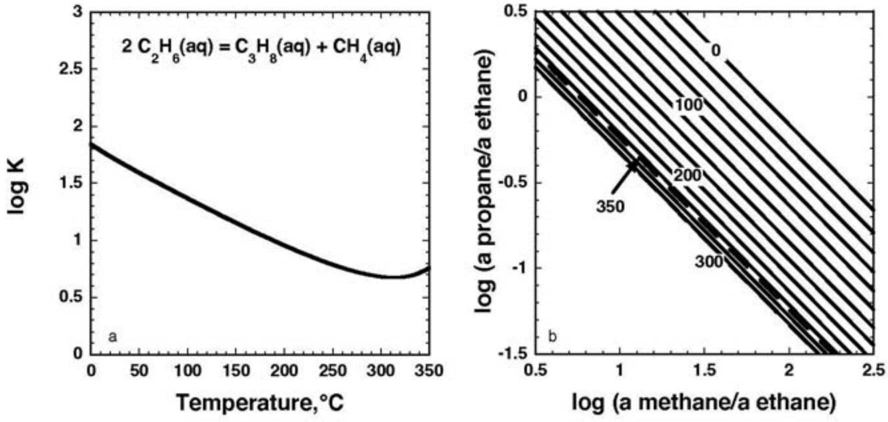

Figure 15. a) The log of the equilibrium constant for the reactions shown (an aqueous version of Reaction 23) as a function of temperature at P_{SAT} calculated with data, equations, and parameters from Shock and Helgeson (1990). In contrast to the reaction shown in Figure 12a, the equilibrium constant for this reaction changes only about one order of magnitude over the same conditions. b) Logarithmic plot of the ratio of aqueous propane to aqueous ethane vs. the ratio of aqueous methane to aqueous ethane derived from the equilibrium constants shown in plot 15a and an assumption of metastable equilibrium. Contours are in °C; note that the 325° and 350 °C contours are shown as dashed lines as they double back into the field defined by the other contours. This type of plot could be used with hydrocarbon data from hydrothermal fluids to estimate reaction zone temperatures, in a manner analogous to using gas data as shown in Figure 14.

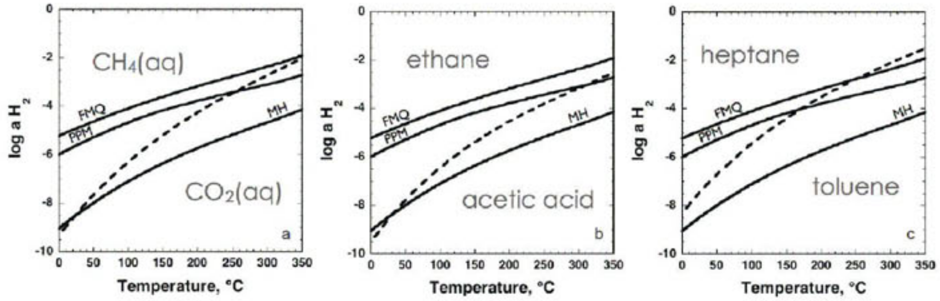

Figure 16. Plot of activities of aqueous hydrogen against temperature at P_{SAT} showing stability relations for iron-bearing mineral assemblages (solid curves, Reactions 17-19), and equal activity ratios (dashed curves) for a) aqueous carbon dioxide and methane (Reaction 24), b) aqueous ethane and acetic acid (Reaction 27), and c) aqueous heptane and toluene (Reaction 28). In all cases the equal activity curves cross-cut the mineral-assemblage curves showing that the more oxidized compound in each case is favored by increasing temperature at values of hydrogen activity consistent with each mineral assemblage. Therefore, the same mineral assemblage can favor oxidation of carbon compounds at one set of temperatures and pressures and reduction at another. Thermodynamic calculations conducted with data, equations, and parameters from Shock and Helgeson (1990), Shock (1995), and Helgeson et al. (1978).

Evidence from natural systems indicates that carbon dioxide is the dominant form of carbon in higher temperature fluids like volcanic gases and submarine and continental hydrothermal solutions. In contrast, methane is commonly encountered in natural gas, which typically occurs at lower temperatures in sedimentary basins. As shown in Figure 16a, the relative stabilities of $CO_{2(aq)}$ and $CH_{4(aq)}$ reveal the underlying thermodynamic drive behind these observations. Aqueous CO_2 is dominant below the dashed curve that shows where activities of $CO_{2(aq)}$ and $CH_{4(aq)}$ are equal as determined from the equilibrium constant for the reaction

$$CO_{2(aq)} + 4H_{2(aq)} \rightleftarrows CH_{4(aq)} + 2H_2O \tag{24}$$

or

$$K = \frac{aCH_{4(aq)}}{aCO_{2(aq)}\,(aH_{2(aq)})^4} \tag{25}$$

when aH_2O can be approximated as unity. The logarithmic form of this equation can be rearranged to yield the expression for the dashed curve in Figure 16a given by

$$\log aH_{2(aq)} = \frac{1}{4}\left[\log\left(\frac{aCH_{4(aq)}}{aCO_{2(aq)}}\right) - \log K\right] \tag{26}$$

Comparison with the log $aH_{2(aq)}$ values consistent with iron-bearing mineral assemblages (Reactions 17-19; solid curves in Fig. 16) shows that $CO_{2(aq)}$ is thermodynamically favored in equilibrium with the MH assemblage at almost all temperatures, and with the PPM assemblage above about 250 °C. In contrast, $CH_{4(aq)}$ is thermodynamically favored in equilibrium with the FMQ assemblage at all temperatures shown, although equal activities of $CH_{4(aq)}$ and $CO_{2(aq)}$ are reached at about 350 °C. This figure helps to explain why $CO_{2(aq)}$ is far more abundant than $CH_{4(aq)}$ in submarine hydrothermal fluids, which typically fall near PPM, and why there is a drive to form methane during serpentinization of ultramafic rocks where the oxidation state would be at or below FMQ.

Observations summarized above indicate that both carboxylic acids and alkanes are abundant and coexist in sedimentary basin brines associated with coal and petroleum reservoirs. If these observations are indicative of a gradual approach to a metastable equilibrium state over geologic time, then the oxidation states of sedimentary basin fluids are likely to fall somewhere between values set by the PPM and MH mineral assemblages as suggested by Figure 16b, which shows relative stabilities of aqueous ethane ($C_2H_{6(aq)}$) and acetic acid ($CH_3COOH_{(aq)}$) consistent with

$$C_2H_{6(aq)} + 2H_2O \rightleftarrows CH_3COOH_{(aq)} + 3H_{2(aq)} \tag{27}$$

It should be kept in mind that this reaction is used to illustrate a point about the attainment of metastable equilibrium in a geologic system and not to indicate a reaction mechanism. Once a metastable equilibrium state is reached between ethane and acetic acid, then the equilibrium constant for Reaction (27) would be satisfied regardless how the actual process happens mechanistically. The case for such metastable redox states was made by Helgeson et al. (1993) and Shock (1994), who took complementary approaches to seek evidence via thermodynamic models.

Several lines of evidence from aqueous organic species in hydrothermal systems, as well as from hydrothermally generated petroleum described above, show that aromatic compounds become more abundant as temperatures increase beyond those usually encountered in petroleum reservoirs. There is a parallel to this trend in the increasing aromatization of coal as the rank increases from bituminous to anthracite (see Manning et al. 2013). The underlying thermodynamic drive toward aromatization can be visualized with the help of Figure 16c, which shows values of log $aH_{2(aq)}$ for metastable equilibrium between aqueous heptane ($C_7H_{16(aq)}$) and toluene ($C_6H_5CH_{3(aq)}$) consistent with

$$C_7H_{16(aq)} \rightleftarrows C_6H_5CH_{3(aq)} + 4H_{2(aq)} \tag{28}$$

As in the case of Reaction (27), Reaction (28) should not be interpreted to imply any particular mechanistic detail. Instead, the comparison of the equilibrium activity of $H_{2(aq)}$ for Reaction (28) with those for equilibrium with the mineral assemblages (Reactions 17-19) can be used to comprehend the thermodynamic drive toward aromatization that is commonly observed in high-temperature/pressure geochemical processes.

Another approach to evaluating relative stabilities is illustrated here with an example using a variety of 3-carbon compounds. As a starting point we can map equal activity curves for propane and a variety of other compounds relative to the same mineral assemblage redox buffer curves shown in Figure 16. Curves of this type are shown in Figure 17 for propane (C_3H_8) paired with propene (C_3H_6), propyne (C_3H_4), 1-propanol ($CH_3CH_2CH_2OH$), propanal (CH_3CH_2COH), acetone (CH_3COCH_3), propanoic acid (CH_3CH_2COOH), lactic acid ($CH_3CHOHCOOH$) and malonic acid ($HOOCCH_2COOH$), and are calculated from the equilibrium constants for the reactions

$$C_3H_{8(aq)} \rightleftarrows C_3H_{6(aq)} + H_{2(aq)} \tag{29}$$

$$C_3H_{8(aq)} \rightleftarrows C_3H_{4(aq)} + 2H_{2(aq)} \tag{30}$$

$$C_3H_{8(aq)} + H_2O \rightleftarrows CH_3CH_2CH_2OH_{(aq)} + H_{2(aq)} \tag{31}$$

$$C_3H_{8(aq)} + H_2O \rightleftarrows CH_3CH_2COH_{(aq)} + 2H_{2(aq)} \tag{32}$$

$$C_3H_{8(aq)} + H_2O \rightleftarrows CH_3COCH_{3(aq)} + 2H_{2(aq)} \tag{33}$$

$$C_3H_{8(aq)} + 2H_2O \rightleftarrows CH_3CH_2COOH_{(aq)} + 3H_{2(aq)} \tag{34}$$

$$C_3H_{8(aq)} + 3H_2O \rightleftarrows CH_3CHOHCOOH_{(aq)} + 4H_{2(aq)} \tag{35}$$

$$C_3H_{8(aq)} + 4H_2O \rightleftarrows HOOCCH_2COOH_{(aq)} + 6H_{2(aq)} \tag{36}$$

It should again be emphasized that writing these reactions is not meant to imply anything in terms of reaction mechanisms. Instead, they are used to examine the directions and magnitudes

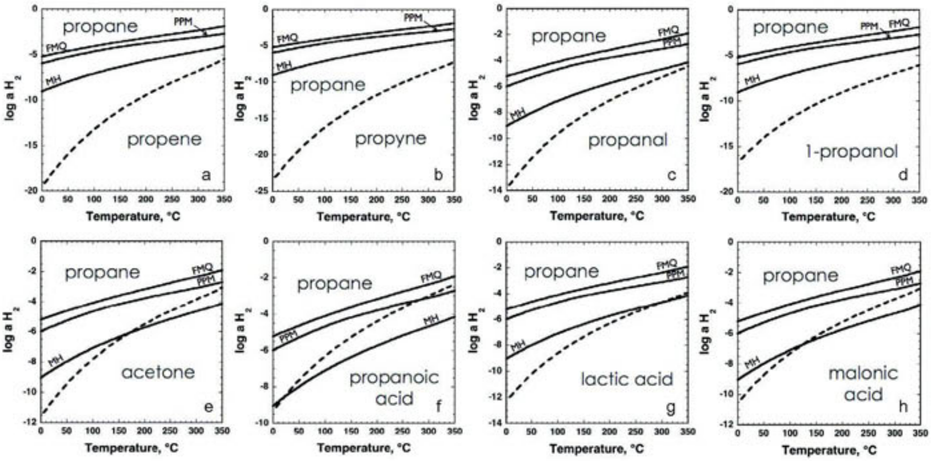

Figure 17. Relative stabilities of aqueous 3-carbon compounds in the C-H-O chemical system. The activity of each aqueous organic compound is equal to that of aqueous propane at the dashed curve in each plot (a-h correspond to Reactions 29-36). As in Figure 16, activities of aqueous hydrogen set by iron-bearing mineral assemblages are shown for reference. Thermodynamic calculations leading to these figures were done with data, equations, and parameters from Shock and Helgeson (1990), Schulte and Shock (1993), Shock (1995), and Helgeson et al. (1978). In each case the more oxidized compound is favored by an increase in temperature either at constant hydrogen activity or at values consistent with mineral assemblages. Comparison of all plots reveals that the equal activity curve between aqueous propane and propanoic acid falls at the most reduced values of the activity of hydrogen, consistent with these two compounds being among the most abundant 3-carbon organic solutes in hydrothermal fluids.

of thermodynamic drives that can be assessed by locating equilibrium relative to conditions that may prevail in nature. Taking Reaction (29) as an example, the curve in Figure 17a is the same as the 3-carbon curve in Figure 10, and is consistent with

$$\log a\mathrm{H}_{2(\mathrm{aq})} = \log K \quad \log\left(\frac{a\mathrm{C}_3\mathrm{H}_{6(\mathrm{aq})}}{a\mathrm{C}_3\mathrm{H}_{8(\mathrm{aq})}}\right) \tag{37}$$

where K is given by

$$K = \frac{a\mathrm{C}_3\mathrm{H}_{6(\mathrm{aq})}\, a\mathrm{H}_{2(\mathrm{aq})}}{a\mathrm{C}_3\mathrm{H}_{8(\mathrm{aq})}} \tag{38}$$

As in the case of Figure 10, setting the activities of the aqueous hydrocarbons equal to one another determines the location of the curve in Figure 17a, again showing that propane is more stable than propene at $\mathrm{H}_{2(\mathrm{aq})}$ activities consistent with the mineral assemblages. In fact, oxidation of propane to yield large amounts of propene requires conditions well into the stability range of hematite. Comparing the curve in Figure 17b showing relative stabilities of propane and propyne (note change in scale of the ordinate) with that for propane and propene in Figure 17a reveals that propyne is less stable than propene relative to propane at oxidation states set by mineral assemblages. Another way of thinking about the consequences of these plots is to consider what it would take for hydrocarbons like propene or propyne to have activities that exceed those of propane at equilibrium in aqueous solutions. Conditions where that is possible occur only at activities of $\mathrm{H}_{2(\mathrm{aq})}$ that are typically orders of magnitude lower than values consistent with the equilibrium presence of magnetite or other ferrous-iron-bearing minerals.

Examination of all of the relative stability plots in Figure 17 shows that in addition to propane, only acetone and propanoic acid can be expected to be abundant at redox conditions consistent with magnetite or other ferrous-iron-bearing minerals at temperatures < 300 °C. Note that lactic and malonic acids may have elevated equilibrium abundances relative to propane at high temperatures at or near $H_{2(aq)}$ activities set by the magnetite-hematite assemblage. Comparison of the plots reveals that the stability field of propanoic acid relative to propane extends to the most positive values of log a $H_{2(aq)}$. The implication is that of all 9 compounds considered in this exercise propane and propanoic acid are the most stable, and that there would be thermodynamic drives to convert the other 3-carbon compounds into these two. Whether those thermodynamic drives are realized depends on reaction mechanisms and their relative rates.

Pair-wise comparisons like those depicted in Figure 17 are useful for thinking about the potential consequences of individual reactions, but many plots of this type are needed to identify the most stable pair. An alternate approach is to assess relative stabilities of many aqueous organic compounds simultaneously, and to include mass balance constraints on carbon or other elements. This approach was taken to modeling the potential for organic synthesis during mixing of hydrothermal vent fluids with seawater at present, and on the early Earth (Shock 1990, 1992; Shock and Schulte 1998; Amend and Shock 1998; Shock and Canovas 2010). The results show how sensitive the potential for organic synthesis is to the combination of oxidation state and temperature.

The preceding theoretical analysis of reactions among organic compounds in hydrothermal fluids shows how thermodynamic drives can be assessed during organic transformation processes. The extent to which any of these thermodynamic drives determines the outcome of organic transformations in nature depends on the existence of reaction pathways and kinetic barriers that may facilitate or impede reaction progress. After all, thermodynamic calculations reveal what *can* happen, but what *does* happen involves many factors outside the realm of a thermodynamic reference frame. Observations of natural systems coupled with thermodynamic calculations can begin to make the link between what is energetically possible and what actually occurs. Likewise, carefully designed experiments can help identify reactions that are reversible and may lead to metastable equilibrium states, as well as those that are irreversible and determine the course of reaction progress in complex systems.

EXPERIMENTAL TESTS

Thermodynamic drives, such as those described above, help to explain the progress of organic transformations observed in natural systems, but the details can be elusive. Turning to experiments can reveal the mechanisms and pathways of organic transformations. Since thermodynamic analyses of hydration/dehydration and oxidation/reduction reactions seem consistent with observations of high temperature/pressure organic transformations, it seems likely that these same processes can be studied experimentally. Examples of successful hydrothermal experiments that explore the details of these processes are summarized in this section, followed by some suggestions for experimental studies that could expedite research progress.

Hydration/dehydration reactions

Dehydration of organic compounds in high temperature aqueous solutions is used in certain textbook organic synthesis schemes (see Shock 1993), but it can still be surprising when examining organic transformations in hydrothermal systems. Nevertheless, as shown in Figure 9, aqueous dehydration of alcohols to alkenes becomes increasingly favorable as temperature increases. As described below, these reactions are rapid and reversible in hydrothermal experiments. Other dehydration, or condensation, reactions have also been demonstrated in hydrothermal experiments, some of which influence how researchers think about the possible involvement of hydrothermal systems in the emergence of life.

Hydration of alkenes to alcohols is central to a proposed conversion of alkanes to ketones (alkenones) as described by Leif and Simoneit (1995) who observed ketones in hydrothermally generated petroleum from the Guaymas Basin with distribution patterns similar to alkanes. Their study included various hydrous pyrolysis experiments using n-$C_{32}H_{66}$ at 350 °C for 72 hours. By combining their experimental results with their analyses of natural hydrothermal petroleum, Leif and Simoneit (1995) proposed the overall scheme shown in Figure 18, where the central role of alkene hydration to alcohols can be seen. Recently, the conversion between alkanes and ketones was explored with the model compound dibenzylketone (DBK) (Yang et al. 2012), and the hydration reaction between the alcohol and the alkene was shown to be reversible, as illustrated in Figure 19. These experiments were conducted for considerably longer than those performed by Leif and Simoneit (1995) and revealed a larger variety of reactions as discussed below.

Dehydration reactions in solution can lead to the production of larger molecules through condensation of smaller molecules. As an example, Rushdi and Simoneit (2006) showed that heating solutions of heptanoic acid and glycerol at temperatures from 100° to 250 °C yields a variety of products through dehydration reactions, as outlined in Figure 20. These experiments were done with and without the addition of oxalic acid (OA in Fig. 20), and variously showed that glyceryl-1-monoheptanoate, glyceryl-2-monoheptanoate, glyceryl-1,2-diheptanoate, glyceryl-1,3-diheptanoate and minor amounts of methyl heptanoate and heptanoic anhydride

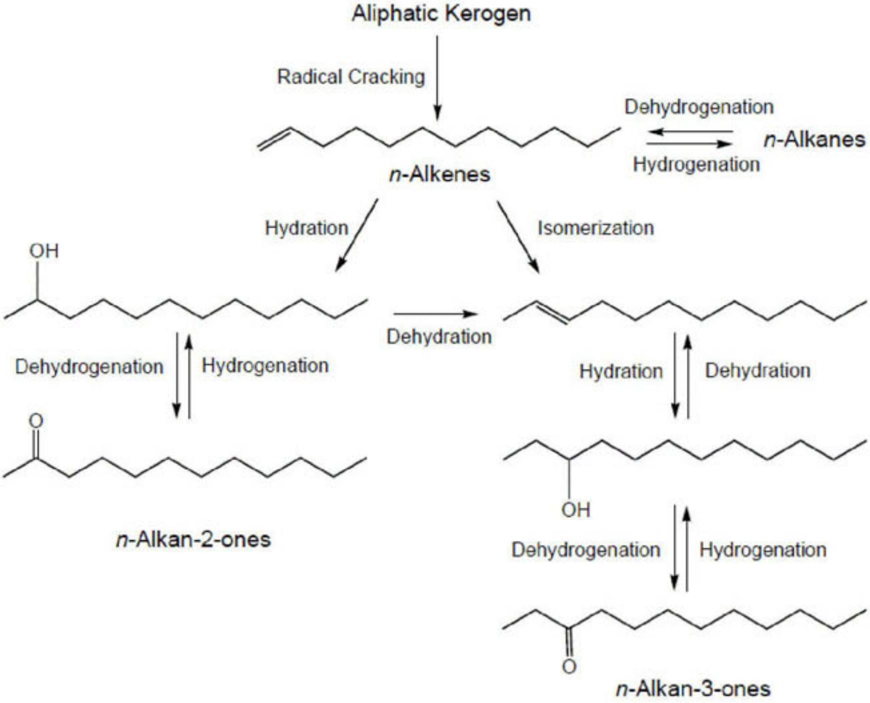
Aliphatic Kerogen
Radical Cracking
Dehydrogenation
n-Alkanes
Hydrogenation
n-Alkenes
Hydration
Isomerization
OH
Dehydration
Dehydrogenation
Hydrogenation
Hydration
Dehydration
O
OH
n-Alkan-2-ones
Dehydrogenation
Hydrogenation
O
n-Alkan-3-ones

Figure 18. A sequence of reactions proposed to connect alkanes and ketones through alkenes and alcohols is shown schematically for C_{12} compounds (modified after Leif and Simoneit 1995). Double arrows indicate reactions that the original authors argued would be reversible, and include hydration/dehydration and oxidation/reduction reactions (the latter called hydrogenation/dehydrogenation in this context). This scheme was derived from observations of ketones in natural hydrothermal petroleum from Guaymas and the results of hydrous pyrolysis experiments.

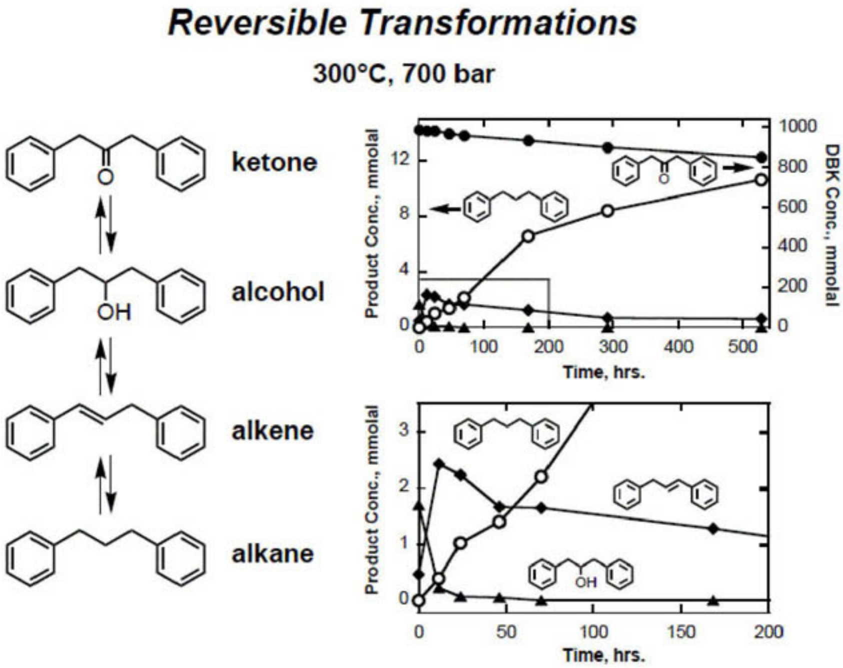

Figure 19. Reversible reactions documented in the study by Yang et al. (2012) who worked with the model compound dibenzylketone (DBK). Note that all reactions between ketone and alkane were found to be reversible. Plots show an example of time-series experiments starting with DBK that produced the other compounds; lower plot shows detail of the boxed region in the upper plot; arrows indicate which axis applies to which compound.

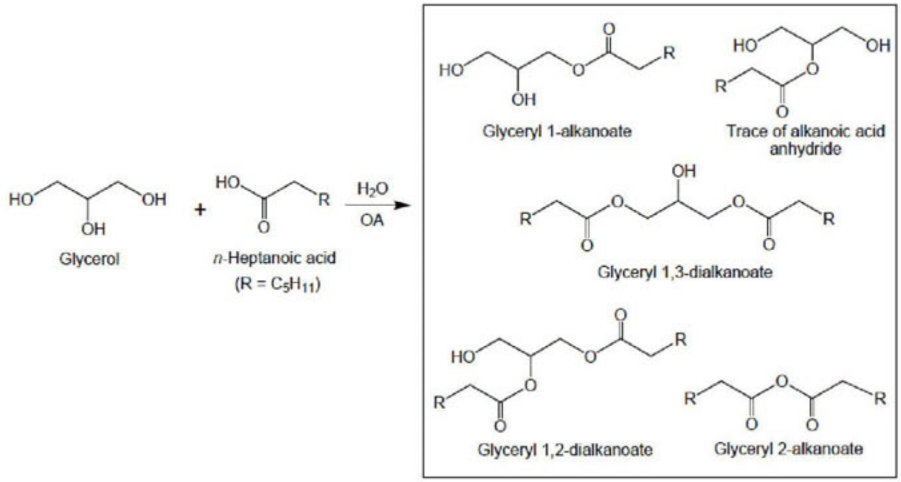
HO
OH
OH
Glycerol
+
HO
R
O
n-Heptanoic acid
(R = C_5H_{11})
H_2O
OA
HO
OH
O
O
R
Glyceryl 1-alkanoate
HO
OH
R
O
O
Trace of alkanoic acid anhydride
OH
R
O
O
O
O
R
Glyceryl 1,3-dialkanoate
HO
O
O
R
R
O
O
Glyceryl 1,2-dialkanoate
R
O
O
O
R
Glyceryl 2-alkanoate

Figure 20. Products formed through dehydration (condensation) reactions starting with glycerol and *n*-heptanoic acid in hydrothermal experiments, and suggested pathways for their formation (modified after Rushdi and Simoneit 2006).

all formed in high-temperature aqueous solutions. In the same study, hydrothermal reactions between ethylene glycol and *n*-nonadecanoic acid yielded mainly ethylene glycolyl monononadecanoate (1,2-ethanediyl monononadecanoate), methyl and ethyl nonadecanoate, *n*-nonadecanol, nonadecyl nonadecanoate (wax ester) and ethylene glycolyl bisnonadecanoate (1,2-ethanediyl bisnonadecanoate) through dehydration reactions. The authors interpret their experiments to indicate that model lipid precursors can form in hydrothermal solutions, and that analogous processes may have contributed to the abiotic synthesis of membranes.

Oxidation/reduction reactions

The hydration/dehydration reactions involving alkenes and alcohols discussed above occur in the context of conversions among alkanes and ketones. The reactions between ketones and alcohols and the reactions between alkenes and alkanes are oxidation/reduction reactions, which is evident because they can be balanced with $H_{2(aq)}$. What may not be evident is that these redox reactions among organic compounds are reversible, although that is observed regularly in hydrothermal experiments.

The first experimental test of whether organic compounds can reach states of metastable equilibrium in hydrothermal systems was the demonstration by Seewald (1994) that ethene and ethane react reversibly at 325 °C (and higher temperatures) at 350 bars (Reaction 14). The results of the 325 °C experiments conducted in the presence of the PPM mineral assemblage (Reaction 18) are shown in Figure 21, which is a variation on a figure from the original paper. The main difference is the location of the equilibrium ratio predicted for equilibrium with the PPM assemblage. The value shown in Figure 21 is based on thermodynamic data for the minerals from Helgeson et al. (1978), which were not used by Seewald (1994) who predicted a lower ratio. Nevertheless, this difference does nothing to detract from the experimental observation that starting either with ethane or ethene, or for that matter cooling from 350 °C to 325 °C, yields ratios of the two hydrocarbons that are close to what can be predicted for metastable equilibrium with the PPM mineral assemblage. This means that Reactions (14) and (18) are linked by the $H_{2(aq)}$ that occurs in both. How the minerals enable this metastable equilibration among the hydrocarbons is still a topic of experimental research, but the involvement of sulfur is implicated by a landmark experimental study of alkane/alkene equilibria and other reactions by Seewald (2001a).

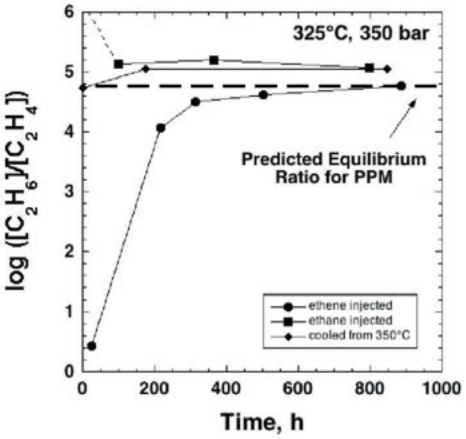

Figure 21. Experimental results at 325 °C and 350 bar showing changes in the ratio of ethane to ethene concentrations in hydrothermal experiments conducted in the presence of the pyrrhotite-pyrite-magnetite mineral assemblage (Reaction 18; Seewald 1994). The lack of change at longer times and the location of concentrations near the activity ratio calculated for the mineral assemblage both show that metastable equilibrium was attained in these experiments. This plot differs from that in the original paper in the location of the predicted ratio (dashed line), which, in this case, was calculated with thermodynamic data, equations, and parameters from Helgeson et al. (1978).

Recently, reversibility of oxidation/reduction reactions among cyclic organic compounds was observed in short-term hydrothermal experiments at 300 °C and 1 kbar (Shipp et al. 2013), as summarized in Figure 22. These experiments also showed reversibility of the hydration/

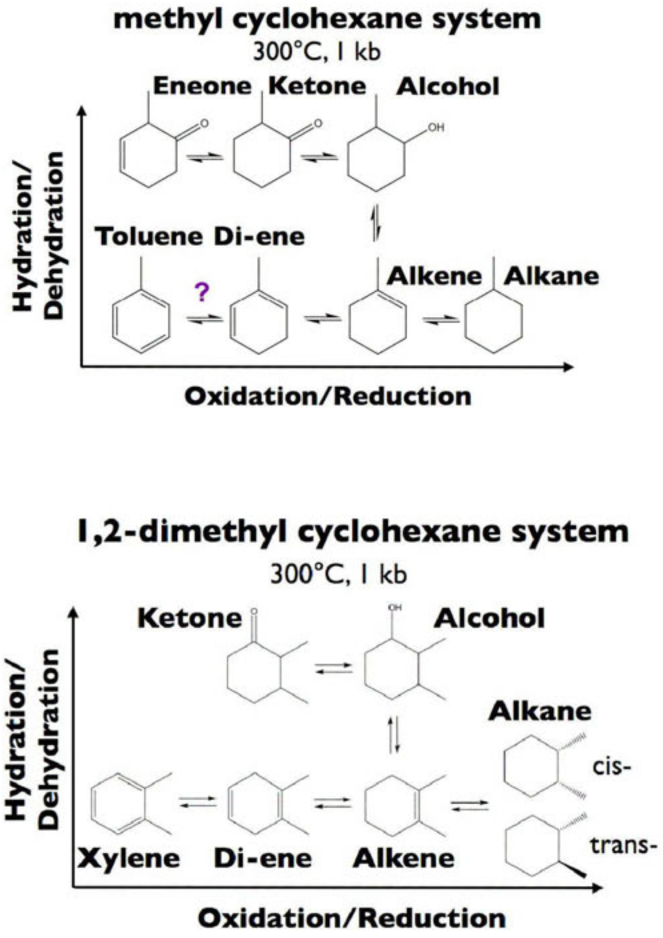
methyl cyclohexane system
300°C, 1 kb
Eneone
Ketone
Alcohol
O
O
OH
Toluene
Di-ene
?
Alkene
Alkane
Hydration/
Dehydration
Oxidation/Reduction
1,2-dimethyl cyclohexane system
300°C, 1 kb
Ketone
Alcohol
O
OH
Alkane
cis-
trans-
Xylene
Di-ene
Alkene
Hydration/
Dehydration
Oxidation/Reduction

Figure 22. Summary of results reported by Shipp et al. (2013) for methylcyclohexane and related compounds (top) and dimethylcyclohexane and related compounds (bottom) in hydrothermal experiments conducted at 300 °C and 1 kilobar pressure. Numerous reversible oxidation/reduction reactions were observed as were reversible hydration/dehydration reactions involving alcohols and alkenes. Short duration experiments in this study allow insight into reactions mechanisms, including carbon cations and radicals.

dehydration reactions among cycloalkenes and cyclic alcohols, as expected from the discussion above. In these experiments it was shown that all of the other compounds could be generated by starting with the alkane, alkene, alcohol, ketone or diene compounds. Reactions leading to aromatic compounds occurred, and those involving xylene appear reversible, but only the formation of toluene and not its reduction reaction was observed possibly owing to the short duration of the experiments. On the other hand, the short durations allowed exploration of reaction mechanisms by quantifying the subtleties of product distributions at early stages of each reaction. It was concluded that carbon-centered cations are involved in the mechanisms of alkene-alcohol reactions owing to the formation of five-membered ring compounds in the methylcyclohexane experiments, which provides unequivocal evidence for carbon-centered cation intermediates via 1,2-alkyl shift reactions of the cationic 6-membered ring (Shipp et al. 2013). The experiments using the dimethylcyclohexane system helped to reveal the mechanism of the oxidation/reduction reactions involving addition and removal of hydrogen. It was concluded that the most likely mechanism is sequential liberation of a hydrogen atom with a carbon-centered radical as an intermediate.

Organic transformations through oxidation/reduction reactions are rampant in geochemical processes, as are overall processes that combine oxidation/reduction with hydration/dehydration reactions akin to Reactions (24), (27), and (31-36). An example is the generation of biomarker compounds and polycyclic aromatic hydrocarbons from steroids and other biomolecules. An example of how cholesterol may ultimately yield phenanthrene, along with biomarker compounds that carry more information, is shown in Figure 23 (McCollom et al. 1999). Each departure of an alkyl group is accompanied by the addition of a hydrogen atom to the remaining structure (reduction), and each step of aromatization of the ring superstructure results in removal of H (oxidation). This balance of redox reactions can be perturbed in a variety of directions during geochemical processes, making it possible that assemblages of biomarker compounds embody a history of redox reactions as well as their more conventional evidence of depositional environments.

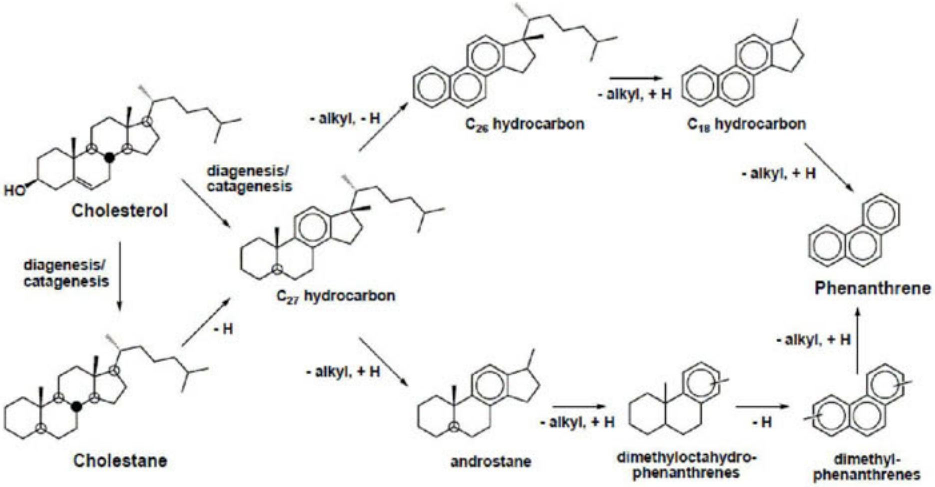

Figure 23. Schematic diagram showing how a biomolecule, cholesterol, can be transformed into cholestane and other biomarker compounds during geochemical transformations that ultimately lead to phenanthrene (modified after McCollom et al. 1999). Note the abundance of oxidation/reduction reactions (indicated by –H or +H) involved in this overall process.

Relative stabilities and irreversible reactions

When writing overall reactions that reflect transformations of organic compounds in hydrothermal fluids, it is common to combine hydration/dehydration reactions and oxidation/reduction reactions. Reactions (31-36) used in the construction of plots in Figure 17 are examples of such merged reactions. As emphasized above, writing reactions this way facilitates thermodynamic analysis of geochemical processes, but does not reflect reaction mechanisms. Once the drives behind organic transformations can be perceived through thermodynamic analysis it can be highly profitable to focus on underlying mechanistic pathways that facilitate or impede the realization of potential reactions. Examples of some experiments that reveal kinetic inhibitions to reactions, or rates and mechanisms of irreversible processes, are summarized here.

Thermodynamic analysis of reactions involving both $H_{2(aq)}$ and H_2O were used by Seewald (2001a) to interpret hydrothermal experiments involving multiple small aqueous organic compounds. Over the course of long-term experiments, analytical data were used to assess values of the activity product, Q_r, defined by

$$Q_r = \prod_i a_i^{\nu_{i,r}} \tag{39}$$

where $\nu_{i,r}$ stands for the stoichiometric reaction coefficient for the i^{th} species in the r^{th} reaction, which is positive for products and negative for reactants. Activity products were then combined with equilibrium constants for the same reactions to evaluate the chemical affinity, A_r, for each reaction, given by

$$A_r = 2.303RT\log\left(\frac{K_r}{Q_r}\right) \tag{40}$$

Positive values of affinity mean that energy would be released if the reaction proceeded in the way it is written (i.e., left to right), and negative values mean that energy would be released if the reaction proceeded from right to left. Either way, the release of energy defines the thermodynamic drive for the reaction. Values of A_r are shown in Figure 24 for several reactions that may have occurred in experiments that included iron-bearing mineral assemblages to control the oxidation state (Seewald 2001a). Note that affinities for many of these reactions are positive. This means that many organic compounds persist in metastable states relative to either $CO_{2(aq)}$ or $CH_{4(aq)}$, which are major constituents of stable equilibrium in the C-H-O chemical system. It can be inferred from the increasing affinity values for reactions involving

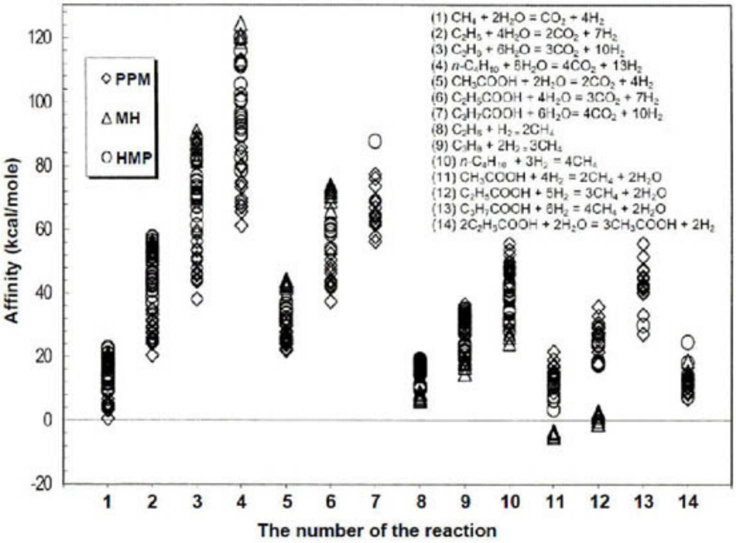

Figure 24. Calculated affinities of reactions among organic and inorganic carbon compounds in hydrothermal experiments conducted in the presence of iron-bearing mineral assemblages (MH and PPM as in Reactions 17 and 18; HMP refers to the hematite-magnetite-pyrite assemblage). Affinities equal zero at equilibrium, and depart to positive values if energy would be released as the reaction proceeds in the direction it is written (and negative if in the opposite direction). The majority of these reactions involve production of either carbon dioxide or methane, which are both constituents of *stable* equilibria in the C-H-O chemical system. These results show that these organic compounds were metastably preserved in these hydrothermal experiments that lasted up to several thousand hours (modified after Seewald 2001a).

homologous series of aqueous organic compounds that larger compounds are further from equilibrium than smaller compounds in these experiments.

The sluggish reactions of metastable aqueous organic compounds in long-term hydrothermal experiments mimics their preservation in geologic processes. It also implies that the rate-limiting steps in the approach to equilibria are sluggish irreversible reactions. The improved understanding of reversible reactions and metastable equilibria described above help to identify the nature of the irreversible reactions that are ultimately in control of the progress of organic transformations. Organic acids are thought to react irreversibly through decarboxylation and other decomposition reactions in sedimentary basin brines (see Shock 1994; Manning et al. 2013). An example of a network of reversible and irreversible reactions involving hydrothermal organic compounds is shown in Figure 25 starting with the reaction of valeric acid (McCollom and Seewald 2003b). Note that rather than a single step decarboxylation of valeric acid, which would produce $CO_{2(aq)}$ and butane$_{(aq)}$, McCollom and Seewald (2003b) deduced that the irreversible reaction produced butene$_{(aq)}$ and formic acid$_{(aq)}$. Butene$_{(aq)}$ then takes part in several reversible reactions to produce butane$_{(aq)}$, butanol$_{(aq)}$ and butanoic acid$_{(aq)}$, and formic acid is shown reacting reversibly to form $CO_{2(aq)}$ and $H_{2(aq)}$. Later work by Seewald et al. (2006) showed that this reaction can also be reversible, as can the corresponding reaction to form H_2O and $CO_{(aq)}$. A cascade of reversible and irreversible reactions emerges from butanol$_{(aq)}$ and butyric acid$_{(aq)}$, ultimately leading to the formation of acetic acid$_{(aq)}$, ethane$_{(aq)}$, ethanol$_{(aq)}$, $CO_{2(aq)}$ and $H_{2(aq)}$.

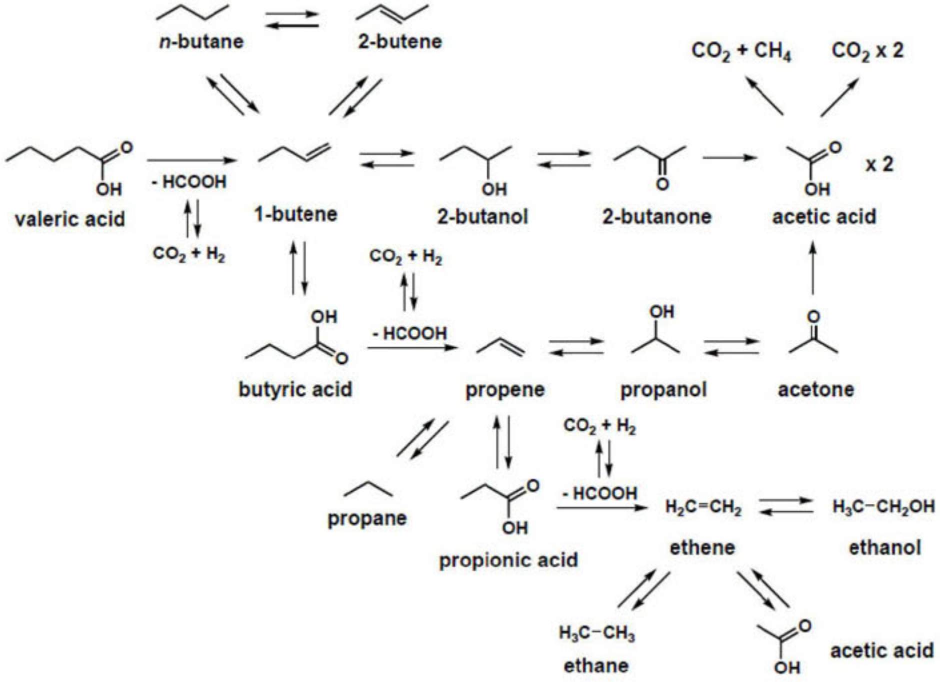
n-butane
2-butene
CO2 + CH4
CO2 x 2
O
OH
valeric acid
- HCOOH
CO2 + H2
1-butene
OH
2-butanol
O
2-butanone
O
OH
x 2
acetic acid
CO2 + H2
OH
O
- HCOOH
butyric acid
propene
OH
propanol
O
acetone
CO2 + H2
propane
O
OH
propionic acid
- HCOOH
H2C=CH2
ethene
H3C-CH2OH
ethanol
H3C-CH3
ethane
O
OH
acetic acid

Figure 25. Summary of observations based on hydrothermal experiments on the reactivity of valeric acid in the presence of various iron-bearing mineral assemblages. Double arrows indicate reversible reactions, and single arrows show irreversible steps in the stepwise transformation of valeric acid to numerous smaller aqueous organic solutes (modified after McCollom and Seewald 2003b). Note that decarboxylation and deformylation followed by reversible production of CO_2 and H_2 from formic acid both produce CO_2.

Decarboxylation or deformylation reactions involve the breaking of C-C bonds in organic molecules, which appear to be sluggish irreversible steps during hydrothermal organic compound transformations. Another example of a C-C bond-breaking reaction was identified by Yang et al. (2012) in studies of the transformations of the model compound DBK mentioned above. The irreversible C-C bond breaking reaction is shown schematically in Figure 26, along with some of the experimental data used to document its occurrence in hydrothermal experiments conducted at 300 °C and 700 bar. Note that when the C-C bond in DBK breaks in the benzyl position the products are a benzyl radical and a phenacetyl radical, which could decarbonylate rapidly to produce $CO_{(aq)}$ and another benzyl radical (Yang et al. 2012). The toluene$_{(aq)}$ that accumulated in the experiments would be a product of the generation of benzyl radicals. Analogous experiments of similar duration starting with toluene$_{(aq)}$ showed no reactivity, suggesting that the C-C bond breaking reaction is an irreversible process at these conditions. It is important to note that no carboxylic acids were detected in these experiments, even though the production of phenacetyl radicals would seem to poise the system for production of phenylacetic acid. This is a major difference between the DBK results and the results obtained by McCollom and Seewald (2003a,b) when starting with organic acids. In their longer-term mineral-buffered experiments with valeric acid$_{(aq)}$ McCollom and Seewald (2003b) saw evidence for the reversible formation of butyric acid$_{(aq)}$ from butene$_{(aq)}$, which is thought to have formed through deformylation of the valeric acid$_{(aq)}$ (see Fig. 25).

Another contrast between the DBK results and the organic acid experiments is the production of larger compounds in the former. Some of these results are illustrated in Figure 27, which shows data reported by Yang et al. (2012). Note that the decreasing concentration of DBK in these plots shows that these data come from the same set of experiments, and that

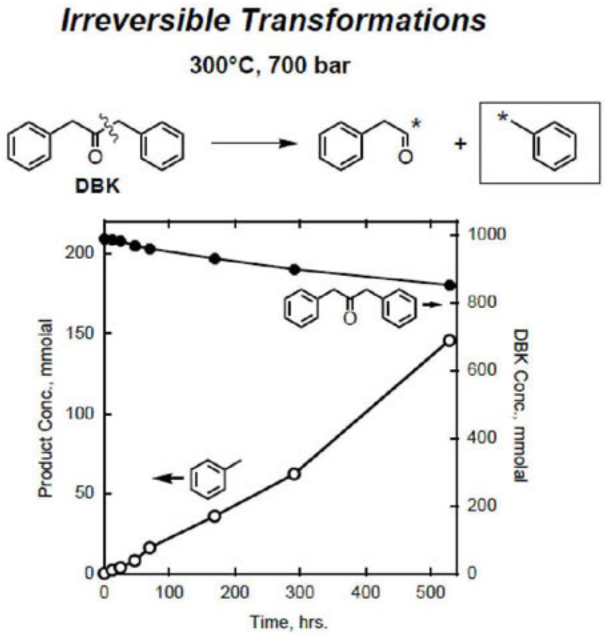

Figure 26. Irreversible transformation of dibenzylketone (DBK) in hydrothermal experiments at 300 °C and 700 bar reported by Yang et al. (2012). Breaking the C-C bond in DBK led to the production of toluene through what is interpreted to be formation of radicals; arrows connect organic compounds with appropriate axes.

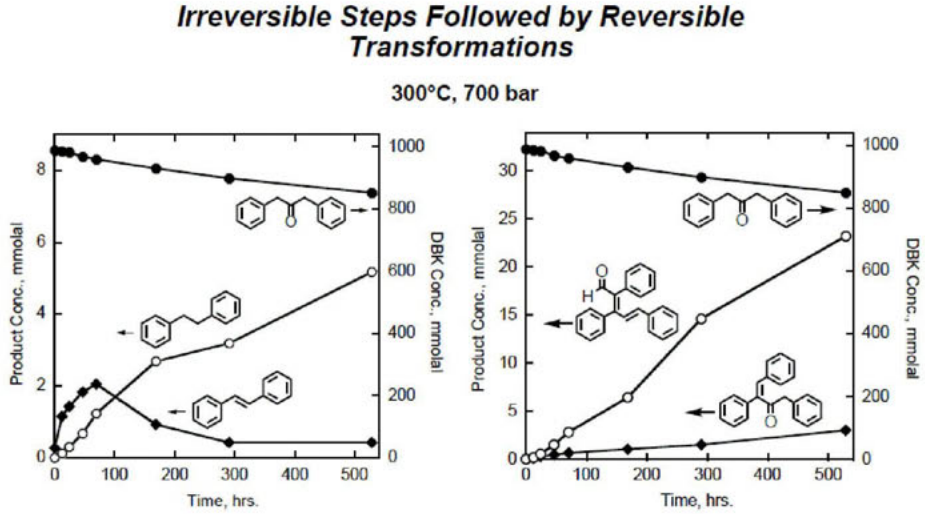

Figure 27. Plots showing some of the products that form when the radicals produced during C-C bond breaking react with another radical (e.g., benzyl radical reaction products, left) or with DBK (right); arrows connect organic compounds with appropriate axes (modified after Yang et al. 2012). Many products of the irreversible C-C bond reaction step went on to participate in reversible reactions (e.g., the production of both bibenzyl and stilbene in the experiments shown in the left plot; production of both three-ring compounds shown on the right).

these are the same results reported in Figure 26. The irreversible production of benzyl radicals shown in Figure 26 can explain the production of bibenzyl, shown in the lefthand plot of Figure 27, as a product of reaction between two benzyl radicals. The production of bibenzyl through the irreversible cleavage of DBK is accompanied by the reversible production of stilbene, also shown in the left-hand plot, through the type of oxidation/reduction now expected between alkanes and alkenes. Additional reactions leading to larger products, such as the three-ring compounds shown in the right-hand plot of Figure 27, can also be traced to the irreversible production of benzyl radicals followed by a variety of reversible transformation reactions. Numerous other examples including the production of 4-ring compounds are documented by Yang et al. (2012). Taken together, the results shown in Figures 26 and 27 suggest that complex networks of irreversible and reversible organic transformations are to be expected in hydrothermal systems.

FUTURE DIRECTIONS FOR HYDROTHERMAL ORGANIC TRANSFORMATIONS

The results summarized above illustrate that investigations of hydrothermal organic transformations have entered an exciting phase where observations of natural systems, thermodynamic models, and hydrothermal experiments can be merged. The progress made in the last 25 years since the first proposal of metastable equilibria among aqueous organic compounds in sedimentary basin brines has revealed unanticipated depth and breadth of reversible processes, as well as the irreversible reactions that maintain metastable states. From this vantage point many directions for research progress can be imagined. Here are a few that seem particularly ripe for investigation.

Analytical advances should allow new observations of small organic compounds in hydrothermal fluids, as well as gases from geothermal and volcanic systems. The need for precision in these measurements should be evident from the preceding discussion, but micromolar (and even submicromolar) detection limits are now possible. Recent progress summarized by Tassi et al. (2012a,b), and Schwandner et al. (2013) provides a strong foundation for such investigations.

Many of the thermodynamic calculations described above use data, equations, and parameters from the 1990's! Since these early developments in theoretical organic geochemistry there have been numerous advances in obtaining experimental data. There are now sufficient data to closely examine the functional forms used for characterizing the thermodynamic properties of aqueous organic compounds at high temperatures and pressures. In addition, regression of dozens of new sets of experimental data can be done in a way that maximizes the potential for building the types of correlation algorithms required to estimate data for the thousands of aqueous organic compounds that may never receive the benefits of experimental study.

New experiments could be designed to attack several lingering mysteries. As an example, despite ample evidence showing that hydrothermal alkane-alkene reactions are reversible, it is still not completely clear how the C-H bonds are broken. One promising direction for such investigations is to explore the involvement of mineral surfaces in facilitating such reactions. Recent studies involving hydrothermal reactions of alkanes (Reeves et al. 2012) and amino acids (McCollom 2013) with and without mineral surfaces point to how such studies could reveal much more than is currently known about organic reaction mechanisms in hydrothermal solutions. Breakthroughs in this arena should be anticipated. Another lingering mystery is the failure of shorter-term hydrothermal experiments to generate carboxylic acids (Yang et al. 2012; Shipp et al. 2013) despite the success of longer-term experiments in the presence of minerals (Seewald 2001a; McCollom and Seewald 2003a,b). This difference raises the possibility that in some cases it may be the production of carboxylic acids rather than their decomposition that is the rate determining process.

Finally, the successful combination of hydrothermal organic transformation experiments and calculations, which has identified and confirmed metastable equilibrium states and begun to clarify the irreversible organic processes during geochemical processes, could be applied to the reactions leading to the production of biomarkers from biomolecules. At present, biomarkers are used to see through all sorts of subsequent geochemical transformations so that parent biomolecules can be identified and constraints placed on depositional environments of sedimentary materials. Perhaps someday soon geochemists will understand enough about all of the hydration/dehydration, oxidation/reduction and other reactions that lead to biomarker formation so that the rest of geologic history can be deduced from the relative ratios and molecular make-up of suites of biomarkers, either coexisting in samples or spread out through a tectonic region. The results would provide a level of detail to geologic history that can, at this stage, only be imagined.

REFERENCES

Abrajano TA, Sturchio NC, Bohlke JK, Lyon GL, Pordea RJ, Stevens CM (1988) Methane-hydrogen gas seeps, Zambales ophiolite, Philippines: Deep or shallow origin? Chem Geol 71:211-222

Albéric P (1986) Composition en acides aminés des particules en suspension autour des vents hydrothermaux (dorsal Est-Pacifique, 13°N). Oceanolog Acta 9:73-79

Alexander DM (1959) The solubility of benzene in water. J. Phys. Chem. 63:1021–1022

Allen ET, Day AL (1935) Hot Springs of the Yellowstone National Park. Carnegie Institute of Washington, Washington, DC

Amend JP, Shock EL (1998) Energetics of amino acid synthesis in hydrothermal ecosystems. Science 281:1659-1662

Anderson FE, Prausnitz JM (1986) Mutual solubilities and vapor pressures for binary and ternary aqueous systems containing benzene, toluene, m-xylene, thiophene and pyridine in the region 100-200 °C. Fluid Phase Equilib 32:63–76

Andreyev PF, Chumachenko AP (1964) Reduction of uranium by natural organic substances. Geokhimya 1:12-22 (in Russian)

Ashworth RA, Howe GB, Mullins ME, Rogers TN (1988) Air-water partitioning coefficients of organics in dilute aqueous solutions. J Hazard Mater 18:25-36

Barnes HL (1979) Solubilities of ore minerals. *In:* Geochemistry of Hydrothermal Ore Deposits, 2nd Edition. Barnes HL (ed) New York: Wiley Interscience, p 404-460

Bergfield D, Lowenstern JB, Hunt AG, Shanks WCP, Evans, WC (2011) Gas and isotope chemistry of thermal features in Yellowstone National Park, Wyoming. United States Geological Survey Scientific Investigations Report 2011-5012

Bittrich H-J, Fahl A, Hartwig F (1983) Zur Löslichkeitsbeeinflussing von Kohlen-wasserstoffen in Wasser. II. Der Einfluss von quarternaren Ammoniumsalzen. Z Phys Chem (Leipzig) 264:891-895

Brault M, Simoneit BRT (1989) Trace petroliferous organic matter associated with hydrothermal minerals from the Mid-Atlantic Ridge at the TAG 26°N site. J Geophys Res 94:9791-9798

Brault M, Marty JC, Saliot A (1984) Fatty acids from particulate matter and sediment in hydrothermal environments from the East Pacific Rise, near 13°N. Org Geochem 6:217-222

Brault M, Simoneit BRT, Marty JC, Saliot A (1988) Hydrocarbons in waters and particulate material from hydrothermal environments at the East Pacific Rise, 13°N. Org Geochem 12:209-219

Brault M, Simoneit BRT, Saliot A (1989) Trace petroliferous organic matter associated with massive hydrothermal sulfides from the East Pacific Rise at 13 and 21°N, Oceanolog Acta 12:405-415

Brown JS, Hallet JP, Bush D, Eckert CA (2000) Liquid-liquid equilibria for binary mixtures of water + acetophenone, + 1-octanol, + anisole, and + toluene from 370 K to 550 K. J Chem Eng Data 45:846-850

Brown RL, Wasik SP (1974) A method of measuring the solubilities of hydrocarbons in aqueous solutions. J Res Natl Bur Stand 78A:453-460

Campos CEPS, Penello JR, Pessoa FLP, Uller AMC (2010) Experimental measurement and thermodynamic modeling for the solubility of methane in water and hexadecane. J Chem Eng Data 55:2576-2580

Capaccioni B, Mangani F (2001) Monitoring of active but quiescent volcanoes using light hydrocarbon distribution in volcanic gases: the results of 4 years of discontinuous monitoring in the Campi Flegrei (Italy). Earth Planet Sci Lett 188:543-555

Capaccioni B, Tassi F, Vaselli O (2001) Organic and inorganic geochemistry of low temperature gas discharges at the Baia di Levante beach, Vulcano Island, Italy. J Volcanol Geotherm Res 108:173-185

Capaccioni B, Taran Y, Tassi F, Vaselli O, Mangani G, Macias JL (2004) Source conditions and degradation processes of light hydrocarbons in volcanic gases: an example from El Chichón volcano (Chiapas State, Mexico). Chem Geol 206:81-96

Chandler K, Eason B, Liotta CL, Eckert CA (1998) Phase equilibria for binary aqueous systems from a near-critical water reaction apparatus. Ind Eng Chem Res 37:3515-3518

Charlou JL, Fouquet Y, Bougault H, Donval JP, Etoubleau J, Jean-Baptiste P, Dapoigny A, Appriou P, Rona PA (1998). Intense CH_4 plumes generated by serpentinization of ultramafic rocks at the intersection of the 15°20'N fracture zone and the Mid-Atlantic Ridge. Geochim Cosmochim Acta 62:2323-2333

Charlou JL, Donval JP, Fouquet Y, Jean-Baptiste P, Holm N (2002). Geochemistry of high H2 and CH4 vent fluids issuing from ultramafic rocks at the Rainbow hydrothermal field (36°14'N, MAR). Chem Geol 191:345-359

Charlou JL, Donval JP, Konn C, Ondreas H, Fouquet Y, Jean-Baptiste P, Fourré E (2010) High production and fluxes of H_2 and CH_4 and evidence of abiotic hydrocarbon synthesis by serpentinization in ultramafic-hosted hydrothermal systems on the Mid-Atlantic Ridge. I*n:* Diversity of Hydrothermal Systems on Slow-Spreading Ocean Ridges. Geophysical Monograph Series 188. Rona P, Devey C, Dyment J, Murton B (eds) American Geophysical Union, Washington DC, p 265-296

Chen H, Wagner J (1994) An apparatus and procedure for measuring mutual solubilities of hydrocarbons + water: benzene + water from 303 to 373 K. J Chem Eng Data 39:470-474

Chiodini G, Caliro S, Lowenstern JB, Evans WC, Bergfeld D, Tassi F, Tedesco D (2012) Insights from fumarole gas geochemistry on the origin of hydrothermal fluids on the Yellowstone Plateau. Geochim Cosmochim Acta 89:265-278

Cipolli F, Gambardella B, Marini L, Ottonello G, Zuccolini MV (2004) Geochemistry of high-pH waters from serpentinites of the Gruppo di Voltri (Genova, Italy) and reaction path modeling of CO_2 sequestration in serpentinite aquifers. Appl Geochem 19:787-802

Cinti D, Procesi M, Tassi F, Montegrossi G, Sciarra A, Vaselli O, Quattrocchi F (2011) Fluid geochemistry and geothermometry in the western sector of the Sabatini Volcanic District and the Tolfa Mountains (Central Italy). Chem Geol 284:160-181

Claussen WF, Polglase MF (1952) Solubilities and structures in aqueous aliphatic hydrocarbon solutions. J Am Chem Soc 74:4817-4819

Comita PB, Gagosian RB, Williams PM (1984). Suspended particulate organic material from hydrothermal vent waters at 21°N. Nature 307:450-453

Cosgrove BA, Walkley J (1981) Solubilities of gases in H_2O and ^2H_2O. J Chromatogr 216:161–167

Crovetto R, Fernandez-Prini R, Japas ML (1982) Solubilities of inert gases and methane in H_2O and D_2O in the temperature range of 300 to 600 K. J Chem Phys 76:1077-1086

Cruse AM, Seewald JS (2006) Geochemistry of low-molecular weight hydrocarbons in hydrothermal fluids from Middle Valley, northern Juan de Fuca Ridge, Geochim Cosmochim Acta 70:2073–2092

Cruse AM, Seewald JS (2010) Low-molecular weight hydrocarbons in vent fluids from the Main Endeavour Field, northern Juan de Fuca Ridge. Geochim Cosmochim Acta 74:6126-6140

Darling WG (1998a) Hydrothermal hydrocarbon gases. 1. Origin and geothermometry. Appl Geochem 13:815-824

Darling WG (1998b) Hydrothermal hydrocarbon gases. 2. Application in the East African Rift System. Appl Geochem 13:825-840

Daumas R, Albéric P, Brault M, Khripounoff A, Hermin M-N, Marty J-C, Saliot A (1988) Matière organique présente dans les eaux d'un site hydrothermal actif du Pacifique-Est (13°N). Oceanolog Acta Spec 8:31-43

Dec SF, Gill SJ (1984) Heats of solution of gaseous hydrocarbons in water at 25 °C. J Solution Chem 13:27-41

Di Gioia ML, Leggio A, Le Pera A, Liguori A, Perri F (2006) Occurrence of organic compounds in the thermal sulfurous waters of Calabria, Italy. Chromatographia 63:585-590

Dohányosová P, Fenclová D, Vrbka P, Dohnal V (2001) Measurement of aqueous solubility of hydrophobic volatile organic compounds by solute vapor absorption technique: Toluene, ethylbenzene, propylbenzene, and butylbenzene at temperatures from 273 K to 328 K. J Chem Eng Data 46:1533-1539

Douville E, Charlou JL, Oelkers EH, Bienvenu P, Jove-Colon CF, Donval JP, Fouquet Y, Prieur D, Appriou P (2002). The Rainbow vent fluids (36°14'N, MAR): the influence of ultramafic rocks and phase separation on trace metal content in Mid-Atlantic Ridge hydrothermal fluids. Chem Geol 184:37-48

Durand R (1948) Chimie physique - Recherches sur l'hydrotropie - Etude de la solubilite de l'heptane, de l'hexane et du cyclohexane dans les solutions aqueuses de quelques sels d'acides gras. C R Hebd Seances Acad Sci 226:409-410

Etiope G, Schoell M, Hosgörmez H (2011) Abiotic methane flux from the Chimaera seep and Tekirova ophiolites (Turkey): Understanding gas exhalation from low temperature serpentinization and implications for Mars. Earth Planet Sci Lett 310:96-104

Fabri MC, Bargain A, Briand P, Gebruk A, Fouquet Y, Morineaux M, Desbruyeres D (2011) The hydrothermal vent community of a new deep-sea field, Ashadze-1, 12°58'N on the Mid-Atlantic Ridge. J Marine Biol Assoc UK 91:1-13

Fekete J, Sajgó C, Horváth I, Kárpáti Z, Vető I, Hetényi M (2009) Interaction and variation of isotopic age, temperature, oragnic and inorganic solutes in Hungarian thermal waters. Central Eur Geology 52:269-285

Fernandez-Prini R, Crovetto R (1989) Evaluation of data on solubility of simple apolar gases in light and heavy water at high temperature. J Phys Chem Ref Data 18:1231-1243

Fiebig J, Chiodini G, Caliro S, Rizzo A, Spangenberg J, Hunziker JC (2004) Chemical and isotopic equilibrium between CO_2 and CH_4 in fumarolic gas discharges: Generation of CH_4 in arc magmatic-hydrothermal systems. Geochim Cosmochim Acta 68:2321-2334

Fiebig J, Woodland AB, Spangenberg J, Oschmann W (2007) Natural evidence for rapid abiogenic hydrothermal generation of CH_4. Geochim Cosmochim Acta 71:3028-3039

Fiebig J, Woodland AB, D'Alessandro W, Püttmann W (2009) Excess methane in continental hydrothermal emissions is abiogenic. Geology 37:495-498

Franks F, Gent M, Johnson HH (1963) The solubility of benzene in water. J Chem Soc 1963:2716-2723

Gherardi F, Panichi C, Gonfiantini R, Magro G, Scandiffio G (2005) Isotope systematics of C-bearing gas compounds in the geothermal fluids of Larderello, Italy. Geothermics 34:442-470

Giordano TH (1985) A preliminary evaluation of organic ligands and metal-organic complexing in Mississippi Valley-type ore solutions. Econ Geol 80:96-106

Giordano TH (2002) Transport of Pb and Zn by carboxylate complexes in basinal ore fluids and related petroleum-field brines at 100 °C: the influence of pH and oxygen fugacity. Geochem Trans 3:56–72

Giordano TH, Barnes HL (1981) Lead transport in Mississippi Valley-type ore solutions. Econ Geol 76:2200–2211

Gize AP (1999) Organic alteration in hydrothermal sulfide ore deposits. Econ Geol 94:967-979

Glynn S, Mills RA, Palmer MR, Pancost RD, Severmann S, Boyce AJ (2006) The role of prokaryotes in supergene alteration of submarine hydrothermal sulfides. Earth Planet Sci Lett 244:170-185

González-Barreiro C, Cancho-Grande B, Araujo-Nespereira P, Cid-Fernández JA, Simal-Gándara J (2009) Occurrence of soluble organic compounds in thermal waters by ion trap mass detection. Chemosphere 75:34-47

Greenwood PF, Brocks JJ, Grice K, Schwark L, Jaraula CMB, Dick JM, Evans KA (2013) Organic geochemistry and mineralogy. I. Characterisation of organic matter associated with metal deposits. Ore Geol Rev 50:1-27

Groves FR Jr (1988) Solubility of cycloparaffins in distilled water and salt water. J Chem Eng Data 33:136-138

Gunter BD (1978) C_1-C_4 hydrocarbons in hydrothermal gases. Geochim Cosmochim Acta 42:137-139

Gunter BD, Musgrave BC (1966) Gas chromatographic measurements of hydrothermal emanations at Yellowstone National Park. Geochim Cosmochim Acta 30:1175-1189

Guseva AN, Parnov EI (1964) Isothermal sections of monocyclic arene-water binary systems at 25°, 100°, and 200°. Russ. J Phys Chem 38:439-440

Helgeson HC (1991) Organic/inorganic reactions in metamorphic processes. Can Mineral 29:707-739

Helgeson HC, Delany JM, Nesbitt WH, Bird DK (1978) Summary and critique of the thermodynamic properties of rock forming minerals. Am J Sci 278A:1-229

Helgeson HC, Knox AM, Owens CE, Shock EL (1993) Petroleum, oil field waters and authigenic mineral assemblages: Are they in metastable equilibrium in hydrocarbon reservoirs? Geochim Cosmochim Acta 57:3295-3339

Helgeson HC, Owens CE, Knox AM Richard L (1998) Calculation of the standard molal thermodynamic properties of crystalline, liquid, and gas organic molecules at high temperatures and pressures. Geochim Cosmochim Acta 62:985-1081

Helgeson HC, Richard L, McKenzie WF, Norton DL Schmitt A (2009) A chemical and thermodynamic model of oil generation in hydrocarbon source rocks. Geochim Cosmochim Acta 73:594-695

Ho ES, Mauk JL (1996) Relationship between organic matter and copper mineralization in the Proterozoic Nonesuch Formation, northern Michigan. Ore Geol Rev 11:71–87

Ho ES, Meyers PA, Mauk JL (1990) Organic geochemical study of mineralization in the Keweenawan Nonesuch formation at White Pine, Michigan. Org Geochem 16:229-234

Hofmann BA (1993) Organic matter associated with mineralized reduction spots in red beds. *In:* Bitumens in Ore Deposits. Special Publication of the Society for Geology Applied to Mineral Deposits 9. Parnell J, Kucha H, Landais P (eds) Springer, p 362-378

Holm NG, Charlou JL (2001) Initial indications of abiotic formation of hydrocarbons in the Rainbow ultramafic hydrothermal system, Mid-Atlantic Ridge. Earth Planet Sci Lett 191:1-8

Hosgörmez H, Etiope G, Yalçin MN (2008) New evidence for a mixed inorganic and organic origin of the Olympic Chimaera fire (Turkey): a large onshore seepage of abiogenic gas. Geofluids 8:263-273

Hulen JB, Collister JW (1999) The oil-bearing, Carlin-type gold deposits of Yankee Basin, Alligator Ridge District, Nevada. Econ Geol 94:1029-1049

Ikorsky SV, Avedisyan AA (2007) Hydrocarbon gases and helium isotopes int he Paleozoic alkaline-ultramafic massifs of the Kola Peninsula. Geochem Int 45:62-69

Ilchick RP, Brimhall GH, Schull HW (1986) Hydrothermal maturation of indigenous organic matter at the Alligator Ridge gold deposits, Nevada. Econ Geol 81:113-130

Jönsson JA, Vejrosta J, Novak J (1982) Air/water partition coefficients for normal alkanes (n-pentane to n-nonane). Fluid Phase Equilib 9:279-286

Joralemon P (1951) The occurrence of gold at the Getchell Mine, Nevada. Econ Geol 46:267-310

Kárpáti Z, Sajgó Cs, Vető, Klopp G, Horváth I (1999) Organic matter in thermal waters of the Pannonian Basin-a preliminary report on aromatic compounds. Org Geochem 30:701-712

Kelley DS, Karson JA, Blackman DK, Früh-Green GL, Butterfield DA, Lilley MD, Olson EJ, Schrenk MO, Roe KK, Lebon GT, Rivizzigno P, the ATSP (2001) An off-axis hydrothermal vent field near the Mid-Atlantic Ridge at 30° N. Nature 412:145-149

Konn C, Charlou JL, Donval JP, Holm NG, Dehairs F, Bouillon S (2009) Hydrocarbons and oxidized organic compounds in hydrothermal fluids from Rainbow and Lost City ultramafic-hosted vents. Chem Geol 258:299-314

Konn C, Testemale D, Querellou J, Holm NG, Charlou JL (2011) New insight into the contributions of thermogenic processes and biogenic sources to the generation of organic compounds in hydrothermal fluids. Geobiology 9:79-93

Konn C, Charlou JL, Donval JP, Holm NG (2012) Characterisation of dissolved organic compounds in hydrothermal fluids by stir bar sorptive extraction-gas chomatography-mass spectrometry. Case study: the Rainbow field (36 N, Mid-Atlantic Ridge). Geochem Trans 13, doi:10.1186/1467-4866-13-8

Kormas KA, Tivey MK, Von Damm K, Teske A (2006), Bacterial and archaeal phylotypes associated with distinct mineralogical layers of a white smoker spire from a deep-sea hydrothermal vent site (9°N, East Pacific Rise), Environ Microbiol 8:909-920

Landais P (1996) Organic geochemistry of sedimentary uranium ore deposits. Ore Geology Reviews 11:33-51

Landais P, Gize AP (1997) Organic matter in hydrothermal ore deposits. *In:* Geochemistry of Hydrothermal Ore Deposits, 3rd Edition. Barnes HL (ed) John Wiley & Sons, Inc., p 613-655

Lang SQ, Butterfield DA, Schulte, MD, Kelley DS, Lilley MD (2010) Elevated concentrations of formate, acetate and dissolved organic carbon found at the Lost City hydrothermal field. Geochim Cosmochim Acta 74:941-952

Lapham L, Wilson R, Riedel M, Paull CK, Holmes ME (2013) Temporal variability of in situ methane concentrations in gas hydrate-bearing sediments near Bullseye Vent, Northern Cascadia Margin. Geochem Geophys Geosys, doi: 10.1002/ggge.20167

Large RR, Bull SW, Maslennikov VV (2011) A carbonaceous sedimentary source-rock model for Carlin-type and orogenic gold deposits. Econ Geol 106:331-358

Leif RN, Simoneit BRT (1995) Ketones in hydrothermal petroleums and sediment extracts from Guaymas Basin, Gulf of California. Org Geochem 23:889-904

Leinonen PJ, MacKay D (1973) Multicomponent solubility of hydrocarbons in water. Can J Chem Eng 51:230-233

Lilley MD, Butterfield DA, Olson EJ, Lupton JE, Macko SA, McDuff RE (1993) Anomalous CH_4 and NH_4^+ concentrations at an unsedimented mid-ocean-ridge hydrothermal system. Nature 364:45-47

Machel HG (1989) Relationships between sulphate reduction and oxidation of organic compounds to carbonate diagenesis, hydrocarbon accumulations, salt domes, and metal sulphide deposits. Carbonates and Evaporites 4:137-151

Mackay D, Shiu WY (1975) Determination of the solubility of hydrocarbons in aqueous sodium chloride solutions. Can J Chem Eng 53:239–242

Magro G, Cherardi F, Bayon FEB (2013) Noble and reactive gases of Palinpinon geothermal field (Philippines): Origin, reservoir processes and geodynamic implications. Chem Geol 339:4-15

Mangani G, Berloni A, Capaccioni B, Tassi F, Maione M (2004) Gas chromatographic-mass spectrometric analysis of hydrocarbons and other neutral organic compounds in volcanic gases using SPME for sample preparation. Chromatographia 59:213-217

Manning DAC (1997) Acetate and propionate in landfill leachates: Implications for the recognition of microbiological influences ont he composition of waters in sedimentary systems. Geology 25:279-281

Manning CE, Shock EL, Sverjensky DA (2013) The chemistry of carbon in aqueous fluids at crustal and upper-mantle conditions: experimental and theoretical constraints. Rev Mineral Geochem 75:109-148

Mazor, E, Wasserburg GJ (1965) Helium, neon, argon, krypton and xenon in gas emanations from Yellowstone and Lassen volcanic National Parks. Geochim Cosmochim Acta 29:443-454

McAuliffe C (1966) Solubility in water of paraffin, cycloparaffin, olefin, acetylene, cycloolefin, and aromatic hydrocarbons. J Phys Chem 70:1267-1275

McCollom TM (2008) Observational, experimental, and theoretical constraints on carbon cycling in mid-ocean ridge hydrothermal systems. *In:* Magma to Microbe: Modeling Hydrothermal Processes at Ocean Spreading Centers. Geophysical Monograph Series 178. Lowell RP, Seewald JS, Metaxas A, Perfit MR (eds) American Geophysical Union, Washington, DC, p 193–213

McCollom TM (2013) The influence of minerals on decomposition of the n-alkyl-α-amino acid norvaline under hydrothermal conditions. Geochim Cosmochim Acta 104:330-357

McCollom TM, Seewald JS (2003a) Experimental constraints on the hydrothermal reactivity of organic acids and acid anions: I. Formic acid and formate. Geochim Cosmochim Acta 67:3625-3644

McCollom TM, Seewald JS (2003b) Experimental study of the hydrothermal reactivity of organic acids and acid anions: II. Acetic acid, acetate, and valeric acid. Geochim Cosmochim Acta 67:3645-3664

McCollom TM, Simoneit BRT, Shock EL (1999) Hydrous pyrolysis of polycyclic aromatic hydrocarbons and implications for the origin of PAH in hydrothermal petroleum. Energy Fuels 13:401-410

McLin KS, Moore JN, Bowman JR, McCulloch JE (2012) Mineralogy and fluid inclusion gas chemistry of production well mineral scale deposits at the Dixie Valley geothermal field, USA. Geofluids 12:216-227

Melchert B, Devey CW, German CR, Lackschewitz KS, Seifert R, Walter M, Mertens C, Yoerger DR, Baker ET, Paulick H, Nakamura K (2008) First evidence for high-temperature off-axis venting of deep crustal/mantle heat: The Nibelungen hydrothermal field, southern Mid-Atlantic Ridge. Earth Planet Sci Lett 275:61-69

Miller DJ, Hawthorne SB (2000) Solubility of liquid organics of environmental interest in subcritical (hot/liquid) water from 298 K to 473 K. J Chem Eng Data 45:78-81

Morrill PL, Kuenen JG, Johnson OJ, Suzuki S, Rietze A, Sessions AL, Fogel ML, Nealson KH (2013) Geochemistry and geobiology of a present-day serpentinization site in California: The Cedars. Geochim Cosmochim Acta 109:222-240

Morrison TJ, Billett F (1952) The salting-out of non-electrolytes. Part II. The effect of variations in non-electrolyte. J Chem Soc 1952:3819-3822

Mottl MJ, Komor SC, Fryer P, Moyer CL (2003) Deep-slab fluids fuel extremophilic *Archaea* on a Mariana forearc serpentinite mud volcano: Ocean Drilling Program Leg 195. Geochem Geophys Geosyst 4, doi:10.1029/2003GC000588

Neal C, Stanger G (1983) Hydrogen generation form mantle source rocks in Oman. Earth Planet Sci Lett 66:315-320

Nelson HD, de Ligny CL (1968) The determination of the solubilities of some n-alkanes in water at different temperatures, by means of gas chromatography. Rec Trav Chim 87:528-544

Neely BJ, Wagner J, Robinson RL Jr, Gasem KAM (2008) Mutual solubility measurements of hydrocarbon-water systems containing benzene, toluene, and 3-methylpentane. J Chem Eng Data 53:165-174

Nivin VA (2011) Variations in the composition and origin of hydrocarbon gases from inclusions in minerals of the Khibiny and Lovozero plutons, Kola Peninsula, Russia. Geol Ore Deposits 53:699-707

Oliveira MLN, Malagoni RA, Fehr M, Franco Júnior MR (2008) Obtaining solubility data from a liquid-liquid equilibrium cell. Chem Eng Comm 195:1076-1084

Pereda S, Awan JA, Mohammadi AH, Valtz A, Coquelet C, Brignole EA, Richon D (2009) Solubility of hydrocarbons in water: Experimental measurements and modeling using a group contribution with associate equation of state (GCA-EoS). Fluid Phase Equilib 275:52-59

Pierotti RA, Liabastre AA (1972) The Structure and Properties of Water Solutions. Georgia Institute of Technology, Environmental Resources Center report ERC-0572

Plyasunov AV, Shock EL (2001) Correlation strategy for determining the parameters of the revised Helgeson-Kirkham-Flowers model for aqueous nonelectrolytes. Geochim Cosmochim Acta 65:3879-3900

Polak J, Lu BC-Y (1973) Mutual solubilities of hydrocarbons and water at 0 and 25 °C. Can J Chem 51:4018-4023

Potter J, Rankin AH, Treloar PJ (2004) Abiogenic Fischer-Tropsch synthesis of hydrocarbons in alkaline igneous rocks; fluid inclusion, textural and isotopic evidence from the Lovozero complex, N.W. Russia. Lithos 75:311-330

Prapaipong P, Shock EL, Koretsky CM (1999) Metal-organic complexes in geochemical processes: Temperature dependence of standard partial molal thermodynamic properties of aqueous complexes between metal cations and dicarboxylate ligands. Geochim Cosmochim Acta 63:2547-2577

Price LC (1979) Aqueous solubility of methane at elevated pressures and temperatures. Am Assoc Petrol Geol Bull 63:1527-1533

Price LC (1991) Aqueous solubility of crude oil to 400 °C and 2,000 bars pressure in the presence of gas. J Petrol Geol 4:195-223

Proskurowski G, Lilley MD, Kelley DS, Olson EJ (2006) Low temperature volatile production at the Lost City Hydrothermal Field, evidence from a hydrogen stable isotope geothermometer. Chem Geol 229:331-343

Proskurowski G, Lilley MD, Seewald JS, Früh-Green GL, Olson EJ, Lupton JE, Sylva SP, Kelley DS (2008) Abiogenic hydrocarbon production at Lost City hydrothermal field. Science 319:604-607

Püttmann W, Hagemann HW, Merz C, Speczik S (1988) Influence of organic material on mineralization processes in the Permian Kupferschiefer formation, Poland. Org Geochem 13:357-363

Püttmann W, Merz C, Speczik S (1989) The secondary oxidation of organic material and its influence on Kupferschiefer mineralization of southwest Poland. Appl Geochem 4:151-161

Püttmann W, Heppenheimer H, Diedel R (1990) Accumulation of copper in the Permian Kupferschiefer - a result of post-depositional redox reactions. Org Geochem 16:1145-1156

Püttmann W, Fermont WJJ, Speczik S (1991) The possible role of organic matter in transport and accumulation of metals exemplified at the Permian Kupferschiefer formation. Ore Geology Rev 6:563-579

Radtke AS, Scheiner BJ (1970) Studies of hydrothermal gold deposition. 1. Carlin gold deposit, Nevada, the role of carbonaceous materials in gold deposition. Econ Geol 65:87-102

Reeves EP, Seewald JS, Sylva S (2012) Hydrogen isotope exchange between n-alkanes and water under hydrothermal conditions. Geochim Cosmochim Acta 77:582-599

Rettich TR, Handa YP, Battino R, Wilhelm E (1981) Solubility of gases in liquids. 13. High-precision determination of Henry's constants for methane and ethane in liquid water at 275 to 328 K. J Phys Chem 85:3230-3237

Rushdi AI, Simoneit BRT (2006) Abiotic condensation synthesis of glyceride lipids and wax esters under simulated hydrothermal conditions. Origins Life Evol Biosphere 36:93-108

Sanemasa I, Araki M, Deguchi T, Nagai H (1982) Solubility measurements of benzene and the alkylbenzenes in water by making use of solute vapor. Bull Chem Soc Jpn 55:1054-1062

Sawamura S, Nagaoka K, Machikawa T (2001) Effects of pressure and temperature on the solubility of alkylbenzenes in water: Volumetric property of hydrophobic hydration. J Phys Chem B 105:2429-2436

Schrenk MO, Kelley DS, Delaney JR, Baross JA (2003) Incidence and diversity of microorganisms within the walls of an active deep-sea sulfide chimney. Appl Environ Microbiol 69:35803592

Schulte MD, Shock EL (1993) Aldehydes in hydrothermal solutions: Standard partial molal thermodynamic properties and relative stabilities at high temperatures and pressures. Geochim Cosmochim Acta 57:3835-3846

Schwandner FM, Seward TM, Gize AP, Hall PA, Dietrich VJ (2004) Diffuse emission of organic trace gases for the flank and crater of a quiescent active volcano (Vulcano, Aeolian Islands, Italy). J Geophys Res 109, doi: 10.1029/2003JD00 3890

Schwandner FM, Seward TM, Gize AP, Hall K, Dietrich VJ (2013) Halocarbons and other trace heteroatomic organic compounds in volcanic gases from Vulcano (Aeolian Islands, Italy). Geochim Cosmochim Acta 101:191-221

Schwarz FP (1980) Measurement of the solubilities of slightly soluble organic liquids in water by elution chromatography. Anal Chem 52:10-15

Seewald JS (1994) Evidence for metastable equilibrium between hydrocarbons under hydrothermal conditions. Nature 370:285-287

Seewald JS (2001a) Aqueous geochemistry of low molecular weight hydrocarbons at elevated temperatures and pressures: constraints from mineral buffered laboratory experiments. Geochim Cosmochim Acta 65:1641-1664

Seewald JS (2001b) Model for the origin of carboxylic acids in basinal brines. Geochim Cosmochim Acta 65:3779-3789

Seewald JS (2003) Organic-inorganic interactions in petroleum-producing sedimentary basins. Nature 426:327-333

Seewald JS, Zolotov MY, McCollom T (2006) Experimental investigation of single carbon compounds under hydrothermal conditions. Geochim Cosmochim Acta 70:446-460

Serra MCC, Mainar AM, Palavra AMF (2011) Solubility of ethene in water and in a medium for the cultivation of a bacterial strain. J Chem Eng Data 56:1596-1601

Sherwood Lollar B, Westgate TD, Ward JA, Slater GF, Lacrampe-Couloume G (2002) Abiogenic formation of alkanes in the Earth's crust as a minor source for global hydrocarbon reservoirs. Nature 416:522-524

Shipp J, Gould I, Herckes P, Shock E, Williams L, Hartnett H (2013) Organic functional group transformations in water at elevated temperature and pressure: Reversibility, reactivity, and mechanisms. Geochim Cosmochim Acta 104:194-209

Shock EL (1988) Organic acid metastability in sedimentary basins. Geology 16:886-890

Shock EL (1989) Corrections to "Organic acid metastability in sedimentary basins." Geology 17:572-573

Shock EL (1990) Geochemical constraints on the origin of organic compounds in hydrothermal systems. Origins Life Evol Biosphere 20:331-367

Shock EL (1992) Chemical environments in submarine hydrothermal systems. Origins Life Evol Biosphere 22:67-107

Shock EL (1993) Hydrothermal dehydration of aqueous organic compounds. Geochim Cosmochim Acta 57:3341-3349

Shock EL (1994) Application of thermodynamic calculations to geochemical processes involving organic acids. *In:* The Role of Organic Acids in Geological Processes. Lewan M, Pittman E (eds) Springer-Verlag, p 270-318

Shock EL (1995) Organic acids in hydrothermal solutions: Standard molal thermodynamic properties of carboxylic acids, and estimates of dissociation constants at high temperatures and pressures. Am J Sci 295:496-580

Shock EL (1998) Co-transport of metals and organic compounds in geochemical, biochemical and environmental processes. *In:* Proceedings of the Rome Seminar on Environmental Geochemistry. Marini L, Ottonello G (eds) Pacini Editore, p 73-102

Shock EL (2000) Thermodynamic response of organic compounds in geochemical processes of sedimentary basins. *In:* Ore Genesis and Exploration: The Roles of Organic Matter. Reviews in Economic Geology Vol. 9. Giordano TH, Kettler RM, Wood SA (eds) Society of Economic Geologists, Inc., Littleton, CO, p 105-117

Shock EL, Canovas PC (2010) The potential for abiotic organic synthesis and biosynthesis at seafloor hydrothermal systems. Geofluids 10:161-192

Shock EL, Helgeson HC (1988) Calculation of the thermodynamic and transport properties of aqueous species at high pressures and temperatures: Correlation algorithms for ionic species and equation of state predictions to 5 kb and 1000 °C. Geochim Cosmochim Acta 52:2009-2036

Shock EL, Helgeson HC (1990) Calculation of the thermodynamic and transport properties of aqueous species at high pressures and temperatures: Standard partial molal properties of organic species. Geochim Cosmochim Acta 54:915-945

Shock EL, Helgeson HC, Sverjensky DA (1989) Calculation of the thermodynamic and transport properties of aqueous species at high pressures and temperatures: Standard partial molal properties of inorganic neutral species. Geochim Cosmochim Acta 53:2157-2183

Shock EL, Schulte MD (1998) Organic synthesis during fluid mixing in hydrothermal systems. J Geophys Res 103:28513-28527

Shulga NA, Peresypkin VI, Revelskii IA (2010) Composition research of n-alkanes in the samples of hydrothermal deposits of the Mid-Atlantic Ridge by means of gas chromatography-mass spectrometry. Oceanology 50:479-487

Simoneit BR (1990) Petroleum generation, an easy and widespread process in hydrothermal systems: an overview. Appl Geochem 5:3-15

Simoneit BRT, Brault M, Saliot A. (1990) Hydrocarbons associated with hydrothermal minerals, vent waters and talus on the East Pacific Rise and Mid-Atlantic Ridge. Appl Geochem 5:115-124

Simoneit BRT, Lein AY, Peresypkin VI, Osipov GA (2004) Composition and origin of hydrothermal petroleum and associated lipids in the sulfide deposits of the Rainbow Field (Mid-Atlantic Ridge at 36°N). Geochim Cosmochim Acta 68:2275-2294

Stephenson RM (1992) Mutual solubilities: water-ketones, water-ethers, and water-gasoline-alcohols. J Chem Eng Data 37:80-95

Summons RE, Powell TG, Boreham CJ (1988) Petroleum geology and geochemistry of the middle Proterozoic McArthur Basin, Northern Australia. 3. Composition of extractable hydrocarbons. Geochim Cosmochim Acta 52:1747-1763

Sverjensky DA (1986) Genesis of Mississippi Valley-type lead-zinc deposits. Annu Rev Earth Planet Sci 14:177-99

Szponar N, Brazelton WJ, Schrenk MO, Bower DM, Steele A, Morrill P (2012) Geochemistry of a continental site of serpentinization in the Tablelands Ophiolite, Gros Morne National Park: a Mars analogue. Icarus, doi:10.1016/j.icarus.2012.07.004

Takai, K, Komatsu T, Inagaki F, Horikoshi K (2001) Distribution of Archaea in a black smoker chimney structure. Appl Environ Microbiol 67:3618-3629

Taran YA, Varley NR, Inguaggiato S, Cienfuegos E (2010) Geochemistry of H_2- and CH_4-enriched hydrothermal fluids of Socorro Island, Revillagigedo Archipelago, Mexico. Evidence for serpentinization and abiogenic methane. Geofluids 10:542-555

Tassi F, Vaselli O, Capaccioni B, Macias JL, Nsncetti A, Motegrossi G, Magro G (2003) Chemical composition of fumarolic gases and spring discharges form El Chichon volcano, Mexico: causes and implications of the changes detected over the period 1998-2000. J Volcanol Geotherm Res 123:105-121

Tassi F, Vaselli O, Capaccioni B, Giolito C, Duarte E, Fernandez E, Minissale A, Magro G (2005a) The hydrothermal-volcanic system of Rincon de la Vieja volcano (Costa Rica): A combined (inorganic and organic) geothermal approach to understanding the origin of the fluid discharges and its possible application to volcanic surveillance. J Volcanol Geotherm Res 148:315-333

Tassi F, Martinez C, Vaselli O, Capccioni B, Viramonte J (2005b) Light hydrocarbons as redox and temperature indicators in the geothermal field of El Tatio (northern Chile). Appl Geochem 20:2049-2062

Tassi F, Vaselli O, Capaccioni B, Montegrossi G, Barahona F, Caprai A (2007) Scrubbing process and chemical equilibria controlling the composition of light hydrocarbons in natural gas discharges: An example form the geothermal fields of El Salvador. Geochm Geophys Geosys 8, doi:10.1029/2006GC001487

Tassi F, Capaccioni B, Capecchiacci F, Vaselli O (2009) Non-methane volatile organic compounds (VOCs) at El Chichón volcano (Chipas, México): Geochemical features, origin and behavior. Geofísica Internacional 48:85-95

Tassi F, Montegrossi G, Capecchiacci F, Vaselli O (2010a) Origin and distribution of thiophenes and furans in gas discharges from active volcanoes and geothermal systems. Int J Molec Sci 11:1434-1457

Tassi F, Capecchiacci F, Buccianti A, Vaselli O (2010b) Sampling and analytical procedures for the determination of VOCs released into air from natural and anthropogenic sources: A comparison between SPME (Solid Phase Micro Extraction) and ST (Solid Trap) methods. Appl Geochem 27:115-123

Tassi F, Aguilera F, Darrah T, Vaselli O, Capaccioni B, Poreda RJ, Delgado Huertas A (2010c) Fluid geochemistry of hydrothermal systems in the Arica-Parinacota, Tarapacá and Antofagasta regions (northern Chile). J Volcanol Geotherm Res 192:1-15

Tassi F, Fiebig J, Vaselli O, Nocentini M (2012a) Origins of methane discharging from volcanic-hydrothermal, geothermal and cold emissions in Italy. Chem Geol 310-311:36-48

Tassi F, Bonini M, Montegrossi G, Capecchiacci F, Capaccioni B, Vaselli O (2012b) Origin of light hydrocarbons in gases from mud volcanoes and CH_4-rich emissions. Chem Geol 294-295:113-126

Tassi F, Capecchiacci F, Cabassi J, Calbrese S, Vaselli O, Rouwet D, Pecoraino G, Chiodini G (2012c) Geogenic and atmospheric sources for volatile organic compounds in fumarolic emissions from Mt Etna and Vulcano Islans (Sicily, Italy). J Geophys Res 117, doi:10.1029/2012JD017642

Thompson JM, Hutchinson RA (1981) Chemical analyses of waters from Boundary Creek thermal area, Yellowstone National Park, Wyoming. United States Geological Survey Open-File Report 81-1310

Tissot BP, Welte DH (1984) Petroleum Formation and Occurrence. Springer, Berlin

Tsonopoulos C, Wilson GM (1983) High-temperature mutual solubilities of hydrocarbons and water. Part I: Benzene, cyclohexane and n-hexane. AIChE J. 29:990–999

Varsányi I, Kovács LO, Kárpáti Z, Matray J-M (2002) Carbon forms in formation water from the Pannonian Basin, Hungary. Chem Geol 189:165-182

Ventura GT, Simoneit BR, Nelson RK, Reddy CM (2012) The composition, origin and fate of complex mixtures in the maltene fractions of hydrothermal petroleum assessed by comprehensive two-dimensional gas chromatography. Org Geochem 45:48-65

Werner C, Brantley S (2003) CO_2 emissions from the Yellowstone volcanic system. Geochem Geophys Geosyst 4, doi:10.1029/2002GC000473

Werner C, Hurwitz S, Evans WC, Lowenstern JB, Bergfield D, Heasler H, Jaworowski C, Hunt A (2008) Volatile emissions and gas geochemistry of Hot Spring Basin, Yellowstone National Park, USA. J Volcanol Geotherm Res 178:751-762

White DE, Muffler ALP, Truesell AH (1971) Vapor-dominated hydrothermal systems compared with hot-water systems. Econ Geol 66:75-97

Wilhelm E, Battino R, Wilcock RJ (1977) Low-pressure solubility of gases in liquid water. Chem Rev 77:219-262

Williford KH, Grice K, Logan GA, Chen J, Huston D (2011) The molecular and isotopic effects of hydrothermal alteration of organic matter in the Paleoproterozoic McArthur River Pb/Zn/Ag ore deposit. Earth Planet Sci Lett 301:382-392

Windman T, Zolotova N, Schwandner, Shock, E (2007) Formate as an energy source for microbial metabolism in chemosynthetic zones of hydrothermal ecosystems. Astrobiology 7:873-890

Yang TF (2008) Recent progress in the application of gas geochemistry: examples from Taiwan and the 9th International Gas Geochemistry Conference. Geofluids 8:219-229

Yang Z, Gould IR, Williams L, Hartnett H, Shock EL (2012) The central role of ketones in reversible and irreversible hydrothermal organic functional group transformations. Geochim Cosmochim Acta 98:48-65